WHAN-FR-50

UC-80, Reactor Technology
UC-25, Metals, Ceramics and Materials

WADCO QUARTERLY TECHNICAL REPORT

JULY-AUGUST-SEPTEMBER, 1970

HANFORD ENGINEERING DEVELOPMENT LABORATORY

UNITED STATES ATOMIC ENERGY COMMISSION

Operated by

WADCO CORPORATION

CONTRACT AT(45-1)-2170

HANFORD ENGINEERING DEVELOPMENT LABORATORY

Richland, Washington
operated by

WADCO CORPORATION

A Subsidiary of Westinghouse Electric Corporation
for the
United States Atomic Energy Commission Under Contract No. AT(45-1)-2170

AEC-RL RICHLAND, WASH

WHAN-FR-50

UC-80, Reactor Technology
UC-25, Metals, Ceramics and Materials

WADCO QUARTERLY TECHNICAL REPORT

JULY-AUGUST-SEPTEMBER, 1970

Issued January 1971

B. Wolfe, Vice President and Technical Director
F. J. Leitz, Consultant to the Technical Director

WADCO TECHNICAL ORGANIZATION

Chemistry and Chem Eng.	J. N. Judy
Engineering	W. M. Gajewski, Manager
Engineering Development Laboratory	H. T. Knight, Manager
Fuels and Materials	E. A. Evans, Manager
Quality Assurance	J. M. Morris, Manager

HANFORD ENGINEERING DEVELOPMENT LABORATORY

UNITED STATES ATOMIC ENERGY COMMISSION

Operated by

WADCO CORPORATION

CONTRACT AT(45-1)-2170

FOREWORD

This is the first issue of the WADCO Quarterly Technical Report. Work reported herein was performed by WADCO Corporation and its subcontractors, under Contract No. AT (45-1)-2170 with the U.S. Atomic Energy Commission, Division of Reactor Development and Technology. The work described is primarily a continuation of programs previously conducted under Contract AT (45-1) 1830 by Battelle-Northwest, and last reported in BNWL-1200-4 (Quarterly Technical Report, Sodium Technology), BNWL-1349-2 (Quarterly Progress Report, Reactor Fuels and Materials, and BNWL-1394 (FFTF Periodic Technical Report).

This WADCO Quarterly Technical Report is subdivided into the "LMFBR Program Plan Elements" defined by the AEC. The tabulation below shows the relationships of the report Chapters to the LMFBR Program Plan Elements.

Chapter I.	Progress Highlights
Chapter II.	Plant Design (LMFBR Element No. 2)
Chapter III.	Components (LMFBR Element No. 3)
Chapter IV.	Instrumentation and Controls (LMFBR Element No. 4)
Chapter V.	Sodium Technology (LMFBR Element No. 5)
Chapter VI	Core Design, Physics and Safety (LMFBR Elements No. 6, 9 and 10)
Chapter VII.	Fuels and Materials Evaluation (LMFBR Element No. 7)
Chapter VIII.	Fuels Processing and Fabrication (LMFBR Element No. 8)

Printed in the United States of America
Available from
National Technical Information Service
National Bureau of Standards,
U.S. Department of Commerce
Springfield, Virginia 22151
Price: Printed Copy $10.00; Microfiche $0.65

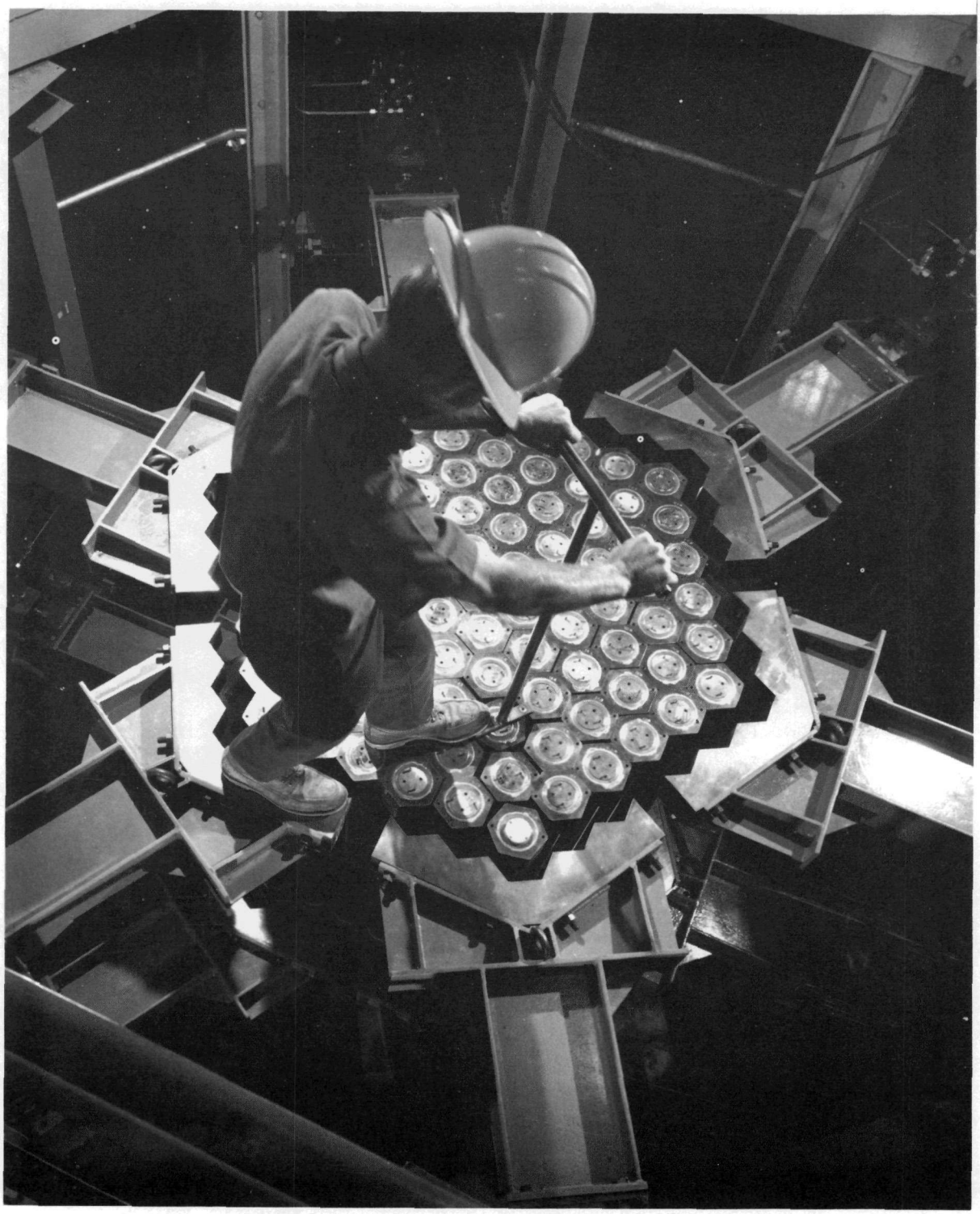

Simulated Core Mockup (SCM)

ACKNOWLEDGEMENTS

Acknowledgement is made of the contributions of the following technical managers in planning and directing the work described in this report.

G. J. Alkire	Analytical Chemistry
H. J. Anderson	Chemistry & Chemical Eng
C. A. Burgess	Component Development
T. T. Claudson	Reactor Metals
T. O. Harves	Mfg. Process & Fuel Handling
R. E. Heineman	Physics & Systems Analysis
P. L. Hoffman	Physics & Systems Analysis
K. M. Horst	Engineering
D. J. Hulbert	Systems Engineering
G. A. Last	Components Evaluation
W. B. McDonald	Plant Design
R. E. Peterson	Safety Technology
W. E. Roake	Core Components
G. J. Rogers	Mechanical Development
W. F. Sheely	Materials Technology
E. Simpson	Safety Technology
C. D. Swanson	Measurement and Controls
J. E. Werle	Reactor Engineering
T. W. Withers	Components Engineering
W. R. Wykoff	Sodium Technology

This report was compiled by WADCO Technical Publications.

CONTENTS

ILLUSTRATIONS

ILLUSTRATIONS
(CONT'D)

ILLUSTRATIONS
(CONT'D)

ILLUSTRATIONS
(CONT'D)

ILLUSTRATIONS
(CONT'D)

ILLUSTRATIONS
(CONT'D)

ILLUSTRATIONS
(CONT'D)

ILLUSTRATIONS
(CONT'D)

ILLUSTRATIONS
(CONT'D)

ILLUSTRATIONS
(CONT'D)

ILLUSTRATIONS
(CONT'D)

ILLUSTRATIONS
(CONT'D)

ILLUSTRATIONS
(CONT'D)

TABLES

TABLES (CONT'D)

TABLES (CONT'D)

TABLES (CONT'D)

I. PROGRESS HIGHLIGHTS

FFTF PLANT DESIGN AND CONSTRUCTION

The AEC has approved the preliminary design of the FFTF, and has issued a directive authorizing FFTF site preparation and the procurement of certain critical equipment. Site preparation contracts have been let and site work has begun. Fabrication of the reactor vessel head has started, and vendors have been selected for the Intermediate Heat Exchanger and the Containment Vessel.

COMPONENTS DEVELOPMENT

The ball screw mechanism proposed for under-sodium service in the FFTF In-Vessel Fuel Handling Machine has been successfully tested at LMEC. Tests are in progress at LMEC and at Todd Shipyards on the N. S. Savannah Replacement Control Rod Drive, and at WADCO on removal and replacement of fuel subassemblies under simulated conditions of irradiation-induced subassembly warpage in the core. Atomics International is investigating the possibility of using explosively-formed fuel ducts for the FFTF.

FUELS PROCESSING AND FABRICATION

Fuel Specifications.-Specifications for FFTF driver fuel are being prepared in the form of RDT standards. Standards have been prepared for: ceramic grade plutonium dioxide; ceramic grade uranium dioxide; uranyl nitrate solution; plutonium nitrate solution; driver fuel pin; mixed oxide fuel pellet; insulator pellet; seamless cladding tube; and end caps, reflector, plenum spacer, plenum spring, and wire wrap for the driver fuel pin.

Prequalification of LMFBR Fuel Suppliers.-Three fuel suppliers are participating in a prequalification program. Evaluation of their products is complete. All three contractors demonstrated the ability to produce PuO_2-UO_2 fuel pins in accordance with specifications.

HIGH TEMPERATURE SODIUM FACILITY

Ground was broken on 26 September 1970 for the High Temperature Sodium Facility (HTSF). A sketch of the HTSF is shown in Chapter VI.

The HTSF will be used to support the FFTF and LMFBR programs, through testing of large hardware, components, systems, and structural materials in high temperature sodium and sodium vapor environments.

PHYSICS

The feasibility of using the Fast Neutron Cavity (FNC) in the Physical Constants Test Reactor (PCTR) for cross-section evaluation has been established by analytical study.

2DB and 3DB runs simulating the fast test reactor showed that two-dimensional mathematical models are adequate for k_{eff} calculations. However, a three-dimensional model is required for accurate design calculations of burnup and reactivity worths, and for analysis of unusual configurations.

SODIUM TECHNOLOGY

A technical comparison of gas-cooled and NaK-cooled forced convection cold traps for the Closed Loop Primary was made; use of NaK-cooled traps was recommended.

A document "Standard FFTF Values for the Physical and Thermophysical Properties of Sodium" has been issued.

CORE DESIGN

Core Mechanics. - A full size mechanical model of the FFTF core has been placed in operation; a photograph is shown as the frontispiece of this report. The core model consists of 91 core lattice positions on a pitch of 4.715 in. Mechanisms are arranged around the core to apply controlled force for core restraint ("clamping") studies. The primary objective of this core restraint system design development effort is to provide a mechanism that, in conjunction with the in-core ducts, will control the core radial motion.

FUELS AND MATERIALS EVALUATION

A theoretical analysis of in-reactor fuel plasticity showed that fast flux increases the plasticity to the greatest extent at low temperatures, but makes little change at temperatures above 2600° K (about 2300° C).

Variation in the stoichiometry of $(U_{0.75}Pu_{0.25})O_{2-x}$ is being measured as a function of the temperature and the oxygen partial pressure. Data obtained at 1100°C in the range of oxygen potentials between -110 and -140 kcal/mole are in reasonable agreement with the data of Markin and McIver.

Fuel-clad gap conductance has been measured for several mixed-oxide SS-clad fuel pins. Test variables included gap widths of 0.0025 in. and 0.011 in. Gap conductances for the small gap pins are significantly higher than previously reported.

The BNW-7-1 capsule containing enriched and depleted B_4C and tantalum specimens has been disassembled after a one-cycle irradiation in a spectrum-hardened ETR flux. Tantalum density changes appear to be independent of irradiation temperature in the 900 to 1500°F range. Swelling rate in the enriched B_4C pellets apparently decreases with increasing density.

Boron carbide materials irradiations in the K reactor have been analyzed to determine the helium gas release ratio and average B^{10} burnup as a function of neutron irradiation fluence. The analysis bore out the experimental observation that lower density absorbers incur greater average burnup and, thus, helium production and gas release ratio are dependent on absorber density.

To develop an accelerated testing method, solution-annealed and 20% cold-worked 316 SS specimens have been bombarded with 5 MeV Ni^{++} ions. Voids and faulted loops were produced as in neutron-irradiated stainless steel. The feasibility of alternating helium injection and heavy ion bombardment, essential to simulation of a fast reactor environment, has been demonstrated on a theoretical basis.

In an effort to enhance resistance to irradiation damage, variations in the microstructure of austenitic stainless steels have been produced by five different thermomechanical treatments. The relative merit of these structures is being evaluated by accelerated ion bombardment and by EBR-II irradiation experiments.

Density measurements and microstructural analyses of volume changes in AISI 316 and 304 SS indicate that, for irradiation temperatures between 700°F and 1400°F and fluences between 2 and 3 x 10^{22} n/cm^2 (E > 0.1 MeV), cold-work limits swelling in 316 SS to negligible amounts. The cold-worked microstructure is stable to 1300°F and is presumably responsible for the absence of voids.

Type 12R72HV SS tubing has been biaxially stress-rupture tested at 1000, 1200, and 1400°F to rupture times of up to ∿ 5000 hr. Results indicate 12R72HV, in the condition tested (cold-worked) possesses about 15% greater rupture stress at 1000°F, and 50% greater rupture stress at 1200 and 1400°F, than does 20% cold-worked 316 SS. Observed ductility ($\Delta D/D$) for 12R72 is lower than the cold-worked 316 SS at all test temperatures.

Burst and stress-rupture tests at 1000 and 1200°F have been performed on PNL-2 series fuel pin specimens (304 SS, mixed-oxide pins, irradiated to 2.5 x 10^{22} n/cm^2 (E > 0.1 MeV). The results indicate no effect of fuel-cladding interaction on the biaxial properties for these irradiation and test conditions.

The effect of strain rate on the mechanical properties of FTR materials is being determined. The initial phase of the program has been completed on unirradiated 304 SS. The following observations have been made from test results:

- Ultimate strength and yield strength appear to slightly increase with strain rate.
- Total elongation remains constant or slightly increases with strain rate at temperatures to 1200°F; total elongation at 1400°F slightly decreases with strain rate.

- Uniform elongation remains almost constant with strain rate to a temperature of 1200°F. At 1400°F, uniform elongation increases with strain rate.

LMFBR dosimetry methods have been applied in an experiment to simulate a pressure vessel in a thermal reactor environment. Measured fluxes in the vessel wall were found to be 1/2 to 1/3 of the fluxes calculated with the one-dimensional transport code DTF-IV.

II. FFTF PLANT DESIGN AND CONSTRUCTION

Present design values of FFTF engineering parameters* are given in Table II-1. Values have been compiled from a draft of the "FFTF Engineering Parameters" document.

Note: Figure II-1 depicts the core map as of August 1970. Figures II-2 and II-3 are reproductions of illustrations used in a 15 July, 1970 design review with AEC/DRDT.

TABLE II-1

PRESENT DESIGN VALUES OF FFTF ENGINEERING PARAMETERS (25 SEPTEMBER, 1970)

	System Parameter	Design Value
1.	ELECTRICAL SYSTEM	
	115 kV Supply Feeder, Number	1
	13.8 kV Supply Feeder, Number	1
	13.8 kV Transformer, Number	1
	13.8 kV Transformer Voltage (kV)	115/13.8
	13.8 kV Transformer Rating (MVA)	22.5/30
	480 Volt Emergency Generators (Diesel), Number	2
	Power, Emergency Generators (kW each)	1200
2.	CONTAINMENT	
	Containment Bldg.	
	Diameter (ft)	135
	Overall Height (ft)	194
	Depth Below Grade (ft)	70

*Compiled by C. W. Higby and J. H. Westsik

TABLE II-1 (Cont'd)

Design Pressure (psig)	
Internal	10
External	0.2
Design High Temp (°F)	250
Design Low Temp (°F)	(-) 10
3. REACTOR CORE	
Power, Excluding Closed Loops (MWt)	400
Peak Flux at 400 MWt (n/cm^2-sec)	7×10^{15}
Doppler Coefficient (T dk/dt)	-0.005
Core Lattice Positions, Number	91
Core Lattice Spacing (in.)	4.715
Drivers, Number	75
Driver Fuel Duct:	
In-Core Section Across Flats O.M. (in.)	4.535
Material	Type 316 SS 20% CW
Wall Thickness (in.)	0.120
In-Core Primary (Safety) Rods, Number	3
In-Core Secondary (Control) Rods, Number	4
Peripheral Control Rods, Number	8
Peripheral Fixed Shim Rods, Number	7
Maximum Velocity, Core Coolant (fps)	30
4. IRRADIATION TEST FACILITIES	
Power, Initial General Purpose Closed Loops, Each of 2 (MWt)	2
Temperature Closed Loop Coolant - Maximum (°F)	1200
Closed Test Loops	
Available Test Diameter (in.)	2.5
Open Test Loops Capability (Number)	3-9

TABLE II-1 (Cont'd)

5. CLOSED LOOP EX-VESSEL MACHINE	
CLEM Machine:	
Bore Diameter (in.)	7.981
Bore Length (ft)	40
Overall Length (ft)	57.5
Weight (tons)	234
CLEM Heat Removal Capability (kw)	10
6. REACTOR VESSEL	
Material	Type 304 SS
Overall Height (ft/in.)	43-2
Inlet Nozzles:	
Number	3
Size (in.)	16
Outlet Nozzles:	
Number	3
Size (in.)	28
7. REACTOR VESSEL HEAD	
Diameter, OD (ft)	25
Thickness (in.)	46
8. HEAT TRANSPORT SYSTEM	
Total System	
Number Cooling Circuits	3
Heat Load Per Cooling Circuit (MWt)	133
Primary System	
Material	Type 304 SS
Hot Leg Piping to Isolation Valve:	
Size, OD (in.)	28
Temp at 15 psig (°F)	1050

TABLE II-1 (Cont'd)

Hot Leg Valves:	
Isolation, Number	3
Size (in.)	28
Cold Leg Piping IHX to Vessel	
Inlet:	
Size, OD (in.)	16
Temp at 225 psig (°F)	830
Cold Leg Valves:	
Isolation, Number	3
Check, Number	3
Size (in.)	16
Primary Pumps, Number:	3
Flow, Each at 500 ft Na (gal/min)	14,500
Temperature (°F)	1050
IHX (Intermediate Heat Exch.), Number	3
IHX Heat Load, Each (MWt)	133
IHX Temp Shell Side (Primary Side) at 225 psig (°F)	1050
IHX Temp Tube Side at 250 psig (°F)	1050
Secondary System	
Main Piping, Size OD (in.)	16
Branch Piping, Size, OD (in.)	12
Pipe Headers, Size, OD (in.)	8
Piping IHX to DHX - Temp at 250 psig (°F)	1000
Piping DHX to IHX - Temp at 250 psig (°F)	830
Valves - Hot and Cold Leg Temp at 250 psig (°F)	1000
Secondary Pumps, Number	3
Flow Each at 260 ft Na Head (gal/min)	14,500
Temp at 250 psig (°F)	830
DHX Units, Number	3
DHX Modules Per Unit, Number	4
DHX Thermal Rating Per Module (MWt)	33
DHX Tube Side, Temp at 250 psig (°F)	1000

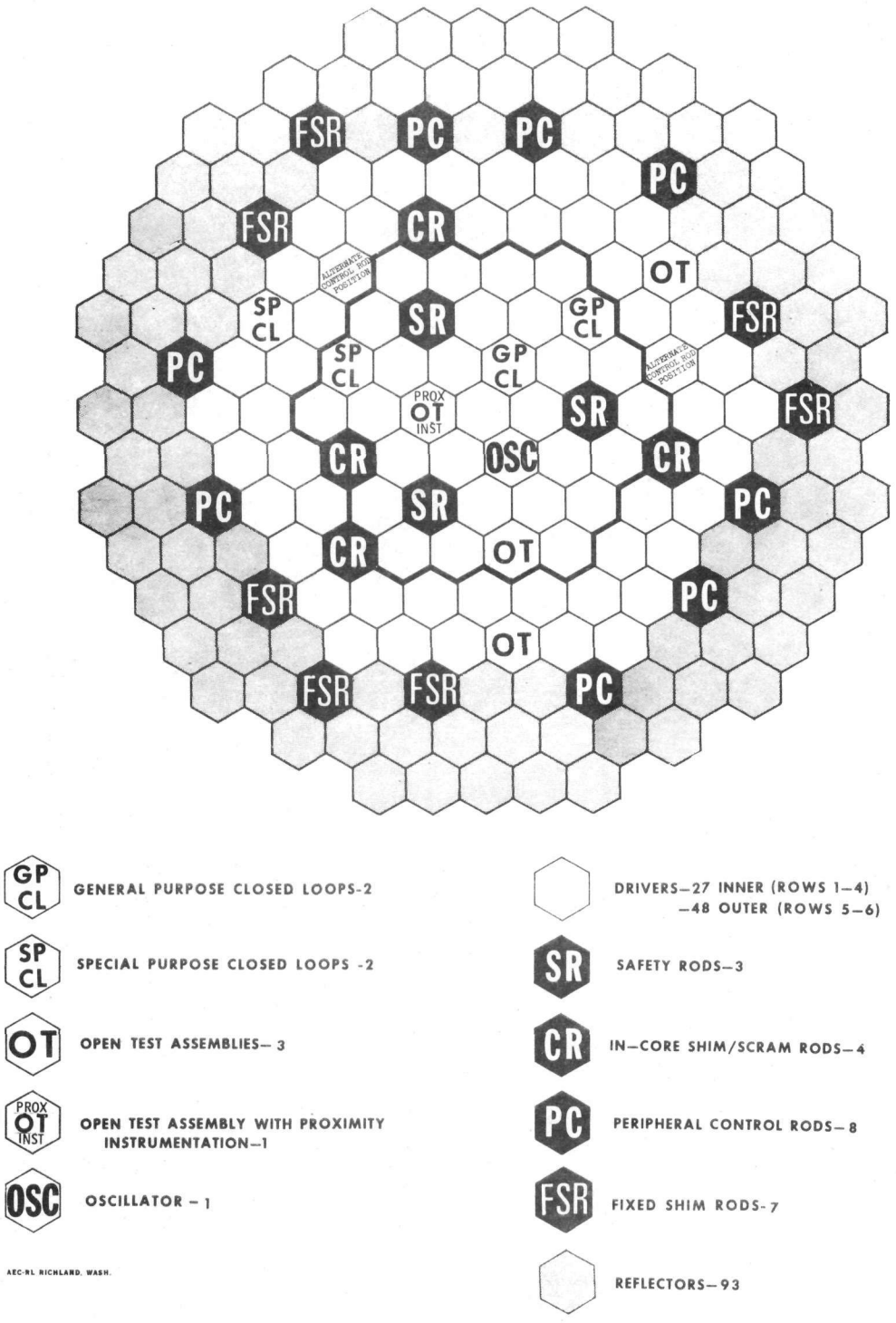

FIGURE II-1 *Core Map, August 1970*

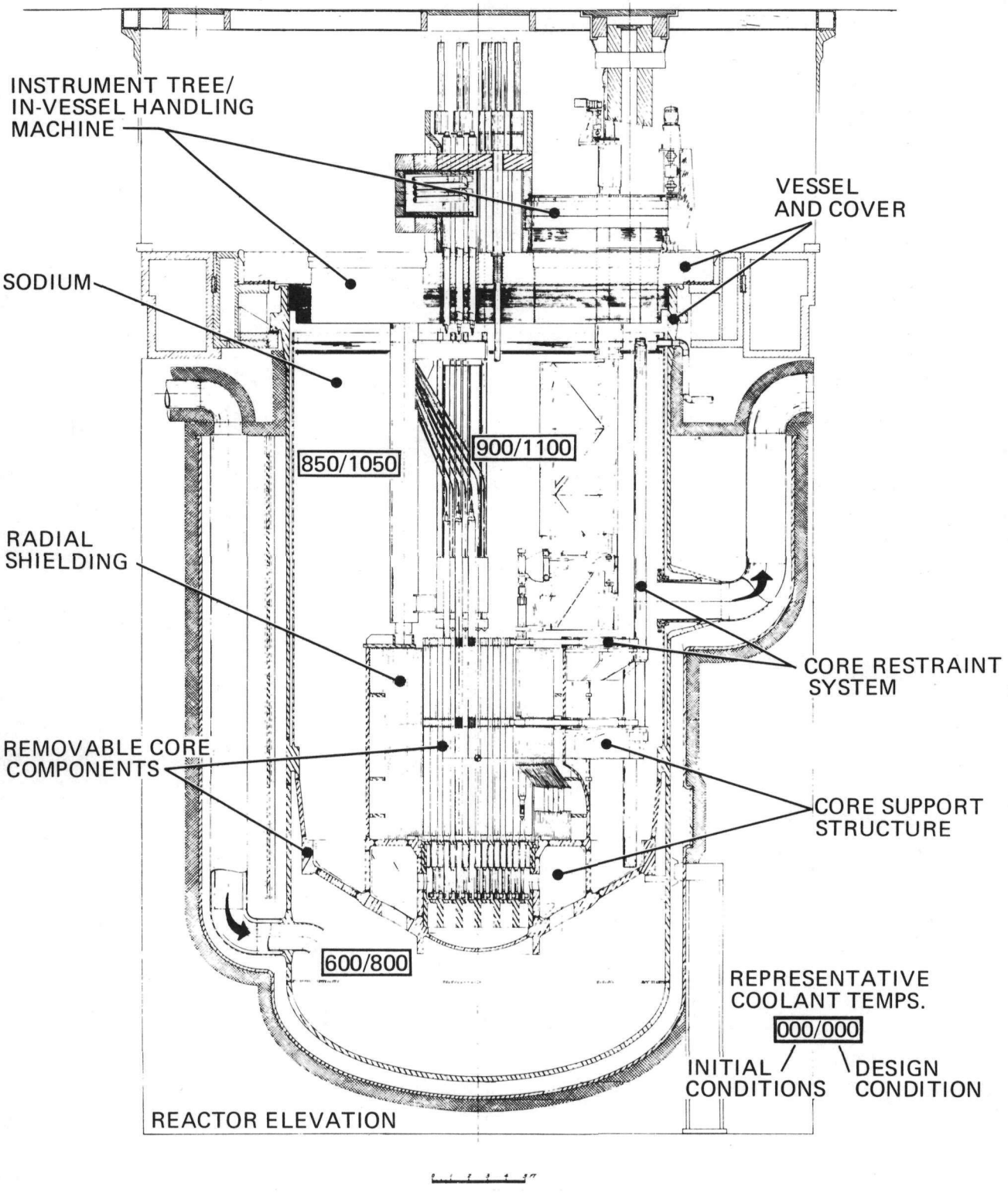

FIGURE II-2 *Review Drawing-Reactor Elevation*

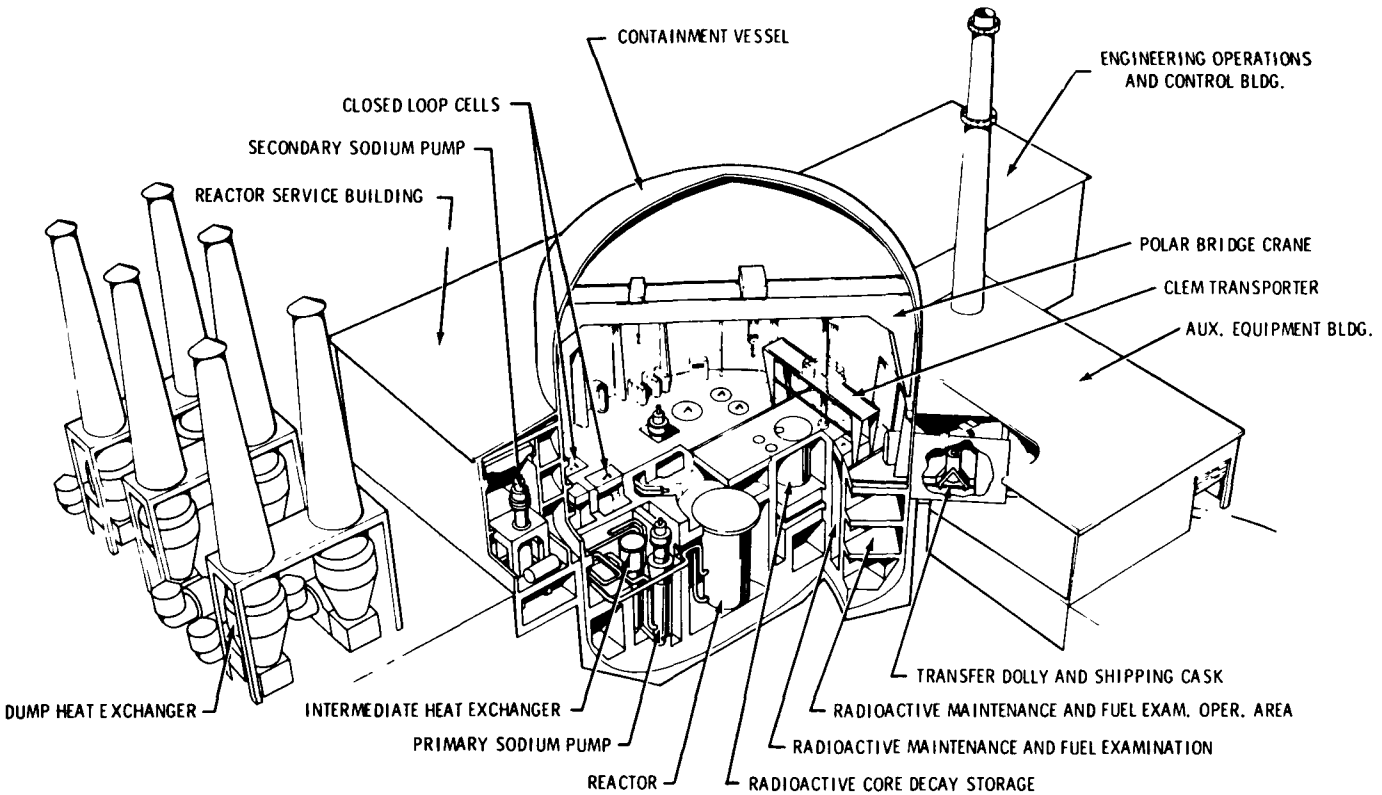

FIGURE II-3 *Review Drawing-FFTF General Building Arrangement*

III. COMPONENTS DESIGN AND DEVELOPMENT

A. REACTOR COMPONENTS

1. Core Support Structure Design

J. F. Wett and D. J. Oakley

At the beginning of the reporting period, major emphasis was placed on a breech-lock mechanical joint between the core support structure and the reactor vessel.

Further analysis of the breech-lock design for attaching the Core Support Structure indicated that the design had major problems associated with excessive bending stresses developed at the upper flange connection.

As a result of these problems, and of the added complexity of this design, a welded skirt design has been selected as the reference concept.

Thermal transient analysis of a severe emergency condition (secondary pump seizure with no scram) indicates that little or no permanent deflection will occur in the structure.

2. Examination of Irradiated EBR-II Components

R. N. Johnson and J. C. Tobin

A safety rod thimble and a control rod thimble with accumulated exposures of greater than 1×10^{23} nvt were recently discharged from the EBR-II. These specimens provide the first opportunity to study core structural ducts exposed to such high fluences; such examinations are of considerable importance in developing design information applicable to the FFTF.

Two WADCO representatives examined the components at the Idaho Falls facility, reviewed the status of the inspections, and participated in planning the remaining destructive and nondestructive examinations.

Some of the more significant preliminary observations and conclusions made on this visit follow.

1) The ducts are laterally supported within the core by raised dimples or buttons in the duct wall which act as spacers and load pads. These pads are located slightly above the midplane of the core; the fact that the components performed satisfactorily could be of some significance to the FTR design. However, the worst damage observable during preliminary inspection of the irradiated components was severe galling on duct walls caused by the stainless steel-to-stainless steel contact of the pads against each other and against the duct walls.

2) Variations in cold work between corners and flats and between the buttons and flats caused no apparent problems with differential swelling.

3) The ducts are seam-welded longitudinally. The weld material has performed satisfactorily for 7 years during exposure to high fluences.

4) Several areas on the components were chrome-plated for wear resistance; these surfaces performed adequately under the EBR-II conditions.

3. Duct Fabrication Development

J. C. Tverberg and R. C. Aungst

The work at Atomics International (AI) was redirected to allow immediate evaluation of explosively formed duct sections. Contract Phase 1 will result in 30 five foot long sections with complete characterization of residual stress, mechanical properties, and microstructure. Three different wall thicknesses will be investigated. Phase 1 will yield up to five complete duct sections to prove the tooling. Phase 2 will produce 25 complete duct assemblies. Atomics International has placed a subcontract with another firm to form the round blanks with the 20 percent cold work. AI intends to make the upper, lower, and wear pad section of the duct in a single piece. The present schedule calls for completion of phase 1 effort by 20 February 1971.

Contract negotiations for a contract similar to that with Atomics International are being conducted with another vendor. The vendor will form the duct by welding and drawing; consequently, the sections will be full length duct sections so that material will be available for flow testing, vibration testing, and general characterization.

B. HEAT TRANSPORT, COOLANT AND GAS COMPONENTS

1. FFTF Simulation and Control Analysis

R. A. Harvey

A detailed digital simulation of the FFTF reactor and heat transport system for pipe rupture studies has been a continuing project. The simulation, HYSIM-2D, is programmed in assembly language on the PDP-9 digital computer, which is part of the WADCO hybrid computer.

The model presently consists of a detailed simulation of the reactor and the primary coolant system for two independent coolant loops (one of these loops simulates identical action for two separate loops). The secondary system is being added and is about 60% complete.

The primary system was completely updated with new system coefficients during the quarter, and all variable properties have been changed from function tables to equations.

A digital program called LINEAR was written; this program simplifies the approximation of complex equations or tabular functions by a minimum number of straight-line segments, and was used in generating the equations used for variable properties in the simulation.

2. Carbon Transport in FFTF

R. R. Borisch, W. F. Brehm and D. W. Shannon

In the last quarter (Ref 1) we presented an analysis of carbon transport in an all-austenitic sodium reactor system; the core should decarburize and the external piping should carburize. Several designs for providing bypass cooling flow and protection from thermal shock at the reactor vessel wall outlet nozzle, and adjacent hot leg piping allow the possibility of the outlet nozzle and adjacent piping being in a rising temperature zone, where they would be subject to corrosion and decar-

---

1. W. R. Wykoff, Ed., Sodium Technology Quarterly Report, April-May-June 1970. BNWL-1200-4.

burization. An addendum to our original report to FFTF Manufacturing Process Engineering was completed this quarter. The analysis of carbon diffusion rates showed that a 1/2-in. thick pipe wall section could decarburize a 0.13-in. zone to less than 2/3 of its original carbon content after 20 years at 1050°F, but only if the pipe were in a decarburization region of the piping. For those parts of the nozzle and piping subject to decarburization, we recommend that section thicknesses be increased and that the allowable minimum carbon content in the stainless steel be changed from 0.04% to 0.06%. This would involve, at most, the outlet nozzle and several feet of hot leg piping. However, the most probable design of the thermal liner at the outlet nozzle is shown in Figure III-1. The rolled insert in the nozzle will allow essentially no flow of sodium along the nozzle itself. The insert and the thermal liner may decarburize, which is of no consequence. The nozzle itself will have a far smaller probability of decarburization. Changing the allowable minimum carbon content in the nozzle from 0.04% to 0.06% was a conservative measure. Since the liner does not extend into the pipe, no decarburization is expected there, and no corrective measures were recommended.

3. Review of Small Valves

R. R. Borisch and D. W. Shannon

During the past quarter, two commercial sodium valves were bisected to determine the degree of physical compliance with RDT E1-19T (Sodium Valves for the Fast Reactor Thermal Engineering Facility). Both valves were bellows seal, butt welded, stainless steel, glove valves. One was 3/8 inch and the other was 1/2 inch; they were from two separate manufacturers. Manufacture of the two valves was very similar; therefore, the areas of noncompliance with this standard are almost identical. These valves were found to deviate from RDT E1-19T as shown in Table III-1.

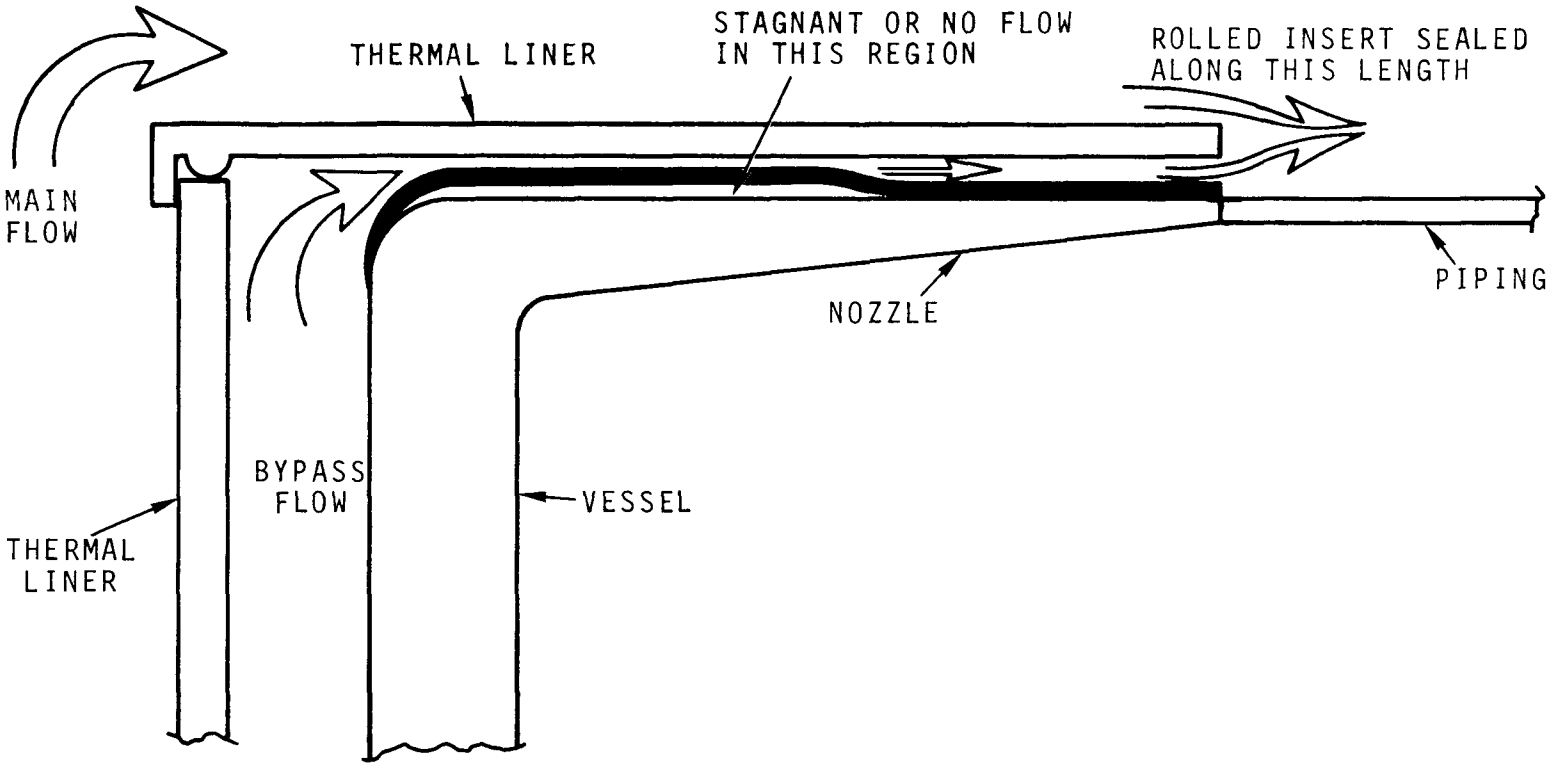

FIGURE III-1 *Schematic of Flow Patterns along Vessel and Outlet Nozzle in One Proposed Design.*

TABLE III-1
DEVIATION OF VALVES FROM STANDARDS

RDT Document Paragraph	Deviation
3.4.1.1	Cold trapping - both valves would require trace heating to prevent cold trapping in the bellows.
3.4.1.2	Crevices - weld adjoining the valve body and bonnet are such that crevices nearly 2/3 of the total wall thickness are formed.
3.4.1.9	Seat and bushing-the valve seat is crimped into a larger block of stainless steel. In one valve, this block is screwed onto the stem and in the other valve, it is held in place with a stainless steel pin. This paragraph and paragraph 3.4.1.21 say that the entire assembly should be welded.

Besides these deviations, it is questionable whether or not the valves meet paragraph 4.3.2.2 on surface roughness of the bellows and paragraph A.3.4.1 g and h on free draining and cleaning.

Although both of these valves are very popular, and have seen many years of use in sodium service, neither could be altered to fully comply with RDT 1-19T without major redesign.

4. Materials List For FFTF Heat Transport Systems

R. R. Borisch and D. W. Shannon

In a liquid metal cooled system such as FFTF, no two materials can be electrically insulated from each other. Also, several materials are known to have short service lives in contact with liquid sodium. Therefore, a vital aspect of materials compatibility studies is a precise knowledge of the materials contained in the system. Table III-2 is a materials list compiled from the most recent drawings for FFTF and consultations with the systems engineers concerned with the heat transport system. This list will be updated semi-annually until the reactor is fabricated.

TABLE III-2
MATERIALS LIST FOR FFTF HEAT TRANSPORT SYSTEMS

Material	Location	Status
304 SS	Basic material	Firm
308 SS	Basic weld material	Firm
316 SS	Fuel cladding and areas of high temperature, accompanied by high stress in reactor	Firm
316 SS	Pump impeller and casing	Conceptual
Stellite 6	Rubbing areas on large valves	Preliminary design
Stellite 12	Rubbing areas on large valves	Preliminary design
Stellite or ?	Cladding for possible self-welding areas in IHX	Conceptual
"Colmonoy" or Stellite	Primary pump bearings	Conceptual
Inconel 718	Wear pads on in-core tubes	Firm
Inconel 718	Driver ducts	Conceptual
Inconel 718 or ?	Bellville washers, upper closure of in-core tube, exposed to dead leg of coolant sodium	Conceptual
Inconel 600 or Nickel	Core reflectors - wholly or partially clad with 304 or 316 SS	Conceptual
Nickel	Hydrogen detector membrane	Conceptual
Armco Iron	Carbon meter membrane	Conceptual
Tantalum	In-core tube melt-down cup exposed to same static cup of liquid Na that tungsten is exposed to Refer to drawing SK-20453	Conceptual
Tungsten	Grid plate for in-core tube melt-down cup. Exposed to small, static container of purified liquid Na	Conceptual
Boron Carbide or possibly tantalum	Poison rods - probably clad with 316 SS	Conceptual
ThO_2-7 w/o Y_2O_3	Oxygen - meter solid electrolyte	Conceptual

5. Dump Heat Exchanger Analysis and Optimization

R. N. Madsen and J. P. Hale

The FFTF heat transport system cost optimization computer code ADOPT (Ref 1) has been significantly modified and expanded. This expanded version, known as ADOPT2, has been utilized to make extensive studies of dump heat exchanger configurations to determine the effect of variations in a large number of design parameters. The parameters studied included: fin thickness, fin spacing, pipe or tube size, fin height, tube length, number of modules, number of passes, and air discharge temperature. A topical report is in process of being issued (Ref 2) which explains in detail the cases studied and the conclusions which were able to be made. A complete documentation of the ADOPT2 code is also being prepared (Ref 3). This code will continue to be a useful analytical tool as the design of the DHX progresses and as additional studies and analyses are made with it.

6. Secondary Coolant Fluid For Atmospheric Cooling

H. C. Martin, C. L. Fies, J. P. Hale and W. R. Wykoff

The FFTF air and nitrogen atmospheres will be cooled by a secondary working fluid. Several major FFTF safety design criteria serve to limit the acceptable coolants to: 1) ammonia: 2) paraffins: and 3) straight sili-

---

1) Goss, C. L. and Johnson, H. G. ADOPT, Program for Steady State Process Design and Cost Optimization of FFTF Heat Removal Systems Using Heat Dumps to Air, BNWL-308. Battelle-Northwest, Richland, Washington, September 1966.

2) Johnson, H. G. and Madsen, R. N. Air Dump Heat Exchanger Optimization for the Fast Flux Test Facility, WHAN-IR-36. WADCO Corporation, Richland, Washington, in preparation.

3) Johnson, H. G. and Madsen, R. N. ADOPT2, A Revised Program for Steady-State Process Design and Cost Optimization of FFTF Heat Removal Systems Using Heat Dumps to Air, WHAN-IR-37. WADCO Corporation, Richland, Washington, in preparation.

cones. More detailed evaluations of these candidates showed ammonia to be satisfactory from a safety standpoint. An investigation of the effect of an ammonia leak concurrent with a gross sodium spill has shown that there is no significant change in peak cell temperatures and pressures.

7. Numerical Modeling of IHX Transient Response

A. E. Waltar, H. G. Johnson and W. W. Little

As part of a study to investigate more efficient numerical schemes for digital computation of reactor system response to transient conditions, initial results have been obtained for one intermediate heat exchanger model. The basic simulation selected was a four-axial node model using a mixed difference nodal hookup(Ref 4). At the present time, the resulting eight first-order differential equations are solved by means of a multistep fourth-order predictor-corrector method using a dynamic systems analyzer code. (Ref 5)

An alternate method, which converts the differential equations to matrix form and uses a Gauss-Seidel iteration process to find the solution vector, has provided adequate results with much less computation time. Although a complete comparison has not yet been accomplished, Table III-3 contains representative results. For the first transient the primary inlet temperature was held fixed for 5 seconds and was then dropped 200°F uniformly over the next 10 seconds. All other variables were fixed. The transient was terminated at 30 seconds. For the second transient, the primary flow was ramped down to 10% flow over the same time interval as above.

---

4) Gunby, A. L. "Intermediate Heat Exchanger Modeling for FFTF Simulation," BNWL-1367, Battelle-Northwest, Richland, Washington, May 1970.

5) Goss, C. L. "Engineers Manual on Fortran IV Version of Dynamic Systems Analyzer (DYNASYAR)," DUN-M-17, Douglas United Nuclear, Richland, Washington, March 1968.

TABLE III-3
COMPARISON OF FOUR-AXIAL NODE MODEL AND GAUSS-SEIDEL ITERATION DATA

Case	Transient	Numerical Method	Primary Outlet (°F)		Secondary Outlet (°F)		Computation Time
			Start	30 sec.	Start		30 sec.
I	Primary Temperature Ramp	4th-Order Predicator-Corrector	600.0	554.4	773.0	625.0	67[a]
		Gauss-Seidel	600.0	554.9	773.0	625.3	1[b]
II	Primary Flow Ramp	4th-Order Predictor-Corrector	600.0	517.0	773.0	572.4	68[a]
		Gauss-Seidel	600.0	517.1	773.0	573.7	1[b]

(a) Total time (including program loading)

(b) Execution time only

Assuming that the fourth-order predictor-corrector method is exact, the maximum error for interior temperatures using the implicit Gauss-Seidel method for Case I was less than 2°F. For Case II, the maximum error was 4°F. Time steps for the latter method, for these cases, were 0.5 seconds. By reducing the time step to 0.1 seconds, accuracy was improved, although at the expense of a corresponding linear increase in running time. The listed computation times are not completely representative, because there was no way to assess actual execution time for the multistep method. However, the method appears attractive enough to warrant further investigation for production use.

C. FUEL HANDLING

1. IVHM Ball Screw Test at LMEC

E. J. Ruane and C. L. Boyd

Candidate materials for the In-vessel Handling Machine (IVHM) drive screw are being tested under prototypic conditions at LMEC. The first screw being tested is a ball screw consisting of an Inconel 718 ball screw shaft, an Inconel 718 ball nut and Stellite 3 balls.

The test article was cycled approximately 11,000 times at loads of 240, 730, and 1710 pounds. The torque naturally varied with load, but all the torque readings were very repeatable throughout the number of cycles. The load vs. torque readings were as follows:

Load (Lb)	Torque (In.-lb)
240	126
730	170
1710	268

After approximately 11,000 dynamic cycles at 450°F, the sodium temperature was raised to 1100°F, and the test article was allowed to dwell for 15 days at a 240-lb load. At the end of the dwell test, the sodium temperature was lowered to 450°F; the test article will be cycled 1590 times at a 240-lb load. This test cycle is in progress, and the results show that the breakaway torque after the dwell period was the same as the running

torque during the previous dynamic tests. The running torque is repeatable from the previous tests.

The 11,000 cycles described above represent an approximate five-year life on the nut and a 40-year life on the screw. (The reason for the 40-year screw life is because the test article is only 18 inches long; the actual length is approximately 15 feet.)

D. OTHER COMPONENTS

1. Elevated Temperature Design Criteria

R. A. Moen and J. C. Tobin

Work in support of the ASME Subgroup on Elevated Temperature Design resulted in development of the following set of information for use in conjunction with the new design methods of revised Code Case 1331:

1) A series of curves using a log stress versus log time plot, showing two-thirds of the minimum stress to cause rupture for times to 3×10^5 hours for temperatures from 1000 to 1500°F.

2) A series of curves using a log stress versus log time plot of 80 percent of the minimum stress to produce the onset of tertiary creep for times to 3×10^5 hours and temperatures from 1000 to 1500°F.

3) Extension of the S_y, yield strength values, found in Section III to 1500°F.

4) Tables of S_u, ultimate strength values, similar to the S_y values found in Section III.

5) A set of short term allowable stress values (S_m') utilizing the tensile portion of the allowable stress criteria.

Data from HEDL's uniaxial creep rupture program on Types 304 and 316 SS, reported by Lovell and Blackburn, were used by Dr. G. V. Smith, Consultant, along with ASTM DS5-S1, to construct isochronous stress-strain curves. These curves are being made available to the ASME Subgroup and FFTF (during this reporting period) for use in the Code Case 1331 revision to define the stress required to produce 1 percent strain in structures.

2. Sodium Technology Summary

W. R. Wykoff

This section is a summary of Sodium Technology progress in support of components work. Further details are given in Chapter V.

A document "Standard FFTF Values for the Physical and Thermophysical Properties of Sodium" has been issued as WHAN-D-3.

A high pressure water spray lance, coupled with a detergent presoak, has demonstrated its effectiveness as a sodium system precleaning technique.

Measurements and calculations of the standard heats of reaction of various heat transfer fluids with sodium have been completed and an appraisal made of these reactions.

Experimental hydraulic and thermal analysis of the diffusion cold trap to be used on the FFTF Closed Loop Secondary and Intermediate Decay Storage Facility (IDSF) were conducted. Geometry, capacity, mixing length, residence time, efficiency and systems clean-up characteristics were determined. The results indicate that diffusion traps are adequate for these applications. Data are being correlated to provide a sound engineering basis for the design of diffusion traps.

Two packages of design data and information for the FFTF purification systems were prepared and forwarded to Bechtel. The first provided detailed heat transfer calculations for the forced convection traps in the FFTF primary and secondary systems. The package also included conceptual design data and drawing for these systems. The second contained the preliminary design information for the diffusion traps for the Closed Loop Secondary and Interim Decay Storage Facility.

A technical comparison of gas-cooled and NaK-cooled forced convection cold traps for the Closed Loop Primary was presented at a joint meeting of WADCO and Atomics International. A recommendation to use NaK-cooled traps was made to RDT.

Engineering evaluation of the controlled cooling profile sodium vapor trap is well underway. Initial studies demonstrated the need for a pre-heater section on the trap to permit it to handle gas streams containing sodium mists.

IV. INSTRUMENTATION AND CONTROL

A. FFTF INSTRUMENTATION AND CONTROL SYSTEMS

J. W. Mitchell, P. F. Shaw, J. B. Williams

A number of tentative design decisions have been made for the FFTF Instrumentation and Control Systems.

1. Instrumentation for Open Test Positions

The following basis for designing the in-vessel portion of the six contact and proximity instrumented open-test positions has been agreed to by WADCO and ARD.

1) Provide for Plant Protection System (PPS) and Process Monitoring Purposes:
   - Three chromel-alumel sheathed coolant thermocouples.
   - A flow straightener, a flow mixer, and a flowmeter.
   - Three separate connectors at the top of the instrument assembly to satisfy the thermocouple PPS requirements.

2) Provide for Experimental Purposes:
   - A 1/2-inch flux monitoring tube and two 3/16-inch cooling tubes.
   - A routing and sealing method for twenty conductors from the test section into the instrument top plug.

2. Closed Test Loop Control System

A control mode recommendation for the closed test loop (CTL) has been received from AI and has been reviewed by WADCO. AI recommended constant 80% flow from 0 to 80% power and increased flow as a function of power from 80 to 100%. Test inlet temperature and test Δt are to be maintained constant for 80 to 100% power. This power-flow relationship is identical to the control mode recommended by ARD for the reactor-HTS.

3. Fuel Failure Monitoring System

WADCO and ARD have approved xenon and krypton gas tagging as the reference concept for locating failed fuel in the initial FTR core.

B. INSTRUMENTATION AND CONTROL DEVELOPMENT

1. Neutron Flux Monitors

a. Measurement of Reactor Thermal Neutron Flux with Microwave Methods

D. P. Brown and W. G. Spear

The concept of microwave neutron detection depends upon the change of the resonant frequency of a microwave cavity caused by a neutron-induced plasma within the cavity. Frequency changes can also occur from plasmas induced by elevated temperatures and by gamma radiation. Thus, experiments have been focused on developing compensation techniques for eliminating the unwanted effects and on smaller millimeter wave sensors for neutron measurement in reactors. [12227]

During this quarter, a fabricated dual-cavity sensor enabled the concept to be tested at temperatures up to 1100°F. During the initial testing, cyclic frequency deviations were observed. Consideration of the measurement technique indicated that the excessive deviation could be caused by reflections in the transmission lines. Alleviation of the problem requires careful impedance matching and isolation of unwanted reflecting boundaries.

Figures IV-1 and IV-2 illustrate the effects of the reflecting boundaries and the effectiveness of attempts to eliminate secondary reflections from the pressure window as the temperature varies from 72°F to 1100°F. Figure IV-1 shows the effect on the measured frequency deviation of reflections occurring both at the cavity and at the pressure window, while Figure IV-2 illustrates the improvement achieved by isolating the window from the system, whereby the frequency fluctuation was reduced from 7.98 MHz to 3.92 MHz.

In further work, the experimental microwave thermal neutron detector, previously tested in the TRIGA reactor at Washington State University, has been readied for tests in the Hanford Co^{60} Gamma Facility to determine the extent of gamma effects on resonant frequency up to about 1×10^7 R/hr.

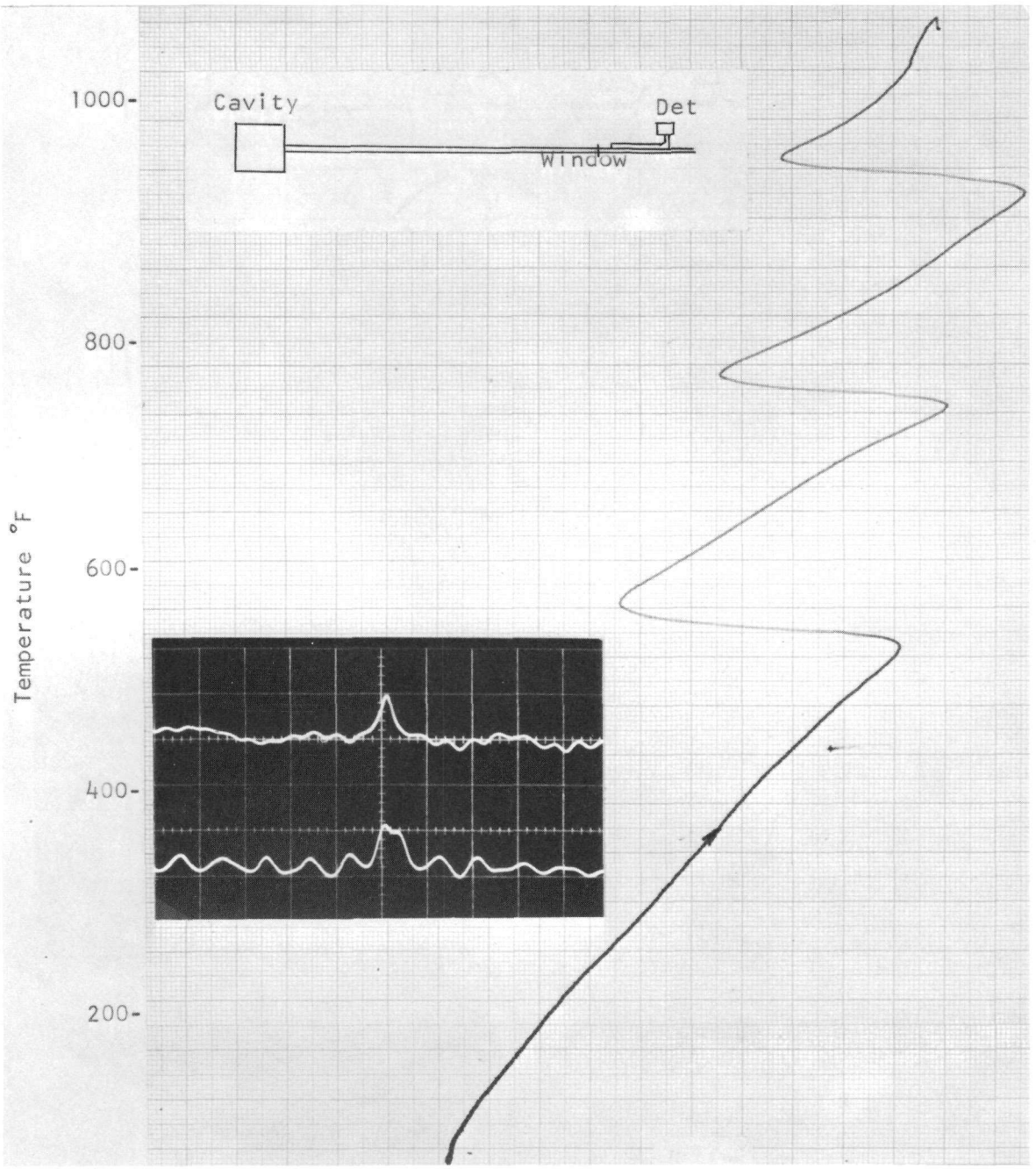

Photo 704622-1

Frequency Deviation - 7.98 MH_2

FIGURE IV-1 *Frequency Deviation as a Function of Temperature. No Isolation.*

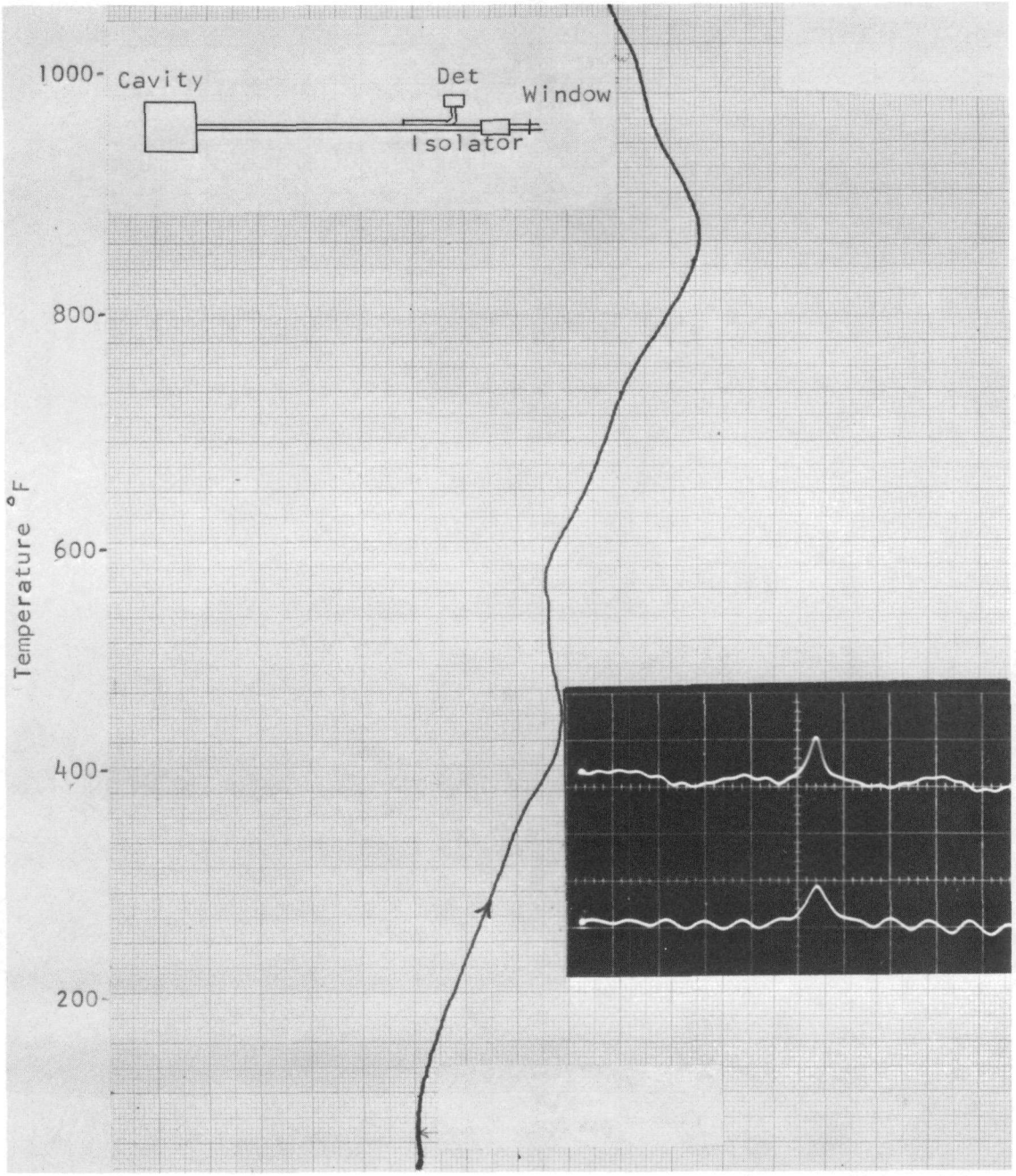

Photo 704622-2

Frequency Deviation - 3.92 MH2

FIGURE IV-2 *Frequency Deviation as a Function of Temperature. Isolator Near Pressure Window.*

The experiments at the TRIGA showed the capability of the concept for measurement of thermal neutron flux from 10^{10} nv to 10^{16}nv.

b. Fast Neutron Measurement With Self-Powered Detectors

J. W. Upton and W. G. Spear

Sensors are needed to measure the fast neutron flux density of sodium-cooled breeder reactors in order to determine power distributions and other neutron-related core parameters. This work is to develop a rugged, self-powered, fast flux monitor of 0.25-in. diameter, operable to 1400°F capable of immersion in liquid sodium up to 50-ft. depths, operable in a 10^9 R/hr gamma field, and having sensitivity for 10^{12} to 10^{16} n/cm^2-sec fast flux. [12227]

The cylindrical geometry of a coaxial detector allows simple design and construction and allows production of a rugged device. Figure IV-3 is a schematic of this concept.

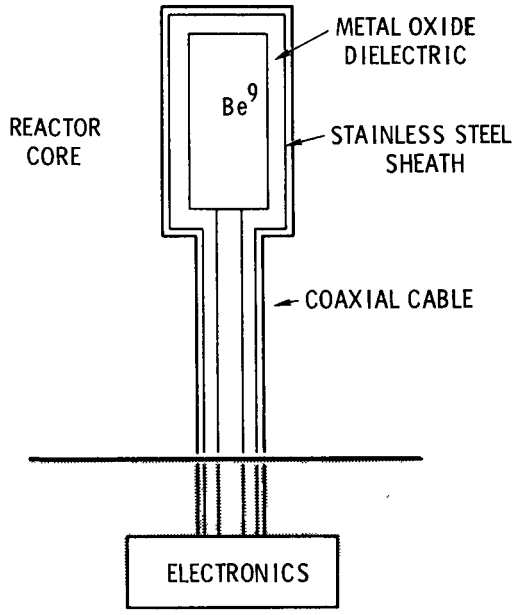

Photo 703906-6

FIGURE IV-3 *Conceptual Design of Self-Powered Fast Neutron Sensor*

During the reporting period, emphasis was on obtaining the materials for fabricating prototype detectors. Vendors of Be wire have supplied information on availability, cost, purity, and other specifications; needs of the first family of experimental devices have been cataloged, and alumina tubing purchased for insulator sheaths for the first tests. Efforts to obtain small size sheaths of MgO or SiO_2 continued. The lack of readily available stainless steel sheathed, semi-rigid coaxial cable of small diameters may affect the experimental effort.

The initial theoretical analysis provided a clear picture of the expected operating parameters, with the coaxial geometry being the focus of the study. The mathematical model involved several assumptions which received continued study this quarter. The assumption of an "infinitely long" detector (i.e., no end effects)produced a negligible error in the calculations centered about a 12.7 cm long detector. The effect of the insulator annulus which surrounds the Be^9 rod should be considered. The analysis centered on estimating the fraction of the electrons stopped within the dielectric in order to confirm previous results. A revised computer program will be used to analyze this effect.

c. Fast Neutron Measurement With Gas-Flow Techniques

D. P. Brown and W. A. Spear

The experimental model, shown in Figure IV-4, has a 0.250-in. diameter stainless-steel cylinder containing Be^9 coated tungsten screens. Helium gas circulating through the in-core sensor will bring beta-emitting He^6 [from the Be^9 (n,α) He^6 reaction] to an ionization chamber external to the reactor. Use of a combination of counting and current measurements should result in a wide-range system having essentially no gamma or thermal neutron interference problems and having a fast flux range from 10^8 to 10^{16} n/cm^2-sec.

Accomplishments during this reporting period included final fabrication and inspection of internal components of the sensor.[12227] The 0.25-in. diameter, 1.5-in. long in-core sensor will contain one hundred 0.2-in. diameter tungsten screens coated with Be^9. Because of fabrication

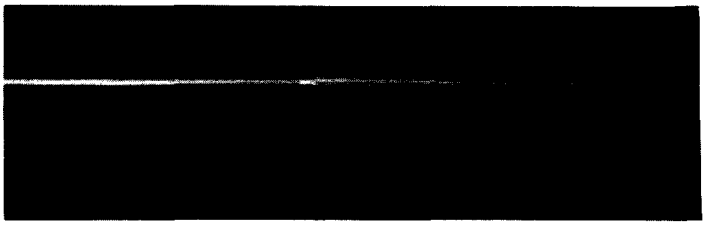

Photo 703516-1

FIGURE IV-4 *Experimental Gas Flow Fast Neutron Detector*

difficulties, a number of original screens were rejected;additional material had to be procured to complete the work. A new technique for making the screens proved successful.

A proportional counter of commercial design received initial tests. Betas from the decay of He^6 will be detected by the 2-in. diameter, 1-ft long, flow-through proportional counter. Test results showed an adequate signal-to-noise ratio; external quenching was provided by an appropriately large resistor in the charge-sensitive preamplifier.

d. Low-Level Neutron Flux Instrumentation

W. A. Spear

This FFTF task focuses on establishing an in-vessel startup channel, which consists of a fission counter, cables and preamplifier. Appropriate standards for acquisition of these components for the FFTF must be generated and a low-level neutron counting system established that can operate under conditions of cooling by inlet sodium but at the stated gamma level.

Significant problems encountered with components include breakdown pulse noise, difficulty in obtaining cables, inadequate detector performance (neutron sensitivity at high gamma levels) and lack of commercial availability of a satisfactory current-sensitive preamplifier.

Continued long-term testing (1000 to 3000 hours) in the Hanford Co^{60} Gamma Facility of commercial, off-the-shelf fission counters,

coaxial cables and preamplifiers has provided the necessary initial evaluation of component performance. [12166 ID-A] One high neutron sensitivity, unguarded fission counter demonstrated stable operation for more than 600 hours of test at a temperature of 319°F and 1.5 x 10^6 R/hr gamma exposure. Because better cables were not delivered, this channel employed, as a substitute, a relatively stiff signal cable that could not be wrapped around the heating mandrel; therefore, the cable was operated without heating (i.e., at about 100°F). The experiment thus provided a "detector test", but with conductive heat raising the connector (detector-to-cable) temperature to about 230°F. With prior exposure for 2400 hours, the present experiment gives a total exposure with detector energized (400 V) of about 3000 hours. Use of the unguarded detector allowed initiation of testing to determine basic characteristics of the sensor.

Other experiments employing a guarded fission counter evidenced stable operation for more than 150 hours under combined conditions of 350° temperature and 1.5 x 10^6 R/hr gamma. Again, because of delayed cable delivery, the assembly used an unheated cable. However, a heat tape around the connector (cable-to-sensor) allowed testing of the critical "cable end zone" including termination and an HN connector (alumina insulator). This channel provided operational experience with a guarded fission counter and signal cable connectors under combined conditions of approximately 350°F and 1.5 x 10^6 R/hr gamma with 400 V dc applied to the detector.

A third channel with an unguarded fission counter has exhibited stable operation for 600 hours with the detector at 110°F and 1.5 x 10^6 R/hr gamma and with SiO_2-insulated cables at 300°F. The connectors remained at about 110°F. During previous testing, this channel had been subjected to over 3000 hours of tests with all components heated to 350°F during the irradiation at 1.5 x 10^6 R/hr and with 400 V detector voltage. Repair work on the neutron source holder in the Hanford Co^{60} Gamma Facility made it necessary to remove the channel from the facility; this apparently caused enough cable damage to result in a marked increase of noise. When the channel was reinstalled, it operated satisfactorily

at the reduced temperature; therefore, continuation of the test to acquire "gamma exposure" information seemed appropriate. The test also provided needed information about temperature effects on the main body of the cable.

Faulty operation of a fourth guarded detector made it necessary to return the unit to the manufacturer under warranty. Laboratory measurements indicated a long collection time of about 350 nanoseconds and a low signal amplitude of 1.1 microamperes, both incorrect by a factor of two from the advertised values. These characteristics result in a substantial loss of gamma tolerance for the detector.

e. Effects of Radiation-Induced Current on Signal Cables

J. L. Stringer and W. G. Spear

This work (12550) defines the coaxial cable parameters, the parametric relationships and the test measurements required to predict the magnitudes of the radiation-induced direct currents that could occur in a given cable and for a specific radiation environment.

During the past quarter, the radiation-induced effects on several cables were measured in the pulsed TRIGA reactor at Washington State University. Analysis of the data obtained at the peak pulse power level of the TRIGA showed the mean-square magnitude of the noise to be proportional to the peak power level and to the induced insulator conductivity, but not proportional to the induced direct current. The noise also proved to be independent of current flow caused by applied voltage on the cable and to be independent of the cable volume on a per-unit-length basis. Figure IV-5 shows the comparison of the mean-square-current (MSC) noise, insulator conductivity and direct current magnitude for the two MgO-insulated, stainless steel conductor cables (4D, 4E) used in the TRIGA tests.

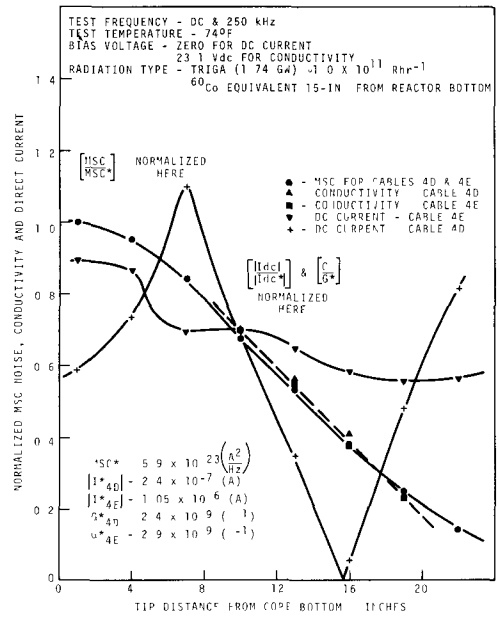

FIGURE IV-5 *Normalized Peak Radiation-Induced Noise Conductivity and Current as a Function of the Cable Tip Position in the Reactor Core.*

f. Effects of Radiation and Temperature-Dependent Electrical Noise on Signal Cables

W. G. Spear

The purpose of this work (12550) is to determine the parameters (electrical, material, thermal, radiation) necessary to characterize the control "breakdown pulse noise" (BPN) generated in metal-sheathed, coaxial signal cables insulated with MgO, SiO_2 and Al_2O_3.

During this quarter, the ac and dc resistance values of the MgO-insulated, stainless-steel-sheathed, coaxial cables were measured using dc bias voltages of 10, 300 and 600 Vdc over a temperature range of 1100 to 1500°F. For the applied voltages, internal insulator polarization caused variation of the dc resistance of almost a factor of 10 at 1100°F; however, this was reduced to a factor of four at 1500°F. The general decrease (slope) in the ac and dc resistance values with increasing temperature suggests an intersection of the values above 1500°F. This intersection could occur if electrons become the dominant charge carrier at higher temperatures.

g. Methods For Improving High Temperature, High Radiation Performance of Reactor Cable Insulation

R. L. Gordon and W. G. Spear

Effort during the past quarter concentrated on conduction mechanisms and breakdown phenomena in order to meet the needs of the FFTF task on low level neutron flux instrumentation in overcoming present problems with breakdown pulse noise (BPN).[12262] A total of 86 references on conduction mechanism and 64 references on breakdown phenomena in SiO_2, MgO and Al_2O_3 were selected from the library for careful review. Preliminary results of this review indicate that space charge polarization (i.e., ion migration to regions of high resistance within the body of the insulator or to blocking contacts at interfaces) had the effect of greatly reducing the breakdown strength of dielectrics. These results support the hypothesis that BPN, the major problem presently affecting signal cables for the neutron fission counters for FFTF, is a manifestation of space charge polarization.

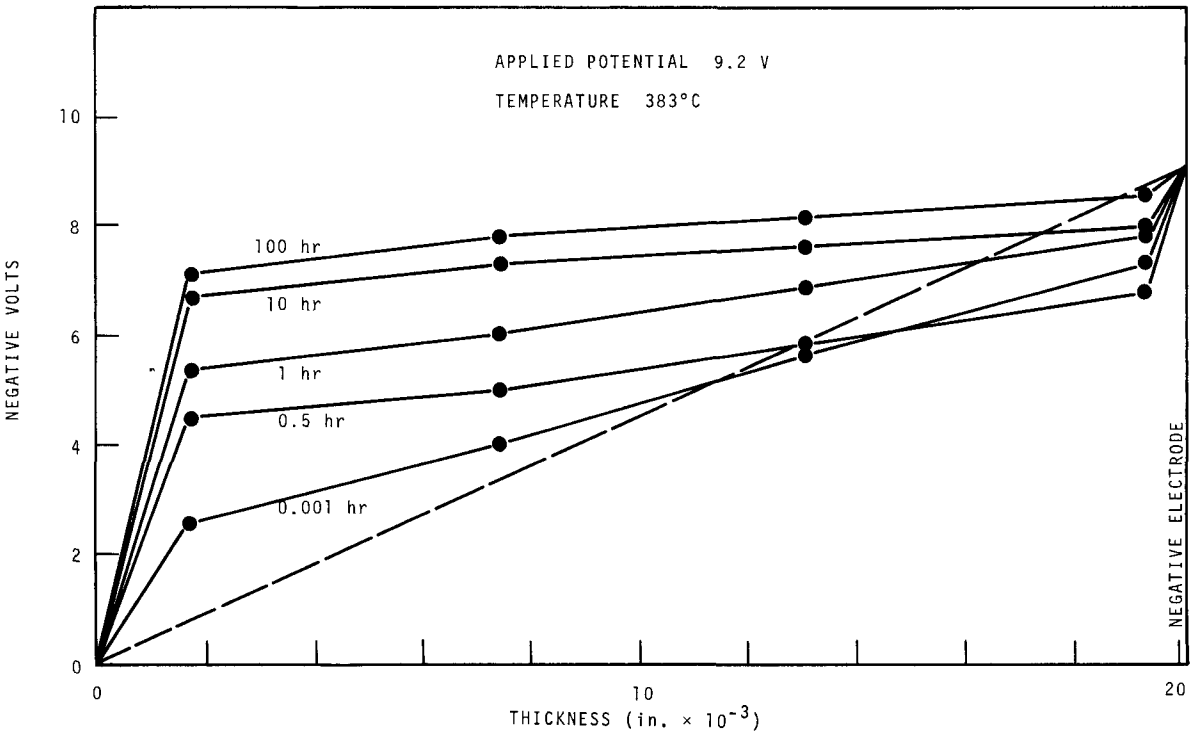

FIGURE IV-6 *Non-Linear Potential Distribution as a Function of Time*

The proposed mechanism for generation of BPN has its basis in the non-linear potential distribution which accompanies polarization. Keller[1] states that in the bulk, "pockets" of charge act to reduce the breakdown threshold for glass (SiO_2 + alkali impurities). Sutton[2] points out that under conditions of interfacial polarization, as much as 90% of the applied voltage appears across an extremely small region of the insulator. Figure IV-6 shows the buildup of potential with time.

2. Fuel Failure Location System

The objectives of this task are to evaluate, develop, and test several Fuel Failure Location (FFL) concepts for application to the FFTF Reactor System. Five concepts are presently under study: xenon and krypton gas tagging of individual fuel pins; fission product detection; conductivity probe monitoring of released gas volume in each subassembly instrument package; fission product deposition on removable tabs located above each subassembly; and acoustical triangulation of the three reactor outlet pipes for released fission gas.

a. Xenon and Krypton Gas Tagging Concept

R. J. Cash, F. A. Scott and T. J. Kabele

The purpose of this phase of the development effort is to evaluate gas tagging as a Failed Fuel Location subsystem for the FFTF. In this concept, 1 to 2 cm^3 of mixed isotopes of xenon, krypton, or both are sealed in each fuel pin as part of the helium fill gas. The same isotopic ratio is used in each pin of a given subassembly with different ratios in different subassemblies. When a fuel pin fails, part or all of the tag gas is released to the sodium coolant and in turn disengages

(1) Keller, K. J., "Formation and Annulment of Space Charges in Glass and Their Influence on Electric Breakdown". Phys. Rev., 86, 804 (1952).

(2) Sutton, P. M., "Space Charge and Electrode Polarization in Glass-II". J. Am. Ceram. Soc., 47, 219 (1964).

into the argon cover gas. A sample of cover gas is then taken and passed through a charcoal bed for adsorption of the xenon and krypton tag gas. Later, the gas is directed into a mass spectrometer to determine the unique tag ratio; by this means, the faulty subassembly is identified.

Gas Tag Loading Costs.-Based on information from the FFTF Fuels Department for the present HEDL method of loading gas tags, a cost analysis per core loading was made. Using the four cases (80 unique tags determined previously), the total cost per core varies from $108,000 to $151,000. This includes all of the costs associated with loading 80 unique tags in 80 subassemblies each containing 217 pins. Table IV-1 presents a breakdown of the costs.

Table IV-1 Tag Gas and Loading Costs for Tagging 80 Subassemblies

	Case I	Case II	Case III	Case IV
Cost of Gas Only[(a)]	$ 48,000	$ 9,000	$ 28,000	$ 52,000
Mixing and Tag Preparation[(b)] @ $167/mixture	13,360	13,360	13,360	13,360
Helium Blending, Glove Box Hookup, and Leak Testing @ $225/Subassembly	18,000	18,000	18,000	18,000
Labor to Load Tag Gas @ $845/Subassembly	67,680	67,680	67,680	67,680
Total Cost	$147,040	$108,040	$127,040	$151,040
Average Cost Per Subassembly	$ 1,838	$ 1,351	$ 1,588	$ 1,888

(a) Gas costs involve 100% wastage factor; i.e., for each 1 cm^3 of tag gas loaded, 1 cm^3 is wasted. Gas costs reflect the current AEC Mound Laboratory prices. Cases I through IV present four methods of selecting and spacing gas tag ratios.

(b) Mixing Costs: $65/mixture; gas cylinder cost: $13/cylinder; mass spectrometer analysis: $45/mixture; and shipping and handling costs FOB Richland, Washington: $44/mixture. Total: $167/mixture.

Dynamic Cover Gas Tag Analysis.-When a tagged fuel pin fails, part of the gas released to the sodium will be tag gas. The tag gas must travel through the sodium to the cover gas spaces and through the cover

gas spaces to the gas sampling position before it can be analyzed. Enough tag gas must be present in the cover gas for a successful analysis (and failure location) to be performed.

Entrainment of tag gas in the sodium and purging of the cover gas spaces both tend to decrease this concentration of tag gas in the cover gas. There is a concentration below which analyses cannot be performed and therefore location becomes impossible. This study is an attempt to estimate the effects of gas entrainment and cover gas purging on the concentration of tag gas in the cover gas following a fuel failure and thereby define the capabilities of the gas tagging approach.

For the cases presented, the concentration of tag gas in the cover gas space is sufficient to permit the successful mass spectrometric analysis for Xe^{124} and Xe^{129}. Only when the entrainment fraction is very large ($y > 0.75$) and the release fraction is very small ($x > 0.001$) would one expect problems in obtaining an adequate tag sample from the cover gas.

The available time during which a sample can be collected appears to be more than adequate. Sufficient tag gas for a successful analysis is present in the cover gas space for at least six hours after a failure in almost all of the cases evaluated. The only exception is, again, if the release fraction is less than 0.001 and the entrainment fraction is greater than 0.75. Indeed, the persistence of the tag gas in the cover gas space may make it difficult to locate a second fuel failure which occurs within a few hours after the first failure.

The cover gas system was assumed to be represented by Figure IV-7. $R_p(t)$ of Figure IV-7 represents the rate of release of tag gas from the fuel pin to the sodium pool as a function of time, and $R_s(t)$ is the rate of release of the tag gas from the sodium to the cover gas. An expression for $R_p(t)$ was selected that was commensurate with the minimum functional requirements for the Fuel Failure Monitoring System; i.e., the FFM system must be able to locate failures when the hole through a fuel pin cladding is large enough to release at least 50 % of the plenum gases within two hours after the failure occurs. Therefore, $R_p(t)$ was taken as constant for two hours at 0.75 cm^3 xenon gas/2 hours.

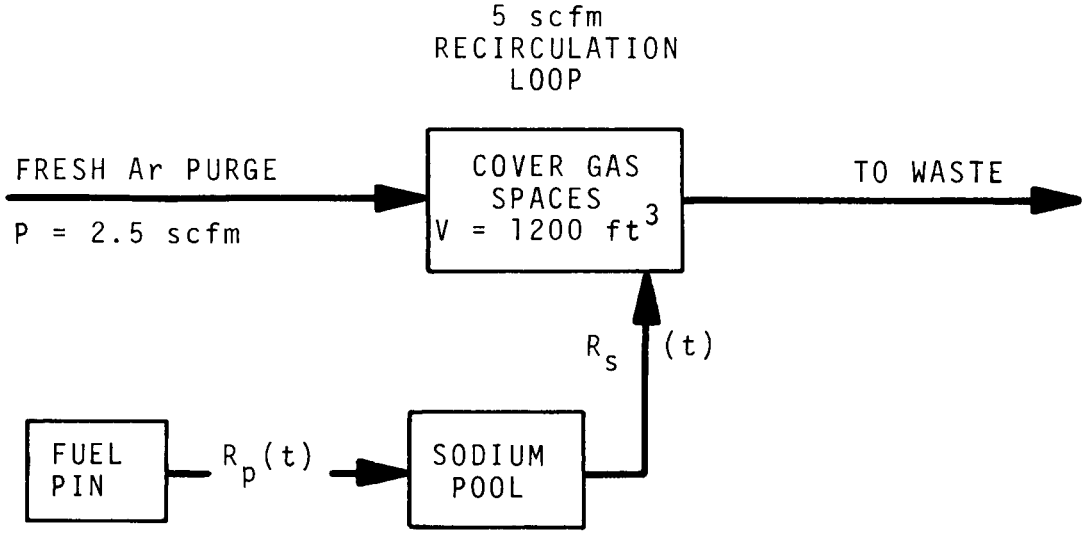

FIGURE IV-7 *Dynamic Cover Gas System Model*

An expression for $R_s(t)$ must be assumed, since little is known about gas disengagement in the FFTF. A material balance on the cover gas spaces following a fuel pin failure gives:

$$\frac{dN}{dt} = R_s(t) - N\,P = R_s(t) - \lambda N \qquad (1)$$

where:

N = amount (atoms, volume, moles, etc.) of xenon tag gas in the cover gas spaces.

t = time, hours.

$R_s(t)$ = release rate of tag gas from the sodium to the cover gas.

V = volume of cover gas spaces.

P = fresh argon purge rate.

λ = P/V, cover gas decay constant.

The release rate $R_s(t)$ is a function of tag gas entrainment and disengagement and a function of $R_p(t)$, the release rate of tag gas from the fuel pin.

The following calculations represent several plausible estimates of the tag gas buildup in the FFTF cover gas system following the type of

fuel pin failure assumed above. The assumption is made that a fraction (1-y) of the tag gas is released directly to the cover gas space while the remainder (y) is entrained in the sodium and released gradually over a period of time.

Thus:

N_p = amount of tag gas entrained in the sodium.

x = fraction of the entrained gas released on each pass of the sodium through the reactor vessel.

t = time required for one cycle of the sodium through the primary circuit.

λ_s = x/T = decay constant for the entrainment-disengagement process.

Therefore:

$$R_s(t) = (1-y)\ R + y\ R\ (1-e^{-\lambda_s t}) \tag{2}$$

for $t \leq 2$ hrs, and for $t > 2$ hrs,

$$R_s(t) = \lambda_s N_{pt=2\ hrs} e^{-\lambda_s (t-2)} \tag{3}$$

Substitution of these equations into Equation (1) yields:

$\underline{t \leq 2 \text{ hrs}}$

$$N = \frac{R}{\lambda}\left[1-e^{-\lambda t}\right] + \frac{yR}{(\lambda-\lambda_s)}\left[e^{-\lambda t} - e^{-\lambda_s t}\right] \tag{4}$$

$\underline{t > 2 \text{ hrs}}$

$$N = N_2\, e^{-\lambda(t-2)} + \frac{N_{p2}\lambda_s}{\lambda-\lambda_s}\left[e^{-\lambda_s (t-2)} - e^{-\lambda(t-2)}\right] \tag{5}$$

Where:

$$N_2 = N \text{ at } t = 2 \text{ hrs}$$

$$N_{p2} = N \text{ at } t = 2 \text{ hrs} \tag{6}$$

Using the model described above and a knowledge of the minimum quantity of tag gas required by the mass spectrometer for analyses of Xe^{129}/Xe^{124} ratios, it is possible to define the effects of: (1) gas release times from the fuel pin; (2) tag gas entrainment; (3) tag gas disengagement; and (4) varying cover gas purge rates on the concentration of tag gas in

the argon. The available sampling time can also be found by determining the length of time that the concentration of tag gas in the cover gas space exceeds the minimum detectable by the mass spectrometer system. Successful sampling can be accomplished during all or a part of this interval.

To make a conservative estimate of the tag gas detection limit, the following assumptions were made:

1) A minimum detection limit at the mass spectrometer of 10^{-12} liters of Xe^{124}(STP);
2) A 90% loss of sample in the charcoal bed and the system piping.
3) A 5 ft^3 gas sampling volume.
4) A 100-fold safety factor to account for adverse system performance and to ensure a conservative estimate.

Using the 1200 ft^3 cover gas space of the FFTF, this represents a minimum concentration of $6.6(10^{-2})cm^3$(STP) in the total cover gas in order to determine the Xe^{129}/Xe^{124} ratio of natural xenon (i.e., 275).

A wide range of values for the purge rate, the release fraction, and the entrainment fraction were used for this analysis. The results of these calculations are summarized in Figures IV-8 through IV-11. The most significant variable appears to be x (the fraction of entrained gas which is released on each cycle of the primary sodium through the reactor vessel). If this fraction is greater than ten percent, entrainment in the sodium pool has little effect on the release of gas from the fuel pin to the cover gas space (Figure IV-8). This is because the entrained gas is rapidly released to the cover gas space. On the other had, if the release fraction is less than 0.001, the entrained gas is released too slowly to be easily detected. Thus, the entrainment fraction (y) becomes the important variable (Figures IV-9 and IV-10). Figure IV-10 shows the influence of the entrainment fraction when the release fraction is 0.001. At release fractions(x) between 0.1 and 0.001, both the release fraction and the entrainment fraction are important variables.

The purge rate determines the rate at which the tag gas in the cover gas space is removed. Figure IV-11 shows the effects of purge rates from

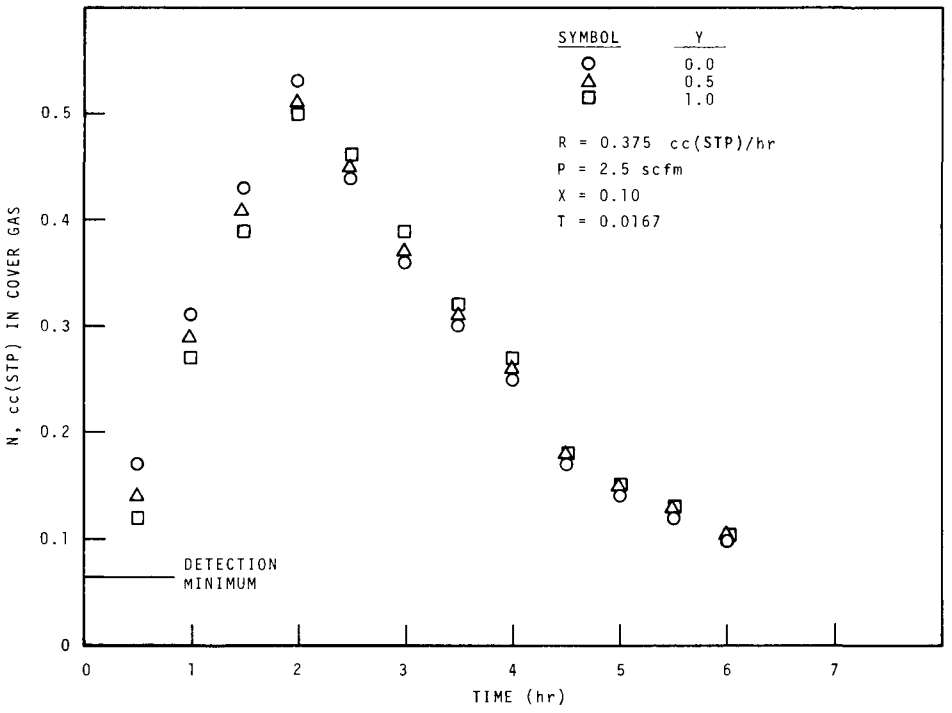

FIGURE IV-8 *Influence of Gas Entrainment on the Cover Gas Tag Concentration for x = 0.10*

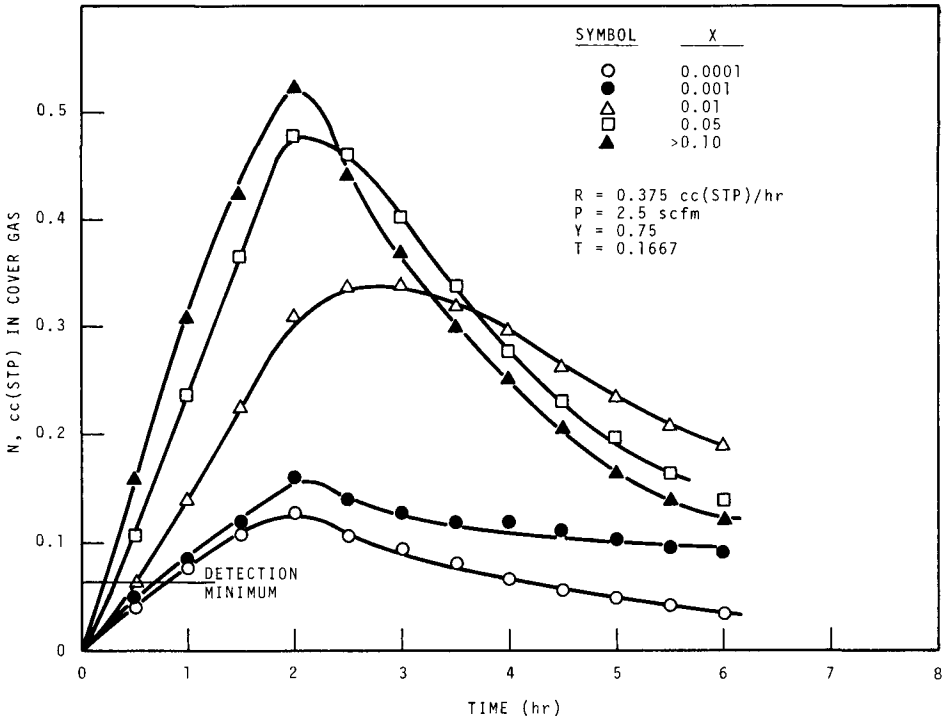

FIGURE IV-9 *Influence of the Estimated Tag Gas Release Fraction (x) on the Cover Gas Tag Concentration*

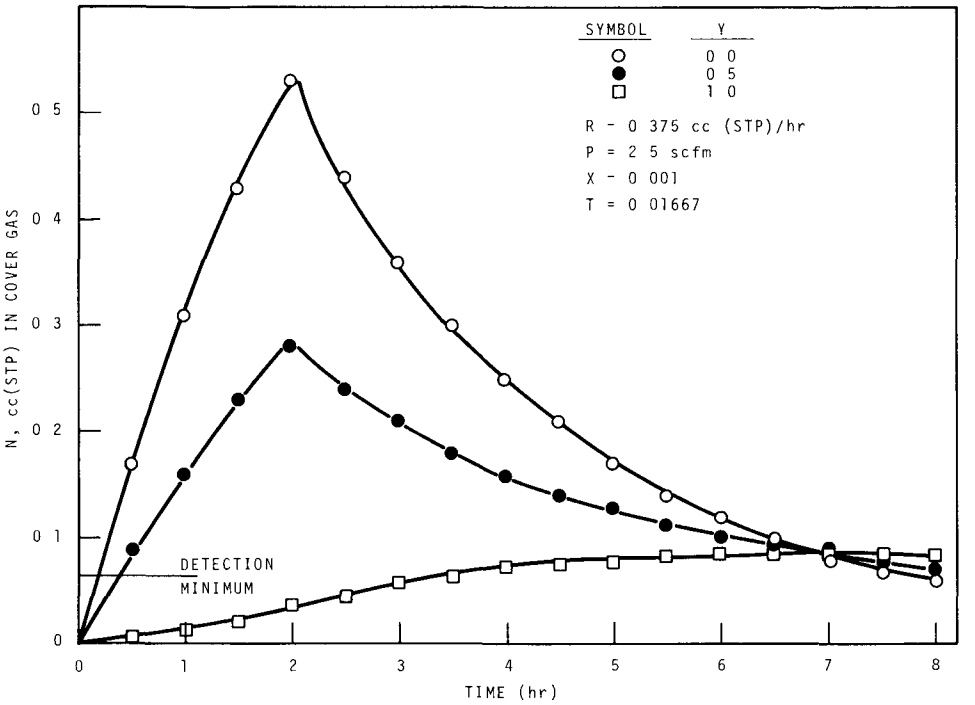

FIGURE IV-10 *Influence of Gas Entrainment on the Cover Gas Tag Concentration for x = 0.001*

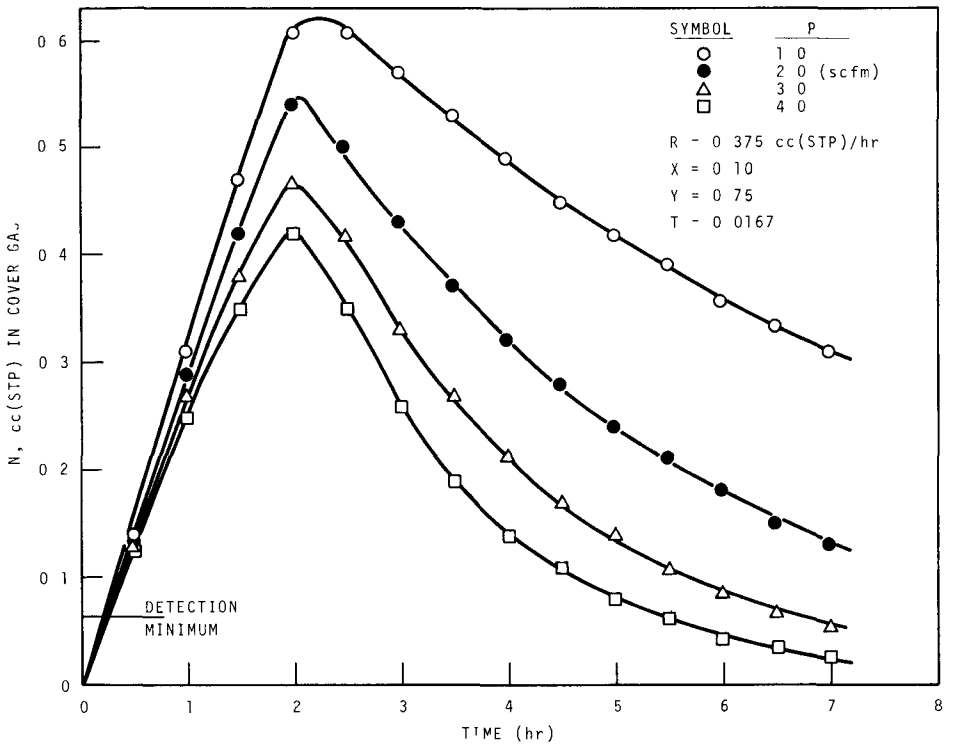

FIGURE IV-11 *Influence of the Purge Rate in the Cover Gas Tag Concentration*

1.0 to 4.0 scfm on the quantity of tag gas in the cover gas.

b. Fission Product Detection

1) In -Vessel Gas Separation Concept

R. J. Cash, F. A. Scott, and D. R. Dickinson

The objective of this phase of the development effort is to test the feasibility of the in-vessel gas separation concept by hydraulic testing using a Plexiglas mockup. In this concept, the sodium flow from each subassembly is passed through a mixer (the same mixer used to achieve sodium mixing for thermocouple sensing) and then past a small diameter sample inlet. Part of the dispersed sodium flow enters the sample line and is carried to the upper guide tube near the sodium to cover gas interface where gas disengagement can occur. Bleed holes below the reactor vessel sodium level permit continuous sodium flow within the sample line. Small fractions (10^{-3} or better) of fission gases released upon failure are collected by natural disengagement in the guide tube. After indication of a fuel failure, each guide tube chamber is sampled for abnormal levels of fission gas. This sampling would probably be done with the reactor shut down.

All proof-of-principle testing has been completed on this concept and a summary report has been prepared by D. R. Dickinson for the FFM Evaluation Board. Tests were conducted at 225 and 450 gal/min with various air injection rates and sample line flows. Tests were conducted with a 1/2 in. diameter sample line and an isokinetic sample line. Disengagement efficiencies of 10^{-3} and better were obtained.

2) Fission Product Detectors

N. S. Potter and W. G. Spear

One task goal centers on the mechanical and operational experimental qualification of the Salford (British) charge-tape detector system for monitoring reactor cover gas for fission products escaping from leaking fuel. A second goal concerns experimental qualification of commercially available detectors in the environment of the delayed neutron detection

system, a technique to monitor the sodium coolant for fission products.

During this reporting period, mechanical evaluation of the charged-tape detector proceeded past the 375,000-cycle mark with no significant failures. Detector sensitivity, which was determined by using a second unit for experiments at the Plutonium Recycle Critical Facility (PRCF), appears adequate for anticipated FTR use. Figure IV-12 compares the detector count rate with the computed neutron flux (extrapolated to lower values) at the fission gas generator (in PRCF) surface. The 2.3 counts/sec observation corresponds to a flux of about 1350 n/cm^2-sec with a signal-to-background ratio of two. The fission gas generator consisted of a 12-in. by 1-in. diameter aluminum tube coated with U^{235} (> 90% enriched) of thickness of 2 mg/cm^2 on the inside diameter. A stainless steel housing around this assembly allowed passage of flowing argon gas which carried the fission products to the detector. Flux foils attached to the housing provided calibration information.

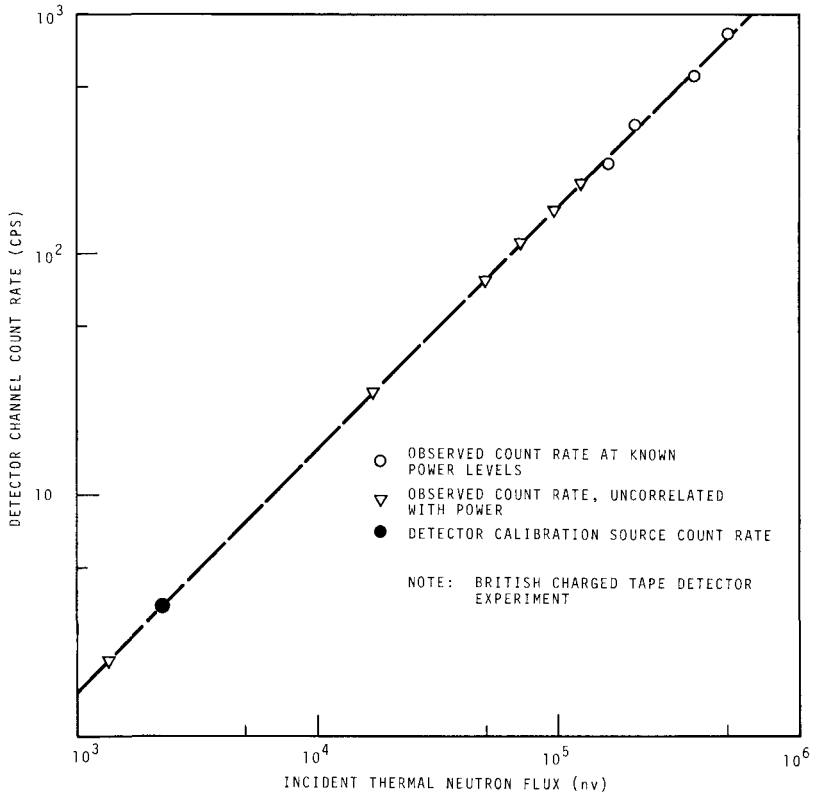

FIGURE IV-12 *Extrapolated Detector Channel Count Rate vs Computed Flux on Fission Gas Chamber Surface*

Experimental evaluation of commercial detectors moved forward during the period with tests completed on one type and initiated on a second. Tests performed on a 0.5-in. diameter by 10-in. long B^{10} lined proportional counter revealed the following information:

- At ambient (114°F) temperature, average (of three detectors) neutron sensitivity at 10^5 R/hr gamma fell to 84.8% of that noted at 10^4 R/hr.
- At rated maximum operating temperature (390°F), the neutron sensitivity reduced to 57.2% for 10^5 R/hr versus that at 10^4 R/hr.
- At 10^4 R/Hr gamma, an increase from ambient to rated temperature reduced neutron sensitivity by only about 3%.
- A 33% sensitivity reduction occurred at rated temperature and 10^5 R/hr.

Preliminary data analysis, following a 586-hour test at rated temperture and gamma, indicated an apparent count-rate decrease of about 16%. However, further data analysis must be done to verify these results. Immediately following this test, evaluation was initiated of a counter having an 0.5-in. diameter and a 24-in. length, with a rating of 10^5 R/hr at 650°F. The initial data obtained indicated that the counter could not operate at the rated gamma level; therefore, present evaluation has been limited to 10^4 R/hr and 550°F. Subsequent tests will be conducted at rated temperature.

During this period, preliminary plans were made to conduct on-line tests with the charged-tape detector system at the EBR-II reactor to obtain operating experience and to secure data for comparison with that from the regular EBR-II instruments. Selected neutron detectors will also be tested EBR-II.

c. Conductivity Probe Monitoring Concept

R. J. Cash, F. A. Scott, and D. R. Dickinson

These studies were made to determine the feasibility of locating a failed fuel element by measuring the released gas with a conductivity probe. The conductivity probe operates on the same principle as a liquid level indicator, i.e., by measuring a change of resistance of the probe.

Test results were presented on this concept last quarter. The summary report has now been completed by D. R. Dickinson for presentation to the FFM Evaluation Board.

d. Fuel Failure Location by Fission Product Deposition

W. F. Brehm, R. J. Cash and F. A. Scott

The purpose of this task is to investigate the feasibility of a method of fuel failure location to complement gas tagging. The basic concept is simple: fission products released from failed fuel elements deposit on tabs located above the fuel pins in the flow channel, the tabs are removed and gamma-scanned and those tabs with adhering fission products identify the leaking subassemblies.

Experiments showed that, while radioactive cesium in easily detectable quantities was collected in residual sodium adhering to tabs, no activity remained after the sodium was removed. While the tabs could still be analyzed to locate a fuel failure, remote handling and radiochemical separation would be required. In addition, the problem of actual location and retrieval of the samples has not been solved.

Tabs of four candidate materials (electropolished stainless steel, passivated stainless steel, ZrO_2 on Zr, TiO_2 on Ti) were loaded into static capsules containing sodium with about 3 mCi of Cs^{134}. Total cesium concentration was about 4 ppm. The tabs were heated for 9.5 and 96 hours at both 900° and 1050°F nominal temperature, a total of four capsules. Using a Ge(Li) diode, the tabs were counted with the adherent sodium film, washed, and counted again. The sodium from each capsule was also counted. Results of the initial counting are shown in Table IV-2.

When the sodium was removed from the specimens, the cesium counting rate dropped to zero for all specimens. In other words, all the cesium was in the sodium or was washed off the specimen by the water and alcohol rinse. This is not surprising, since cesium is very soluble in sodium and any cesium on the tab surface probably reacted with the water and alcohol.

TABLE IV-2
COUNTING RATES OF TAB SPECIMENS *

9.5 hr--900 °F	Counts/min	Approximate Counts/min/cm^3 of Sodium in Capsules
SS-E **	817	
SS-P **	241	
Zr **	412	960
Ti **	582	
96 hr--900 °F		
SS-E	421	
SS-P	323	920
Zr	134	
Ti	488	
9.5 hr--1050 °F		
SS-E	1051	
SS-P	133	1100
Zr	190	
Ti	286	
96 hr--1050 °F		
SS-E	503	
SS-P	332	
Zr	300	970
Ti	350	

* The 0.600 MeV peak of Cs^{134} was tabulated.

** SS-E = electropolished stainless steel, SS-P = passivated stainless steel, Zr = ZrO_2 on Zr, Ti = TiO_2 on Ti.

These results are disappointing, because attempting to locate a fuel failure with Cs^{134} deposition would require chemical separation of the Cs from the overwhelming Na^{24} background. While chemical separation is possible, it would complicate the procedure for locating the fuel failure.

The difference in activity reported in Table IV-2 must be a function of the amount of sodium adhering to the different tabs, or a function of the amount of cesium segregating to the different solid-liquid interfaces during the test, since there is no systematic variation in counting rate with temperature or time of exposure. (Segregation during cooling could not have occurred because the capsules were inverted before cooling and all but the residual sodium drained off the tabs.)

Cesium segregation to interfaces has been reported. A rough estimate of the cesium segregation to the surfaces occurring in this experiment can be obtained as follows: the stainless steel tabs had a surface area of about 2 cm^2; it has been reported that the amount of sodium adhering to stainless steel pulled from a sodium pool into a hot argon atmosphere is 1 to 5 mg/cm^2 (about 1.1 to 5.5 x 10^{-3} cm^3/cm^2). If we assume that 5 x 10^{-3} cm^3/cm^2 of sodium adhered to the electropolished stainless steel specimens, then the concentration of radioactive cesium in the adherent sodium ranged from 4.27 x 10^4 to 1.051 x 10^5 counts/min per cm^3 of adherent sodium, as compared to 920 to 1100 counts /min per cm^3 of sodium taken from the capsules. A segregation factor of about 50 for cesium to a stainless steel sodium interface is indicated. The other tabs either had less sodium adhering to them or less cesium segregating to the interface. (The true segregation factor is probably less because the counting efficiency of the tabs is greater than that of the sodium from the capsules which was poured into bottles and counted. It would not be expected, however, that the difference in counting efficiency could account for all the apparent segregation.)

e. Fuel Failure Location by Triangulation

1) Summary

A test series was run on the nominal quarter-size outlet region hydraulic model of the FTR to demonstrate the feasibility of locating failed fuel positions by ultrasonic measurement of gas bubbles in the model outlets.

Air was injected at selected core positions and the three outlet pipes of the model were monitored. The distances between the core position and the outlet nozzles were correlated with the percent of air leaving the model at each outlet and the arrival time of the air at each outlet.

Two empirical formulae were found to predict the distance between the source of injected air and the model outlets.

$$L = 47.513\ A^{-0.131}$$

$$L = 30.631\ \Delta t^{\ 0.054}, \text{ where}$$

L is the distance, measured in the plan view, from the air source to any of the three outlets.

A is the percent of air leaving by way of the outlet corresponding to the distance L.

Δt is the time interval between the arrival of air at the first outlet, and the arrival at the second and third outlets (i.e., air would first be detected in one outlet, later in a second, and in the third outlet in turn, the order being determined by the distance between the selected core position and the outlet).

By using the lengths given by these formulae, it was found during a proof test that the source of air could be predicted to within a zone of two or three core lattice positions.

2) Discussion

The concept works on the principle that flow from a given subassembly is strongly biased toward the closest outlet nozzle of the reactor vessel. This will be true for FFTF as long as there is no

contrivance above the subassemblies for mixing or deflecting the flow exiting in the vessel. Thus, flow from each subassembly should be effectively split, with the largest flow moving to the nearest outlet in the shortest time. If the effect is reproducible and capable of being mapped and measured, then it is practical to determine a zonal location based upon synchronous monitoring of released gas bubbles (or delayed neutrons) in the three outlet pipes.

Feasibility tests on this concept were performed on the Hydraulic Core Mockup (HCM) by injecting air at selected core positions. The amount of air and its arrival time were measured at each of the three model outlets using three 2.25 MHz transducers. The following variables were correlated:

1) The percent of air which reached each outlet.
2) The arrival time of air in each outlet.
3) The distance from each selected core position to each outlet.

It was thus possible to develop two empirical expressions relating the three variables:

1) The distance from a selected core position to each of the model outlets as a function of the percentage of air which reached that outlet.
2) The distance from a selected core position to each outlet as a function of the arrival time at the outlets.

Experimental Arrangement and Procedure.-Figure IV-13 is a schematic of the model showing the air injection system and the ultrasonic instrumentation. The three outlets pipes of the HCM were each fitted with 2-1/2 inch diameter ultrasonic transducers molded to fit the pipe. These transducers were coupled to an ultrasonic pulser-receiver (P/R) unit. The output of the P/R units was fed to an attenumeter which, in turn, was connected to the strip chart recorder. The output signal of the system was linear and proportional to the void fraction (air content) of the water flowing past the transducers.

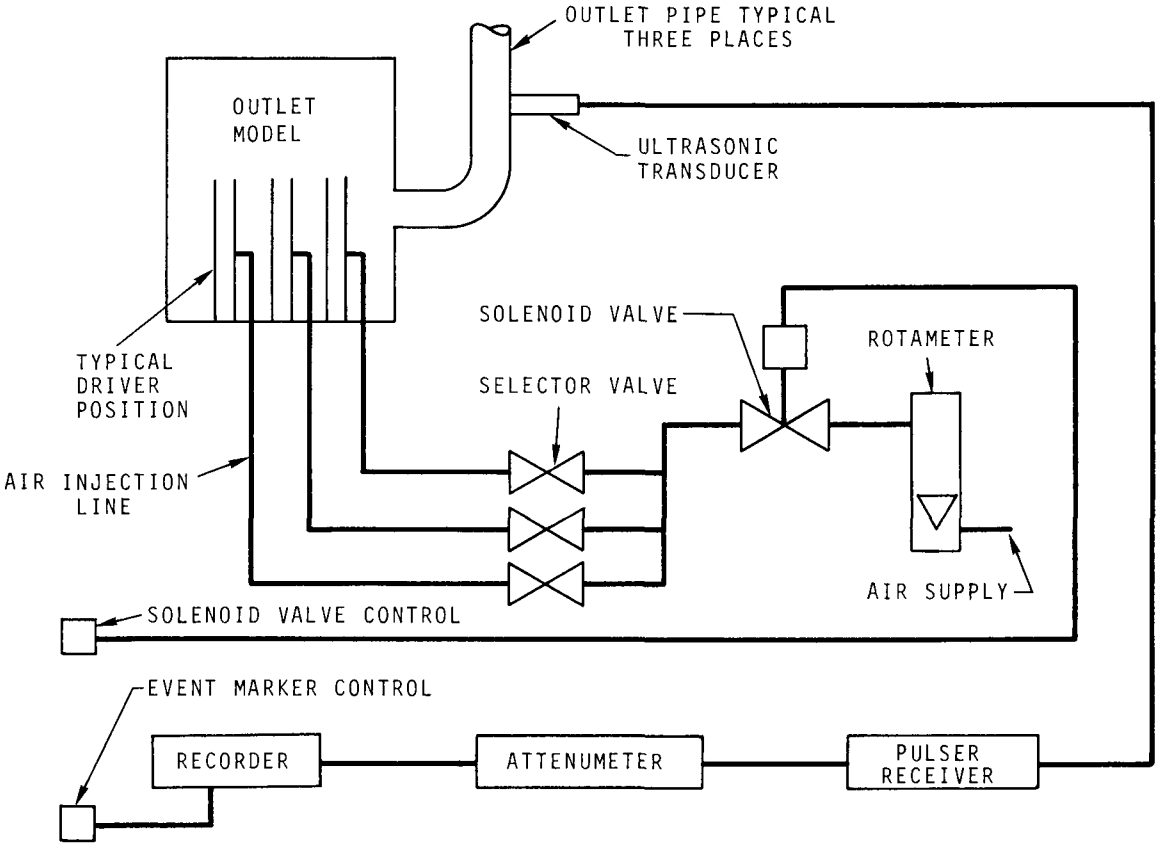

FIGURE IV-13 *Schematic of Experimental Air Injection System and Instrumentation.*

A solenoid valve was installed in the air supply line to the model's injection manifold. This was used to start and stop the air flow to selected core positions in the model. The strip chart recorder was equipped with an event marker which could be triggered simultaneously with the solenoid valve to note a reference point for arrival time measurements.

Calibration.-The model was operated at the normal flow of 3010 gpm. Air was injected into each of the three outlet pipes in turn at rates of 0.5, 0.75, 1.0, 1.25, 1.5, 1.75 and 2.0 SCFH. While these rates are greater than would be expected from a slow "gas leaker type" failure, they are representative of "burst type" failures. In addition,

considerable improvement in the detection level may be possible through refinement of equipment and because of the inherently lower gas solubilities in a sodium system. A record of the response of the ultrasonic system was made by the strip chart recorder for each of the injection steps.

Air Volume Test Runs.-The solenoid valve and the selector valve to the desired injection point were opened. The flow of air was regulated to a set value, usually 1 SCFH. The solenoid valve was then closed and the model was allowed to dispel the air accumulated during flow regulation.

After establishing a "zero" on the strip charts, the solenoid valve was opened to inject air in a selected core position. The transducer responses were recorded for each of the following 13 core positions (Figure IV-14): C-7, D-6, F-4, F-8, F-11, G-7, H-6, H-9, K-10, K-13, L-6, M-8, and N-13.

Arrival Time Test Runs.-For these tests, no calibration runs were necessary, because only the time at which the response began was required; the magnitude of the transducer signal was of no interest. The air injection rate was again regulated as described above with the solenoid valve open. The solenoid valve was then closed, and the air level was allowed to drop to "zero". It should be noted that the air level was never truly zero, because the model always contained a background of entrained air. When "zero" was established, the solenoid valve and strip chart event markers were actuated simultaneously. The arrival time then was represented by the length of chart travel between the event marker and the trace departure from zero. Injections were made from each of the 13 positions shown in Figure IV-14.

A facsimile of a typical strip chart response trace is shown in Figure IV-15.

Since the three transducers each responded differently to the same air injection rate, it was necessary to relate the different responses. This was possible because the responses were linear; i.e., the calibration

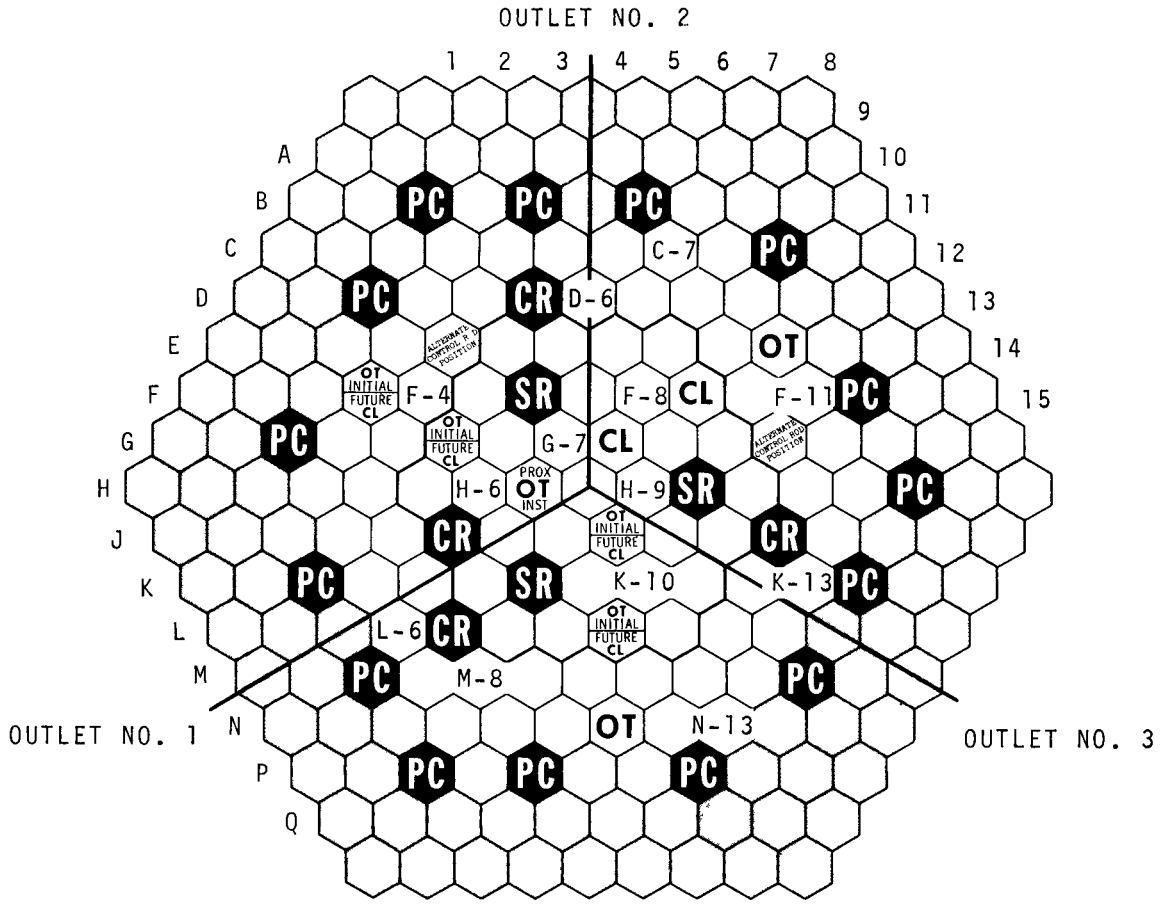

FIGURE IV-14 *Hydraulic Core Mock-Up Arrangement*

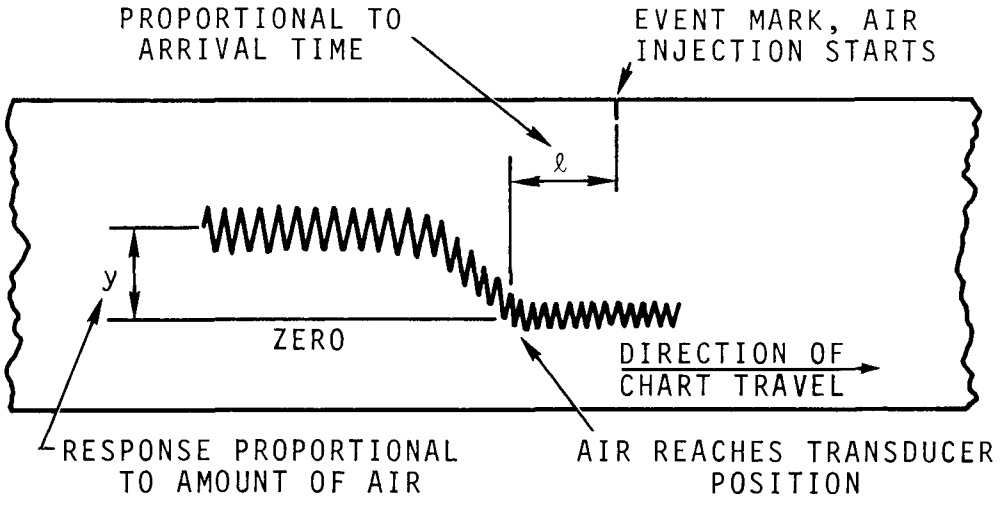

FIGURE IV-15 *Facsimile of a Typical Strip Chart Response*

curves for each could be written as follows:

$$Y_1 = m_1\ x+b_1;\ Y_2 = m_2\ x+b_2;\ Y_3 = m_3\ x+b_3 \qquad (7)$$

Eliminating x, the air injection rate, allows one to choose one response; e.g., Y_2, as the reference and relate the other two responses as follows:

$$Y_2 = \frac{m_2}{m_1}\ (Y_k - b_1) + b_2;\quad Y_2 = \frac{m_2}{m_3}\ (Y_3 - b_3) + b_2 \qquad (8)$$

Thus, if the responses Y_1 and Y_3 are changed to an equivalent Y_2 response, measurements from all three outlets will behave as if transducer no. 2 had been used in every case, and the responses can be compared directly.

3) Results and Conclusions

Air Volume Data.-All responses were converted to equivalent No. 2 responses. The sum of the equivalent responses of all three outlets is proportional to the total amount of air reaching the outlets. Thus, each equivalent response divided by this sum is the percent of air exiting the corresponding outlet. These percent values were calculated and tabulated. The distances between the core position, into which air was injected, and outlets 1, 2 and 3 were scaled from the design drawings of the model and tabulated. The calculated data, A (%) and L (in.) for the 13 injection points were plotted and found to be a power function of the form $L = K A^n$. A least-squares fit of the data resulted in the expression:

$$L = 47.513A^{-0.131}. \quad (9)$$

The graph of this function and the associated data points are shown in Figure IV-16. The similarity of this function to the function found from electrolyte conductivity data taken during mixing tests earlier this year is noteworthy. In this case, the resulting empirical expression was:

$$L = 46.336\ Q^{-0.116}. \quad (10)$$

Arrival Time Data.-The chart travel was scaled between the instant of air injection and the point where a response was seen, and the data tabulated. These chart distances were divided by the chart speed and the resulting arrival times were tabulated.

In an actual situation, where the three outlets of the reactor are being monitored for entrained gas, the arrival time would not be known as such; instead, only the difference between arrival times could be measured. Gas would first be detected in one outlet, then a second outlet, and later, the third outlet would be reached. Because of this, the arrival time data were converted to values of the difference in arrival time by subtracting the first arrival time from the other two and tabulating the results, showing Δt in seconds.

The Δt values and the corresponding L values were also found to plot linearly on log-log paper and could be expressed by a least-squares fit as:

$$L = 30.631\ (\Delta t)^{0.054}. \quad (11)$$

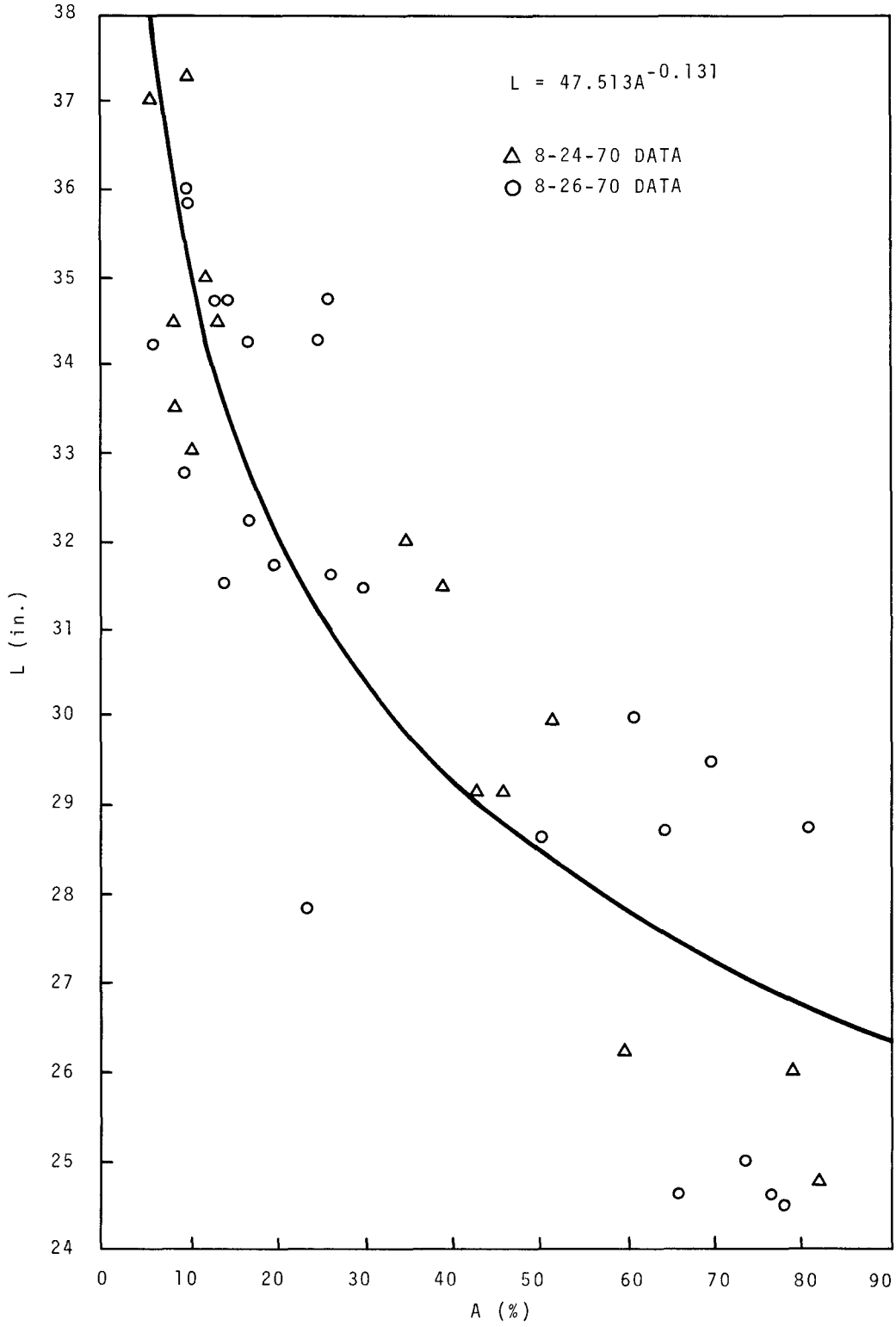

FIGURE IV-16 *Calibration Curve for Air Volume Tests in the Hydraulic Core Mock-Up*

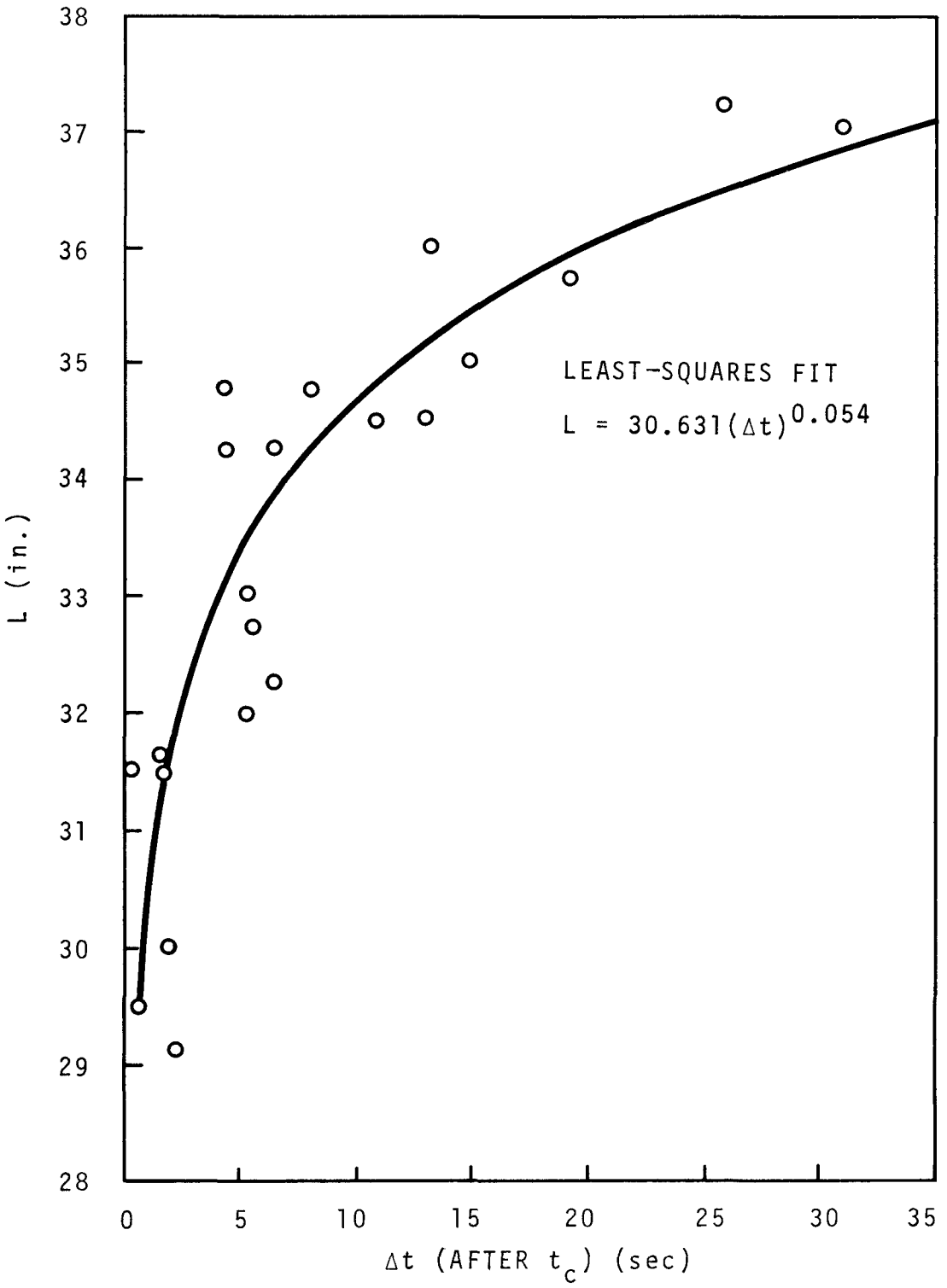

FIGURE IV-17 *Calibration Curve for Arrival Time Tests in the Hydraulic Core Mock-Up*

The graph of this function and the associated data points are shown in Figure IV-17.

Proof Test.-As a final test, air was injected into five core locations that had not been used during prior data runs. The coordinates of these injection points were recorded, but were not known to the experimentor. Air volume and arrival time measurements were taken. The data were reduced and values of L were calculated from both empirical formulae. Using these values of L, the five locations were predicted by triangulation. All predicted locations were within three core lattice spaces of the actual source location. In the best case, the prediction was adjacent to the true location. The results for the proof test are presented in Table IV-3 and clearly illustrate that this technique can predict the location of a gas source to within a small zone of the core. The concept is feasible.

TABLE IV-3
ACOUSTICAL TRIANGULATION
PROOF TEST CORRELATED DATA

Injection Point	Outlet No.	Response	Corrected Response	A (%)	Arrival Time (sec)
Unknown No. 1 (G-10)	1	2.4	1.720	7.2	19.95
	2	14.4	14.4	60.3	3.23
	3	13.7	7.754	32.5	4.58
Unknown No. 2 (C-3)	1	3.0	2.087	11.1	7.20
	2	15.3	15.3	81.5	4.20
	3	2.3	1.382	7.4	15.15
Unknown No. 3 (M-11)	1	4.4	2.942	13.9	10.65
	2	2.0	2.0	9.4	30.60
	3	28.9	16.251	76.7	2.85
Unknown No. 4 (N-10)	1	7.8	5.020	29.7	6.75
	2	1.3	1.3	7.7	14.18
	3	18.8	10.605	62.7	3.68
Unknown No. 5 (J-5)	1	24.1	14.979	68.8	3.23
	2	4.9	4.9	22.5	6.60
	3	3.2	1.835	8.7	18.75

3. Evaluation of Pressure Sensors for Sodium Service

a. Commercial Sensors

Testing of commercial pressure transducers in the static sodium test facility started in January 1968 and was completed in September 1970. [12168 ID-C] Fourteen absolute and gage pressure transducers were purchased and subjected to a sodium environment with temperatures ranging from 300°F to 1200°F. Transducer pressure ratings ranged from 0 to 30 psia to 0 to 250 psig. Absolute pressure transducers rated at 0 to 30 psia were tested at pressures ranging from 50 percent to 90 percent of rating. Gage pressure transducers were tested at pressures ranging from 10 percent to 80 percent of rating.

Several types of electromechanical transducers were tested:

1) One bonded and four unbonded strain gages
2) Two LVDT
3) Four variable impedance
4) One NaK capillary
5) Two hybrid NaK capillary-unbonded strain gages.

One unbonded strain gage, one LVDT and the NaK capillary system operated for over 4000 hours with satisfactory results. The other transducers failed at times varying from a few hours to about 2000 hours. The LVDT and strain gages do not meet the present FFTF temperature requirements and are not being considered further. The NaK capillary system has a diaphragm which separates the high temperature, high pressure sodium from the NaK pressure transmitting fluid. The NaK, which is contained in a capillary tube, transmits pressure to the transducers. The transducer can be located in a cooler area. This combination is capable of operating under wide temperature ranges and can provide acceptable performance.

In summary, the one NaK capillary system was operated for 4280 hours in the static sodium test facility with temperatures ranging from 300°F to 1200°F and pressures up to 200 psi. System characteristics noted:

1) Linearity ±1% with a 95 percent confidence level
2) Maximum thermal zero set is 1.25 percent after ∿2723 hours operation
3) Thermal zero shift is +0.5% for 900°F rise in temperature
4) Maximum thermal sensitivity set was 0.835%; three long-term drifts of 1% were observed after 240 hours at constant operating temperature and input pressure.

b. Reactor Pressure Measurement Using Microwave Methods.

T. R. Billiter and W. G. Spear

A major objective of this work (12225) is the development of pressure measurement methods applicable to severe environments, expecially to liquid-metal reactors. Rapid response to pressure variations within an LMFBR requires a fast method of pressure sensing. Accordingly, development of a fast-reaction microwave technique operable between 75°F and 1200°F and directly immersible in liquid metals is underway.

During the quarter, effort has been applied to methods to reduce the temperature-dependent response of the dual-cavity pressure sensor. Specifically, materials with minimum thermal expansion would increase the operating temperature range of the sensor. Previously developed dual cavities composed of a single billet of metal to reduce temperature gradients have exhibited small "tracking" errors of about 3 MHz over a total range of 300 MHz for general operation at about 35 GHz. Improvement by a factor of at least ten of this error with improved instrument operational characteristics should be realized by using quartz resonators.

A representative microwave sensor with 0.005-in. thick, 0.5-in. diameter pressure diaphragm evidenced rapid response to an abrupt pressure change of 15 psi. The recorded data Figure IV-18 indicates a response to 63% of final value of about 7.5 milliseconds. System noise limited pressure measurement accuracy to approximately 0.25 psi for the particular sensor and test conditions. Reduction of system instability should be possible with improved stabilization of the microwave oscillator.

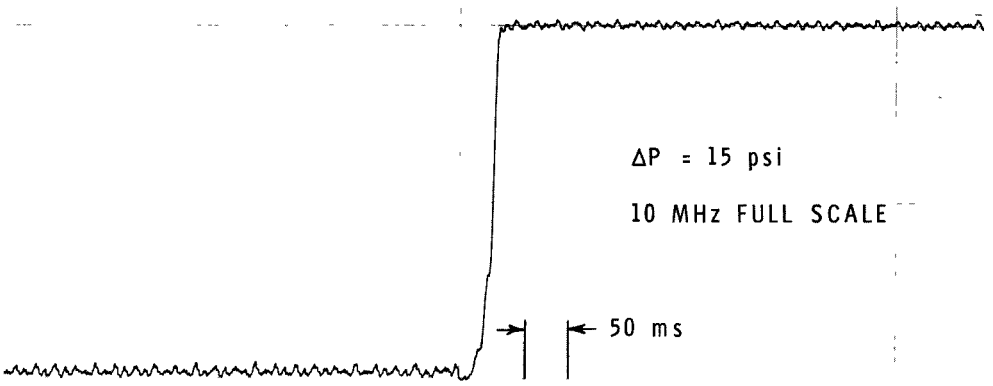

FIGURE IV-18 *Output Signal Response of the Dual Cavity Pressure Sensor for Abrupt Pressure Change*

4. In-Reactor Coolant Thermocouples

W. G. Spear

This task (12171 ID-F) investigates effects of the expected FTR environment on performance of Chromel/Alumel thermocouples. Characteristics under examination include: emf versus temperature calibration, wire resistance, insulation resistance and time response.

During this reporting period, completion of preliminary data reduction provided necessary information for the pre-irradiation testing series on the new 0.125-in. diameter sensors. The detailed analysis of the data will be performed after the post-irradiation tests scheduled for FY-1972. An issued topical report and a technical paper presented during the quarter described the results of irradiation tests performed on the 0.0625-in. diameter thermocouples previously irradiated to about 7×10^{21} nvt in EBR-II.

As a result of the data reduction work completed recently, several observations can be made regarding the test procedure used. The time response data, reduced to 0 to 63% time constant values, revealed values from 1.0 sec to 1.7 sec. These exceed the maximum specified time constant of 0.9 seconds for tests conducted in boiling water. However, the pre-irradiation tests used a salt bath rather than water. Later tests on eight sensors with boiling water resulted in time constants ranging from 0.47 sec to 0.93 sec. Thus, the marked changes probably center on the difference between heat transfer coefficients of the salt bath and the

boiling water bath. This will present no difficulty to the planned test program.

Traveling gradient tests performed on about 35 of the thermocouples provided useful information concerning wire homogeneity along the sensor length. For post-irradiation tests, this information will help to establish calibration changes as a function of neutron fluence along the wire. The measurements determined the differential emf between each test thermocouple and the reference with both lowered into a deep water bath and with differential emfs measured in two-inch increments along the lengths. This technique scans the thermocouple with a rather sharp temperature gradient, and since the emf results from that part of the sensor in a temperature gradient, the measurements establish the homogeneity of the entire length of wire.

All the thermocouples for irradiation have been shipped to EBR-II and should be in the reactor by the end of October.

5. Surveillance Sensors

Vibration and displacement surveillance of the FTR vessel, piping and components requires transducers capable of operating for long periods of time at elevated temperatures and high gamma levels. This program (12179 ID-N) includes evaluation of three different types of transducers (i.e., accelerometers, LVDT devices and eddy current proximity sensors); these will be subjected to acceptance, short-term, long-term reliability and life tests. Most of the sensors and test equipment have been received during the reporting period and evaluation programs have been started. The shaker table system and Kistler Corporation vibration calibration standard, traceable to the National Bureau of Standards, permit accurate evaluation of the ten piezoelectric charge accelerometers available. Eight of these units feature ratings to 1050°F, vibration to 200 g for frequency response from 2 Hz to 4 kHz and a charge sensitivity of 60 pC/g. The units also have stainless steel, hermetically sealed cases and cables suitable for under sodium use.

The other two units have temperature ratings to only 550°F but are 20 times as sensitive. Preliminary results of completed acceptance tests and temperature-effects tests on the eight high temperature devices indicated satisfactory performance.

6. Reactor High Temperature Measurement with Microwave Resonant Cavities

T. R. Billiter and W. G. Spear

Employing a small microwave (35 GHz) cavity resonant at a frequency dependent upon its temperature, the microwave technique being developed under budget 12225 should provide temperature measurements to 2500°F, thus providing an excellent margin of safety for LMFBR's. As a prime objective, the sensors will provide accurate data over extended periods of time without need of replacement. Reactor tests of the sensor will be conducted in the EBR-II "INCOT" facility. Measurement requirements could possibly include temperatures up to 2500°F and pressures up to 550 psia. An experimental sensor of niobium-1% zirconium received evaluation to temperatures up to 2500°F in a laboratory oven. The sensor response remained easily detectable over the temperature range of 75 to 2500°F, with only a minor degradation of cavity quality factor at the higher temperatures. Differences between the output signal for specific temperatures during increasing or decreasing cycles remained minimal. Data obtained confirmed a linear sensor response for temperature change with a detection sensitivity of 140 kHz frequency change per °F change. Neglecting other expansion coefficients, the linear coefficient of thermal expansion at a particular temperature may be approximated by

$$\alpha = \frac{\Delta f}{\Delta T \, f_o} \qquad (12)$$

for $\Delta f/\Delta T$ the determined sensor detection sensitivity and f_o, the resonant frequency at the specified temperature. For the resonant frequency of about 35,000 MHz and for the noted detection sensitivity, the calculated metal thermal expansion coefficient of $\sim 4 \times 10^{-6}$ in/in/°F agrees very closely with corresponding values noted in handbooks of properties of materials.

A heated (∿ 700°F) sensor subjected first to 60°F water and later to immersion in static air at 75°F, yielded unit time constants of 0.5 second and 100 seconds, respectively, (Figure IV-19). Because of the similarity of cooling environments, the first test results are applicable to liquid metal environments; the second more closely approximates results for a gas coolant.

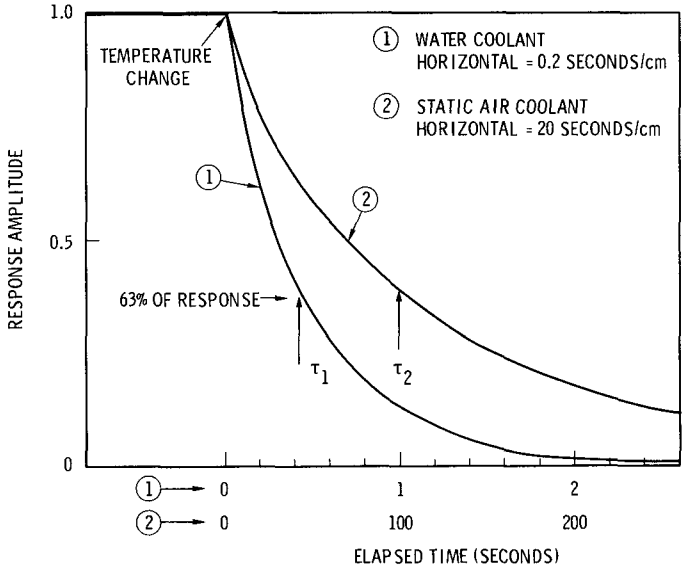

FIGURE IV-19 *Time Response of Nb - 1% Zr Sensor for Abrupt Temperature Decrease*

7. Microwave Methods of Measuring Coolant Impurities.

T. R. Billiter and W. G. Spear

The basic objective of this work (12225) is to develop microwave sensors and instrumentation applicable to measuring, under severe environmental conditions, various impurities in nuclear reactor coolants. Technique concepts will first be proven for moisture measurements in high temperature helium gas and should result in a prototypic system for reactor experiments early in FY-1972.

During this quarter, a fabricated microwave dual-cavity moisture monitor of Invar, intended primarily for laboratory tests, has undergone minor modifications to enable tests at the Gulf General Atomic test gas loop. Experiments conducted with the dual Invar cavity device yielded a detection sensitivity of about 15 ppmv/V dc for moisture in helium gas

over the range ∿ 1 ppmv to ∿ 1500 ppmv, as illustrated in Figure IV-20. Ordinate values refer to an amplified error signal voltage proportional to instrument response to moisture changes. Stability of the instrumentation for periods up to 15 minutes permits determination of moisture content within ± 2 ppmv at STP. For introduction of a constant moisture content sample, long-term variations of the detected error signal result predominantly from variations of sample gas pressure, although temperature fluctuations also cause minor sensor response.

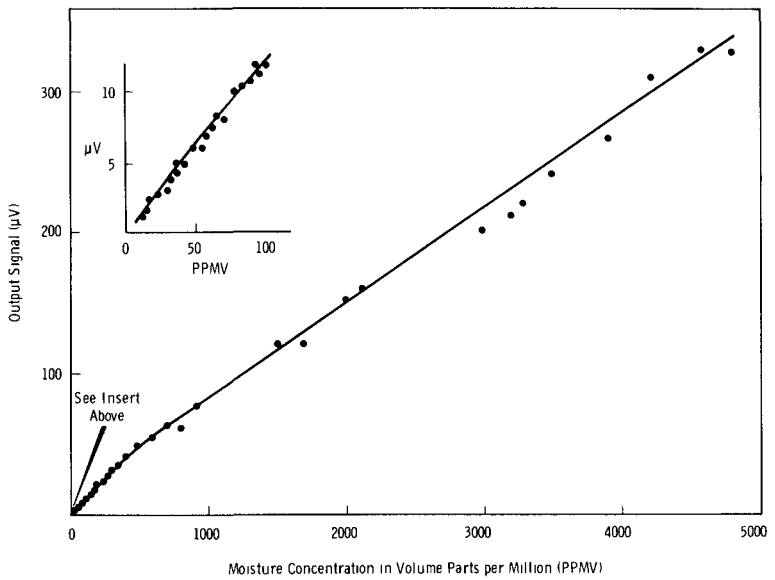

FIGURE IV-20 *Dual Cavity Microwave Moisture Monitor Response*

Sensor time response to abrupt changes of moisture content proved rapid (< 5 seconds) and independent of equilibrium moisture level. Selected values of time constant for the system lock-in amplifier influence speed-of-response for moisture variations. At low moisture content, the microwave instrument yields valid measurements much more rapidly than does the commercial dew point hygrometer, employed as a standard moisture measurement device. Consequently, coolant monitoring applications requiring highly responsive (at low moisture content), rather than highly accurate, measurements (as obtainable with a dew point hygrometer), should be satisfied by the microwave instrument system.

8. Advanced Non-Destructive Testing

a. Application of Mechanical Energy to Non-Destructive Testing

1) Measurement of Irradiation Effects on Steels

D. O. Hunter and H. N. Pedersen

Because of degradation of mechanical properties in neutron-irradiated steel, we have tried to establish the feasibility of nondestructive measuring of irradiation damage in reactor structural components (such as the pressure vessel) by means of ultrasonics. Earlier work has revealed readily measurable changes in elastic properties in steels irradiated at 140 to 350°F; however, changes in steels irradiated at 610 to 680°F, were found to be so small as to be inseparable from experimental error, the greater part of which was normal elastic properties variations within the donor plate. (Ref 1)

To reduce the experimental error, pre-irradiation dimensional ultrasonic measurements were made on some A533-B W.O.L. (wedge opening loaded) fracture toughness specimens and miniature tensile specimens which were to be irradiated as part of the Heavy Section Steel Technology Program requirements. Post-irradiation measurements at the same locations and using similar methods would then, ostensibly, provide a more accurate assessment of changes due to irradiation.

Changes in ultrasonic velocity and attenuation on the first two groups of specimens have been reported in an earlier quarterly report.(Ref 2) Specimens comprising the third group have recently been post-irradiation measured for changes in ultrasonic velocities and attenuation. Determining velocity changes depends on accurate dimensional changes. Upon completion of dimensional measurements on the third group of specimens, it is clear that these measurements are inaccurate; so are the measurements on the previous groups. Causes of the inaccuracies are identified as:

1) Presence of scale and other corrosion products
2) Burrs and dents as a result of handling
3) Pitting as a result of corrosion.

Practically all measured dimensions were on the large side; this results in calculated velocity changes being too large in the increased velocity direction for WOL specimens and too large in the decreased velocity direction for tensile specimens. It is impractical to determine the true dimensions of the specimens; consequently, estimates of dimensional changes were made on the basis of isotropic swelling. This results in a density change of -0.03%, and in an assumed effective oxide layer of 0.0001 in. Based on these estimates, the changes in velocities have been re-calculated.

Observations from these data are:

1) Ultrasonic velocity changes in a typical low alloy steel irradiated up to 9 x 10^{19}nvt (E>1MeV) at 500 to 550°F are too small to be accurately measured because of surface damage during irradiation and post-irradiation handling.

2) Although, for tensile specimens, there is some evidence of a trend in the decreasing velocity direction after first having experienced an increase in velocity, as fluence increases, changes are too small and scattered to enable correlation with neutron fluence.

3) Attenuation changes are predominantly in the increasing direction as fluence increases; scatter exists and changes are thought to be caused partly by the deteriorated condition of specimens' surfaces. Longitudinal velocity changes in WOL specimens when measured at 10.5 MHz (data not shown here) are, in general, slightly greater than when measured at 4MHz, indicating a possible frequency dependence on irradiation-caused changes in elastic properties.

Although the data reported here are inconclusive for the range of neutron fluence under consideration, it does not imply that data for steel irradiated to 2 x 10^{20}nvt (anticipated lifetime dosage to many thermal reactors' pressure vessels at beltline) would also be inconclusive. Nor does it imply that changes would be scattered and inconclusive if measurements were to be made on specimens which had surfaces restored to pre-irradiation condition (by hot-cell machining/polishing operations). Data do show, however, that changes due to irradiation, will be small at 500 to 550°F at $\sim$ 9 x 10^{19} nvt (E$\sim$1MeV) when measured at low ultrasonic frequencies with the present technique. These changes

will, in fact, be less than the scatter in unirradiated material and detectable in random scanning insitu on pressure vessels.

2) Fundamental Ultrasonic Studies

F. L. Becker and H. N. Pedersen

We have been investigating ultrasonic critical angle reflectivity as a method for determining material properties non-destructively. Our previous resport (Ref 3)indicated that there is a frequency, F_o, for which the reflected amplitude at the Rayleigh critical angle is zero. Anomalies in the phase of the reflected wave at F_o are also noted in the vicinity of the Rayleigh critical angle. Analysis of changes in F_o as a function of material properties is important to better understand the basic reflection phenomenon and to determine its usefulness as a nondestructive testing tool.

The relationship between F_o and the material properties has been established. The next step in this investigation is to analyze the effects and relationships to determine whether they can be useful in determining material properties; we must also find the expected accuracy of such a determination. The investigation will also be extended to cover many other materials.

b. Application of Electromagnetic Energy to Non-Destructive Testing

1) Eddy Current Methods

R. L. Brown, D. M. Romrell and H. N. Pedersen

As part of the eddy current development task, an effort is being made to automatically classify and segregate eddy current data as it is generated by a test system handling material such as cladding, ducting, etc. The feasibility of this approach was shown previously (Ref 4) using machined defects in a one-inch I. D. stainless steel tube; present effort is directed toward classifying natural defects.

Present categorization of the eddy current signal is performed on the bases of : 1) the maximum amplitude of the differential voltage derived from a differentially wound eddy current probe coil; and 2) the

phase angle of that voltage. As each signal is received, it is digitized and compared with the various classes of symbol categories. When a signal matches a given class, the computer registers one count. After each tube is run, or a complete batch of tubes is run, the data (being in statistical form) allows the distribution of the types of defects present to be known, and hence allows comparison to such variables as drawing method, batch chemistry, etc. The processed data are printed out after each test sequence, thus providing permanent record of all detectable defects in each tested specimen. Complete analysis of the collective data is provided on a real-time basis.

Upon successful operation of the basic system, additional data handling criteria will be developed to improve data collection techniques. Graphical data printout will be considered.

In order to accomplish this objective, signal conditioning hardware is being assembled and the coil design optimized for the intended application of this system, (i.e.),testing the FFTF fuel cladding.

2) Thermal/Infrared Methods

D. R. Green and H. N. Pedersen

Density of FFTF fuel pellets is presently determined from calculations employing pellet dimensions and weight.

Initial experiments to determine whether or not a thermal image transducer developed under this program could be used to sense density differences in green (non-fired) ceramics were carried out on ceramic chips borrowed from commercial manufacturers. Results of these experiments are shown in Figure IV-21. Density differences in the chips caused the brightness of the thermal images to be different. (Scan lines in the images are the result of using a video camera for image enhancement.)

The transducer used to make these images was described in a recent article (Ref 5). It is comprised of a thin foil coated with a thermally sensitive phosphor. The foil is pressed into contact with the test specimen by means of a transparent flexible backing. A thermal image of the test specimen is seen on the back of the foil after the foil is given a pulse of heat by passing an electrical current through it. The actual

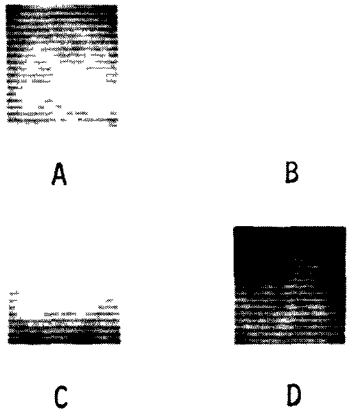

FIGURE IV-21 *Thermal Transducer Images of Green (Non-Fired)Ceramic Chips*

A. Normal Density, Uniform.
B. High Density, Uniform
C. Greater than Normal Density on One Side.
D. Lower than Normal Density on One Side

magnitude of density differences in the samples in Figure IV-21 could not be determined with sufficient accuracy, since the specimens had to be returned to the manufacturers intact and we could not immerse them or cut them.

Density differences of 8% in FFTF fuel pellets were thermally detected after the pellets were sealed inside their stainless steel sheath. The method used to do this is illustrated in Figure IV-22. The fuel pin sheath was coated with thermographic phosphor. This material fluoresces when irradiated with ultraviolet light. The intensity of fluorescence decreases with increasing temperatures, so that high temperature areas appear darker. Heat was produced in the sheath by passing a large electrical current pulse through it. Temperatures along the fuel pin were scanned with a rotating mirror - photomultiplier system, as shown in Figure IV-22. The output of the photomultiplier during one scan made 30 seconds after termination of the heat pulse is shown in Figure IV-23. The 8% lower density of pellets in a 10-inch long section on one end of

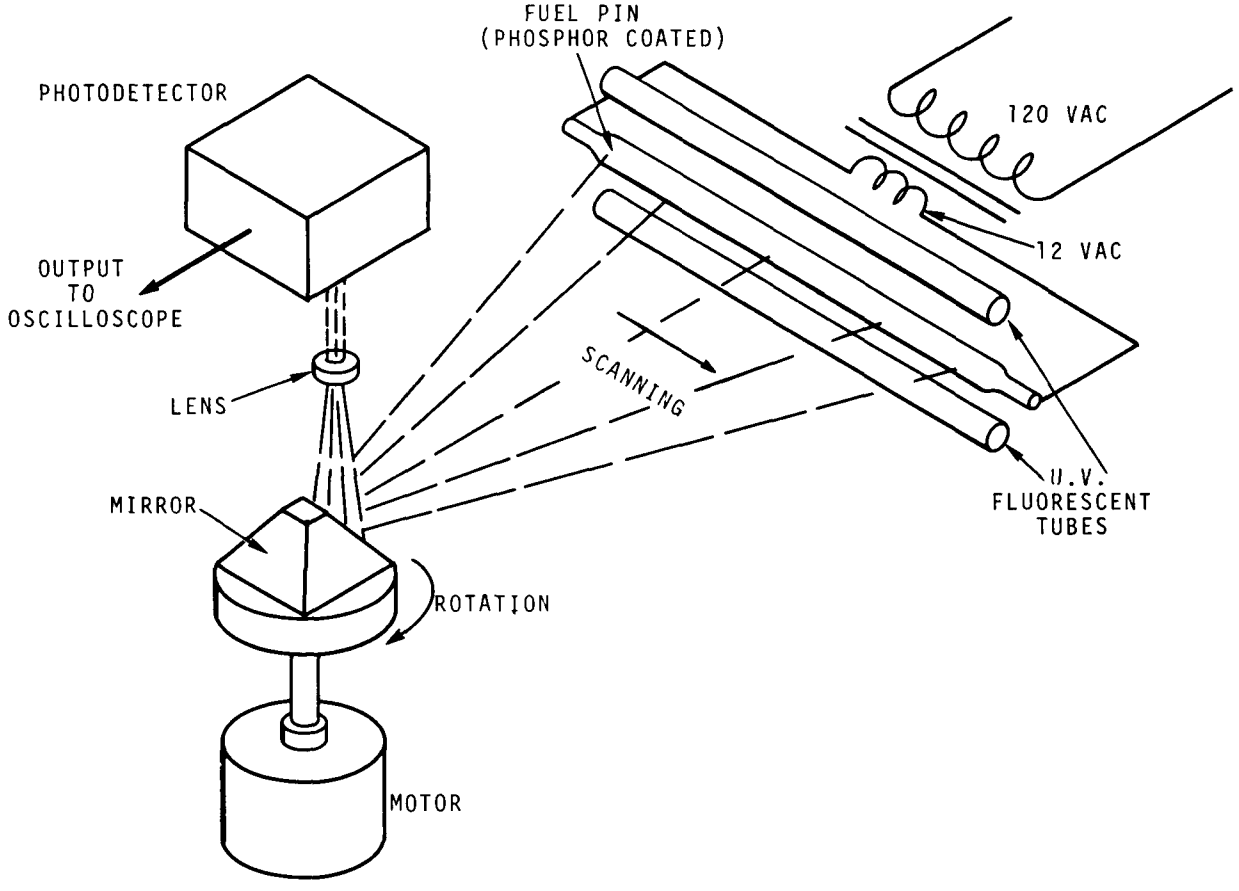

FIGURE IV-22 *Arrangement used in Experiments on Thermal Phosphor Detection of Fuel Density Differences in LMFBR Pins.*

the fuel pin can clearly be seen as an increase in photomultiplier output. Signal decrease due to a 2% density increase is lost in the noise.

Higher sensitivity can be obtained by making thermal measurements of density on the bare fuel pellets before they are inserted in the sheath. Experiments using the flat thermal image transducer, together with a video system for higher sensitivity, are being carried out on UO_2 pellets of known density in a manner similar to those performed above on the ceramic chips.

3) Neutron Radiography

C. B. Shaw, J. L. Cason

The limitation of thermal neutron radiography lies in the maximum penetration that can be achieved in a material. The penetration can be improved in many instances by using neutrons of an energy group where the specimen neutron cross section for that group is minimum, and then employing a detector having a maximum cross section to the same group.

A theoretical analysis was performed to aid in selecting epithermal neutron imaging materials in radiography of FTR fuels during pre or post-irradiated examination for measurements of fuel pellet enrichment (Pu and U), enrichment distribution and density (% theoretical).

The degree of increase in penetration of fuel materials by use of epothermal neutrons instead of thermal neutrons can be defined by Σ thermal /Σ epithermal. This factor is 40.0 and 46.0 for U^{235} and Pu^{239} respectively, and is graphically demonstrated in Figure IV-24 by a comparison of the neutron cross sections for U^{235} and Pu^{239} below and above the cadmium cutoff (0.4 ev.)

The theoretical analysis included use of THERMOS, HRG and ANISN computer epithermal resonance detectors. These detectors yield the highest response for discrimination between and penetration through U^{238}, U^{235}, Pu^{239} and Pu^{240} The detectors considered were Au^{197}, In^{115}, and Mn^{55}. The prototypic fuel assumed was 75% UO_2, 25% PuO_2 and 0.85 theoretical density. Cases for fully and naturally enriched uranium

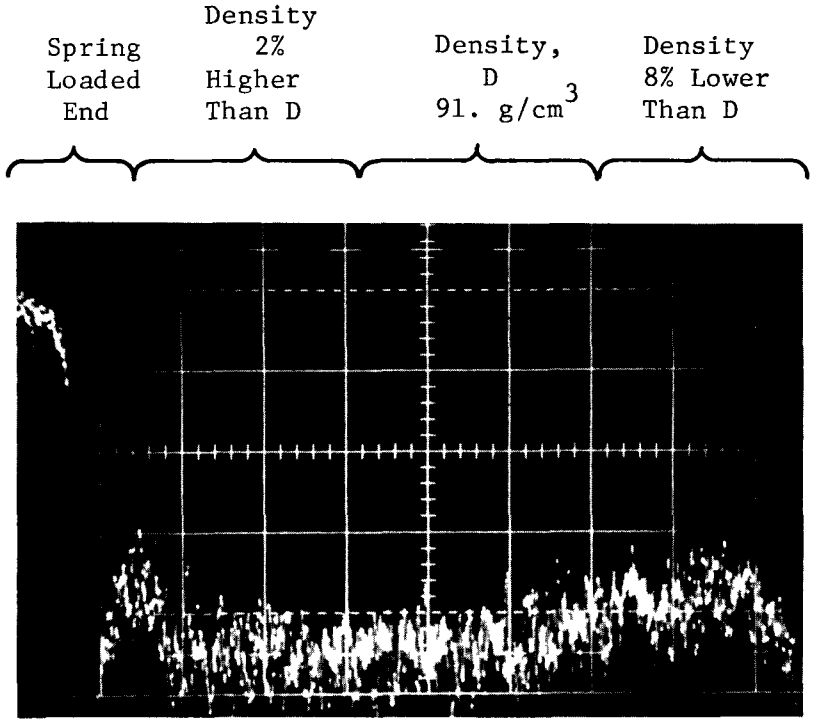

FIGURE IV-23 *Ceramic Fuel Pellet Density Differences of LMFBR Fuel Pins*

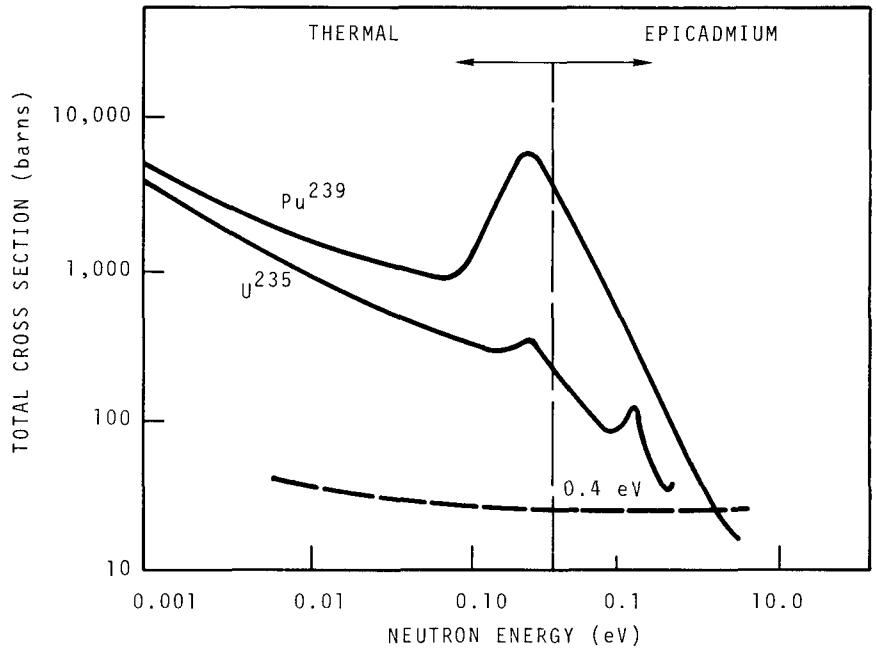

FIGURE IV-24 *Cross Section Comparison as a Function of Energy for Pu^{239} and U^{235}.*

were included. The neutron source selected for computational purposes was Cf^{252} (Fission Spectrum) moderated by 4.5 cm. of ZrH_2.

The Mn^{55} (n,α) reaction is activated by neutrons in an energy range in which the absorption by heavy elements differs the most from the thermal values. This gives an effective increased penetration; therefore, less exposure time is needed to produce an image of the attenuated beam after passing through the fuel. In order to eliminate the thermal response, each of the resonance detectors should be used with a Cd beam filter. In addition to the sensitivity of Mn^{55}, the half-life of 2.58 hours (compared to 64.8 hours for gold and 54 minutes for indium) makes it useful for applications with non-reactor sources where the ability to integrate the neutron flux over a period of several hours is important, yet, where long exposures (i.e., with Au) are not mandatory.

The mean expected levels of detection and variance of Pu^{239} and U^{235} using resonance detectors are 0.125% and 0.349%, respectively. Comparison of Σ_{th}/Σ_{epi} for Pu^{239} and U^{235} shows that increased penetration can be achieved with epicadmium neutrons rather than thermal neutrons. It is expected that the use of epicadmium neutrons and resonance detectors will prove to be a useful approach for radiography of fuels.

4) Application of Mössbauer Effect

R. N. Ord and H. N. Pedersen

The Mössbauer effect is a promising new tool for nondestructive testing. Several applications of the technique to the area of surface effects in materials are being studied. These include, (but are not limited to) corrosion products, material phase, surface strain, etc. The present effort is concerned with the identification of the various compounds of iron using the nondestructive backscatter geometry (Ref 6).

A series of ASI 1010 mild steel plates was oxidized under the conditions shown in Table IV-4 to produce the oxides and total thickness of oxide layer shown. A summary of results of qualitative analysis employing Mössbauer spectra is also shown on Table IV-4.

TABLE IV-4

OXIDATION CONDITIONS AND RESULTS OF
MÖSSBAUER SPECTRA FOR TEST SPECIMENS

Sample	Sample Preparation	Oxide Thickness (mil)	Oxides Formed	Compound
1	Heat in air at 650°C for 1 hour--furnace-cool to ambient	2.6	Fe_xO Fe^{3+} Fe_2O_3 Fe_3O_4	Fe^{3+} FeO Fe_2O_3 Fe_3O_4
2	Heat in O_2 at ∿ 5 torr at 850°C for 1 hour--furnace-cool to ambient--overcoat oxide surface with Krylen	2.1	Fe Fe_3O_4	Fe^{3+} Fe_3O_4
3	Heat in O_2 at ∿ 5 torr at 650°C for 1 hour, then furnace-cool to ambient--overcoat oxide surface with Krylen	0.96	Fe^{3+} Fe_3O_4	Fe^{3+} Fe_3O_4
4	Heat in air at 640°C for 1 hour--furnace-cool to ambient--overcoat oxide layer with Krylen	1.2	Fe_xO Fe^{3+} Fe_2O_3 Fe_3O_4	Fe^{3+} FeO Fe_2O_3 Fe_3O_4

Estimates of the peak areas for each spectra allows us to estimate the amount of each oxide present. However, until the spectra are computer fit, quantitative measurements can not be determined. Also, knowing the peak areas and the mass absorption coefficients, a determination can be made of the thickness of the oxide layers.

The purpose of this study was not to perform corrosion analysis, as such, but to show the applicability of the Mössbauer reflection geometry to corrosion analysis; therefore, further studies need to be done in conjunction with corrosion analysis studies.

9. Sodium Technology Instrumentation Development Summary

W. R. Wykoff

A summary of sodium technology instrumentation development work is given below. Details are given in Chapter V, Sodium Technology.

Preliminary requirements for the FFTF on-line instrument package (OLIP) have been based on present FFTF on-line instrument cell concepts. These concepts are being reviewed to optimize the cell arrangement. The Sodium Purity In-Line Analytical Module design is progressing toward a final design review. Oxygen meter ceramic tubes have been demonstrated to be considerably more resistant to thermal shock than was expected, (some withstanding shock rates as high as 200 °F/min). Three plugging meter designs have been selected for evaluation as an FFTF standard. A laboratory model of the LASL distillation sampler has been installed on SCEL.

A process employing isostatic pressing and sintering in inert gas has been developed for producing ThO_2 - 7.5 wt% Y_2O_3 electrolyte tubes. Tubes have been fabricated as a preliminary demonstration of the process. Characterization of Zircoa-produced slip-cast tubes has shown that there is a large variation in sodium resistance within individual tubes. Specifications have been prepared and procurement initiated for obtaining solid electrolyte tubes from a commercial source.

A process gas chromatograph has been received and is being installed

on the Small Components Evaluation Loop. It will be evaluated for FFTF application and will provide analytical information in support of the in-line instrumentation program being conducted on this loop.

The first order of new automatic power controllers for trace heaters has been received, tested and installed on the SCEL sampling header. This represents the first major step in an effort to establish commercial availability of an inexpensive automatic proportioning type controller with feed-back control and voltage limitation.

References:

1. Hunter, D. O., "Ultrasonic Velocities and Critical-Angle-Method Changes in Irradiated A302-B and A542-B Steels," BNWL-988. Battelle Northwest, Richland, Washington, April 1969.

2. Hunter, D. O., "Ultrasonic Measurements on Irradiated Steel," Quarterly Progress Report, Oct, Nov, Dec, 1969, Reactor Fuels and Materials Development Programs for Fuels and Materials Branch of USAEC Division of Reactor Development and Technology, BNWL-1279, p. 8.7. Battelle Northwest, Richland, Washington, Feb. 1970.

3. Becker, F. L. and Richardson, R. L., Research Techniques in Non-destructive Testing, edited by R. S. Sharp. (Accepted for publication by Academic Press, London) Vol. 1, Chap. 4, p. 91.

4. Ord, R. N., "Eddy Current Test Pattern Recognition Program," BNWL-942 Nov. 1968

5. Green, D. R., "High Speed Thermal Image Transducer for Practical NDT Applications," Materials Evaluation Vol. 28, pp 97-102, 110, May 1970.

6. Ord, R. N., Mössbauer Effect Using Backscatter Geometry as Applied to Nondestructive Testing - BNWL-1276, Dec. 1969.

V. SODIUM TECHNOLOGY

A. SODIUM INSTRUMENTATION AND SAMPLING SYSTEMS DEVELOPMENT

1. On-Line Sodium Purity Monitors

V. P. Kelly, W. H. Caplinger and D. W. Shannon

The objective of this activity is to develop and standardize on-line monitoring devices for the measurement and control of FFTF sodium coolant purity. Three major efforts are required to meet this objective:

1) Define and develop reference concepts for the FFTF on-line instrument package (OLIP) to provide design bases for experimental and prototype instrument packages.

2) Design, fabricate, and test an experimental system to be installed in the HEDL Sodium Studies Facility (325 Building) and to be used for engineering development and evaluation of on-line instruments developed at ANL and elsewhere. This system has been designed as the Sodium Purity In-Line Analytical Module (SPIAM).

3) Future fabrication of a prototypical on-line instrument system (POIS) for test at the EBR-II reactor.

a. FFTF On-Line Instrument Cell Concepts

W. H. Caplinger and V. P. Kelly

Work is continuing to firmly establish the cell concept and on-line instrument system within the next quarter. Continued design and study effort has confirmed these system requirements:

1) FFTF on-line instruments will be located in a shielded cell.

2) Sodium will be circulated through piping located in a below-grade pipeway, from the reactor sampling point to the cell and returned to a collection vessel or system.

3) One on-line instrument package (OLIP) will be provided for each reactor sampling point designated for the closed loops and the primary heat transfer system. Provisions for five OLIP's are being planned.

4) Each OLIP will consist of carbon, oxygen, hydrogen, and plugging meters connected in parallel or series to a sodium distribution

loop. The distribution loop in turn will be connected to the reactor sampling system.

5) The OLIP concept must provide reliability, maintainability, and operability consistent with the radioactive environment.

The FFTF on-line instrument cell concept proposed to meet these requirements is shown in Figure V-1. Separate cells 4-1/2 ft high and 7 ft long are provided for each OLIP to allow access to and maintenance on the individual package without interfering with others. Hinged steel shielding doors are indicated for each cell. Penetrations through the cell floors, walls and ceilings are provided for sodium piping, service feedthroughs, and cell ventilation ducts. The concept was considered to be the best of five candidates, based on technical and economic considerations.

b. Sodium Purity In-Line Analytical Module (SPIAM)

SPIAM design based on current FFTF on-line instrument package concepts, Figure V-2, features upper and lower sections of the distribution loop for sodium supply and return, with space and connections along the loop for installing instrument test sections in modular array. Functional requirements for SPIAM are given in BNWL-1200-4.

Sodium enters the SPIAM pump section from a separate source of supply and is pumped through the 1/2-in. pipe supply header, returning to the source of supply through the upper return header. Isolation valves and connectors at each test section permit independent removal or replacement of the instrument sections. SPIAM is housed in a metal enclosure for confinement of sodium or sodium smoke. An exhauster circulates cooling air through the duct and test sections during normal operation. If smoke is detected, power-operated dampers at the inlet and outlet of the enclosure close to shut off the air flow to facilitate fire control. Automatic safety shutoff valves near the sodium inlet and outlet also close in emergency to isolate SPIAM from the source.

In addition to providing an experimental test facility for development and nonradioactive design verification testing of FFTF in-line instruments, SPIAM will also be used where possible to demonstrate or extend

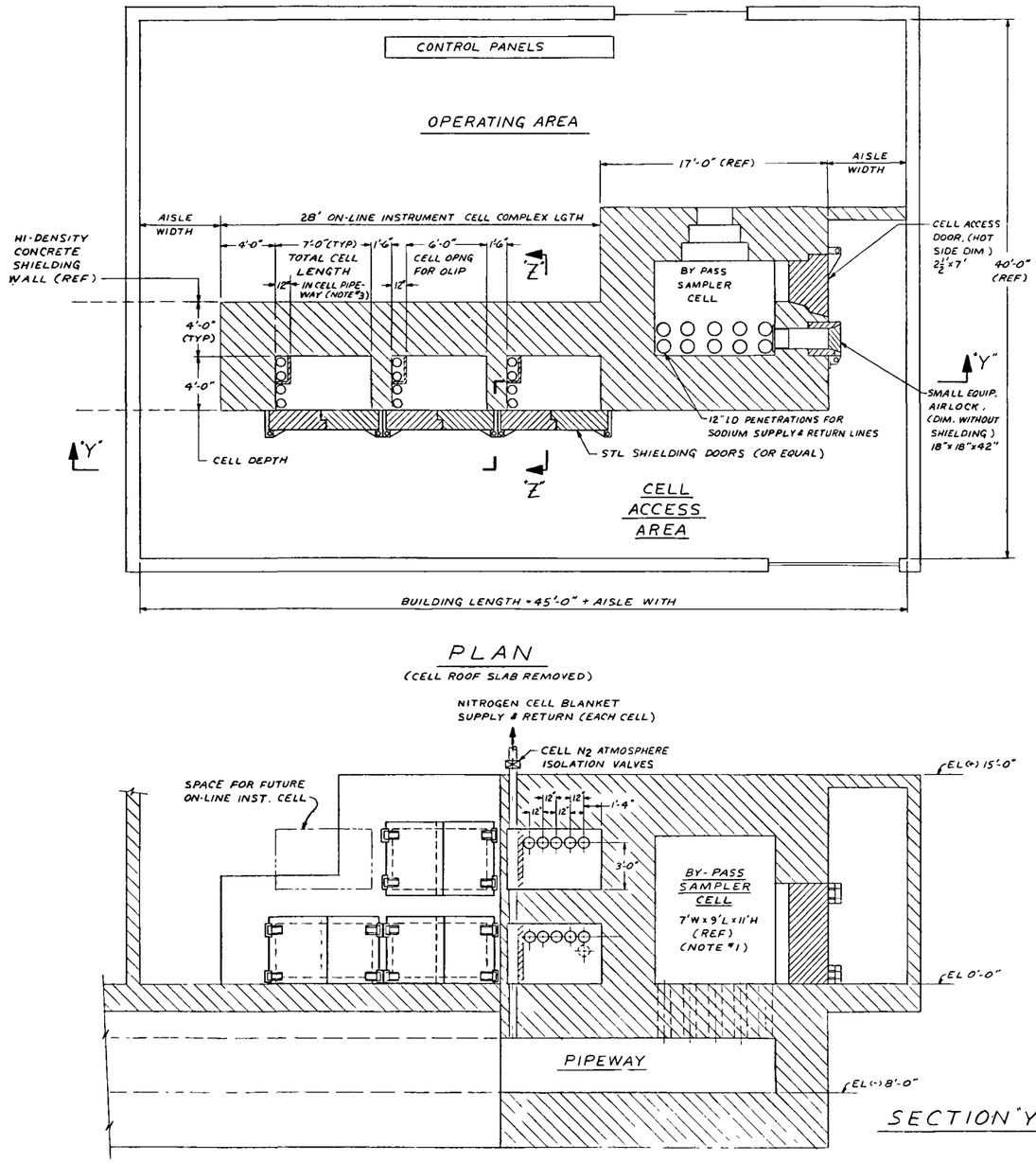

PLAN
(CELL ROOF SLAB REMOVED)

SECTION "Y-Y"

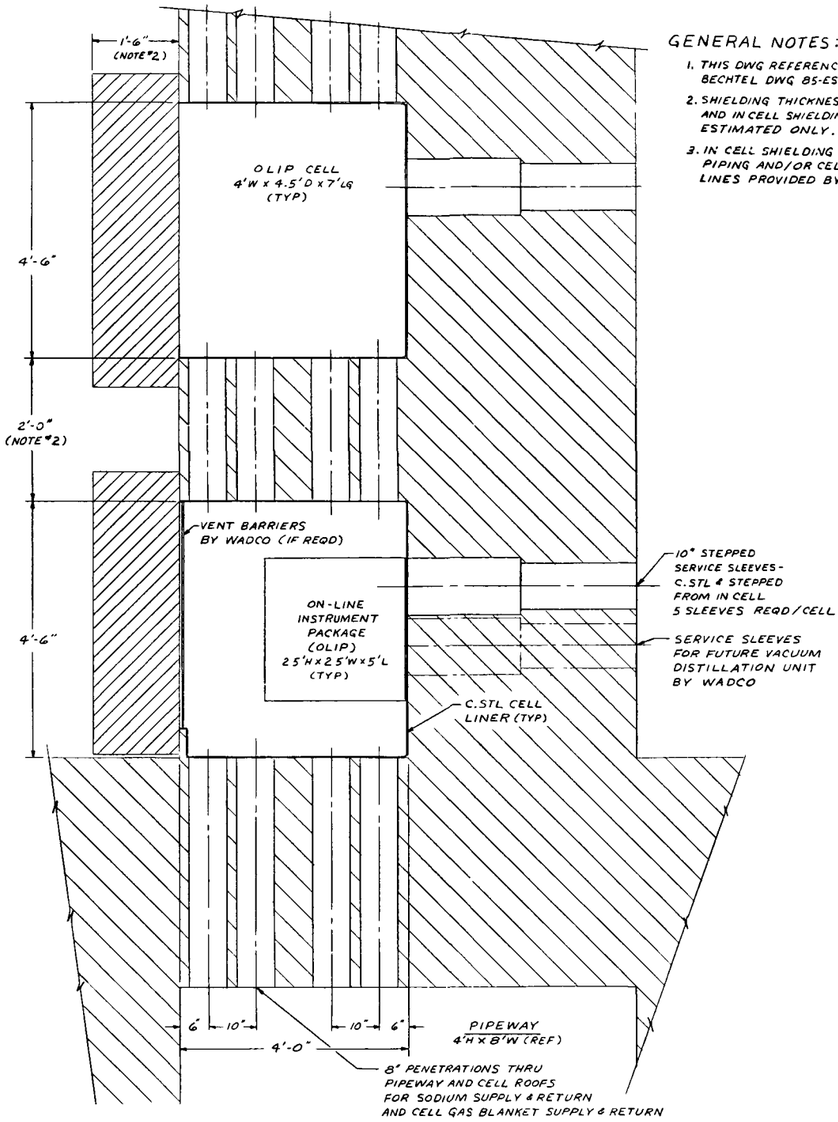

GENERAL NOTES:

1. THIS DWG REFERENCED TO BECHTEL DWG B5-ESK-M-150.
2. SHIELDING THICKNESS FOR DOORS AND IN CELL SHIELDING ARE ESTIMATED ONLY.
3. IN CELL SHIELDING FOR SODIUM PIPING AND/OR CELL VENT LINES PROVIDED BY WADCO.

SECTION "Z-Z"

FIGURE V-1 *Sodium Sampling Facility.*

LEGEND

EM = ELECTROMAGNETIC
FM = FLOWMETER
FR = FLOW RECORDER
JC = POWER CONTROLLER AUTOMATIC
JE = POWER SUPPLY
JK = POWER CONTROLLER MANUAL
P = PRESSURE
TE = TEMPERATURE ELEMENT
TC = TEMPERATURE CONTROLLER
TR = TEMPERATURE RECORDER
LL = LIQUID LEVEL
PT = PRESSURE TRANSMITTER
PI = PRESSURE INDICATOR
LA = LEVEL ALARM
TA = TEMPERATURE ALARM
LR = LIQUID LEVEL RECORDER

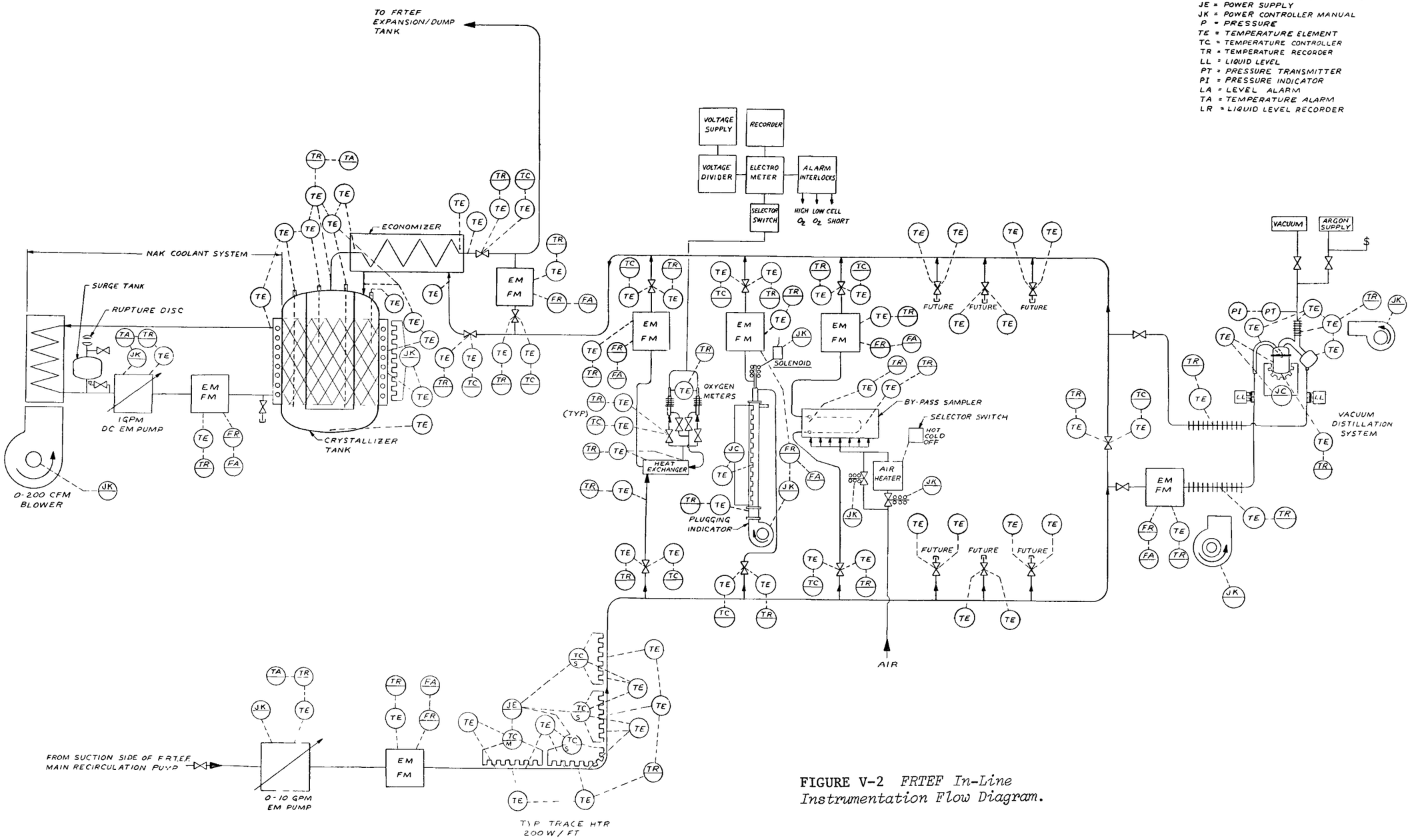

FIGURE V-2 *FRTEF In-Line Instrumentation Flow Diagram.*

the testing for other FFTF components or concepts. Two candidates identified to date are (1) FFTF trace heating system, using dual sheathed resistance heaters; and (2) FFTF differential pressure systems proposed for use in the bypass flow section.

The preliminary designs for SPIAM are presently being reviewed preparatory to final design review and processing of design documents for shop fabrication. Procurement of long-lead items has been initiated.

2. Selecting and Testing Cover Gas Instruments and Sampling Systems For FFTF

G. B. Barton , H. P. Maffei and F. A. Scott

The objective of this activity is to provide proven sampling and analysis equipment and technology for the cyclic on-line monitoring of impurities (including fission gases) in the FFTF argon cover gas.

Engineering testing of an analytical-scale, controlled-cooling-profile, reflux vapor trap has been started on the CGEL. These tests are to evaluate the vapor trap and one of Argonne National Laboratory (Kimont) design (Ref 1) for their effectiveness in removing sodium vapor from a flowing reactor cover gas argon stream. A primary objective of the present tests is to determine whether the trap will plug with sodium compounds when impure argon is passed through the sodium cover gas space and out the trap. On a system with sodium at 800°F, argon containing 500 ppm air could result in vapor with approximately 57% of the sodium present as sodium oxide. Operation for an extended period with such a leak is not anticipated, but its effects should be examined.

Prior to the introduction of such an impure gas stream, it is necessary to verify the satisfactory operation of the vapor traps with pure argon. Testing on this phase of the work was started this quarter. Some difficulty was encountered in adjusting temperature conditions so that the high decontamination factors previously measured in calibrating the controlled-cooling-profile trap could be duplicated. The vapor trap is being tested over flowing sodium at 800 °F and 1100 °F with argon cover gas flow

rates into the sodium pot of 0.75 to 1.5 liters/min.

The data are summarized in Table V-1 with an argon flow rate of 1.5 liters/min over 800°F sodium; the sodium concentration at the vapor trap outlet ranged from 13 to 120 ppm. It appears that the amount of sodium vapor escaping from the vapor trap is correlated to the trap's temperature profile. As the inlet vapor trap temperature was raised from an average of 600 °F to 900°F, the sodium vapor concentration at the outlet was lowered to 13 ppm, provided the outlet trap temperature was maintained at approximately 325°F. The same results can be seen for the tests over 1100°F sodium at a flow rate of 0.75 liters/min. The actual temperature profiles along the trap for the most efficient sodium removal runs at 800°F and 1100°F are shown in Figure V-3. The desired profiles are also shown for comparison.

TABLE V-1

SODIUM REMOVAL BY CONTROLLED-COOLING-PROFILE VAPOR TRAP

Sodium Temperature in Test Pot (°F)	Argon Cover Gas Flow Rate (liter/min)	Vapor Trap Temperature Inlet (°F)	Vapor Trap Temperature Outlet (°F)	Sodium Concentration in Argon Gas at Outlet of Vapor Trap (ppm)
800	1.5	644	365	67
	1.5	600	345	61
	1.5	700	345	80
	1.5	650	315	62
	1.5	750	400	120
	1.5	850	400	26
	1.5	850	400	20
	1.5	850	325	28
	1.5	900	325	13
	0.75	900	325	3
	0.75	900	325	1
1100	0.75	1185	405	0.5
	0.75	1400	?	1.5
	0.75	1100	450	5.0
	0.75	1200	420	1.5

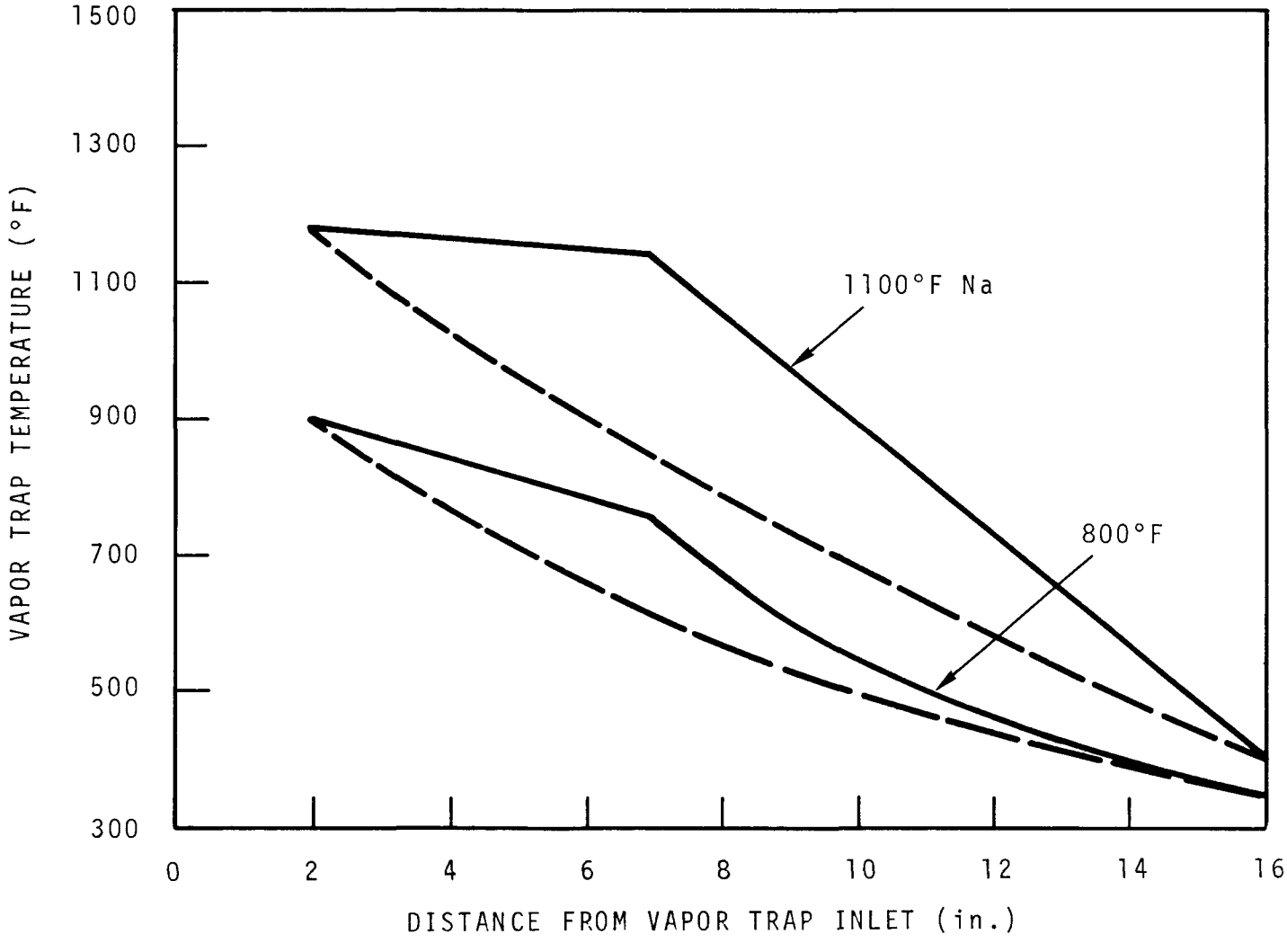

FIGURE V-3 *Actual Temperature Profiles of The Controlled-Cooling-Profile Vapor Trap Compared With the Desired Profiles.*

The low sodium removal rates at 800°F compared to those at 1000°F were surprising. Preliminary measurements of the source terms in the two pots reveal that the gas phase in the 800°F pot contains a very large quantity of mist (approximately 200% of saturation) while that in the 1000°F pot is close to saturation. The marked improvement in sodium removal obtained by raising the trap inlet temperature on the 800°F pot undoubtedly results from a partial revaporization of this mist. To permit the trap to handle vapor from any source, the heaters are being redesigned to include a pre-heater section to vaporize any mist prior to passage through the controlled-cooling profile region.

3. Vacuum Distillation Sampling

G. E. Meadows and D. W. Shannon

HEDL has the lead responsibility for developing and proof testing a remotely operated distillation sampler for the FFTF. In addition to being used for trace metal and other non-volatile residue analyses, the sampler may be required to provide bulk sodium samples for other chemical analyses.

A review of operational distillation sampler designs has not revealed a sampler design that fulfills all of the requirements for an on-line distillation sampler for FFTF. The LASL laboratory model distillation sampler and the EBR-II trace metal distillation sampler have been selected as the basis for the development of the FFTF sampler; these designs have documented sampling histories.

Initial testing of in-line distillation sampling will begin on the SCEL. A LASL laboratory model (fabricated and received from LASL as surplus) has been modified and incorporated in the SCEL sample station.

4. FFTF Plugging Meters Selection

G. E. Meadows and D. W. Shannon

A review of the on-line instrument needs for FFTF and related facilities indicates the need for selecting a "standard" plugging meter for

application to all FFTF facilities; this would ensure a uniform approach for using a plugging meter for measuring sodium purity. Prior to this report period, two basic designs were evaluated:

1) The plugging meter developed at LASL, which incorporates an orifice plate as the plugging restriction, and
2) The EBR-II operations plugging meter, which has a modified valve with a fluted stem as the plugging restriction.

During this report period, an additional meter design has been selected for evaluation, which is a modified version of the experimental plugging meter undergoing recent development at EBR-II. The design incorporates a 60-micron filter as the plugging restriction; it offers some additional capabilities that designs 1 and 2 do not. Preliminary evaluation of the concept at EBR-II indicates that the meter has extreme sensitivity to impurities and a capability for quick determination of low (<250°F) plugging temperatures.

The three plugging meter designs will be evaluated on the SCEL to select a "standard" meter and to establish a uniform operating procedure.

5. Surveillance Methods for Deposited Radioactivity in FFTF

W. F. Brehm and D. W. Shannon

The purpose of this activity is to establish possible methods for monitoring the reactor core and heat transport system for materials degradation and radioactivity buildup. This activity has just begun; initial efforts are concerned with identifying critical system components and regions. It is planned to monitor radioactive buildup rates during FFTF operation. During this past quarter, tests were run to see if activated corrosion products could be identified by counting through the pipe walls.

A section of pipe from the Radioisotope Transport Loop containing deposited Mn^{54} and Co^{60} was counted on the Ge(Li) diode in four configurations (Figure V-4):

1) Pipe flush against the diode
2) One-quarter inch of stainless steel between diode and pipe.

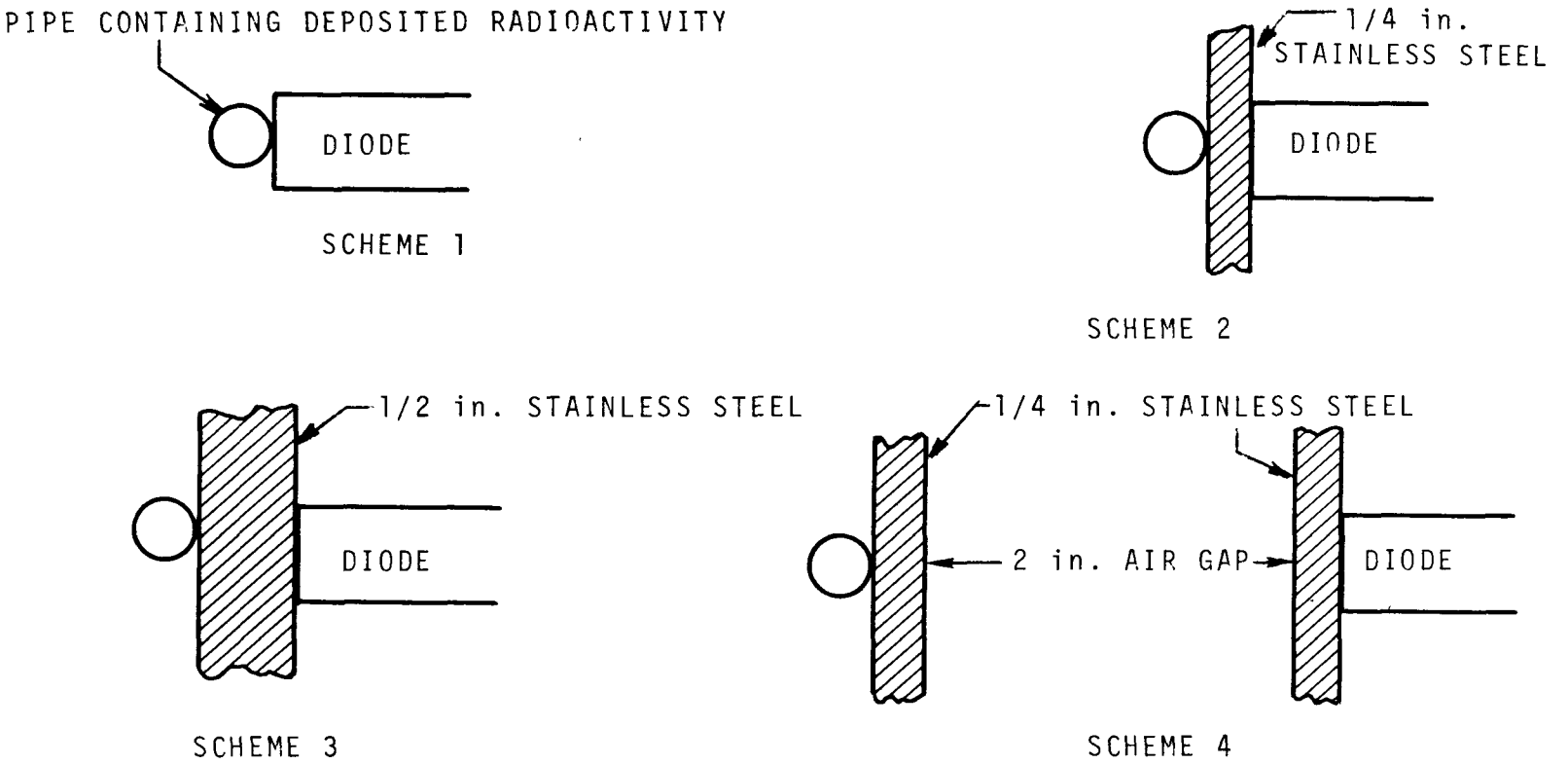

FIGURE V-4 *Counting Configurations Tested With Radioisotope Transport Loop Pipe*

3) One-half inch of stainless steel between diode and pipe

4) One-quarter inch of stainless steel, two inches air, one-quarter inch stainless steel between diode and pipe.

These configurations attempted to duplicate the FFTF piping thickness with and without a guard vessel, such as will be placed around the pump and IHX.

The spectra of the Mn^{54} and Co^{60} were attenuated (peak height decreased) by the presence of the stainless steel, but the spectra were not distorted, as seen in Figures V-5 and V-6. The attenuation in the steel-air gap-steel configuration was a factor of five; less attenuation occurred in the other configurations. These results show that monitoring radioactivity buildup by gamma scanning is a good possibility provided it is conducted when the sodium twenty four activity has decayed.

6. Oxygen-Sensing Solid Electrolytes

W. A. Ross and E. T. Weber

This program provides fabrication technology, characterization, testing and procurement of ceramic electrolyte tubes in support of oxygen meter development programs for liquid sodium applications.

a. Fabrication Process Development

Fabrication technology development has progressed in four areas during this quarter:

1) Furnace installation,

2) Powder preparation method,

3) Isostatic pressing methods, and

4) Sintering methods.

The Centorr graphite resistance furnace received from ANL has been installed. The power control system and safety interlocks are operating. The furnace response and behavior has fulfilled all expectations.

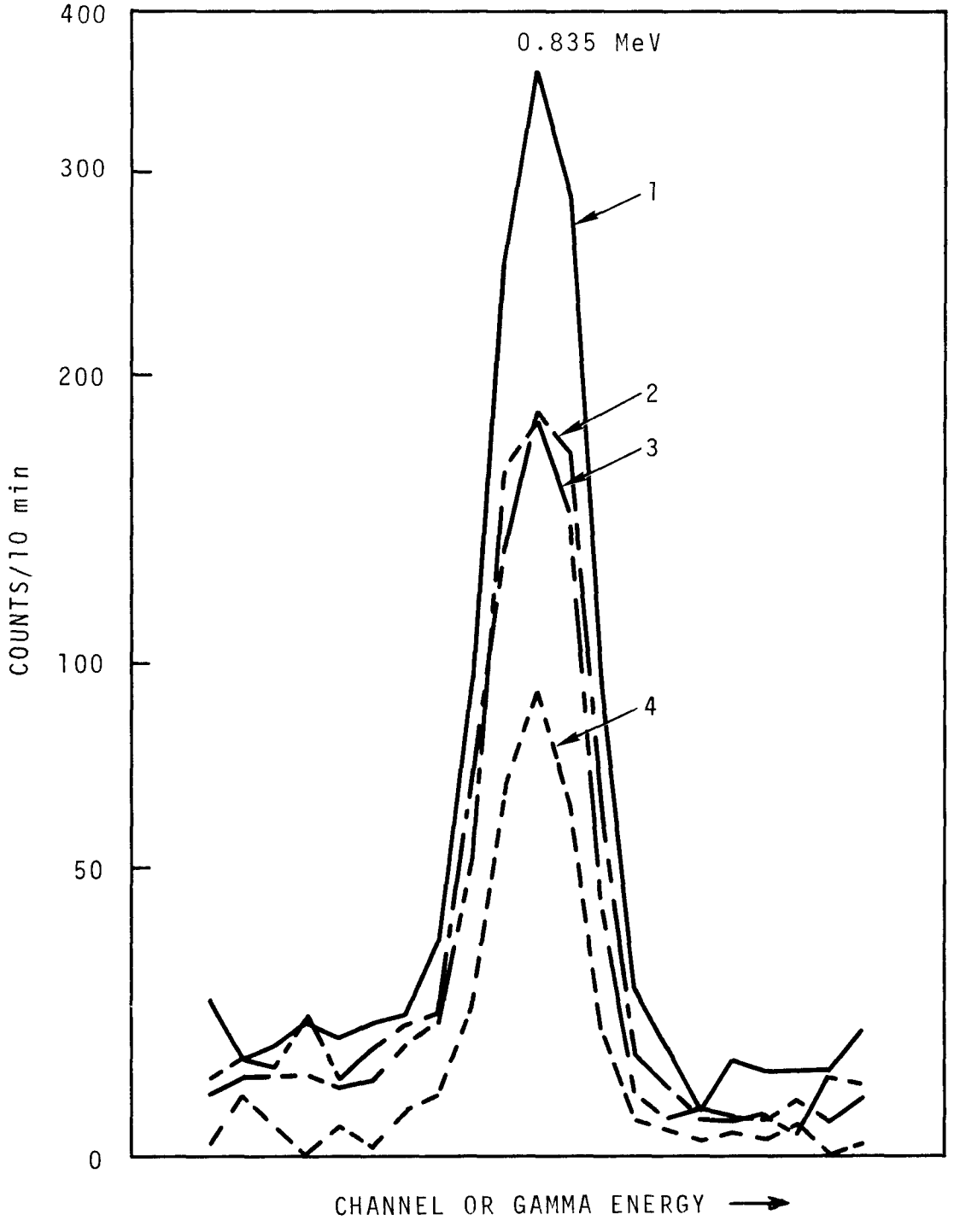

FIGURE V-5 *Spectrum From Deposited Mn^{54} Under Various Counting Configurations.*

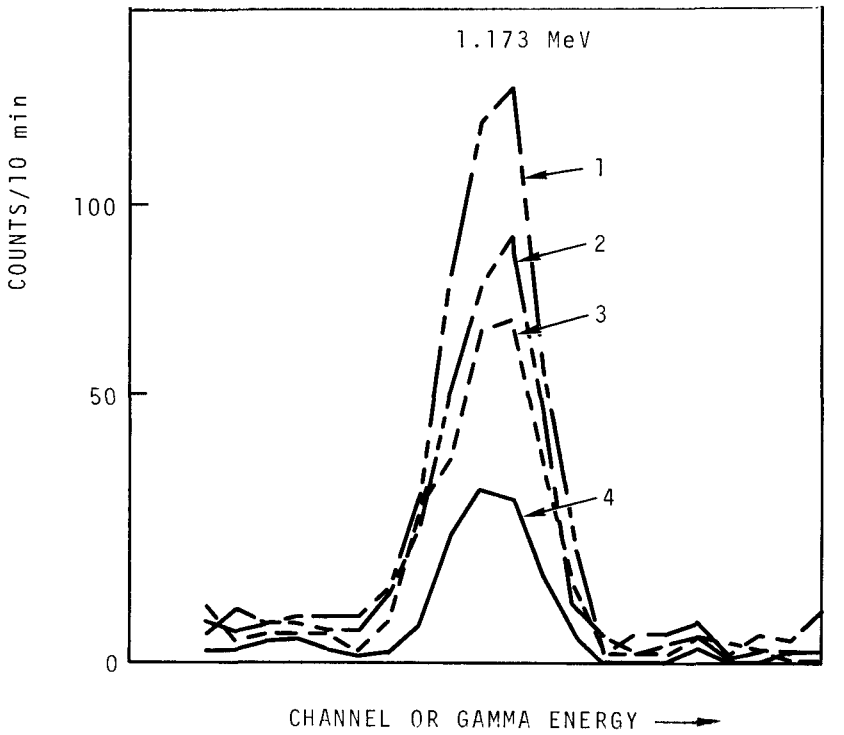

FIGURE V-6 *Spectrum From Deposited Co^{60} Under Various Counting Configurations.*

For efficient tube production, it is necessary to scale up the powder preparation methods from the 100 gram batch used for laboratory samples. The initial attempt was to use a larger 00 (0.3 gal) Burundum mill with ZrO_2 balls. However, ball milling time doubled to four hours (to activate the powder for high sintered density) which resulted in increased impurities and less resistance of the material to sodium attack.

A rubber-lined mill with tungsten carbide balls has also been tried without success to date. The white starting powder is gray after a three-hour ball milling and the powder still does not have sufficient activity to sinter to desired density of 96% T.D.

A high purity Al_2O_3 mill with ZrO_2 balls has been used with the four-hour milling time to achieve the desired density. A test of sodium com-

patibility of sintered tubes obtained from this powder is now in progress. The rubber lined mill is being used with ZrO_2 balls as a backup to the high purity Al_2O_3 mill.

A mold for isostatic pressing the solid electrolyte tubes has been designed and developed (see Figure V-7). The mold consists of a mandrel (C) with a silicon rubber boot (B) surrounding the mandrel. The boot and mandrel are held in the desired positions by a mold (A). Powder is fed into the region between the mandrel and boot through holes in the top of the mandrel. Powder is packed into the mold assembly by a combination of vibration and by hand to obtain a uniform fill. The mandrel and boot are then removed from the surrounding mold and inserted into the isostatic pressing chamber. Successful pressing has occurred at a pressing pressure of 10,000 psi. Item D in Figure V-7 is a ThO_2 - Y_2O_3 tube fabricated in this mold and partially sintered. A new mold and mandrel are now being fabricated to obtain the dimensions required by revised specifications for tubes for the Westinghouse oxygen meter.

Tubes sintered in the Centorr furnace at 1800° and 1900°C show a gradient of gray coloring from top to bottom. The upper end of the tube is typically quite dark. The darker region is used to support the tubes and is separated from the graphite holder by a 0.005-inch molybdenum foil. A carbon analysis of an upper and lower region of the tubes sintered at 1900°C showed that approximately 500 ppm of carbon was picked up by the upper (supporting) section of the tube. A large refractory metal insert will be fabricated to further separate the ThO_2 - Y_2O_3 and graphite; this should reduce the carbon concentration. A discolored tube was reheated in air at 1000°C, and it returned to its normal white, but all effects of the re-oxidation have not yet been determined. In previous work (Refs 2 and 3) carbide inclusions were formed at much higher temperatures (2150°C). Re-oxidation reduced the strength of the material and also its compatilility with sodium.

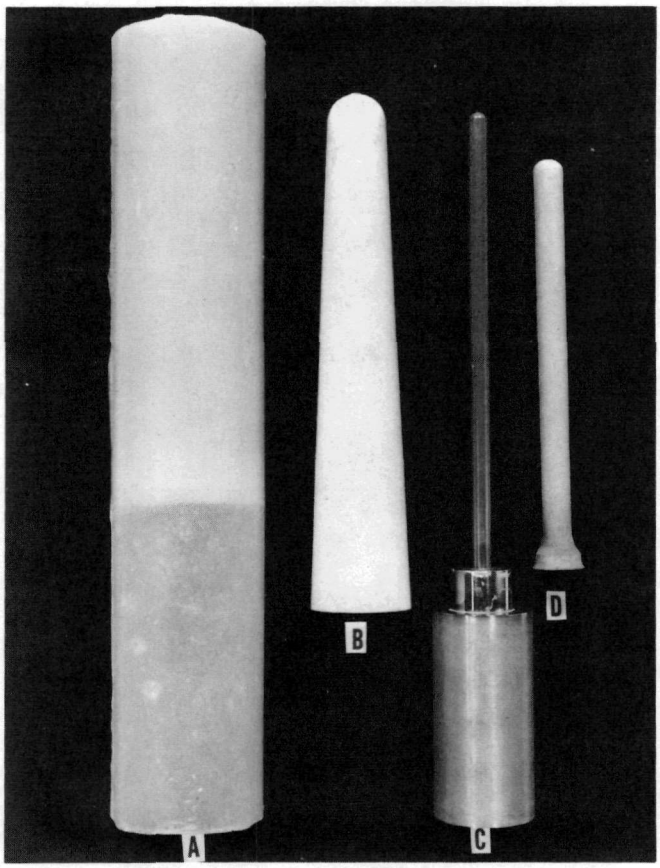

FIGURE V-7 *Isostatic Pressing Assembly. A-Alignment Mold. B-Silicon Rubber Boot. C-Pressing Mandrel. D-Electrolyte Tube Produced From Mold.*

The sintered isostatic-pressed tubes have exhibited a high degree of wall uniformity and have been well within the 0.015-inch maximum bow specifications.

b. Characterization of Electrolyte Tubes

The final PNL-Zircoa "improved" (7% Y_2 - ThO_2) tubes (Z-4) have been tested and characterized. It should be noted that "Improved" denotes tubes fabricated by slip casting from pre-calcined powder. "Standard" denotes Zircoa production tubes. Table V-2 compares a chemical analysis of three

TABLE V-2

COMPARISON OF IMPROVED ELECTROLYTE TUBES WITH STANDARD TUBES

Sample	Z-4-1*	2-4-7*	2-4-10*	Standard**
Al	60	30	30	>575
Ca	300	90	90	120
Mg	60	200	6	>1000
Si	60	200	200	270
Zr	3000	3000	3000	-

* Analysis by spark source mass spectrography
Accuracy est. at ± 300%.

** Analysis by emission spectrochemical methods
Accuracy est. at ± 200%.

"improved" tubes, which were fabricated with minor process variations, to a "standard" 15% Y_2O_3 - ThO_2 tube (Ref 5). The Al and Mg have been reduced in the "improved" tubes by about an order of magniture relative to the "standard" tube. Ca and Si are nearly the same in both types. The microstructure of the "improved" tubes does not contain the large areas of second phase. However, a very fine and dispersed second phase exists, apparently concentrated at grain boundary triple points.

The sodium compatibility tests on these tubes revealed a large variation in the sodium resistance of a single section of a tube. Micrographs in Figures V-8 and V-9 were taken of a section of tube Z-4-1 tested in sodium containing approximately 9 ppm Na_2O at 800°C for 100 hours. Figures V-10 and V-11 are micrographs of tube Z-4-1 tested in sodium containing saturated Na_2O (∿9000 ppm) at 800°C for 100 hours. Examination of an as-received section of tube Z-2-1 revealed a gradual increase in second phase from one side to the opposite side. Figures V-12 and V-13 illustrate the

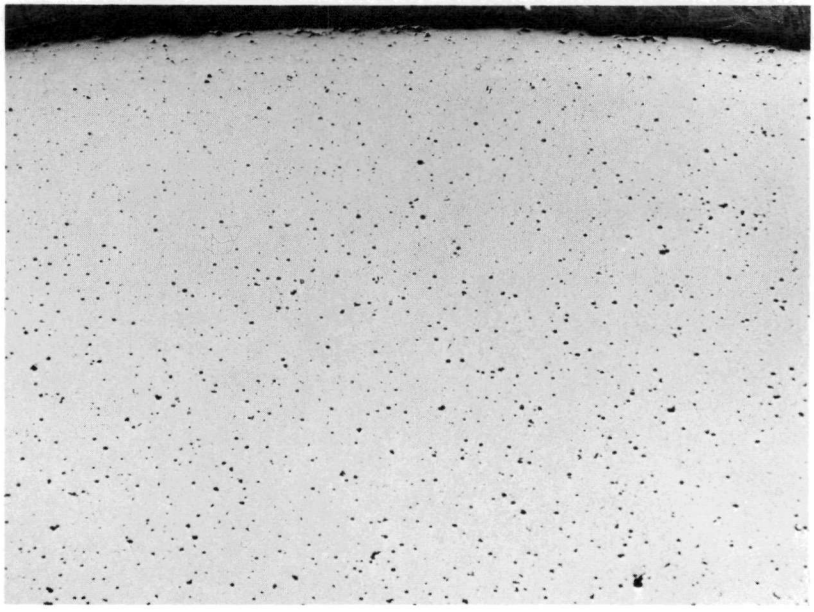

80X

FIGURE V-8 *Photomicrograph showing Unattacked Surface Section of Z-4-1 tested in Clean Sodium at 800°C for 100 hours.*

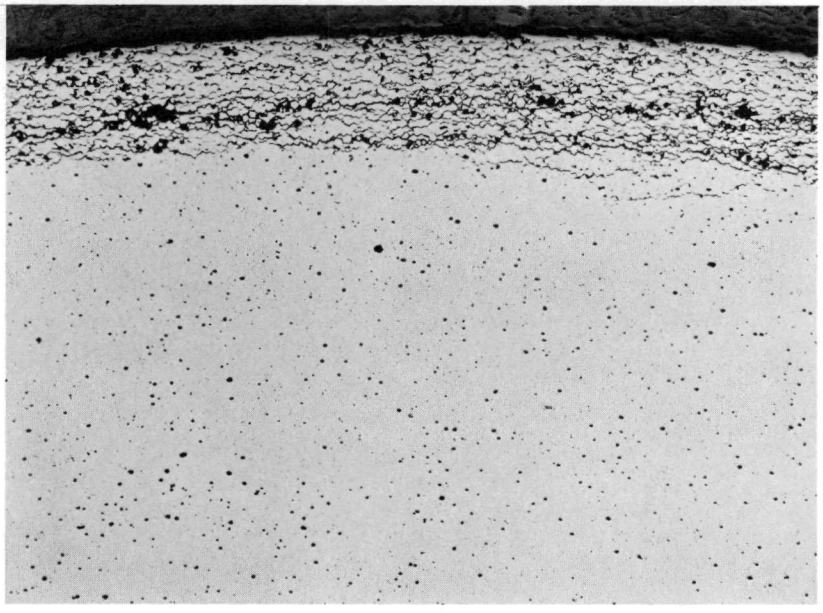

80X

FIGURE V-9 *Photomicrograph showing Attacked Surface Section of Z-4-1 Tested in Clean Sodium at 800°C for 100 Hours.*

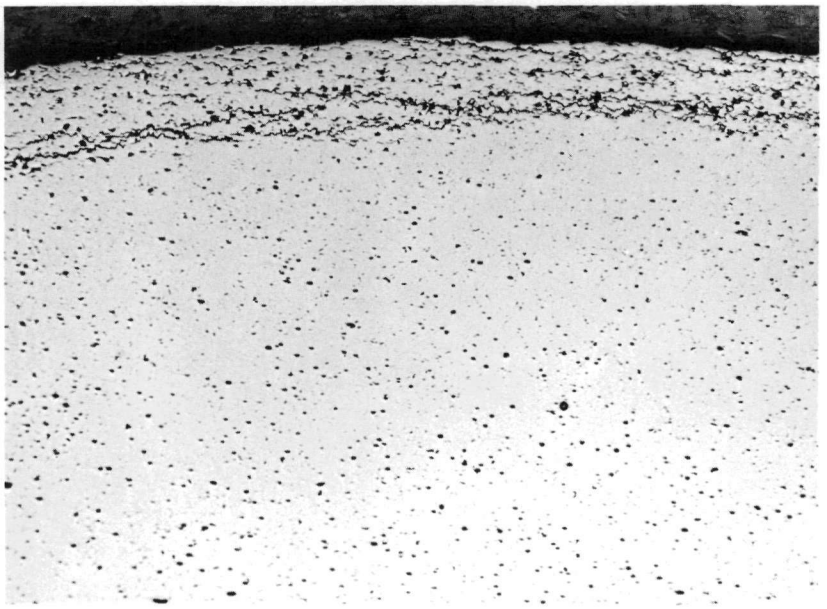

80X

FIGURE V-10 *Photomicrograph showing Slightly Attacked Surface Section of Z-4-1 Tested in Na_2O Saturated Sodium at 800°C for 100 Hours.*

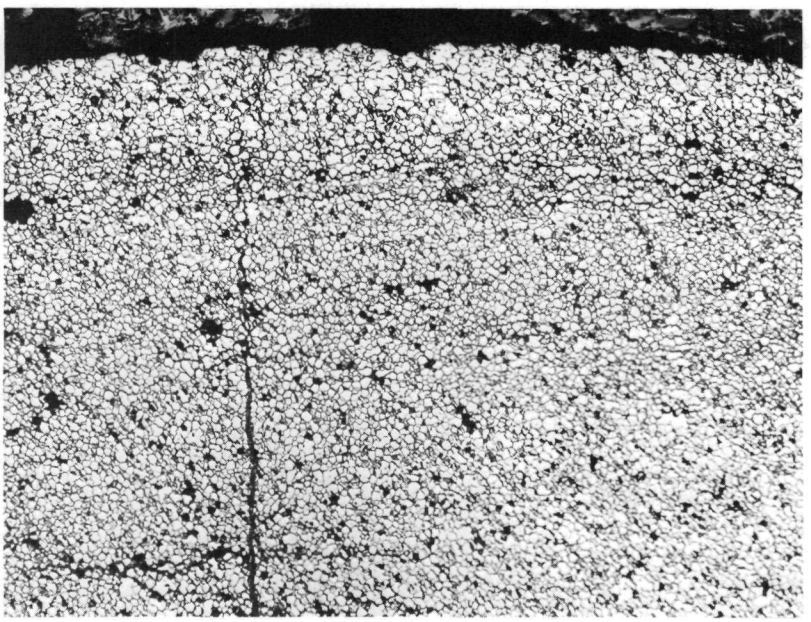

80X

FIGURE V-11 *Photomicrograph Showing Highly Attacked Surface Section of Z-4-2 Tested in Na_2O Saturated Sodium.*

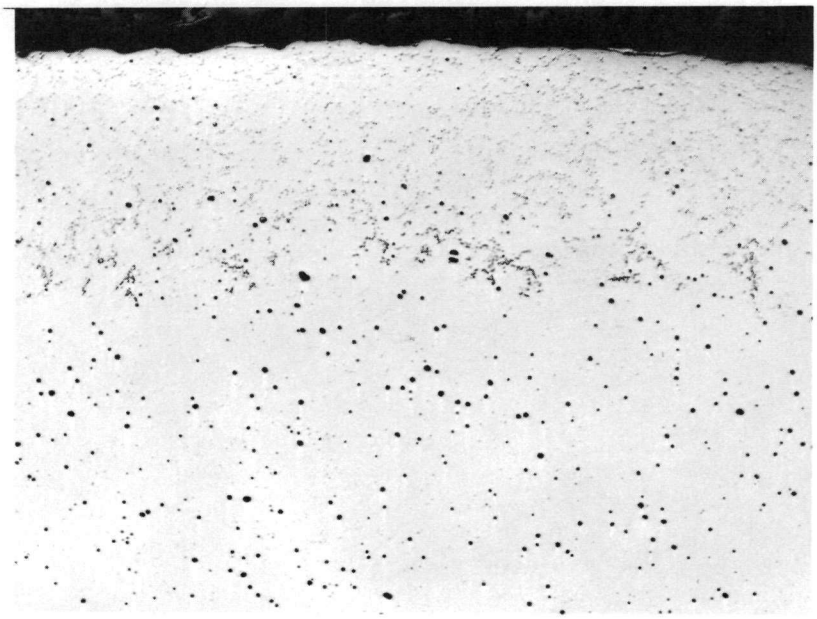

100X

FIGURE V-12 *Photomicrograph of As-Received Section of Tube Z-2-1 Showing High Concentration of Second Phase Near Surface.*

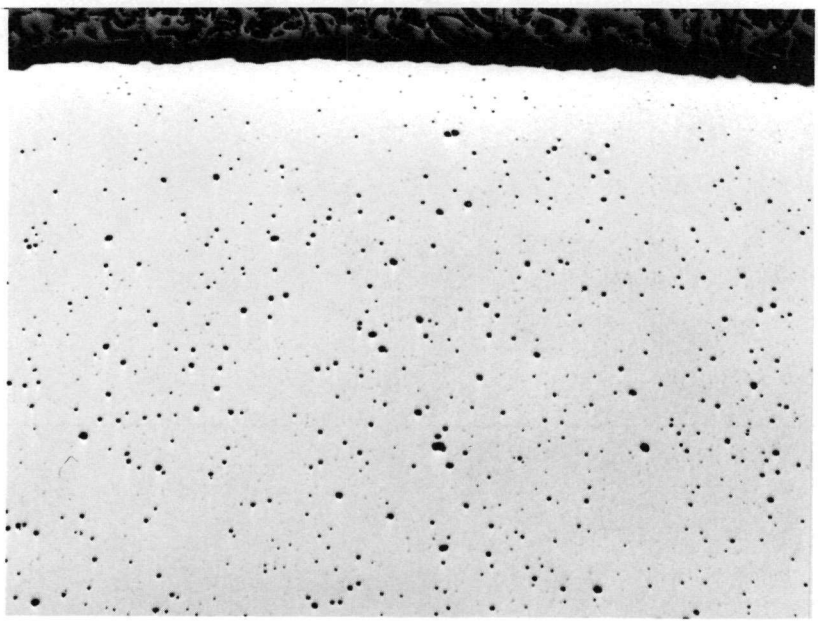

100X

FIGURE V-13 *Photomicrograph of As-Received Section of Tube Z-2-1 Showing Absence of Second Phase Near Surface.*

degree of difference in concentration of the second-phase in one tube. A spark source mass spectrographic analysis of the regions in the tube sections with and without second-phase is summarized in Table V-3. Also included in Table V-3 is impurity data on two HEDL-produced materials which are quite resistant to sodium attack. The analysis indicates that Zr, Si, Mg, and K are main contributers to the second phase. Silicon is the most highly suspect material for decreasing the resistance to sodium attack.

TABLE V-3

COMPARISON OF TWO HEDL-PRODUCED SAMPLES

	Tube Section Z-2-1 with second-phase	Tube Section Z-2-1 without second-phase	HEDL Sample 18-8	HEDL Sample 78-7
Al	90	90	300	30
Ca	100	100	20	4
Cr	5	2	5	0.5
K	40	3	3	1
Mg	200	200	7	10
Mn	5	0.6	3	0.5
Na	20	10	40	0.6
P	3	1	3	0.3
Si	200	60	60	20
Zr	10,000	4000	20	60

It was previously reported that a correlation between resistance to sodium attack and resistance of the microstructure to etching by concentrated phosphoric acid might be possible. To define the etch test temperature for obtaining the best correlation with sodium resistance, samples were selected from "improved" Zircoa fabricated tubes (slip cast) and HEDL fabricated material. This gave materials which previously had been shown to be resistant to and prone to sodium attack. Temperatures of 90°C, 112°C and 135°C were used in etching the material in phosphoric acid. The only temperature at which the materials etched was 135°C. At that temperature, all materials appeared to be affected, contrary to the tentative correlation.

c. Impurity Test

An experiment to determine the effect of specific impurities on resistance to sodium attack is in progress. Samples were taken from a single batch of material and then doped with 50 and 500 ppm of SiO_2, CaO, Al_2O_3, MgO, Fe_2O_3, or ZrO_2. Pellets were formed and sintered in one firing. An undoped pellet was sintered and tested as a control. All pellets have been exposed to liquid sodium containing 6000 ppm Na_2O at 800°C for 100 hours. The pellets are now being examined to determine susceptability to sodium attack.

d. Electrolyte Tube Procurement

A goal of this program is to establish specifications to be used to obtain high integrity solid electrolyte tubes from a commercial supplier. A preliminary set of specifications has been written; this will be used to establish a commercial source of electrolyte tubes, for which procurement activity has been initiated. Tubes received from a vendor will be fully characterized to determine conformance with the specifications and to test sodium compatibility. Tubes meeting specifications and showing adequate protection against sodium attack will be supplied to Argonne National Laboratory for use in large-scale testing of oxygen meters.

7. Thermal Shock Test of Oxygen Meter Ceramic Tubes

W. H. Caplinger, V. P. Kelly and D. W. Shannon

Objectives of this task are to determine the thermal shock rate which causes failure of the ceramic in the standard UNC oxygen meter geometry, and to compare this shock rate with that for an improved purity electrolyte tube and the electrolyte tube selected for the Westinghouse standard oxygen meter.

The results of thermal shock tests on four tubes indicate that the oxygen meter ceramic, when installed in the standard UNC housing, is more resistant to thermal shock than was expected. Temperature ramping rates of less than 100°F/min were expected to break the cells; however, three of the four tubes withstood rates of over 200°F/min, and the one tube which broke did so at a rate of about 150°F/min. A photograph of the broken tube is shown in Figure V-14. The experimental procedure used placed the electrolyte tube in the standard UNC housing on the Small Heat Transfer Loop (SHTL) in a special thermal shock test section. The temperature was then ramped from 500°F to 600 to 700°F at increasing rates. Temperatures, as measured by thermocouples immersed in the sodium and inside the ceramic, were followed to determine the point where failure occured. An initial ramping rate of 20°F/min was used. This was increased, in about 20°F/min steps, until rates of >200°F/min were attained.

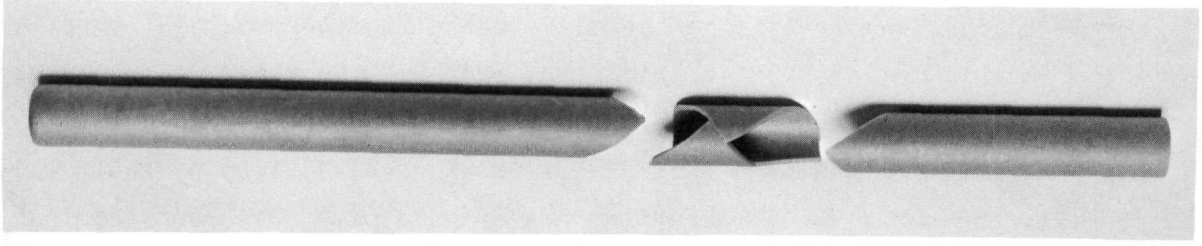

FIGURE V-14 *Broken Oxygen Meter Ceramic Tube After Thermal Shock Test.*

The broken tube,as shown in Figure V-14, broke about 4 to 4-1/2 inches above the bottom of the ceramic, or about three inches above where the maximum temperature gradient was expected. From the angle and the appearance of the fracture, shear or torsional forces were apparently present. Not only was the location of the failure a bid odd, but the mode of the failure does not indicate thermal shock.

Of the four tubes tested, two had hemispherical shaped bottoms and two had flat bottoms. The tubes received no pre-treatment except a vacuum drying and outgassing in a furnace at 250°F. All four of the tubes had been slip cast by Zircoa some time ago and did not include the improvement in purity as developed by HEDL.

The data suggests that the failure mechanism of the ceramics which have failed previously in service likely involves stresses in addition to thermal shock.

8. Segregation of Impurities During the Cooling and Freezing of a By-Pass Sodium Sample

T. J. Kabele and F. A.Scott

An analytical study has been made to estimate the degree of segregation of impurities (such as sodium oxide) due to diffusion in a sodium by-pass flow sampling tube during cooling and freezing. The driving force for segregation would be a radial concentration gradient, established as a result of the radial thermal gradient present during the cooling process. Any significant segregation of impurities near the tubing walls could lead to erroneous analytical results if the frozen sodium were removed from the sample tubing by melting or extrusion, as both processes tend to leave some sodium on the wall of the tubing after the sample has been removed.

Results showed that diffusion of sodium oxide toward the tube wall as a result of the thermal gradients established during cooling is insignificant. Even with a high thermal gradient, diffusion is very small and is probably negligible in the real system.

a. Thermal Gradients

In modeling the process, many simplifying assumptions were made. However, each was made conservatively; therefore, the resulting model is far more conducive to segregation than the real system. Briefly, the major assumptions are:

1) No convection occurs in the liquid sodium.
2) The heat of fusion was neglected in the heat transfer calculations.
3) The resistance to heat transfer of the tube wall and gas boundary layer was ignored.
4) The thermal properties of liquid and solid sodium were assumed to be independent of temperature and nearly equal.
5) Mass is transferred only by the method described in the previous section. (No thermal diffusion.)

All of these assumptions led to the formation of the steepest thermal gradients possible, and hence, to the largest diffusion rates.

When the cooling begins (t = 0), the outside temperature of the tube is dropped to about 100°F. The sodium cools rapidly, freezing from the tube wall inward. If the liquid sodium is treated as a physically immobile medium (no convection), with thermal properties similar to the solid sodium, then the problem, thermally, approaches that of the cooling of an infinite, solid cylinder, as given by Carslae and Jaeger (Ref 4).

b. Concentration Gradient

If a temperature gradient can be established for the system, the concentration gradient for any impurity whose saturation temperatures are known can be calculated. Once the concentration gradient is known, one can directly estimate the diffusion rate along that gradient using Fick's Law in cylindrical coordinates,

$$R \frac{\partial C_i}{\partial t} = D_i \frac{\partial C_i}{\partial R} \qquad (1)$$

where:

t = time

R = radius of tube

α = thermal diffusivity of the cylinder

C_i = concentration of impurity in sodium

D_i = diffusivity of impurity in sodium

The only remaining information needed to calculate a diffusion rate based on Equation (1) is the diffusivity of sodium oxide in liquid sodium. This information is almost totally lacking, with only questionable values reported. The best, conservative estimate is that a diffusivity of about 10^{-5} cm^2/sec should suffice for most of the impurities found in sodium systems.

c. Results and Discussion

At values of $\alpha t/R^2$ greater than 1.0, the temperature gradients predicted by Ref. 4 are quite small and not conducive to segregation by the diffusion mechanism under consideration here.

Table V-4 presents values of $\alpha t/R^2$ versus time for 600°F sodium and 1/2 in. diameter tubing.

TABLE V-4

VALUES OF $\alpha t/R^2$ VERSUS TIME

Time	$\alpha t/R^2$
1 sec	1.65
30 sec	49.5
1 min	99.0
5 min	495.0

Since all values of $\alpha t/R^2$ in Table V-4 are greater than 1.0, it is evident that a significant temperature gradient exists only for an extremely short time after cooling begins. This rapid equilibration of temperatures across the tube radius is a result of the high thermal conductivity of sodium.

Using the model, it is instructive to calculate a diffusion rate for a severe thermal gradient to see just how much diffusion could occur in an extreme situation. Using oxygen as the impurity, it is assumed (again

conservatively) that the sodium is saturated with sodium oxide before cooling begins. The following parameters were used to estimate local changes in concentration, with respect to the radius, caused by diffusion toward the tube wall (Table V-5)

$\alpha t/R = 0.1$

$R = 0.25$ in.

$D_i = 10^{-5}$ cm^2/sec

$T_o = 600$ °F

$T_1 = 100$ °F

TABLE V-5
LOCAL CONCENTRATION CHANGES FROM DIFFUSION CAUSED BY COOLING

Position	Concentration Change
0.5 R	0.28 wppm/min
0.7 R	0.20 wppm/min
0.9 R	0.16 wppm/min

B. SODIUM PROPERTIES AND PURIFICATION

1. Sodium Properties

W. H. Yunker and D. W. Shannon

The document "Standard FFTF Values for the Physical and Thermophysical Properties of Sodium," (WHAN-D-3) has been published. The purpose of the document is to present a single set of values for the physical and thermophysical properties of sodium for use by all individuals and organizations contributing to or associated with the FFTF Project.

2. Reactivity of FFTF Coolant Fluids With Sodium

W. H. Yunker and D. W. Shannon

An assessment was made of the chemical reactivity of several proposed coolant fluids for the FFTF Plant Heating and Ventilation System (including the nitrogen cell coolers). Of primary interest were the hazards that might be created by accidental discharge of the coolant into various parts

of the plant (in particular, the containment vessel). The proposed fluids were Freon 113* (1, 1, 2- trichloro, 1, 2, 2-trifluorethane), water, organic liquids (hydro-carbons and silicone oil) and ammonia. Since the specific reaction conditions affect the amounts of the various reaction products generated, a precise estimate of the energy released is virtually impossible to predict. In the summary below, typical examples of reactions are shown for comparative purposes.

Freon 113 is a common halocarbon refrigerant. As a class, halocarbons are known to react vigorously with sodium. However, no specific or comparative information on reaction conditions, products or rates was found for Freon 113 and sodium. It can be assumed, however, that the reaction would be chemically complex.

To illustrate, the heat of reaction for

$$1/2\ [2\ CClF_2CCl_2F_{(g)} + 2\ Na_{(l)} = 2\ NaCl_{(s)} + CClF_2CClFCF_2CCl_2F_{(g)}] \quad (2)$$

was calculated to be -87 Kcal/mole per halide atom reacted at 1400°F. (Probably more than one halide atom per molecule will react.) This is compared to

$$2\ Na_{(l)} + H_2O_{(g)} = Na_2O_{(s)} + H_{2(g)} \quad (3)$$

with a heat of reaction of -41 Kcal/mole at 1400°F.

To check the rate of reaction experimentally, 1/2 gram of sodium was heated to 400 to 500°F in a nickel crucible under an argon blanket. With a syringe, 0.05 ml of Freon TF Solvent (113 high purity) was injected into the center of the sodium drop. The reaction was instantaneous, violent, gave a large yellow flame and the sound of a small firecracker. It was repeated several times. For comparison, the same quantity of water was injected in the same manner. The reaction gave a sputtering sound, and a small yellow flame was sustained only while the water was being injected.

The heat of reaction of water and sodium is given above. The absence of oxygen in the nitrogen cells would prevent the subsequent burning of hydrogen commonly observed when the reaction occurs in air. The caustic formed during the cleanup of a spill could cause additional problems in some circumstances.

* U.S. Patent Office for E.I. DuPont DeNemours & Co.

While organic liquids (hydrocarbons and silicone oil) are relatively inert to sodium, they undergo thermal decomposition (cracking) at temperatures of 600°F and above and are subject to radiation damage. Such products (e.g., additional gas formation, soot, clouds of condensed vapor) can contribute to the problems of an already difficult situation. Discharge of hot hydrocarbons in air obviously would be a fire hazard.

In the presence of sodium, the reaction to form sodium amide

$$Na + NH_3 = NaNH_2 + 1/2\ H_2 \quad \Delta H^\circ_{25^\circ C} = -17\ \text{Kcal/mole} \tag{4}$$

proceeds with either liquid or gaseous NH_3. Sodium amide decomposes above 335°C

$$NaNH_2 \rightarrow Na + 1/2\ N_2 + H_2 \tag{5}$$

Amide could accumulate and later decompose rapidly as the temperature was raised above 335°C, forming the gaseous products. A mixture of 15 to 25% of ammonia and air can be ignited at temperatures above 1200°F. The reaction can occur at considerably lower temperatures on the surface of a heated metal oxide (such as iron oxide) or platinum catalyst. The overall reaction for complete oxidation:

$$4\ NH_3 + 3\ O_2 = 6\ H_2O + 2\ N_2 \quad \text{Temperature} = 900^\circ K\ (1160^\circ F), \tag{6}$$

has a standard heat of reaction of -75 Kcal/mole of Nh_3. For comparison, the complete oxidation of propane

$$C_3H_8 + 5\ O_2 = 4\ H_2O + 3\ CO_2 \quad \text{Temperature} = 900^\circ\ K\ (1160^\circ F), \tag{7}$$

has a standard heat of reaction of -490 Kcal/mole of C_3H_8. On the basis of equal volumes of the respective reaction mixtures (which are mixed in the above mole ratios to give complete combustion with the oxygen component of air) the heats of reaction are -16 Kcal/mole of mixture of NH_3 and -19 Kcal/mole of mixture of C_3H_8.

These properties, and the associated engineering requirements for the systems, are under consideration for final selection of a coolant fluid.

3. Cold Trap Mockup Facility

G. R. Bloom, D. H. Lester and V. E. Fitzpatrick

Present program plans include evaluating methods to improve thermal, hydraulic and crystallization performance of cold traps. Water mockups in "see through" glass systems are being used for testing internal crystallizer flow patterns and mixing behavior in scaled test systems. A diffusion cold trap model has been built and evaluation tests begun. A forced convection cold trap mockup has progressed to the engineering design stage.

4. Diffusion Cold Trap Studies

G. R. Bloom, D. H. Lester, A. P. Bohringer and V. F. Fitzpatrick

The diffusion cold trap is an unheated, uninsulated, finned vertical deadleg, pointing down, in a sodium system. Any sodium containing oxide impurities which enters the diffusion cold trap becomes saturated; this causes the sodium oxide to crystallize and remain in the trap. One operating problem is that the trap loses sodium oxide back into the sodium system; this results in increased oxygen levels when the normal sodium flow rate is increased appreciably. Also, there has never been any estimates of a sodium recirculating rate for the diffusion cold trap. As a result, trap design for new sodium systems has been difficult and sodium system recovery characteristics hard to predict.

a. Purpose of Tests

The goal of the present work is to be able to predict sodium oxide trapping rates and recovery times from sodium oxide excursions in a system using diffusion cold traps. The equation relating solute concentration to refreshment rate and time for a system can be expressed by:

$$C = C_t + (C_0 - C_t)e^{-(K(\frac{F_t}{V_s}\theta)} \qquad (8)$$

where:

C = system solute concentration at time, θ

C_0 = system solute concentration at time, θ

V_s = system volume

C_t = saturation concentration at the trapping temperature

F_t = trapping flow rate

θ = Time

K = pseudo trapping efficiency

LASL work for cold traps has given sufficient data from which pseudo trapping efficiency (K) can be calculated. The efficiency depends on trap residence time (θ_t) and type of packing. The fluid flow rate into the diffusion cold trap (F_t) is also related to the trap residence time (θ_t) by the expression:

$$F_t = \frac{V_t}{\theta_t} \tag{9}$$

Thus, the diffusion cold trap residence time must be determined before K and F_t can be determined. The trap volume (V_t) must be determined experimentally. The true cold trap volume (V_t) is that part of the deadleg which is: 1) below the system plugging temperature; and 2) in that portion of the cold trap with recirculation.

The purpose of the present tests are to provide required design data for the closed loop secondary and the interim decay storage pool. Specific goals are to:

1) Determine penetration depth of the recirculating loop fluid into the deadleg or "fluid mixing length".
2) Determine deadleg depth required to prevent reintroduction of sodium oxide crystals back into the loop flow.
3) Determine fluid mean residence time in the diffusion cold trap.
4) Determine fluid temperature profiles in the cold trap to verify thermal hydraulic models assumed for theoretical temperature calculations.

With these data, it will be possible to predict sodium oxide trapping rates and sodium oxide excursion recovery time for a system using diffusion cold traps.

b. System Description

A scaled FFTF closed loop secondary diffusion cold trap has been constructed for hydraulic testing; this is shown in Figure V-15. The loop consists of two pumps in series, a venturi flow tube for flow measurement, an electrically operated bypass system for dye injection, a surge tank and a glass test section. Flow is recorded by means of a D.P. cell, flow transmitter and recorder. Temperature of the water entering the test section and at five locations of the deadleg outside surface is also recorded. System heat-up is accomplished with the pumps and auxiliary heating tapes. Inlet water filters and system drains are provided. The dye injection system consists of motor-operated ball valves, which direct flow through a bypass containing dye. Loop flow is regulated by a throttle valve and a pump flow bypass.

c. Procedure

A typical test run for determining "fluid mixing length" consisted of:

1) Filling deadleg with 70°F water and heat loop fluid to temperature.
2) Adjusting fluid flow with flow through dye injection system.
3) Valve out dye injection system with bypass valving and add dye.
4) Valve in dye injection system and measure dye penetration depth into deadleg as a function of time.

The loop flow rate and deadleg temperature profile were continuously recorded. The Reynolds number of 4.6×10^5 (same as FFTF closed loop secondary system) was obtained in a one-inch glass pipe test section with a 58 gpm water flow at 160°F.

d. Results and Discussion

The data obtained are shown in Figure V-16 where the fluid mixing length is plotted against the log of the fluid Reynolds number. The Reynolds number was calculated by:

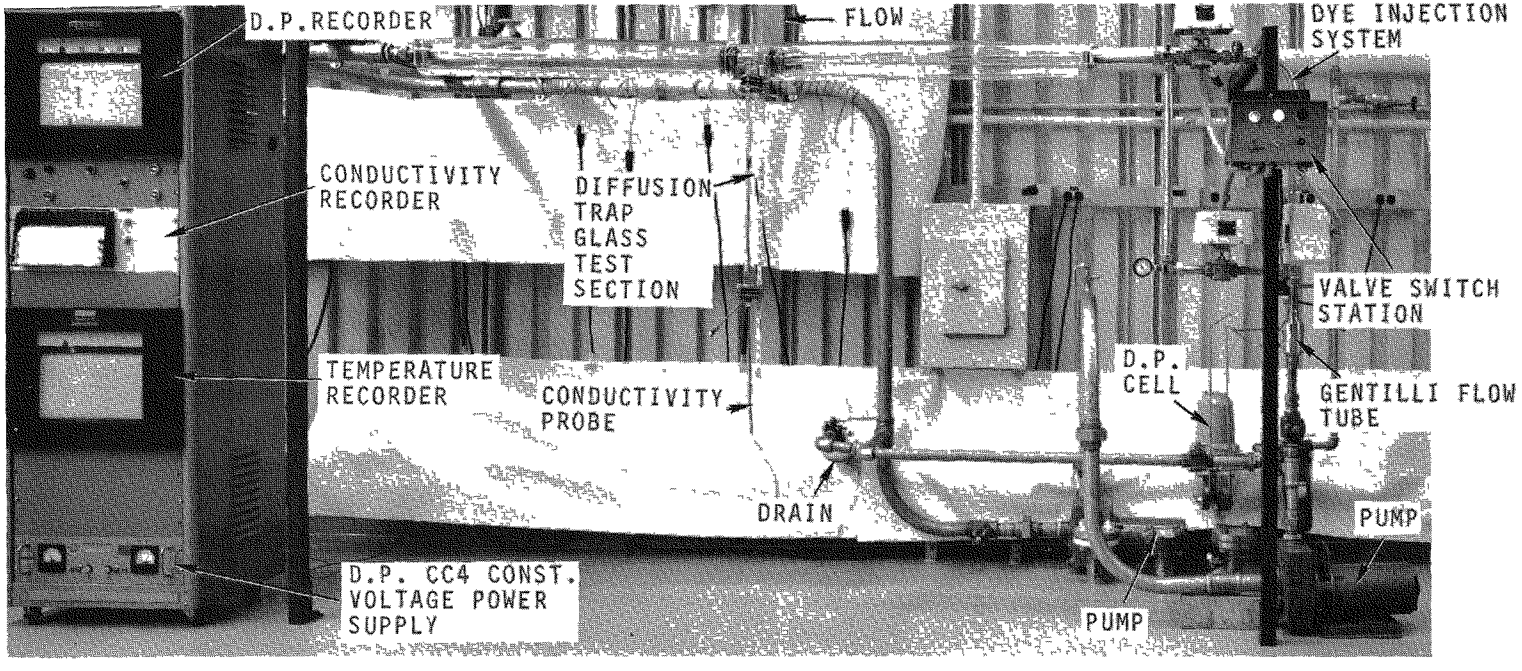

FIGURE V-15 *Diffusion Cold Trap Mock-up.*

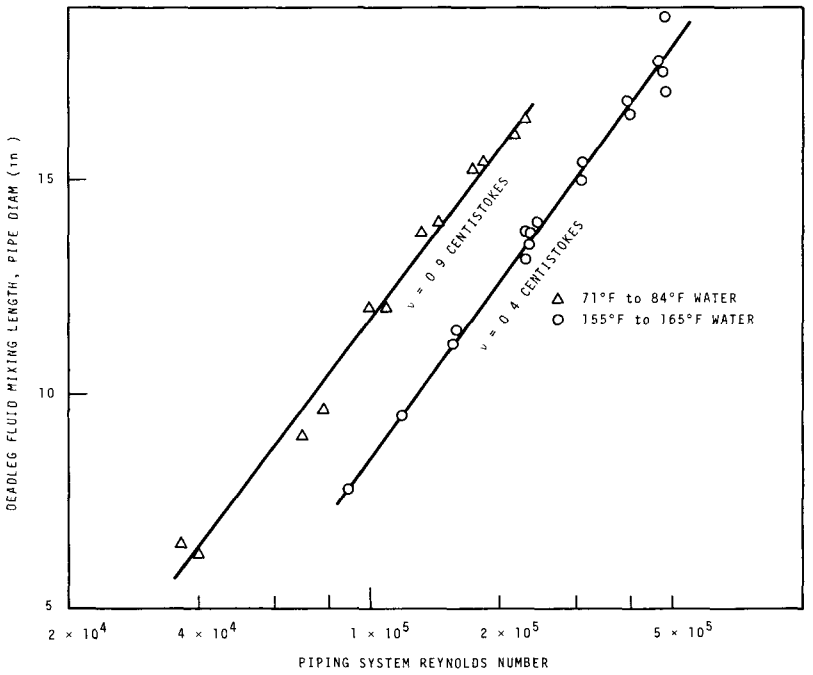

FIGURE V-16 *Fluid Mixing Length Curves - Diffusion Cold Trap Mock-up.*

$$Re = \frac{DV}{\nu} \qquad (10)$$

where:

Re = Reynolds number

V = Bulk fluid velocity

ν = Kinematic viscosity

D = Pipe diameter

A straight-line relationship was observed between fluid mixing length and the log of the Reynolds number for each temperature range. At 155°F to 165°F, the fluid mixing length varied between eight pipe diameters at a Reynolds number of 9×10^4 and 18 pipe diameters at a Reynolds number of 5×10^5. At 71°F to 84°F, the mixing length varied between 6-1/2 pipe diameters at a Reynolds number of 4×10^4 and 16-1/2 pipe diameters at a Reynolds number of 2.2×10^5. The data obtained demonstrates that fluid mixing occurs very deep in the cold trap for the higher fluid Reynolds

numbers. Thus, as observed on operating systems, sodium oxide deposited in a diffusion cold trap at low sodium flow rates could easily be washed back into the sodium system if the deadleg were not long enough and a large enough increase in sodium flow rate occurred.

The temperature profiles obtained for the water system at a main loop temperature of 160°F are shown in Figure V-17. A local temperature gradient was measured for 60 gpm flowrate and a gross temperature grid was measured for five lower flowrates. The temperature profile was assumed similar for all flowrates and drawn as a dashed line to fit the gross observed temperature grid for the 10, 20, 30, 40 and 50 gpm flow rates. The temperature profiles agreed well with the dye penetration data. The detailed temperature gradient obtained for the 60 gpm flowrate will be used to check the theoretical heat transfer equations now being used for sodium diffusion cold trap thermal analysis.

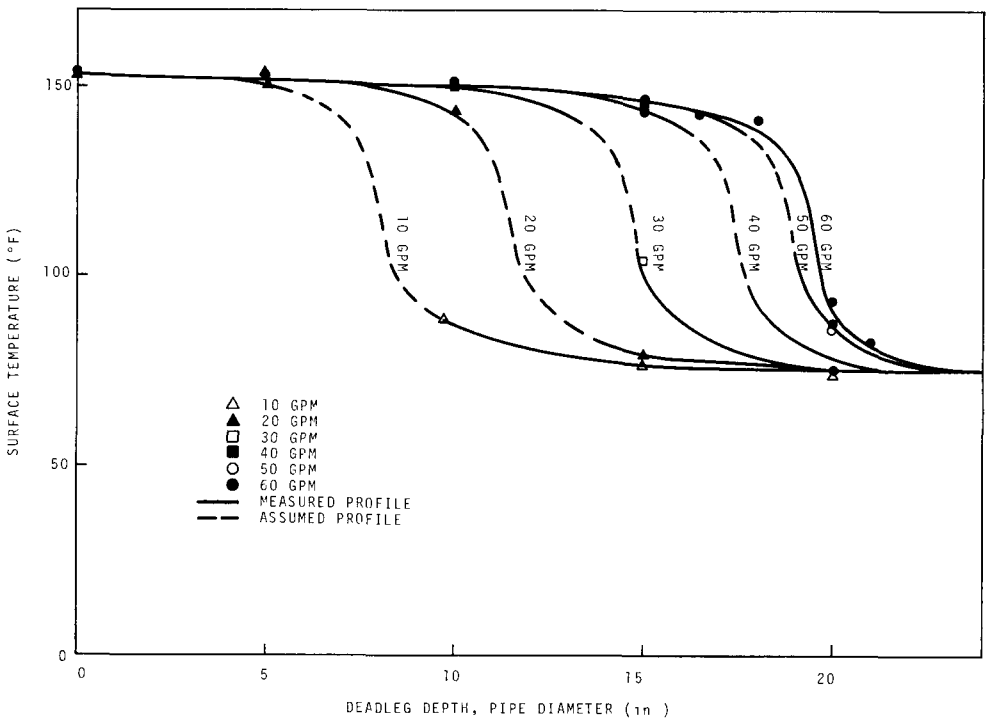

FIGURE V-17 *Temperature Profile Curve*

The mean residence time was determined using tracer methods based on the following equation for an ideal backmix reactor:

$$C = C_0 e^{-\frac{\theta}{\theta_t}} \tag{11}$$

where:

C = system solute concentration at time, θ

C_0 = system solute concentration at time, $\theta = 0$

θ_t = Mean trap residence time

θ = time

The experimental procedure was to measure concentration and time, then calculate mean trap residence time θ_t. First, a visual dye spiked with sodium chloride was injected into the deadleg. Tracer concentration was measured with a small conductivity probe so constructed that it could be positioned at any vertical position in the deadleg. Duplicate test runs were made at two-inch intervals from two to 16 inches into the deadleg and a semilog plot of log conductivity versus time was made for each run. The half-life (time required for the concentration at one point to be reduced to half its former value) was determined for each location in the deadleg. The point residence time was calculated from the half-life using equation (9) assuming the deadleg to be a back mixed system. Equation (11) can be arranged to:

$$\overline{\theta} = \frac{\theta_{1/2}}{\ln 2} \tag{12}$$

where:

$\overline{\theta}$ = point residence time

$\theta_{1/2}$ = half life

The tracer concentration decay curve was determined at a system Reynolds number of 2×10^5 obtained with a loop flow of 60 gpm water at 75 to 80°F in a one-inch test section.

A plot of log point residence time versus deadleg depth in pipe diameters is given in Figure V-18. The point residence time increased sharply in the first eight pipe diameters to a value of about 1 minute then leveled off. At 16 inches, the point residence time increased sharply up to infinity.

The net result is that there is rapid mixing in the first eight pipe diameters, with moderate mixing from eight to 14 pipe diameters and poor mixing from 14 to 16 pipe diameters into the deadleg. Diffusion cold trap volume can be determined exactly. These data will be obtained from thermal analysis the next reporting period.

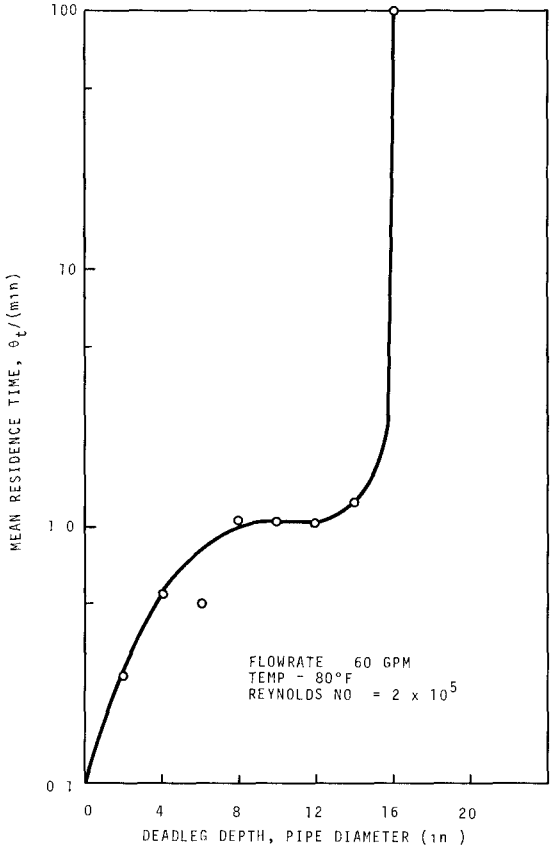

FIGURE V-18 *Residence Time Distribution--Diffusion Cold Trap Mock-up.*

e. Sample Calculation

This section demonstrates how the data obtained would be used to predict the sodium oxide concentration in the closed loop secondary sodium system at any time (θ) after a sodium oxide excursion. If the three-inch pipe system containing 440 gallons had a 165 gpm sodium flow rate at 400°F, an initial oxygen concentration (C_o) of 9 ppm and a trapping temperature of 250°F, the sodium oxide concentration would be calculated as follows. The kinematic viscosity of the sodium is 0.49 centistokes and the Reynolds number would be calculated by Equation(10)to be 3.55×10^5. The saturation concentration (C_t) at the trapping temperature of 250°F would be approximately 1 ppm 0. Reference to Figure V-16 shows that a fluid with a kinematic viscosity near 0.4 centistokes and a Reynolds number of 3.55×10^5 would give a fluid mixing length of 16 pipe diameters into the deadleg. If it is assumed that the sodium temperature in the region of 8 pipe diameters to 16 pipe diameters is below the 300°F plugging temperature, then the trap volume, V_t, is calculated by:

$$\begin{aligned} V_t &= \text{cross sectional area} \times \text{length} \\ &= \pi \frac{D}{4}^2 \times 8D \\ &= 2\pi D^3 \end{aligned} \tag{13}$$

Therefore, the trapping volume would be 0.73 gallons for the three-inch deadleg. Examination of Figure V-18 shows that the mean trap residence time would be approximately one minute at a distance from 8 to 16 pipe diameters deep in the deadleg. Using equation (2) where:

$F_t = V_t/\theta_t$; the trap flowrate (F_t) would be 0.73 gpm. Reference to the LASL work (2) for unpacked cold traps with a residence time of one minute gives a calculated pseudo efficiency (K) of 0.33. Now substitute K, V_s and F_t into equation (1) where:

$$C = C_t + (C_o - C_t)\, e^{-K(\frac{F_t}{Vs})\,\theta} \tag{14}$$

and:

$C_t = 0$

$C_0 = 9$

$K = 0.33$

$V_s = 440$ gal.

$F_t = 0.73$ gpm

With these substitutions, equation (14) reduces to

$$C = 1 + 8\ e - .00055\ \theta$$

The sodium oxide concentration in the FFTF closed loop secondary system can now be calculated for any time, θ, in minutes. For example, with all parameters constant, the oxygen concentration after 24 hours would be

$$C = 1 + 8\ e - (.00055\ (24)\ (60) \text{ or } C = 5 \text{ ppm } 0 \qquad (15)$$

5. Forced Convection Cold Trap Mockup

G. R. Bloom, D. H. Lester, A. P. Bohringer and V. F. Fitzpatrick

The design of the forced convection cold trap water mock-up has been delayed in favor of the short-term hydraulic testing of diffusion traps. It is expected that the forced convection mock-up design and construction will be resumed soon.

6. FFTF Design Support

D. H. Lester and V. F. Fitzpatrick

a. Information Packages

Two packages of design information were provided during the last quarter. The information package detailing heat transfer calculations for forced convection cold traps was completed and transmitted to Bechtel. The package contained details leading to the conclusion that forced convection crystallizers should not have volumes exceeding 300 gallons.

A second package was prepared on diffusion cold traps. Diffusion traps have been proposed for the Closed Loop Secondary and Interim Decay Storage Facility. An assessment of the purification requirements in the two systems was included in the package, along with preliminary estimates of cold trap sizes required. A copy of the preliminary thermal analysis of diffusion cold traps which appeared in the last quarterly was included in the information package. A more rigorous analysis will soon be developed as a result of hydraulic mock-up data described above.

b. Presentation of WADCO Design Basis

At an Auxiliary Systems meeting on 25 August 1970, a presentation of the WADCO design basis for the proposed cold traps was made. The presentation included:

1) The highlights of a parametric study leading to the conclusion that the NaK jacket inlet temperature to the reactor primary cold traps should be 125°F.
2) Review of trapping requirements in all FFTF systems.
3) Presentation of self-contained sodium to NaK to gas cold trap concept proposed for use on the reactor secondary and closed loop primary.
4) Discussion of diffusion trap design basis.

c. RFP for Cold Trap Design Study

A draft of a Statement of Work for Liquid Metal Cooled Sodium Cold Trap Detailed Design Studies was prepared and sent for internal review. The work will encompass cold traps for the reactor primary and secondary heat transport systems. Comments have been received and a revised draft will be issued shortly.

C. SODIUM TEST FACILITIES

1. Prototype Applications Loop (PAL)

The Prototype Applications Loop (PAL) is an isothermal, forced convection sodium loop for sodium technology tests. The PAL is a versatile sodium system, capable of operating to 1200 °F and 40 psig, and is de-

signed for experimental flexibility without the need to modify the basic loop system.

a. Design Work This Quarter

V. F. Fitzpatrick

The effort during the quarter was centered on establishing the codes and standards to be used for PAL. This was accomplished, and RDT approval has been obtained to proceed with PAL. The substance of the agreement is:

1) The mixing tank will be ordered to RDT Standard E10-3T, Tank-Liquid Metal Service.
2) Appropriate nondestructive examinations will be performed on materials (pipe, fittings, plate, etc.) purchased to ASTM specifications, to upgrade materials to meet RDT standards. The additional NDT tests to be run are those that would be normally specified if the materials had been procured to RDT standards originally.
3) Flow meters will be purchased to RDT Standard C4-5T, Flow Meter, Small Permanent Magnet.
4) Thermocouple and liquid level sensors will be procured to RDT Standards C7-6T and C5-2T, respectively.
5) The following RDT Process Standards will be employed for purchase specifications, equipment qualification procedures, cleaning procedures and fabrication instructions that are discussed in the PAL Quality Assurance Plan.

F2-2T Quality Assurance Program Requirements.

F2-4T Quality Verification

F3-2T Calibration Requirements.

F3-6T Nondestructive Examination.

F3-8T Ultrasonic Examination of Metal Pipe and Tubing for Longitudinal Discontinuities.

F5-1T Cleaning and Cleanliness Requirements for Nuclear Reactor Components.

F6-1T Welding.

F7-3T Requirements for Identification Marking of Reactor Plant Components and Piping

A detailed review of the PAL design and action plan is in progress. Procurement activities and materials qualification activities will begin

early in the next quarter. Based on the above agreement, PAL is expected to be completed in 14 months (December, 1971).

b. Sodium System Precleaning Methods

W. H. Yunker, A. P. Bohringer and D. W. Shannon

System precleaning techniques were developed during the design, fabrication, and construction of the Prototype Applications Loop (PAL).

A high pressure water spray lance (3/8 in. O.D., 10 ft long) was used for cleaning the inside of several test sections of 304 stainless steel pipe. The lance emits a radial spray pattern at pressures up to 6,000 psi. Several split pipe sections were coated with a "standard" oil-dirt mixture (for comparison purposes) and the halves clamped together. Pieces which were presoaked for 15 minutes in a hot detergent bath just prior to spray cleaning showed an oil residue of less than 0.05 mg oil/ft^2 on the 1/2 in. pipe and 0.3 mg/ft^2 on the 1-1/2 in. pipe. Particulate residues were very low. The method appears to give excellent results.

From our cleaning experience to date, and from the information contained in the RDT Standards for Cleaning and Cleanliness, detailed layout and operating procedures are being written for application in a shop which fabricates small sodium loops and components.

2. Small Components Evaluation (SCEL) Modifications

T. J. Owen, D. W. Bennett, J. L. Gibson and V. F. Fitzpatrick

a. Background

The existing Small Components Evaluation Loop (SCEL) is being modified to provide capability for near-term sodium technology tests. A header system has been installed in the existing sampling cubicle, along with several instrument packages.

b. Work This Quarter

The sodium supply header system was installed in the sampling cubicle, complete with thermocouples, trace heating and insulation. An EBR-II style plugging valve and a LASL-style plugging orifice and vacuum distillation

sampler have been fabricated and installed. The installed system is shown in Figures V-19 and V-20.

The acceptance test procedures (ATP's) and operator training programs have been completed. The system was filled with sodium and testing started. A flow-through expansion tank has been designed for installation in the sampling cubicle to provide a gas interface for tests of the prototype FFTF gas chromatograph. The proposed flow arrangement is shown in Figure V-21.

Table V-6 summarizes the work to date, including provisions for future work.

TABLE V-6
SUMMARY OF WORK ON SMALL COMPONENTS STATUS

Header System	Complete and operating.
Plugging Meters	Complete and operating.
Vacuum Distillation Sampler	Complete and operating.
Bypass Loop Sampler	Detail design 80% complete.
Oxygen Meter	Design 30% completed.
Carbon Meter	Design 30% completed.
Flowmeter Calibrator Station	Not started.
Expansion Tank Relocation	Scope drawing completed.

3. CGEL Modifications

H. P. Maffei and F. A. Scott

Modifications, initiated during the previous report period (Ref 3) to the Cover Gas Evaluation Loop have been completed, and the loop has been in operation for most of this report period. It has operated smoothly, requiring virtually no attendance. The feed tank has been maintained at 850°F; two test pots have been maintained at 800°F, and the other two test pots run at 1100°F. The cold trap has been operated continuously at 300°F.

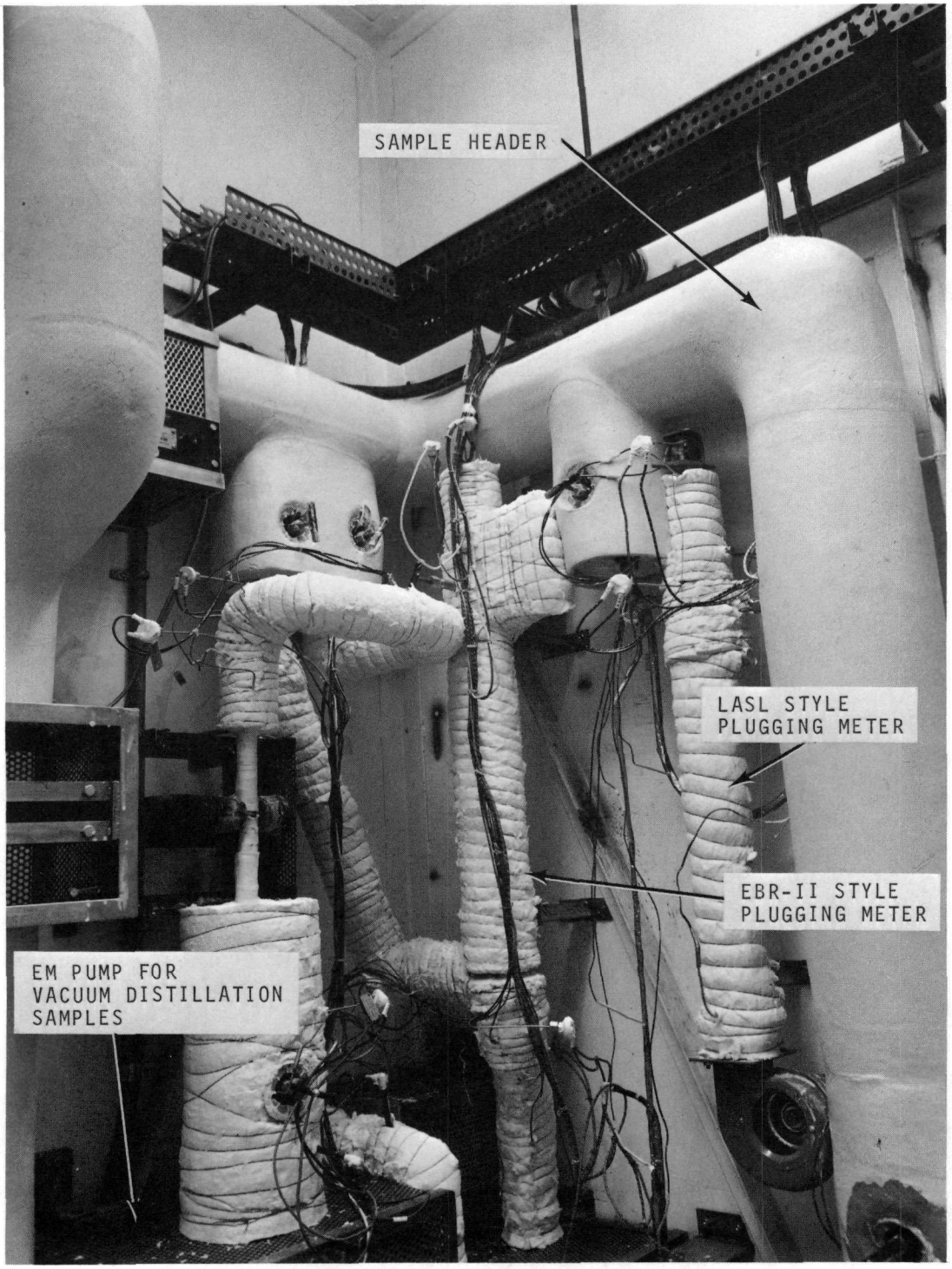

FIGURE V-19 *SCEL Sample Station and Plugging Meters (Vacuum Distillation Unit is Behind Wall)*

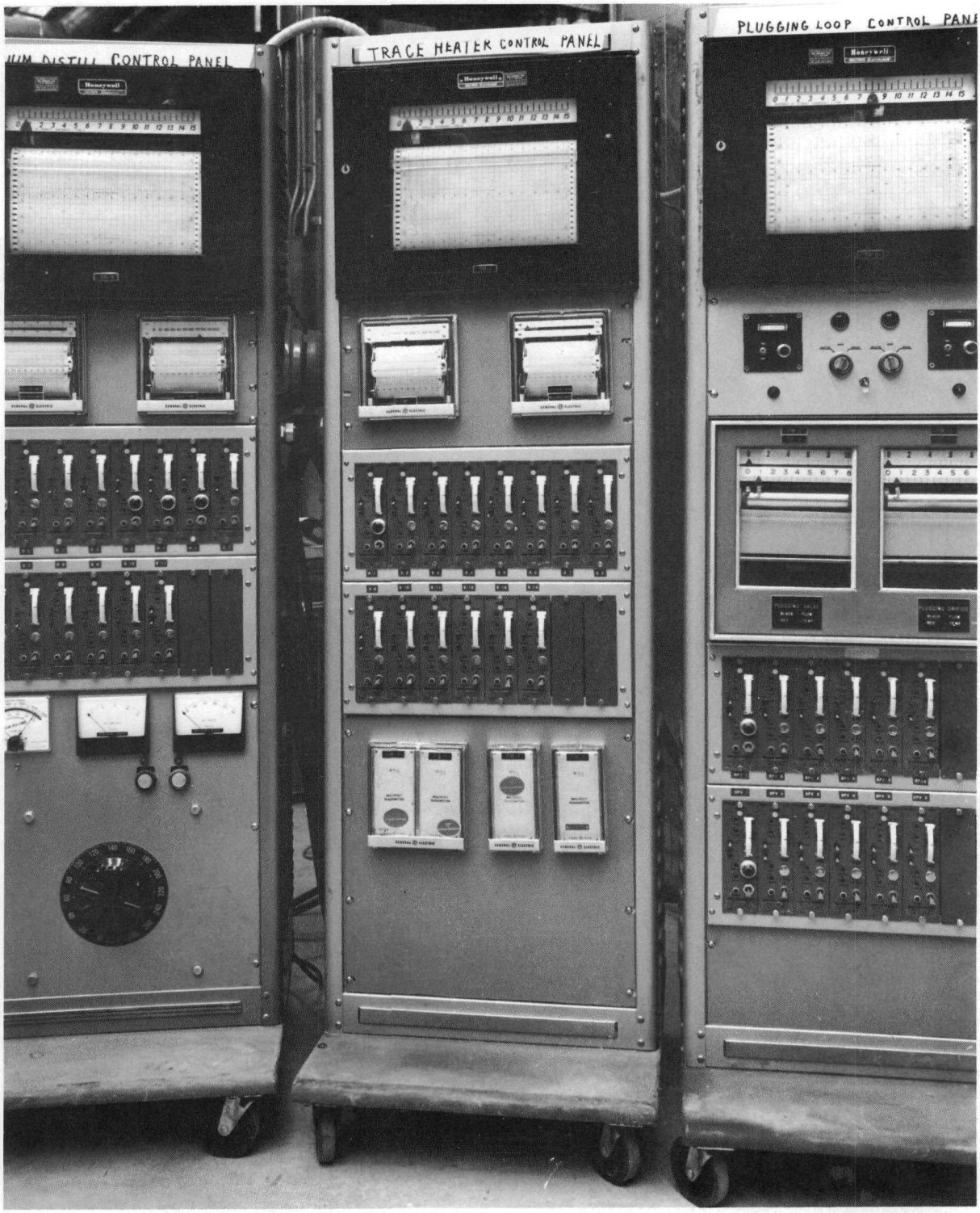

FIGURE V-20 *Control Panels for SCEL Sample Station*

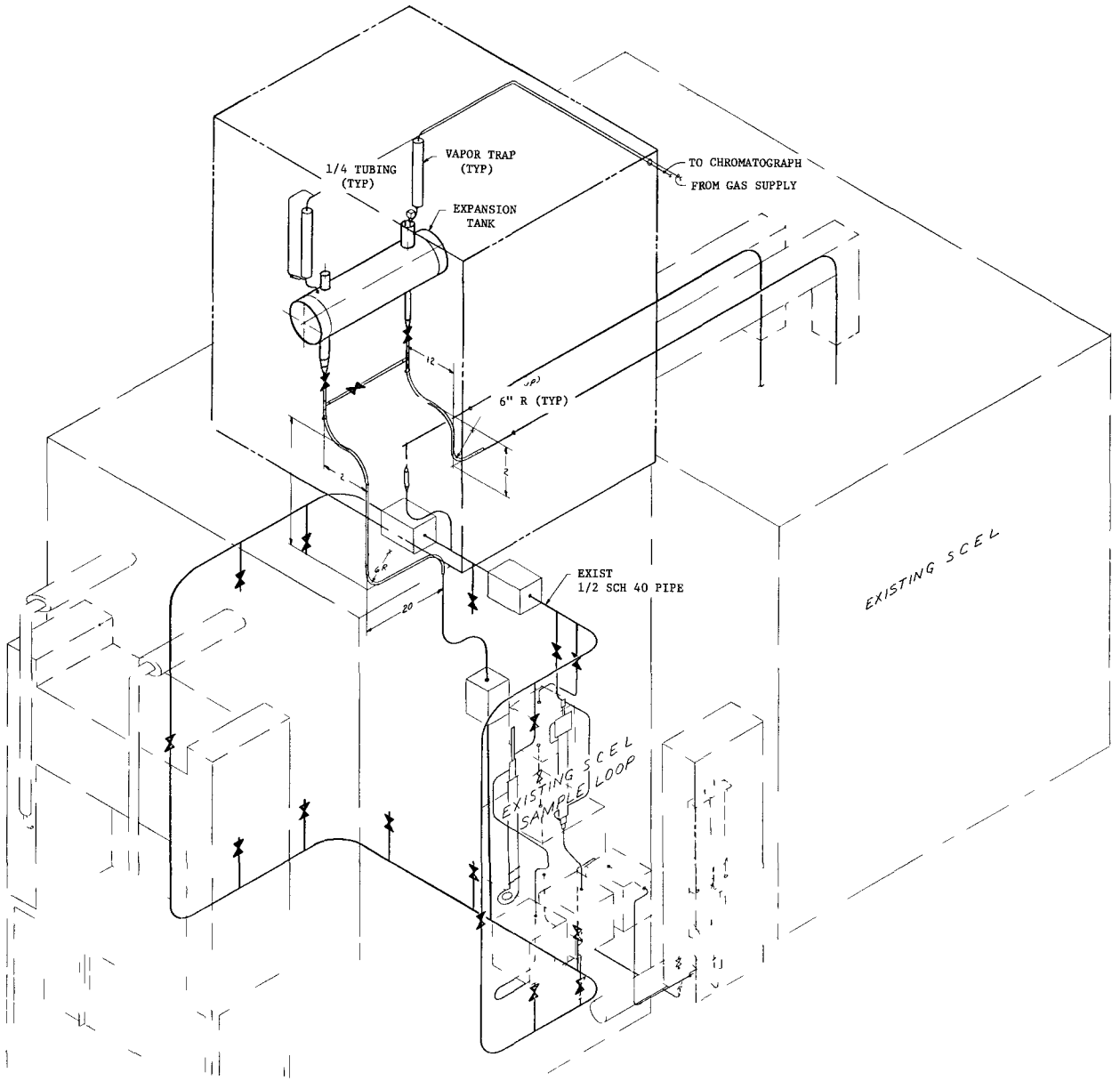

FIGURE V-21 *Expansion Chamber Arrangement*

at 300°F. The sodium flow rates through test pots and cold trap have been maintained at 0.3 gpm and 0.4 gpm, respectively.

4. FRTEF Systems

V. F. FitzPatrick, D. W. Bennett, and T. J. Owen

The preliminary design of the FRTEF (Fast Reactor Thermal Engineering Facility) sodium purification and characterization, and cover gas systems, has been completed and forwarded to the FRTEF project to begin detailed design. The sodium purification and characterization systems are designed to replace the surplus CANEL Oxide Control and Indicating (OCI) System originally scheduled to be used for the FRTEF. The new system will fit into the space envelop designated for the OCI system, and will provide additional instrumentation and flexibility of operation. The cover gas system remains essentially unchanged, except that new vapor traps and a chromatograph typical of FFTF units will be provided.

The piping for the sodium purification and purity monitoring system will take off of the suction side of the FRTEF main recirculation pump and return to the free surface of the FRTEF expansion/dump tank, shown schematically in Figure V-22. A separate EM pump (0 to 10 gpm) and EM flow meter (0 to 10 gpm) will be required.

The sodium characterization system is a header which supplies sodium to a LASL style oscillating plugging meter, a pair of Westinghouse oxygen meters, a bypass sampler, and an EBR-II style vacuum distillation sampler, which operate in parallel. The characterization system is located upstream of the cold trap so that any sodium is purified before returning to the main FRTEF recirculation loop, except when the bypass line is in service.

The vapor traps will be a refluxing type with three zone heating to control the temperature profile and to minimize misting. The traps will be used for both the level probe chamber and expansion/dump tank. An aerosol trap will be located immediately upstream of each trap. The gas chromatograph will analyze the gas from the two-inch gas equalizing line. The

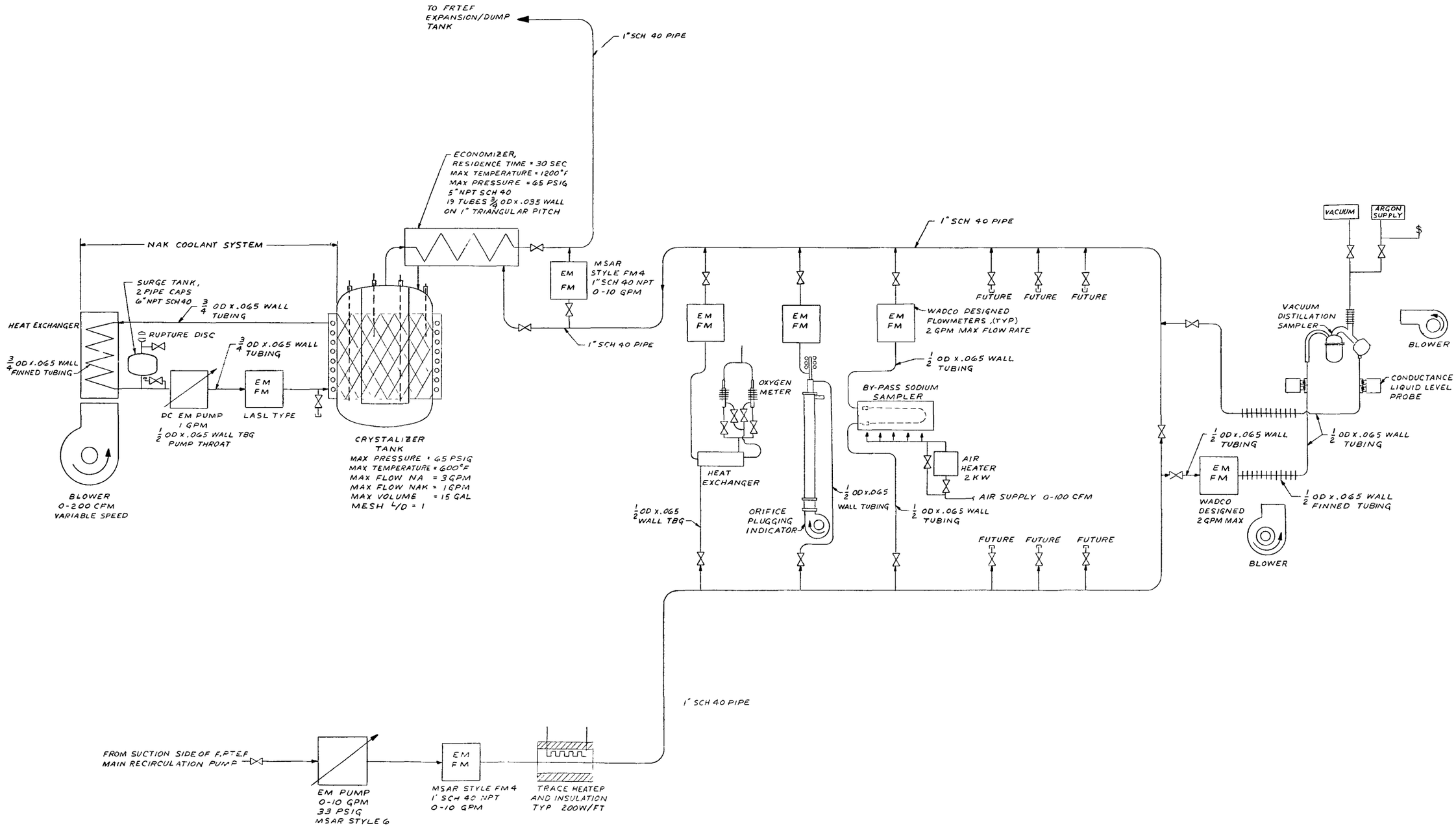

FIGURE V-22 *Sodium Purification and Purity Monitoring System.*

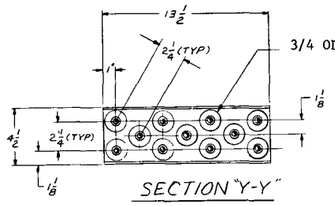

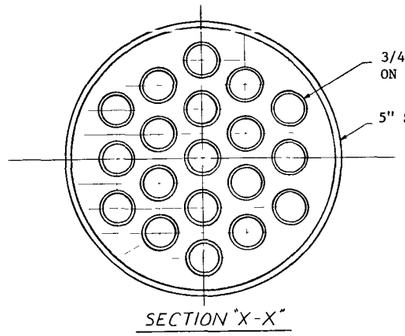

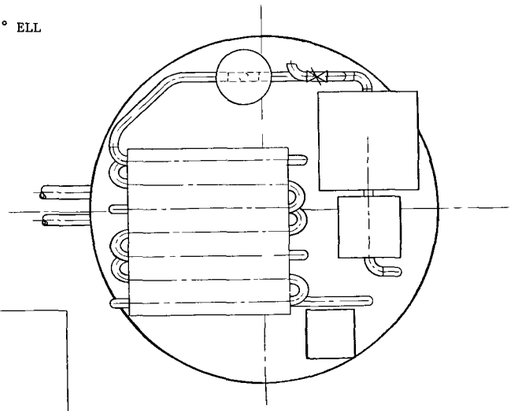

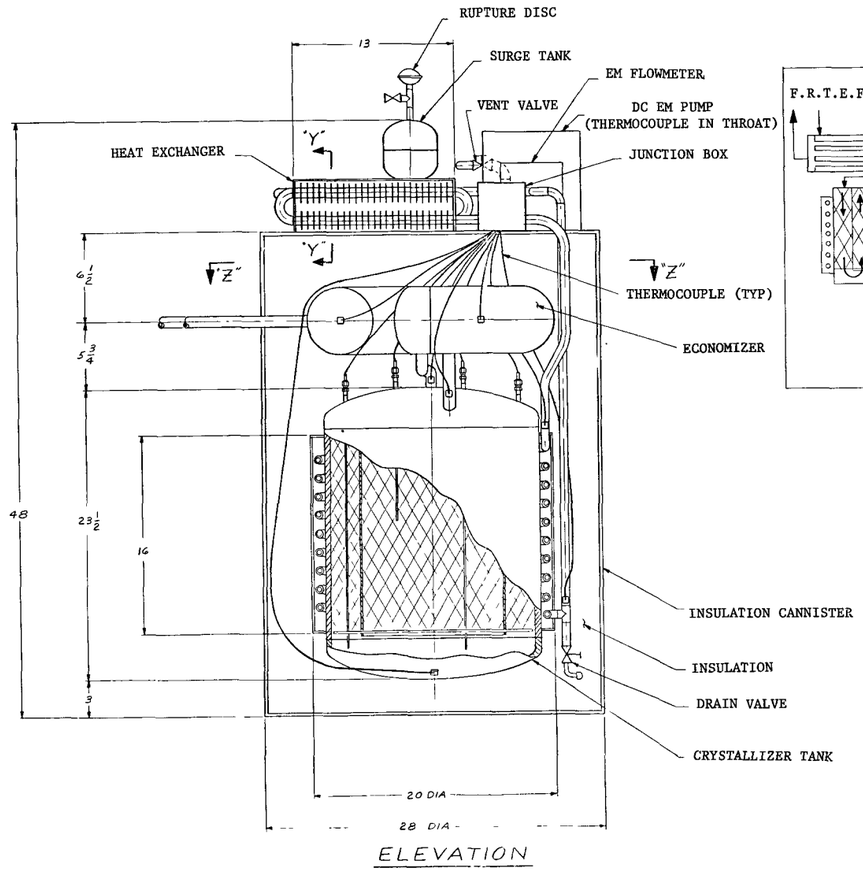

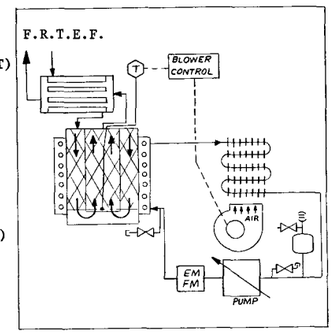

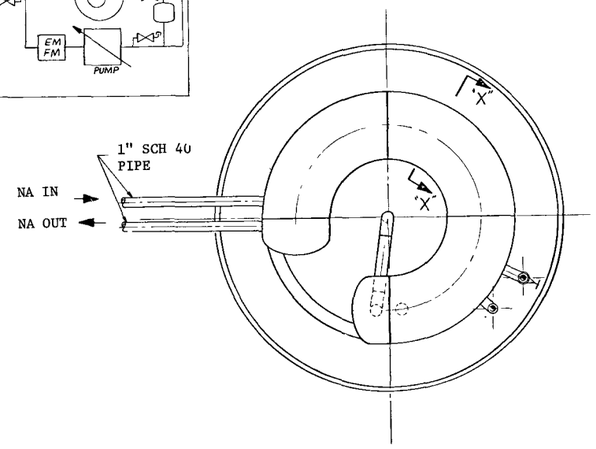

FIGURE V-23 *Sodium Purification Unit.*

gas flow rate to the chromatograph will be about 20 cm^3/min and will be vented to the building exhaust system.

It is intended that free access be permitted to the cubicle containing the sodium purification and sodium purity monitoring system during operation. Therefore, the detail design will provide a suitable barrier between the cubicle and the FRTEF system for personnel safety. A light gauge sheet metal barrier will be provided around all pieces of equipment in the cubicle that are not insulated to a minimum thickness of three inches.

The sodium purification unit for FRTEF shown in Figure V-23 is a crystallizer tank, closely coupled torroidal economizer. A 1 gpm NaK cooling system is an integral part of the purification system and is mounted within the same frame. The purification system is a self-contained unit 2.3 feet in diameter and about 3.5 feet high, and is similar to the purification unit to be used in the FFTF closed loop primary systems.

The cold trap is designed for a 3 gpm flow rate and a 250°F trapping temperature. The residence time in the section of the crystallizer tank containing mesh is five minutes and the length-to-diameter ratio of the mesh section is about one. Both the cold trap and NaK cooling are forced circulation. The ΔT of the sodium across the cold trap is about 30°F, at a sodium flow rate of 3 gpm and a trapping temperature of 250°F. The NaK flow rate can be varied between 0.3 and 1 gpm and the ΔT across the cooling jacket will be about 190°F. The NaK is cooled by a small NaK-to-air heat exchanger mounted above the cold trap.

The LASL style oscillating plugging meter in the sodium characterization system is identical to the meter installed on the SCEL for evaluation. If the EBR-II unit or some other model is selected as the FFTF standard design, the standard design will be substituted. The bypass sampler is a simple standard design and is also similar to the sampler to be installed on the SCEL.

The oxygen meters will be standard FFTF modules based on the design currently being prepared by the Argonne National Laboratory. The module contains the valves required for operation, a flow meter, and an economizer, in addition to the two oxygen meters.

The vacuum distillation sampler is similar to the sampler developed for trace metals analysis at EBR-II. Some improvements have been made in the area of liquid level sensing and of minimizing the number of valves required for operation. The design of the unit is shown in Figure V-24.

5. SCEL Power Controllers

D. W. Bennett, T. J. Owen, J. L. Gibson and V. F. FitzPatrick

Eighty power controllers for trace heating systems were procured for the SCEL. This represents the first major step in an effort to establish commercial availability of an inexpensive, automatic, proportioning-type controller with feedback control and voltage limitation for sodium loop trace heat application. The need for such a controller was established during the initial design of PAL, and has received serious attention at HEDL for possible use on the FFTF secondary system.

All of the heater controllers were tested for operability and durability in an actual heater circuit (Figure V-25) before they were installed in the SCEL instrument panels. This test apparatus consists an eight-controller plug-in rack wired to eight infrared lamps. Two thermocouples are mounted on each lamp so that the master-slave sequential control mode can be demonstrated. The controllers were tested in both the manual and automatic modes, and their control systems were characterized to provide a basis for a startup procedure for the SCEL sampling station.

D. LABORATORY SODIUM ANALYSIS

The objective of this activity is to provide analytical support for existing HEDL sodium technology programs.

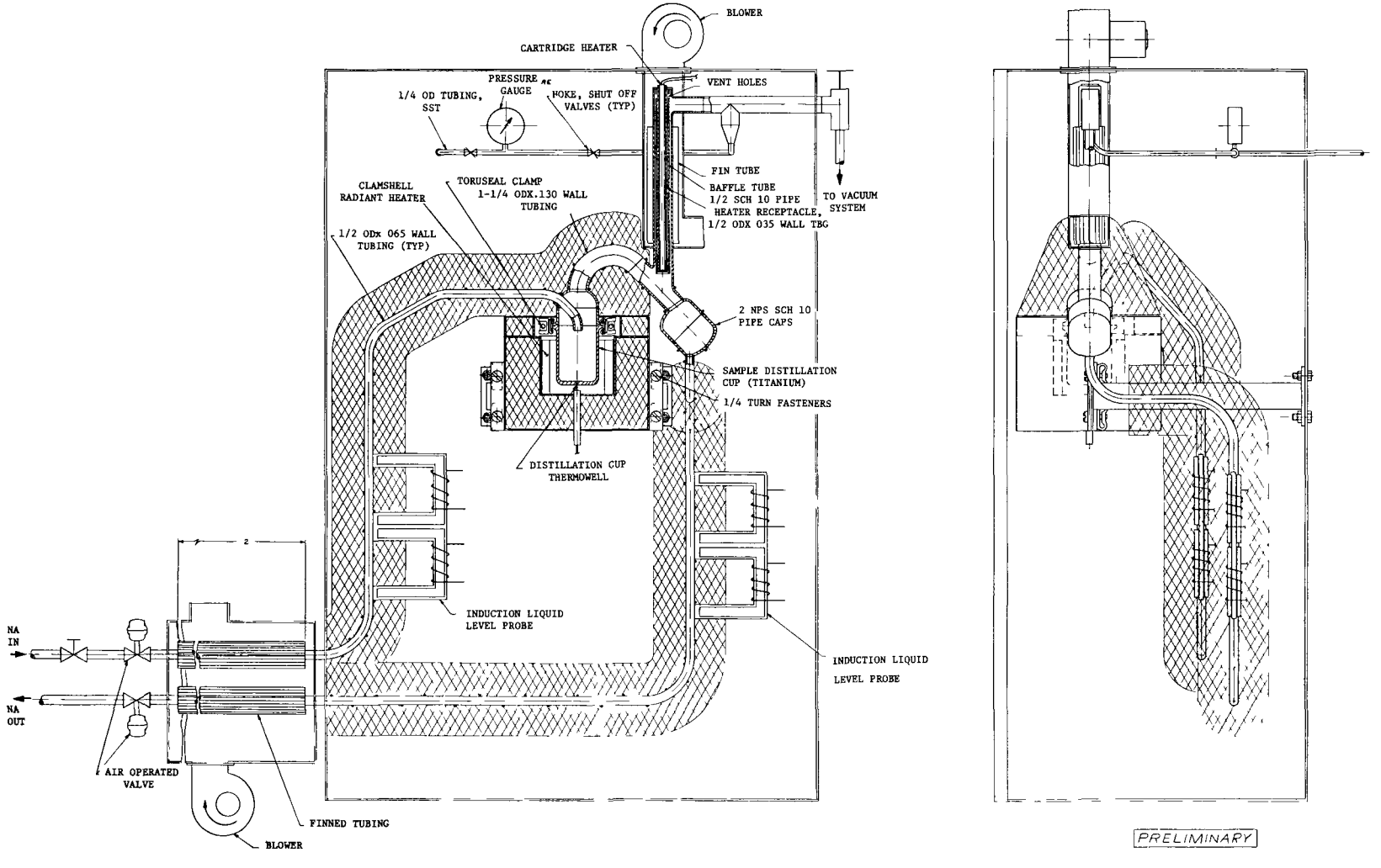

FIGURE V-24 *Vacuum Distillation Sampler.*

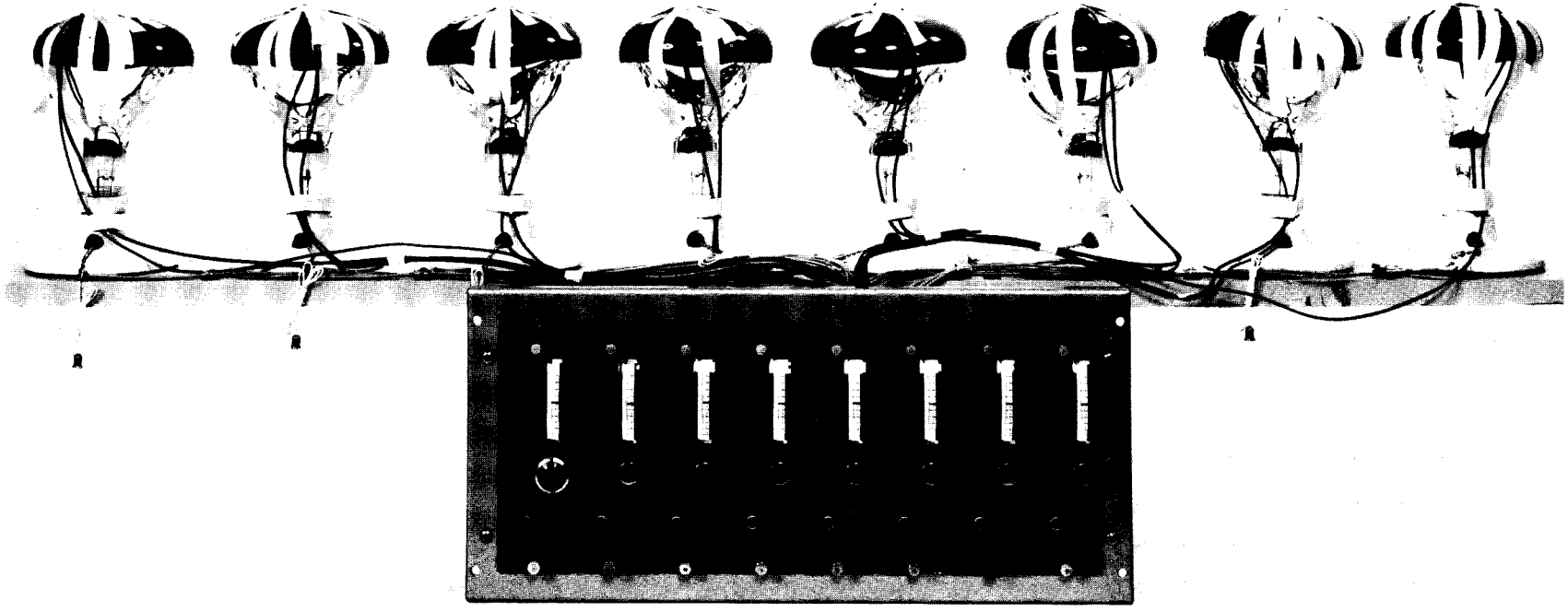

FIGURE V-25 *Controller Test Stand--Each Controller Regulates One Heat Lamp*

1. High Radiation Level Analytical Facility Design

L. F. Lust, S. E. Nichols and F. A. Scott

The objectives of this activity were to provide proven equipment and techniques to analyze radioactive sodium from the FFTF and to develop design criteria and requirements for the FFTF chemical analysis laboratory.

Operation of the remote analytical mock-up facility was discontinued. After having maintained a pure argon atmosphere for eight weeks, the purification units were shut down and the inert atmosphere portion of the mock-up mothballed. The air atmosphere portion of the mock-up was removed from the EDL-146 Mezzanine in the 324 Building. A terminal report describing the facilities, the experimental work, and the accomplishments of the program for the laboratory analysis of radioactive sodium is being prepared. An oral presentation of this work has been prepared (Ref 5) and has been accepted for delivery at the Winter Meeting of the American Nuclear Society in Washington, D. C., 15-19 November, 1970.

2. Interim Methods for the Analysis of Reactor Sodium

R. F. Keough, L. F. Lust, M. B. Hall, S. E. Nichols and F. A. Scott

In compliance with the Argonne National Laboratory (ANL) plan for selecting interim methods for the analyses of reactor sodium, work was started to establish the capability of analyzing sodium for oxygen, hydrogen, trace metals, carbon and radionuclides by the selected interim methods. The goal is to have this capability in place in time to participate in the interlaboratory sample interchange program. The Reactor Standard Working Group has agreed to start the sample interchange program on or about 1 November, 1970. Some of the methods in use at HEDL are identical to the interim methods; others require modification. The interim methods for oxygen and hydrogen have been put in place and tested. The method for trace metals is undergoing final testing. Equipment for the interim standard method for determining carbon (oxyacidic flux) is being assembled. Details of this method, the required apparatus, and the analytical techniques were discussed with ANL-EBR II personnel at their laboratories. Actual setup and operation of the equipment will begin early next quarter.

a. Oxygen Determination

The interim method for the determining oxygen by amalgamation proposes three modifications to the procedure presently used by HEDL. Two of the suggested modifications were considered previously (Ref 3). The third, extrusion sampling, was examined in this quarter. A comparison of oxygen determinations on sodium amalgamated directly from the stainless steel tubing versus sodium extruded from the tubing prior to amalgamation clearly shows that extruded sodium appears lower in "oxygen" (See Table V-7). Low results were also observed when sodium was melted from the tubing, rather than extruded. Comparison of apparent oxygen values for extruded and complete cross-section samples will be continued as more sodium samples become available.

TABLE V-7
COMPARISON OF "OXIDE" IN SODIUM SAMPLES

Source	Oxide (ppm)	
	Extruded	Tubing Section
CGEL	3	12
SCTL	6	15
POT[a]	4	40
FPTL[b]	8	250
PL	3	11
PL	3	16
PL	4	13
PL	4	11
PL	3	6

(a) Sodium flow limited to less than 1 Kg through sample tube

(b) Loop contaminated with boron nitride prior to sampling

A re-examination of the blank contribution of the outer surface of the tubing has been completed. Earlier work indicated that the tubing blank was equivalent to 0.5 ppm of oxide for 1/2-in. diameter tubing.

The assumption was made that the inner surface did not contribute to the blank because it had been cleaned or "conditioned" by flowing sodium for several hours.

Type 304 stainless steel strips, or 1/2-in. diameter tubes (ASTM-A-269) were heated overnight in various manners to prepare surfaces similar to those found on typical sample tubes. The metal exposed to air after heating was allowed to stand in the laboratory for 24 hours and was then wiped with cotton moistened with toluene. From this point, the metal was allowed to contact only glass or stainless steel as it was taken into an argon atmosphere glove box.

Metal samples were contacted with sodium amalgam in two ways: by adding 50 ml of 6%, oxide-free, sodium amalgam preheated to 120°C to the metal in a separatory funnel; and by adding three to four g of extruded sodium to a funnel containing the metal and a 50 ml pool of mercury at room temperature. The funnels were then carried through the normal oxygen analysis procedure. The resulting blank contributions of the stainless steel (Table V-8) are expressed as ppm of oxide in sodium, based on 1/2-in. diameter tubing containing 2.2 g of sodium/in. Conclusions reached from the most recent work may be summarized thus:

1) The tubing blank is much too low to explain the discrepancies illustrated in Table V-7 between sodium analyzed in the presence of its containment tubing and sodium analyzed after extrusion from the tubing.
2) Tubing blanks, in actual practice, will range from 0.5 to 1.5 ppm oxide equivalent. (Sets 2, 3 and 5, Table V-8).
3) Tubing blank values with hot amalgam average roughly 75% of comparable blanks with sodium added to a pool of mercury containing the tubing (sets 1 through 4, Table V-8). The correct metal blank for amalgamations of sodium in tubing is probably between the two values. The outer surface is not exposed to sodium or very rich amalgams, but it is exposed to localized heating due to the amalgamation occurring within the tubing.
4) All of the heating treatments, simulating sampling of a system, reduced the blank from the value obtained with off-the-shelf (set 1, Table V-8) tubing.

TABLE V-8
BLANK CONTRIBUTIONS OF STAINLESS STEEL TUBING

Set	Treatment	Oxide Equivalent	
		Sodium Plus Mercury (ppm)	Hot Amalgam (ppm)
1	No heating - off the shelf	1.7 1.7 1.7	1.3 1.3 1.6
2	Heat in air at 400 °C; equilibrate with room air	1.1 1.4	0.6 0.7
3	Heat in argon at 400 °C; no exposure to air	0.4 0.2 0.0 0.2	0.2 0.1 0.4 0.3
4	Heat in argon at 400 °C; equilibrate with room air	1.0 0.7	0.5 0.5
5	Heat in air at 650 °C; equilibrate with room air		0.5 0.4 0.6
6	Heat in air at 650 °C; equilibrate with room air. Remove tarnish with emery cloth inside glove box (strips)		1.1 1.1
6A	Control - tarnish not removed		0.6
7	Heat in air at 400 °C; equilibrate with room air. Store in antechamber at 0.02 torr for 18 hours		0.4 0.6 1.1
7A	Control - 10 minutes under vacuum in antechamber		0.4 0.7

5) The previous estimate of 0.5 ppm for normal samples is slightly low. 0.8 ppm appears to be a better value.

6) Heating the tube of sodium in the inert atmosphere glove box before the analysis produces the lowest metal blank. However, heating of actual samples is unacceptable, because melting the sodium is likely to change its apparent oxygen concentration through segregation. Vacuum drying in the unheated glove box antechamber does not reduce the blank. Apparatus was not available for vacuum drying at 90 to 95°C in the antechamber.

7) The blank values appear to be caused by the reaction of sodium with adsorbed water, rather than with metal oxides, and therefore could be a major problem in the proposed modification of the amalgam reflux method for hydrogen, where the tubing remains in the reaction vessel.

8) Exposure to air after heating results in some readsorption of moisture; the amount or perhaps the rate depend on the heating temperature (sets 3 and 4, Table V-8).

9) Removal of the blank source with emery cloth in the glove box appears to be ineffective (set 7 vs. 7A, Table V-8), and the emery cloth may contaminate the metal with dust, adhesive, etc.

10) No practical method has been found to reduce the tubing blank consistently below the 0.5 ppm level.

11) The tubing blank does not contribute a significant error to the amalgamation oxygen values because of its small size (0.8 ppm) and relative constancy (±0.2 ppm).

An additional interim method (vanadium wire equilibration) has been suggested for oxygen by ANL. Funding limitations will not permit the installation of equipment for the procedure at HEDL until FY-1972.

b. Hydrogen Determination

A number of hydrogen determinations have been made on EBR-II sodium for W. H. Olson, and more samples are in transit.

c. Trace Metal Determination

A simple loop tap (drain) sampler was built and attached to the purification loop (Figure V-26). Ten 50 to 75-gram cup samples were taken over a period of a week with no problems. Most of the samples were used in evaluating vacuum distillation/flame spectrometry techniques.

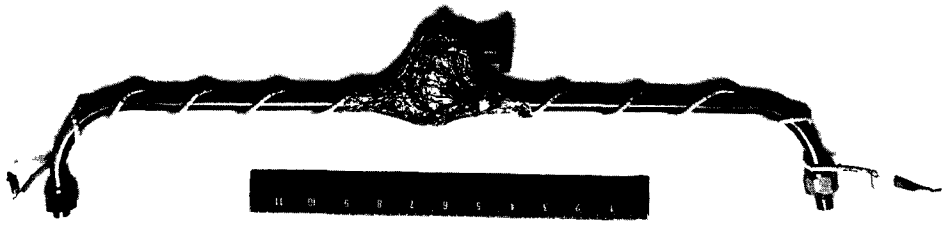

FIGURE V-26 *Loop Tap (Drain) Sampler for Sodium Purification Loop.*

Data gathered incident to this work indicate that the levels of the common metallic impurities (excluding potassium) are well below 0.1 ppm for this loop.

3. Analytical Support for Engineering Facilities

W. O. Greenhalgh and F. A. Scott

The objective of this activity is to establish the extended analytical capability needed to support the fast flux test facilities and the sodium technology programs at HEDL.

a. The Analysis of Sodium Particulates

An electron microscope and x-ray probe examination of two in-line stainless steel filters from the Sodium Purification Loop were made. The seven micron pore filters were placed on the by-pass loop sampler and sodium was passed through the filters at the rate of 0.25 gpm. The lengths of exposure were 72 hours and 8 days, respectively.

A substantial number of particles were deposited on each filter. On the first filter, three typical areas were distinguishable: an area containing a rosette shaped particulate; a dark area which was possibly a void; and the bulk sodium (Figure V-27). The x-ray analysis of these three areas identified the rosette as stainless steel. The bulk sodium contained large amounts of iron and chromium in approximately equal molar

quantities and trace amounts of nickel and aluminum. The emission x-ray spectrum of the dark areas was found to be essentially the same as that of the bulk sodium, except that the sodium peak was much smaller. Analysis of the filter surface itself gave a typical stainless steel profile indicating that the regions investigated were authentic.

Several particulate regions on the second filter were analyzed by the x-ray probe. A grouping of three similar looking rods, a rosette, a cluster of small various shaped particles, and a rod with an attached kidney-shaped appendage were all identified and examined. Analysis of two of the three rods showed that one was stainless steel with minor impurities of calcium and silicon, and the other was nearly all silicon with traces of iron and chromium. The cluster and the rod with the attached kidney-shaped appendage are shown in Figures V-28 and V-29, respectively. The rosette and cluster were both found to be stainless steel. Analyses of the rod showed it to be primarily silicon with some iron and chromium, while the kidney-shaped appendage contained both calcium and silicon, with minor quantities of sulfur, chromium and iron.

The in-line filters and the sodium metal for both samples were also examined with the Unitron metallograph using the sample preparation procedure reported earlier (Ref 6). Two different views of the filter are shown in Figures V-30 and V-31. The first photomicrograph is an overall view of the filter surface, and the second is a closeup of some of the individual particulates. The type of particulates observed were similar to those examined by the electron microscope, but they are more readily distinguished with the metallograph. Most of the particulates are metallic. There was no deposition pattern across the filter surface; in fact, the population density varied from sparse to very dense. Figure V-31 was taken in the more densely populated region.

The sodium, both upstream and downstream of the filters, contained "metallic crystallites." Many of the inclusions observed downstream of the filter measured 10 microns or greater. They must have been formed or increased in size during cooling, since they are larger than

1000X

FIGURE V-27-*Three Distinguishable Areas on the Surface of a Stainless Steel Filter from the Sodium Purification Loop.*

1000X

FIGURE V-28-*Particulate Clusters on the Surface of a Stainless Steel Filter from the Sodium Purification Loop.*

1000X

FIGURE V-29 *Rod-like particulate On The Surface of a Stainless Steel Filter from the Sodium Purification Loop.*

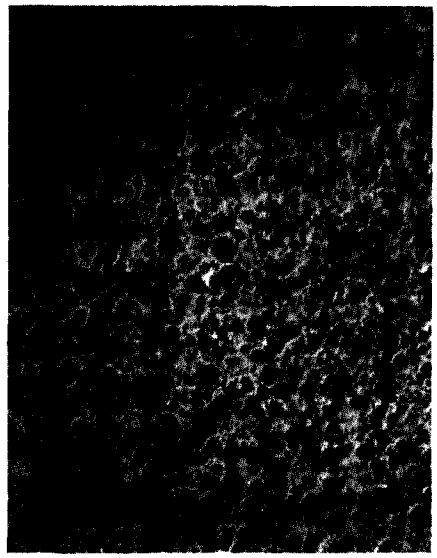

16X

FIGURE V-30 *High Population Density Area on the Surface of a Stainless Steel Filter from the Sodium Purification Loop.*

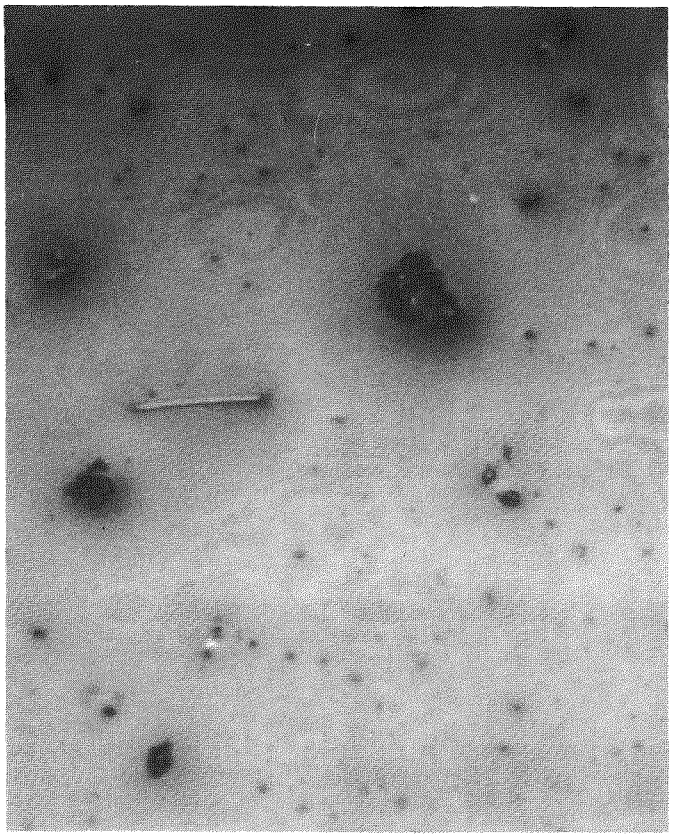

160X

FIGURE V-31 *Closeup of Individual Particulates on the Surface of a Stainless Steel Filter from the Sodium Purification Loop.*

the absolute rating of the filter.

X-ray techniques, the emission spectrograph, and Coulter Counter methods were evaluated for analysis and characterization of aqueous insoluble particulates. X-ray diffraction and fluorescence analyses were not sensitive enough to detect impurities in the residues of 10 gram aliquots of sodium from the Sodium Purification Loop. Emission spectrographic analysis of the same sample source, however, indicated major impurity levels of silver, calcium, chromium, copper, iron, and magnesium and minor impurity levels of aluminum, bismuth, manganese, nickel, and lead. Interferences prevented the determination of silicon. Examination of a GCEL sample residue with the Coulter Counter indicated it contained approximately 5 ppm particulates by volume with a mean particulate dia-

meter of 5 microns. The Coulter Counter appears to provide a rapid routine method for determining the number and the size distribution of aqueous insoluble particulates in sodium at a very reasonable unit cost. The accuracy should be limited only by the counting statistics.

b. The Analysis of Carbon Species

Carbon species development analyses on samples from CGEL startup have been completed. Table V-9 summarizes the results.

TABLE V-9
CARBON SPECIES ANALYSIS

Run No.	Sodium Loop Temp. (°C)	Carbon as CO_2 (ppm)	Carbon as C_2H_2 (ppm)	Carbon Solids (ppm)	Total Carbon (ppm)	Carbon Reference* (ppm)
Fill sample	∿150	2.7	0	8	11	12
5-001		1.6	0.1	6	8	11
5-003	200	1.5	0.3	results contaminated		not analyzed
5-005	230	1.5	0.5	6	8	3
5-009	320	2.7	0.3	7	10	12
5-010	350	2.3	0.6	2	5	5
5-011	370	1.8	0.5	6	8	10
5-012	410	0.9	0.3	4	5	5
5-016	410	3.3	0.2	3	7	2
5-017	440	2.2	0.2	3	5	1 5 Rerun
5-020	530	1.8	0.4	2	4	3

* The reference carbon values were run independently in another apparatus using combustion for total carbon.

Carbon solids, carbonate species (C envolved as CO_2), and alkaline earth and refractory carbide species (C envolved as C_2H_2) were successfully analyzed. In some of the earlier runs, problems were encountered with methane retention by the liquid nitrogen trap, and the results may be as much as 20% low. The trap has been modified and 100% retention of all evolved gases can now be demonstrated.

A new apparatus for carbon species analysis was designed, built, and set in place this quarter. The system is presently being checked out and should be suitable for making routine analyses. Preliminary tests with the system indicate that the gas species CO_2, CH_4, and C_2H_2 can be suitably handled.

References for Chapter V

1. Kemont, E. L. "Engineering Development of a Practical 1200°F Sodium-Vapor Trap" Trans. Am. Nucl. Soc. 8 (1):147 (1965).

2. Dillon, R. L., ed. "Sodium Technology Quarterly Report, October, November, December 1969", BNWL-1200-2. Battelle-Northwest, Richland, Washington, February 1970.

3. Wykoff, W. R., ed. "Sodium Technology Quarterly Report, April, May, June 1970", BNWL-1200-4. Battelle-Northwest, Richland, Washington, August 1970.

4. Carslaw, H. S. and Jaeger, J. C. "Conduction of Heat in Solids, Second Edition, Oxford University Press, 1959, p. 200.

5. Lust, L. F., Scott, F. A., and Jarosch, J. F. "Mock-up of Remotely Operated High Purity Inert-Atmosphere Sodium Analysis Facility, BNWL-SA-3437. Battelle-Northwest, Richland, Washington, June 1970.

6. Dillon, R. L., ed. "Sodium Technology Quarterly Report, January, February, March 1970", BNWL-1200-3. Battelle-Northwest, Richland, Washington, April 1970.

VI. CORE DESIGN, PHYSICS AND SAFETY

A. CORE MECHANICS

1. Core Restraint

a. Design Concepts

J. F. Wett and G. R. Waymire

The primary objective of the core restraint system design effort is to provide a mechanism that, in conjunction with the in-core ducts, will control the core radial motion so that responses to steady-state and transient operating conditions are predictable and safe.

Evaluation of alternate conceptual designs is continuing, including the "Vertical Push-Pull Concept" shown in Figure VI-1, the "Flexible Strap Concept" shown in Figure VI-2, and the concept shown in Figure VI-3.

The thermally actuated concept has been discarded because of limited travel capability and variations in the outlet temperature (e.g., 900° to 1100°F).

b. Simulated Core Model (12149)

W. C. Kinsel

The Simulated Core Model (SCM) was built recently to evaluate kinematic and structural design problems related to core restraint, duct insertion and withdrawl, and interfaces with the fuel handling machine and the instrument trees. The SCM is a full scale structural model of the FTR core; it is intended to provide preliminary design information (clamping forces, alignment precision, force distribution, optimum load sequence, etc.) and proof-of-design information (functional proof tests) of the core restraint mechanisms. A photograph is shown as the frontspiece of this report.

The SCM is presently operational. A partial core (consisting of driver ducts only) representing startup configurations, is now being

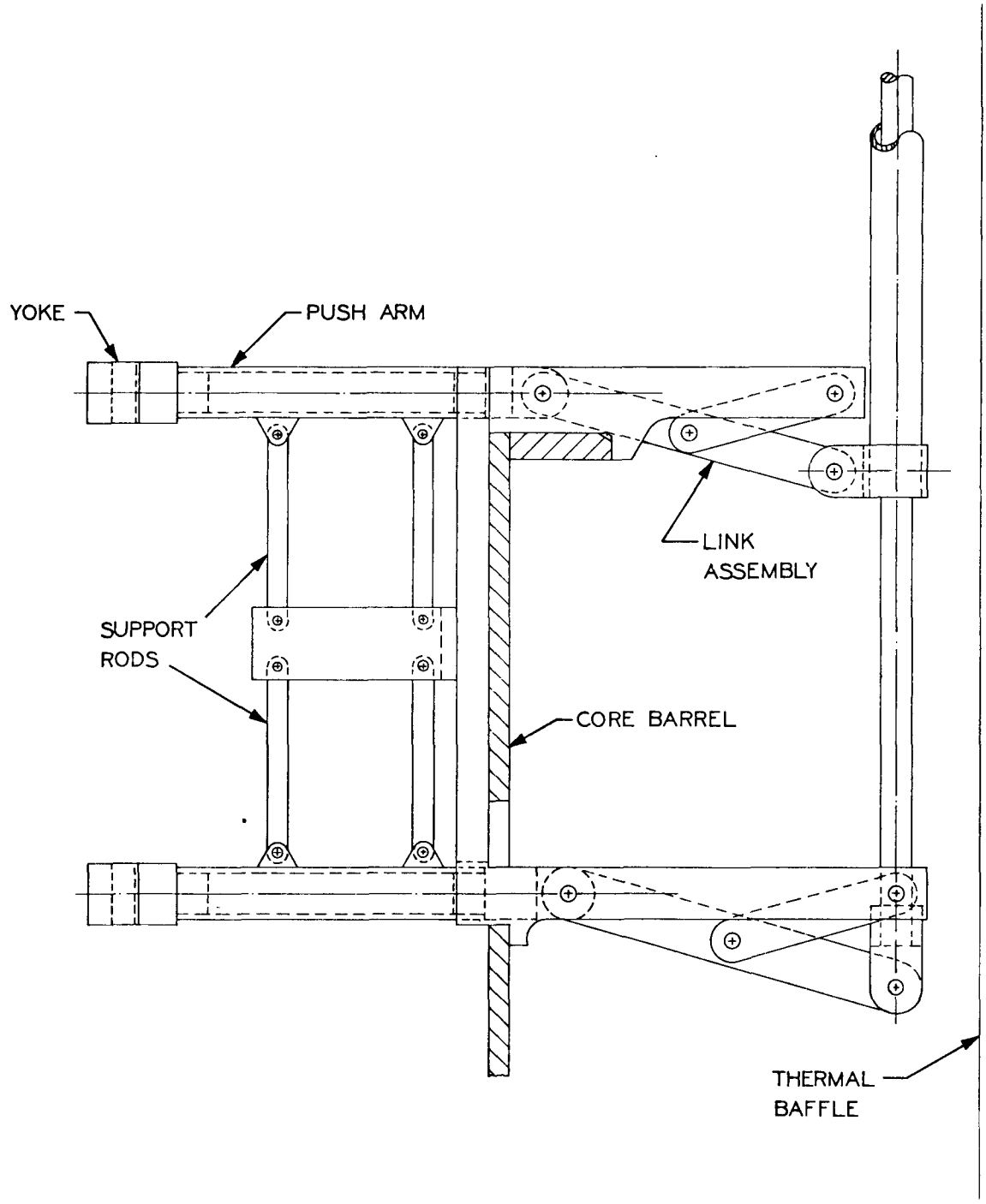

FIGURE VI-1 *Core Restraint Mechanism - Vertical Push-Pull Concept*

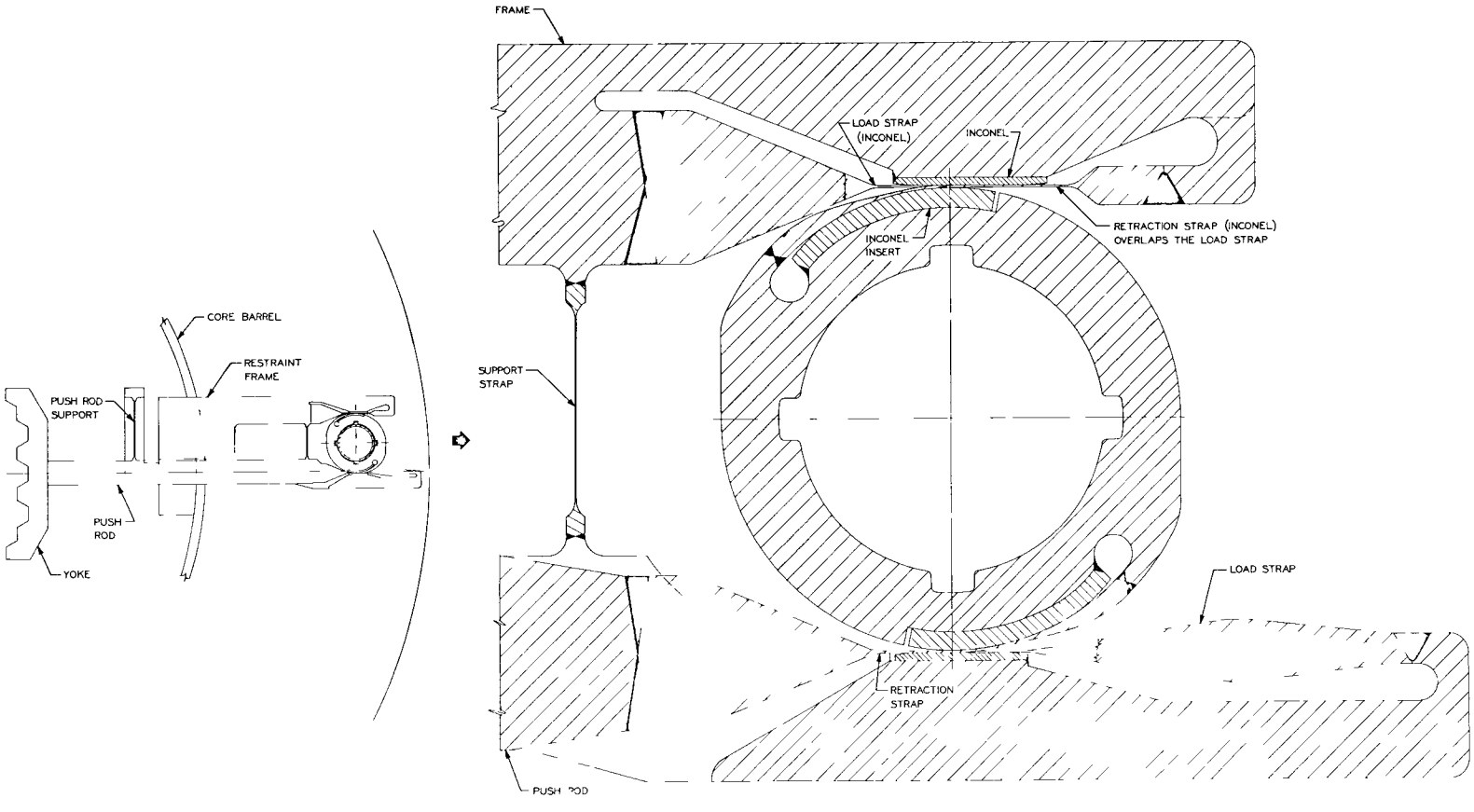

FIGURE VI-2 *Flexible Strap Core Restraint Layout*

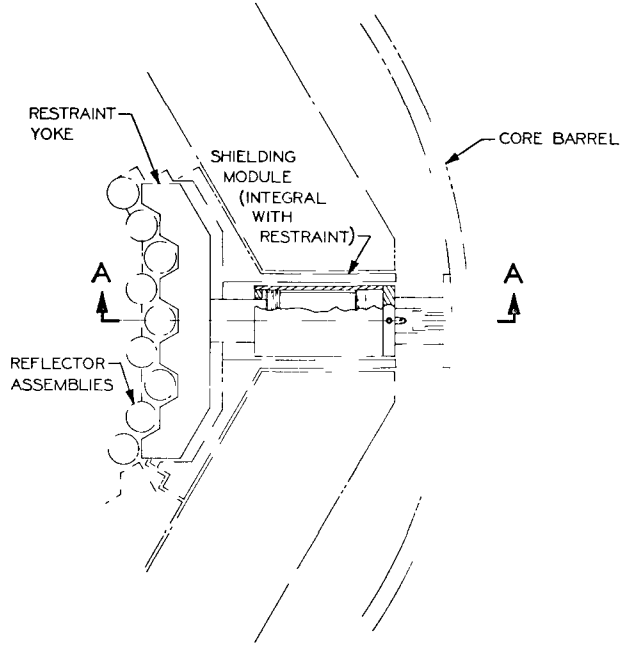

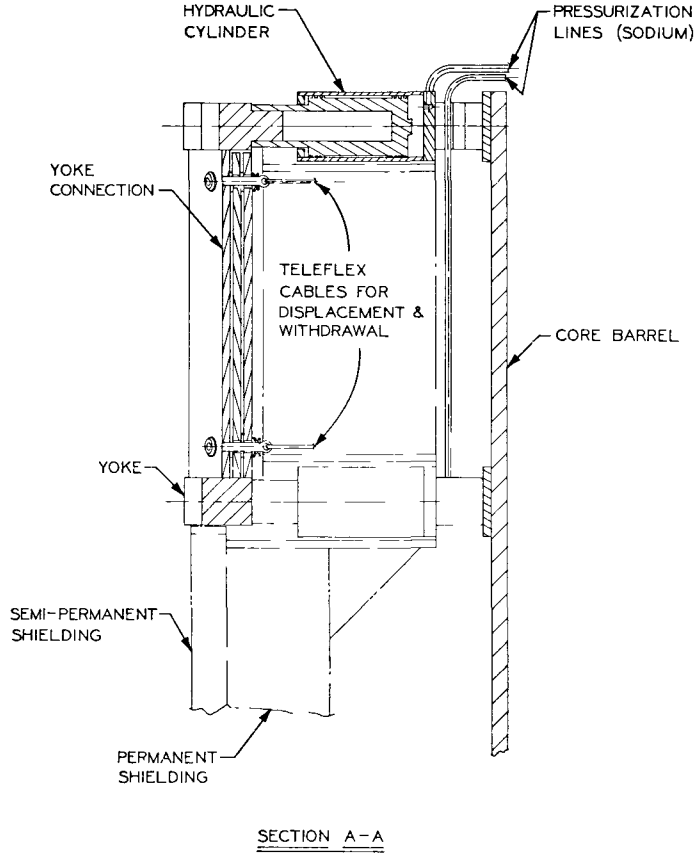

FIGURE VI-3 *Hydraulic Actuator Concept*

tested. Significant results to date include:

1) The verticality of the core depends upon the clamping sequence and the synchronization of diametral clamping mechanisms.

2) Clamping all mechanisms simultaneously is not effective in realigning a disarrayed core.

3) The lower clamping mechanisms are more effective than the upper for realigning the core.

4) The instrumented duct in the center position experiences virtually no load under full clamping forces of 10,000 lb. - - this implies that ducts are bridging.

5) The presence of the center duct appears to aid the realignment of other ducts during the clamping action.

6) Friction appears to play a significant role in aligning the ducts (i.e., friction influences bridging).

7) When ducts are skewed from their theoretical compacted position, ducts cannot be realigned perfectly - - regardless of the clamping forces.

c. Mechanics Code Development (12116)

W. H. Sutherland and W. C. Kinsel

BMCRP.-The initial 3-dimensional version of finite element code BMCRP for analyzing the effects of thermal camber, stainless steel swelling and creep has been completed and implemented.

The BEAMCRP computer code is being developed principally to predict time-dependent structural deformations of FTR flow ducts during the fuel cycle. BEAMCRP now can be used to analyze stresses and deformations arising from thermal creep, irradiation creep, and irradiation swelling plus loading due to pressure, concentrated loads and thermal gradients.

BEAMCRP is operational both at the Hanford 1108 computer and the Westinghouse Penn Center (Pittsburgh) CDC 6600 computer. Significant design results obtained by BEAMCRP:

1) An active above-core restraint mechanism is essential.

2) An active below-core restraint mechanism is desirable.

3) Displacements of the ducts (which influence power coefficients) and reactions on the ducts (which determine their configurations) are highly sensitive to material behavior laws (creep, swelling) and to the thermal profiles.

Comparison of test case results with the 2-D code DUCBO II and BMCRP indicate good agreement.

AXICRP.-The AXICRP computer program was developed to predict the time-dependent stresses and deformations in two-dimensional idealized structures. AXICRP has been used to evaluate the thermal creep strains in cross-secitons of FTR flow ducts. AXICRP has been used to show that thermal creep strains are insignificant in the FTR ducts.

2. Fuel Assembly Nozzle Insertion Tests (12149)

L. J. Defferding

Structural materials, including austenitic stainless steel, are subject to dimensional changes during irradiation in a fast reactor. One potential consequence of this phenomenon is the gradual bowing of the fuel assemblies during reactor operation, which could cause binding of the lower portion of the fuel assembly (the nozzle) in the receiving receptacle during the process of replacing or repositioning the fuel.

The objective of this test program is to identify and evaluate potential problems caused by remote insertion and withdrawl of various designs of FFTF fuel assembly nozzles and orifice receptacles. It is specifically desirable to find a correlation between the nozzle-receptacle design and the extent of nozzle-receptacle misalignment, ease of nozzle insertion and withdrawl, and to determine the effect of misalignment on galling, fretting, and wear of nozzle and receptacle surfaces.

Testing completed to date has involved two nozzle-receptacle designs, a single-diameter cylindrical wall and a stepped wall (see Figures IV-4 and IV-5). Both a straight fuel assembly and a bent fuel assembly (to represent the bowing expected with 270 days of reactor operation) were used in the tests; the nozzles were aligned with the orifice receptacles or were misaligned by measured amounts up to 0.5 in. Radial guides with 1/2-in. annular clearance were located about 6 ft. and 10 ft. above the top of the orifice receptacle; these guides approximated the effect of a core restraint on the fuel assembly. The tests were performed with pressurized air at ambient temperature flowing through the receptacle

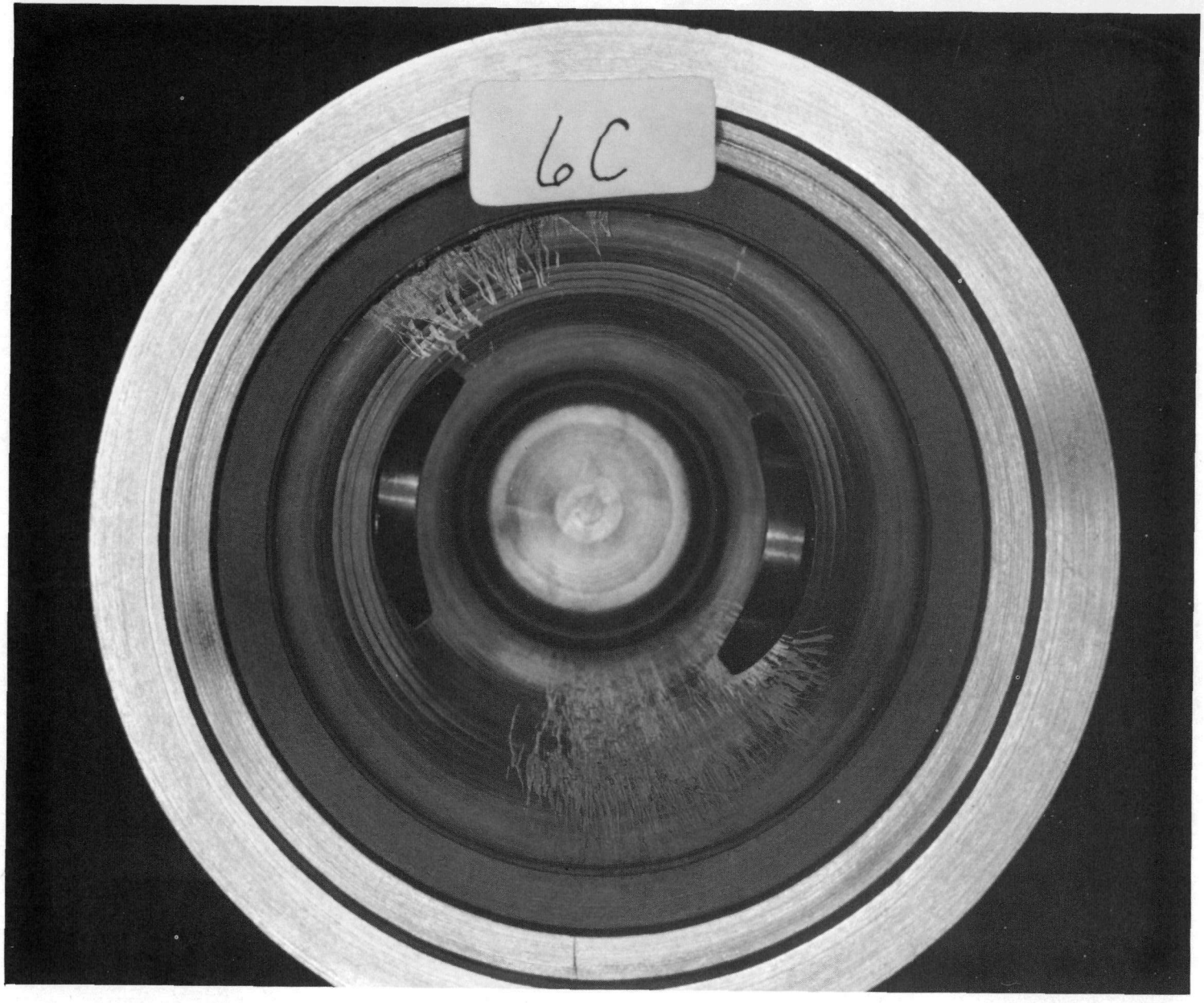

FIGURE VI-4 *Scratches and Galling Inside a Straight Receptacle After 50 Insertion-Withdrawal Cycles With a Bent Fuel Assembly.*

FIGURE VI-5 *Two Views of Stepped Cylinder Nozzle Showing Scratches and Galling Near Tip and in Upper Steps After 50 Insertion-Withdrawal Cycles With Nozzle and Receptacle in Correct Alignment.*

to simulate the shut-down sodium flow.

a. Tests With Bowed Fuel Assemblies

Test results indicate that both designs of nozzles and receptacles require high loads and undergo significant damage during withdrawl and insertion of the bowed fuel assemblies. In testing a bent fuel assembly with the nozzles in alignment, forces exceeding 500 lbs were required to insert either nozzle design; forces of 900 to 1000 lbs. were required for withdrawal, and the nozzle and receptacle surfaces were scratched and galled to an estimated depth of 15 mils (Figures VI-4 and VI-5). Minor radial restraint on the upper part of the assembly greatly increased the difficulty of nozzle movement. With the assembly guides in place, a misalignment of only 0.25 in. required more than 1000 lbs after two insertion-withdrawal cycles. The stepped cylinder design was successfully tested to a misalignment of 0.50 in., but required 200 to 500 lbs. for withdrawl and insertion. With both guides removed from the assembly (leaving only a cable guide located about 18 in. above the top of the assembly), the nozzles were inserted and removed with up to 200 lb force at misalignments of up to 0.50 in.; the top of the fuel assembly moved around quite a bit but there was no significant scratching or galling of nozzle or receptacle surfaces (Figure VI-6). The top of the assembly was out of plumb by 1 to 1 1/4 in. when the nozzles and receptacles were in alignment and fully inserted; it was out by an additional 0.5 in. when fully inserted at a misalignment of 0.50 in.

b. Tests With Straight Assemblies

With a straight fuel assembly, no insertion or withdrawl forces, except the weight of the assembly, were required for either the straight or stepped cylinder design, and damage was limited to light burnishing of nozzle and receptacle surfaces at the contact points. Nozzle-to-receptacle misalighments as great as 0.50 in. had negligible effect on insertion, withdrawl, or damage.

Further testing is planned when nozzle and receptacle components of new design become available.

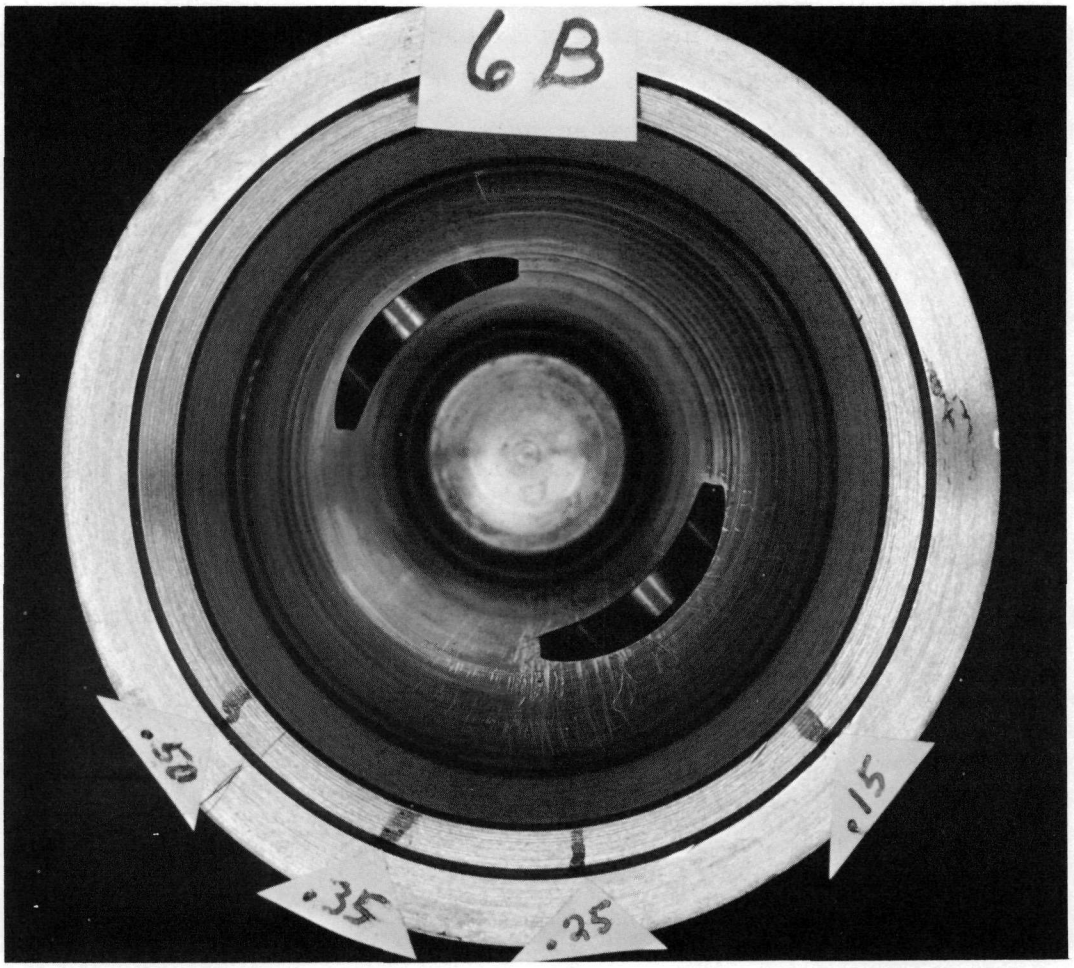

FIGURE VI-6 *Straight Cylinder Receptacle after 5 Insertion-Withdrawal Cycles at Each of Four Misalignment Positions with a Bent Fuel Assembly. Note some scratches and galling at 0.15 and 0.25 positions (fuel assembly partly restrained by lower radial guide) and absence of damage at 0.35 and 0.50 positions (no guides; fuel assembly completely free).*
Neg. # 704241-14

B. CORE PROCESS TECHNOLOGY

1. Fuel Management

R. J. Hennig and J. F. Wett

Analysis of certain aspects of fuel management have led to decisions about initial core(s) design and operation. Some of these decisions are:

1) No axial enrichment zoning will be used.

2) Equilibrium feed enrichments will be used.

3) Selected driver fuel assemblies will be replaced with special nonfueled test assemblies to achieve fixed shim requirements in excess of the capability of the seven Ta peripheral shims.

4) For the purposes of better estimating fuel enrichments and for planning the engineering mockup critical experiments, the following nominal test loadings will be used:

- Two general purpose closed loops, containing 37 pin oxide bundles operating at 15 kw/ft peak power.
- Two special purpose (safety oriented) closed loops containing seven pin oxide fuel bundles operating at 18 kw/ft peak power.
- Four open test positions containing 217 pin oxide fuel bundles with grid spacers, of the same composition and enrichment as adjacent driver fuel.

2. Core Arrangement

J. F. Wett, R. J. Hennig, G. R. Waymire

Potential modifications to the core presently being evaluated include:

1) Rotating the three Row 5 shim/scram rods one lattice position clockwise, and moving the Row 4 rod to that position in Row 5 which would provide additional similarity amongst the three instrument trees and tri-sections of the vessel cover.

2) Moving the oscillator rod to that Row 4 test position which would permit moving the two special purpose closed loops to adjacent Row 2 and Row 4 positions, thus easing radial restraint problems.

3) Providing an alternate means of instrumentation and backup hold-down for the center test assembly to permit contact instrumentation (or a closed loop) in the proximity instrumented open test position and to make each instrument tree identical.

3. Heat Transfer Characteristics of FFTF Fuel Assemblies (12146)

R. E. Collingham, V. R. Hill, J. M. Yatabe

The goals of this task are to provide heat transfer information to support LMFBR fuel assembly design, reactor safety evaluations and reactor operation. The immediate objectives are to define the thermal hydraulic behavior of both normal and abnormal seven-pin bundles of electrically heated pins in sodium to support the FFTF fuel design and to develop heater pins for safety tests.

During the reporting period, two tests were completed. In these tests, the internal pin thermocouples consisted of two bare wires welded separately to the inside surface of the sheath. Conclusions, based on preliminary analysis of the data, are given below:

a. Conclusions

1) The measured heat transfer coefficient from inside the sheath was consistent with analytical and experimental literature values (approximately 30,000 Btu/hr-ft^2).

2) Bundle bowing caused the maximum temperature difference between the outer coolant channels to increase by about 20%. This may be important in structural analyses that consider the maximum temperature difference across a duct.

3) The measured clad hot spot due to pin bowing at the point of contact was within the 100°F maximum determined by analytical techniques.

4) The measured coolant enthalpy distribution was only slightly disturbed by pin bowing; no signigicant increase in the coolant enthalpy was found two in. downstream of the bowed pin contact point.

5) The measured clad temperature difference across the outer bowed pin was about twice that across an outer unbowed pin in this test. Under typical FFTF conditions, the measured temperature difference across the bowed pin was about 100°F.

6) The cladding temperature increase beneath a wire wrap (when the wrap was located between pins) was small (about 20°F) and not significantly different from earlier measurements where the

orientation of the wire was 30 deg. (angular rotation) from that position.

These results imply that the fuel pins can sustain the abnormal event of two pins bowing together without immediate clad failure.

b. Test Data

Typical data from tests of a seven-pin fuel bundle centered in the duct are shown in Figure VI-7. The uniformly heated pins were 0.230-in. diameter, 39 in. long and were wire wrapped with a 0.056-in. diameter tube containing two thermocouples. The instrument plane was 36 in. downstream. There was a 15-mil clearance between the overall bundle size and the duct on each side. Figure VI-7 also shows the local coolant temperature based on thermocouples in the wire wraps and on the hex flow duct. Figure VI-8 shows the strong temperature gradients that were measured by a traversing thermocouple midway between Pin Nos. 2 and 7.

4. Fuel Assembly and Poison Control Rod Vibration Testing (12119)

G. R. Sawtelle and W. C. Kinsel

Coolant flowing through a reactor core at high velocities is a source of energy that can induce and sustain vibration in reactor core components. Fuel assembly internals may be damaged by fretting, wear, weld failure, and fatigue caused by this flow. These short and long term vibration effects may lead to component failure, which, in turn, could cause severe accident conditions that would necessitate reactor shut-down.

In general, theoretical methods to predict flow-induced vibrations are not available; any theoretical treatment would be extremely difficult because of the complex geometric and time-varying boundary conditions present in the spiral wire wrap fuel design. Furthermore, the forcing function associated with flow-induced vibrations is not well defined. Because of the uncertainties in predicting flow-induced vibrations, experiments are required.

Preliminary flow-induced vibration testing has been conducted as part of a conductivity cell instrument development program. The conductivity cell, which measures relative displacement between two fuel pin

$q = 541{,}000$ BTU/HR-FT^2

$Pe = 474$

$T_{bulk} = 767^oF$

$T_{inlet} = 578^oF$

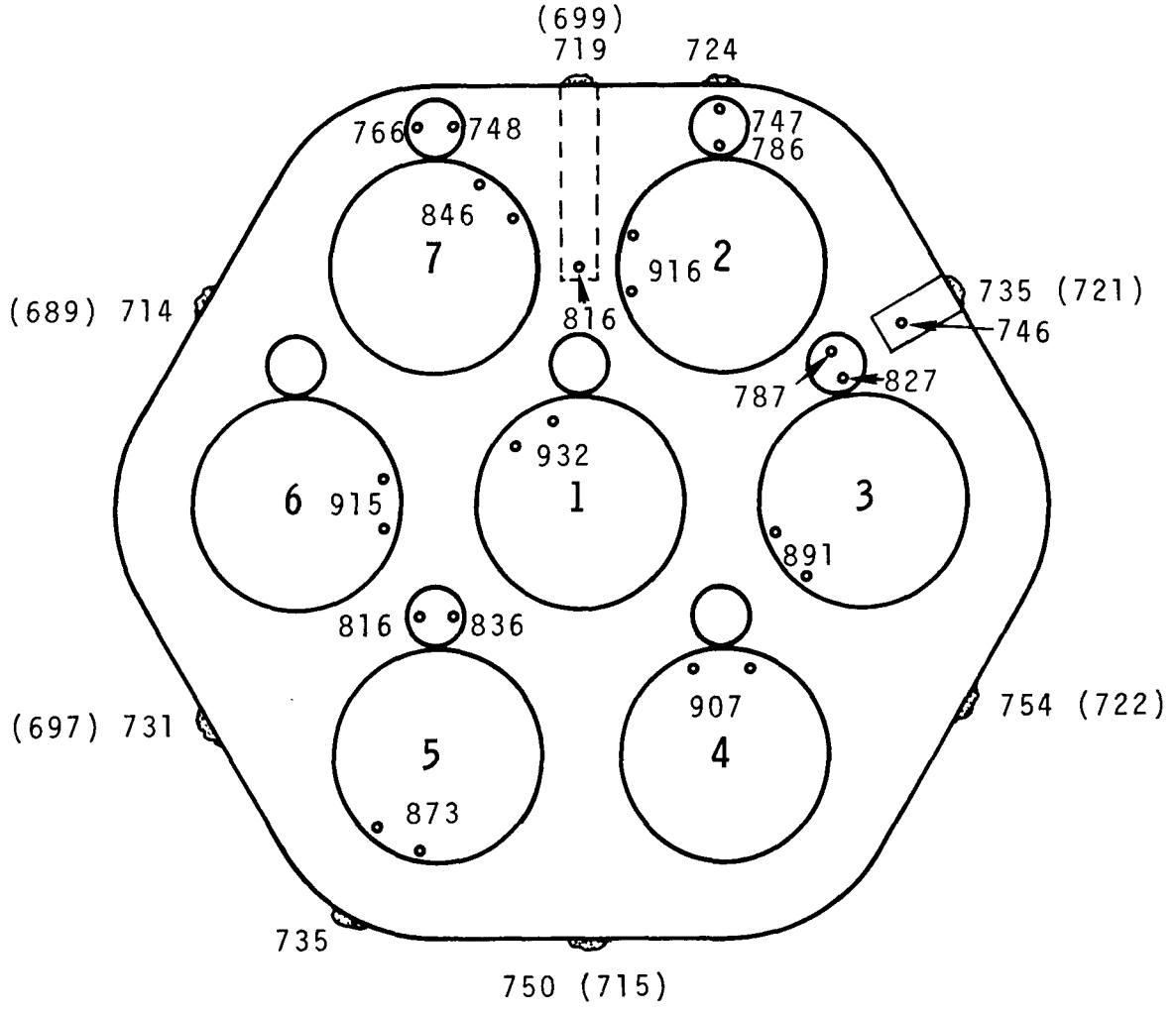

FIGURE VI-7 *Temperature Map, Wall-to-Wall, Looking Downstream Clockwise. NOTE: All temperatures in °F.*

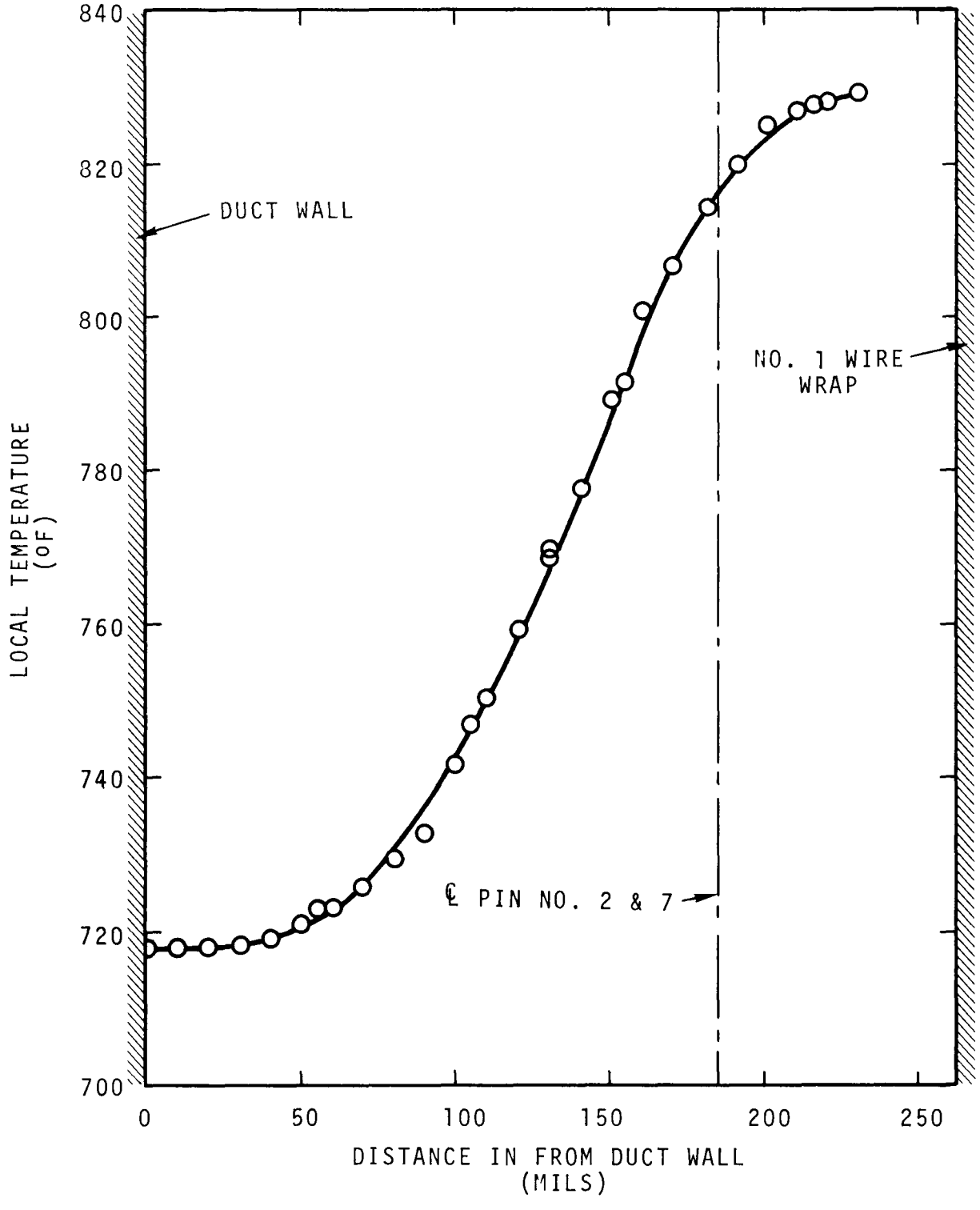

FIGURE VI-8 *Temperature Traverse of Outer Channel.*

surfaces in water (0.75% N_aNO_3), was shown to be feasible for the FTR fuel geometry. Testing is in progress to evaluate a reliable cell construction for the 60 to 200°F temperature cycling of the water coolant.

Commercially available miniature accelerometers small enough to fit on the inside of the fuel cladding have been tested; some were found which will survive 200°F and provide a reliable output with an accuracy of 5 to 10 percent. Strain gages are available that are small enough to be mounted on the inside of a fuel cladding. Testing of these gages is planned to determine their dynamic response characteristics at elevated temperatures. These gages are advertised as being operable to 1500°F for dynamic measurements.

The SAMIS computer program has been implemented to provide natural frequency and mode shape data for a typical fuel pin using simple and multiple supports. Preliminary results indicate that maximum amplitudes occur below the center of mass for the multiply-supported case, but for the simply-supported fuel pin, the maximum amplitudes occur away from the mass center and nearer the gas plenum area. Preliminary natural frequencies for a typical fuel pin are approximately 1.5 Hz and 300 Hz for simply and multiply-supported fuel pins, respectively.

C. IRRADIATION TEST FACILITIES

1. Closed Test Loop In-Reactor Assembly (CLIRA)

M. A. Vogel and R. C. Walker

ARD, under WADCO technical direction, continued to develop the conceptual design of this component. The concept developed by ARD and approved by WADCO is shown on Figure VI-9 and Figure VI-10.

Major features of the approved concept are:

· A double walled 316 SS pressure tube; this pressure tube has a moderate (0.035 in.) helium conductance gap in the core region and a somewhat more insulative (0.050 in.) helium gap above the core region. The pressure tube interfaces directly with the core fuel subassemblies and the core support structure. A meltdown cup is provided in the bottom of the pressure tube to contain any test fuel meltdown.

· The flow tube is a double walled tube of 316 SS with a 0.035 in. helium conductance gap in the core region and a 0.100 in. helium gap above the core region. The usable test diameter in the flow tube is 2 1/2 in.

· The test section is located inside the flow tube, and is supported by the instrument tube. The instrument tube contains the instrumentation leads from the test section, plus a separable instrument connector to permit shortening the test train to 12 ft; the instrumentation can be reconstituted after an interim examination of the test section.

· The pressure tube, flow tube, integral pot and instrument tube are all supported from the spool piece that is attached to the reactor vessel head standpipe for the CLIRA. The spool assembly directs the inlet and return flow of the test coolant to the appropriate flow annulus formed by the CLIRA tubes. Two welded seals near the top of the spool piece isolate the test coolant from the FTR containment. A welded seal near the bottom inside of the spool piece isolates the test coolant from the FTR cover gas

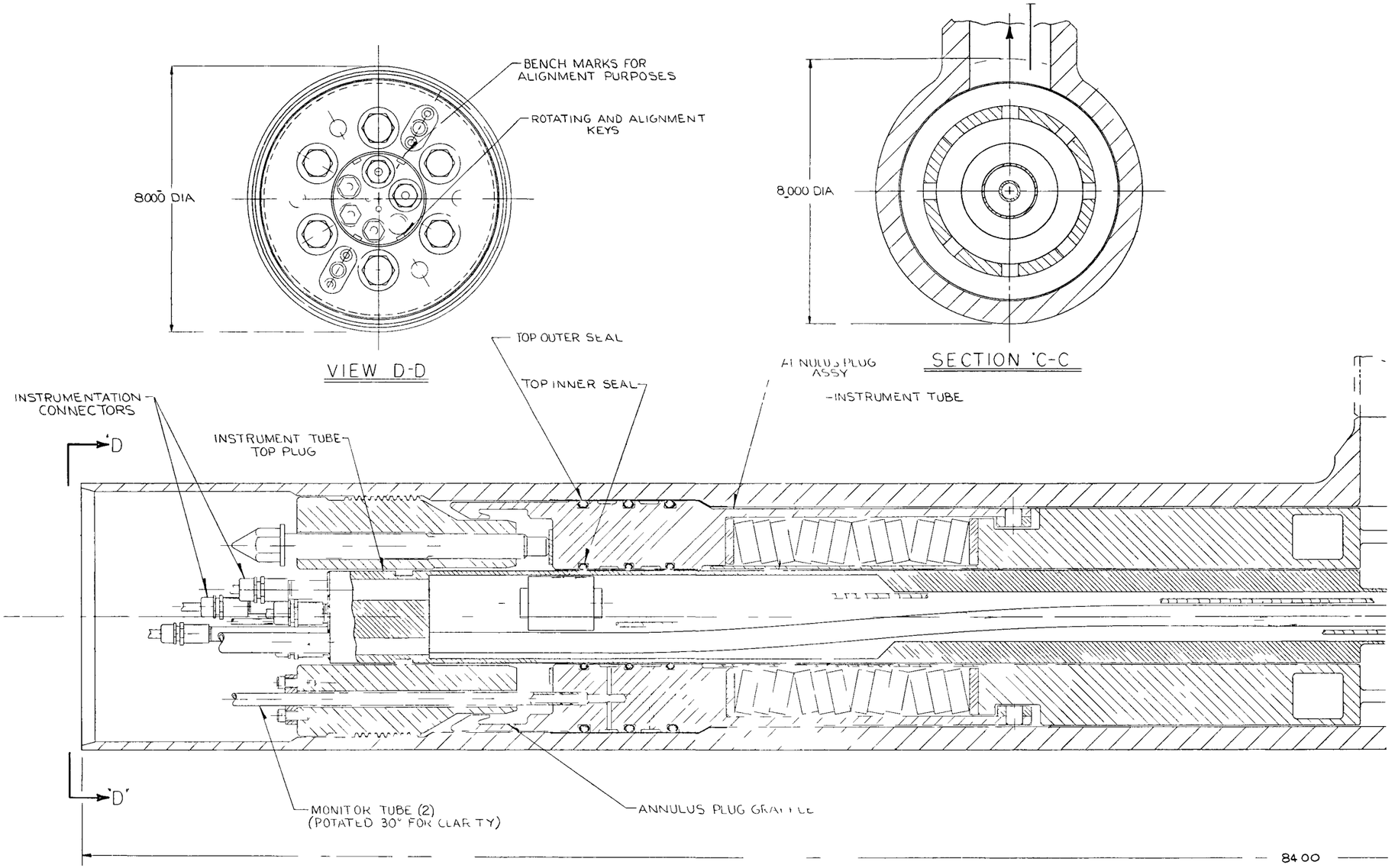

FIGURE VI-9 *Closed Loop In-Reactor Assembly--Upper Section.*

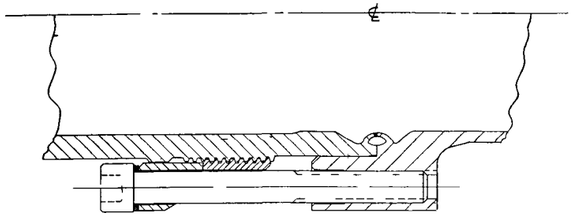

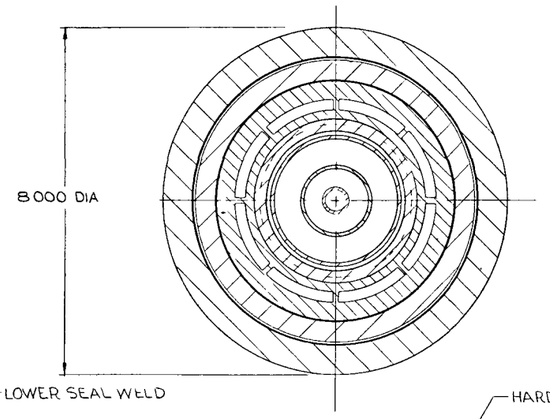

Notes 1 All Materials 316 SS or as Indicated
2 All Parts Fabricated and Inspected in Accordance with RDT E8-11

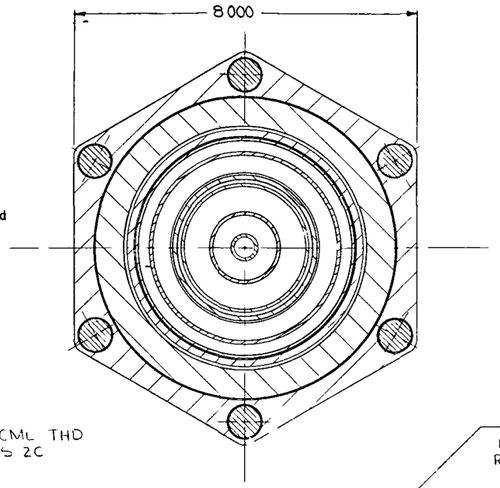

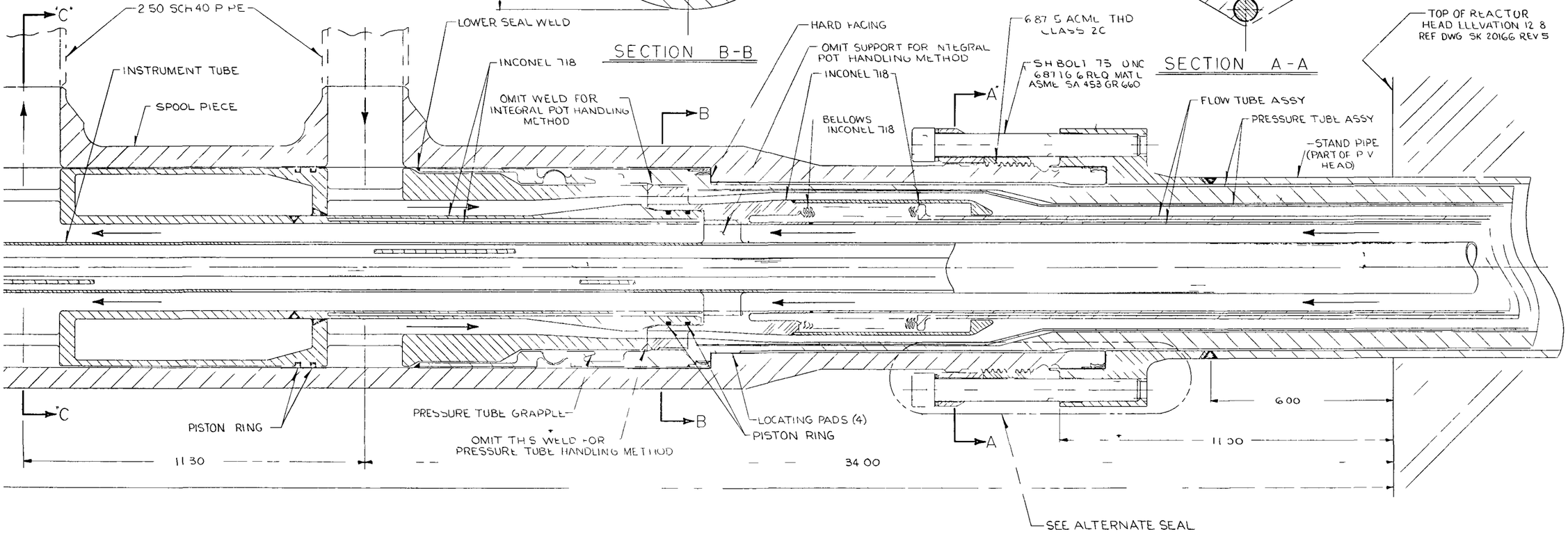

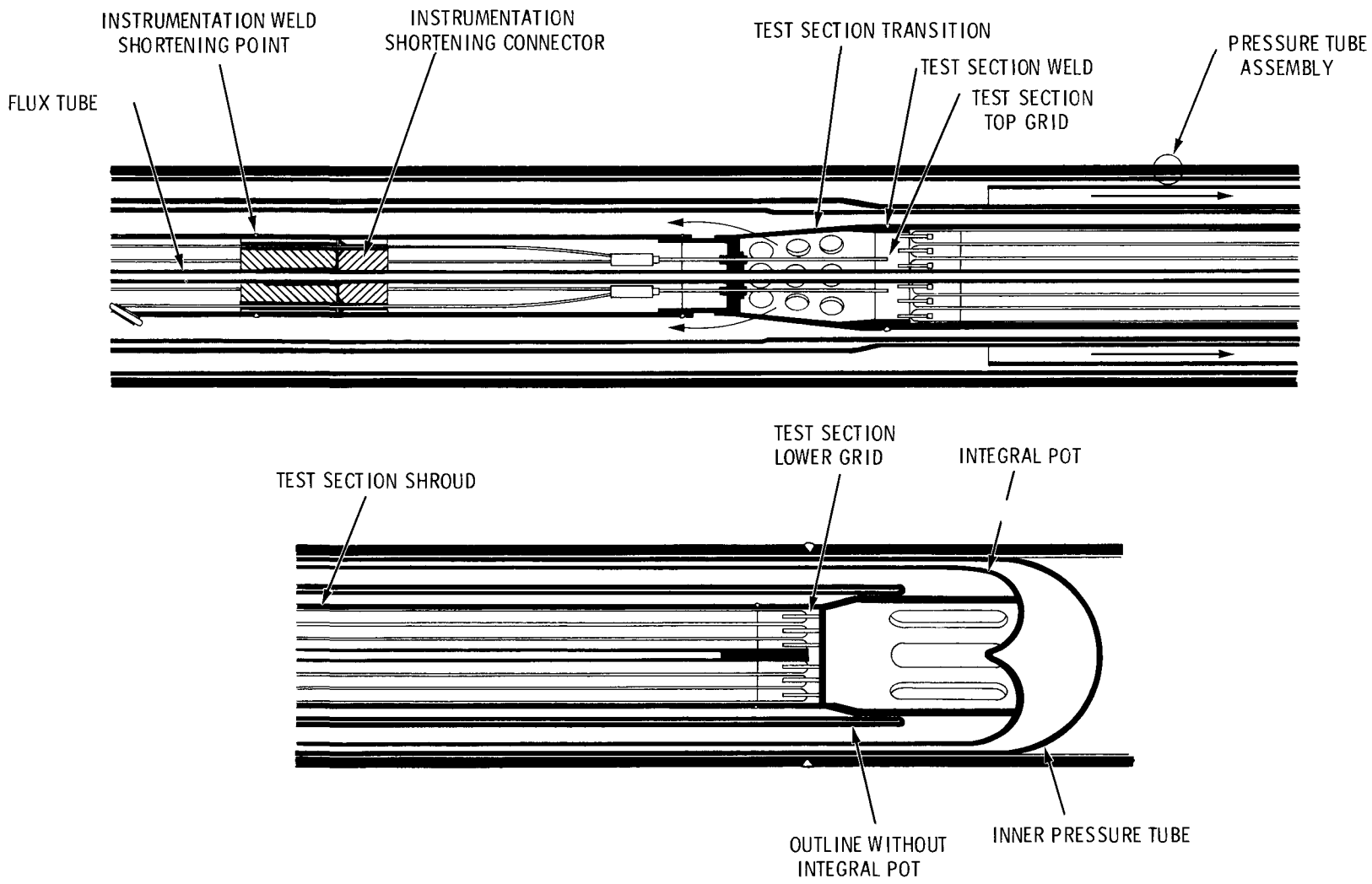

FIGURE VI-10 *Closed Loop In-Reactor Assembly--Lower Section.*

and sodium coolant. An autoclave type closure secures the removable annulus plug and spool assembly to the spool piece. Removable instrument connectors are located on top of the spool assembly for manually disconnecting the instrumentation.

· An integral pot, approximately 11 1/2 ft long, is assembled to the flow tube and test train to provide a sodium pool for cooling the test section during handling operations. This permits removal of a test from the pressure tube while the tube remains in the reactor.

· The CLIRA test train, including the integral pot, can also be handled inside the pressure tube, which acts as a long sodium-filled pot. In order to improve decay cooling during closed-loop handling, an adaptor has been provided to effect natural circulation.

2. Closed Test Loop Analysis

A. L. Gunby and J. P. Hale

In the process of performing an evaluation of the closed loop design, a test section model was developed and employed. The results showed that decreasing the initial test section ΔT to 200°F results in a decreased transient rate for the scram with full flow case. Figures VI-11 and VI-12 show the responses for 400°F and 200°F ΔT, respectively, to be 110°F/sec and - 65°F/sec. The model used consisted of three axial nodes with separate fuel, clad and coolant nodes in the fueled region, plus additional nodes for axial reflectors.

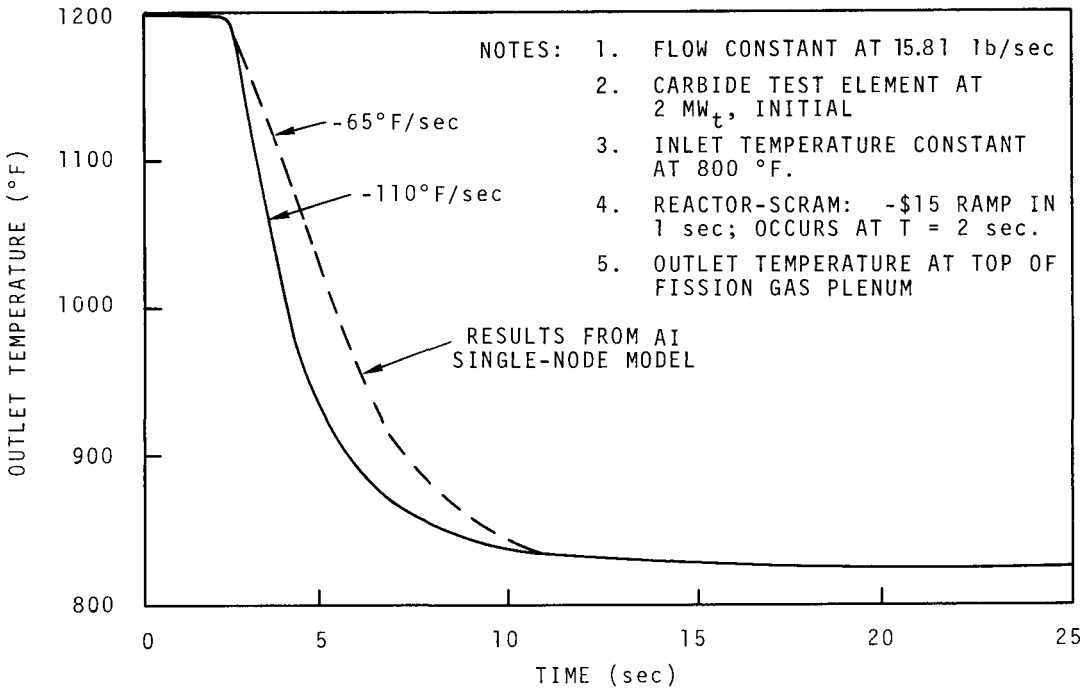

FIGURE VI-11 *Closed Loop Test Section Coolant Outlet Response, Reactor Scram with Full Flow.*

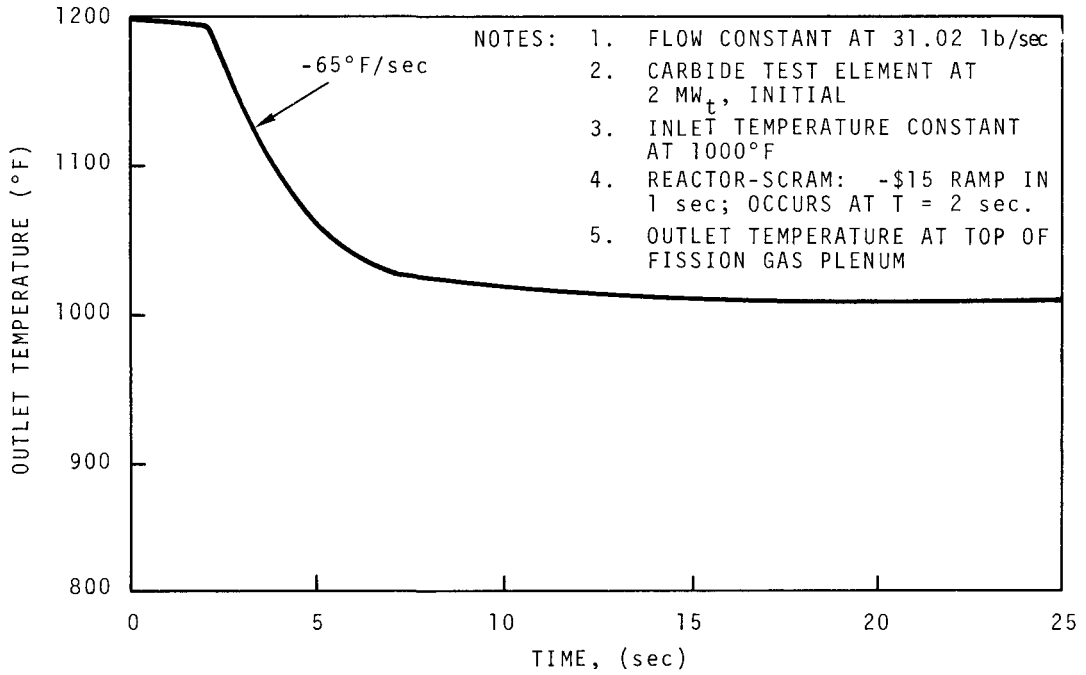

FIGURE VI-12 *Closed Loop Test Section Coolant Outlet Response, Reactor Scram with Full Flow.*

D. OTHER CORE DESIGN PROGRESS

1. High Temperature Sodium Facility

a. Project Progress

D. B. Whitford, K. L. Young, C. E. Linderoth, K. G. Toyoda

Ground was broken on 26 September 1970 for the High Temperature Sodium Facility (HTSF). Figure VI-13 is an exterior sketch of the HTSF.

The HTSF will be used to support the FFTF and LMFBR programs, through testing of large hardware, components, systems, and structural materials in high temperature sodium and sodium vapor environments. The HTSF will have a gross area of approximately 99,000 sq.ft. It will have working space for approximately 370 people, a high bay area for LMFBR development programs, and a service wing containing support facilities and building services.

b. CRCTA Mixing Tests

D. H. Lester and V. F. Fitzpatrick

As part of the sodium technology support for the FFTF test systems, a water model mixing study of the large vessel in the High Temperature Sodium Facility for the Reactor Components Testing Activity (HTSF/CRCTA) was initiated. The vessel in the sodium facility will contain prototypes of FFTF fuel-handling machinery in a high temperature sodium environment. The driver loop flow in the system will be used to maintain a mixed environment in the tank through the use of nozzles and jets.

The water model system has been completed and has undergone preliminary shakedown tests resulting in some modifications to the system. The system is a once-through flow system pumping fresh water at 1 gpm through a 74-gal. tank containing "boxed in" models of the core segment, instrument tree, fuel handling machine and other miscellaneous in-tank hardware. Two 0.18-in. nozzles in one water model scale to 1.4-in. nozzles in the sodium system. (See Figure VI-14.)

Solution conductivity probes are located in the vessel and in the inlet and outlet piping. The probes are connected to recording system

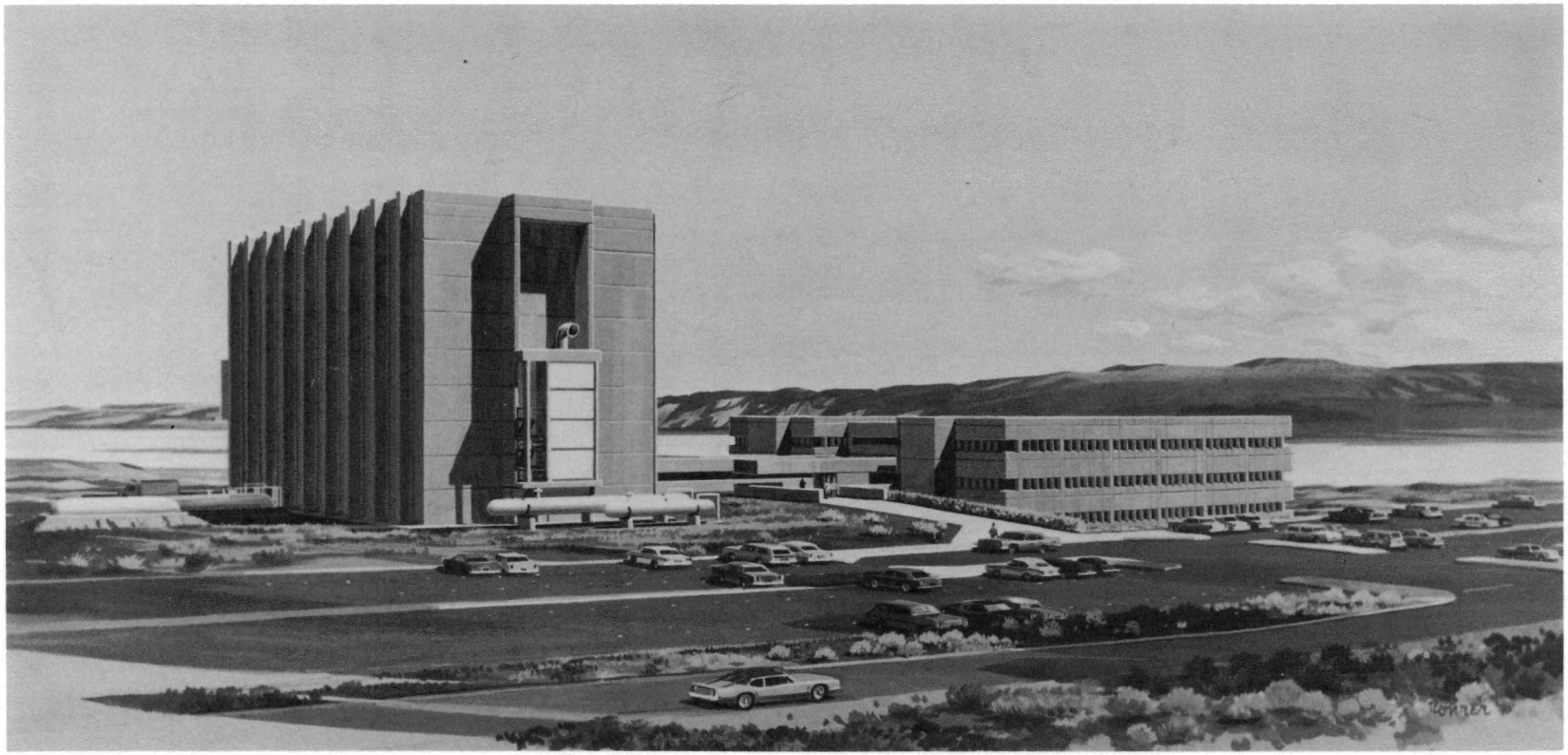

FIGURE VI-13 *High Temperature Sodium Facility.*

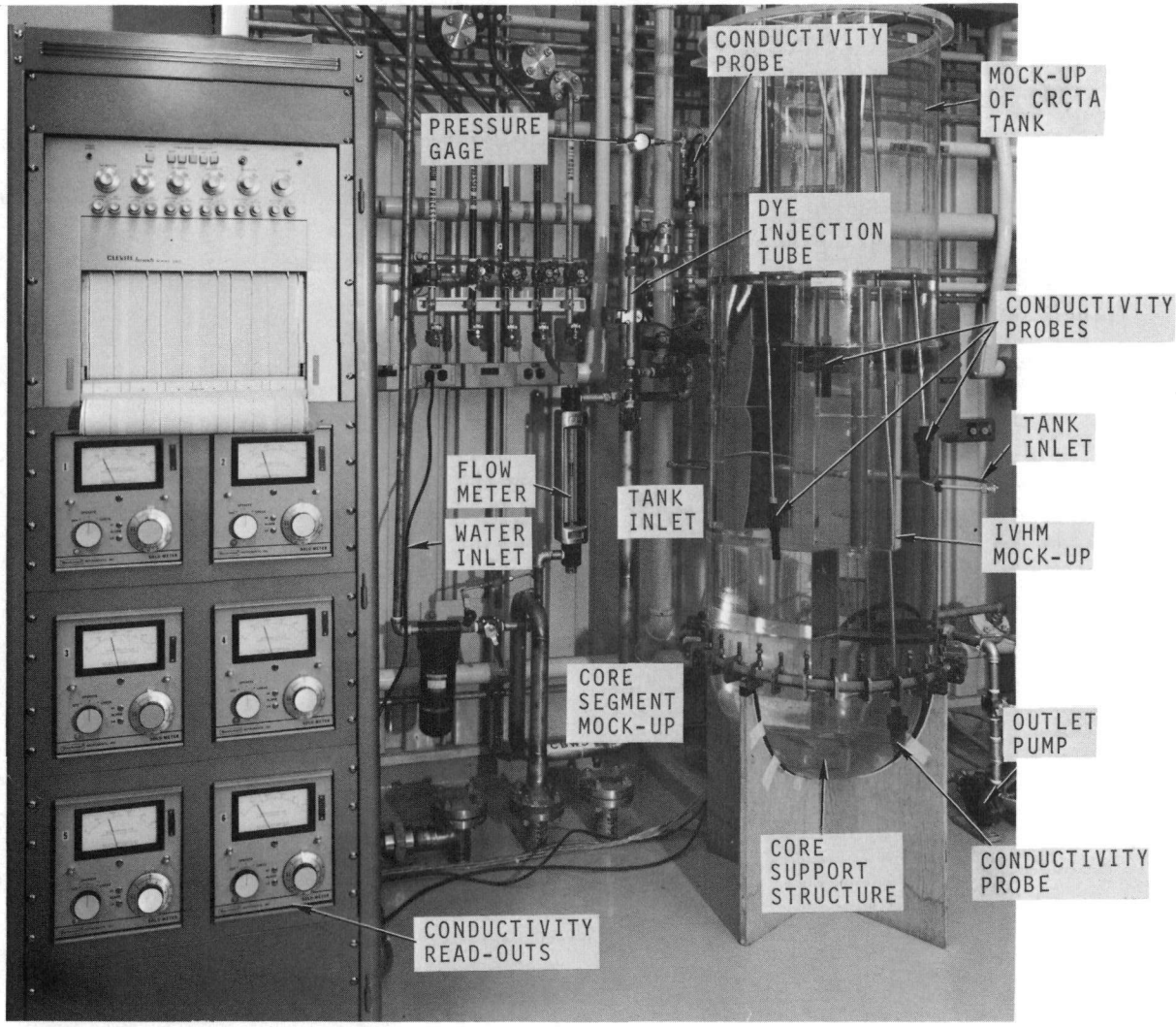
CONDUCTIVITY PROBE
MOCK-UP OF CRCTA TANK
PRESSURE GAGE
DYE INJECTION TUBE
CONDUCTIVITY PROBES
TANK INLET
FLOW METER
WATER INLET
TANK INLET
IVHM MOCK-UP
CORE SEGMENT MOCK-UP
OUTLET PUMP
CORE SUPPORT STRUCTURE
CONDUCTIVITY PROBE
CONDUCTIVITY READ-OUTS

for continuous readout of conductivity at the measuring points. A salt solution tracer is injected into the system and followed with the conductivity probes. Testing has begun and early data on a pair of cylindrical 0.18-in. diameter nozzles indicated that smaller nozzle diameters are required.

2. Hydraulic Core Mockup (12439)

The objectives of this task include evaluation of hydraulic characteristics of the FFTF vessel and core components using reduced scale, isothermal, hydraulic models. The complexity of the hydraulic system encountered in a nuclear reactor vessel does not permit an accurate analytical analysis. Thus, the methods of hydraulic modeling are often applied to examine these systems. The hydraulic core mockup program uses this approach and consists of two "future models" characterizing the inlet and outlet plenum regions respectively.

The two feature models have been modified to simulate the current reactor design arrangements. Model arrangements are shown in Figure VI-15.

a. Inlet Plenum Feature Model

This model was modified to represent the current inlet plenum zone including downcomers, plenum, core support structure, and duct receptacle regions. Preliminary flow distribution and pressure drop tests have been performed. The data indicate that flow distribution across the core is quite uniform, even when system flow was varied from 67% to 112% of design flow, or by closing off any one of the three coolant circuits. Plenum velocities were sufficient to cause a broken injector tube (1/4 OD x 1/8 ID x 4 in. long steel tube) to pass from a downcomer up through the core support structure and lodge in the removable basket region of the model.

b. Outlet Region Feature Model

This model was modified to represent the current outlet plenum region design and includes hydraulic simulation of pool hardware. The resulting model scale is 0.268.

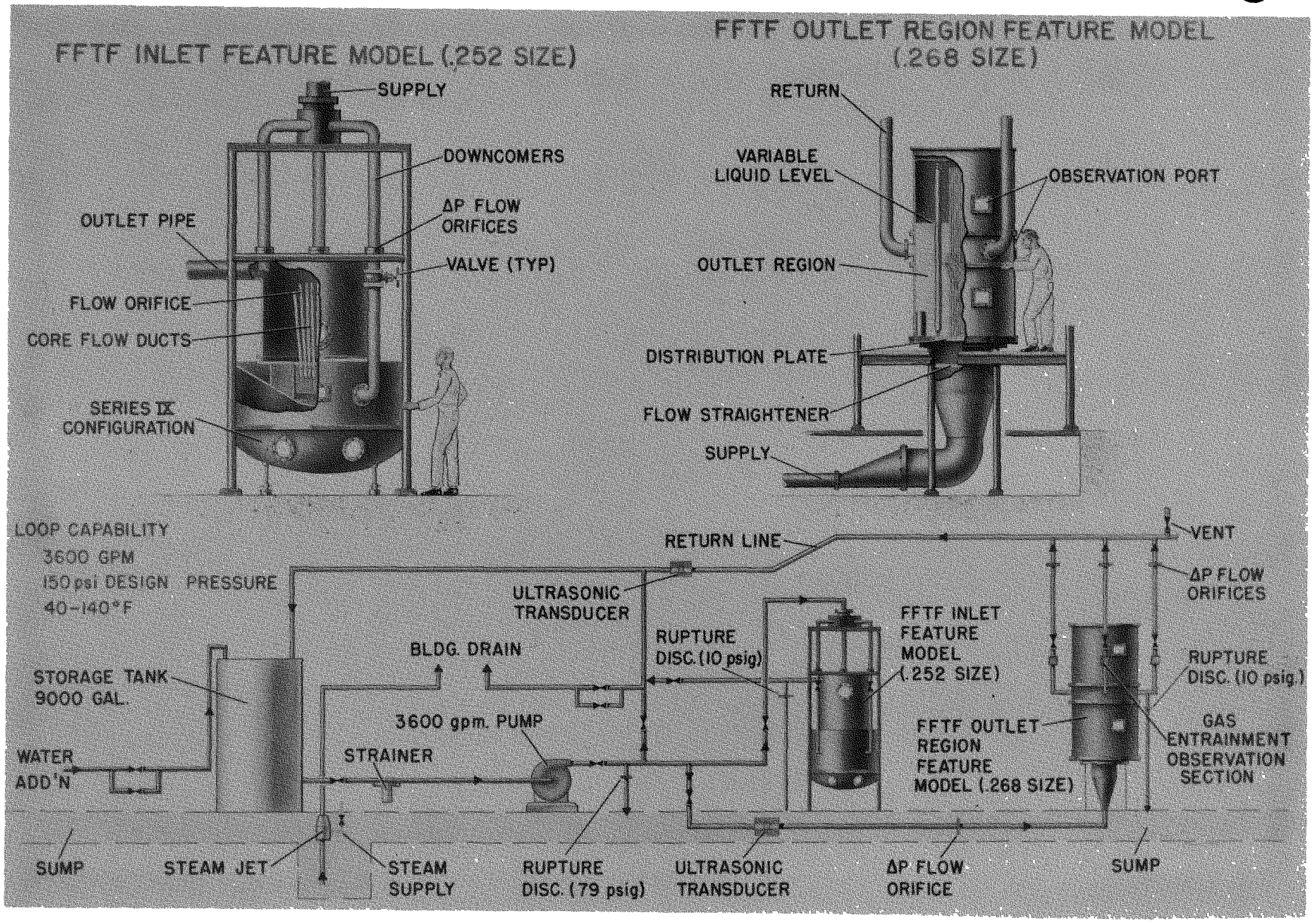

FIGURE VI-15 *HCM Feature Models.*

1) Effect of Vortex Suppression Plate

Tests were conducted for evaluating pool surface conditions and resultant air entrainment with and without a vortex suppression plate (VSP) installed. This plate is located 2 in. below the model pool surface, and is fabricated of two layers of perforated plate with 1/8 in. diameter x 3/16 in. triangular lattice. Three tests were performed for each condition at flow rates of 3010, 1575, and 300 gpm. Figures VI-16 and VI-17 show values of entrained air vs. pool height for the two higher flow rates with and without the VSP, respectively.

The 3010 gpm flow rate represents a model flow velocity equal to that in the reactor; the 1575 gpm rate results in Froude Number ratio of one to one.

As Figures VI-16 and VI-17 show, the VSP is effective in eliminating the minor air carry-under which occurs when the model is operated at a pool surface of 40 in. to 42 in., and at Froude Number equality. This relates to a reactor pool elevation of 12 1/2 ft. to 13 ft. above the outlet nozzle. More significantly, the VSP is quite effective in quieting the pool surface and in reducing the amount of entrained air present in the outlet pool.

2) Flow in Outlet Pool

The results of six tests were averaged to produce data which represent hydraulic pressure drop values chargeable to the reactor outlet pool. The data show that the expenditure of static pressure in the pool is small, and is predicted at <0.25 psi for the reactor.

Localized fluid velocity data are being obtained for a nominal 1/3 sector of the outlet pool. Data points are located in 20 planer positions, and at least seven elevations between the outlet nozzles and the pool surface. Although the plotting of velocity profiles is not complete, it is evident that the main bulk of the coolant travels directly upward, with relatively minor mixing occuring, until it strikes the

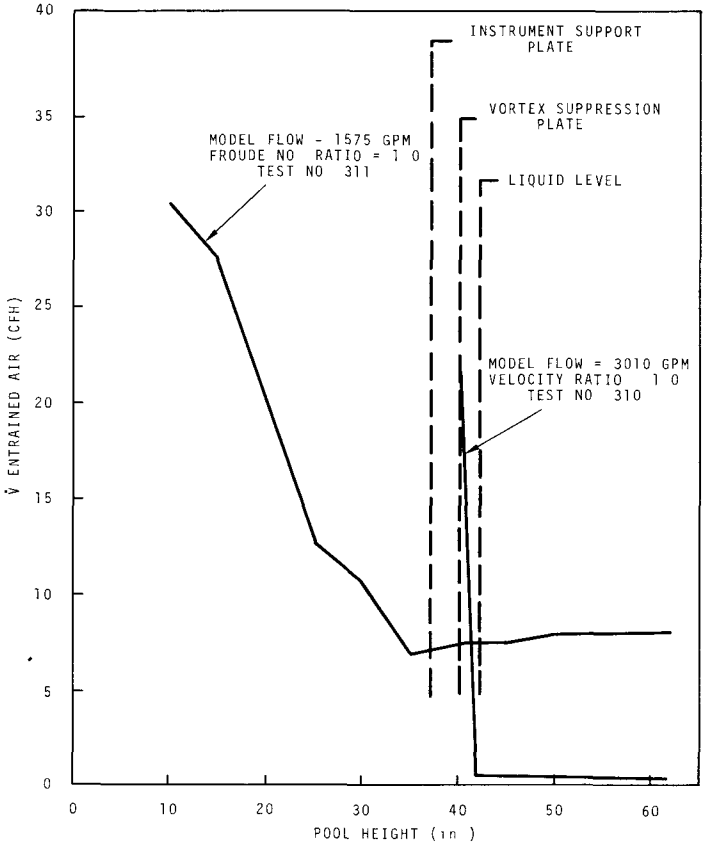

FIGURE VI-16 *Pool Height vs Entrained Air.*

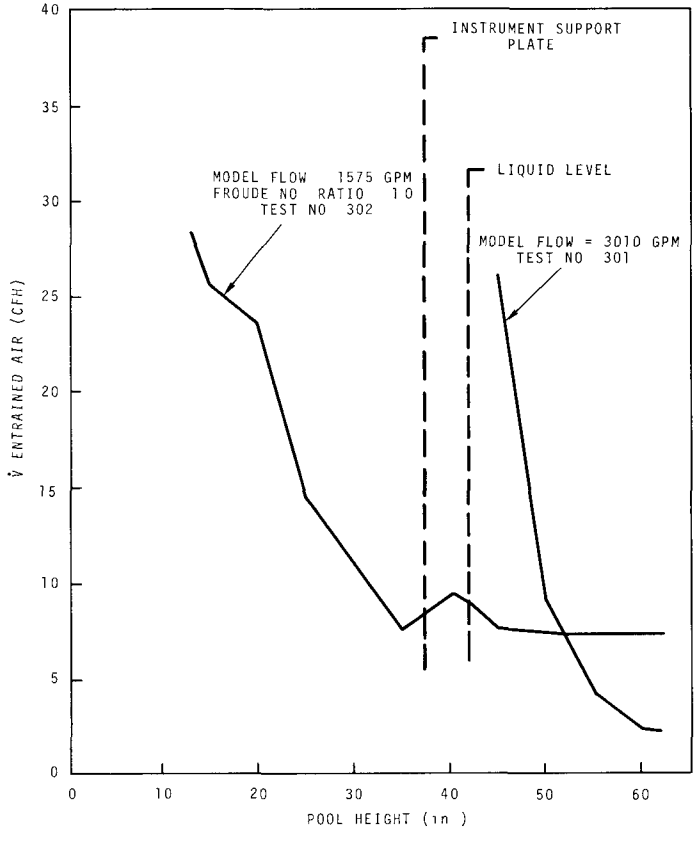

FIGURE VI-17 *Entrained Air vs Pool Height.*

instrument support plates located near the pool surface. The flow is then deflected horizontally in a mushroom effect, travels outward, and thence downward near the vessel wall. Pool velocities range from about 15 fps down to less than 1 fps.

c. HCM Instrumentation

The data logging equipment for the outlet feature model has been modified and supplemented to provide up to 100 channels of signal con ditioners and recording capability.

A high speed digital data acquisition system utilizing a small general purpose digital computer is being constructed for the HCM test facility. Data collected from the transducers will be properly formatted by the computer and put on IBM-compatible magnetic tape so that it may be processed directly by the Univac 1108. Limited on-line preliminary analysis will be made on the data to determine if the data from each channel falls within valid limits.

E. CORE PHYSICS

1. Analysis of Critical Experiments

P. L. Hoffman, R. E. Heineman, H. J. Anderson, G. J. Alkire, W. F. Sheely

a. Comparison of Calculated and Experimental Worths of Large Samples of Plutonium and B_4C in FTR Criticals

R. P. Omberg, R. A. Bennett and J. V. Nelson

Measurements made in the FFTF Critical Experiments Program are primarily to assure the absolute accuracy of the methods used in the design of the FTR. Phase B of this program is being carried out by ANL in critical assemblies in which the complexities of the FTR design are being introduced progressively. Analyses reported here are of experiments conducted in ANL SPPR Assembly 1 (FTR Criticals, FTR 1 and 2), the initial critical assembly in that facility. Specifically, comparisons between

calculational and experimental results (Ref 1) are presented for reactivity worths of large samples of fuel (plutonium) and control (B_4C) materials. Portions of the results were presented earlier (Ref 2). These comparisons are being used to assess the accuracy of design values of the reactivities of FTR control and test loops. These data are to be combined with the results of experiments and analyses presently underway in SPR-9 Assembly 26, FTR-3.

Table VI-1 shows a calculation-experiment comparison for a set of fissile-for-fertile, fuel-for-reflector, and B_4C-for-reflector exchanges. The fissile, fuel, and B_4C exchanges vary in location and mass; for example, No. 1 is at the core-reflector interface and involves an exchange of approximately 1 kg; No. 3 is located between the core edge and the B_4C ring in the interior of the reflector and involves 160 kg; No. 5 is located in the center of the core and is the average of five exchanges totaling 32 kg.

The table shows that the C/E ratio for large sample B_4C-for-reflector exchanges is approximately 0.9 ± 0.1. The C/E ratios for fissile material show larger variations. The ratio for fertile-for-fissile exchanges at the core center is 1.2 ± 0.1, and the ratio for core-for-reflector exchanges at the core edge is approximately 1.1. The replacement of reflector by fuel between the B_4C ring and the core produces a C/E ratio of 1.43 ± 0.15.

Table VI-2 shows a comparison between the calculated and experimental multiplication constants for a set of FTR-1 and -2 loadings. It can be seen that k_{eff} is undercalculated in the B_4C-free loadings (1-17, 1-33, and 1-113) and is overcalculated in the highly poisoned loadings (1-52 and 1-96). The loading with B_4C in the interior of the reflector (loading X) is also undercalculated. The table indicates the reason for the single high C/E of 1.43. This value was obtained from the difference in k_{eff} between loadings X and 1-52, that is, the transition from under-calculating k_{eff} to overcalculating it.

TABLE VI-1
CALCULATED AND MEASURED WORTHS OF LARGE SAMPLES OF FISSILE AND B_4C CONTROL MATERIAL IN CRITICAL ASSEMBLIES FTR-1 and -2

No.	Loading	Type of Exchange	Location	Description	C/E*
1	1-17	Core for reflector	Core-reflector interface	1 and 1/2 kg fissile respectively	1.06 & 1.13
2	1-17 to 1-33	Core for reflector	Core-reflector interface	30 kg fissile	1.10 ± 0.05
3	X to 1-52	Core for reflector	Annular space between B_4C ring and core	160 kg fissile	1.43 ± 0.15
4	1-70	Core for reflector	At B_4C ring (involves translation of B_4C across the ring)	1 and 1/2 kg fissile respectively	0.96 & 1.11
5	1-96 to 1-113	Fissile for fertile	Core center	Average of 5 exchanges totaling 32 kg	1.2 ± 0.1
6	1-17 to X	B_4C for reflector	Interior of reflector	304 kg B_4C	0.90 ± 0.09
7	1-70	B_4C for reflector	Core-reflector interface	285 kg B_4C, the experimental value	0.82
8	1-96 to 1-113	B_4C for reflector	Core-reflector interface	Average of 5 exchanges totaling 152 kg B_4C	0.9 ± 0.1

* The uncertainties shown reflect the propagation of the statistical experimental error into the C/E ratios; if no uncertainty is shown, the statistical experimental error is negligible.

Thus, large samples show a bias similar to that of small samples, with a difference between the C/E's for fuel and B_4C of 5% to 35% (3) and, therefore, sample size cannot be the source of this bias.

TABLE VI-2

CALCULATED AND MEASURED MULTIPLICATION CONSTANTS FOR VARIOUS LOADINGS IN ASSEMBLIES FTR-1 AND -2

Loading	Description	C/E (mk)*
1-17	363 kg fissile and no B_4C	-4.2
1-33	333 kg fissile and no B_4C	-5.3
X**	333 kg fissile and 304 kg B_4C in center of reflector	-2.5
1-52	523 kg fissile and 304 kg B_4C adjacent to core	+6.5
1-96	527 kg fissile and 285 kg B_4C adjacent to core	+6.8
1-113	495 kg fissile and no B_4C	-9.9

*The calculated k_{eff} has been corrected for transport effects and includes a uniform 10 mk heterogeneity correction.

**The experimenters did not assign a number to this loading; for convenience it is labeled X.

b. Measurements of Large Negative Reactivities in FTR by the Source Multiplication Technique

S. L. Engstrom, J. V. Nelson and R. A. Bennett

Subcriticality states of FTR during refueling and during approaches to critical will be monitored with the low flux monitoring system using the source multiplication technique. This method can be extremely sensitive to the nature of the reactor perturbation producing a multiplaction change.

Quantitative estimates of the effects of a few perturbations in the FTR Engineering Mockup Critical (EMC) have been made as a part of the planning for the EMC program. The EMC configuration is shown in Figure VI-18 and the location of three sensors is indicated. Various perturbations of this system were made as listed in Table VI-3. Corresponding reactivity changes are inferred from source free k_{eff} calculations and from source multiplication calculations. In the latter, the reactivity change was simply based upon the calculated change in the absolute value of total flux level. Using the Δk values from k_{eff} calculations as reference values, the source multiplication values from the three chambers variously over and underestimate the reactivity changes due to local flux perturbations as shown in the "% Overestimation of Worth" column of Table VI-3.

Actually, these calculated values simply illustrate the extreme magnitudes of the errors that can occur for the uncorrected source multiplication technique. This type of calculation and actual experiments to be carried out in the FTR Critical Experimental Program will be used to develop the correction scheme to allow the utilization of the source multiplication method in FTR.

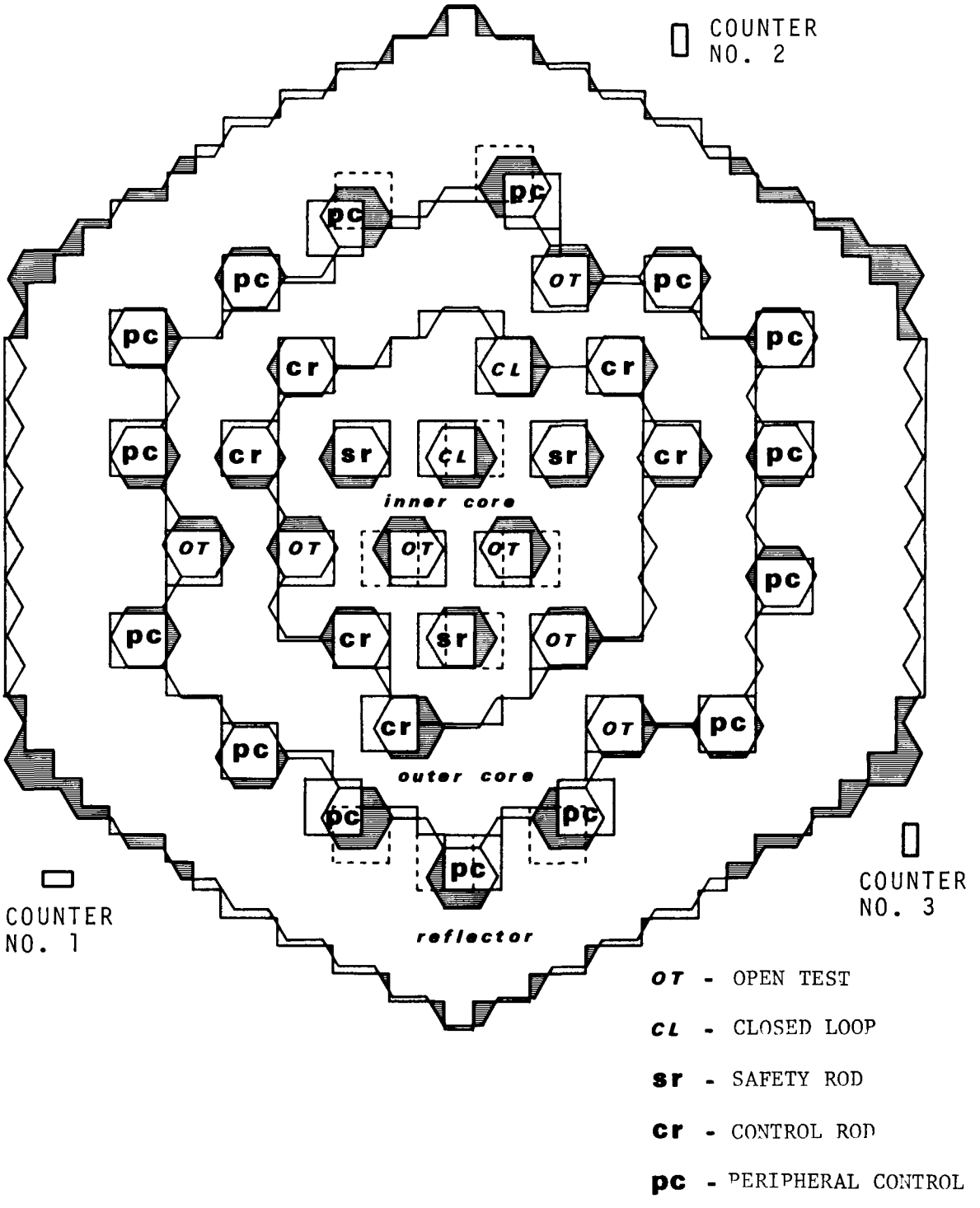

FIGURE VI-18 *Engineering Mockup--FTR Overlay.*

TABLE VI-3
OVERESTIMATION OF WORTH OF CONTROL AND FUEL MOVEMENTS

Description of Perturbation	Counter No.	k_{eff}*		% Overestimation of Worth
		Base Case	Pert Case	
1. Removal of peripheral control rod, zone 6, from fully shutdown core	1 2 3	0.9018	0.9028	+182.02 - 59.04 +236.75
2. Removal of safety rod, zone 39, from fully shutdown core	1 2 3	0.9018	0.9278	- 41.74 + 23.72 - 6.64
3. Removal of peripheral control rod, zone 6, from near critical core	1 2 3	0.9743	0.9755	+ 53.42 - 28.22 + 84.50
4. Replace open test material, zone 29, with closed loop material	1 2 3	1.0030	0.9962	+ 0.167 + 1.23 + 5.51

* Diffusion theory calculations

c. Inverse Kinetics Experiments Precision and Accuracy

R. A. Bennett

Reactivity measurements of control loop strengths requested of ANL are being made using "Rod Drop" techniques and are being analyzed with "Inverse Kinetics Algorithms". Since the range of subcriticality states required is large; (a small fraction of a percent ΔK to as much as 3 to 4% ΔK), required accuracy on the measurements is difficult to obtain. Reptition was recently begun to obtain the required precision.

Significant scatter in the data was observed c.g., for single Δk excess measurement, the unofficial preliminary experimental values were $2.8 \pm 0.2\%$ Δk for fuel "drop" and $1.9 \pm 0.2\%$ Δk for poison "drop" experiments. These results were unacceptable and an investigation has revealed that a modified algorithm for analysis is required to improve the precision.

Accuracy of this method has been evaluated by ANL for reactivity effects of a few inhours but not for reactivities of 100 and 1000 inhours. It is our intent to request calibration experiments for a few hundred inhour reactivity effects as a part of the Subcriticality Experiments in FTR-3.

d. Analysis of FTR-3 Experiments on the ZPR-9

J. V. Nelson and R. A. Bennett

The measurement of Pu^{239} (n,f), U^{238} (n,f) and B^{10} (n,α) reaction rate distributions was done as a part of the FTR-3 critical experiments on the ZPR-9. Four distributions were measured, two radial and two axial. The radial traverses were taken near the core midplane and near the core axial reflector interface. Axial distributions were measured at the core center and at the middle of the outer core zone. Fission rates were measured with a gas flow counter and the (n,α) reaction rates with a proportional counter.

To date, only the radial reaction rates near the core midplane have been calculated. These were done using 2DBS with an X-Y model and a 13-group cross-section set.

2. Three-Dimensional FTR Calculations

S. L. Engstrom, R. A. Bennett and J. V. Nelson

Perturbations in axial distributions of power density in FTR due to partially inserted in-core secondary rods have been calculated using the computer program 3DB (Ref 4). The FTR model was a half core with symmetry about a vertical midplane. This approximation was made to reduce the problem memory requirements to within the present capability of the UNIVAC-1108. To achieve symmetry, the core and control arrangements of FTR were modified to that shown in Figure VI-19, which represents the upper and lower zone of the core. A four broad-group energy model for cross sections was used. Additional details of the model have been reported elsewhere(Ref 4).

Figure VI-20 illustrates the power perturbations induced by the half insert rod in position 2 of Figure VI-19. The power density distribution in Assembly 3, next to the half-inserted rod, is significantly altered, while those for Assemblies 1 and 4 remain fairly symmetric. Comparisons with a similar unperturbed core are not available. Such a comparison can be inferred from the axial power density distributions obtained earlier in an R-Z model of FTR (Ref 5). The core average axial peak-to-average power there was reported as 1.24. Here values for Assemblies 1,3, and 4 are 1.27, 1.29, and 1.26, respectively.

These calculations indicate that, where possible, 3DB calculations on the FTR preliminary design should be made.

3. Results of the FTR Prototypical Reactivity Meter Test in ZPR-IX (Task SRA)

R. W. Albrecht, R. M. Fleischman, G. M. Hess, J. R. Sheff and R. A. Bennett

An on-line reactivity meter which uses a recently developed polarity spectral analysis technique (Refs 6 and 7) was tested in the ZPR-IX reactor at Argonne National Laboratory to aid in evaluating the potential of an operational instrument for FTR. The reactivity meter compares the coherent portion of the fluctuating counter signal to the incoherent portion. The coherent portion results from the fission events and the incoherent portion

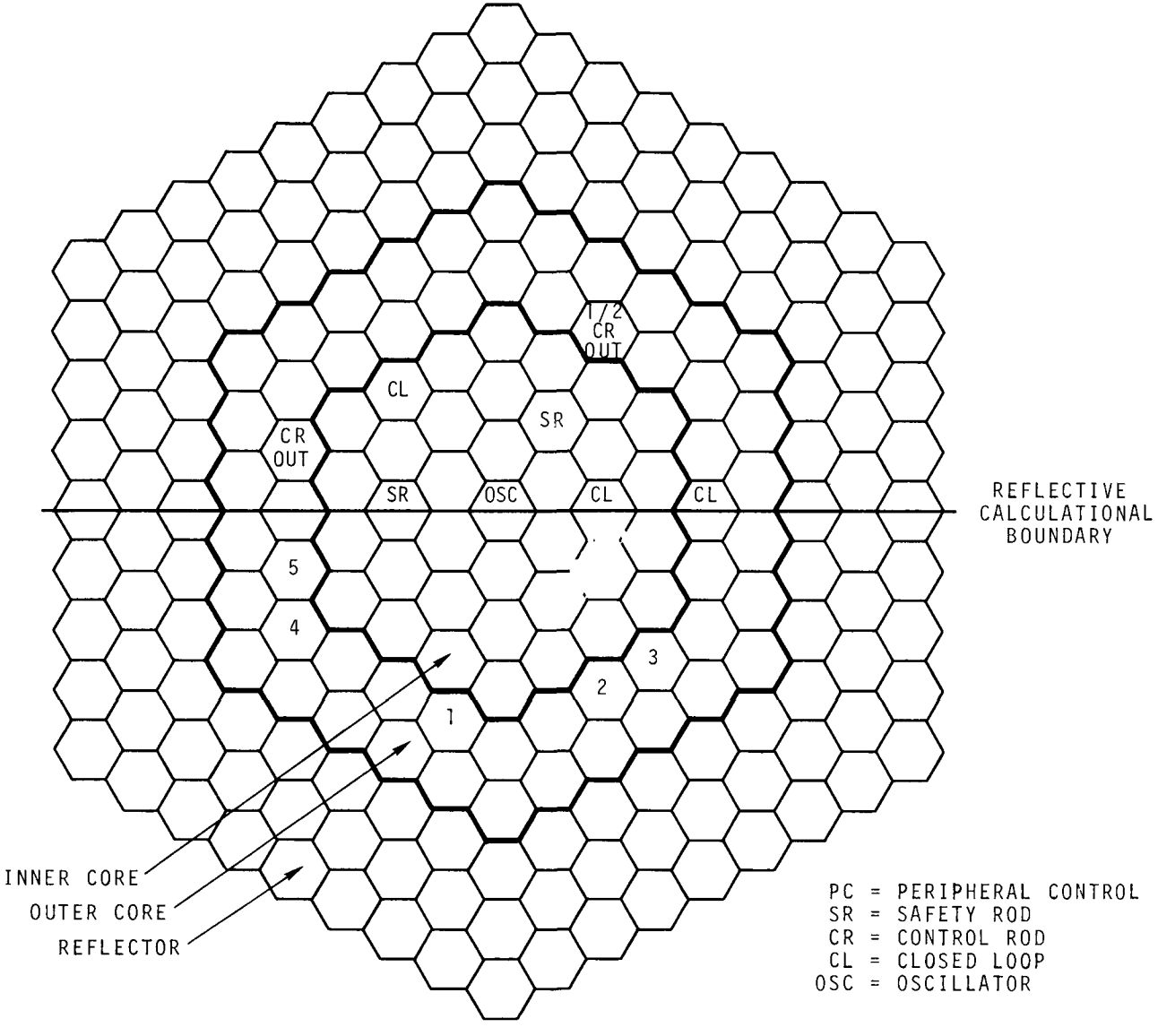

FIGURE VI-19 *Mid-Plane Areal Profile--3D FTR Calculation.*

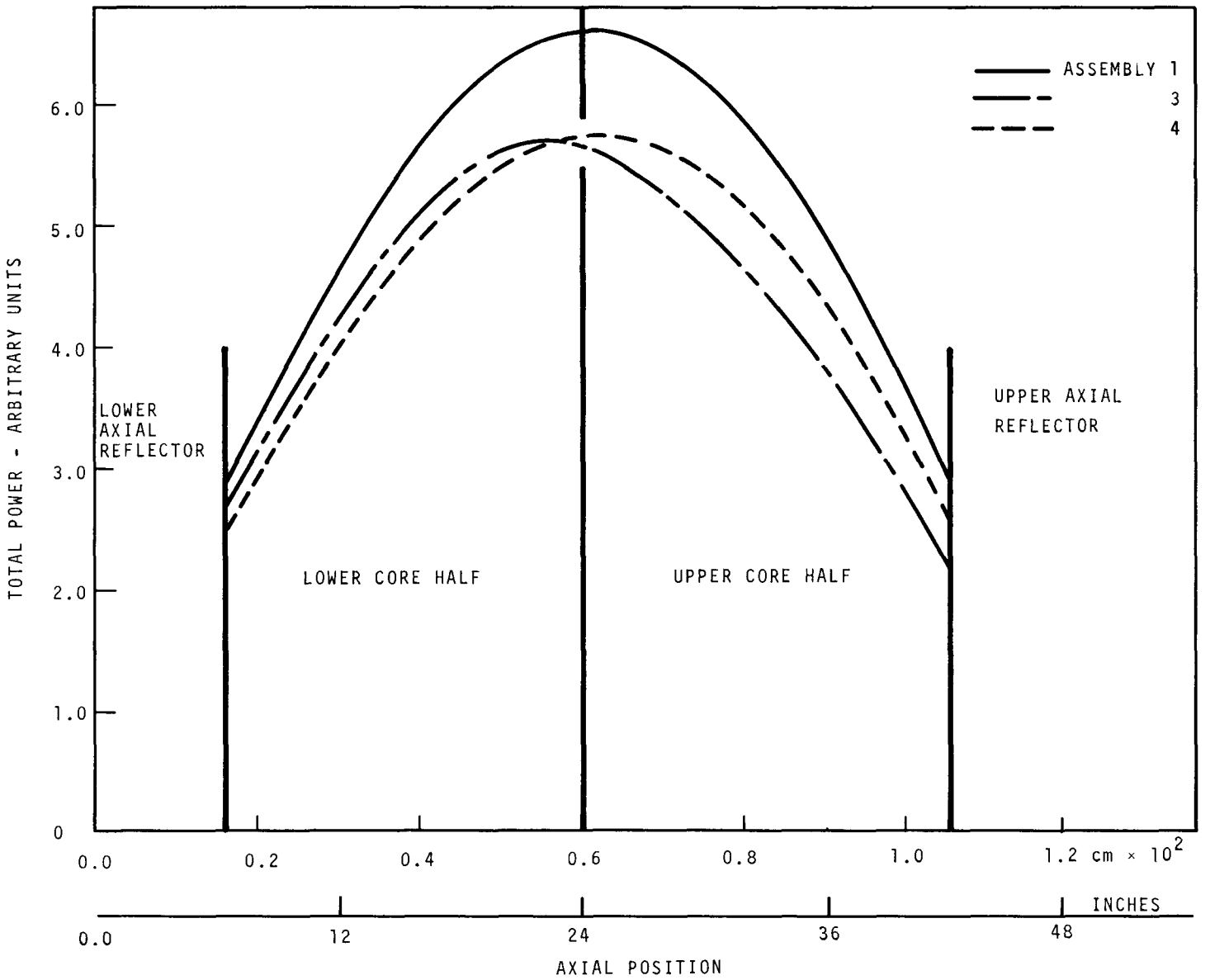

FIGURE VI-20 *Axial Power Distribution.*

from the other stochastic processes occurring in the reactor, such as neutron absorptions, neutron scattering, and neutron source emissions.

The reactivity meter tests were made during rod-drop measurements made by ANL. Several conclusions were drawn from the tests:

1) There is an apparent systematic discrepancy of approximately 15% between the polarity spectral analysis results and the rod-drop results. The polarity spectral analysis method consistently predicts smaller reactivity worths than the rod-drop method.

2) The polarity spectral analysis results show a high degree of consistency with the expected precision. In fact, it is apparent that the standard deviation calculated "on-line" using the polarity spectral analysis systems is an overestimation of the true standard deviation.

3) The consistency of the worth of all fuel rods when measured from a far shut-down state of \$-5.30 ± .07 and from a more reactive state of \$-91 ± .02 was excellent. The estimated worth of the fuel rods in the first case was \$2.16±.23 and in the second case the worth was measured to be \$2.14±.08.

4) All sensitivity tests to small reactivity changes fell within expectations using the polarity spectral analysis system.

The results of the polarity spectral analysis measurements are compared to those of the rod-drop measurements in Figure VI-21 and Table VI-4. It is known that temperature corrections should be applied to the data; however, these corrections should be small and, in the interests of reporting the data as soon as possible, these corrections have been ignored.

The standard deviations reported for the polarity spectrum measurements are calculated standard deviations which depend on the critical coherence, the measured subcritical coherence, the measuring time and the bandwidth. These should be interpreted as estimates of the expected standard deviation about the true mean for the experimental parameters obtained. The rod-drop (or inverse kinetics) estimates of reactivity in \$ were obtained from the measurements in inhours using the conversion factor factor obtained from ANL which depends weakly on an estimate of β_{eff}. The time after the initiation of the experiment at which the polarity spectrum results were available to the experimenters is essentially equal to the measuring time noted under "configuration".

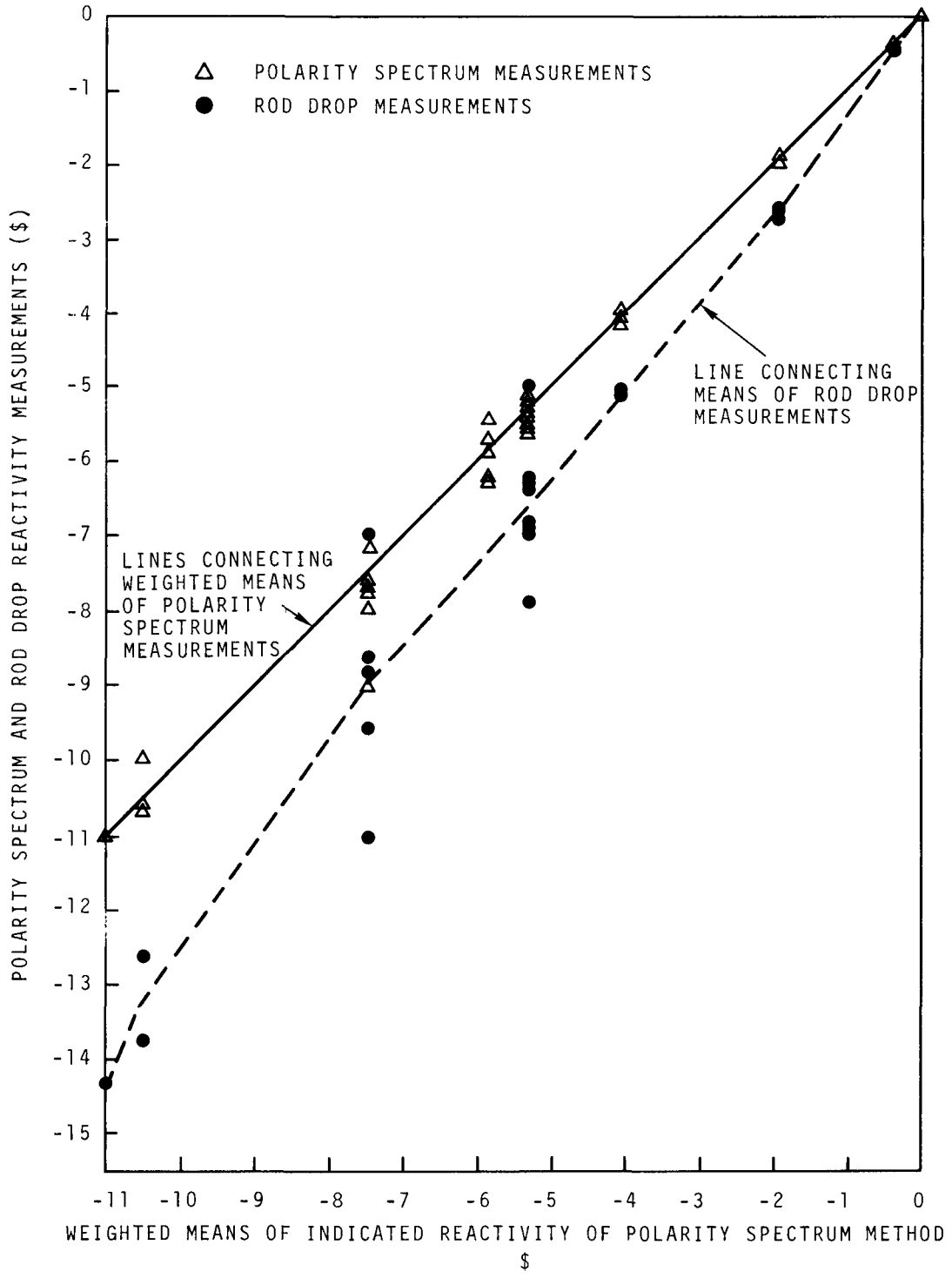

FIGURE VI-21 *Pictorial Comparison of Polarity Spectrum and Rod Drop Reactivity Results--ZPR-IX, Loadings 90, 91, 92.*

TABLE VI-4
COMPARISON OF POLARITY SPECTRAL ANALYSIS MEASUREMENTS
AND ROD-DROP MEASUREMENTS

Loading	Configuration	Polarity Spectrum "$"	Inverse Kinetics
90 8/10/70	Critical average for ρ_c 13 min = .840425	0	0
	Dropped B-rod #3 from critical flux falling 2 min	0.38±.02	143.75 Ih → $.457
	Same as above flux falling 2 min	0.39±.02	
	Same as above flux steady 5 min	0.38±.01	
91 8/11/70	B rods out, F rods in except 2&9 sources in 2 min	5.90±.37	
	Reference config. - loading 91		
	B rods out F in sources out 10 min	5.25±.13	2774.6 Ih → $6.34
	same as above 2 min	5.35±.30	2167.9 Ih → $6.89 1963.3 Ih → $6.24
	same as above 2 min	5.56±.33	2486.9 Ih → $7.90
	same as above 2 min	5.49±.32	1572.1 Ih → $4.99
	same as above 4 min 3 1/2 hr later	5.11±.19	2135.5 Ih → $6.78
	same as above 10 min next day	5.29±.13	1963.6 Ih → $6.24
	B rods out, F rods in sources out 2 min	5.21±.28	2189.5 Ih → $6.95
	same as above 2 min	5.25±.29	
	same as above 4 min	5.46±.22	

TABLE VI-4 (CONT'D)

Loading	Configuration	Polarity Spectrum "$"	Inverse Kinetics
91 (cont'd)	38 min sum for B rods out, F rods in sources out	5.30±.07	
	B rods 3 & 9 dropped from B rods out F rods in 1 min	6.20±.59	
	same as above 2 min	5.47±.32	
	same as above 4 min	5.87±.26	
	same as above 2 min	5.71±.35	
	same as above 2 min	6.23±.42	
	11 min sum for B rods 3 & 9 dropped from B out, F in	5.85±.16	
	all F rods dropped from B out, F in 2 min	7.67±.69	2774.6 Ih → $8.81
	same as above 4 min	7.17±.42	3015.8 Ih → $9.58
	same as above 4 min	7.98±.54	3472.2 Ih → $11.03
	same as above 4 min	6.94±.36	2193.1 Ih → $6.97
	same as above next day 4 min	7.60+.48	2723.4 Ih → $8.65
	same as above 4 min	7.63±.49	
	22 min sum for F rods dropped from B out, F in	7.46±.20	
	dropped all B rods and F rods except #4 4 min	10.62±1.11	3990.4 Ih → $12.67
	same as above 4 min	9.99±.95	4328.9 Ih → $13.75
	same as above 20 min	10.63±.50	

TABLE VI-4 (CONT'D)

Loading	Configuration	Polarity Spectrum "$"	Inverse Kinetics
91 (cont'd)	28 min sum for above	10.53±.41	
	B rods out, F in except 4 & 8 sources in 2 min	5.72±.35	
	dropped all B rods and F rods from B out, F in 4 min	11.04±1.23	4519.4 Ih → $14.36
92 8/13/70	B rods out, F in sources out 4 min	1.87±.04	808.06 Ih → $ 2.57 817.06 Ih → $ 2.60
	same as above 10 min	1.91±.03	861.42 Ih → $ 2.74
	same as above 4 min	1.92±.04	
	same as above 4 min	1.91±.04	
	22 min sum for B rods out, F in sources out	1.90±.02	
	F in, B out except B #4 in ∿ 25% 4 min	1.89±.04 (sensitivity test)	
	F in, B out except B #4 in ∿ 50% 4 min	1.93±.04 (sensitivity test)	
	Drop all F rods from B out, F in 4 min	4.03±.12	1586.9 Ih → $ 5.04
	same as above 4 min	3.95±.12	1597.2 Ih → $ 5.07
	same as above 4 min	4.18±.13	1612.1 Ih → $ 5.12
	12 min sum for drop F rods from B out, F in	4.05±.08	
	F out, B out except B #4 10 min	4.18±.08 (sensitivity test)	
	F out, B out except B #4 & 5 10 min	4.31±.08 (sensitivity test)	

The data reported in the table is summarized in Figure VI-21. Calculated standard deviations have been omitted for clarity. For the sake of visualizing the results, the values of the polarity spectrum reactivity measurements and the rod drop reactivity measurements have been plotted against the weighted means of the indicated reactivity produced by the polarity spectrum method. Note that this generates a straight-line fit for the polarity spectrum data. Data points shown in Figure VI-21 are for a variety of measuring times which can be found by referring to Table VI-4. The 45 deg line indicates the weighted mean versus weighted mean of the polarity spectrum results. The dashed line is drawn through the means of the rod drop data.

4. Fast Reactor Cross Sections

R. E. Schenter

The evaluation and theoretical calculation of neutron reaction cross-sections in support of the FFTF and LMFBR programs is the object of this research.

Studies have been continuing on the theoretical calculation of the capture cross-section of selected fission product isotopes. Emphasis has been on analyzing those fission product isotopes for which experimental data are inadequate or nonexistent.

We have emphasized more realistic optical model potentials for use in neutron reaction theory codes, such as NEAREX, HELENE, AND FISPRO. In collobaration with Professor A. D. MacKellar, (University of Kentucky) we have developed a system of equations and computer codes which calculate "equivalent" local optical potentials from the more complicated non-local optical potentials. The nonlocal potentials correspond to the "true" optical model potential, which describes neutron-nucleus scattering, and is obtained in some approximation from many-body theory. The "equivalent" local potentials give the same elastic scattering as the nonlocal potentials. The philosophy of this work is to replace the usual phenomenological optical potentials with the more realistic "equivalent" local potentials. Figure VI-22 shows typical results of these calculations, where the

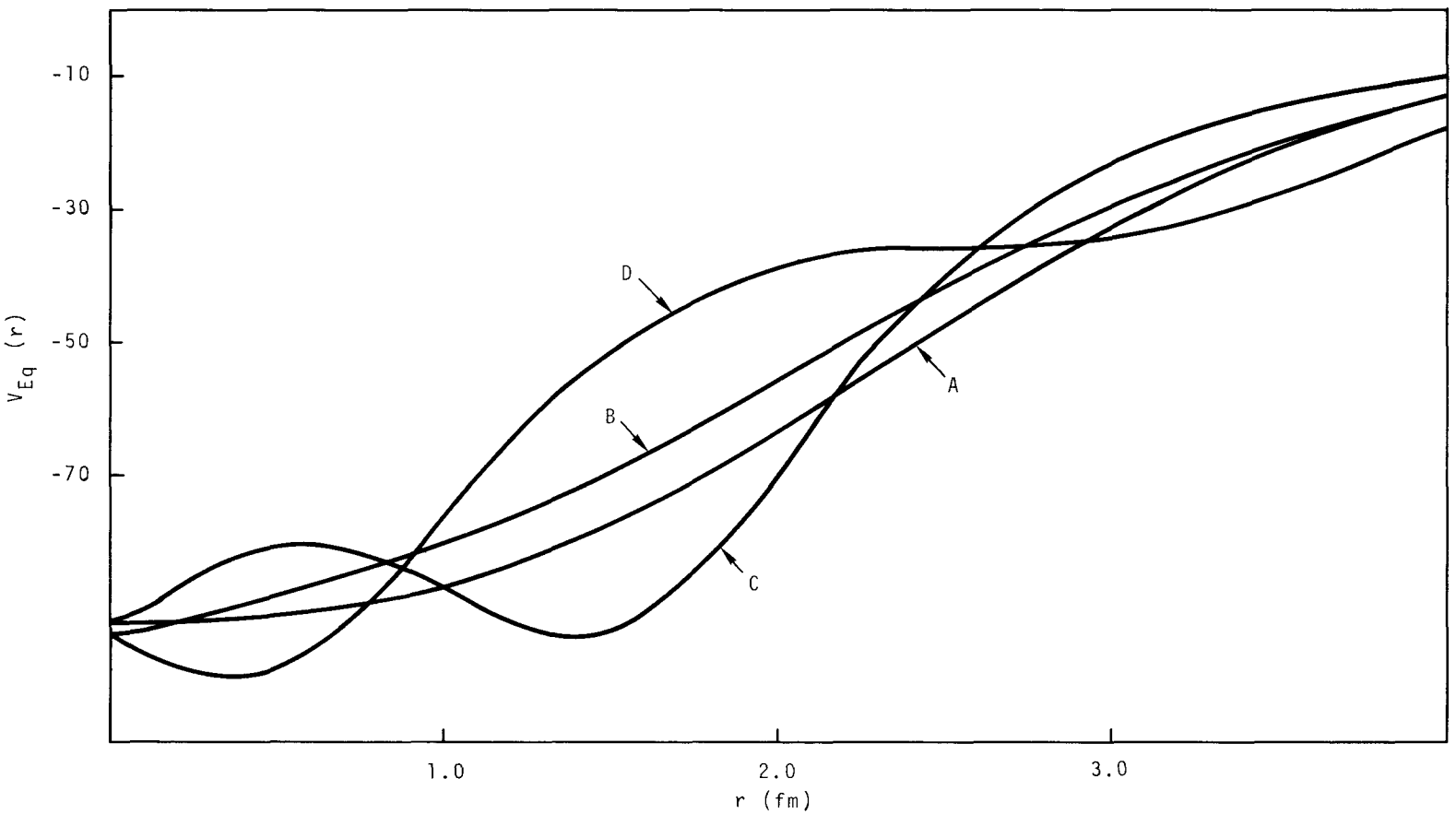

FIGURE VI-22 *Equivalent Local Potentials for the Elastic Scattering of Low Energy Neutrons by O-16 Targets*

dependence of the "equivalent" local potential, $V_{EQ}(r)$, is given for the elastic scattering of low-energy neutron by Oxygen-16 targets. Curve A represents the usual phenomenological potentials, whereas curves B, C and D are "equivalent" local potentials obtained using various approximations in many-body theory.

5. Code Interfacing

R. W. Hardie and W. W. Little Jr.

The 1DX, (Ref 6),2 DB, (Ref 7), 3DB (Ref 8) and PERT-V (Ref 9) codes have been programmed to read and write standard interface files containing groups of similar data.

Briefly, 1DX is a one-dimensional diffusion theory program designed to compute resonance-shielded multi-group cross-sections using data in the "Russian" format (Ref 10) and collapsed-group cross-sections using flux-weighting over any specified reactor zone. 2DB and 3DB are two- and three-dimensional diffusion theory burnup codes containing a material shuffling scheme. The above codes also perform criticality searches on time absorption, reactor composition, reactor dimensions, and buckling using either a flux or adjoint model. PERT-V is a one- and two-dimensional perturbation code designed to calculate reactivity coefficient traverses, the effective delayed neutron fraction, the neutron generation time, and the inhour/δk conversion factor.

Most of the standard interface data files are nearly the same as the ones specified by the Committee on Computer Code Coordination (Ref 11). The additional files were defined so that the standard data files encompass virtually all input data for all coes. Thus, for example, if one wishes to run a 1DX case to generate cross-sections, followed by 2DB flux and adjoint cases, and finally a PERT-V case, the number of input cards is greatly reduced by uniting the appropriate standard files to tape. A brief description of each data file is given in Table VI-5.

TABLE VI-5

STANDARD FILE CONTENTS

Standard File Name	Contents of Standard File
ADMNSTR.	Control card data (e.g., No. groups, No. space points, etc.)
GRP FLXS	Fluxes
GEO DIST	Geometry specifications
EXTRA	Buckling modifiers and delta search data
MULTIGRP	Resonance shielded cross sections
MIX DATA	Mixture specifications
COLLAP	Group collapsing specifications
RESSHD	Resonance self-shielding specifications
INTQUANT	Integral quantities
ZONE DENS	Material densities by zone
BETEFF	Data for β_{eff} calculation
DELTAK	Data for reactivity traverse calculations
ACTVTY	Data for activity calculations
GRP ADJF	Adjoint fluxes
PRTMOD	Print modifiers

6. Reactivity Effects of Fuel Duct Thermal Deflections (12116)

R. B. Rothrock and W. W. Little

A computer code ("BOW") written in 1968 by R. L. Burnett and R. B. Kidman to calculate the reactivity effects of small core component replacements by perturbation theory has been modified for greater ease of data handling, and checked out on the present computer system. A test case for uniform radial motion of all core components was run, with excellent agreement in eigenvalue perturbation as calculated by BOW and by direct comparison of eigenvalues from 2DB runs in the perturbed and unperturbed states. Calculations of reactivity effects are now proceeding with a more detailed core map, using calculated fuel duct thermal deflection values.

7. Evaluation of Nuclear Design Model for Flux and Power Distributions Near Core-Reflector Interface

L. D. O'Dell, W. W. Little and R. B. Rothrock

A set of calculations was made of flux and power distributions near the core-reflector interface in simplified geometries, to compare results from calculations that treat the nuclear behavior in varying degrees of detail. Calculational model features examined were the description of flux anisotropy (SN vs. diffusion theory), scattering anisotropy (transport approximation, P0, P1 and P3 moments), number of energy groups, and spatial mesh interval size. Results of the calculations were compared with respect to group flux, total flux, and power density distributions near the core edge; flux spectrum; and eigenvalue. Nuclear behavior at core-reflector boundaries remote from control rods was modeled by a one-dimensional reflected spherical reactor, while effects of peripheral poison rods were studied with a quarter core XY model having a single B_4C poison rod located on the core-reflector boundary. Additional calculations in triangular geometry (diffusion theory only) were made in which an FTR half core was described in detail, and the effects of changing the mesh size from six triangles per 12 cm core lattice position to 24 were evaluated.

In the 1D calculations (fuel/reflector only), it was found that diffusion theory results correspond very closely with those calculated from S8-P3, generally within $\gtrsim$2%. The lower order calculation (diffusion or modified S2) tended to yield a slightly softer spectrum at the core edge, and predict a slightly higher power density when compared with higher order results. Reducing either the number of space mesh points near the reflector ($\gtrsim$1 cm interval) or the number of energy groups $\gtrsim$20 resulted in loss of most of the detail in the low energy flux distributions near the reflector. The resulting change in local power density depends on the sensitivity of the fission cross section to low energy neutrons, and was found to be $\gtrsim$2% for typical FTR fuel compositions employing resonance self-shielding corrections.

The two dimensional X-Y geometry calculations were made with 2DB and DOT computer codes, and were used to examine the effects of mesh spacing near the control rod and of angular detail in the flux description. Again, differences in local power density as calculated by the different models were generally $\gtrsim$2%, but the total flux in the interior of the poison rod and in the reflector near the poison rod was calculated about 5 to 10% higher by diffusion theory than by S4. Similar differences were found in going from 5-cm mesh intervals to 2.5-cm mesh intervals in the region of the poison rod, with higher flux values resulting from larger mesh intervals. A typical total flux traverse through the poison rod is shown in Figure VI-23.

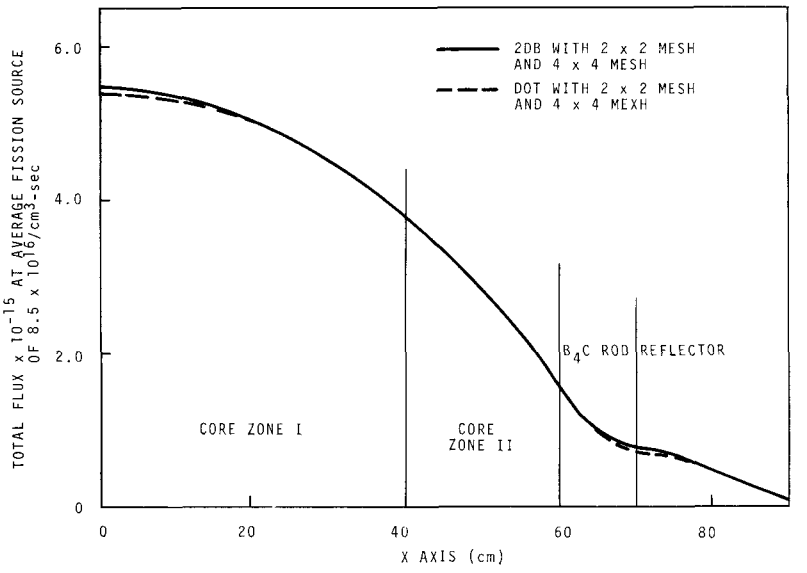

FIGURE VI-23 *Total Flux Traverse through B_4C Rod*

The same trends were observed in triangular geometry, where two diffusion theory calculations of a half-core FTR model were made using 6 and 24 mesh triangles per core lattice position, respectively. Results of the two calculations agreed within 1 to 2% in the core, and within about 10% in the interior of the reflector. Agreement to within about 1 to 2% was found in the interior of the peripheral poison rod.

It was concluded from these results that a few-group diffusion theory calculation in triangular geometry with six mesh triangles per 12 cm core lattice position yields a good description of the total flux and

power density near the core edge. Greater detail is required, in the form of more energy groups and smaller mesh intervals, if interest is focused on spectral detail or on the spatial distribution of low energy flux.

8. Fast Breader Physics - Improved Analysis(12532)

R. B. Kidman

a. Cross-Shielding

The present structure factor method (the use of correction factors to account for resonance shielding) accounts for only self-shielding. It neglects that accidental resonance overlap might have an effect on the resulting effective group cross-sections.

In order to determine the magnitude of this effect, the particular resonance overlap between U^{238} and Pu^{239} was studied for a range of hypothetical compositions. Work on this first study has been completed and the results are presently being published as document BNWL-1509, "Resonance Cross-Shielding in Reactor Analysis."

If one neglects accidental resonance overlap, results show that one can expect as large as a five % cross-section error. Future work will be concerned with generalizing the procedure of determining overlap effects and with developing a method of incorporating these overlap corrections into 1DX.

b. Structure Factor Interpolation

ETOX can be run several times to obtain self-shielded structure factors (f-factor) for a large number of σ_o and temperature values. This allows one to construct smooth curves of f-factors vs. σ_o (or f-factors vs. temperature) showing the actual behavior of factors.

Thus, for the first time, the adequacy of the 1DX structure factor interpolation schemes can be accurately tested. In fact, the shape of the actual f-factor curves has suggested new interpolation schemes.

Figures VI-24 and VI-25 compare the old and new interpolation schemes on the f-factors of U^{238}. It is obvious that the new schemes

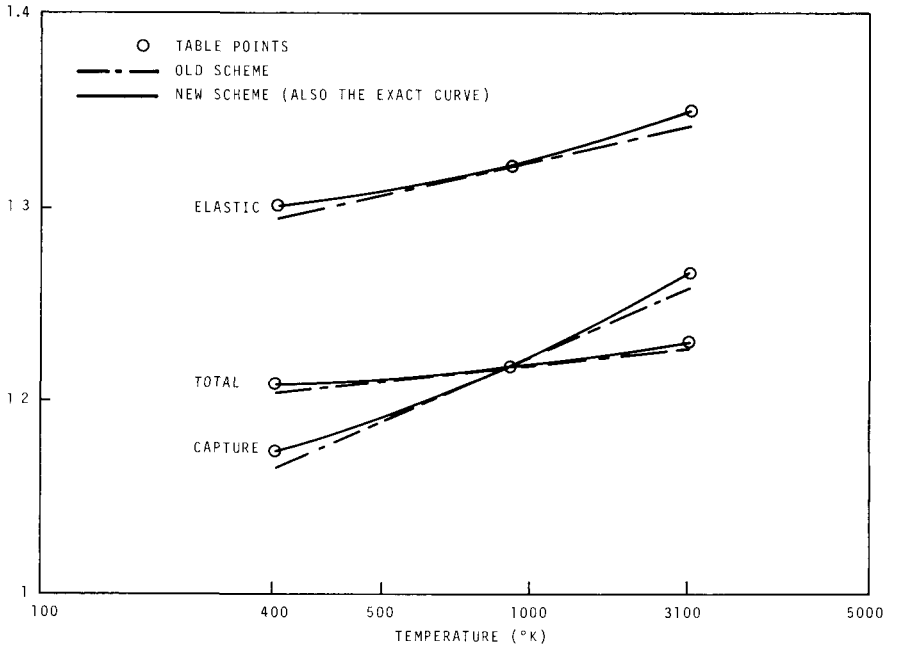

FIGURE VI-24 *Group 22 (275-454ev) U^{238} f-factors vs Temperatures (σ_o = 100b).*

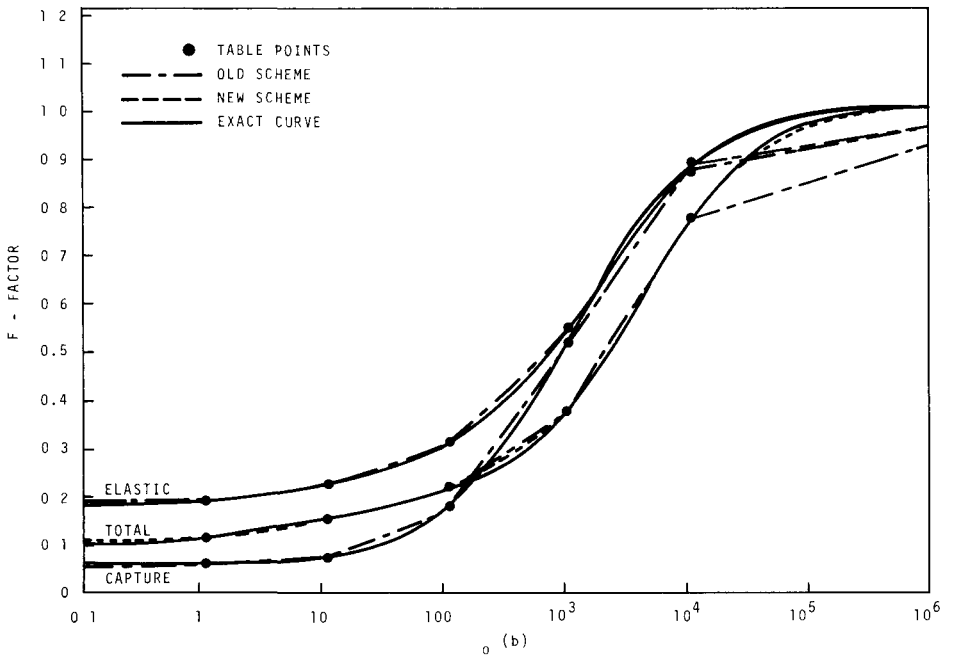

FIGURE VI-25 *Group 22 (275-454ev) U^{238} f-factors vs σ_o (Temp = 300°K).*

better follow the U238 f-factor behavior. More testing is required to assure that the new schemes are correct for all possible cases.

References:

1. Davey, W. G. and Amundson, P. I., "ZPPR Operations and Analysis", Reactor Development Program Progress Report, ANL-7581, p. 16-26, June, 1969.
2. Bennett, R. A. and Nelson, J. V., "Central Fuel and Peripheral Control Worths in the FTR-2 Critical", Trans. Am. Nucl. Soc., 13, p. 322 (1970).
3. Little, W. W. and Hardie, R. W., "Discrepancy Between Measured and Calculated Reactivity Coefficients in Dilute Plutonium Fueled Fast Criticals", Nucl. Sci. & Eng., 36, p. 155 (1969).
4. Hardie, R. W. and Little, Jr., W. W.,3DB, A Three Dimensional Diffusion Theory Burnup Code, BNWL-1264.
5. Little, Jr., W. W. and Maas, L. I., "Nuclear Parameters and Parametric Studies for the Fast Test Reactor (FTR)," June, 1969, SNWL-1067.
6. Hardie, R. W. and Little, Jr., W. W., 1DX, A One-Dimensional Diffusion Code for Generating Effective Nuclear Cross Sections, BNWL-954, Battelle-Northwest, Richland, Washington, 1969.
7. Little, Jr., W. W. and Hardie, R. W., 2DB User's Manual -- Revision 1, BNWL-831 REV1, Battelle-Northwest, Richland, Washington, 1969.
8. Hardie, R. W. and Little, Jr., W. W., 3DB, A Three-Dimensional Diffusion Theory Burnup Code, BNWL-1264, Battelle-Northwest, Richland, Washington, 1970.
9. Hardie, R. W. and Little, Jr., W. W., PERT-V, A Two-Dimensional Perturbation Code for Fast Reactor Analysis, BNWL-1162, Battelle-Northwest, Richland, Washington, 1969.
10. Bondarenko, I. I., et al., Group Constants for Nuclear Reactor Calculations, Consultants Bureau, New York, 1964.
11. Hannum, W. H. and Lewellan, J. W., "Some Thoughts on AEC Funded Coding," Proc. of the Conf. on The Effective Use of Computers in the Nuclear Industry, Knoxville, Tennessee, (1969).

F. RADIATION AND SHIELDING

1. Lifetime of FTR Structural Components(12121)

E. L. Boulette and W. L. Bunch

The primary function of in-vessel shields is to reduce the flux intensity to assure tolerable lifetimes for key structural components. For FTR design purposes, it is presently assumed that radiation damage to stainless steel is independent of the energy of the incident neutron. Various energy-dependent damage functions have been employed or proposed previously to account for spectral differences between test specimen locations used to establish fluence limits, and structural component locations of interest. This study was made to determine the variation in the calculated lifetime of seven key structural components in the FTR by employing five different energy-dependent damage functions.

For this study, it was assumed the total fluence limit for stainless steel is 10^{22} nvt (total) at a temperature of 600°F, based on test samples irradiated in a fast reactor (EBR-II) environment. The "damage effectiveness" (DE) of a particular spectrum is calculated for any of the proposed energy-dependent damage functions, D_X, by the relation:

$$DE\Big|_X^P = \frac{\sum_g D_X^g \phi_P^g}{\sum_g \phi_P^g} \qquad (1)$$

where the subscript X refers to the damage function and the superscript g to the energy group. The neutron flux, ϕ_P^g, is given by energy group (g) at the point of interest (P).

The fluence limit for the spectrum at location P is related to the experimentally established fluence limit by:

$$\phi t_{lim}\Big|_X^P = \frac{DE\Big|_X^{EXP} \quad \phi t_{lim}\Big|^{EXP}}{DE\Big|_X^P} \qquad (2)$$

where the superscript EXP refers to the experimental measurement in which the physical characteristic of a test sample was degraded to the established limiting value.

Two-dimensional R-Z diffusion theory calculations were made using the 2DBS code and the 31-group transport corrected HOMSET cross-section library to define the intensity and spectral distribution of the neutron flux incident on each of the seven structural components of interest. No attempt was made to treat possible neutron streaming through the below-core shield and through the fission gas plenums above the core. Peripheral control rods were assumed to be fully withdrawn and homogenized into an annular ring above the core.

The five different damage weighting functions employed are defined below:

D_{EI} All neutrons are assigned unit weight (present FTR criterion).

$D_{1.0}$ All neutrons having an energy greater than 1 MeV are assigned unit weight; all other neutrons are assigned zero weight.

$D_{0.1}$ All neutrons having an energy greater than 0.1 MeV are assigned unit weight; all others are assigned zero weight.

D_{GD} Gross displacement damage function, theoretically derived and normalized to unity in the most damaging energy group.

D_{CV} Clustered vacancy damage function, theoretically derived and normalized to unity in the most damaging energy group.

Results of the study are summarized in Table VI-6. It is evident from these results that the calculated lifetime of a given component is strongly dependent on the damage weighting function employed. It is also evident that the total fluence criterion being used for the design of the FTR results in a more conservative design than any of the other damage functions considered. The study does not validate any of the damage functions, but simply indicates their impact on design lifetimes.

2. Fission Product Decay Heat (12121)

D. R. Marr and W. L. Bunch

The fission product decay heat associated with irradiated fuel is required as a basis for the design of emergency or backup cooling systems for the FTR, for establishing shutdown cooling requirements, for the design

TABLE VI-6
STRUCTURAL COMPONENT LIFETIME vs. DAMAGE WEIGHTING FUNCTION

Component	Lifetime (years)				
	D_{EI}	D_{GD}	D_{CV}	$D_{1.0}$	$D_{0.1}$
Grid Plate (Removable Section)	11	130	170	2,200	45
Grid Plate (Fixed Section)	32	370	470	62,000	130
Core Barrel*	320	3,900	5,400	3,700,000	1,800
Reactor Vessel*	5,600	470,000	860,000	590,000,000	280,000
Instrument Tree Support Plate	30	390	537	11,000	230
Upper Radial Restraint Mechanism	180	2,400	3,500	120,000	1,500
Lower Radial Restraint Mechanism	3	14	15	70	10

*Does not include spectral shift due to stored fuel

of in-vessel fuel storage and handling systems, and for the design of ex-vessel fuel handling, storage, examination, shipping, and processing equipment. Figure VI-26 provides a reference decay heat curve for use in designing the FFTF; this way, a consistent basis can be employed in all systems. The reference curve is for FTR fuel irradiated to goal exposure. Results are given in per cent of operating power; thus, the information can be applied to the reactor as a whole, or to any given volume of fuel (such as subassembly, fuel pin, test assembly, unit length, unit volume, etc.) whose operating power is known. The uncertainty shown is the estimated standard deviation based on extensive comparisons with the pertinent experimental data. For the design of safety systems, it is possible to generate higher upper limit estimates by employing alternate confidence limits.

The reference curve is based on calculations with the code RIBD employing a fission product libray containing approximately 800 different isotopes and isometric states. It was assumed that 90% of the fission events would be induced in plutonium and 10% in uranium. Direct fission product yields are a function of both the isotope undergoing fission and the energy of the incoming neutron. The total decay energy, as well as the time distribution, is dependent on the direct yield distribution and the average charge displacement from stability. The newly developed product library includes a large number of predicted isotopes whose individual characteristics (half-life, decay energy) have not been measured. Empirical values were generated for these isotopes in order to obtain agreement with available integral fission product measurements. Thus, the RIBD method of summing individual isotopes has been extended to short decay times. The code can now be employed to consider various combinations of fissile material, and any exposure and decay history, including the formation of shielded isotopes by neutron capture.

3. Shield Design Guidelines

W. L. Bunch

The radiation protection standards applicable to the FFTF, as contained in AEC Manual Chapter 0524 Appendix, established annual and

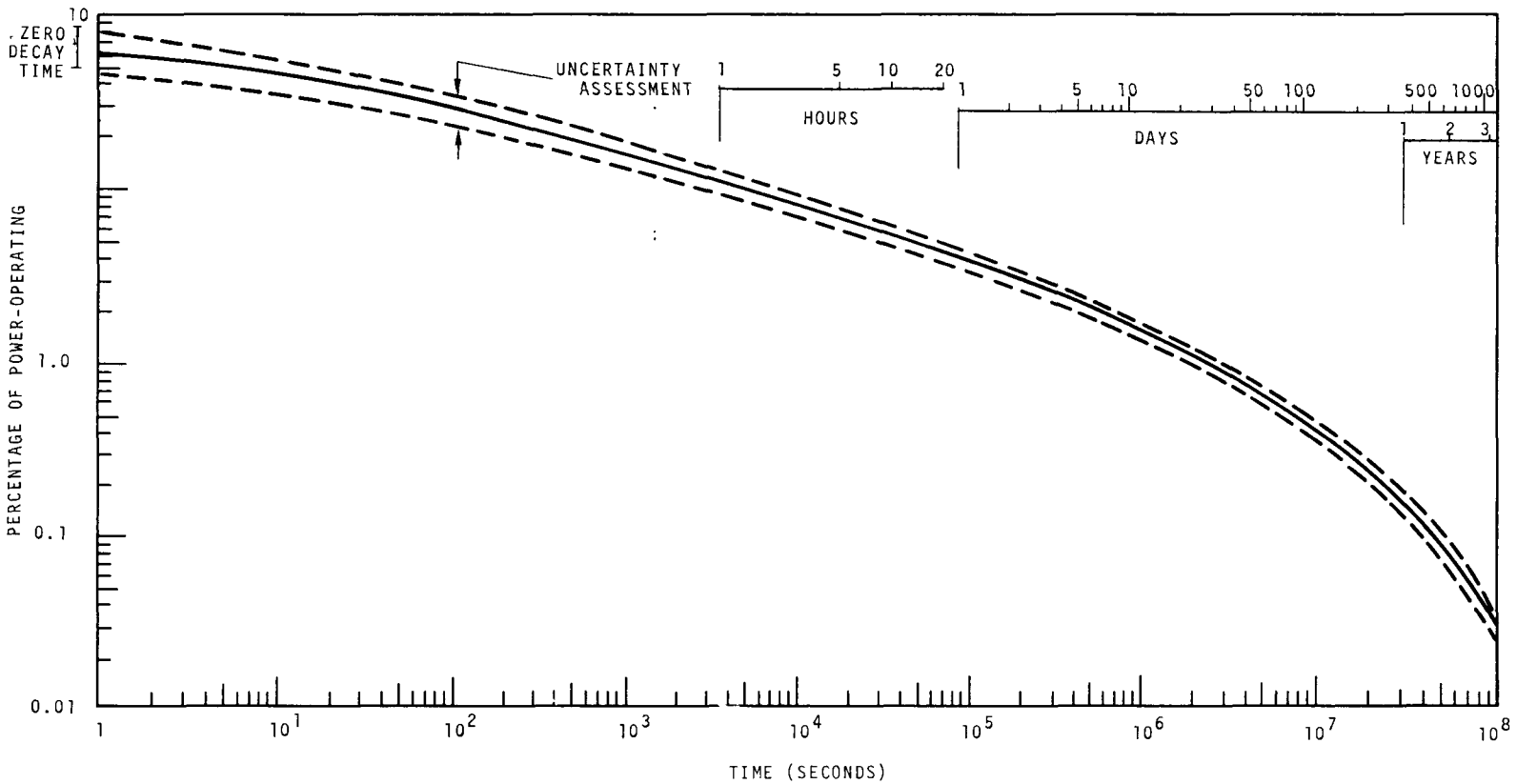

FIGURE VI-26 *Reference Fission Product Decay Heat Curve for FFTF.*

quarterly personnel exposure limits. Radiation protection procedures, established administrative procedures and methods for operating radiation facilities within the limits established by the AEC. To plan for operation of the FFTF in a practical, efficient, and economical manner within the established AEC limits, it has been necessary to prepare a set of shield design guidelines.

Basically, the guidelines assume that the size of the operating crew is establised by the work load, and is not influenced by radiation exposure considerations. Preliminary guidelines, for use by individual system engineers in establishing basic shield requirements prior to the time the integrated plant features are evolved, are based on estimated access requirements for that system. Five radiation zones are defined.

ZONE	ACCESS REQUIRED	DESIGN LEVEL (mrem/hr)
I	Full Time	0.2
II	Less than two hours per day	2
III	Less than one hour per week	20
IV	Less than one-half hour per month	200
V	No access permitted	>1000

All of the rooms within the FFTF containment building have been placed in one of the five zone categories defined above. The size and makeup of the operating crew has not been established at this time. However, a preliminary radiological evaluation of the overall design based on preliminary estimates of the operating crew size and composition, and employing the relation defined above, indicates the design to be satisfactory.

G. REACTOR DOSIMETRY

1. Comparison of Measured and Calculated Integral Fluxes and Spectra in a Pressure Vessel Mockup

R. L. Simmons, L. S. Kellogg, K. M. Barry*, C. Z. Serpan, Jr.**,
W. Y. Matsumato, H. H. Yoshikawa

Thermal reactor facilities are used to irradiate structural and fuel cladding materials for the LMFBR program. As part of a continuing effort to improve dosimetry methods for thermal reactor applications, an experiment to measure the flux and spectra in a simulated pressure vessel environment has been performed in cooperation with Westinghouse Nuclear Engineering Systems and the Naval Research Laboratory. Typically, these fluxes and spectra are determined by neutron transport or diffusion theory calculations. In this section, such calculations are compared with integral fluxes and spectra derived from foil activation data taken at five locations along the centerline of a thermal shield and pressure vessel mockup.

The pressure vessel mockup consisted of an 18 x 18 x 8-in. block of iron one in. behind a one-in. thick thermal shield placed $\sim$ seven in. from the Industrial Research Laboratory reactor core edge. The foil measurements were made at the front of the thermal shield, at the front of the block, and are four and seven in. into the mockup block. The 15 to 18 activation foil reactions [including (n,f), (n,γ), (n,p), and (n,α) reactions] for each of the five positions were analyzed using the SAND-II code (Ref 12). An analytical calculation for the vessel was made with the physics code DTF-IV, a 25-energy group, one-dimensional, transport calculation (Refs 13, 14).

In Figure VI-27, a ratio comparison of the multiple foil derived and DTF-IV calculated integral fluxes (>E) versus energy (E) are shown for the five locations in the pressure vessel experiment. A ratio of unity indicates exact agreement between the calculation and the multiple foils

---

* Westinghouse Nuclear Engineering Systems

** Reactor Materials Branch, Naval Research Laboratory

results. The estimated absolute uncertainty in the multiple foils derived integral fluxes (>E) is 15% to 30% ($\pm 1\sigma$). The lowest uncertainty is for fluxes at energies above 0.5 MeV.

The comparison shown in Figure VI-27 indicates the following:

1) For this experiment (as modeled for the DTF-IV calculation), the calculated integral flux exceeds that indicated by the multiple foils results for all energies, but particularly above 1 Mev. This suggests a significant difference in the spectrum shape above 1 MeV.

2) The multiple foils integral flux magnitudes decrease more rapidly with penetration into the pressure vessel block than those calculated with DTF-IV. At four in. and seven in. into the vessel block, the measured values are only 1/2 to 1/3 of the calculated values.

Based upon the above observations, the DTF-IV results imply a higher damage rate than the multiple foils results. For example, at the four in. and seven in. depths, the time to accumulate the fluence required for a 200°F change in nil ductility temperature in A302B steel, estimated by an empirically derived damage function (Ref 15) and the measured spectra, is longer by a factor of two to three than the time estimated using the same damage function and the DTF-IV calculated spectra.

2. Feasibility of Using the Fast Neutron Cavity in the PCTR for Cross-Section Evaluation

W. N. McElroy, H. H. Yoshikawa and D. F. Newman*

A feasibility study of using the Fast Neutron Cavity (FNC) in the Physical Constants Test Reactor (PCTR) for cross-section evaluation has been completed. The results indicate that the FNC can be used successfully for this purpose.

The timely evaluation and definition of energy-dependent reaction cross-section $\sigma(E)$ in the energy region between $\sim 10^{-5}$ and 10 MeV is important for both reactor physics and engineering in the LMFBR program. Previous studies have demonstrated the feasibility of using a multiple foil activation iterative method for $\sigma(E)$ definition and evaluation

* Battelle-Northwest

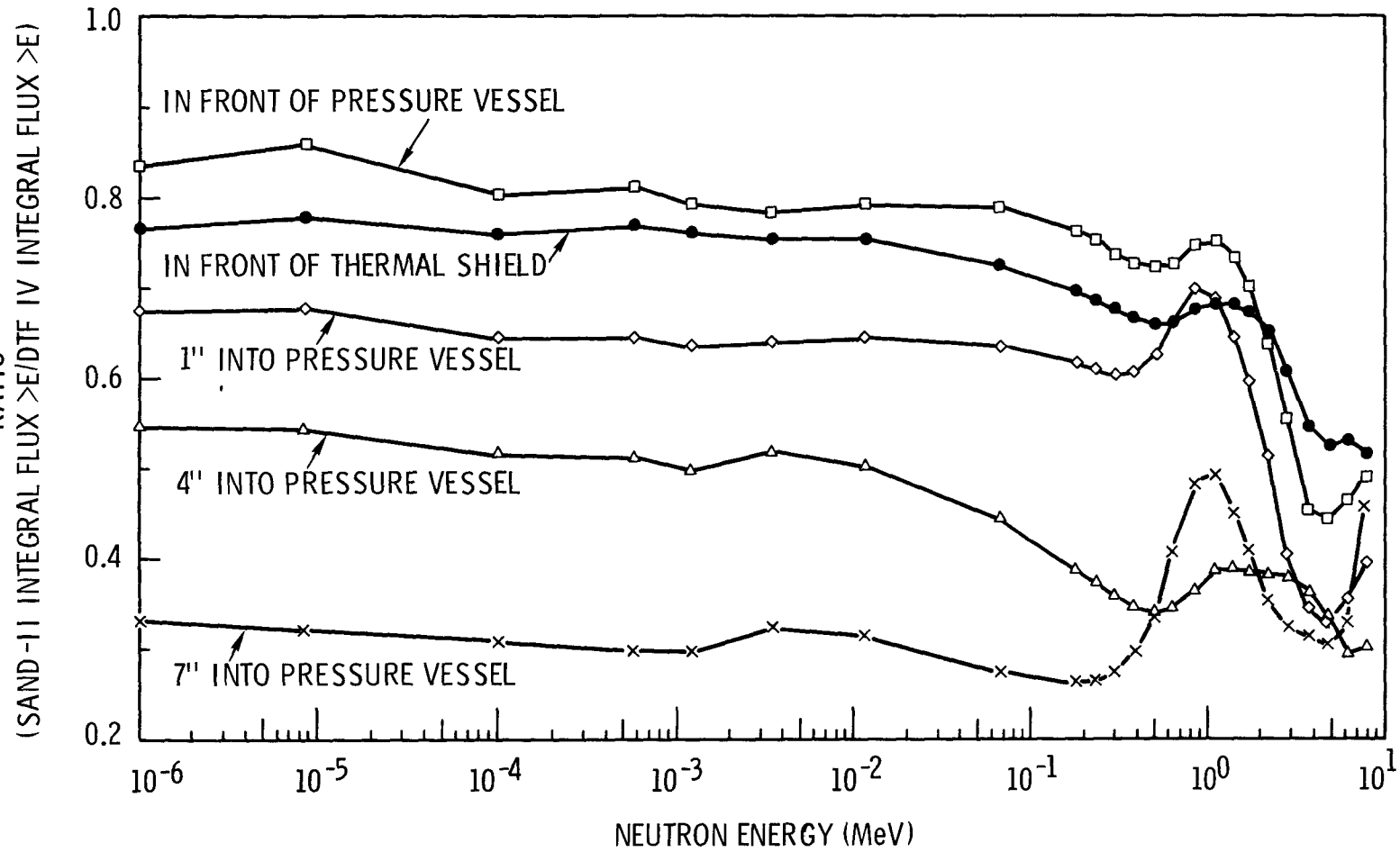

FIGURE VI-27 *Activation Foil vs Transport Calculated Integral Flux Comparison in a Pressure Vessel Mockup.*

(Refs 16 through 19). The method involves irradiating a selected set of detectors (usually 10 to 15) in different reference spectra, measuring resultant reaction rates, and determining, by iterative solution, of the flux spectra for the different reference neutron environments. These reference spectra, and corresponding measured reaction rates for a single reaction, are used in an inverted iterative process to define and evaluate an energy-dependent cross-section (Refs 16 through 18).

The accuracy of the method can be improved by the simultaneous irradiation of a single type of foil (for a specified reaction) in an appropriate set of reference spectra (Ref 16). This analytical study establishes the feasibility of using PCTR/FNC facility with a multi-region central core of beryllium and Al-30 wt. % uranium (93% U^{235}) to produce a suitable set of reference spectra. Results of some multiple foil/proton-recoil neutron flux-spectral measurements in the FNC central cavity have been previously reported (Ref 20).

The calculated spectra for several positions in the central region and one position in the FCTR graphite reflector region are shown in Figure VI-28. Nine such spectra from these regions were selected as the set of reference spectra for this study.

Because of its importance to the LMFBR program, the $U^{238}(n,\gamma)U^{239}$ reaction was selected as a typical reaction to be re-evaluated by this method in the PCTR/FNC. The existing SAND-II code (Ref 12)cross-section (Ref 17) for this reaction was used with the nine reference spectra to calculate a set of reaction rates which might have been measured during a simultaneous irradiation of identical U^{238} foils in each location of the PCTR/FNC.

These nine reaction rates and the corresponding nine reference spectra were then input to the SAND-II code with a number of different initial (and extreme) estimates of $\sigma(E)$ for the U^{238} reaction -- considered to be unknown. For each from $\sigma^{(o)}(E)$, the SAND-II iterative procedure generated a solution $\sigma^{(K)}(E)$ where "K" is the number of iterations required to achieve the solution. The results are presented in Figure VI-29.

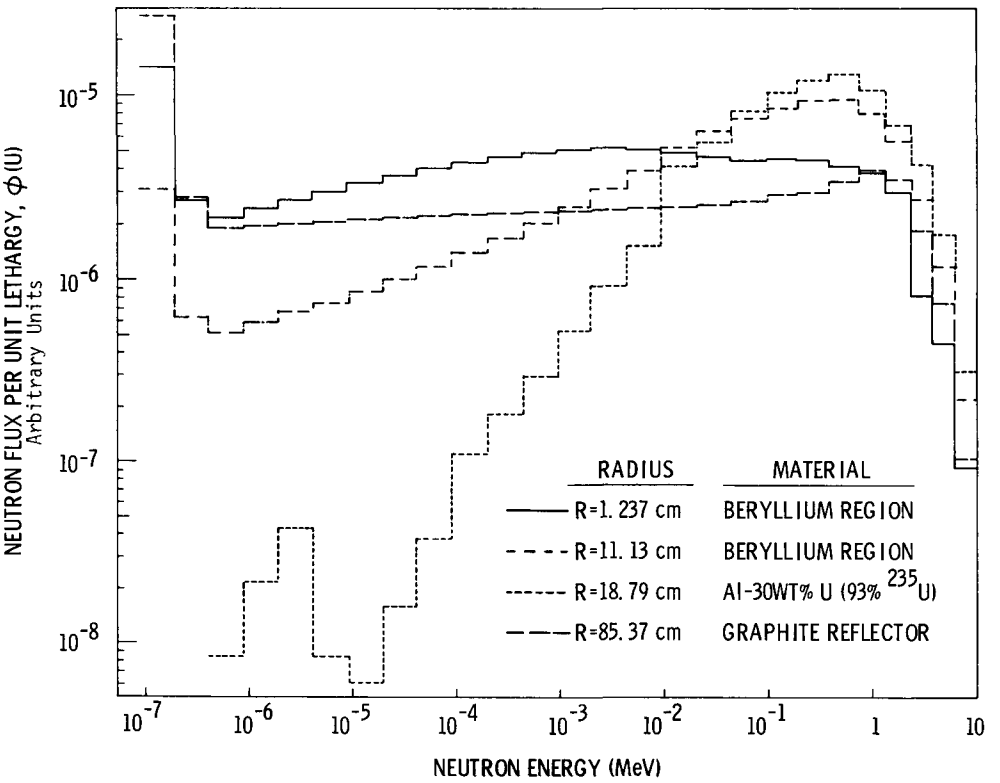

FIGURE VI-28 *Neutron Spectra in the PCTR/FNC Cross Section Evaluation Study*

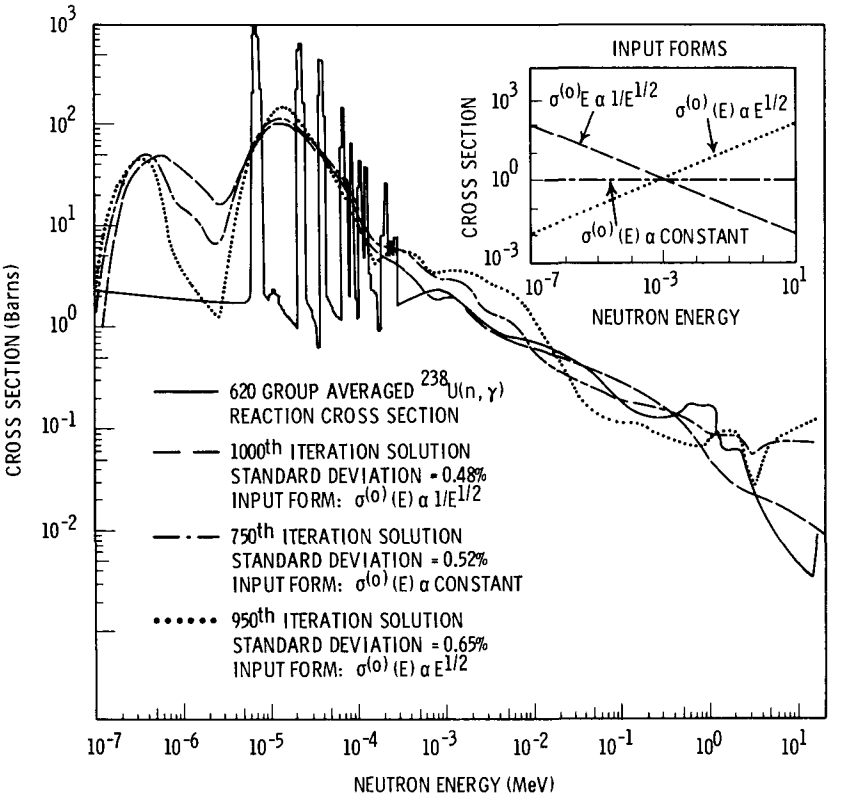

FIGURE VI-29 *SAND-II Solution Uniqueness Study for the U^{238} (n,γ) U^{239} Reaction.*

The small inset figure shows the three extreme input forms used. The dashed curve represents an initial guess $\sigma^{(o)}(E)$ that has a $1/E^{1/2}$ shape (corresponding to a 1/v cross section). In Figure VI-29, the solution for this input is also represented by the dashed curve. Similar results are given for a constant and $E^{1/2}$ input form. The solid curve is the existing SAND-II cross-section and is, therefore, the correct solution. As expected, it is approximated best by the solution based on the 1/v input form.

Although there are differences among the three solutions shown in Figure VI-29, the overall agreement is excellent considering the extreme differences in input forms. This implies that the nine reference spectra are sufficiently different to establish a unique solution over approximately six decades of energy by one irradiation. Thus, if the best available $\sigma(E)$ for the $U^{238}(n,\gamma)$ reaction (based on monoenergetic measurements and theoretical estimates) were used for $\sigma^{(o)}(E)$, together with reaction rates from a PCTR/FNC irradiation, the resulting $\sigma^{(K)}(E)$ solution could be expected to produce excellent integral consistency over the energy interval of $\sim 10^{-5}$ to ~ 3 MeV.

Energy-dependent cross-sections, usually based on monoenergetic measurements and theoretical estimates, are generally inconsistent with activation measurements that are inherently of an integral nature. Energy-dependent cross-sections determined as described here do not suffer from this inconsistency.

Below $\sim 4 \times 10^{-5}$ and above ~ 3 MeV, the derived cross-sections must be disregarded, since the nine reference spectra do not have adequate reaction sensitivity in these regions. Irradiations in additional spectra would be required to provide reliable results for these regions.

The results of this study also show that if a previously undefined cross-section were needed (such as for a tag gas used in fuel element leak detection), a smoothed energy-dependent cross-section could be easily defined for immediate engineering application. That is, the derived cross-section could be expected to give reliable estimates of reaction rates for engineering applications for most LMFBR type spectra.

3. EBR-II Dosimetry Test

J. L. Jackson, W. N. McElroy, J. A. Ulseth and H. H. Yoshikawa

A joint WADCO-ANL dosimetry test is planned for the EBR-II reactor during 62.5 Mw operation. The test is necessary because:

1) Uncertainties in the calculation of flux-spectra in EBR-II have been reported as potentially ranging from 20% at core center to a factor of 3 or more at blanket positions (Ref 18).

2) Published calculations by Miller and Jarka indicate that local distortions of the energy-dependent integral flux and fission rate caused by compositional differences between fuels and materials subassemblies are significant (Ref 21).

3) Separation of the energy and temperature dependences of radiation damage to structural materials requires accurate knowledge of both flux-spectra and temperatures. Irradiation temperatures are known best at below core midplane, but flux-spectra information below core midplane is inadequate. Some data bearing on this point are discussed below.

Activation data from control thimble samples and flux gradient wires from EBR-II have been analyzed for possible vertical asymmetry. Figures VI-30 and VI-31 show a comparison of the below-core midplane to above-core midplane reaction rates for two neutron activation reactions, $Fe^{54}(n,p)Mn^{54}$ and $Fe^{58}(n,\gamma)Fe^{59}$. The ratios are plotted vs axial distance from reactor midplane for three radial positions, Rows 2, 4, and 7.

The $Fe^{54}(n,p)Mn^{54}$ reaction, due mainly to neutrons with energies >2 MeV, shows below/above core differences of 10 to 20% near core bottom and top, with differences exceeding 20% at far out blanket positions. Although the uncertainties associated with counting the Mn^{54} activity are large, as shown by the error bars, the indicated trend is nevertheless significant.

The $Fe^{58}(n,\gamma)Fe^{59}$ reaction, due mainly to neutrons with energies <2 MeV, shows below/above core differences of up to 10% near core bottom and top and up to ~19% at blanket positions. The asymmetry far exceeds data uncertainty.

The ratios shown are useful in estimating the difference in flux below and above core; however, they are not a measure of the flux

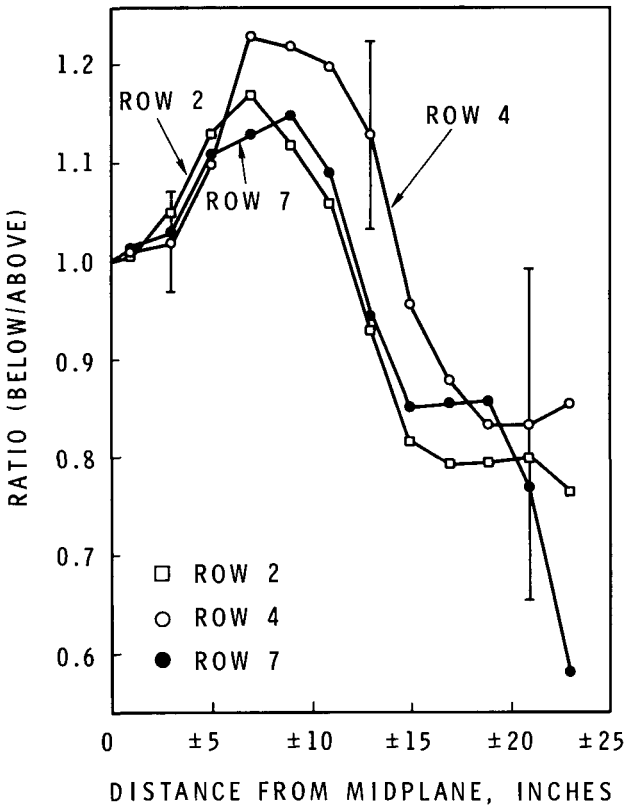

FIGURE VI-30 *Ratio of Saturated Activities below and Above Midplane for Fe^{54} (n,p)Mn^{54}.*

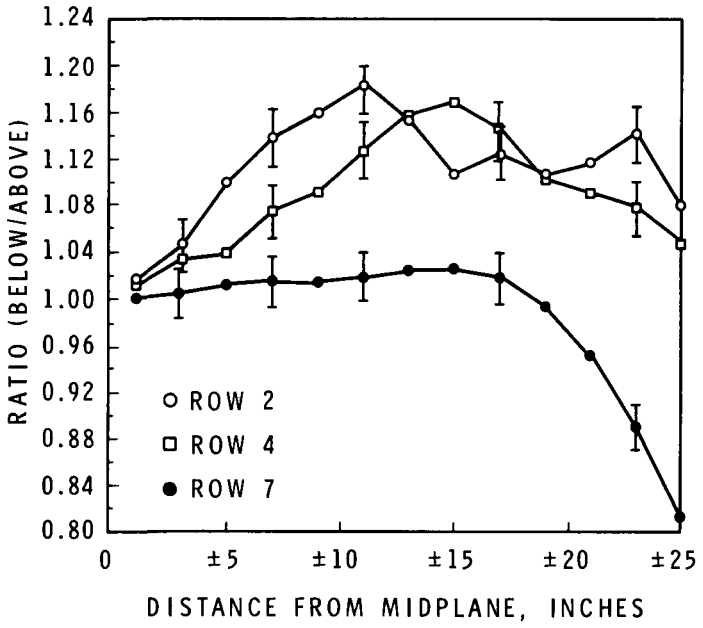

FIGURE VI-31 *Ratio of Saturated Activities below and above Midplane for Fe^{58} (n,γ) Fe^{59}.*

differences until it has been established that no spectral differences exist. Consequently, flux-spectra measurements must be made below core midplane and these data tied into our present knowledge of flux-spectra above core midplane. Until this is done, the large body of below-midplane material property data will not be amenable to damage function analysis uncertainties associated with the fluence and spectra data.

These results emphasize again the need for adequate dosimetry in each specific irradiation experiment.

The number and location of spectral sets for the joint WADCO-ANL test are under discussion with ANL. Present plans emphasize the region below midplane and Rows 7 and 8. Locations above the core would be limited to those needed to confirm agreement with the previous Run 31F dosimetry test.

4. Fast Reactor Dosimetry Capsule

J. A. Ulseth, J. L. Jackson, W. N. McElroy and H. H. Yoshikawa

The last quarterly reported on the identification of optimum and minimum dosimetry sets for fast reactor irradiation experiments. Some experimental details involved in including such monitor materials in experiments are described here.

Figure VI-32 shows how a typical optimum monitor set is assembled ready for placement in a fast reactor irradiation experiment. The materials are kept to minimum size to reduce the need for spatial interpolation of the data, to reduce self-shielding of the foils, and to lower radition levels to facilitate handling and counting. The fission foils and other types that require encapsulation are welded in pure vanadium tubes. These materials need not be removed from the containers for analysis, since the activation of vanadium does not interfere with counting the monitor materials. Counting these monitors in sealed containers after irradiation minimizes handling and the possibility for radioactive contamination.

The vanadium capsules are placed in a 304 SS container which is sealed into the 19-pin subassembly. The containers are spaced by SS tubes

which typically contain lengths of iron and cobalt wires for flux gradient measurements.

5. Dosimetry for Irradiation of Large Specimens in ATR and ETR (12242)

C. W. Hunter, J. A. Williams, J. A. Hiseth, R. L. Knecht and H. H. Yoshikawa

a. ATR Gamma Heating and Neutron Flux

Values of gamma heating (γ) and neutron flux (ϕ) have been measured in the ATR north reflector, to obtain data for planning irradiation of four-in. specimens. It was found that an unacceptable long irradiation period of seven years would be required to achieve a fluence of 5×10^{19} n/cm^2.

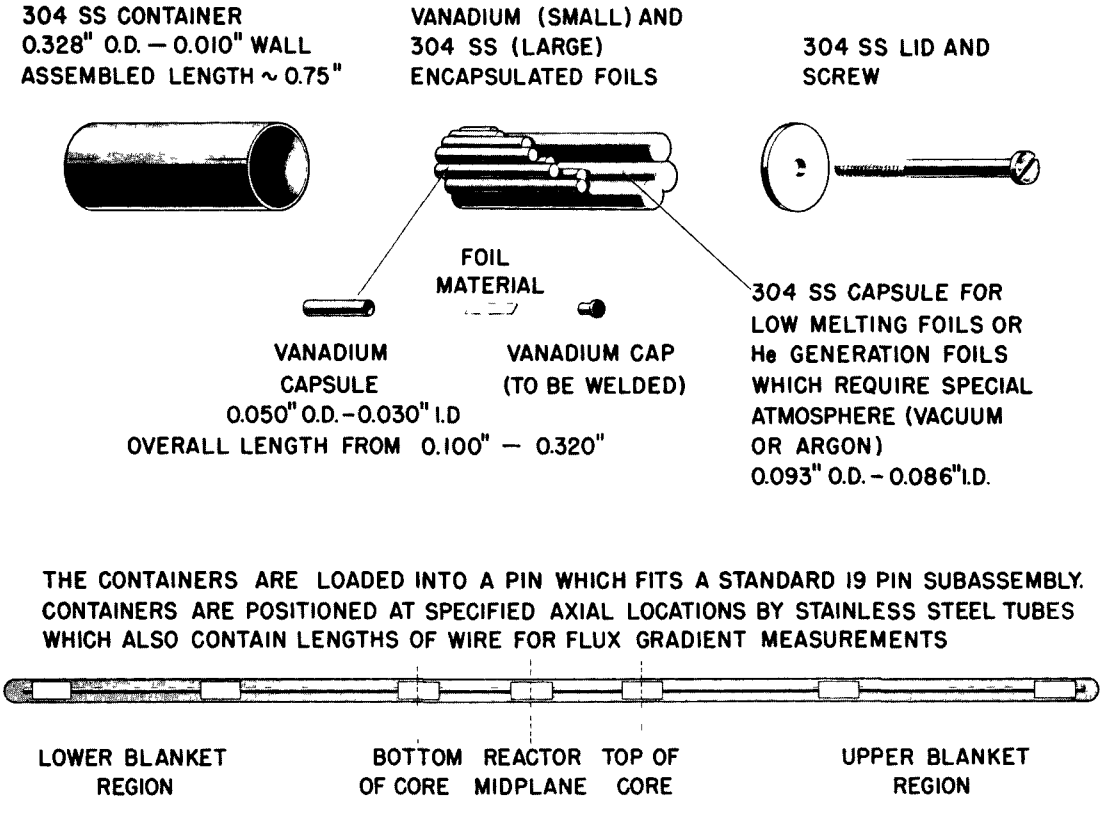

FIGURE VI-32 *Fast Reactor Dosimetry Capsule.*

The recently measured values of γ and ϕ are listed in Tables VI-7 through VI-10. Positions ON-3 through ON-5 were in the front row of the reflector and ON-9 in the back row. The fast ϕ in Table VI-8 was determined with Ni using the fission spectrum averaged cross-section. Since the neutron energy spectrum out in the reflector differs from the fission spectrum, and the energy response range of Ni is above 2.2 MeV, the Ni dosimetry with the fission spectrum can produce an erroneous value of ϕ E>1 MeV. To resolve this problem, multiple-foil dosimetry was used in the ATR north reflector during cycle 3-A and the absolute neutron ϕ level was unfolded using the SAND II iterative computer program (Ref 12, 23). The monitors used, reactions analyzed, and the neutron energy response range are listed in Table VI-9. The neutron ϕ above specified energy levels are listed in Table VI-10. It is evident that this procedure of spectrum unfolding with multiple foil dosimetry more precisely determines the neutron flux.

TABLE VI-7
GAMMA HEAT GENERATION IN NORTH REFLECTOR
POSITIONS IN THE ATR

Determined with Graphite during Cycle 2-C at
1.65Mw, Extrapolated to 250W

Position Above Core Bottom (in.)	ON-3	ON-4	ON-5	ON-9
9	0.21	0.21	0.29	0.11
15	0.26	0.29	0.34	0.14
21	0.26	0.33	0.39	0.16
27	0.26	0.32	0.39	0.16
33	0.24	0.27	0.34	0.14
39	0.19	0.23	0.26	0.12
45	0.12	0.15	0.18	0.08
51	0.07	0.08	0.08	0.05

b. Requirements for Thick Specimen Irradiations

To produce a meaningful irradiation of a thick specimen in a reasonable time, a high ratio of fast ϕ to γ is desirable. High γ heating results in too large temperature gradients in the specimen, and low ϕ , of course, leads to long reactor tenure. For both the ETR and ATR reflector positions, the values of γ and ϕ that would exist through a four-in. thick specimen are plotted in Figure VI-33. The markers on each line indicate the front and back faces of the four-in. specimen, with the higher values of γ and ϕ being nearest the core. The general relation of γ to ϕ is evident, and probably the γ and ϕ for any water test reactor fall on nearly the same line. The arrows on the lines in Figure VI-33 indicate the values of γ and ϕ that may be obtained by moving the four-in. specimen in the reflector. In the ETR, the vessel wall prevents movement of the specimen away from the core, while in the ATR, the reflector construction precludes movement of the specimen closer to the core. Thus, the ATR is too "cool" for a high-fluence irradiation, the ETR is too "hot" and a more favorable γ - ϕ range is not covered by either. Therefore, the following three alternative methods of irradiating a four-in. specimen are being evaluated.

TABLE VI-8

NEUTRON FLUX IN THE NORTH REFLECTOR OF THE ATR

(MEASURED DURING CYCLE 1-A AT 155.3 Mw, EXTRAPOLATED TO 250 Mw)

Position Above Core Bottom (in.)	FAST NEUTRON FLUX (n/cm^2-sec (E>1 Mev) Ni Monitor, Fission Spectrum			THERMAL NEUTRON FLUX (n/cm^2-sec) 0.5% Co Al Monitor		
	ON-4	ON-5	ON-9	ON-4	ON-5	ON-9
0	1.1×10^{11}	1.0×10^{11}	3.6×10^{10}	3.2×10^{12}	3.1×10^{12}	1.5×10^{12}
6	1.7	1.6	5.6	5.4	5.3	2.3
12	2.4	2.2	7.7	8.5	7.0	3.2
18	2.7	2.4	8.7	9.2	8.2	3.6
24	2.8	2.5	8.6	9.2	8.5	3.7
30	2.6	2.3	8.1	8.3	7.5	3.3
36	1.9	1.8	6.0	6.1	5.9	2.7
42	1.2	1.1	4.1	4.0	3.7	1.8

TABLE VI-9
MONITOR DETAILS FOR FLUX DETERMINATION
IN POSITION ON-4 OF THE ATR REFLECTOR
DURING CYCLE 3A

Monitor Type	Dimensions (in.)	Reaction to be analyzed	$t_{1/2}$	90% Response Range[a] E_L Mev	90% Response Range[a] E_U Mev
Enriched U	0.001 foil	$U^{235}(n,f)Ba^{140}$	12.80 d	5.5×10^{-7}	2.1×10^{-1}
Cu	0.0005 foil	$Cu^{63}(n,\gamma)Cu^{64}$	12.84 hr	5.8×10^{-7}	4.5×10^{-2}
Fe	0.020 wire	$Fe^{58}(n,\gamma)Fe^{59}$	44.5 d	6.0×10^{-7}	9.2×10^{-7}
Co	0.0005 foil	$Co^{59}(n,\gamma)Co^{60}$	5.268 yr	7.6×10^{-7}	1.5×10^{-4}
AlCo (.1% Co)	0.020 wire	$Co^{59}(n,\gamma)Co^{60}$	5.268 yr	7.6×10^{-7}	1.5×10^{-4}
AlAu (.13% Au)	0.020 wire	$Au^{197}(n,\gamma)Au^{198}$	2.698 d	4.3×10^{-6}	7.2×10^{-5}
Np	0.006 foil	$Np^{237}(n,\gamma)Ba^{140}$	12.80 d	4.5×10^{-1}	5.7
Depleted U	0.003 foil	$U^{238}(n,f)Ba^{140}$	12.80 d	1.5	7.5
Ti	0.020 wire	$Ti^{47}(n,p)Sc^{47}$	3.43 d	2.1	7.7
Ni	0.020 wire	$Ni^{58}(n,p)Co^{58}$	71.3 d	2.2	8.1
Fe	0.020 wire	$Fe^{54}(n,p)Mn^{54}$	313.5 d	2.4	8.5
Ti	0.020 wire	$Ti^{46}(n,p)Sc^{46}$	84.0 d	3.6	10.5
Cu	0.020 wire	$Cu^{63}(n,)Co^{60}$	5.268 yr	6.1	12.1
Ti	0.020 wire	$Ti^{48}(n,p)Sc^{48}$	44.0 hr	6.7	13.9
Al	0.020 wire	$Al^{27}(n,)Na^{24}$	15.0 hr	6.5	12.8

(a) Based on Cd-covered foils in a highly thermalized position in a heterogeneous water-moderated reactor.

TABLE VI-10
INTEGRAL FLUX (ϕ) VALUES ABOVE SPECIFIED ENERGIES (E_L)
FOR THE ATR ON-4 MIDPLANE POSITION

E_L, MeV	$\phi n/cm^2$-sec
6	1.39×10^{10}
4	4.16×10^{10}
2	1.43×10^{11}
1	4.48×10^{11}
5×10^{-1}	1.04×10^{12}
1×10^{-1}	1.84×10^{12}
1×10^{-2}	2.36×10^{12}
1×10^{-3}	2.80×10^{12}
1×10^{-4}	3.25×10^{12}
1×10^{-5}	3.95×10^{12}
1×10^{-6}	4.50×10^{12}
4×10^{-7}	4.74×10^{12}
$<4 \times 10^{-7}$ Thermal	1.08×10^{13}
1×10^{-10}(Total)	1.56×10^{13}

Note: Measured during Cycle 3-A at 220 Mw,
Extraploated to 250 Mw.

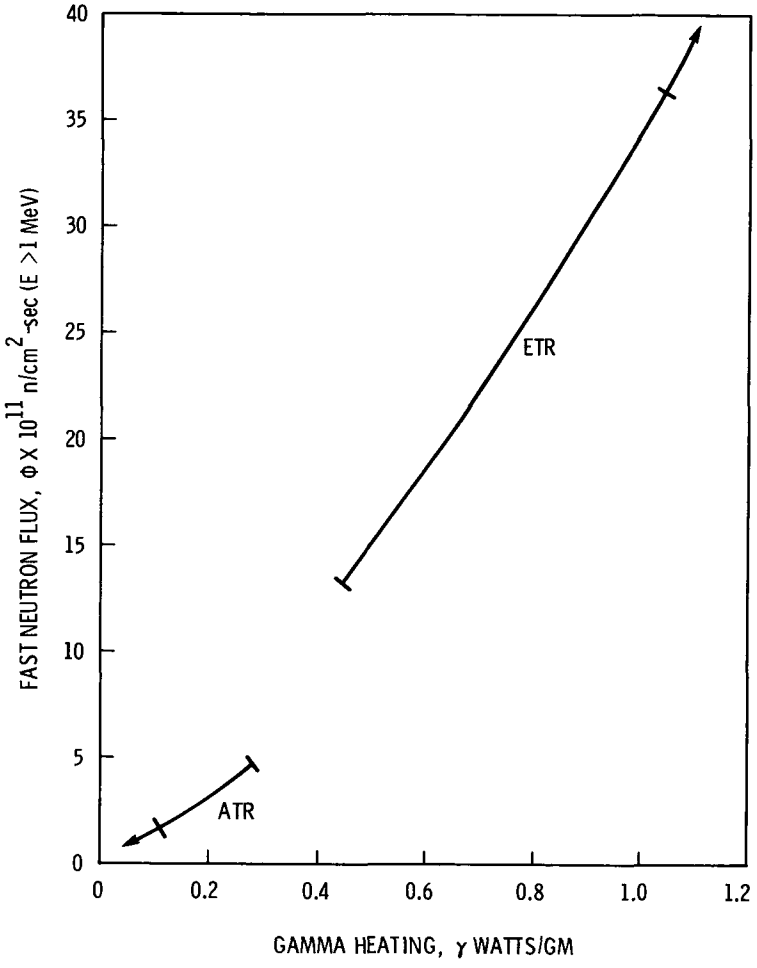

FIGURE VI-33 *Fast Neutron Flux and Gamma Heating Relation for the Irradiation of 4T-CT Fracture Mechanics Specimens.*

1) Achieve a uniform crack-tip temperature in a high γ-heating position, such as the ETR reflector, by controlling the heat flow in the specimen with appropriately located insulating patches;

2) Produce a higher ratio of ϕ/γ in the ETR reflector with shielding materials which preferentially reduce γ heat generation;

3) Evaluating other potential reactors with specific ϕ and γ determinations.

Until recently, large specimen irradiation capsules have been the type in which specimens are completely encapsulated, and the temperature of the specimen is controlled by varying the conductivity of a fixed gas gap by varying the He - Ar mixture in the gap. In such a design, the heat flow is out the two large parallel surfaces of the specimen, and, since the crack-line (region of interest in a fracture initiation test) is perpendicular to these surface and intersects their centers, the largest temperature gradient in the specimen will exist along the crack line.

However, by insulating only a small area at the ends of the crack line, heat flow parallel along the crack line will be greatly reduced, thus reducing the temperature gradient along the crack line. In a fracture initiation test, the material outside the plastic zone along the crack tip will be strained only elastically; since irradiation temperature does not affect the elastic properties, proper irradiation temperature is essential only within the plastic zone. In the ETR reflector, a 4T CT specimen with insulated areas of 16 sq. in. centered on the ends of the crack line will have a maximum temperature differential of about 25°F in the plastic zone from the face of the specimen nearest the reactor core to two-thirds through the thickness of the specimen. During the irradiation, the back one-third of the specimen would receive less than 25% of the neutron exposure and would be maintained at a cooler temperature than the front two-thirds of the specimen. As described previously, the specimen would be rotated half way through the irradiation period to achieve a symmetrical exposure through the specimen thickness. Two specimens could be irradiated simultaneously in one reflector of the ETR to a fluence of $5 \times 10^{19} n/cm^2$ in less than a year. The principal disadvantage to such an irradiation experiment is that the periphery of the specimen would have been irradiated

at a cooler temperature and therefore would be of questionable value as a source of irradiated material for machining smaller specimens. This insulation concept is, of course, applicable to irradiation in any other reactor, but is of decreased significance at lower γ and ϕ values and longer irradiation times.

It is possible to preferentially decrease γ with respect to ϕ with suitable shielding and adsorber materials. Heating results from specimen adsorption of γ rays generated outside the specimen and from γ rays generated by capture of low-energy neutrons in the specimen. This latter source is likely the dominant one, and may be greatly reduced by Li, which will capture the low-energy neutrons without generating γ rays. Also, the externally generated γ rays may be reduced, without appreciably disturbing the fast neuton ϕ , by a heavy metal shield such as Pb or W. The potential of such shielding is being evaluated with 31 group neutron diffusion calculations to determine the spatial and spectral distributions of neutrons and γ rays in the ETR, and the influences caused by Li, Pb, and W shielding. If such shielding is effective and practical, it will enable the meaningful irradiation of thick specimens afforded by no other means.

The γ - ϕ relation indicated in Figure VI-33 for the ATR and ETR reactors is quite similar to that existing in all water reactor reflector positions. Thus, it is unreasonable to expect that a very favorable ratio of ϕ to γ will exist in another reactor. Nevertheless, the ϕ and γ conditions in several other reactor reflector positions are being evaluated. Reactors being considered are the BAWTR, ORR, and GETR. Hopefully this information will reveal which reactor positions fill the gap in γ - ϕ values between the ETR and ATR, and which reactor has a more favorable ϕ/γ ratio.

H. SAFETY ANALYSIS OF HYPOTHETICAL ACCIDENTS

1. Primary Loop Piping Integrity in a Hypothetical Core Disruptive Accident

G. L. Fox and D. D. Stepnewski

Cooling of fuel material must be continued after a hypothetical core disassembly accident in order to retain control of fission products and fuel debris. Cooling capability can be provided by any of the three primary loops, if they survive the accident with sufficient integrity to transfer the core heat to the intermediate heat exchanger. The purpose of this study was to investigate primary loop piping integrity. The analysis identified no loading mechanisms that would cause primary piping failure.

Under the postulated conditions of such an accident, three mechanisms were selected as the most likely to cause failure:

1) Piping movements caused by motion at reactor vessel nozzles.
2) A quasi-steady residual gas bubble pressure (from vaporized core material).
3) An intense pressure pulse for very short times (from coolant impact with vessel cover).

Piping movements were investigated first. From the results of analyses using the ASPRIN code, and an accident work energy of 150 Mw-sec, the outlet nozzle motion was estimated to be five in. outward radially and six in. downward. The piping system was then modeled by the piping code MEL-21. In the initial calculation, no pipe restraints were assumed at the radiation barrier between the pipeway and the heat transport cells. This assumption produced pipe stresses near the yield point, but well below failure. The next calculation was conducted with the pipe held rigid at the radiation barrier so that an upper-limit situation was obtained. An effective "reduced modulus" (Ref 24) was calculated which includes plastic deformation in the outermost pipe fibers. The reduced modulus equaled the strain at indicated stress. Results indicated the maximum piping strains to be approximately 0.5 to 1%. Since the ultimate strain for type 304 SS at 1050 °F is 21.5%, the piping should not fail for the nozzle displacements specified.

The next phase investigated was the effect of a quasi-steady residual pressure. The burst strength of the 28-in. OD outlet piping was calculated using the ultimate strain of 21.5%, and was found to be 1300 psi. A pressure of about 400 psi is sufficient to cause yielding. The present analysis of disassembly accident residual pressure history indicates pressures in excess of 400 psi would only last a few milliseconds. Thus, the major pipe strain occurs from pressures within this time period and it is concluded that quasi-steady pressure does not present a problem.

The third phase, investigation of the effects of an intense pressure pulse over a short period of time is still underway. A computer model has been formulated which brackets the pipe deformation and the pressure wave decay during progression down the pipe. Preliminary results indicate the wall strains will be quite small and there is a very rapid attenuation of the pressure pulse down to that which causes yield in the piping wall (400 psi) with no further deformation thereafter.

In summary, the present analyses have identified no loading mechanisms that would cause primary pipe failure. The effects of accident loading on the primary pump and IHX will be analyzed next.

2. Parametric Analysis of Sodium Spills

R. D. Peak and D. D. Stepnewski

A parametric study of sodium spills in the reactor cavity and in one of the three HTS cells was accomplished. The spills, due to hypothetical pipe rupture, ranged from 20,000 lb to 200,000 lb at 965 °F to 1050 °F. The floor and submerged walls in direct contact with the pool formed from the spilled sodium was assumed to be insulated with firebrick (thermal conductivity of 0.167 Btu/hr-ft-°F) or with calcium silicate insulation (thermal conductivity of 0.038 Btu/hr-ft-°F). The heat capacity of the insulation on the floor was not found to be a significant factor (8.45 Btu/ft^3-°F for firebrick and 2.42 Btu/ft^3-°F for calcium silicate insulation) 8 in. of firebrick or its equivalent, 2 in. of calcium silicate insulation, was sufficient to keep the bulk of the floor concrete below 200°F. However, the liners of the roofs and walls of the cavity and cell were heated above

the 250°F design limit due to heat radiation from the surface of the sodium pool. Note that a 250°F limit for liners permits full recovery from a spill accident with no permanent damage to cell liners; hence, this limit is based on economic considerations, rather than safety.

Further analysis is required to establish realistic spill quantities and temperatures.

3. Thermal Analysis of Molten Debris Following a Hypothetical Core Disruptive Accident

A. Padilla, Jr. and D. D. Stepnewski

Previous analyses of post-accident heat removal suggested that the molten debris may breach the bottom head of the reactor vessel. A more comprehensive analysis has shown that breaching of the vessel should not be expected.

The previous models lacked similitude in assuming that the molten debris covered the reactor vessel bottom in a continuous layer immediately following the accident. If a mechanistic analysis of the mechanical and thermal interaction of the core debris with the core structures is carried out, it would be found that most of the molten debris would solidify on core structures within a few hours. Such an analysis is currently being carried out, but the present study assumes that some of the molten debris does find its way past the bottom core structure.

When the molten debris contacts the sodium below the inlet plenum structure, experiments at Argonne National Laboratory indicate that a process will occur that results in fragmentation of the molten material into small particles of the order of a few hundred to a few thousand microns in diameter. A thermal analysis of these particles shows that they are solidified and cooled to the temperature of the sodium before reaching the bottom head. Therefore, the settling debris would form a porous bed on the surface of the vessel, rather than a molten pool.

As the porous bed begins to heat up because of the decay heat generation within the debris, heat is transferred to the sodium pool above the porous bed and to the reactor vessel below. Although a significant amount

of convection within the porous bed would be expected, the present study considers only conduction as the mechanism for removing heat within the porous bed. If the thickness of the porous bed is small (less than one inch), the temperatures within the porous bed will rise only a few hundred degrees above the temperature of the sodium pool. As the thickness of the porous bed is increased, sodium boiling temperatures are attained. A thermal analysis (Figure VI-34) shows that this critical thickness is about two inches, assuming that the debris reaches the bottom head a few seconds after the termination of the core disruptive accident.

For porous beds larger than the critical thickness, it is assumed that the sodium boiling process creates sufficient agitation of the porous bed to bring the temperatures down to the level of the sodium pool temperature. The heat removal capability of a boiling bed of fuel particles is currently being investigated experimentally and analytically at Argonne National Laboratory.

The temperature of the bottom head of the reactor vessel would remain somewhat below the sodium boiling temperature as long as there is a sodium pool above the porous bed to act as a heat sink. Therefore, failure of the reactor vessel would not be expected.

4. Analysis of Cold Sodium Accident

A. L. Gunby and J. P. Hale

A cold sodium accident can only occur if the reactor is operating at a power level somewhat less than full power, where an idle heat transport loop contains sodium at a lower temperature. With this in mind, an analysis was performed, based on the following assumptions:

1) The reactor is at two-thirds power (267 Mw_t).
2) Heat is being removed with two heat transport loops operating at flows such that the full vessel ΔT (600°F to 858°F) is maintained.
3) The other loop is isothermal at 400°F.
4) At time zero, the cold loop begins pouring cold sodium into the reactor inlet plenum as a result of the inadvertent starting of the pump and opening of the isolation valve.

References:

12. McElroy, W. N., et al., "A Computer Automated Iterative Method for Neutron Flux Spectra Determination by Foil Activation," Volumes I-IV, AFWL-TR-67-41, Air Force Weapons Laboratory (1967).

13. Lathrop, K. D., "DTF-IV, A Fortran-IV Program for Solving the Multigroup Transport Equation with Anisotropic Scattering," LA-3373, Los Alamos Scientific Laboratory (1965).

14. Jenquin, U. P., Private Communication, Pacific Northwest Laboratory, Richland, Washington, 1970.

15. McElroy, W. N., Dahl, Jr., R. E., and Serpan, Jr., C.Z., "Damage Functions and Data Correlation," Nuclear Applications and Technology 7, 561 (1969).

16. McElroy, W. N., et al., "Neutron Differential Cross Section Evaluation by a Multiple Foil Activation Iterative Method," NBS Special Publication 299, Vol. I., September 1968.

17. Simmons, R. L. and McElroy, W. N., "Evaluated Reference Cross Section Library," BNWL-1312, Battelle-Northwest, May 1970.

18. McElroy, W. N., et al., "EBR-II Dosimetry Test Data Analysis (Reactor Runs 31E and 31F)," BNWL-1402, Battelle-Northwest, June 1970.

19. McElroy, W. N. and Dahl, Jr., R. E., "Neutron Dosimetry for Fast Reactor Applications," BNWL-SA-2887, June 1970.

20. Newman, D. F. and Davenport, L. C., "Neutron Flux Spectrum Measurements in the PCTR Fast-Neutron Cavity," Trans. Am. Nucl. Soc. 12, 714 (1969).

21. Miller, L. B. and Jarka, R. E., "Asymmetry and Local Distortions of the Flux Due to Gross Heterogeneities in EBR-II," Trans. Am. Nucl. Soc. 12, p. 772 (1969).

22. Doran, D. G., "Computer Simulation of Displacement Spike Annealing," Radiation Effects 2, 249 (1970).

23. "QPR, April, May, June, 1970, Reactor Fuels and Materials Development Programs for Fuels and Materials Branch of USAEC DRDT," BNWL-1349-2, W. F. Sheely (ed), July 1970.

24. Timoshenko, S. P., "Strength of Materials," Part 2, p. 362 (1941).

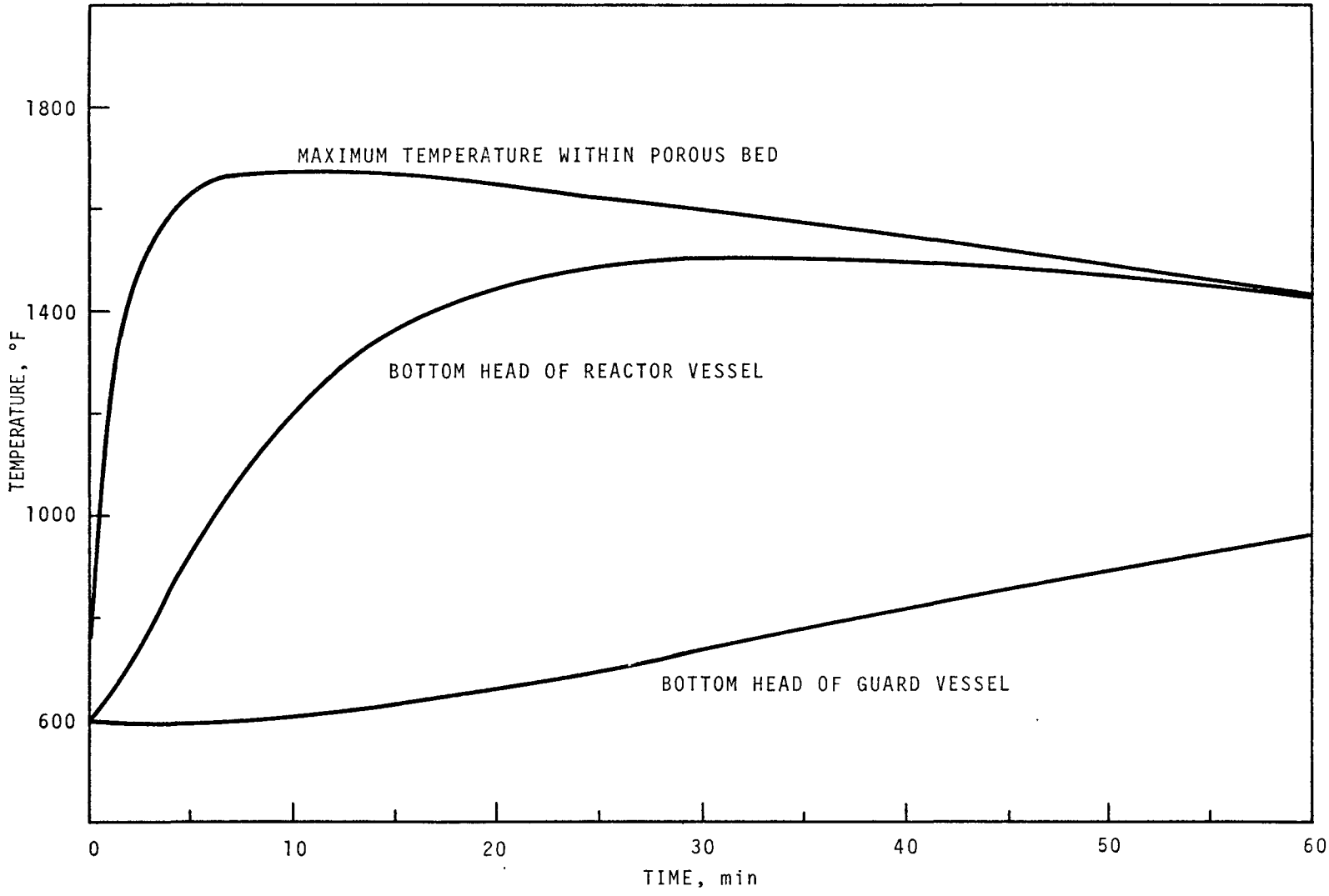

FIGURE VI-34 *Transient Temperatures for 2-in. Thick Porous Bed: Gas Gap between Reactor and Guard Vessels.*

5) Doppler and sodium expansion coefficients provide the only reactivity feedback.

The results presented in Figures VI-35, VI-36, and VI-37 show that the incident is extremely mild. The reactivity inserted as a result of the accident is only 3.3¢. The power rises from 267 Mw_t to a maximum of 318 Mw_t. Fuel and clad temperatures decrease as a result of the accident.

5. Sodium Pool Fire Analysis for HTS Cell Open to Outer Containment

P. R. Shire, C. L. Fies and J. P. Hale

The SOFIRE-I code has been utilized to calculate the transient reaction and heat transfer problem involving a pool fire in an open heat transport system (HTS) cell. Initially, it is assumed that the heat transport loop in question has been isolated from the reactor coolant system for a time sufficient for radioactive decay, at which time shielding plug(s) may be opened, allowing 80°F air from outer containment to circulate into the HTS cell. An assumed double-ended failure in either the primary or secondary HTS piping spills a quantity of 500°F sodium onto the HTS cell floor where the burning takes place. The large reservoir of air (1.5 million ft^3) in the outer containment supplies the fire by natural convection. For the cases analyzed, no leakage into or out of containment was assumed.

The air pressure rose to a peak at between one to three hr and then slowly diminished. The peak pressure and time of occurrence varies with the quantity of sodium spill, but in all cases, the peak pressure was below containment design internal pressure.

6. Sodium Pool Fire Analysis for Closed HTS Cell

P. R. Shire, C. L. Fies and J. P. Hale

The SOFIRE-II code one-cell version has been utilized to analyze pool burning for a closed HTS cell with no leakage. Initially, the 20,000 ft^3 cell contains 1 vol% oxygen in inert gas at atmospheric pressure and ambient temperature of 100°F. A hypothetical double-ended failure in primary HTS piping is assumed to spill 150,000 lb of 1050 °F sodium onto the cell floor.

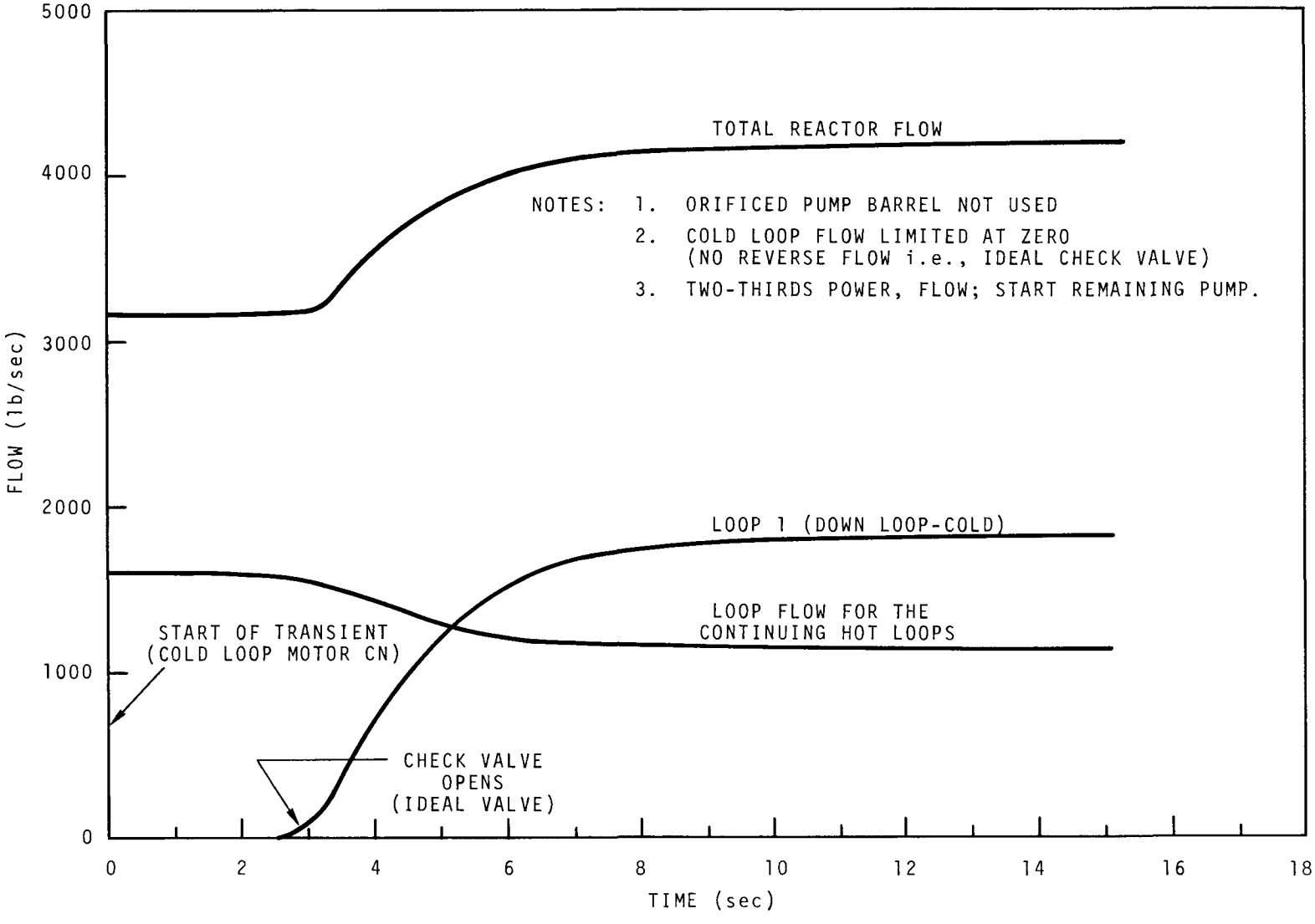

FIGURE VI-35 *Cold Na Accident--Flow Transients.*

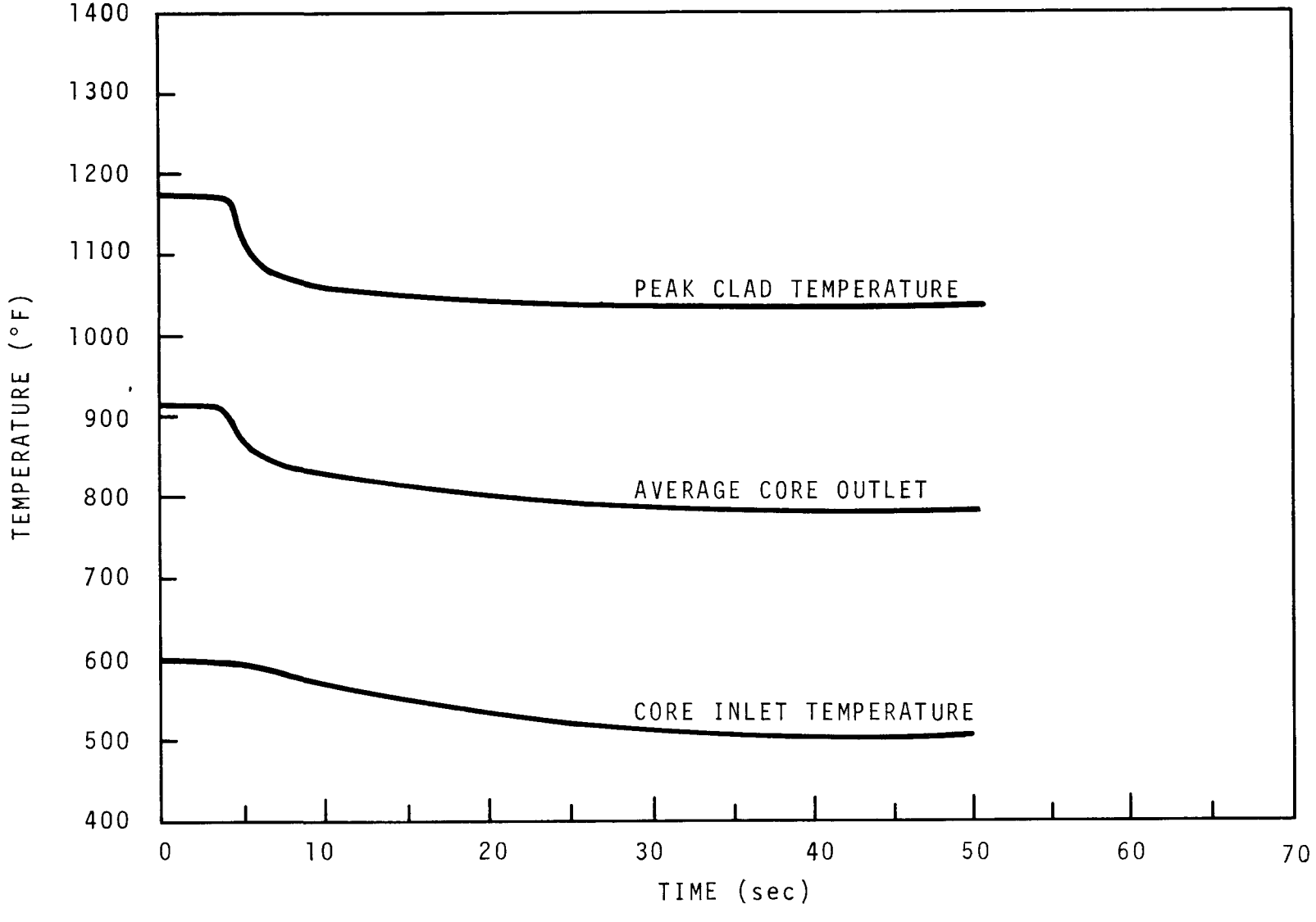

FIGURE VI--36 *Cold Na Accident--Temperature Transients.*

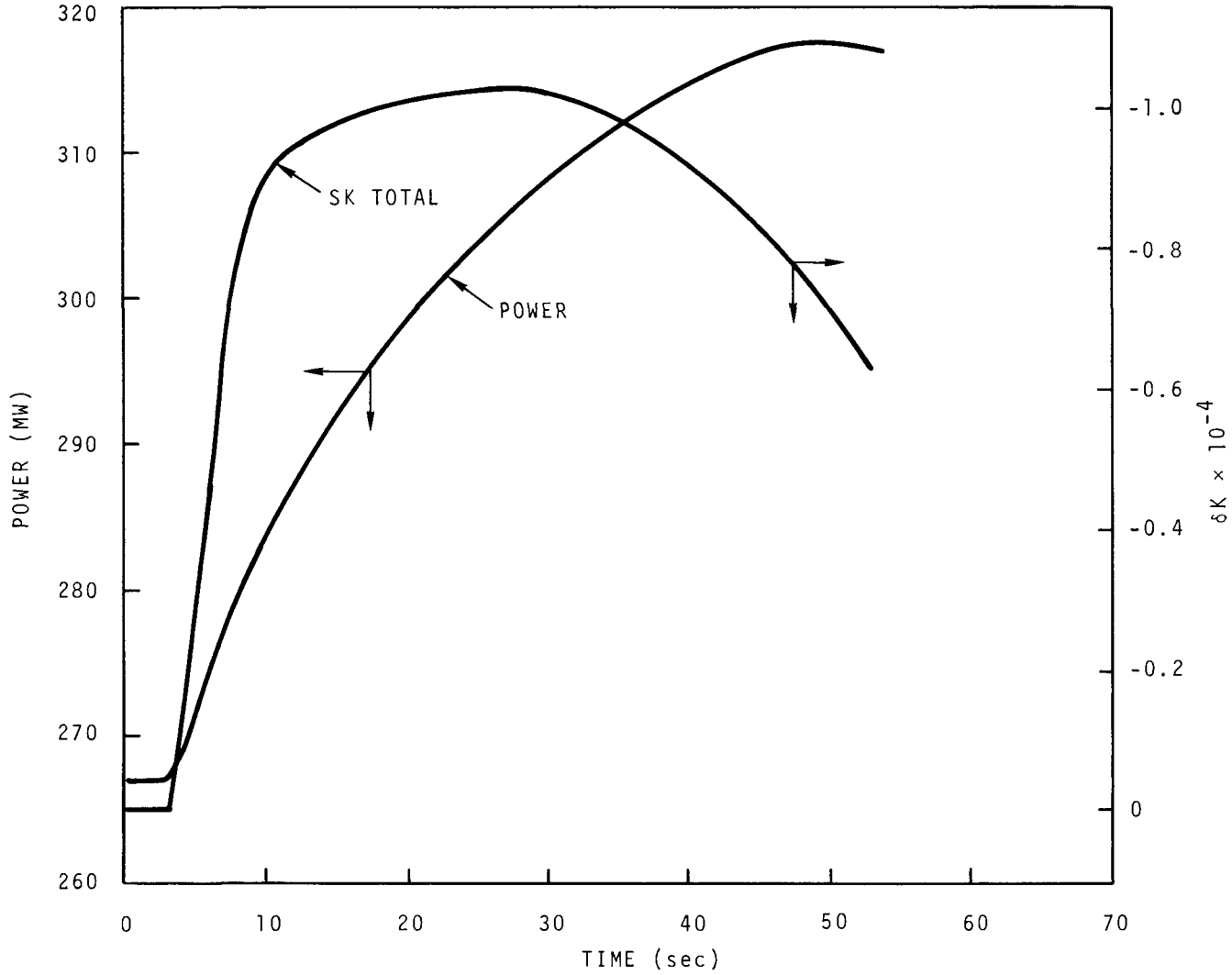

FIGURE VI-37 *Cold Na Accident--Power and Reactivity Transients.*

Several cases considered the cell floor with and without insulation forming a catch basin for the sodium with and without recirculation gas cooling. In cases where insulation protected the steel floor liner, the steel wall liner reached a peak of 320°F at two hr and then diminished slowly. (See subsection 2 above) This local temperature in the steel wall liner, which is not a safety problem, occurs as a result of direct heat radiation from the high temperature sodium surface.

1. METHODS FOR SAFETY ANALYSES

1. Simulation of Sodium Piping

A. L. Gunby and J. P. Hale

A simplified model for simulating the effects of stored heat in sodium piping has been developed, and a topical report on the subject has been completed. The simplified model consists of a pure transport delay in series, with a first-order lag representing total stored heat, with appropriate factors applied to the pipe volume and total stored heat. Comparison with the detailed reference model (see Monthly Technical Progress Report for May 1970) showed the simple model to be highly satisfactory. An example is shown in Figure VI-38 for an extreme temperature and flow transient. Equations for the simple model are:

$$\frac{dT_o}{dt} = \frac{W}{K_2 \left[(\rho VC)_{steel} + (\rho VC)_{Na} \right]} (T_d - T_o) \quad . . . \quad (1)$$

$$T_d = T_i \, (t - T) \quad . . . \quad (2)$$

where T_o = pipe outlet, T_i = pipe inlet, T_d = delayed inlet and T is a function of flow, W, and sodium volume, $K_1 V_{Na}$. The K-factors are chosen to match the reference model for thermal transient response.

2. Development of SOCOOL-II

A. Padilla, Jr. and D. D. Stepnewski

The SOCOOL-II computer program for calculating the work energy due to a molten fuel-sodium interaction has been generalized to apply to the interaction of sodium with any molten material. Due to the uncertainty of extrapolating sodium properties beyond the range of the experimental data, several different options for calculation of sodium properties have been incorporated into the program. Documentation is currently in progress and should be completed by the next reporting period.

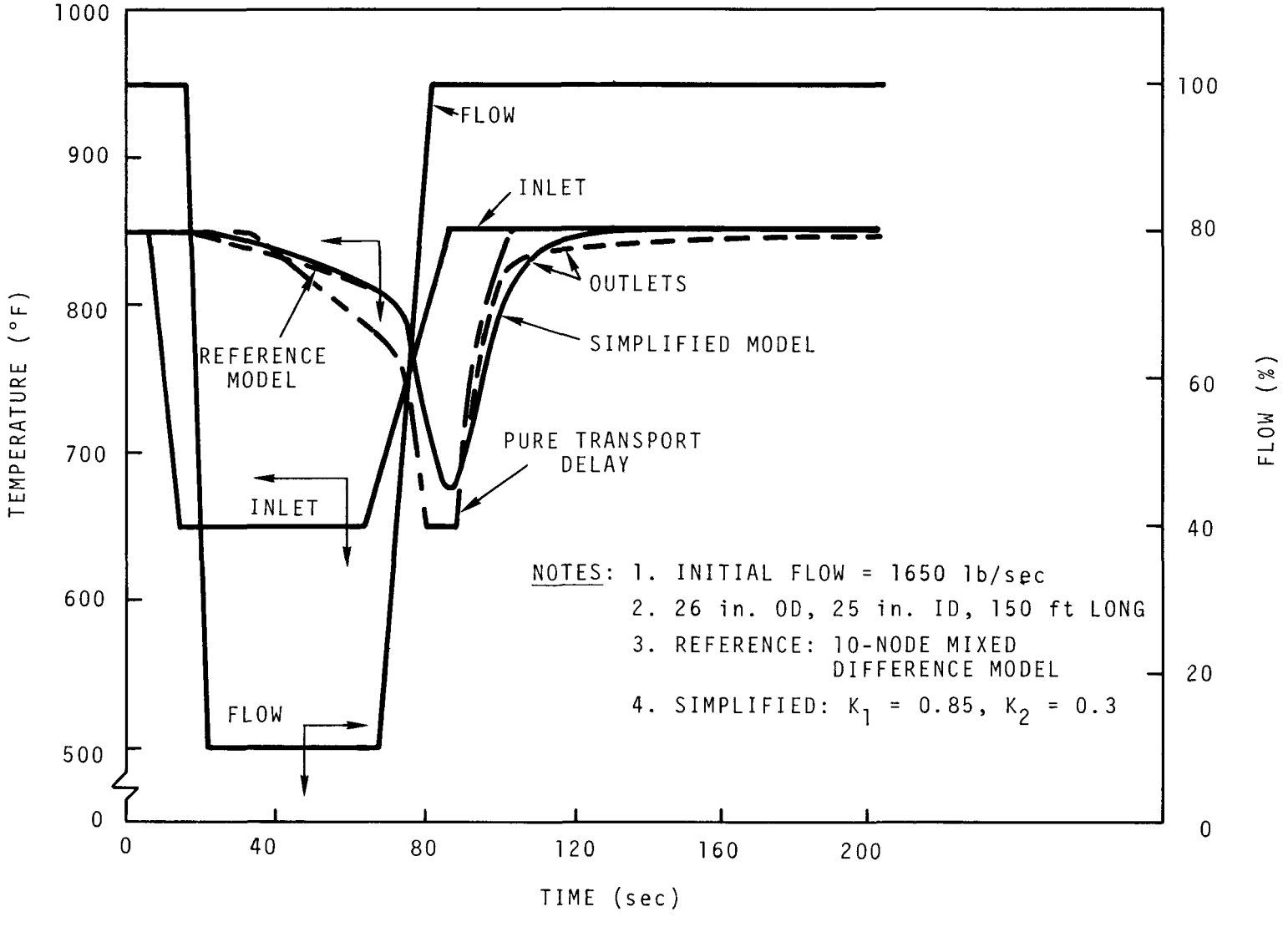

FIGURE VI-38 *Pipe Heat Study--Comparison of Simplified Model to Reference Model for Combined Flow and Temperature Ramp.*

3. Development of MELT-II Code

A. Padilla, Jr., A. E. Waltar, D. D. Stepnewski and W. W. Little

The MELT-II neutronics-heat transfer computer program for accident analysis is being prepared for general distribution. The voiding routines, which previously were applicable to a specific FFTF subassembly design, were generalized and a more accurate numerical integration scheme was incorporated. Extensive comment statements have been incorporated throughout the program to aid the user in following the logic so that future modifications can be made easily. Documentation is currently in progress and should be completed by the next reporting period.

4. CACECO Code Development

R. D. Peak and D. D. Stepnewski

CACECO is a digital computer code developed for the analysis of containment temperature and pressure transients resulting from sources associated with sodium-cooled reactors. The CACECO code was checked against the SOFIRE-II code (developed by Atomics International) for the case of an HTS cell subjected to a 150,000 lb, 1050 °F sodium spill due to a hypothetical pipe rupture. A spill of this magnitude and temperature was selected to obtain limiting effects. This spilled sodium, some 50,000 lb in the first 10 min. of the accident, forms a pool on the cell floor. The model of the cell consisted of roof and upper wall area of 4,166 ft^2 which could not receive heat radiation from the sodium pool on the floor, lower wall area of 2,100 ft^2 which did receive heat radiation from the sodium pool, and floor and submerged wall area of 1,159 ft^2 in direct contact with the sodium pool. The pool, itself, had a surface area of 375 ft^2. The roof, walls, and floor were all modeled with a 0.25-in. steel liner, a 0.25-in. nitrogen gap due to concrete shrinkage, and 60-in. of concrete wall. Heat transfer across the gap was due to conduction and radiation. Good agreement was achieved between these two codes by modifying CACECO in the following respects:

1) Sodium, newly spilled (during a time step) into a containment space, mixes uniformly with the sodium pool already in the space.

2) Natural convection heat transfer coefficients for vertical and horizontal surfaces are increased by a factor of two, and

3) Natural convection mass transfer coefficients for oxygen diffusion to the sodium pool surface and for sodium evaporation from this surface are increased by a factor of two.

The SOFIRE-II code has been checked against experimental data for pool fires in a closed vessel. Thus, the increase in natural convection heat and mass transfer coefficients by a factor of two would appear to be due to convection currents in the experimental vessel that were not accounted for by normal methods of predicting these coefficients.

In either of the above assumed mechanisms, the movement can be simply based on a core average fuel or cladding temperature or by actually considering expansion within each row of subassemblies. In the latter case, reactivity is computed according to the equation:

$$\rho^*_{\substack{\text{Axial}\\ \text{Expansion}}} = \sum_{i=1}^{I} \left[\sum_{j=1}^{J} M_f(1,j) W_f(i,j) \left\{ \frac{\sum_{n=1}^{j-1} \alpha\Delta T(i,n)}{1 + \alpha\Delta T(i,j-1)} - \frac{\sum_{n=1}^{J} \alpha\Delta T(i,n)}{1 + \alpha\Delta T(i,j)} \right\} \right.$$

$$\left. + M_f(i,J) \frac{\sum_{j=1}^{J} \alpha\Delta T(i,j)}{1 + \alpha\Delta T(i,J)} \left\{ W_f(i,J) + \left[W_f(i,J) - W_f(i,J-1) \right] \left[\frac{1}{2} + \frac{\sum_{j=1}^{J} \alpha\Delta T(i,j)}{2} \right] \right\} \right]$$

where: α = thermal expansion coefficient (fuel or cladding)

$W_f(i,j)$ = fuel worth at node (i,j) ($\delta\rho$*/unit fuel mass)

$M_f(i,j)$ = fuel mass at node (i,j)

$\Delta T(i,j)$ = change in temperature from initial condition (average nodal fuel or caldding)

i = radial ring of subassemblies

J = axial level

This model assumes the pins to be rigidly fastened at the bottom of the core, but free to expand in the vertical direction. The first term represents the elongation and resultant density change of the fuel within

the original core length and the second term accounts for the fuel which has expanded above the original core region. A linear thermal expansion coefficient has been used, although a more sophisticated functional relationship could be incorporated.

Figure VI-39 contains representative results for a power transient (5 $/sec unbounded ramp) wherein fission gas release was assumed to cause rapid voiding of the coolant from near the axial center of the core. As can be noted from the curves, the power rose very quickly when no feedback due to axial fuel expansion was taken into account. In the other three cases, expansion due to heating of the fuel was assumed. For the lumped temperature (spatially independent) case, a reactivity coefficient of -2.04×10^{-6} $\delta K/\delta T(°K)$ was used. For the spatial model, using Equation 1, an $\alpha = 6.8 \times 10^{-6}$ $\delta L/K-°K$ was chosen. The spatial model is noted to yield a weaker feedback than the lumped approximation, and the resultant power is higher. The differences are small, however, due mainly to the judicious selection of the lumped reactivity coefficient and the nature of the excursion (little temperature skewing occurs during a rapid power transient; substantially more would be expected in a lost of flow type accident).

Within the spatial model, two variations were made. The base case assumed continual axial fuel expansion even though fuel melting and squirting into the coolant channel occurred. The other case assumed such expansion to terminate in any ring when cladding failure occurred. Figure VI-40 illustrates the variation in the net reactivity and power after initial cladding failure (start of fuel collapse and coolant voiding). Substantially high power is achieved when axial expansion is assumed terminated when fuel collapse begins. It is not clear which variation of the spatial model represents the more realistic situation. Fuel melting should result in a sizable decrease in fuel density (unless sufficient internal porosity is available prior to melting) and a consequent axial expansion. On the other hand, such fuel may expand into the coolant channel and cease to contribute to the axial expansion.

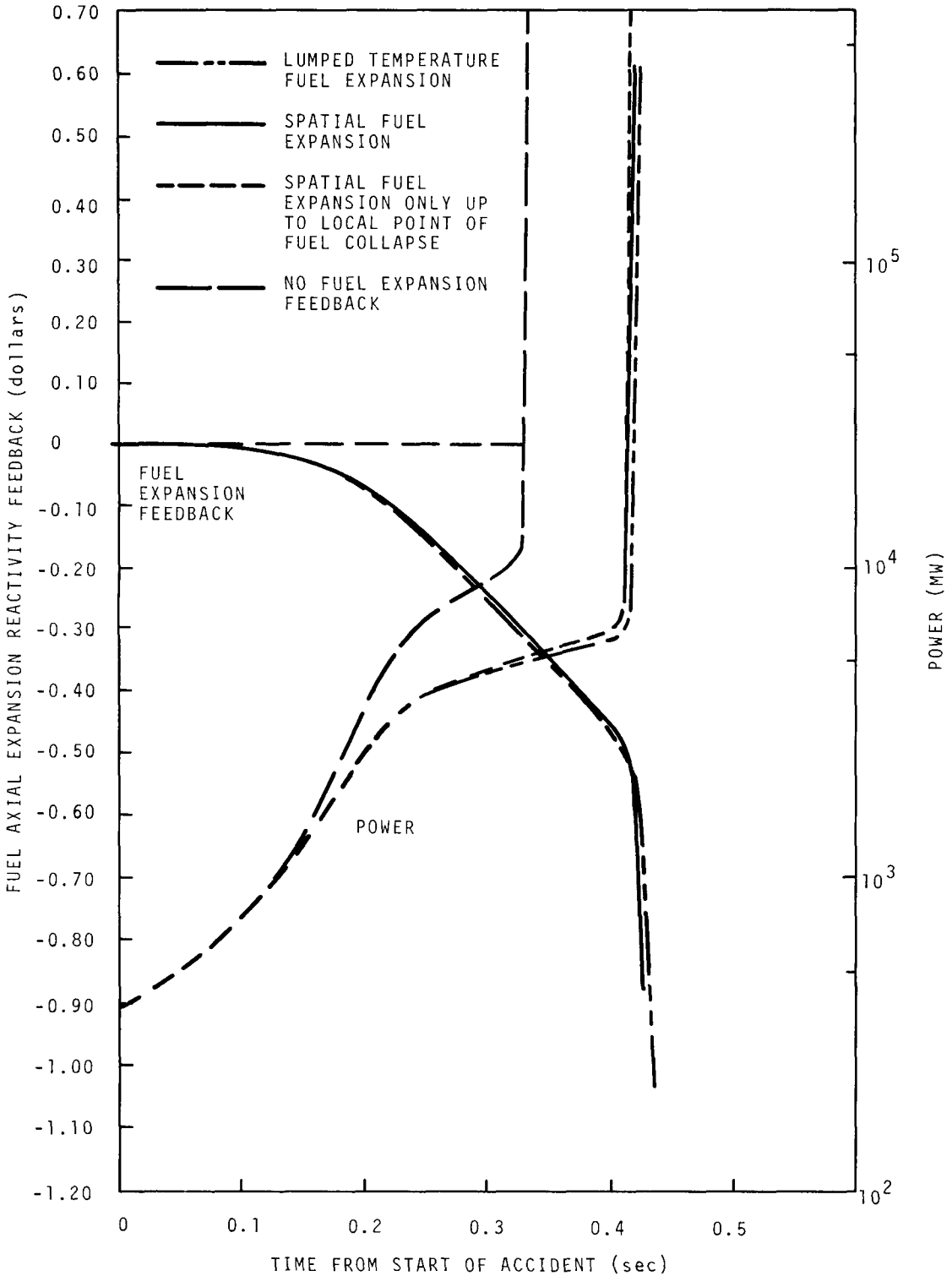

FIGURE VI-33 *Power Transients with Fission Causing Rapid Coolant Voiding.*

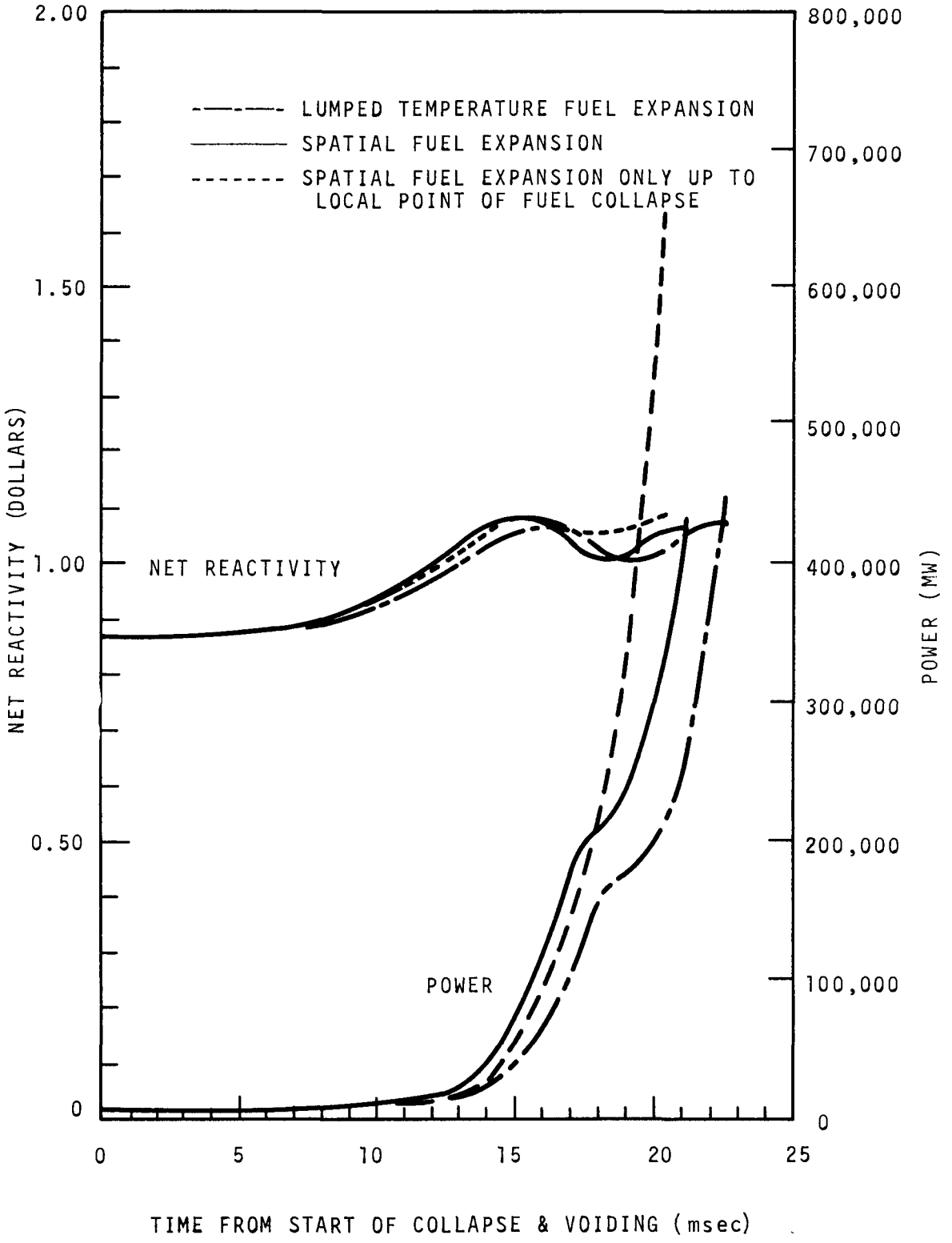

FIGURE VI-40 *Net Reactivity and Power Comparisons for Lumped vs Spatial Axial Fuel Expansion Feedback Models.*

6. Application of Monte Carlo Technique to Reliability Analysis

O. B. Monteith and D. D. Stepnewski

The reliability study of the Plant Protection System (PPS) is continuing through fault-tree analysis employing the Monte Carlo Fault-Tree Simulation Program. The code was checked out against the System 99 reliability study, for which analytical results have been computed in BNWL-1201. In addition, the code was exercised to check results of spurious scrams of the PPS due to component failure. Listed below are some of the results of the MFTS fault tree simulations as compared to the analytical computations.

	Fault-Tree Top Event	MFTS Code	Analytical Result
1.	Seismoscope Trip Fail Unsafe 168 hr	4.281×10^{-7}	1.4×10^{-7}
2.	Primary Rod Release Fail Unsafe - 168 hr	7.734×10^{-7}	8.8×10^{-7}
3.	Seismoscope Trip and Primary or Secondary Rod Release Fail Unsafe - 168 hr	5.63×10^{-7}	1×10^{-6}
4.	Flux/Flow and Primary or Secondary Rod Release Fail Unsafe - 8 hr	3.338×10^{-9}	5×10^{-9}
5.	Flux/Flow and Primary or Secondary Rod Release Fail Unsafe - 168 hr	1.355×10^{-5}	2×10^{-5}
6.	Flux/Flow and Primary or Secondary Rod Release Fail Unsafe - 1500 hr	1.036×10^{-2}	5×10^{-3}
7.	Seismoscope Trip Spurious Scram - 1500 hr	1.421×10^{-5}	1.6×10^{-5}
8.	Seismoscope Trip Spurious Scram - 168 hr	2.152×10^{-6}	1.8×10^{-6}
9.	Flux/Flow Spurious Scram - 1500 hr	5.458×10^{-4}	5.1×10^{-4}

	Fault-Tree Top Event	MFTS Code	Analytical Result
10.	Primary or Secondary Rod Release Spurious Scram - 1500 hr	6.442×10^{-6}	6.9×10^{-6}
11.	Flux/Flow and Primary or Secondary Rod Release Spurious Scram - 1500 hr	6.565×10^{-4}	5.15×10^{-4}
12.	3-out-of-4 Spurious Scram - 1500 hr	3.773×10^{-10}	6.3×10^{-10}
13.	2-out-of-4 Spurious Scram with long repair item - 1500 hr	8.213×10^{-3}	1.2×10^{-2}
14.	3-out-of-4 Fail Unsafe 1500 hr	2.379×10^{-3}	3.0×10^{-3}

Owing to the complexity of the algebraic expressions, certain simplifications were required to obtain the analytical solutions. The agreement between the two methods is considered good, and the Monte Carlo program has been shown to be an efficient way for evaluating complex systems. For example, the fault trees of items 4,5,6, and 11 contained 71 logic gates and 128 independent input events. The average computer time to evaluate these trees by the MFTS code was 17 sec.

VII. FUELS AND MATERIALS EVALUATION

A. FUELS IRRADIATION AND EVALUATION

1. Fast-Flux Fuels Irradiation and Evaluation

The purpose of this task (12138/FI-B) is to provide statistically significant fast-flux irradiation experience with reference and alternate UO_2 - PuO_2 FTR driver fuel. The transient behavior of fast-flux irradiated fuel pins is being investigated in TREAT. Fuel pin performance limits and failure mechanisms of fuel pins irradiated in a fast flux are being investigated.

a. EBR-II Subassemblies PNL-9, PNL-10 and PNL-11

L. A. Pember, E. O. Ballard and J. E. Hanson

Subassembly PNL-9 (X087) will have accumulated an estimated peak burnup of 9400 MWd/MTM at the end of EBR-II Run 45.

The fuel pins for Subassembly PNL-10 were shipped to EBR-II on 6 July 1970 and are to be assembled into the subassembly in the near future. The pins for these subassemblies are mixed-oxide fueled, clad in Type 316 SS, 20% cold worked, 0.230 OD by 0.015 in. thick. Fuel-to-cladding gap is nominally 0.006 in. and the smeared density is 85.5% TD.

b. Run-to-Failure Testing

M. K. Millhollen and J. E. Hanson

Flow testing is being conducted to develop a dependable 100-hour plus, fuel pin defect mechanism for use in EBR-II run-to-failure tests. Three out of four 100-hr tests in flowing, 950°F sodium have been successful; no sodium has penetrated into the dummy fuel pin.

For all tests, a 0.005-in. hole drilled through the cladding wall was filled with Silfos (a copper, silver, phosphorus material). The outer surface of the cladding tube surrounding the filled hole was covered with a coating of Silfos $\sim$0.002 in. thick. In turn, a layer of nickel, 0.001 to 0.002 in. thick, was plated on top of the Silfos.

The three successful tests were conducted with the filled defect hole located centrally under a relatively large layer area of Silfos and nickel.

In one case, the layer was ∿1/8 in. wide by 1/4 in. long; in the other two, the layer was ∿3/4 in. long and continuous around the entire tube. The single test failure in less than 100 hours with this method was where the filled defect hole was located very near the edge of the plated patch.

Two of the test specimens surviving the 100-hr. test were placed back in test, one for an additional 100 hours and the other for an additional 200 hours. Both of these specimens were failed at the end of the test period.

Further flow testing will be conducted before in-reactor failure test pins are fabricated.

c. Linear Heat Rating for Melting Test

E. O. Ballard, J. L. Metcalf, R. D. Leggett and J. E. Hanson

The principal purpose of this test is to confirm the bases for limits on FTR driver fuel thermal performance by determining the effect of initial, cold, diametral fuel-cladding gap on the heat rating required to cause incipient fuel melting in mixed oxide fuel pins clad with 0.230 and 0.250-in. diameter Type 316 SS. Another objective is to evaluate the influence of burnup on the linear heat rating to melting by including several preirradiated pins (from PNL-1 and PNL-2 subassemblies) in the EBR-II subassembly. These latter pins will also provide information about the effects of fuel shuffling and about fuel-cladding damage criteria. Since melt radius provides a known temperature isotherm in the fuel, this test will also allow more comprehensive postirradiation analysis of the important thermal characteristics of the fuel.

The EBR-II Heat Rating for Melting Test is proceeding on schedule. The Engineering Test Plan, final design and safety analysis are in the final stages of completion. Material inspection and fabrication were initiated in anticipation of receipt of Approval In Principle.

Analysis, based on the operating conditions shown in Table VII-1, and the predicted thermal gap conductances shown in Figure VII-1, indicates that incipient melting will occur in the unirradiated 0.250-in. diameter,

TABLE VII-1
OPERATING PARAMETERS FOR THE POWER-TO-MELT TEST

Number of Pins/ Subassembly 1	Diametral Gap (in.)	Pin Diameter (in.)	Pellet Density (% TD)	Planar Smeared Density (%TD)	Pellet Diameter (in.)	Element Position in Subas-sembly	Peak Pin Power (kw/ft)
2	0.004	0.230	90.9	87.30	0.196	13 and 14	16.95 & 16.91
2	0.006	0.230	90.9	85.53	0.194	2 and 5	16.61 & 16.65
2	0.008	0.230	90.9	83.77	0.192	8 and 9	16.40 & 16.31
2	0.010	0.230	90.9	82.04	0.190	1 and 4	16.06 & 16.08
2	0.004	0.250	90.9	87.59	0.214	12 and 19	19.83 & 19.88
2	0.006	0.250	90.9	85.97	0.212	15 and 16	19.63 & 19.54
2	0.008	0.250	90.9	84.35	0.210	7 and 11	19.21 & 19.26
2	0.010	0.250	90.9	82.75	0.208	17 and 18	18.99 & 18.85
PNL-1-11 (Annular)	Preirrad.	0.250	90.78 (initial)	80.29 (initial)	.212 (initial)	3	18.27
PNL-2-16 (Annular)	Preirrad.	0.238	90.57 (initial)	80.91 (initial)	.212 (initial)	6	17.81
PNL-2-18	Preirrad.	0.238	90.05 (initial)	85.28 (initial)	.21225 (initial)	10	18.77

Pellet Geometry (New Pins) - Solid with dished ends.

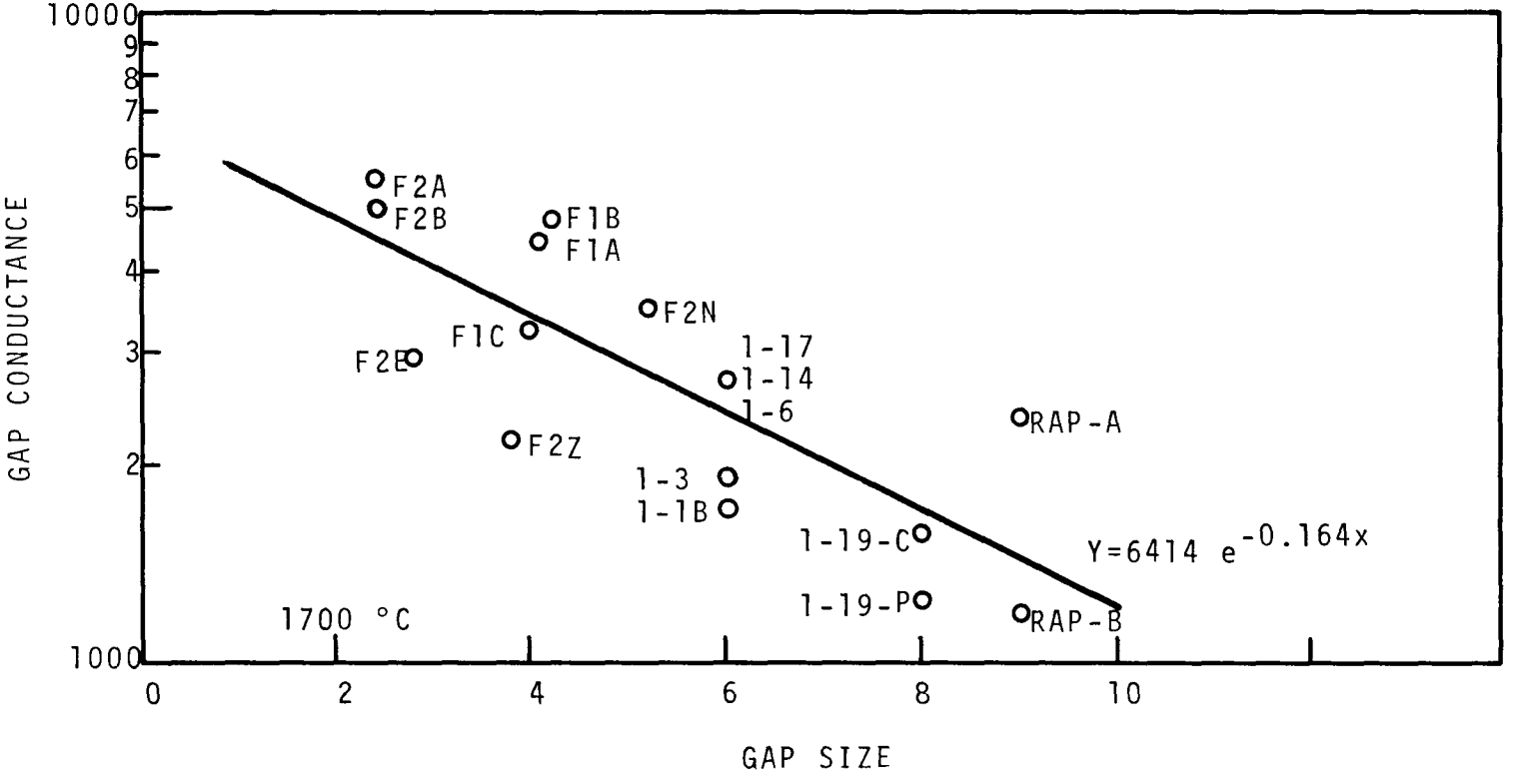

FIGURE VII-1 *Predicted Gap Conductance as a Function of Diametral Gap.*

but not the 0.230-in. diameter fuel pins when irradiated at full reactor power of 62.5 MW.

d. EBR-II/TREAT Test Series

G. E. Culley, D. O. Sheppard, J. C. Gustafson and J. E. Hanson

Transient irradiations are being conducted on prototypic FTR fuel pins that have been previously irradiated under steady-state conditions in fast neutron flux test reactors. The fuel pin response to transient overpower conditions is being studied to determine the failure mechanisums and thresholds.

Analysis of the first EBR-II/TREAT test (PNL-1-2) was completed, and a second fuel pin (PNL-1-1) was transient irradiated. Examination of the PNL-1-2 fuel pin revealed a significant diameter increase, twice the fission gas release of a sibling pin irradiated at steady-state only, and no detectable fuel melting. This response to a transient overpower condition is not in full agreement with existing performance models, which would require fuel melting for either cladding deformation or significant gas release.

The response of the capsule thermocouples during the PNL-1-2 test was not as anticipated, (see Figure VII-2). The much lower equilibrium capsule temperatures observed at 15 sec indicate that not as much energy was released as was expected. A thorough reevaluation of the transient heat transfer prediction by the ARGUS computer code resulted in the conclusion that the ratio of power generated in the fuel pin to the power generated by the reactor had been overestimated by 22%. When this ratio was reduced to 0.78×10^{-4} W/cm^3 of fuel per watt of reactor power, the agreement between predicted and observed thermocouple response shown in Figure VII-3 was achieved. The adjusted fuel pin temperatures shown in Figure VII-4 agree with the observed metallographic evidence (i.e., no fuel melting).

The second test assembly was prepared with the PNL-1-1 fuel pin. This pin was identical to the PNL-1-2 pin. The TREAT reactor test conditions required to produce 50 areal % fuel melting and 1480 °F cladding temperature were determined using the experience gained on the previous PNL-1-2

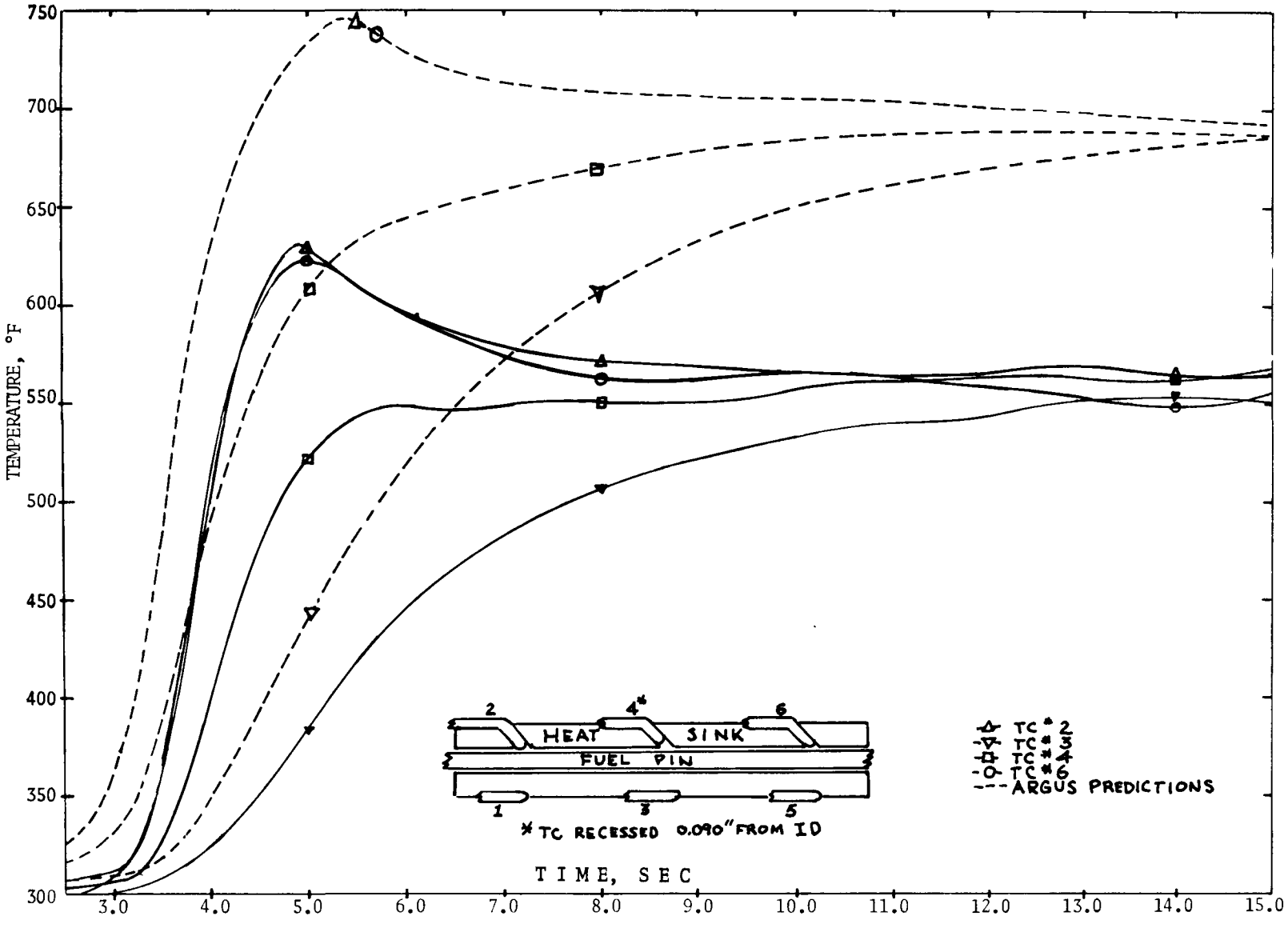

FIGURE VII-2 *PNL-1-2 Transient Data Comparison With Initial ARGUS Prediction.*

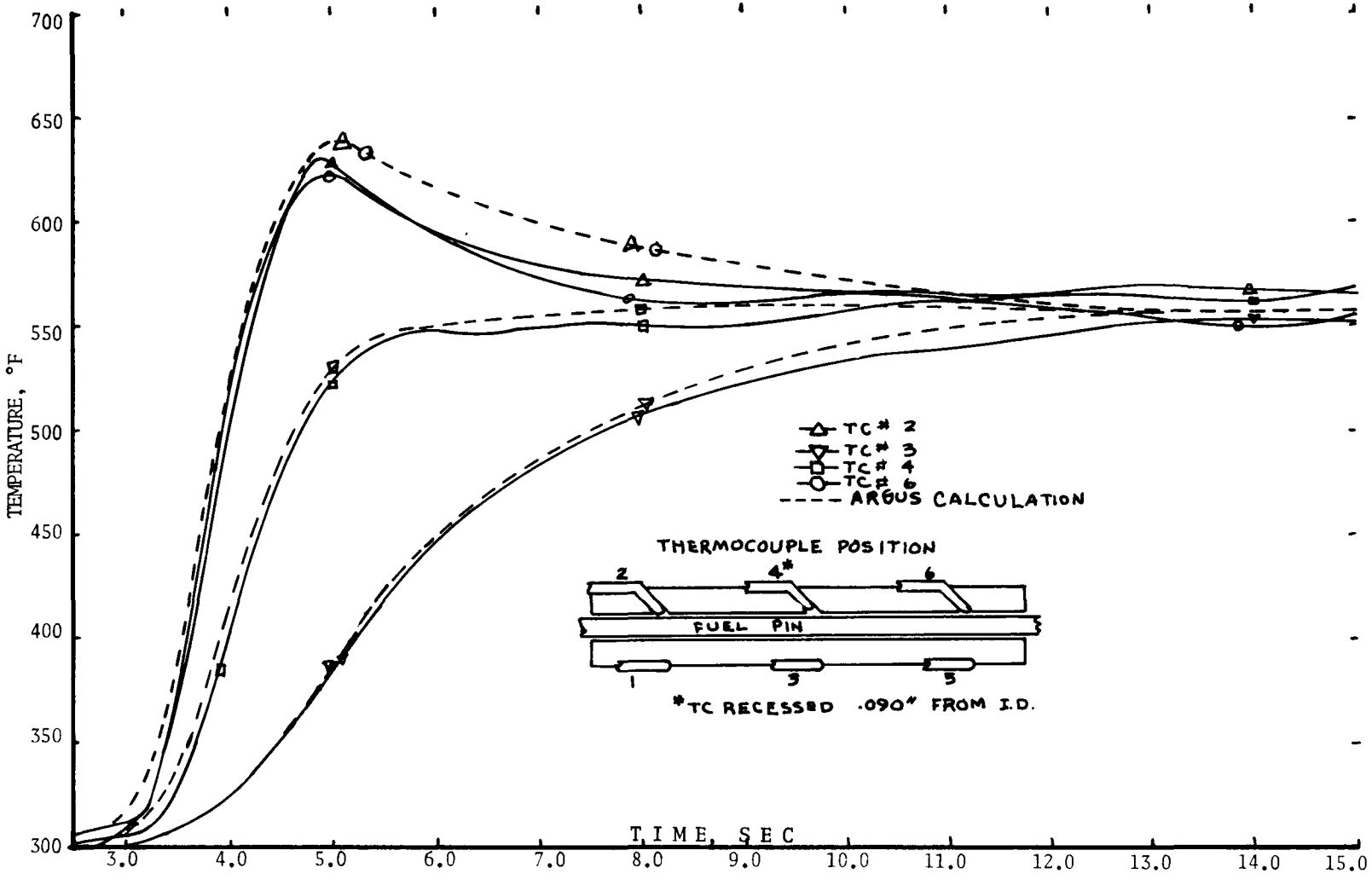

FIGURE VII-3 *Corrected ARGUS Analyses of PNL-1-2 Transient Test Data.*

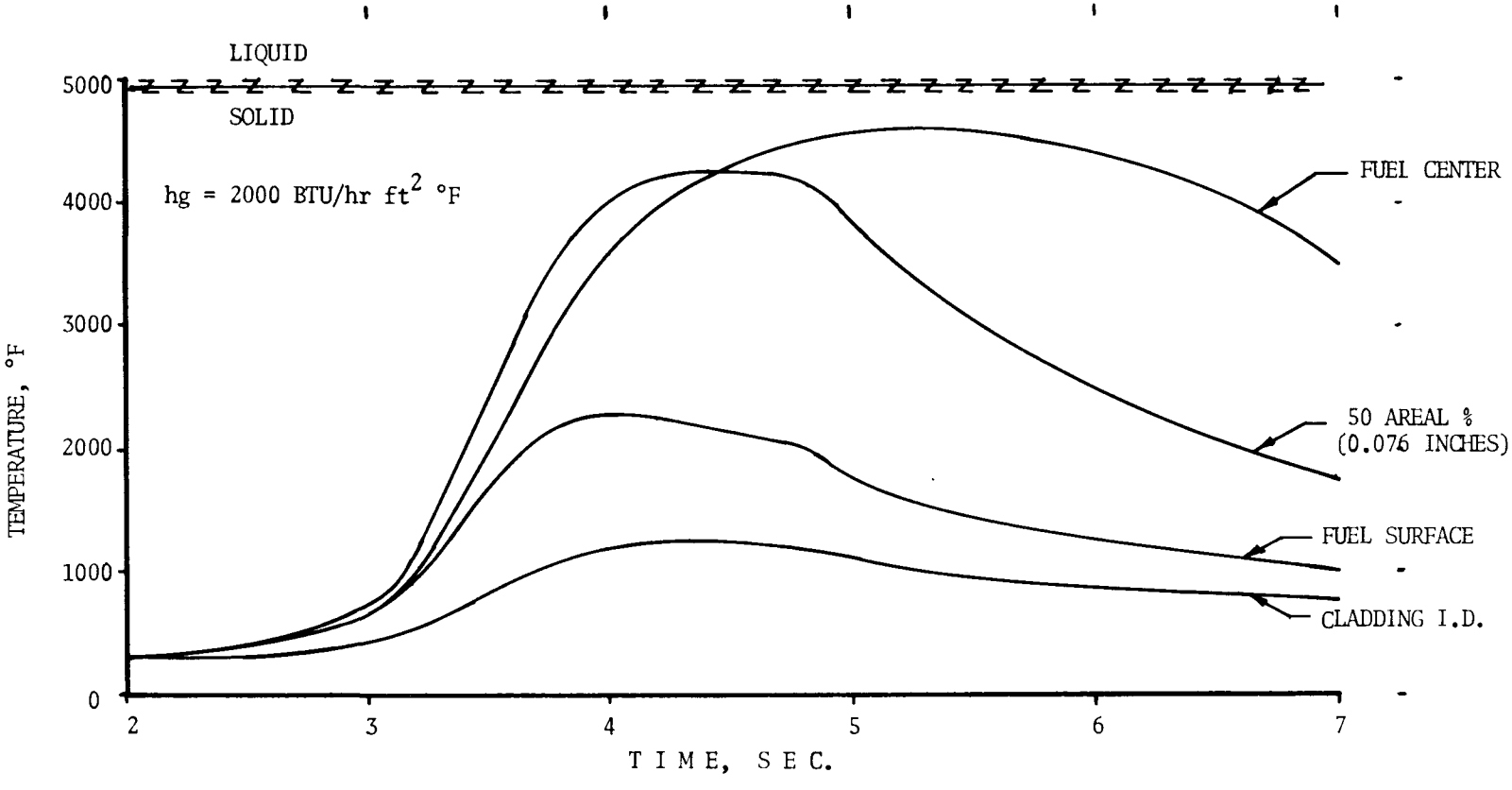

FIGURE VII-4 *Temperature History of PNL-1-2 Fuel Pin.*

test. Figure VII-5 shows the requested reactor power transients. The peak reactor power was overshot by 40%, although the integrated power was within 5% of that requested. The observed response of the capsule thermocouples is compared with that anticipated for the requested transient in Figure VII-6. Since the integrated power (energy released by the fuel pin) was the same as that anticipated, and the expected and observed equilibrium capsule temperatures (at 10 sec.) are identical, the correction to the power ratio must have been in the right direction.

Fuel pin response to the received transient is a different matter. Subsequent ARGUS calculations indicate 80 areal % fuel melting and 1600°F cladding temperature were experienced instead of the 50% and 1480°F values desired. Figure VII-7 depicts the pre- and post-transient condition of the fuel pin. The fuel pin underwent radial expansion to the limit of the ID of the heat sink (36% $\Delta D/D$) and, apparently, the resulting gun barrel effect produced the upward movement of the top of the fuel pin and the accompanying ejection of molten fuel into the capsule. The initiating mechanism was excessive internal pressure from the release of entrapped fission gas upon fuel melting. This behavior is consistent with transient performance predictions.

Other work during the reporting period involved the modification of the EBR-II/TREAT inner capsule to accept PNL-17 (EBR-II instrumented subassembly) fuel pins. Neutronic calculations were also made to determine the power distribution within the PNL-17 test pin in the TREAT neutron flux. The possibility of adding cadmium to the outside of the TREAT capsule heater can to absorb thermal neutrons and to flatten the radial power profile was also evaluated. The calculations indicate this may be feasible.

e. Error Analysis for HEDL Remote Profilometer

J. W. Weber, N. H. Johnson and J. E. Hanson

The errors associated with irradiated fuel pin diameter measurements made on the HEDL remote profilometer were re-estimated. This estimate of errors applies to the fuel pins measured subsequent to the

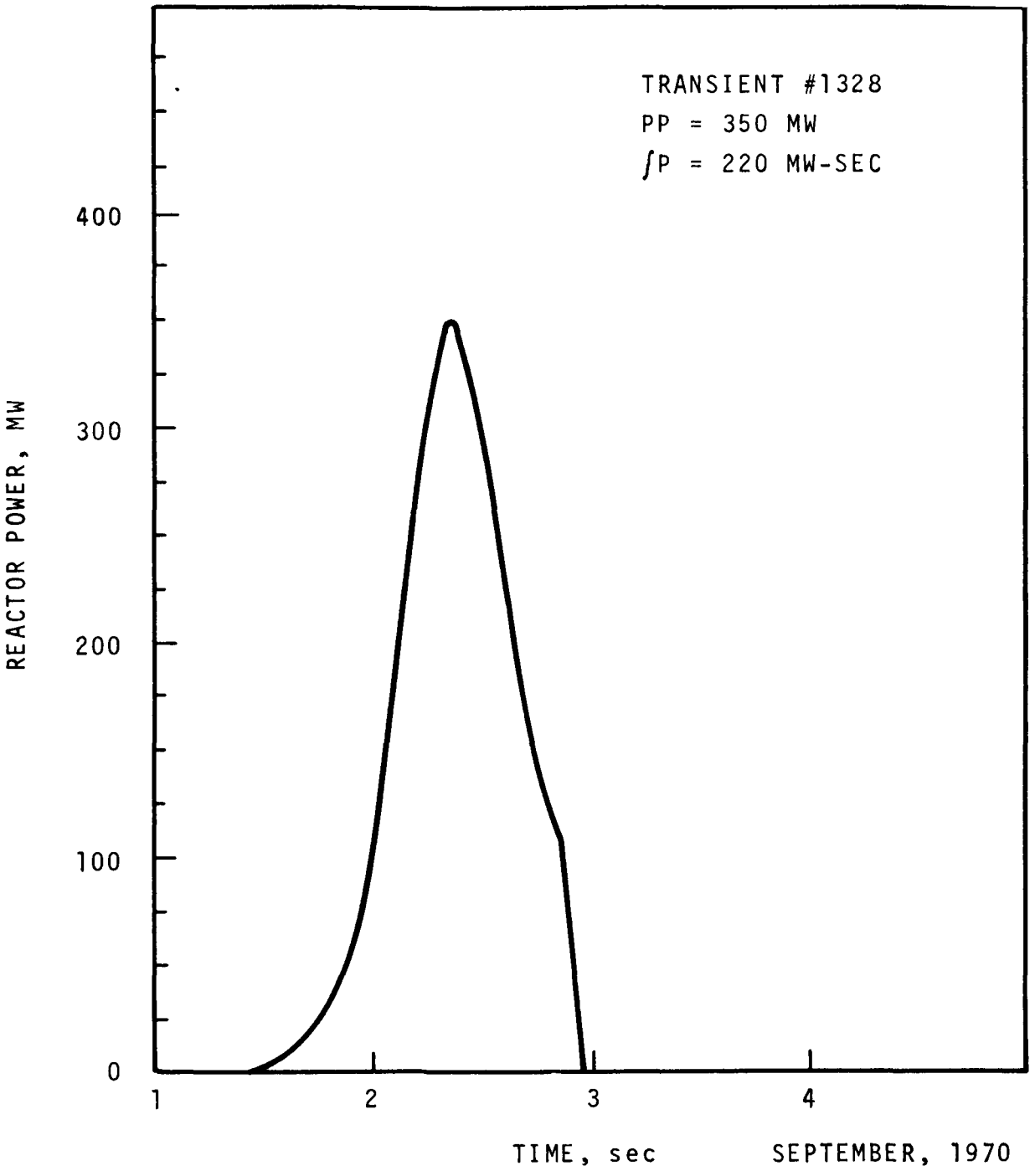

FIGURE VII-5 *Reactor Transients Requested for PNL-1-1 TREAT Test.*

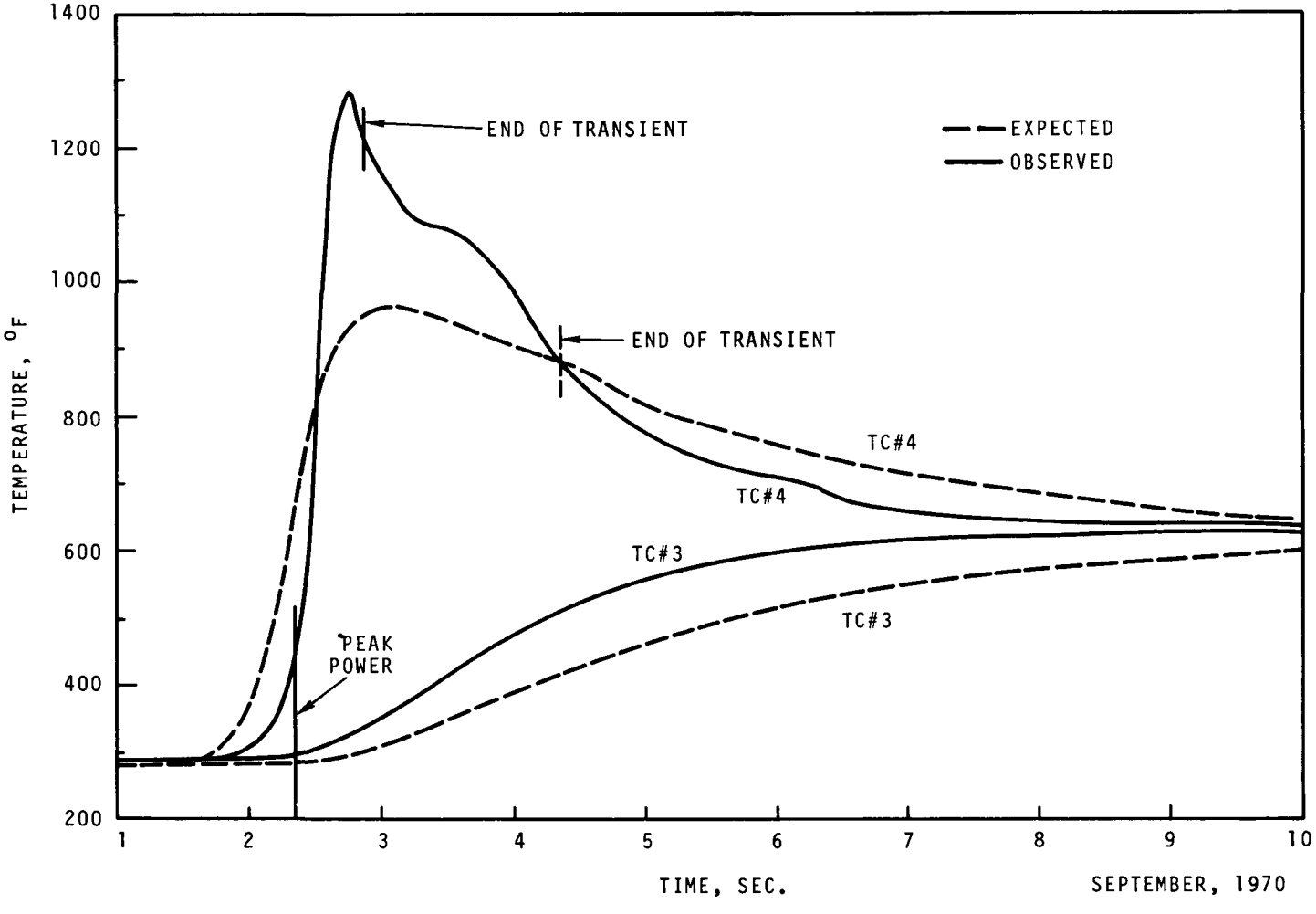

FIGURE VII-6 *PNL-1-1 Expected and Observed Capsule Temperature History.*

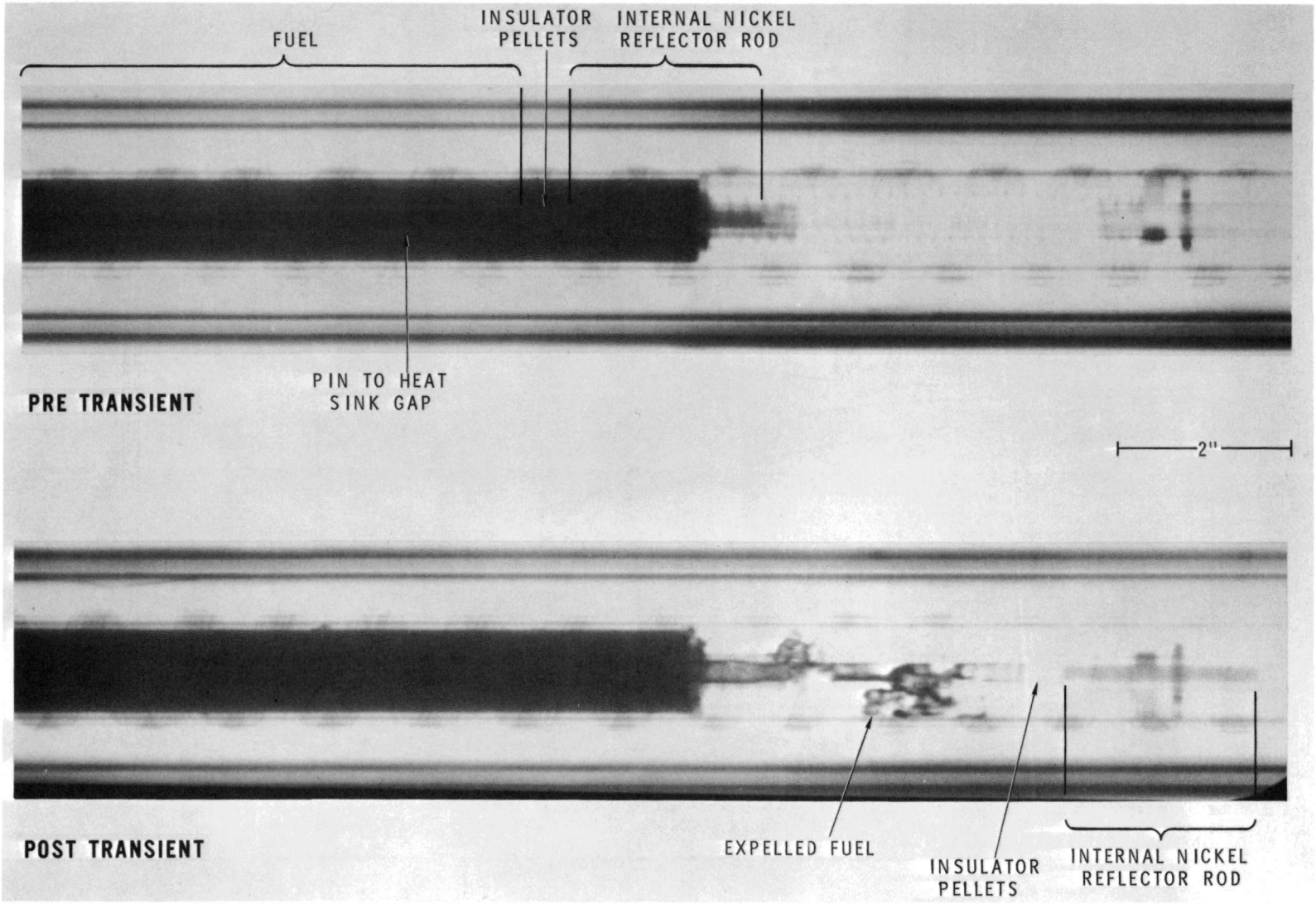

FIGURE VII-7 *Capsule PNL-1-1 Neutron Radiography*

modifications to the profilometer completed in March 1970.

Diameter measurements were made on a standard, certified by the BNW Standards Laboratory to the nearest 5×10^{-6} inch, using standards blocks traceable to the National Bureau of Standards.

Upper and lower limits to the errors calculated for 95, 99, and 99.9% confidence levels are shown in Table VII-2 for each step diameter of the standard.

These error limits indicate that, for any fuel pin diameter measurement to the chosen confidence level, the error of the diameter read from the recorder trace minus the true diameter will be between the upper and lower limits for the respective diameter range. That is, for a pin diameter near 0.250 in., the error at a 99.5% confidence level will range between -0.00003 in. and -0.00005 in. For a pin with diameter near 0.245 in., the error for a 99.9% confidence level will range between -0.00002 in. and -0.00004 in. The errors estimated in Table VII-2 are less than the accuracy to which the diameter traces are normally read (to the nearest 0.0001 inch).

2. Steady-State and Transient Performance Limits

The objective of this task (12160/FP-B) is to evaluate the performance of fuel pins with prototypic FTR-length fuel columns under steady-state and transient irradiation, primarily to verify fuel pin performance under possible abnormal conditions.

a. Steady-State Irradiations

G. E. Culley, J. C. Gustafson and J. E. Hanson

The last two capsules of the 12 original GETR/TREAT test capsules continue under steady-state irradiation. They are operating satisfactorily at 17 kW/ft, and will have an axial average burnup of approximately 48,000 MWd/MTM at end of irradiation.

A capsule was designed for the steady-state and transient irradiation of 0.230 in. diameter, 316 SS clad (present FTR reference design) fuel pins

TABLE VII-2
PROFILOMETER MEASUREMENT ERRORS

	Error Limits (-in.)					
	95% Confidence Level		99% Confidence Level		99.9% Confidence Level	
Standard Diameter (in.)	Upper	Lower	Upper	Lower	Upper	Lower
0.250	-0.00004	-0.00005	-0.00003	-0.00005	-0.00003	-0.00005
0.255	-0.00004	-0.00005	-0.00004	-0.00006	-0.00004	-0.00006
0.245	-0.00002	-0.00003	-0.00002	-0.00004	-0.00002	-0.00004

to update the data from the original 12 capsules. The capsule design is such that when the fuel pin is operated at 13.5 kW/ft in the GETR, the fuel and cladding temperatures will simulate the temperatures that will exist in the FTR peak pin operating at 12.2 kW/ft. The transient thermal performance was also considered; the design will allow test conditions such as 50 areal% fuel melting, 1480°F cladding temperature with an initial pretransient temperature of 480°F.

b. Transient Irradiations - GETR/TREAT Test Series

G. E. Culley, J. C. Gustafson and J. E. Hanson

The transient irradiation of two zero burnup fuel pins in the GETR/TREAT test series was reported in the previous report. The capsule thermocouple data have been analyzed with the following conclusions. Capsule PNL-59-14 probably underwent only 2 areal% fuel melting and the pin-to-reactor power ratio was 0.92×10^{-4} cm^{-3}. The goal was 20 areal% fuel melting. Capsule PNL-59-16, with a goal of 70 areal% fuel melting, probably attained 60 areal% with a pin-to-reactor power ratio of 0.96×10^{-4} cm^{-3}. The initial analytically determined power ratio was 0.90×10^{-4} cm^{-3}.

Nondestructive examination of the two zero burnup fuel pins continued. Neutron radiographs of the bare fuel pins showed no central voids in either fuel pin. The fuel pellets in both pins are cracked extensively, and there are many pellet separations in the PNL-59-16 fuel pin.

3. Fast Flux Steady-State Pin Irradiations

This task (12161/FP-C) is to provide statistically significant steady-state, fast-flux irradiation experience with reference and alternate UO_2-PuO_2 FTR driver fuel at peak, average and minimum anticipated FTR pin linear power ratings. Data on fuel performance at fuel burnup-cladding fluence ratios typical of those anticipated in FTR will be generated during these irradiations. The data provided will be used in developing models to describe mixed oxide fuel pin behavior as a function of fuel and cladding parameters.

a. EBR-II Subassemblies PNL-3, PNL-4 and PNL-5

L. A. Pember, E. O. Ballard and J. E. Hanson

Two of the three, 37-unencapsulated-pin experimental subassemblies (25 wt% PuO_2-75 wt% UO_2, Type 304 SS cladding, 0.250-in. OD) in EBR-II are operating well. These subassemblies will have attained the following estimated peak burnup at the end of EBR-II Run 45.

Subassembly	Burnup MWd/MTM
PNL-3(X051)	28,100
PNL-4(X059)	43,100
PNL-5(X054)	50,300

Subassembly PNL-5, which was discharged at the end of Run 42 after reaching a goal exposure of 50,000 MWd/MTM, is still in the EBR-II basket. Approval of the proposed examination and reconstitution scheme has been requested from DRDT. We propose that this subassembly be given an interim examination and reconstitution into two Mark E 19 subassemblies for continued irradiation.

Subassemblies PNL-3 and -4 will be reconstituted between Runs 45 and 47 and will be reinserted into EBR-II for continued irradiation with the reactor operating at 62.5 MW for Run 47.

b. EBR-II Subassemblies PNL-6, PNL-7 and PNL-8

L. A. Pember, E. O. Ballard and J. E. Hanson

These three 37-pin experimental subassemblies (which contain annealed Type 316 SS clad, 0.250-in. diameter mixed oxide fuel pins) continue their successful operation. Estimated peak burnups at the end of EBR-II Run 45 will be:

Subassembly	Burnup, MWd/MTM
PNL-6(X073)	18,500
PNL-7(X069)	25,200
PNL-8(X074)	28,900

Subassemblies PNL-7 and -8 were discharged at the end of Run 44 and were put in the EBR-II basket. They will be reconstituted for 62.5 MW operation and are scheduled for reinsertion into EBR-II for Run 47. PNL-6 does not require reconstitution and will continue irradiation without interruption.

c. Instrumented Subassembly - PNL-17

M. K. Millhollen and J. E. Hanson

The PNL-17 instrumented subassembly continued to operate satisfactorily in EBR-II during its fourth reactor run at a reactor power level of 50 MW. Data in the form of thermocouple readings were being collected continuously.

The subassembly was fabricated with thermocouples substituted for wire wraps on 16 of the pins to obtain direct subchannel coolant temperatures at two levels in the subassembly. Readings taken during the first reactor run at reactor power levels of 20 MW and 50 MW have been compared to calculated values made with the COBRA II A Program. A statistical analysis of the results, described below, showed to be very good in most cases. The comparison of measured and calculated temperatures indicates that calculational methods used to predict coolant channel performance of fuel test assemblies in EBR-II are satisfactory. (The data and the analysis of the temperatures have been published in BNWL-1424, "PNL-17 EBR-II Instrumented Subassembly Test Interim Report" by M. K. Millhollen and A. M. Sutey, June 1970.)

A request was made to continue the irradiation test for three additional reactor runs at a reactor power level of 62.5 MW. The Hazards Analysis was updated to reflect the results of the additional irradiation periods and was submitted to EBR-II Project for approval. Calculations indicated that the additional irradiation periods would not jeopardize the integrity of the fuel pins.

A statistical analysis of the results of temperatures measured in the PNL-17 Subassembly was performed. It was found that there was no

power-dependent bias in the temperature measurements.

4. Thermal Flux Irradiation of Hypostoichiometric UO_2-PuO_2 Fuel

This task (12213) includes irradiation testing of mixed oxide fuel specimens of different stoichiometries to high burnups in a thermal flux. Substoichiometric mixed oxides are expected to exhibit better fuel-cladding-Na compatibility at high burnups than the nearly stoichiometric oxides. System compatibility, swelling and gas release characteristics of UO_2-PuO_2 fuel as a function of stoichiometry and fuel form must be determined at high burnup before an optimum fuel can be designed.

a. Status of Thermal Flux Irradiation Tests

J. W. Weber and J. E. Hanson

The general status of the fuel pins is summarized in Table VII-3. The reported burnup values were derived from Nd^{148} analyses of sections removed from the center of the fuel pins. The burnup values for those pins not yet examined were estimated from the reported fluence, assuming a linear relationship between fluence and burnup. During this report period, the burnup on samples from fuel pin BNW 1-3 and 1-5 were determined by chemical analysis for Nd^{148}, to be 113, 500 MWd/MTM and 137,200 MWd/MTM, respectively.

Metallographic examinations of samples from BNW 1-1, 1-2, 1-3 and 1-5 fuel pins continued. Longitudinal cross sections, designated A, from the bottom of the fuel columns of BNW 1-3 and 1-5 are shown in Figures VII-8 and VII-9, respectively. Each of the fuel sections exhibits a deposit of material in the central void. The α- autoradiographs, Figures VII-8 and VII-9, show only faint evidence of fuel in the material in the central void. Strong beta or gamma emission from the material is shown in the β-γ autoradiographs. Examinations of the polished fuel sections on the metallograph showed a discontinuous low density structure for the material. Gamma scan data obtained during the nondestructive examination of the BNWL 1-5 fuel pin showed two broad peaks of high gamma activity at the same logitudinal position as the material shown in the central void.

TABLE VII-3
SUMMARY STATUS OF IRRADIATION EXPERIMENTS

Status Issue Date: 9/3/70

Test Designation	Description[1] Fuel Form	O/M	Facility	Goal Exposure MWd/MTM	Actual Exposure MWd/MTM	Discharge Date	
BNW 1-1	Solid	1.93	MTR	100,000	122,000	2-69	Being examined at BNW
BNW 1-2	Solid	1.93	ETR	50,000	82,800	2-69	Being examined at BNW
BNW 1-3	Solid	1.96	MTR	100,000	113,500	2-69	Being examined at BNW
BNW 1-4	Solid	1.96	MTR	50,000	71,000	6-68	Examined at BNW
BNW 1-5	Solid	2.00	MTR	100,000	137,200	2-69	Being examined at BNW
BNW 1-6	Solid	2.00	MTR	50,000	75,200	10-68	Examined at BNW
BNW 1-7	Annular	1.93	MTR	50,000	<1,000		Lead tube failed. Examined at BNW
BNW 1-8	Annular	1.93	MTR	100,000	29,000	1-68	Failed. Examined at BNW
BNW 1-9	Annular	1.96	MTR	50,000	81,800	6-68	Examination completed at LASL
BNW 1-10	Annular	1.96	ETR	100,000 (Est)	92,200	11-69	(2)
BNW 1-11	Annular	2.00	MTR	50,000	87,400	8-68	Examination completed at LASL
BNW 1-12	Annular	2.00	ETR	100,000 (Est)	96,500	11-69	(2)

(1)
Fuel

25% PuO_2 - 75% UO_2

Pellets 0.212 in. OD (0.052 in. ID for annular pellets)
Smeared density 87.5% TD
Pellet density - solid pellet 93% TD, annular pellet 95% TD
Fuel column length 13.5 in.

Cladding

OD - 0.250 in.

Wall thickness - 0.016 in.
304 SS

(2) Discharged 2-69 for interim examination. Recharged 5-69
Discharged 11-9-69 for final examination.

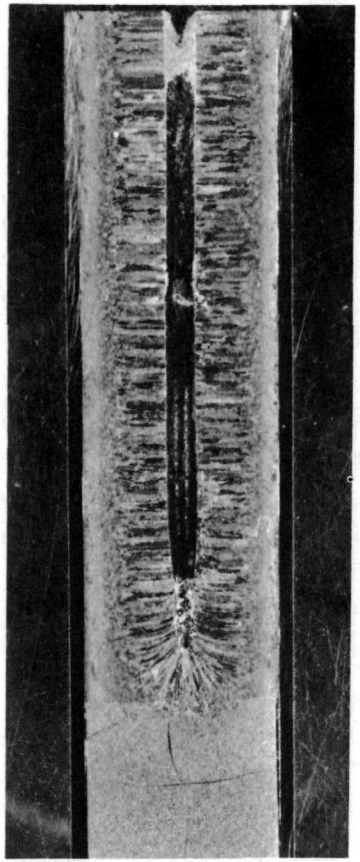

Macro F1786

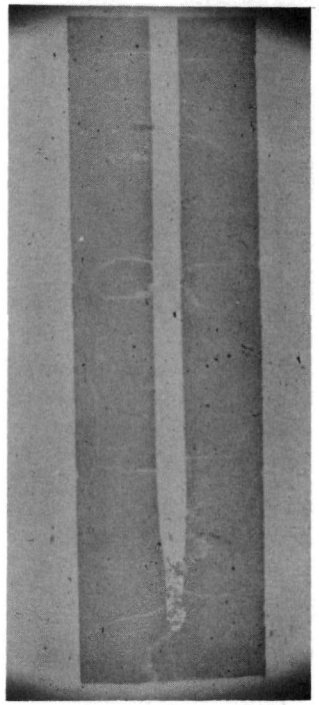

α Autoradiograph
1763

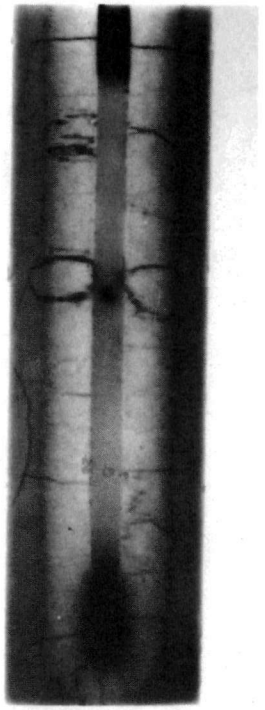

β-γ Autoradiograph
1762

FIGURE VII-8 *Longitudinal Cross Section from Bottom of BNW-1-3 Fuel Pin As-polished, 4.75x.*

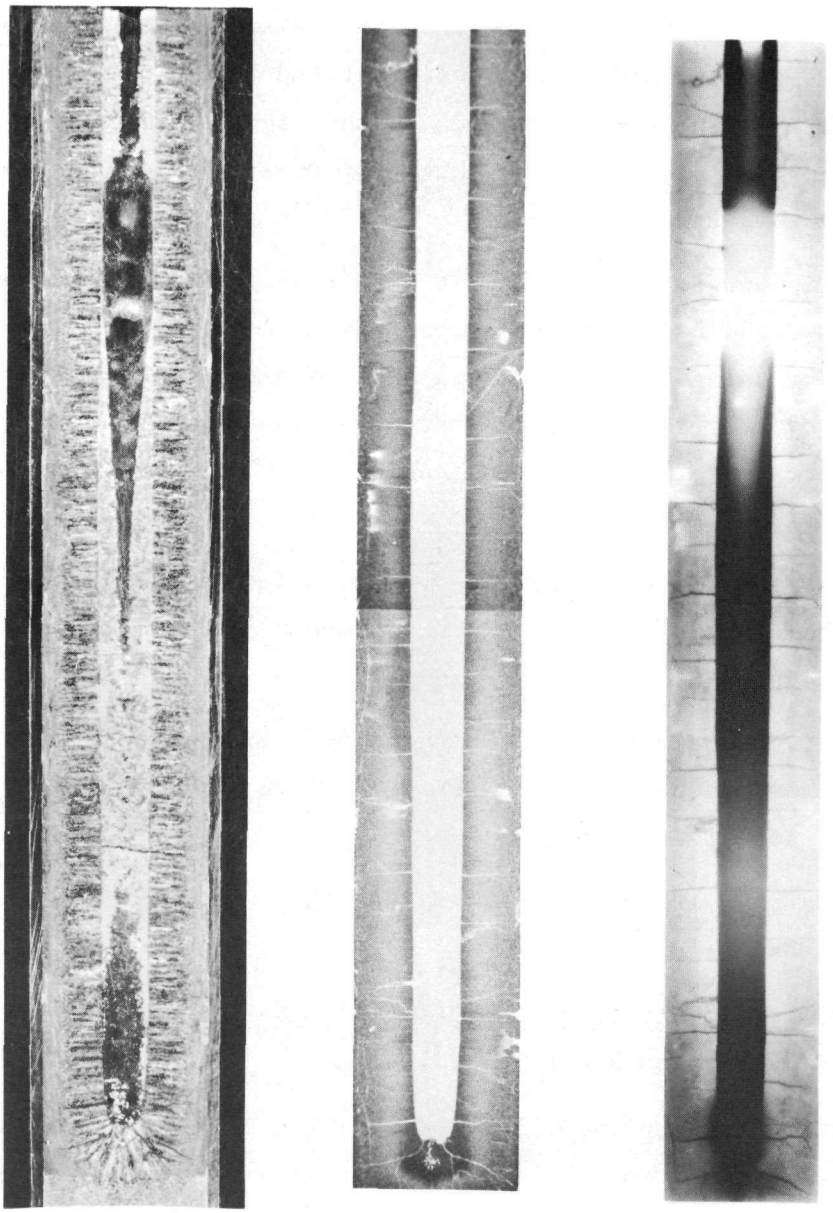

Macro 17662 | α Autoradiograph 1809 | β-γ Autoradiograph 1810

FIGURE VII-9 *Longitudinal Cross Section From Bottom of BNW 1-5 Fuel Pin. As-polished, 4.75x.*

Analysis of spectral gamma scan data obtained at these peak locations showed Cs to be the primary gamma emitter. A peak of gamma activity was found on the gamma scan of BNW 1-3 at the same longitudinal position as the material filling the central void at the top of the fuel section (Figure VII-8). The presence of Cs in the higher temperature portion of the fuel has been postulated by ANL to be possible by the formation of a stable compound of Cs-U-O.

A continuous layer, distinctly different from the fuel, was observed at the fuel-cladding interface of the BNW 1-5A fuel section. The fuel, layer, and cladding are in intimate contact along the interface, other than for a quarter inch of fuel just above the depleted pellet. Adjacent to the layer, the cladding has extensive grain boundary attack to a depth of 3 mils.

The BNW 1-3A section exhibited only an intermittent layer between the fuel and cladding. There was no evidence of grain boundary attack in the cladding.

These two sections will be studied more extensively to determine whether the Cs concentration in the central void and the cladding grain boundary attack are related.

Preparations are being made to open the last two BNW-1 series capsules, 1-10 and 1-12.

b. Shielded Electron Microprobe Examination

E. D. Jenson and L. A. Hartcorn

A radial cross section (D-1) of fuel pin BNW 1-2 has been examined in the Shielded Electron Microprobe. The most prominent feature of this sample is a two-phase region adjacent to the central void. Figure VII-10 shows the surface and some of the areas examined in detail. The continuous phase has flowed into radial cracks and extends nearly to the equiaxed grain region. The composition was examined in more than 20 locations and was very similar at all locations, averaging 30 to 40% barium, 8 to 14% molybdenum, a small amount of tellurium and the balance fuel. Figure VII-11

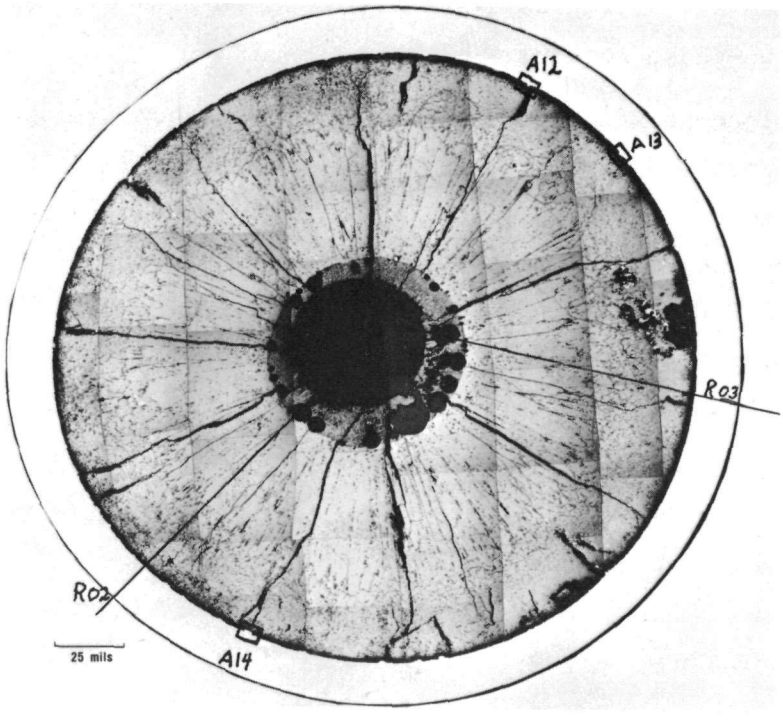

FIGURE VII-10 *Surface of BNW 1-2, D1 examined. Radii and 3 Areas of Palladium on Cladding also indicated.*

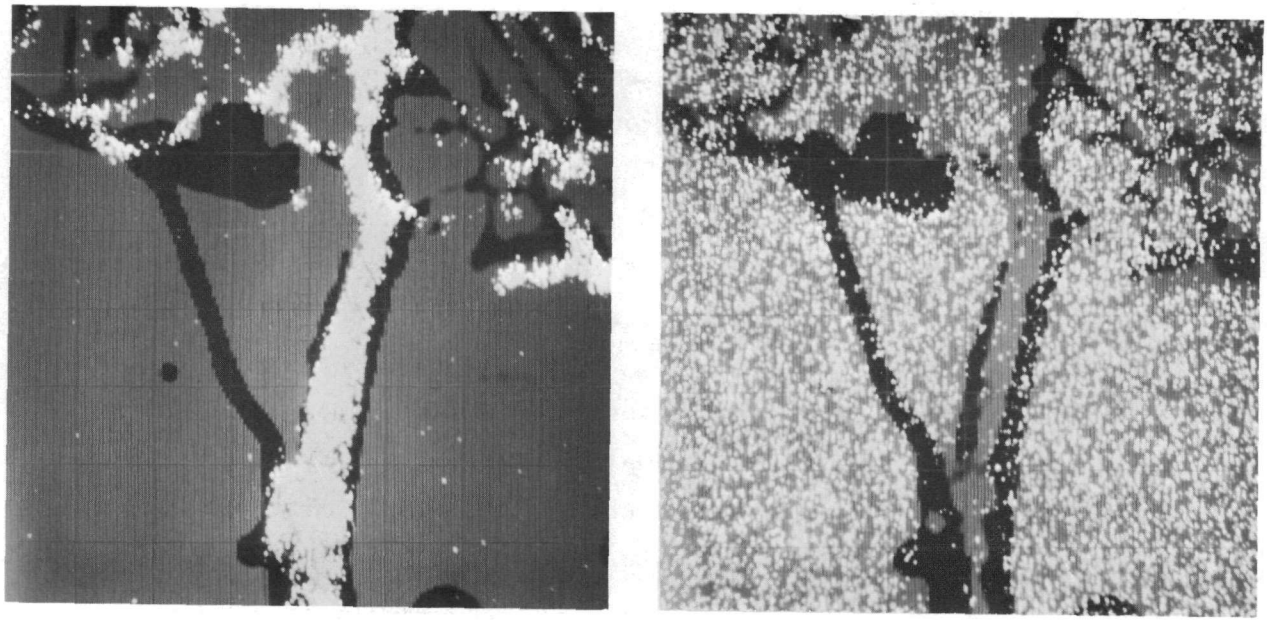

FIGURE VII-11 *Distribution of Barium & Plutonium in the Two-Phase Region, Normal Fuel & a Crack.*

shows the barium and plutonium distribution in an area overlapping the fuel and the two-phase region.

The radial composition of metallic inclusions containing fission product molybdenum and ruthenium was examined along several radii (Figure VII-12). Two types of inclusion are apparent; a 30% molybdenum deposit and an 80 to 90% molybdenum deposit. The high molybdenum deposit occurs only at 0.60 to 0.85 radial fractions, while most of the low molybdenum deposit occurs in the inner half of the radius; deposits do occur out to 0.9 radial fraction.

The distribution of uranium, plutonium, zirconium, and neodymium across two radii of BNW 1-2, D1 has been determined. Figure VII-10 shows the surface and the two radii examined. The distribution of uranium and plutonium (as oxides) is shown for radius RO2 in Figure VII-13. The plots begin at the center of the fuel including the two-phase region and extend to the cladding. The interval between points analyzed was 5.0 microns. Corrections for X-ray and radiation background were made, as well as instrumental drift. Single sharp spikes in U and Pu concentration are not real.

The zirconium concentration was determined across each radius at 10 to 50 micron intervals. Backgrounds were determined for each point on each side of the X-ray peak. The average composition in the bulk of the fuel appears to be 0.15 to 0.3%, with higher concentration at the fuel OD. Figure VII-14 shows the zirconium distribution across radius RO2. An indication of the 2-sigma error limits (counting statistics only) is given by the error bars. Zirconium segregation was found just inside the cladding (between the fuel OD and the palladium layer on the cladding). Considering the burn-up of this pin, (82,800 MWd/MTM) and the fission yield of zirconium there should be about 2% zirconium present by now. The discrepancy between the determined and expected values indicates that much more zirconium is located somewhere in the pin.

The relative neodymium distribution across radius RO2 and RO3 was determined manually (separate determinations on and off the peak to

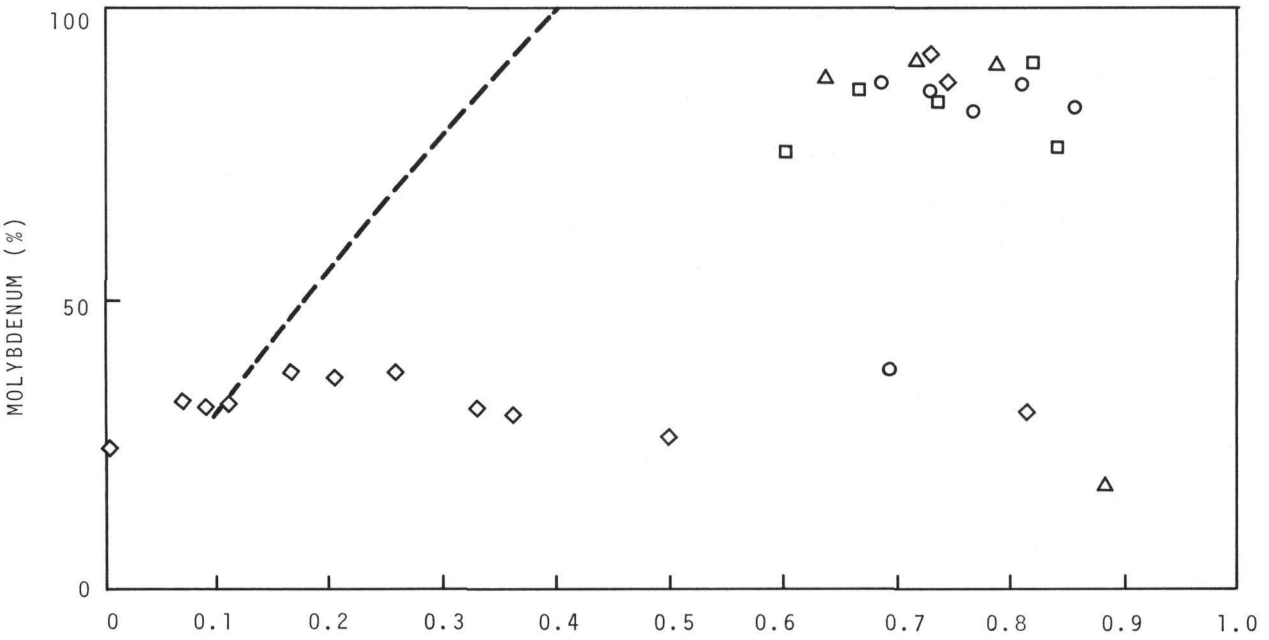

FIGURE VII-12 *Radial Fraction (From ID Of Fuel) Molybdenum Content of Inclusions in BNW 1-2, DI Each Type of Symbol Represents A Different Radius.*

correct for background). The counting rate was low (50 to 100 counts/sec) resulting in appreciable errors from statistical fluctuation in the high background counting rate. Figure VII-15 shows the neodymium count rate (approximately proportional to concentration) across radius RO2. A slight increase in neodymium near the central void (probably indicative of the higher plutonium content) and a dramatic increase near the fuel OD (indicative of the higher burnup) are apparent. No segregation of neodymium could be found.

The fuel-cladding interface shows a layer of palladium on the cladding. In some areas, a mound of palladium has been deposited. Between the palladium and the fuel is a region of fission products rich in cesium and tellurium. One such area (area 12 in Figure VII-10) is shown in Figure VII-16 with the location of the main fission products labelled (area 12 in Figure VII-10).

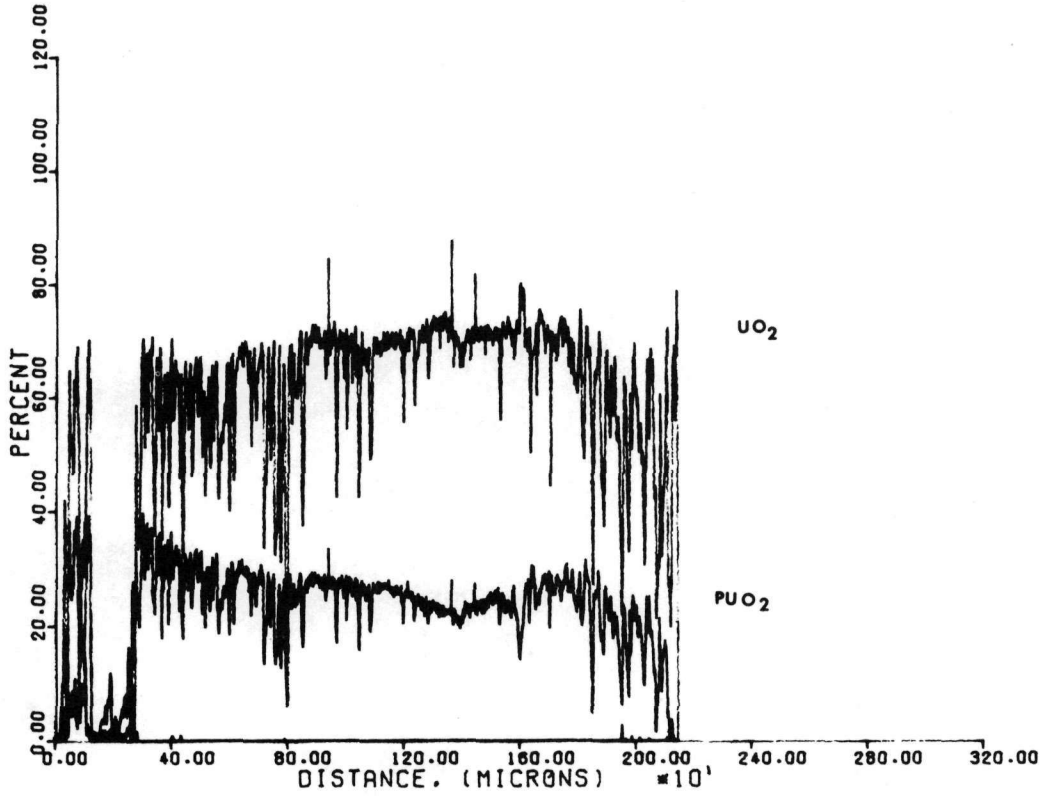

FIGURE VII-13 *UO_2 and PuO_2 on Radius 02 of BNW 1-2, D1. Distance is from ID of fuel.*

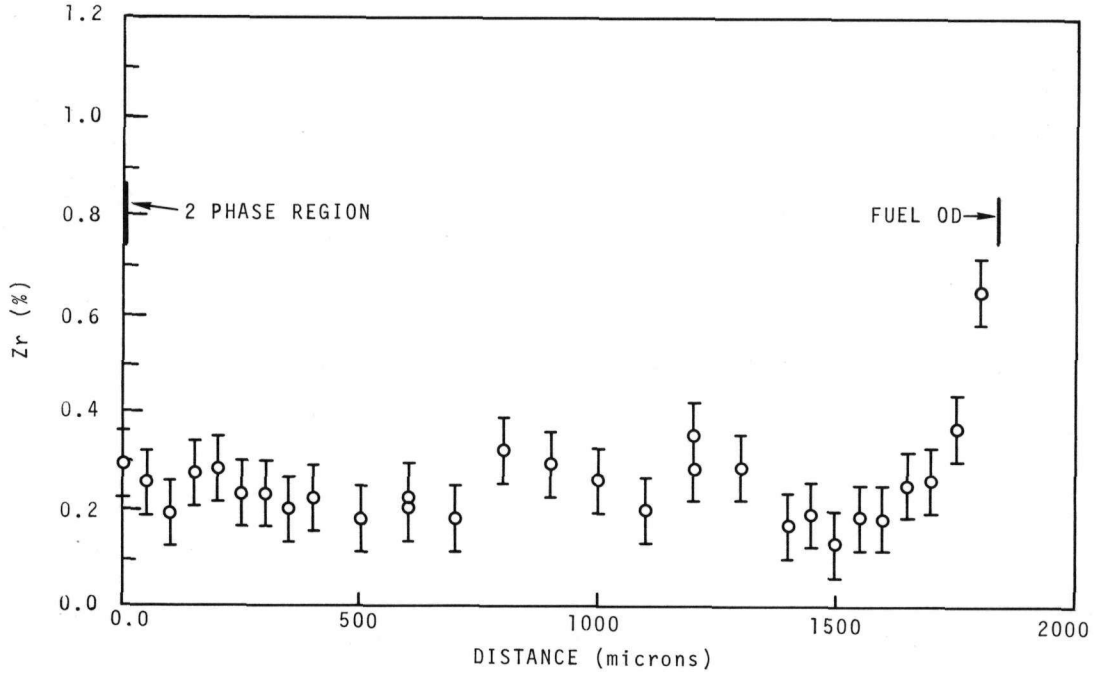

FIGURE VII-14 *Zirconium Distribution Across Radius RO2 of BNW 1-2, D1.*

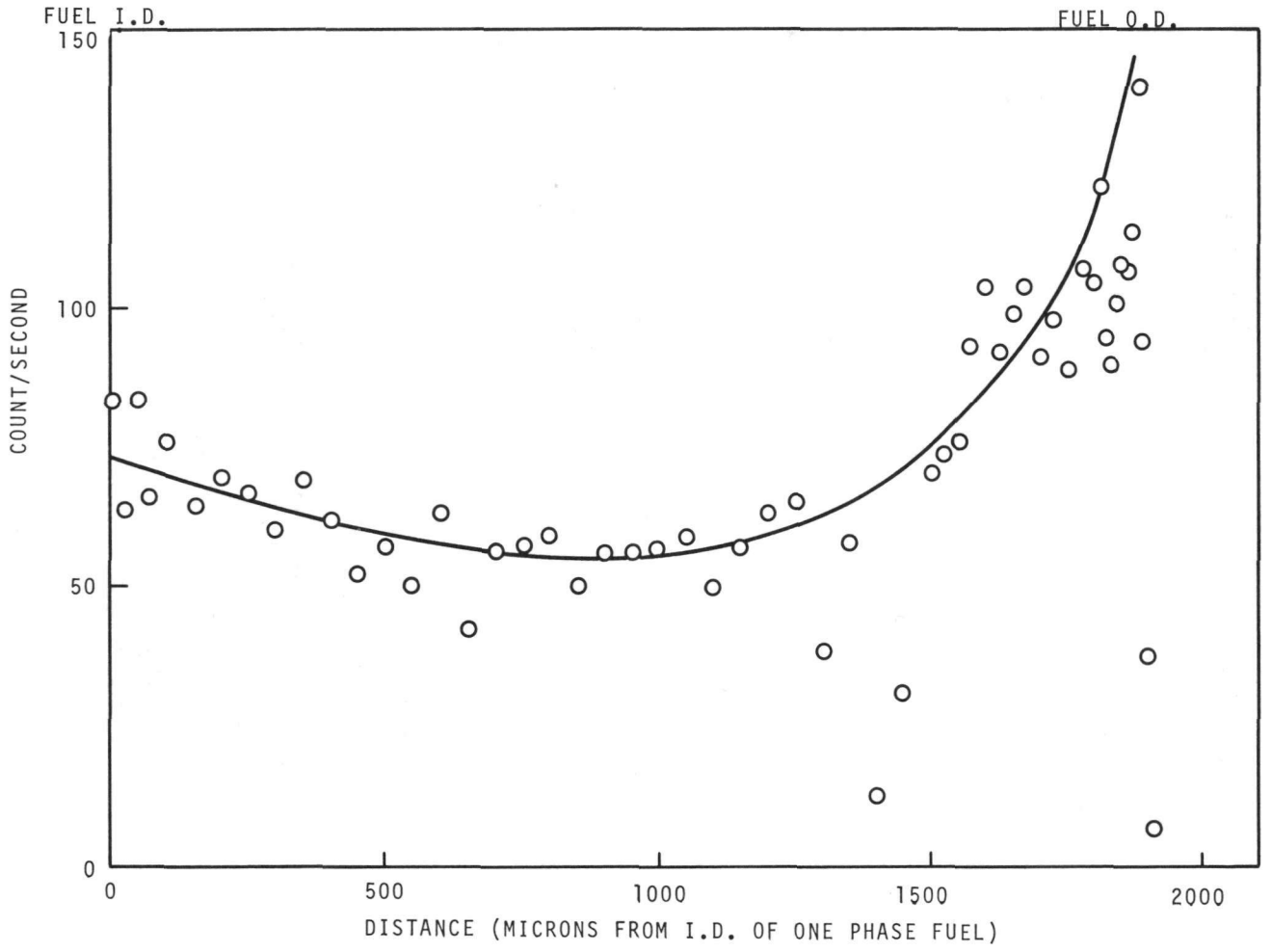

FIGURE VII-15 *Neodymium Counting Rate Across Radius (RO2) of BNW 1-2, D1.*

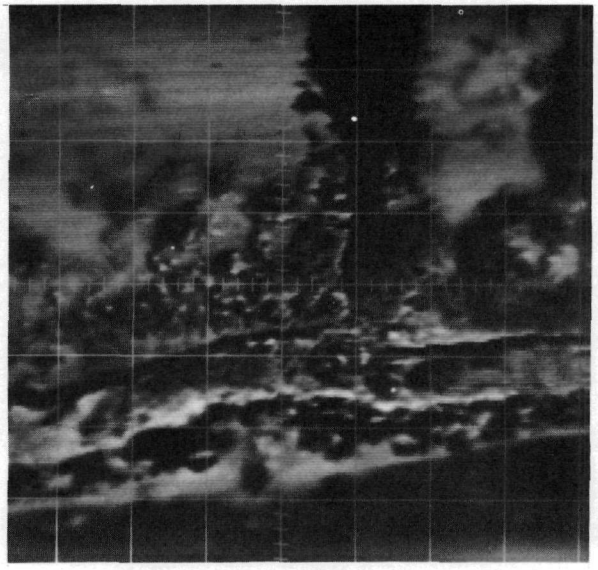

50 microns

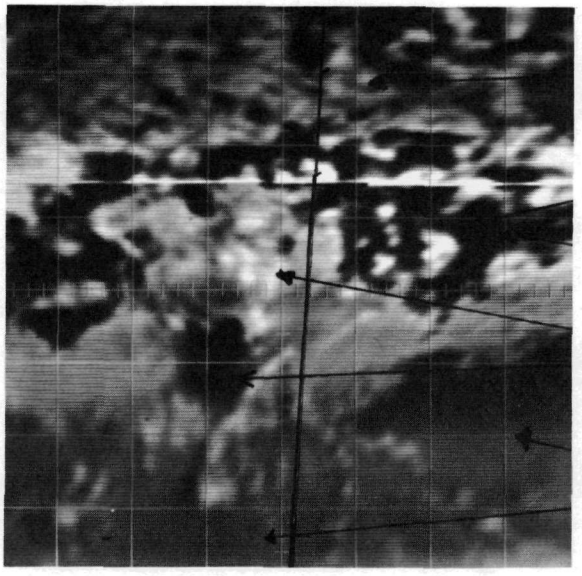

20 microns

FIGURE VII-16 *Identification of Features in Area of Fission Product-Cladding Interaction Zone.*

The distribution of iron, chromium and palladium across the path shown in Figure VII-16 is shown in Figure VII-17. All three determinations were done simultaneously. The sharp drop in iron concentration and sudden rise in palladium is probably the cladding edge. If so, then iron has migrated about 25 microns into the palladium, while chromium has only migrated 7 microns into the palladium. Palladium has apparently penetrated 2 to 3 microns into the cladding. However, the apparent palladium penetration could be an error due to the beam spreading in the sample. The chromium particle at 52 microns could not be found again and is apparently a single, small point. The low iron concentration on the cladding edge is due to rounding of the cladding edge. Other areas of palladium mounds on the cladding show less penetration of iron into the palladium. Protuberances of palladium up to 5 microns long extend into the cladding.

Conversion Program "MAINLN". - A computer program (MAINLN) has been developed to convert raw data on uranium and plutonium concentration to intensity ratios and to correct for instrumental drift, radiation, and sample background. This program makes automatic operation of the microprobe feasible for unattended data collection, along a single radius. It collects data on paper tape for computer processing. The output is a table of position and composition, and a plot of the composition of each element analyzed and the specimen current. Voids are indicated in the plots by increased specimen current and decreased fuel components.

5. EBR-II Test Fuel Characterization

M. C. J. Carlson and J. P. Keenen

a. PNL-6 Fuel Porosity Characterization

As a part of the fuel characterization for PNL-6 fuel (12213), 30 areas previously examined by the scanning electron microprobe on a section of a pellet from fuel batch MEE-63-4 were photographed in the scanning electron microscope. The diameters of the void intercepts shown were measured with a Zeiss particle analyzer. The true void size distribution for voids in the size range 0.375 to 4.3 microns was determined from the tabulated intercept frequencies by use of program LINEST (Ref 1). The photographs obtained during a previous microprobe examination were also

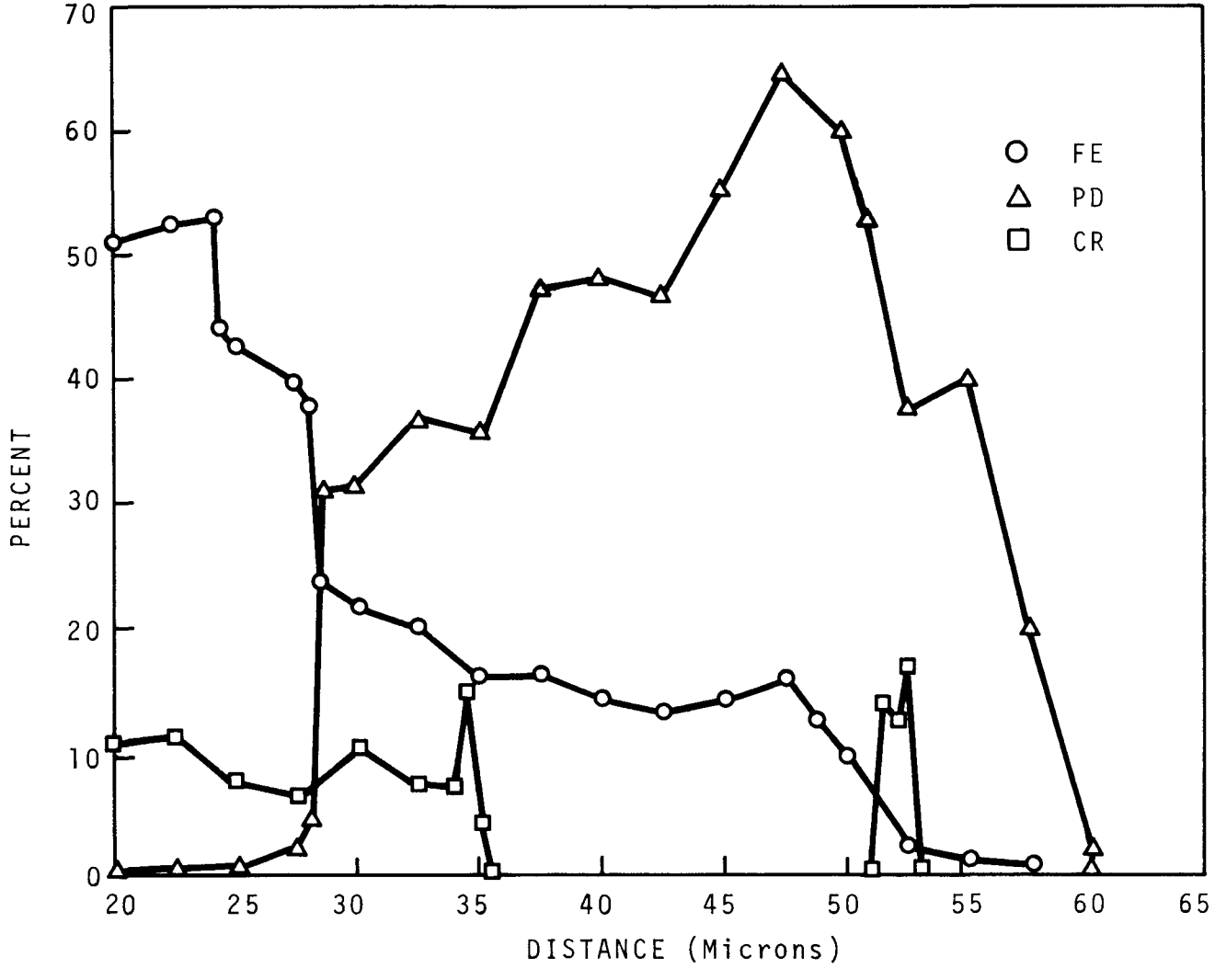

FIGURE VII-17 *Iron, Palladium and Chromium Concentration On A Line Across Cladding-Fission Product Interface Shown in Figure VII-16.*

analyzed by the same technique. The results of these analyses are shown on Figure VII-18. The solid line was obtained by using Computer Sciences Corporation's program ***POLFIT, which provides a least-squares fit of a polynomial of the form $Y = K_1 + K_2 x + K_3 x^2 \ldots$ of arbitrary order. The natural logarithm of the variables was taken prior to using ***POLFIT to provide more equal weighting for all of the data points. The expression shown in Figure VII-18, a third-order fit, was chosen by examining the coefficient of determination for polynomials up to the 10th order.

The increase in the coefficient of determination for expressions of order greater than three was very small and was generally achieved by introducing small "wiggles" in the smooth curve predicted by the lower order expressions as the higher order terms were used to attempt to follow individual data points.

It is anticipated that experimentally derived analytical expressions can be obtained for irradiated fuels using the techniques developed during the unirradiated fuel examinations. A program using this approach is being formulated for a fuel swelling study to be performed in cooperation with the Reactor Ceramics Section. A sample of an MEE-63-4 fuel pellet irradiated during FY-70 as a part of development work on a swelling capsule is now being examined to provide guidance in designing the fuel swelling program.

b. Microprobe Output Analysis Program "MITRAN"

A program, MITRAN, designed to provide automated tabulation of void intercepts and tabulation by size and concentration for regions of higher than nominal element concentrations has been completed by a CSC programmer.

Void intercept data output from MITRAN is provided both in written form and as punched cards in a format suitable for direct input to program PROBE (Ref 1) for conversion of the intercept counts to a "true" void size frequency distribution.

Data on regions of higher than average element concentrations is presented as tables listing the number of regions by size and peak concen-

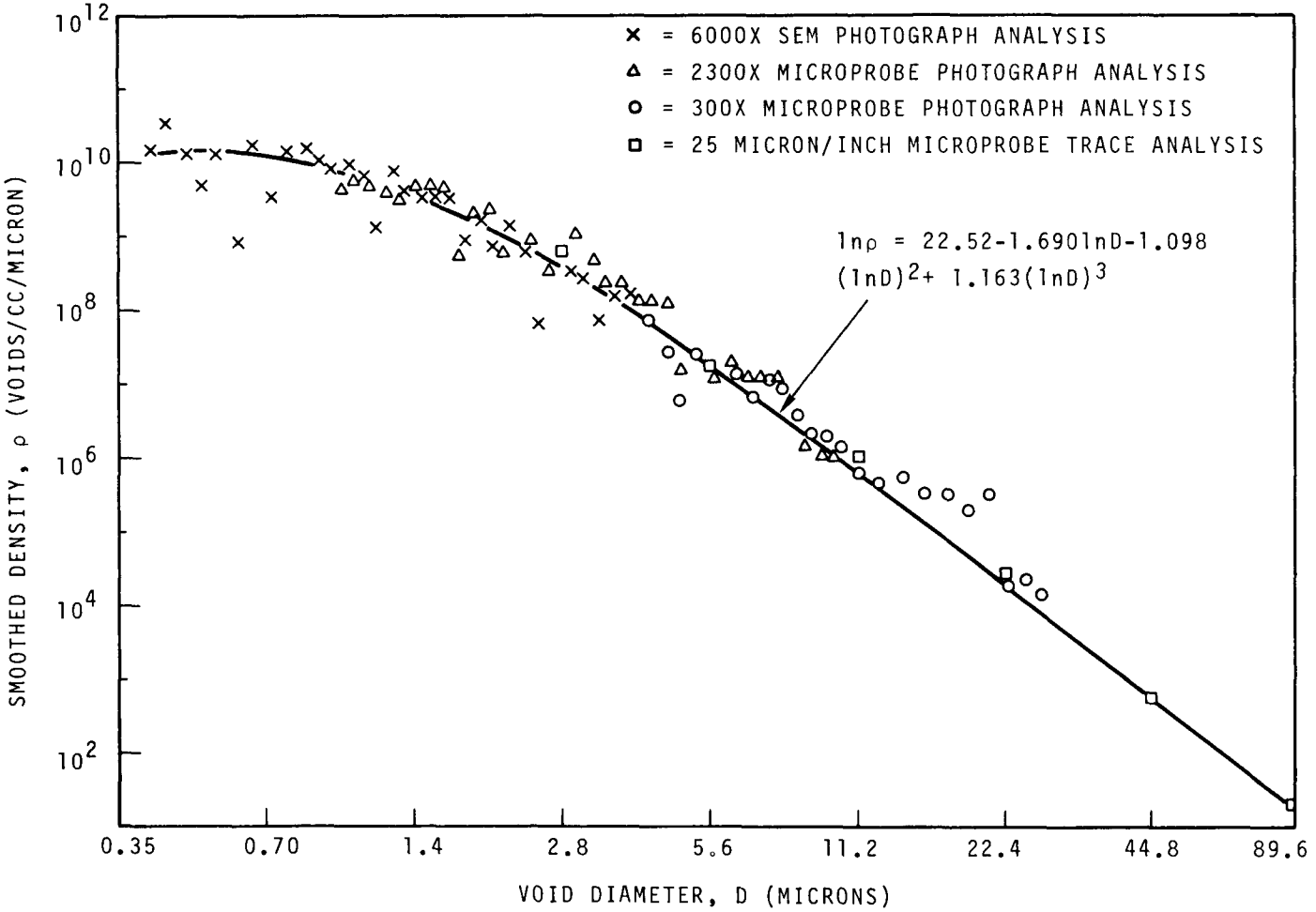

FIGURE VII-18 *Void Size Frequency Distribution For A HEDL- P-6, Batch MEE-63-4 Fuel Pellet.*

tration. Up to 16 arbitrarily chosen size ranges and up to 20 arbitrarily chosen composition ranges can be selected.

The program format is not specific to UO_2-PuO_2 material, but can be used equally well for other materials, such as B_4C, within the limits of sensitivity of the microprobe to composition changes in the material.

6. Fuel-clad Gap Heat Transfer in Fast Reactor Oxide Fuels

a. Experimental Measurements of Gap Conductance (12213)

L. A. Lawrence, G. R. Horn, J. A. Christensen and E. T. Weber

High heat fluxes and large fuel-clad gaps are characteristic of oxide, fast-reactor fuel pins. The resulting large temperature drops across the fuel-clad interface may decrease allowable heat rating 30 to 40% compared to pins with closely mating fuel and clad. Addditional data are needed for the accuracy required to reduce design conservatism. Measurements were made for eight UO_2 - 25 wt% PuO_2 fuel pins from capsules FP-34, FP-36 and FP-37. Test variables included heat rating, gap width (0.0025 in. and 0.011 in.) and fill gas composition. Various amounts of xenon were added to the fill gas, in the large gap pins, to simulate fission gas contamination of the initial helium bond. Fuel characteristics and test conditions are listed in Table VII-4. Fuel pins were irradiated under conditions that ensured thermal and structural steady-state, after which they were rapidly quenched to preserve structures representative of peak power operation.

Fuel-clad gap conductances were determined by matching observed fuel structures with temperature profiles calculated for the measured heat ratings. Accepted FTR design values for fuel thermal conductivity, grain growth temperatures, and melting point, were used in the calculations.

1) Summary of Results

Results for the change in gap coefficient (for pins with 0.011 in. gap) as a function of xenon content of the fill gas, using a nominal value of 25 kW/ft for heat generation rate, were consistent with results pre-

TABLE VII-4
FUEL AND TEST CHARACTERISTICS AND POST-IRRADIATION RESULTS

Pin	Preirradiation Fuel/Clad Gap (in.)	Preirridation Fill Gas	Time at Steady-State Power (hr.)	Q/L kw/ft	Outward Extent of Fuel Structural Feature as % of Fuel Radius[2]		
					R_1	R_2	R_3
1	0.0025 ± 0.0005	He	10	31.1	16.3	25.2	65.0
2	0.0025 ± 0.005	He	10	34.7	25.2	42.0	72.2
3	0.0025 ± 0.005	He	10	35.5	31.2	39.4	72.5
4	0.0025 ± 0.005	He	10	36.4	32.5	47.2	76.0
5	0.0111 ± 0.005	He	100	25.0	0	0	68.9
6	0.0117 ± 0.005	59%He-41%Xe	100	25.0	0	0	69.7
7	0.0116 ± 0.005	24%He-76%Xe	100	25.0	17.2	23.8	75.4
8	0.0113 ± 0.005	Xe	100	25.0	41.0	49.2	83.6

Notes:
1. Fuel consisted of cold pressed and sintered pellets -- UO_2 - 25 wt % PuO_2-95% theoretical density - oxygen/metal 1.96 ± 0.01 - Pu ^{239}/Pu 87%; Pu ^{240}/Pu 11%; U^{235}/U normal - Clad 304 L SS.
2. Values are avg. of 12 equally spaced measurements on the circumference
3. R_1 = Inner boundary pore-free zone
   R_2 = Outer boundary pore-free zone
   R_3 = Columnar grains; assumed 1800° isotherm
   R_1 and R_2 min and max, respectively, of fuel melting at steady-state - melting temp 2750°C
4. Rate of power increase during charging - 60 %/hr
   Rate of power decrease during discharge - 3%/sec

viously reported (Ref 2--Figure VII-19). Values calculated for the 0.0025-in. gap pins using the nominal values for heat generation rates are consistently higher than those reported in the literature (Refs 3 through 6) (Figure VII-20). These differences reflect inconsistencies in structure - temperature associations among the various sets of data and also the inherently low precision of gap conductance values inferred from fuel structures.

2) Experimental Methods and Evaluation of Results

Post-irradiation radiochemical burnup results were obtained for all eight pins using Zr^{95}, Ba-La^{140}, and Ce^{141} determinations. For Pins 1 through 4, additional data were obtained from in-pile calorimetry, using thermocouples positioned at two different radii in the capsule's thick aluminum sleeve. See the table below. The uncertainties quoted correspond to one standard deviation from the mean of the individual values (a 68% confidence level for a normal distribution).

Pin	Heat Generation Rate, kW/ft
1*	31.1 $\pm$ 1.1*
2	34.7 $\pm$ 2.3
3	35.5 $\pm$ 2.7
4	36.4 $\pm$ 2.8

* One of the thermocouples failed during irradiation; the results reflect only the burnup data.

Pins 5 through 8 were all from the same capsule, FP-37. This capsule design did not have thermocouples in the aluminum sleeves, but thermocouples were located in the four coolant annuli to monitor increases in coolant temperature. Assuming an equal flow split between the four coolant channels, heat generation rates were calculated to range from 19 to 33 kW/ft, with an average value of 27 kW/ft. Heat generation rates for Pins 5 through 8 obtained from burnup, assuming all the pins operated at the same flux density, were 25.0 $\pm$ 1.0 kW/ft. The uncertainty corresponds to one standard deviation from the mean.

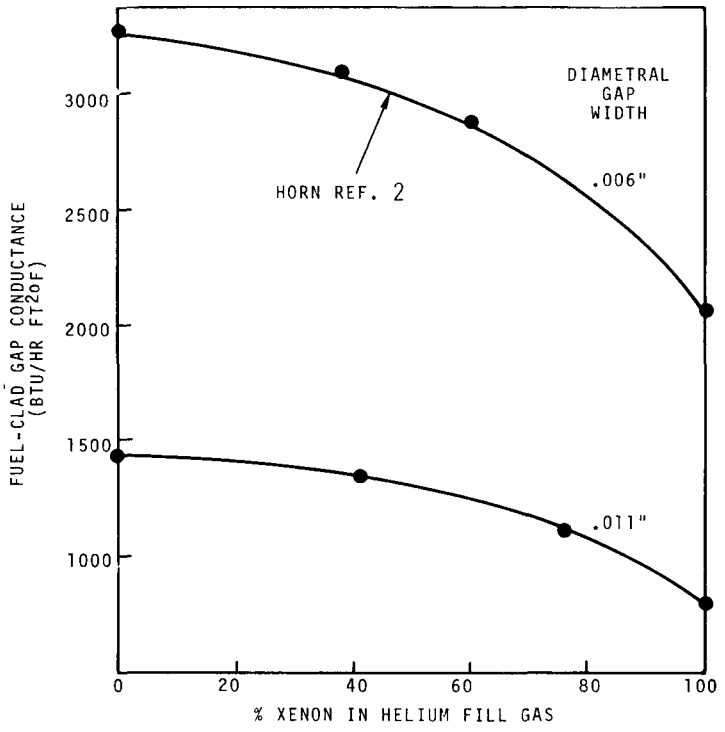

FIGURE VII-19 *Effect of Xenon On Fuel-Clad Gap Conductance.*

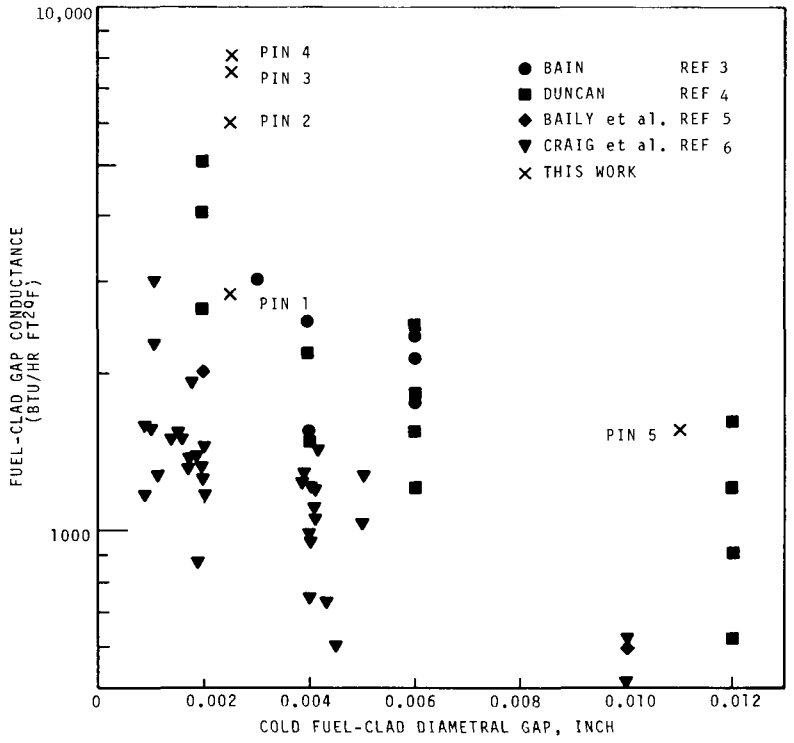

FIGURE VII-20 *Fuel-Clad Gap Conductance As A Function of Cold Diametral Gap.*

Heat generation rates for the eight pins were calculated using the THERMOS code to be:

Pins 1, 2, 3, 4 - Q/L = 33 to 36 kW/ft

Pins 5, 6, 7, 8 - Q/L = 24 to 27 kW/ft

Calculations to include the errors introduced into the values of gap conductance because of uncertainties in heat generation rate and fuel thermal conductivity have been completed. Additional calculations to consider uncertainties in temperature and location of the microstructural feature fuel flux depression data, clad thermal conductivity, and coolant temperature are in progress. The differences in gap conductance calculated by the thermal conductivity equation used by G.E. (Ref 7) or the equation in the SINTER program (Ref 8) as compared to values calculated with the WARD design equation are on the order of 5%. Varying the heat generation rates over the ranges suggested by the data produced very large changes in calculated gap conductances (Table VII-5). Table VII-5 also includes the values predicted using the two microstructural features that are associated with fuel melting. The high apparent gap conductance (some greater than 25,000 Btu/hr-ft^2°F) reflects the fact that for small gaps and their associated small DT's, small variations in factors used in deriving an experimental value result in large variations in the values of the gap conductance. These large values of gap conductance calculated for small diametral gap widths are consistent with those predicted from the Ross and Stoute Model in the GAPCON (Ref 9) program.

3) Tests in Progress

Closure of the fuel-clad gap has been observed and is anticipated early-in-life for FTR fuel pins. Three capsules are planned to study the rate of gap closure and associated change in ΔT across the fuel-clad gap as a basis for specifying reactor startup schedules. The first of two noninstrumented capsules (FP-37) was successfully irradiated for 100 hours (Ref 10). Postirradiation examination included measurement of residual fuel-clad gap. Results show for the 0.011-in. gap approximately

TABLE VII-5
CALCULATED GAP CONDUCTANCE

Pin	Heat Generation Rate, kW/ft	Gap Conductance Btu/hr/ft^2/°F			
		R_1	R_2	$\frac{R_1 \& R_2}{2}$	R_3
1	29	1,750	1,600	1,675	4,600
	31	2,950	2,500	2,700	14,000
	33	6,100	4,675	5,375	>25,000
2	33	4,625	2,550	3,550	7,900
	35	16,250	4,425	7,900	>25,000
	37	>25,000	12,150	>25,000	>25,000
3	33	3,850	2,800	3,350	7,300
	35	9,850	5,250	7,250	>25,000
	37	>25,000	20,000	>25,000	>25,000
	39	>25,000	>25,000	>25,000	>25,000
4	33	3,650	2,100	2,750	4,250
	35	8,850	3,350	5,000	7,750
	37	>25,000	6,600	18,000	>25,000
	39	>25,000	>25,000	>25,000	>25,000
5	23	-	-	-	1,070
	25	-	-	-	1,410
	27	-	-	-	1,950
6	23	-	-	-	1,040
	25	-	-	-	1,360
	27	-	-	-	1,880
7	23	630	600	610	860
	25	840	795	820	1,080
	27	1,150	1,080	1,110	1,420
8	23	520	490	500	650
	25	675	640	600	780
	27	890	780	840	950

* R_1, R_2, R_3 defined in Table VII-4

a 50% decrease in gap width even though the fuel pins operated for only 100 hours. The decrease in gap width is equivalent to that calculated, assuming irreversible thermal expansion of the fuel.

A recently derived model, which predicts fuel-clad gap closure arising from radial crack ratcheting of the fuel, indicates that the rate of gap closure is directly related to the number of thermal cycles. The second noninstrumented capsule (FP-33) has been assembled and is scheduled for irradiation in October 1970. The capsule will be irradiated in exactly the same manner as FP-37, except it will experience five carefully controlled, evenly spaced, thermal cycles.

Closure of the fuel-clad gap during irradiation results in a lowering of the fuel center temperature. The third capsule (FP-316) is designed to monitor fuel center temperatures during irradiation using refractory metal thermocouples. Capsule hardware has been fabricated and the WADCO Special Products Fabrication Section has made a batch of cored fuel pellets (Figure VII-21). One fuel pin has been loaded and successfully shrink-fitted into the aluminum sleeve. Two pins with 0.002-in. gaps and two pins with 0.011-in. diametral gaps will be placed in a flow basket. Calculations indicate that during irradiation the fuel with the 0.002-in. gap will be in contact with the cladding, and any change in fuel center temperature of the pins with the 0.011-in. gap, as compared to the 0.002-in. gap pins, will indicate closure. In addition, the data obtained with Chromel-alumel thermocouples positioned in the aluminum sleeve, combined with fuel center temperature measurements, will provide an absolute value for fuel-clad gap conductance.

b. Digital Computer Prediction of Fuel-to-Cladding Heat Transfer Coefficients (12213)

G. R. Horn, F. E. Panisko, L. J. Parchen and E. T. Weber

The preliminary version of a computer program (GAPCON) for predicting fuel-to-cladding heat transfer coefficients in operating ceramic fuel elements has been completed. The program will also predict gap conductances as a function of time in-reactor (burnup) taking into account calculated

FIGURE VII-21 *Capsule FP-316 Pin Prior to Assembly*

changes in fill gas composition (due to fission gas buildup) and fuel swelling.

Gap conductances are calculated using the model proposed by Ross & Stoute. As shown in the simplified flow sheet in Figure VII-22, the calculation is an interative process, wherein a gap conductance is assumed, temperature profiles are calculated, thermal expansion of the pellet is calculated, and the hot gap (or fuel-cladding interface pressure) is determined. Knowing the latter, gap conductance is calculated by the Ross & Stoute method and the calculated value compared to the assumed value. This process is continued until the calculated and assumed values agree.

Several calculations have been made with the program to compare predicted values to those measured at various sites. The preliminary comparisons indicate good agreement between predicted and measured values. Results of these preliminary calculations are shown in Figures VII-23, VII-24 and VII-25. Figure VII-24 is particularly interesting, because it shows a significant increase in gap conductance with increasing linear heat rating. This increase is due primarily to the effect of increased thermal expansion with increase in power rating. The result, as shown in Figure VII-25, is that GAPCON predicts that the temperature drop across the gap is essentially independent of linear heat rating over the range of heat ratings of interest in the FTR.

Several improvements to the program are being made prior to final documentation. The most important of these improvements is a provision for restructuring the fuel. It is anticipated that the addition of this feature will cause the predicted values shown in Figure VII-22 to be somewhat lower.

c. Hybrid Computer Prediction of Gap Conductance

R. D. Leggett, R. B. Baker, L. E. Addison, D. S. Dutt
J. D. Lodge and R. A. Harvey

A study (12163-FPE) was made of fast-flux irradiated, mixed oxide

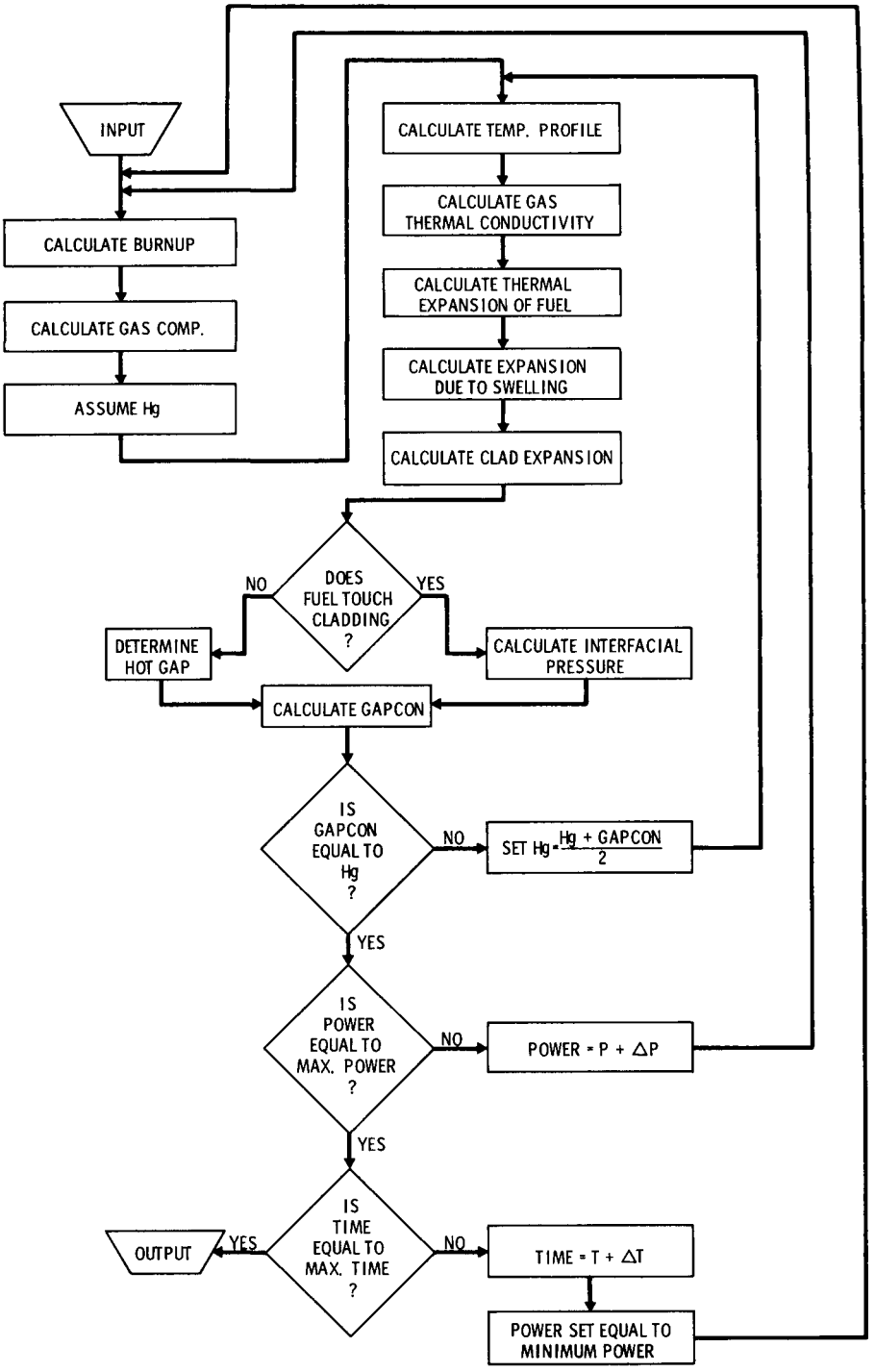

FIGURE VII-22 *Simplified Flow Diagram for Calculating Gap Conductance*

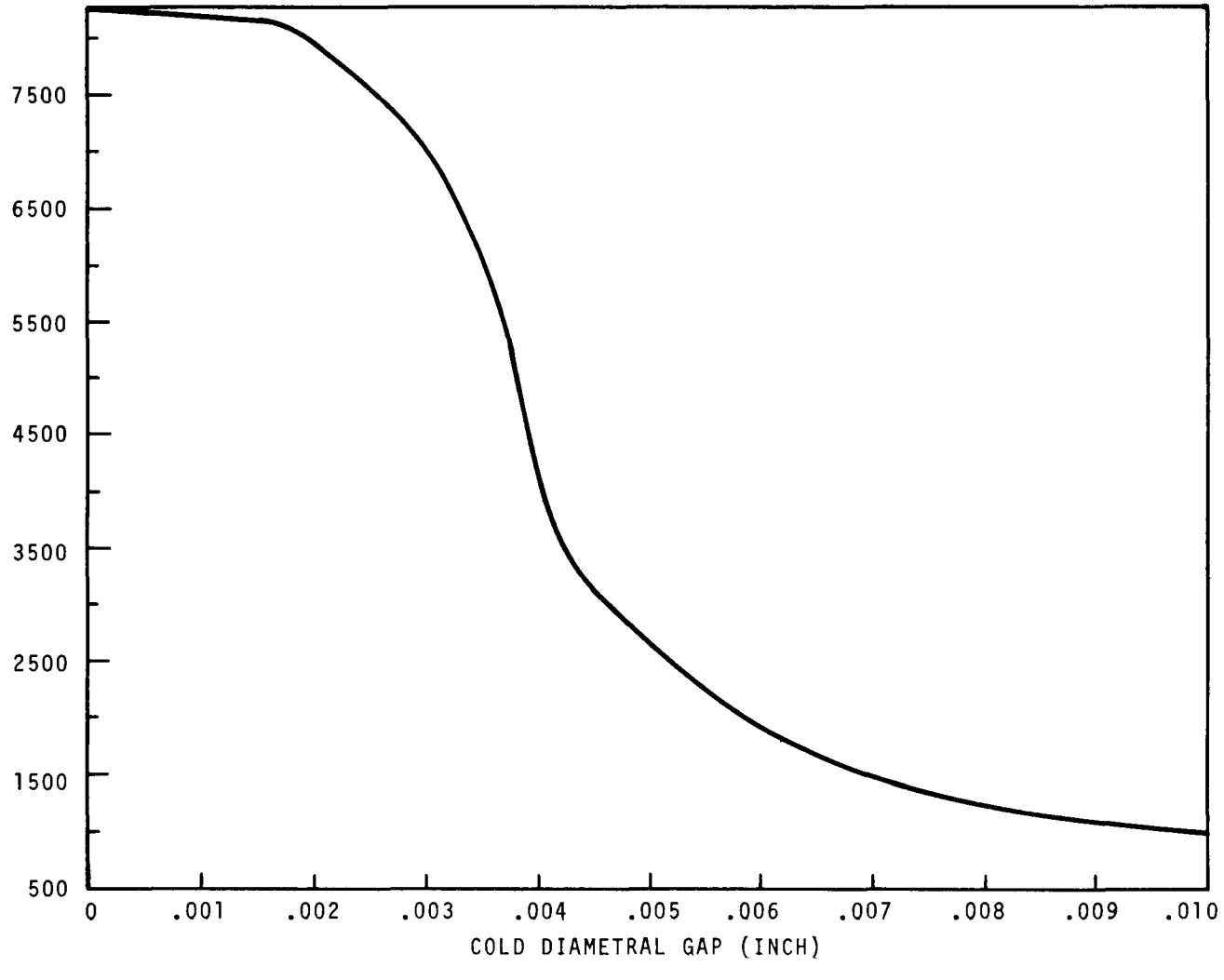

FIGURE VII-23 *Gap Conductance vs Cold Diametral Gap*

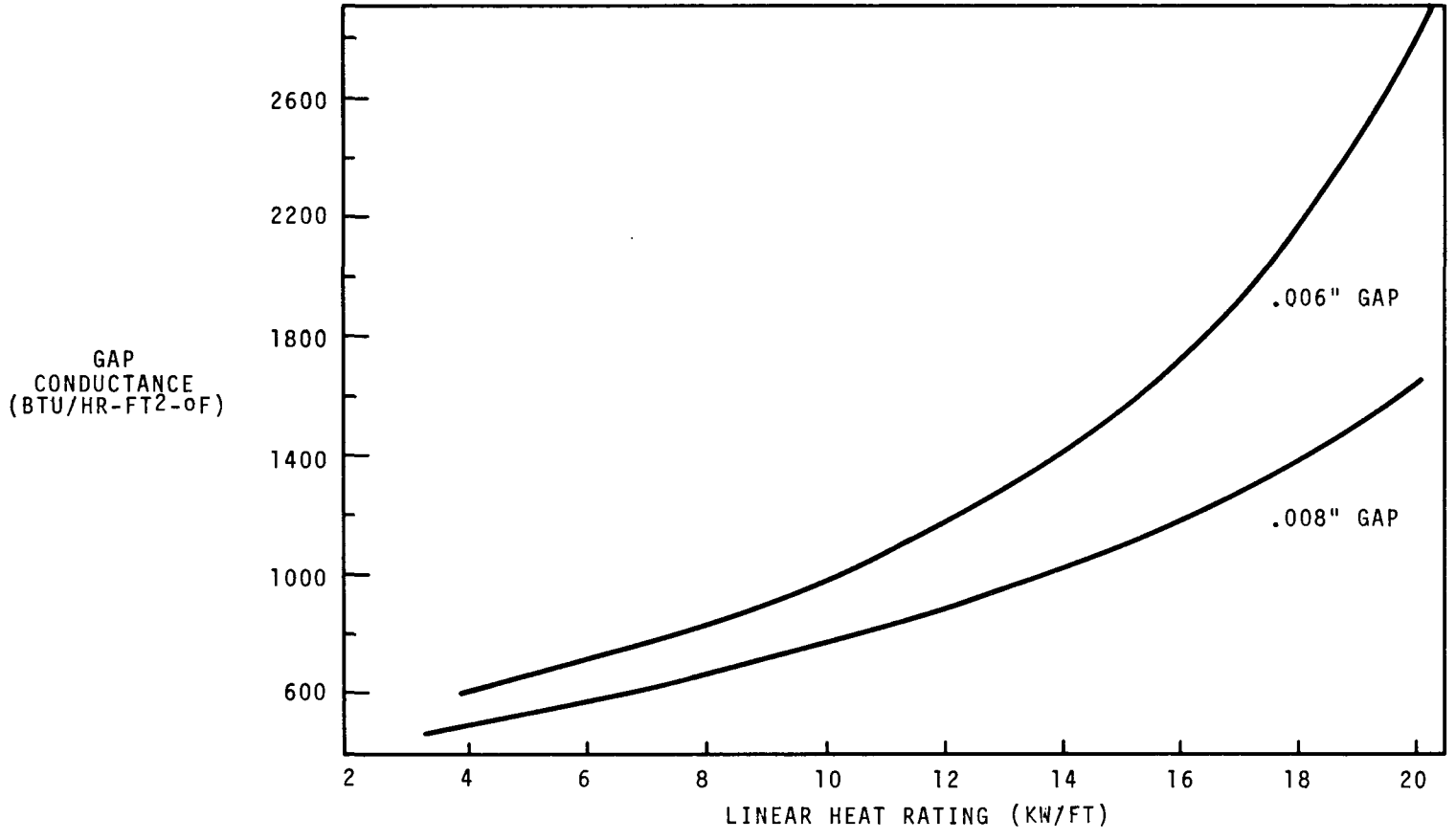

FIGURE VII-24 *Increase In Gap Conductance With Increase In Linear Heat Rating*

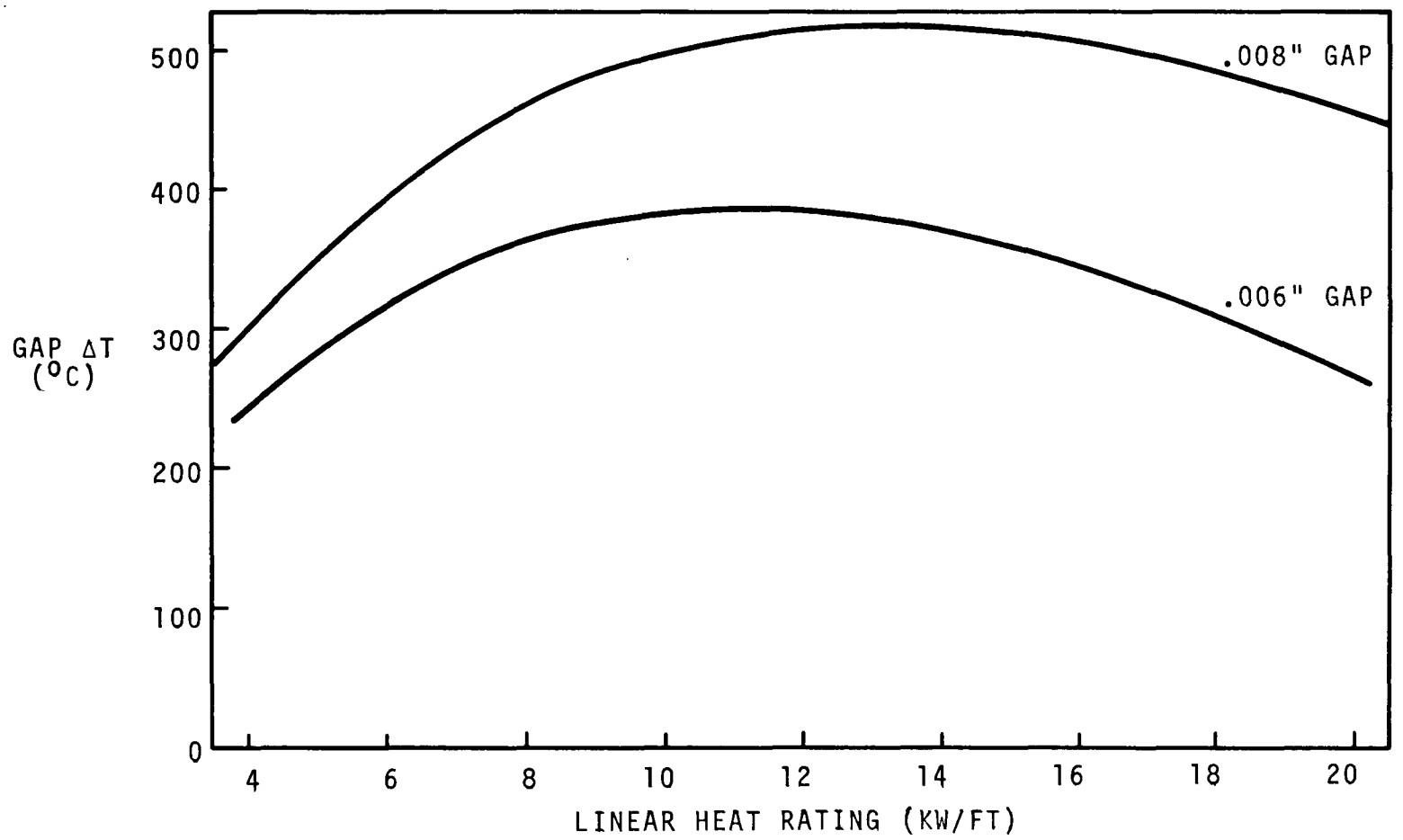

FIGURE VII-25 *Gap ΔT vs Linear Heat Rating for 0.008-in. and 0.006-in. Gaps.*

(75% UO_2 - 25% PuO_2) fuel microstructures to determine fuel-cladding gap conductance. The principal technique used in this analysis was structure matching with the Hybrid Computer (Ref 11). Sections of PNL-1 pins (Ref 12) and GE/BRDO Series F-1 and F-2 (Ref 13) pins provided the bulk of the data analyzed. A few GE/BRDO Series F-6 and F-8 pins and Rapsodie fuel data (Refs 14,15,16) were also included.

1) Summary of Results

Figures VII-26 and VII-27 depict the exponential relationships derived between gap conductance, power to melt and cold gap for T_{CG}= 1700 °C (data points are shown). For design conservation, we selected the T_{CG}= 1700 °C curve for nominal values and the 1800 °C curve for the lower limit of gap conductance. For these data, gap conductance and power to melt tend to decrease with increasing gap size. The extent of the decrease, however, may be somewhat misleading, since all of the large gap data were obtained from fuel that operated at relatively low power. If all of the fuel had operated at high power, curves of the type shown in Figures VII-26 and VII-27 would be expected to be much flatter.

2) Discussion

Table VII-6 summarizes the physical characteristics of the pins, the estimated operating conditions, the structure radii, and the results of the Hybrid Computer analysis assuming 1700°C as the temperature for the initiation of columnar grain formation. In each case, the steady-state operating power reported is that calculated from reactor physics data. In our previous work (Ref 11) time-averaged linear heat ratings based on burnup analyses were used. However, recent data obtained with an instrumented mixed oxide subassembly (PNL-17) in EBR-II have shown (Ref 17) that the physics estimate of fission rate in EBR-II (Ref 18) is very nearly correct and should be used to calculate pin power.

A structure match was obtained by assigning a value (1600, 1700 or 1800 °C) to the temperature for the formation of columnar grains, T_{CG}, and varying gap conductance, hg, density of columnar grains, and temperature

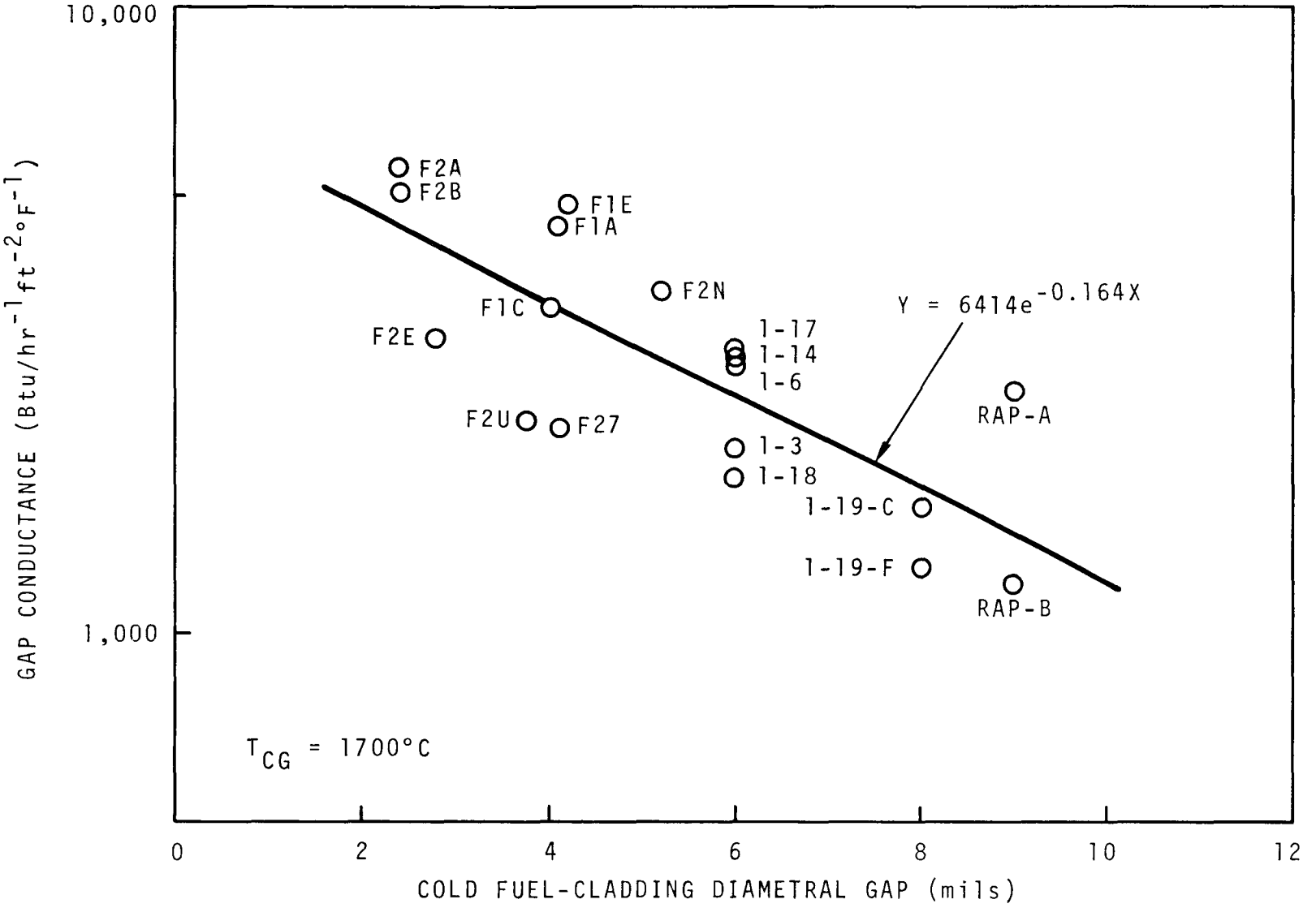

FIGURE VII-26 *Gap Conductance as a Function of Cold Fuel Cladding Diametral Gap for a Columnar Grain Growth Temperature of 1700°C.*

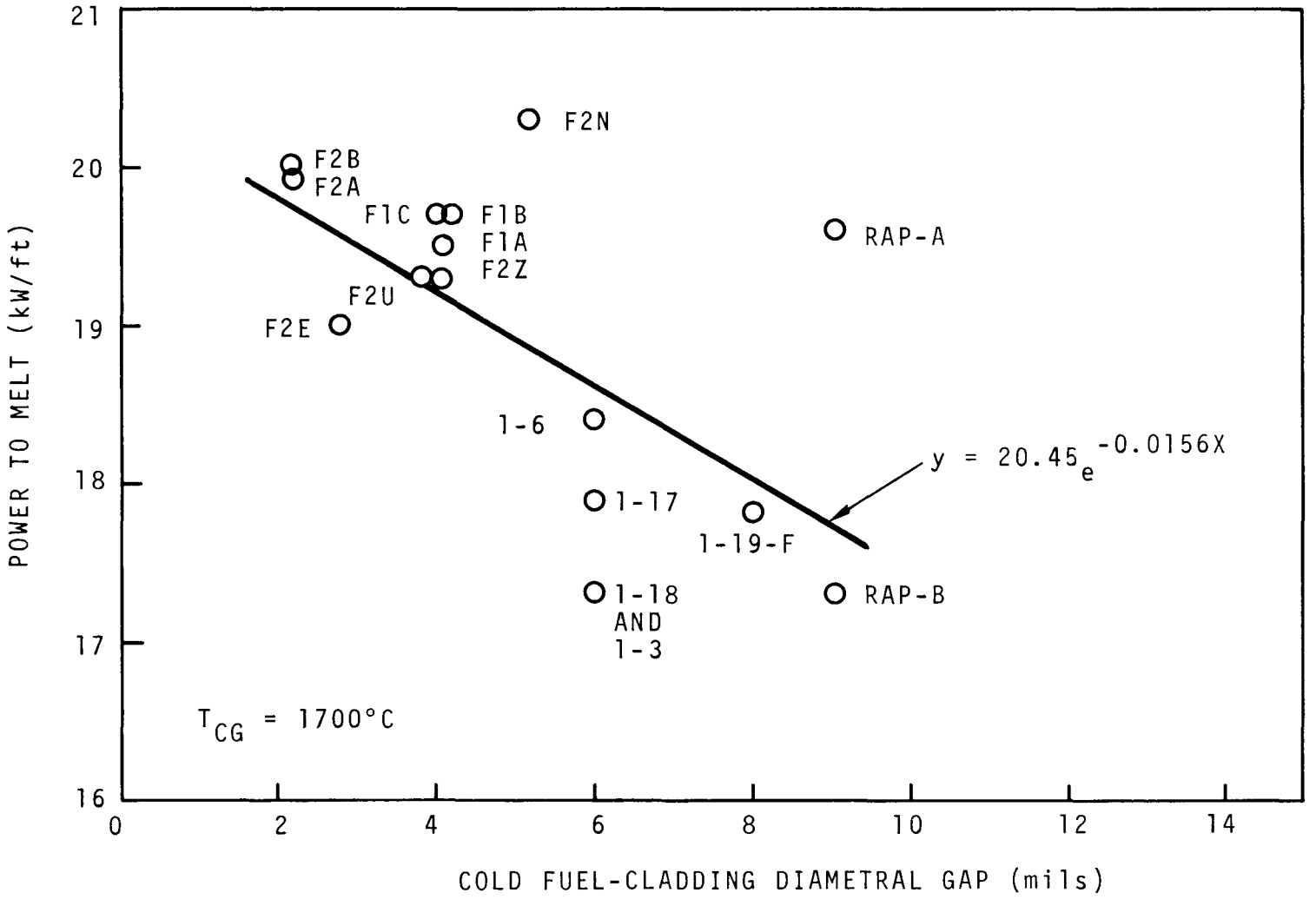

FIGURE VII-27 *Power to Melt Fuel as a Function of Cold Fuel-Cladding Diametral Gap for a Columnar Grain Growth Temperature of 1700°C.*

TABLE VII-6
SUMMARY OF HYBRID ANALYSIS

Pin	Clad OD (in.)	Clad ID (in.)	Cold Fuel To Clad Gap Start (diam) (in.)	Fuel Diam. (in.)	Fabri-cated Density (% TD)	Steady State Power, (kW/ft)	Structure at Cross Section with this Power (radii)			Gap Conduct. to Match Columnar G. G. Temp of 1700 °C (Btu/ft²-hr-°F)	Power to Melt (1700 °C Columnar G.G. Temp), (kW/ft)	Columnar Density Needed to Match Structure, (% TD)	Fuel Form
							Equiaxed G.G. (in.)	Columnar G.G. (in.)	Central Void, (in.)				
PNL-1-3	0.250	0.211	0.006	0.212	93.06	10.94	0.0659	0.0415	0.005	1980	17.3	94.50	SP
1-6	0.250	0.211	0.006	0.212	89.49	10.49	0.0587	0.0370	0.0077	3300	18.4	93.65	SP
1-14	0.238	0.211	0.006	0.212	90.19	10.30	0.0475	0.0244	0.00	3900	17.5	- - -	SP
1-15	0.238	0.211	0.006	0.212	94.92	10.49	0.0679	0.000	0.0265	1190	18.8	- - -	AP
1-16	0.238	0.211	0.006	0.212	90.10	9.85	0.0521	0.000	0.0265	1970	20.9	- - -	AP
1-17	0.238	0.211	0.006	0.212	90.00	10.66	0.0544	0.0366	0.0051	3200	17.9	91.9	SP
1-18	0.238	0.211	0.006	0.212	90.14	10.81	0.082	0.0498	0.0095	1780	17.3	93.52	SP
1-19	0.238	0.211	0.008	0.210	90.14	10.73	0.0763	0.0563	0.0175	1285	17.8	>99.9(1)	SP
1-19	0.238	0.211	0.008	0.210	90.14	10.31	0.0650	0.0431	0.0104	1626	17.5	95.91	SP
GE-F1A	0.2488	0.2213	0.0041	0.2162	94.1	15.37	0.0920	0.0656	0.0085	4400	19.5	96.0	SP
F1C	0.251C	0.2213	0.0040	0.2163	96.1	16.07	0.0920	0.0673	0.0089	3500	19.7	97.8	SP
F1E	0.2492	0.2213	0.0042	0.0042	90.1	13.66	- - -	0.0636	0.0154	4800	19.7	95.93	SP
F1F	0.2524	0.2213	Vipac	0.2203	85.3	15.52	0.885	0.0741	0.0219	>5500(1)	19.3	93.5	VP
F2A	0.2510	0.2214	0.0022	0.2182	95.7	16.38	0.0823	0.0598	0.0055	>5500(1)	19.9	96.5	SP
F2B	0.2496	0.2213	0.0022	0.2181	96.8	16.37	0.0821	0.0630	0.0028	5100	20.0	97.0	SP
F2E	0.2510	0.2210	0.0028	0.2182	96.7	15.90	0.0850	0.0666	0.0030	2900	19.0	96.9	SP
F2N	0.2410	0.2205	0.0052	0.2153	97.3	16.54	0.0887	0.0660	0.0153	3300	20.3	>99.9(1)	SP
F2S	0.2808	0.2300	0.0008	0.2192	98.2	16.26	0.0839	0.0735	0.0054	2100	18.2	98.9	SP
F2U	0.2509	0.2302	0.0038	0.2164	89.7	13.75	0.0899	0.0717	0.0235	2200	19.4	>99.9(1)	SP
F2W	0.2505	0.2200	Vipac	0.2200	83.8	14.91	0.0930	0.0752	0.0236	>5500(1)	19.6	92.9	VP
F2Y	0.2407	0.2210	Vipac	0.2200	83.9	14.99	0.0914	0.0741	0.0261	>5500(1)	20.4	95.8	VP
F2Z	0.2501	0.2203	0.0041	0.2162	90.2	13.80	0.0909	0.0706	0.0230	2273	19.3	>99.9(1)	SP
F8A	0.2523	0.2203	0.0038	0.2165	90.18	10.	0.042	0.00	0.000	>5500(1)	20.2	- - -	SP
F8C	0.2495	0.2202	0.0034	0.2168	89.48	10.	0.042	0.00	0.000	>5500(1)	20.3	- - -	SP
F8E	0.2505	0.2201	0.0037	0.2164	89.87	10.	0.042	0.00	0.000	>5500(1)	20.3	- - -	SP
Rapsodie	0.264	0.228	0.009	0.219	94.80	11.5	- - -	0.0325	0.0065	2457	19.60	98.89	SP
Rapsodie	0.264	0.228	0.009	0.219	94.80	10.	- - -	0.0325	0.0065	1185	17.26	98.89	SP

(1) Upper Limit of Hybrid Settings

for the formation of equiaxed grains, T_{EG}. By varying the density of columnar grains, the extent of sintering required to account for the formation of a central void (when present) was obtained. T_{EG} was determined for each structure match, but this information was not used in the statistical treatment of the data to evaluate gap conductance.

The power required to produce melting in those pins containing a center void was estimated. A structure match was made for T_{CG} = 1600, 1700 and 1800 °C, yielding sintering conditions and hg. Using these values, and adjusting the cladding OD temperature to 900 °F, the power simulation was increased until the initiated maximum fuel temperature reached 5000 °F (the assumed melting point for 25 wt% PuO_2 - 75 wt% UO_2). This extrapolation is probably conservative for pins irradiated at low power (∿10 kW/ft), since it would be expected that both sintering and gap conductance would be enhanced as the power is increased. The extrapolation should be fairly reliable for pins that operate at 15 to 16 kW/ft.

All of the thermal analysis data were subjected to curve-fitting routines for gap conductance and linear-power-to-melting versus initial, cold, diametral fuel-cladding gap. Table VII-7 summarizes the data used. First-, second-, and third-order polynomials and an exponential relationship were obtained.

TABLE VII-7
SUMMARY OF DATA USED FOR CURVE FITTING

Sample Number	Gap Size (Mils)	T_{CG} = 1600°C		T_{CG} = 1700°C		T_{CG} = 1800°C	
		h_G*	P_{melt}**	h_G*	P_{melt}**	h_G*	P_{melt}**
F2B	2.2	10,000	20.7	5060	20.0	3050	19.1
F2A	2.2	9990	20.6	5500	19.9	3400	19.9
F2E	2.8	5350	20.0	2960	19.0	2350	18.3
F2U	3.8	2930	- - -	2200	19.4	1550	- - -
F1C	4.0	4500	20.8	3480	19.7	2500	18.8
F1A	4.1	6000	20.4	4430	19.5	2700	18.6
F2Z	4.1	3350	20.8	2270	19.3	1600	18.1
F1E	4.2	10,000	20.5	4810	19.7	2750	18.5
F2N	5.2	5900	21.4	3350	20.3	2280	19.3
PNL-1-18	6	2240	18.3	1780	17.3	1300	16.3
1-17	6	3600	19.0	2790	17.9	2010	17.0
1-14	6	3400	- - -	2760	- - -	2120	- - -
1-6	6	3450	19.6	2700	18.4	2000	17.3
1-3	6	2470	18.4	1930	17.3	1380	16.4
1-19-F	8	1710	19.2	1270	17.8	1000	16.6
1-19-C	8	2200	- - -	1600	- - -	1200	- - -
RAP-A	9	3100	20.8	2400	19.6	1650	18.4
RAP-B	9	1630	18.5	1200	17.3	1000	16.1

*h_G = Gap Conductance (BTU/hr/ft^2/°F

**P_{melt} = Power to Melt (kw/ft)

References

1. Nicholson, W. L. and Merckx, K. R., "Unfolding Particle Size Distribution," Technometrics, Vol. 11, No. 4, pp. 707-723, 1969.

2. Horn, G. R., "The Effects of Xenon on Fuel-to-Cladding Gap Conductivity," Trans. ANS, Vol. 23, No. 2 p. 607, November 1969.

3. Bain, A. S., "Microscopic, Autoradiographic, and Fuel/Sheath Heat Transfer Studies on UO_2 Elements," AECL-2588, June 1966

4. Duncan, Robert N., "CVTR Fuel Capsule Irradiations," CVNA-153, August 1962.

5. Baily, W. E., et al., "Effects of Diametral Gap Size on the In-Pile Performance of Fast Reactor Ceramic Mixed-Oxide Fuel," Trans. ANS, Vol. 9, No. 1, p. 40, June 1966.

6. Craig, C. N., et al., "Heat Transfer Coefficients Between Fuel and Cladding in Oxide Fuel Rods," GEAP-5748, January 1969.

7. Baily, W. E., Aitken, E. A., Asamato, R. R., Craig, C. N., "Thermal Conductivity of Uranium-Plutonium Oxide Fuels," Proceedings of 1967 Nuclear Metallurgy Symposium, Scottsdale, Arizona, October 1967.

8. Merckx, K. R., Fox, G. L., "Sinter-A Program for Calculating Radial Temperature Distributions in Oxide Fuel Pins Undergoing Sintering," BNWL-1241, Pacific Northwest Laboratory, Richland, Washington, January 1970.

9. Horn, G. R., Unpublished Data, Hanford Engineering Development Laboratory, Richland, Washington, September 1970.

10. Sheely, W. F. (Ed.), "Reactor Fuels and Materials Development Program for Fuels and Materials Branch of USAEC Division of Reactor Development and Technology," BNWL-1349-2, Quarterly Progress Report, April, May, June, 1970.

11. Leggett, R. D., Ballard, E. O. and Cole, C. R. "Simulating the Performance of Mixed Oxide Fuels with the Hybrid Computer," ACS 72nd Annual Meeting, May 2-7, 1970, Philadelphia, Pa.

12. Hanson, J. E. "Experiment Description and Hazards Evaluation for the Pacific Northwest Laboratory Mixed Oxide (UO_2-PuO_2) Irradiations in EBR-II, Task A, Subtask 1 Irradiations," BNWL-650, July 1968.

References (Cont'd)

13. Craig, C. N., Hull, G. R., and Bailey, W. E. "Heat Transfer Coefficients Between Fuel and Cladding in Oxide Fuel Rods," GEAP-5748, January 1969.

14. Claudson, T. T., Peterson, R. E., and Hanson, J. E. "Trip Report U.S. FFTF Fuels and Materials Team Trip to the United Kingdom and France," BNWL-569, December 1967.

15. Sebilleau, F. "Fuel Considerations," ANS Winter Meeting, Washington, D. C., November 1968.

16. Anselin, F., Mas, R. G., and Mustilier, J. P. "Irradiation Behavior of Plutonium Mixed Oxide Driver Fuel of Rapsodie," ANS Winter Meeting, Washington, D. C., November 1968.

17. Millhollen, M. K. and Sutey, A. M. "Subchannel Coolant Temperatures of EBR-II Instrumented Subassembly PNL-17," (XX02) Submitted for ANS Winter Meeting, Washington, D. C., 1970.

18. Guide for Irradiation Experiments in EBR-II, Rev. 3., Argonne National Laboratory, Argonne, Illinois, July 1969.

19. Manson, S. S., "A Simple Method for Estimating High Temperature Low-Cycle Fatigue." High Temperature Low-Cycle Fatigue, Edited by W. H. Tuppeny, Jr., Society for Experimental Stress Analysis, May 1967.

20. Vogel, R. C., et al Chemical Engineering Division Research Highlights, January-December 1969. Argonne National Laboratory, ANL 7650, p. 26.

B. PROPERTIES AND BEHAVIOR OF MIXED OXIDE FUEL MATERIALS

1. Properties of Molten Fast Reactor Oxides

O. D. Slagle, E. T. Weber, and J. A. Christensen

A program (12212) is in progress to measure several physical properties of molten uranium-plutonium oxide that relate to the mechanical design and safety of LMFBR fuels. The properties of interest are density, surface tension, viscosity and compressibility. The equipment has been assembled and initial results on UO_2 have been obtained.

Figure VII-28 is a plot of the velocity of sound in UO_2 versus $T^{1/2}$ with a least-squares line fit to the data. Assuming a temperature uncertainty of $\pm$ 10°C, the line falls within the expected range of experimental error. The equation for UO_2 obtained for the line in Figure VII-28 is

$$v = 5.268 \times 10^5 - 6.198 \times 10^3 \, T^{1/2} \text{ (cm/sec)}$$

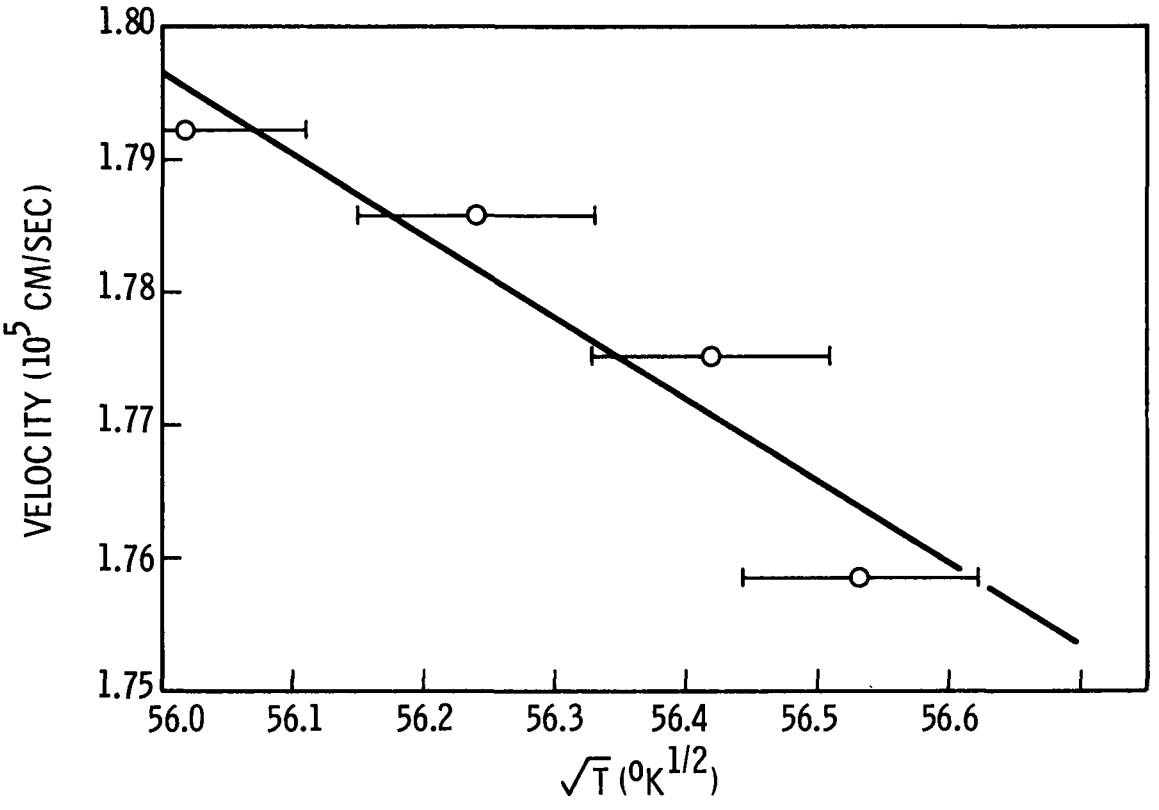

FIGURE VII-28 *Velocity of Sound vs $T^{1/2}$ For Molten UO_2.*

Although the line falls within experimental error, the short temperature range over which the data were taken limits its usefulness for extrapolation to higher temperatures.

Measurements of viscosity and compressibility have been carried out on CaF_2 to serve as a check on the apparatus, and also to aid in interpreting the results of the mixed-oxides. Calcium-fluoride and UO_2 have the same cyrstal structures in the solid form because of their similar ratio of anion to cation radii. Therefore, it can be expected that the liquid structures will be similar. If this is so, one can further hypothesize that the temperature-dependences of viscosity and compressibility will be similar. This may be useful in analyzing the results on UO_2,since high melting point and the temperature limitations of the furnace place restrictions on the temperature range over which data can be obtained.

Measurements of the period and decay constant for CaF_2, using the oscillating cup viscometer (Refs 21,22) were carried out in the temperature range from 1780 to 2290°K. The sample was contained in a tungsten crucible with ID of 1.1 cm and height of 6.54 cm. The viscosities were calculated by two ways; one method used a program similar to the one used by Finucane (Ref 21) which makes use of an approximation given earlier by Roscoe (Ref 23). The other used the curve given by Wittenburg, et al (Ref 22) which was calculated from a different expression. Results from the two methods are in close agreement.

Figure VII-29 presents the calculated values of viscosity versus temperature. Data were taken while increasing and decreasing temperature; in general, there is good agreement between values. These measurements will be repeated and extended to higher temperatures to test the reproducibility of the results and ascertain if there is anomalous behavior.

Measurements of the velocity of sound in molten CaF_2 were made using the phase comparison technique (Ref 24) and tungsten crucible similar to the one used in the previous molten UO_2 results (Ref 25). Figure VII-30 gives the resulting values of velocity and compressibility versus temperatures. Data were taken both during increasing and decreasing temperature

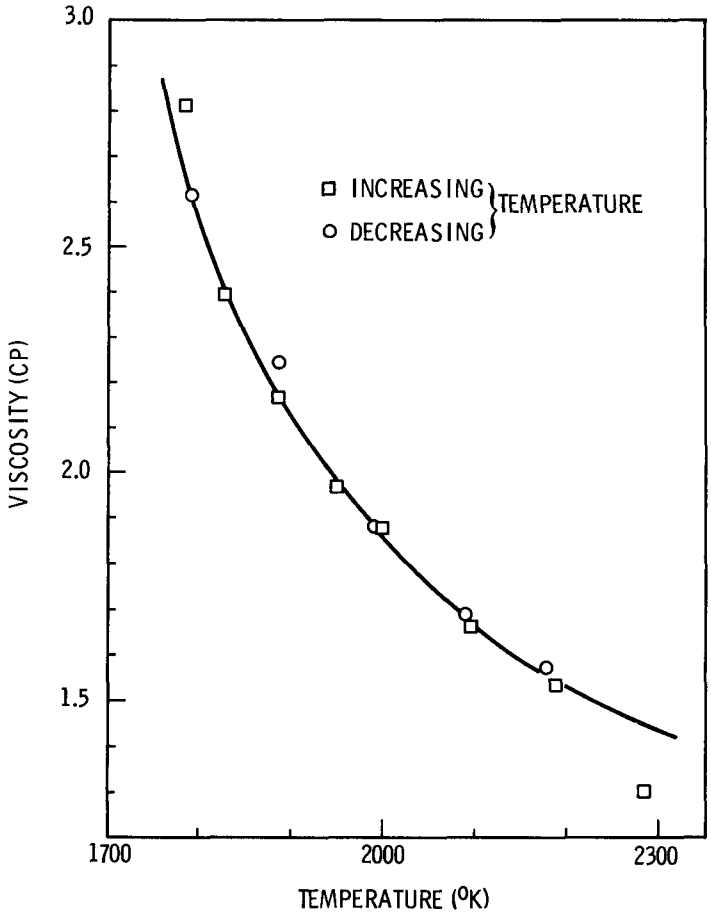

FIGURE VII-29 *Viscosity vs Molten CaF_2.*

and good agreement was found between the two sets of data. Values of density used in computing the compressibility were calculated by the expression given by Kirshenbaum, et al (Ref 26):

$$\rho = 3.179 - 3.91 \times 10^{-4} T \ (g/cm^3)$$

where T is in degrees Kelvin.

The dependence of measured velocity on temperature is nearly linear, with a slight concave upward dependence. From consideration of the effect of thermal expansion, a linear dependence of velocity versus $T^{1/2}$ is expected. Such a dependence has been observed for liquids of lower melting salts (Ref 27). Figure VII-31 is a plot of velocity versus $T^{1/2}$ for molten CaF_2; the data are fit quite well by a straight line. By analogy between molten CaF_2 and UO_2, it was reasonable to expect that the velocity of UO_2 should also exhibit a linear dependence when plotted versus $T^{1/2}$. (Figure VII-28).

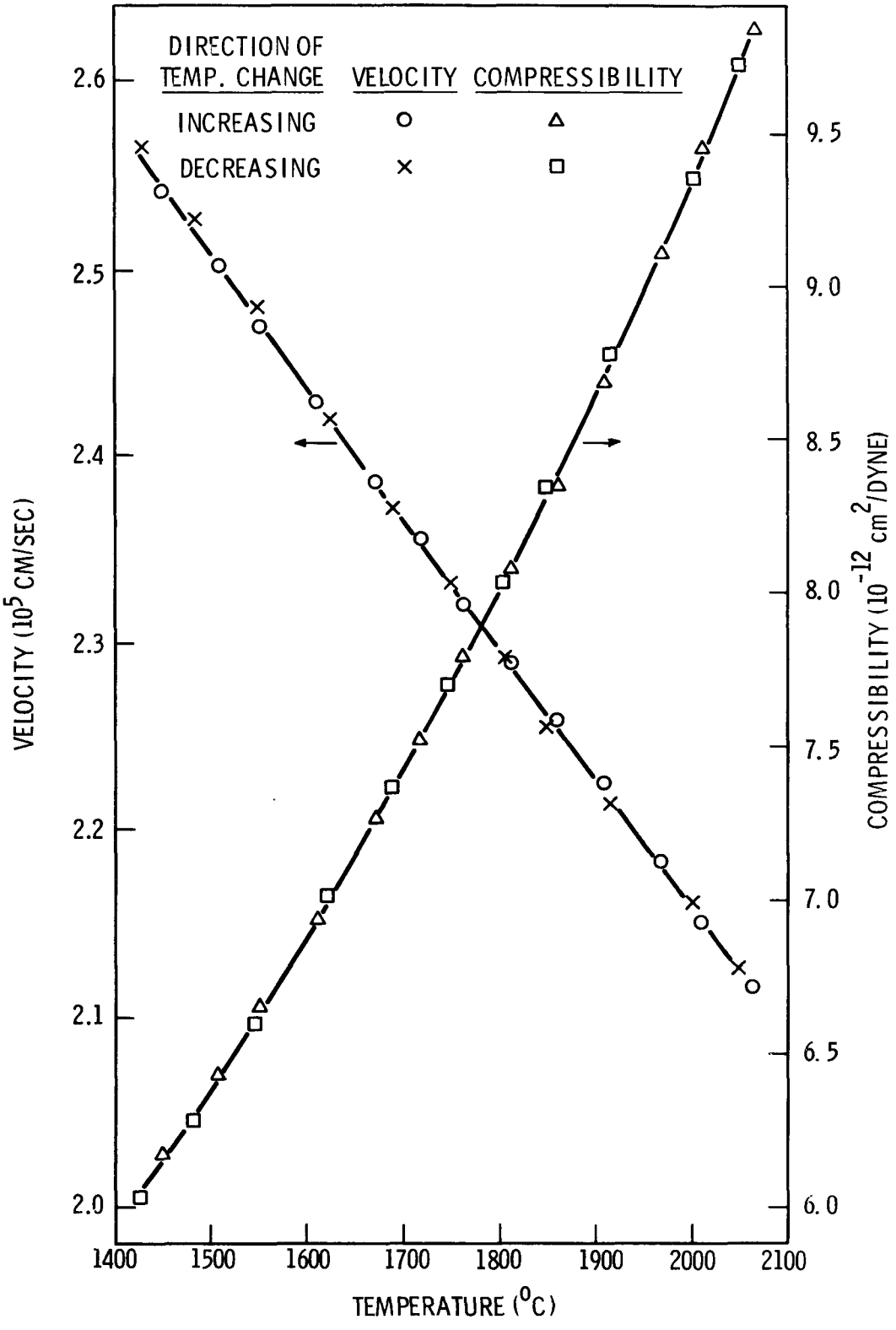

FIGURE VII-30 *Velocity of Sound and Compressibility vs Temperature For Molten CaF_2.*

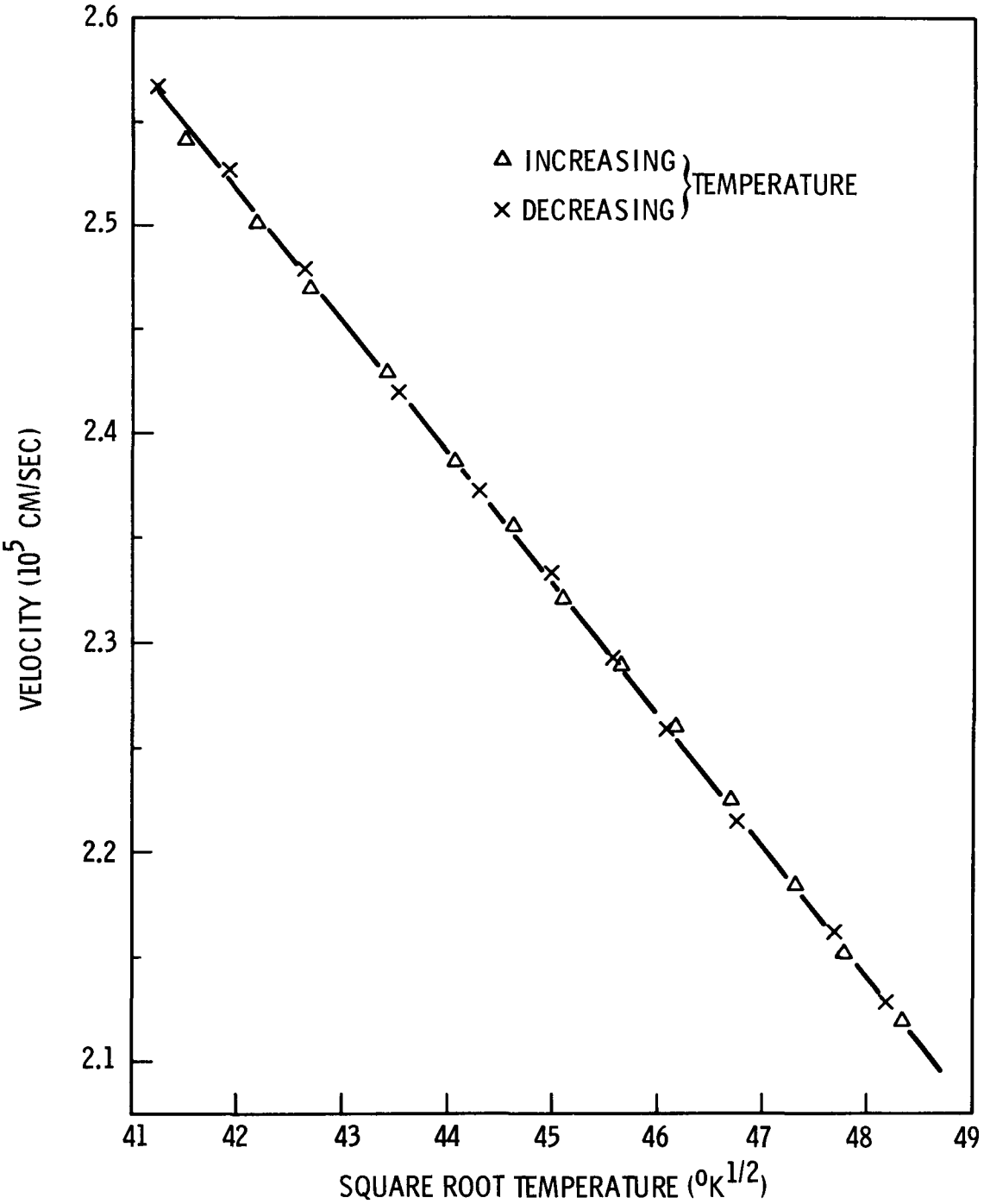

FIGURE VII-31 *Velocity vs Square Root Temperature for Molten* CaF_2.

References

21. Finucane, J. S., "The Viscosity of Uranium Metal and some Uranium-Chromium Alloys," UCRL-16988.

22. Wittenberg, L. J., Ofte, D., and Curtiss, C. F., "Fluid Flow of Liquid Plutonium Alloys in an Oscillating Cup Viscosimeter," J. Chem. Phys. 48, 3253 (1968).

23. McSkimin, H. J., "Use of High Frequency Ultrasound for Determining the Elastic Moduli of Small Specimens," IRE Trans. on Ultrasonic Engineering PGUF-5, 25 (1957).

25. Quarterly Progress Report, October, November, December 1969, Reactor Fuels and Materials Development Programs for Fuels and Materials Branch of USAEC Division of Reactor Development and Technology, edited by W. F. Sheely, BNWL-2179, Battelle-Northwest, Richland, Washington, February 1970.

26. Kirshenbaum, A. D., Cahill, J. A., and Stokes, C. S., "The Density of Molten Metal Fluorides in the Range of 1600°-2500°K," J. Inorg. Nucl. Chem. 15, 297 (1960).

27. Bockris, J. O'M, and Richards, N. E., "The Compressibilities, Free Volumes and Equation of State for Molten Electrolytes: Some Alkali Halides and Nitrates," Proc. Roy. Soc. 241A 44 (1957).

2. Phase Studies

R. E. Woodley, E. T. Weber and J. C. Christensen

The variation in stoichiometry of $(U_{0.75}Pu_{0.25})\ O_{2-x}$ as a function of the temperature and oxygen partial pressure is being determined by a thermogravimetric technique (12212). A knowledge of these relationships is essential for controlling fuel fabrication procedures and for specifying fuel compositions with acceptable radiation stability.

A balance pan machined from molybdenum was installed in the experimental system and its compatibility with the gas atmospheres of interest examined in the absence of a fuel sample. At temperatures up to 1250°C and oxygen potentials approaching -109 kcal/mole, the molybdenum pan exhibited only a small weight loss, presumably resulting from the reduction of a small quantity of oxide on its surface.

Because any additional weight change of the molybdenum pan appeared unlikely, a sample of $(U_{0.75}Pu_{0.25})O_{2\pm x}$, weighing about 1 gram, was installed in the experimental system and equilibrated to an O/M value of 2.000 by exposing it to a hydrogen-water vapor mixture with an oxygen potential of -111.7 kcal/mole. The sample temperature was maintained near 800°C during the equilibration period. This and subsequent measurements on the sample are tabulated below.

Initial Thermogravimetric Measurements on $(U_{0.75}Pu_{0.25})O_{2-x}$

Sample Temp. (°C)	$-\Delta\bar{G}_{O_2}$ (kcal/mole)	O/M
802	111.7	2.000
1095	110.0	1.999
1096	120.3	1.995
1093	130.7	1.988
812	110.1	2.000
800	110.2	2.000
1092	120.2	1.993
1092	131.1	1.984
1092	140.9	1.964
802	107.6	2.000

The O/M values observed at temperatures near 1100°C are in good agreement with results obtained using the iridium pan and are in reasonable agreement with values obtained by interpolation of data measured by Markin and McIver (Ref 28) by electrochemical means. These comparisons are presented in Figure VII-32. The scatter of points about the 1100°C isotherm is of about the same magnitude as the scatter of the points used to define the isotherm originally.

According to Rand and Markin, (Ref 29), for hypostoichiometric solid solutions $U_{1-Y}Pu_YO_{2-x}$ with $y \leq 0.3$, the oxygen potential at any temperature is, to a close approximation, a function only of the plutonium valence and not of the U/Pu ratio. This fact should allow all 1100°C data meeting the above composition requirement to be plotted on a single curve. In Figure VII-33, the 1100°C isotherms for $(U_{0.89}Pu_{0.11})\ O_{2-x}$ and $(U_{0.70}Pu_{0.30})O_{2-x}$ (taken from Figures 44-C and 44-D, respectively, of Markin and McIver (Ref 28)) as well as the present experimental data for $(U_{0.75}Pu_{0.25})O_{2-x}$ are plotted in this manner. While the two lines and the individual points are not coincident, they easily fall within the normal scatter band expected for a plot of this nature (as indicated by the scatter of points in Figure 44-E of Ref 28) and therefore exhibit reasonable agreement.

An attempt is being made to extend the 1100°C data to an oxygen potential of -145 kcal/mole or below, after which the sample temperature will be increased to 1200°C and the measurements repeated over the same range of oxygen potentials.

References

28. Markin, T. L. and McIver, E. J., Proc. Third Int. Conf. on Plutonium Inst. Metals, London, 1965 pp. 845-857.

29. Rand, M. H. and Markin T. L., Thermodynamics of Nuclear Materials, IAEA, Vienna, 1968, pp. 637-650.

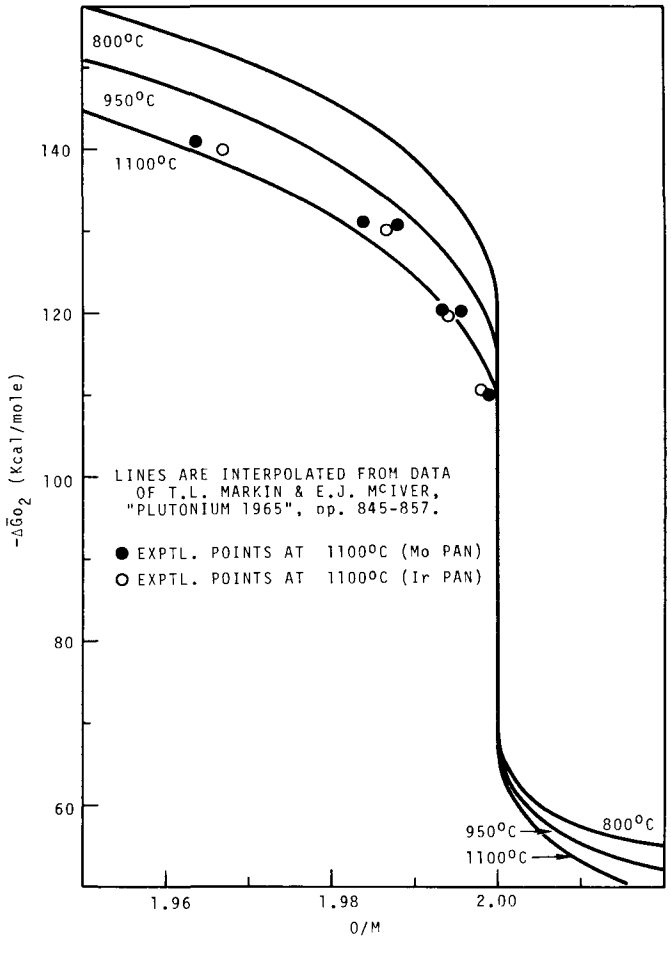

FIGURE VII-32 $\Delta\bar{G}o_2$ *vs Oxygen/Metal Ratio for* $(U_{0.75}Pu_{0.25})O_{2+x}$

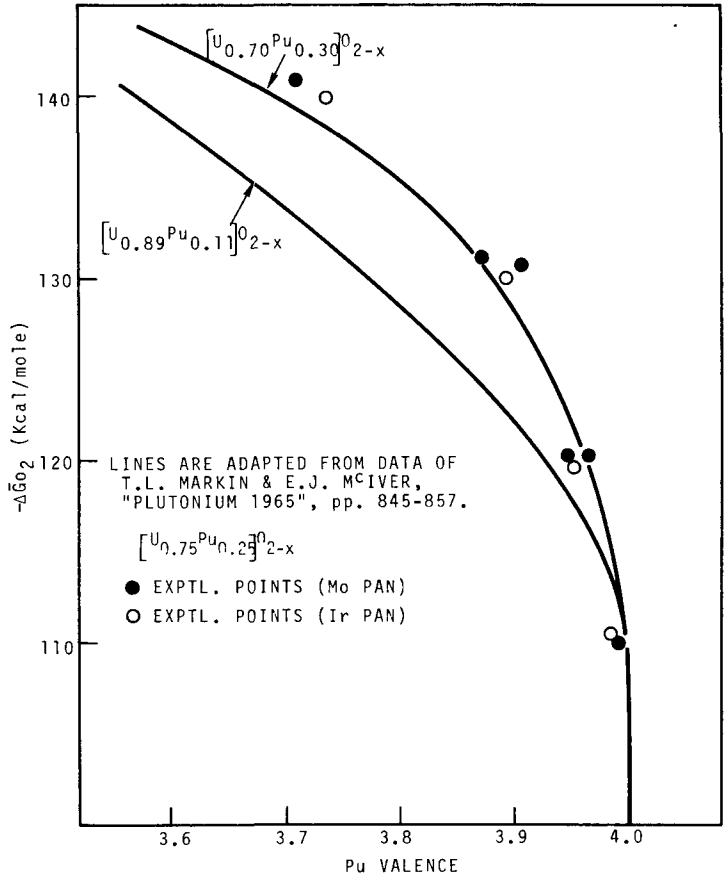

FIGURE VII-33 $\Delta\bar{G}o_2$ *vs Plutonium Valence For* $(U_{1-y}Pu_y)O_{2-x}$ *at 1100°C.*

3. Basic Property Measurements

R. L. Gibby, E. T. Weber & J. A. Christensen

The purpose of this study (12212) is to determine the high temperature (1600°C) thermal transport properties of UO_2 - 25 wt% PuO_2 FTR fuel. The approach being taken is to measure thermal diffusivity and heat capacity, followed by a calculation of thermal conductivity from these data. Thermal diffusivity measurements will also be made on low density fuel material (88-92% TD) currently being used in FTR prototype fuel testing.

A high temperature laser heat pulse apparatus for measuring thermal diffusivity was installed in a plutonium glove box. During the last quarter, the apparatus was tested at temperatures greater than 2300°C. Because of problems with the sample support system, several minor modifications were made, and the apparatus can now be operated above 2300°C without any difficulty.

A narrow band filter with a 0.45-micron band pass width at 4.40 microns has been incorporated in the temperature monitoring system. This has greatly improved the performance of the indium antimonide detector at temperatures above 1600°C.

Thermal diffusivity measurements were made on a round-robin UO_2 sample to approximately 2000°C in an argon 8% H_2 atmosphere; however, because of mechanical vibrations in the temperature monitoring system, the thermal response curves from which thermal diffusivity values are calculated were of poor quality. Minor modifications in the detector system are expected to alleviate this problem. Measurements on the UO_2 sample will be repeated prior to initial measurements on mixed oxide.

4. Restructuring Phenomena

a. Restructuring Effects on Melting Heat Rating

L. A. Lawrence, J. A. Christensen and E. T. Weber (12213)

Densification and restructuring of oxide fuels during irradiation is expected to reduce center temperature and alter the shape of the temperature profile within the fuel. As a consequence, restructured fuels

should be capable of higher unit power outputs than nonrestructured fuels. The magnitude of the effect has potential significance presently unknown, but it will be a function of fuel density, void deployment, time, and heat rating. Experiments intended to quantify these relationships are in progress.

Two capsules, FP-313 and FP-314, were successfully irradiated in the SNOUT facility to study effects of fuel restructuring on the temperature profile of UO_2 - 25 wt% PuO_2. FP-313 was inserted slowly into the reactor to permit fuel restructuring prior to melting; FP-314 was inserted as rapidly as possible to preclude or minimize restructuring. The two capsules contained thermocouples located at two different radial positions in the outer aluminum sleeve to monitor power generation continuously in the two pins during irradiation. Fuel characteristics and test conditions are listed in Table VII-8.

Post-irradiation examination of FP-313 has been completed (Figures VII-34, VII-35 and VII-36) and measurements of post-irradiation structures are summarized in Table VII-9. Measurements of residual fuel-clad gap width show approximately a 30% decrease in the initial 0.009-in. diametral gap. Radiochemical burnup determinations using Zr^{95}, $Ba\text{-}La^{140}$, and Ce^{141} showed the pins to have operated at power densities within 4% of each other.

Fuel-clad gap conductance was calculated by matching observed fuel structures with temperature profiles calculated for the measured heat ratings. Using nominal values for the heat generation rates, the gap conductance for the 0.009-in. gap pin was approximately 2000 Btu/hr-ft^2°F.

Close examination of the fuel's post-irradiation structure showed the pores to have what appears to be a "tail". These "tails" are aligned somewhat on radii to the thermal center of the fuel and are most heavily concentrated in the area of equiaxed grains (Figure VII-37). Examination of the fuel in the unetched condition showed no such decoration of the pores. It is probable that the fuel is of a slightly different chemical

TABLE VII-8
FUEL CHARACTERISTICS AND TEST CONDITIONS
FOR CAPSULES FP-313 AND FP-314

1. Fuel	
Form	Cold pressed and sintered pellets
Composition	UO_2 - 25 wt% PuO_2
Oxygen/Metal	1.96 ± 0.01
Density	95% T.D.
Pu^{239}/Pu	87%
Pu^{240}/Pu	11%
U^{235}/U	Normal
Cladding	304L SS
Fuel-Clad Diametral Gap Width (in.)	
Pin A	0.002
Pin B	0.009
Fill Gas	He at one atmos
Impurity Content	>400 ppm cation impurity
2. Test Conditions	
Rate of Power Increase During Charging	
FP-313	45%/hr to 90% full power Remained at 90% full power for 24 hr. 1.25%/ hr to full power
FP-314	3%/second to full power

Rate of Power Decrease During Discharge--3%/sec

Time at Steady-State Power--10 hr.

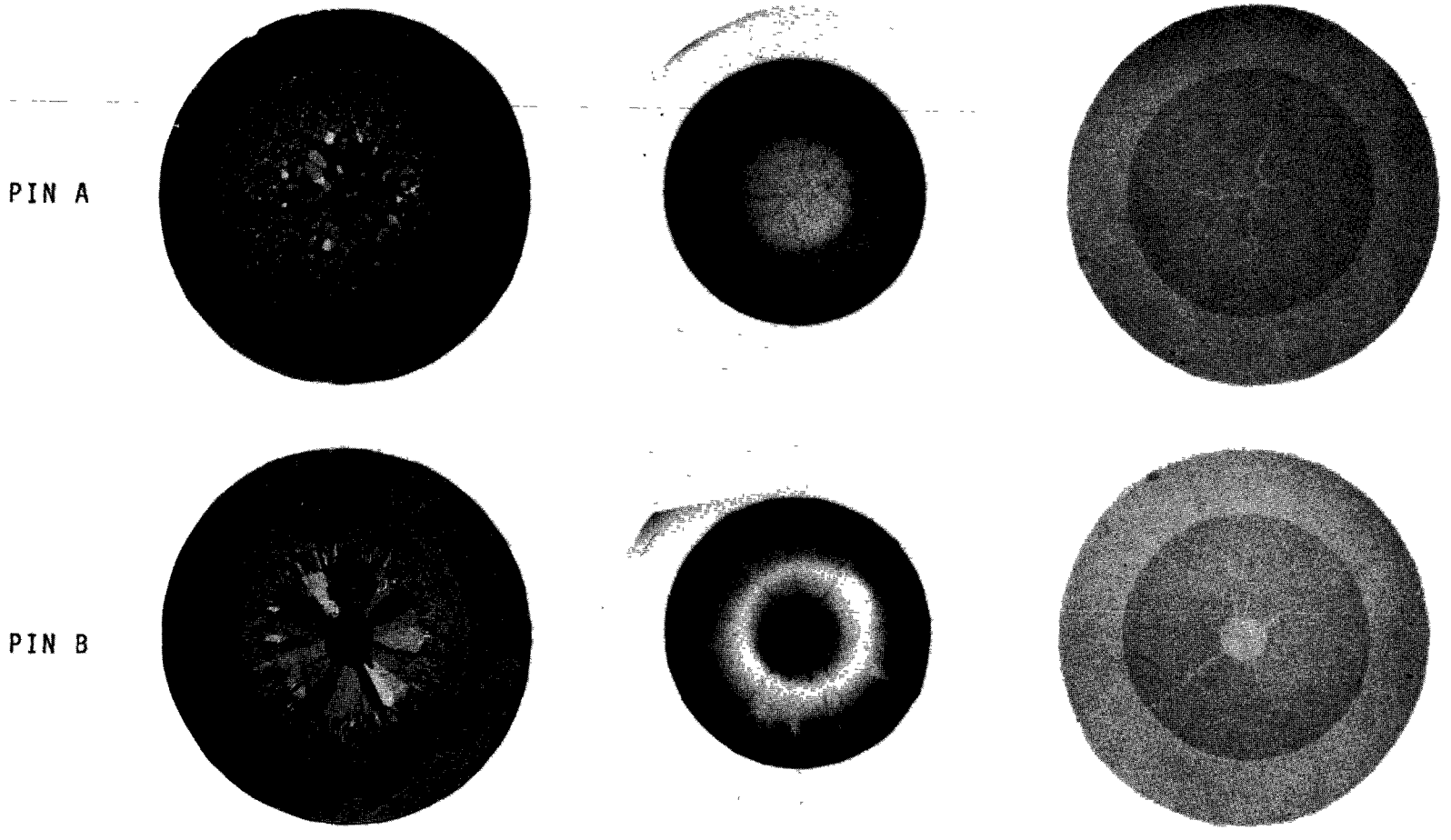

FIGURE VII-34 *Post-Irradiation Structures From Capsule FP-313*

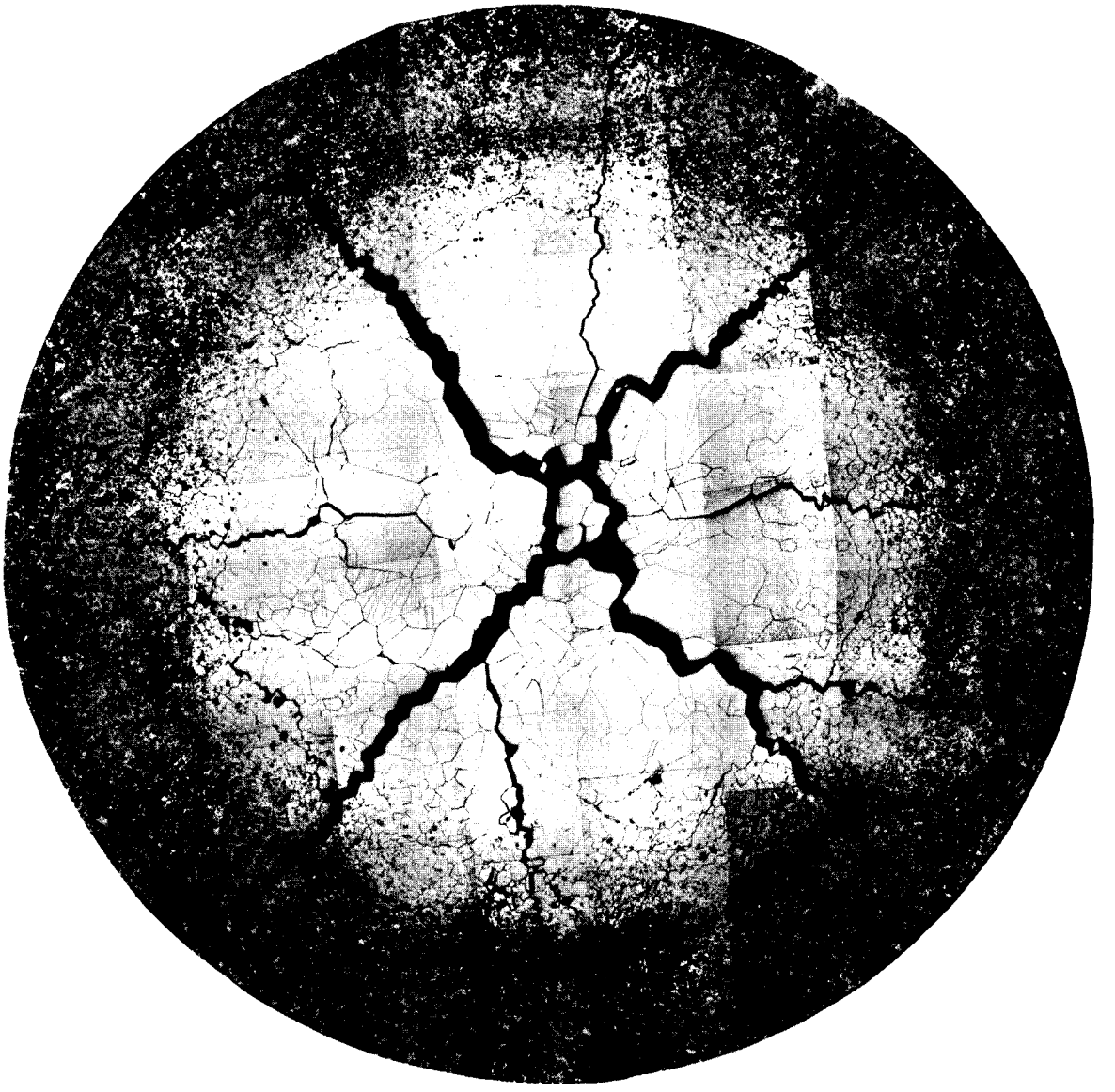

FIGURE VII-35 *Post-Irradiation Structures of Pin FP-313A Showing No Evidence of Fuel Melting.*

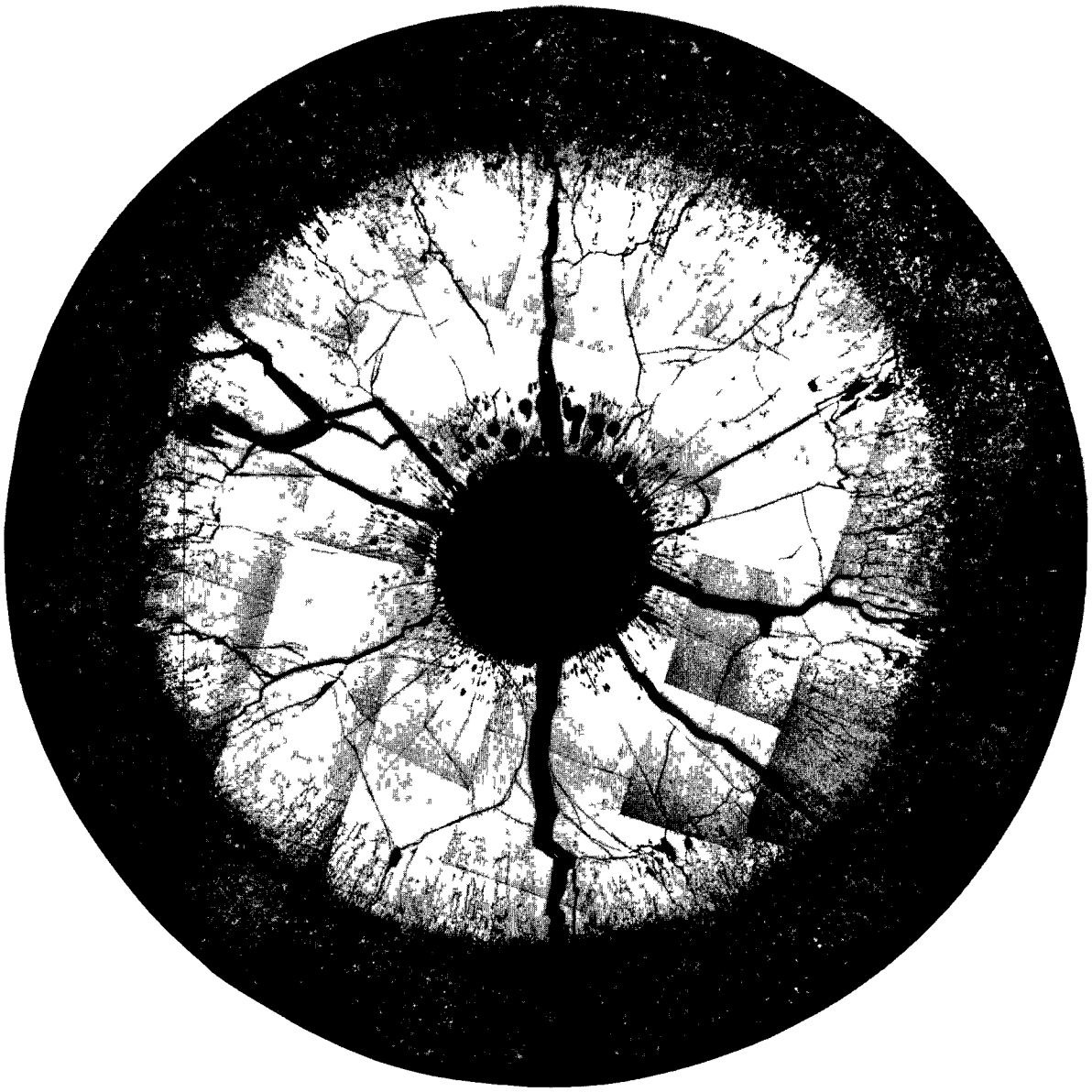

FIGURE VII-36 *Post-Irradiation Structures of Pin FP-313B Showing Structures Associated with Operation for Short Periods with Center Melting.*

TABLE VII-9

POST-IRRADIATION STRUCTURES OF PINS FROM FP-313

Feature	Location* (% Fuel Radius)	
	313A	313B
Beta-Gamma Autoradiographs		
Inner boundary of light gray annulus	--	30.4
Inner boundary of bright annulus	--	41.8
Outer boundary of bright annulus	45.0	50.6
Outer boundary of light gray annulus	73.2	68.5
Micrographs		
Central Void	--	18.3
Inner boundary pore-free zone	--	31.7
Outer boundary pore-free zone	--	46.6
Maximum extent of columnar grains	--	60.0
Beginning of columnar grains	--	75.0
Beginning of equiaxed grains	72.5	82.5

*Avg. of 12 equally spaced measurements on the circumference

composition in the immediate area traversed by the pore, thereby having different etching characteristics. This same explanation has been presented by Rosenbaum (Ref 30) to explain these tails. He postulated that they arose from increased solubility of the fuel in the area traversed by the pore for the fission gases present.

The outer and inner boundaries of the pore-free zone in the fuel's microstructure (Figure VII-36) probably represent the beginning and end of life melt radii, respectively. Therefore, the outer boundary should represent the extent of fuel melting in unrestructured fuel, and the inner boundary should represent the extent of melting in the restructured fuel

prior to discharge. Because of the sensitivity of extent of fuel melting to variations in power density, the two melt indicators could also be the result of fluctuations in power density rather than fuel restructuring. Data analysis, including that from the in-pile thermocouples for both capsules, is still in progress to determine which factors have most strongly influenced fuel structure.

TABLE VII-10
FUEL CHARACTERISTICS AND TEST CONDITIONS
FOR FP-38 AND FP-39

1. Fuel			
Composition			UO_2 - 25 wt% PuO_2
Oxygen/Metal			1.96 ± 0.01
Pu^{239}/Pu (%)			87
Pu^{240}/Pu (%)			11
U^{235}/U			Normal
Cladding			304L SS
Average Fuel-Clad Gap (in.)			0.003
2. Test			
Capsule	Pin No.	Fuel Form	Smeared Density (% TD)
FP-38	1A	Vipac	83
	1B	Pellet	83
	2A	Pellet	87
	2B	Pellet	90
	3A	Pellet	93
	3B	Pellet	90
	4A	Pellet	96
	4B	Pellet	90
FP-39	Same as FP-38		

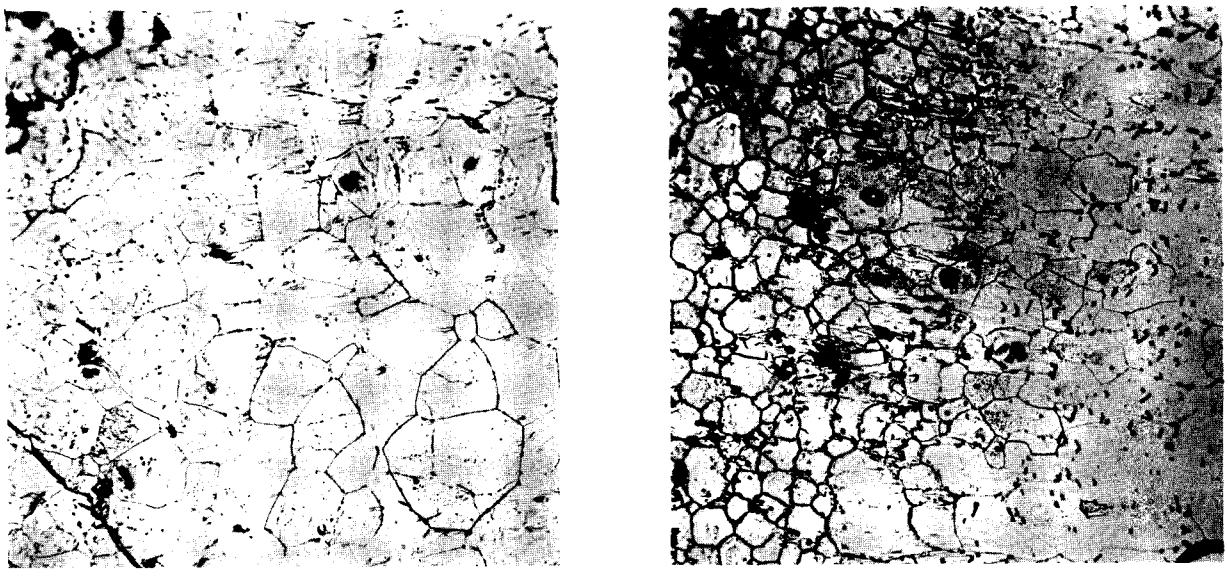

FIGURE VII-37 *Etched Fuel Microstructures of Pins FP-313A and FP-313B Showing Bubble Trails. Fuel Thermal Center is to the Right.*

Two eight-pin capsules designed to determine the melting heat rating for four different fuel densities and for a packed powder fuel related to pelleted fuel of comparable density are under construction. Fuel characteristics and test variables are listed in Table VII-10. The first capsule, FP-38, will be irradiated for 24 hours at a heat rating just below fuel melting to achieve an equilibrium fuel structure. The capsule will then be inserted very slowly into the high power regions to cause enough fuel melting to deduce melting heat ratings. The second capsule, FP-39, will be rapidly inserted into the peak power region. Results from FP-39 will be relevant to nonrestructured fuel of various densities. All the fuel has presently been fabricated and loaded except the 87% and 96% smeared density pins. Fabrication, assembly and irradiation of FP-38 and FP-39 should be completed by December, 1970.

References

30. Rosenbaum, H. S., "Bubble Trails in Oxide Fuels," J. Nucl. Mat. 28, (1968), p. 225.

b. Program Plan-Studies of Restructuring Phenomena

C. A. Hinman, E. T. Weber and J. A. Christensen

A project to investigate the temperature-induced restructuring characteristics in mixed-oxide systems, both in-reactor and ex-reactor, has been initiated. (12212) The objective is to improve confidence in interpretations of radial structure-temperature profiles and to provide data on restructuring kinetics of virgin fuel. The data obtained from the ex-reactor work will be used as a base-line comparison to the grain-growth observed in various in-reactor experiments.

An extensive literature survey is being carried out covering grain-growth theory, experimental techniques, and available data for both metallic and ceramic systems. A relatively large amount of grain-growth data exists for UO_2, but relatively little is available for (U,Pu) O_2. Some of the major conclusions drawn from the survey to date are:

1) A satisfactory model for the atomistic structure of a grain boundary does not exist.
2) The mechanisms involved in grain-growth are not fully understood.
3) The most probable theoretical formulation describing grain-growth is given by:

$$D^n - D_o^n = Ke^{-\frac{E}{kT}}t$$

where D = grain diameter as a function of time and temperature,

D_o = grain size at t=0,

n = a constant which ranges from about 2 to 4 depending upon the mechanisms of boundary migration,

K = a constant,

E = an activation energy for migration,

T = absolute temperature,

k = Boltzmann's constant,

t = time.

4) Grain-growth rates are very sensitive to small amounts of impurities; these impurities may either increase or decrease the migration rate, depending upon the type and amount.

5) Boundary migration rates are also very sensitive to inclusions, such as precipitates, pores, and/or bubbles, a very important factor when considering grain-growth in reactor fuels.

6) The grain-growth rates are probably affected by the local fission rate density in operating fuels, as are most rate activated processes.

It is possible that, given adequate pre-irradiation characterization of the fuel and proper base-line test results, the observed in-reactor grain-growth characteristics can be used to obtain radial temperature profile data from relatively short-term irradiations. This would be applicable to initial startup behavior of virgin fuel.

c. Simulation on Hybrid Computer

R. D. Leggett, R. B. Baker, L. E. Addison, D. S. Dutt and J. D. Lodge

A prediction (12163 FP-E) of fuel restructuring for PNL-1-1 and PNL-1-2 pins while in EBR-II was made with a hybrid fuel model. Based on analyses made on similar PNL-1 pins, for which a structure was known, the following simplifying assumptions were made:

1) Gap conductance should equal 2400 BTU/ft^2 - hr-°F.
2) Density of the columnar and equiaxed regions should be equal to the density of the unrestructured region.
3) The cold fuel diameter gap at finish was equal to that at start.
4) The peak power should be derived from EBR-II fission rates.

Table VII-11 shows input parameters. An extra case was run for each pin with a 1% densification of the columnar region, since the behavior of this quantity is not exactly known. However, the uniform density fuel prediction (no central void resulting) is considered the most probable.

TABLE VII-11
SUMMARY OF INPUT PARAMETERS AND MIDPLANE
RESTRUCTURING PREDICTIONS FOR PNL-1-1 AND PNL-1-2

Input Parameters	PNL-1-1		PNL-1-2	
Fuel Column Length (in.)	13.328		13.563	
Extrapolation Distance (ft)	0.458		0.458	
Max. Pin Power (kW/ft)	10.66		10.55	
Pin Diameter (in.)	0.250		0.250	
Clad Thickness (in.)	0.016		0.016	
Coolant Mass Flow Rate (lb/hr)	703.		703.	
Coolant Specific Heat (BTU/lb-°F)	0.3070		0.3070	
Film Coefficient (BTU/ft^2-°F-hr)	4855		4855	
Gap Conductance (BTU/ft^2-°F-hr)	2400		2400	
Clad Conductivity (BTU/ft-°F-hr)	11.4		11.4	
Inlet Coolant Temp (°F)	700		700	
Columnar Temp (°C)	1700		1700	
Equiaxed Temp (°C)	1450		1450	
Unrestructured Density (% TD)	91.74		92.94	
Equiaxed Density (% TD)	91.74		92.94	
Columnar Density (%TD)	91.74	93.00	92.94	94.00
Fuel Diameter (in.)	0.212		0.212	
Restructuring at Midplane				
Radii (Mil) — Central Void	0.0	4.1	0.0	2.6
Radii (Mil) — Columnar G.G. Boundary	36.7	36.8	29.1	27.9
Radii (Mil) — Equiaxed G.G. Boundary	58.7	58.7	55.0	54.3
Radii (Mil) — Fuel Radius	106.0	106.0	106.0	106.0

Included in Table VII-11 are the predictions of restructuring at the center of the fuel column.

Restructuring and temperature predictions made for the whole pin are available. The predictions will be used in connection with transient tests being run on these pins.

5. High Burnup Effect on Melting Heat Rating

F. E. Panisko, E. T. Weber and J. A. Christensen

The objective of this program (12213) is to determine the effect of burnup on the melting heat rating of UO_2 - 25 wt% PuO_2. Fission products may significantly lower the fuel melting heat rating by changing the melting point and thermal conductivity. The latter may be a result of lower thermal diffusivity and also lower density which results from fission gas swelling. An irradiation test will be performed to determine the effect of burnup on melting heat rating.

We plan to irradiate simultaneously, for about 1 hour in a thermal reactor, two similar fuels with different burnups from prior irradiations to observe any differences in their melt radii. Re-encapsulated clad fuel sections from PNL-1 (~10,000 MWd/MTM fast fluence burnup in EBR-II) and PNL-2 or PNL-5 (~50,000 MWd/MTM fast fluence burnup in EBR-II) will be used in this test.

Figures VII-38a and VII-38b are photographs of the remotely operated welding system which was designed for re-encapsulation by P.K. McDaniel. The system is being used to develop a technique to remotely weld end caps to stainless steel cladding sections.

6. In-Reactor Creep

a. Prediction of Fuel Plasticity In-Reactor

D. C. Bullington and D. S. Dutt

A study was made (12163 FPE) to estimate the change in the creep rate of the fuel during irradiation. Grain boundaries were assumed to act as sinks for cation vacancies and the energy required to form a cation

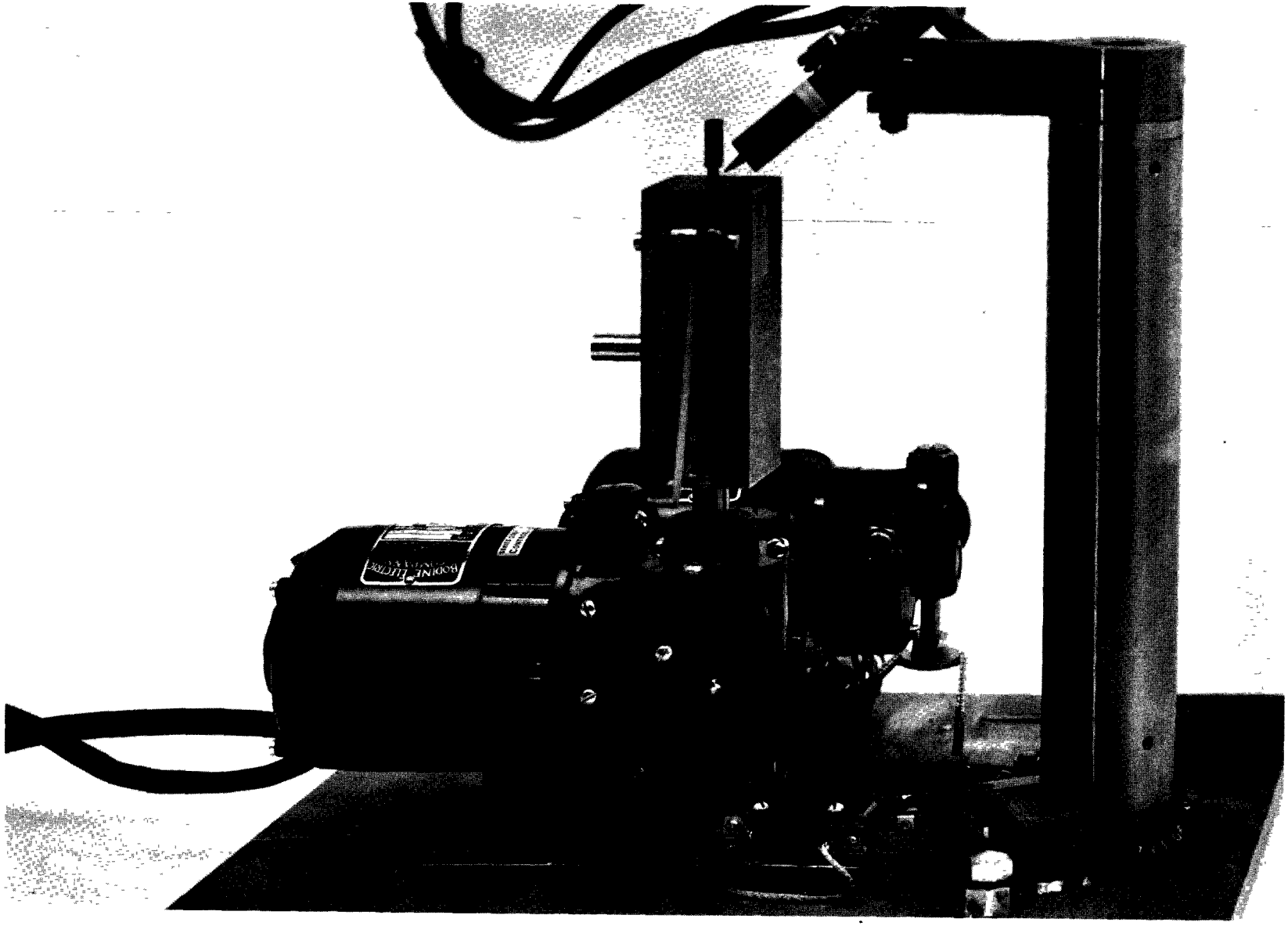

FIGURE VII-38a *Remotely Operated System for Welding End Caps to Cladding Sections.*

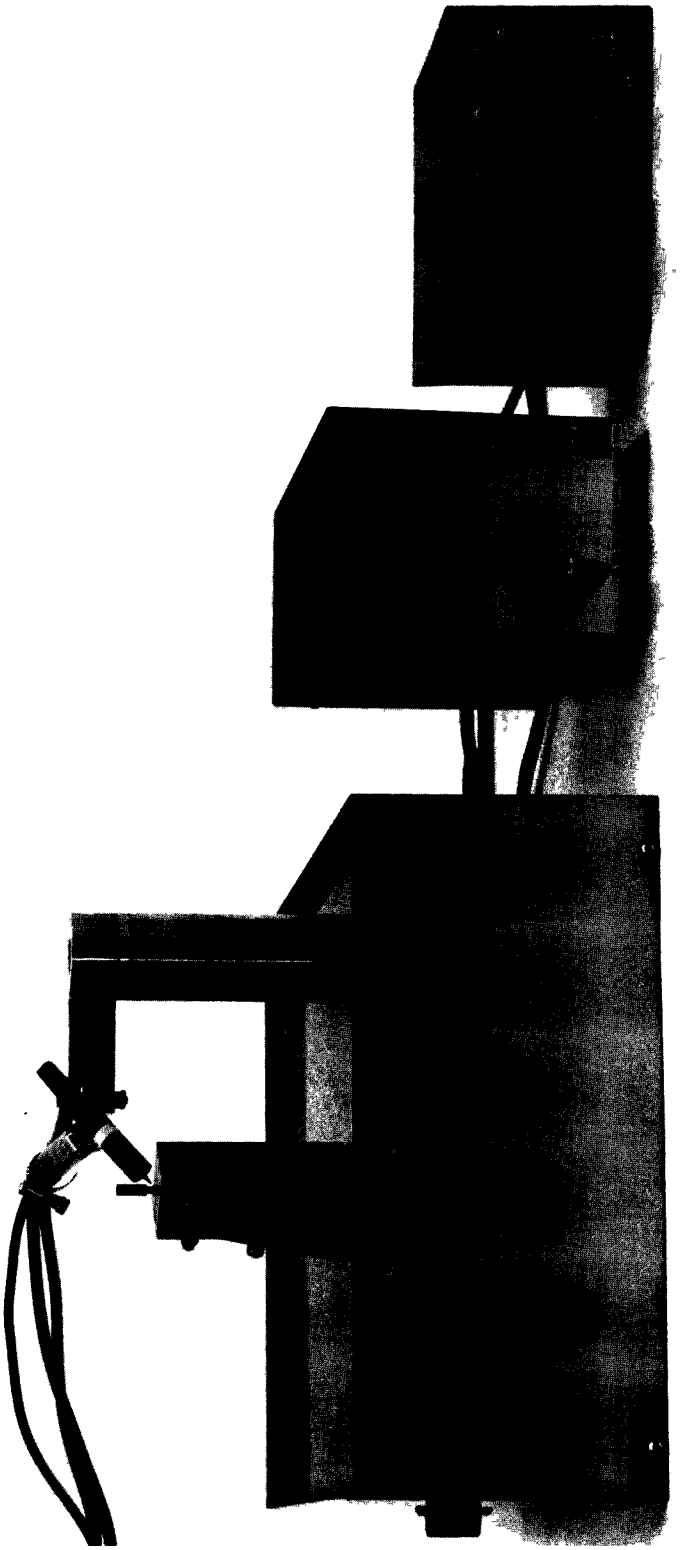

FIGURE VII-38b *Another View of End Cap Welder.*

vacancy (E*) was assumed to be two electron volts. The excess vacancy concentration created by the fast flux in excess of that supplied by thermal activation ($\nu^*-\nu$) is calculated to be:

$$\nu^*-\nu = \left[\sqrt{\frac{2}{2}}\right]^Z \left\{\exp\left[-\frac{E^*+Q}{RT}\right] - \exp\left[-\frac{E^*}{RT}\right]\right\}$$

where Z = coordination number

E^* = energy for cation formation

Q = additional energy supplied by neutron flux

Assuming the equillibrium cation vacancy concentration is C, where

$$C = \phi\, \sigma_s\, \frac{S^2}{D}$$

ϕ = neutron flux n/cm^2-sec

σ_s = scatter cross-section for heavy metal

S = distance to nearest vacancy sink

D = cation diffusion rate (cm^2/sec)

Setting the two above expressions equal enables one to estimate Q, the energy supplied by the neutron flux. Assuming an activation energy for cation diffusion in mixed oxide of 105 kcal/mole and the following material constants:

Z = 12

ϕ = 2×10^{15} n/cm^2-sec

E^* = 2 eV or 46 kcal/mole

σ_s = 2 barns

and since

$$\exp\left(\frac{-46000+Q}{RT}\right) >> \exp\left(\frac{-46000}{RT}\right)$$

for Q large with respect to E* and for cation diffusion

$$D = D_0 \cdot \exp\left(\frac{-E^*+Q}{RT}\right)$$

We may write

$$\phi \frac{\sigma_s S_2}{D_o} = 64.5 \exp\left(\frac{-151000+2Q}{RT}\right)$$

Figure VII-39 shows calculated values of Q, the reduction in activation energy for creep, as a function of temperature and the parameter S^2/Do, the ratio of the square of the distance to cation sinks to the coefficient for cation diffusion. The fast flux increases the plasticity of the fuel to the greatest extent at low temperatures. For expected S^2/D_o ($\sim 10^{-2}$ sec) the fast flux is expected to make little or no contribution to fuel plasticity above 2600°K. This temperature is quite dependent upon the value assumed for the cation binding energy. A lower assumed value would reduce the prediction of Q. A modified form of computer code SIEX was used for these calculations.

b. In-Reactor Creep Capsule

J. A. Basmajian, O. D. Slagle, E. T. Weber and J. C. Christensen

A program (12212) has been underway to measure both in- and out-of-reactor creep on fast reactor mixed-oxide material using a four-point bending technique. In the last quarterly report, the assembly of the in-reactor creep capsule was discussed and the results of high temperature creep measurements on high density UO_2 were presented (Ref 31).

The final assembly of the in-reactor creep capsule was completed and loaded with three specimens: two samples of high density (99% TD) hot pressed UO_2 - 25 wt% PuO_2 and one sample of 92% TD UO_2. Prior to loading, one of the mixed-oxide samples was subjected to a stress of 5000 psi for

---

Reference

31. Quarterly Progress Report, April, May, June, 1970. Reactor Fuels and Materials Development Programs for Fuels and Materials Branch of USAEC Division of Reactor Development and Technology, BNWL 1349-2 UC-25, August 1970.

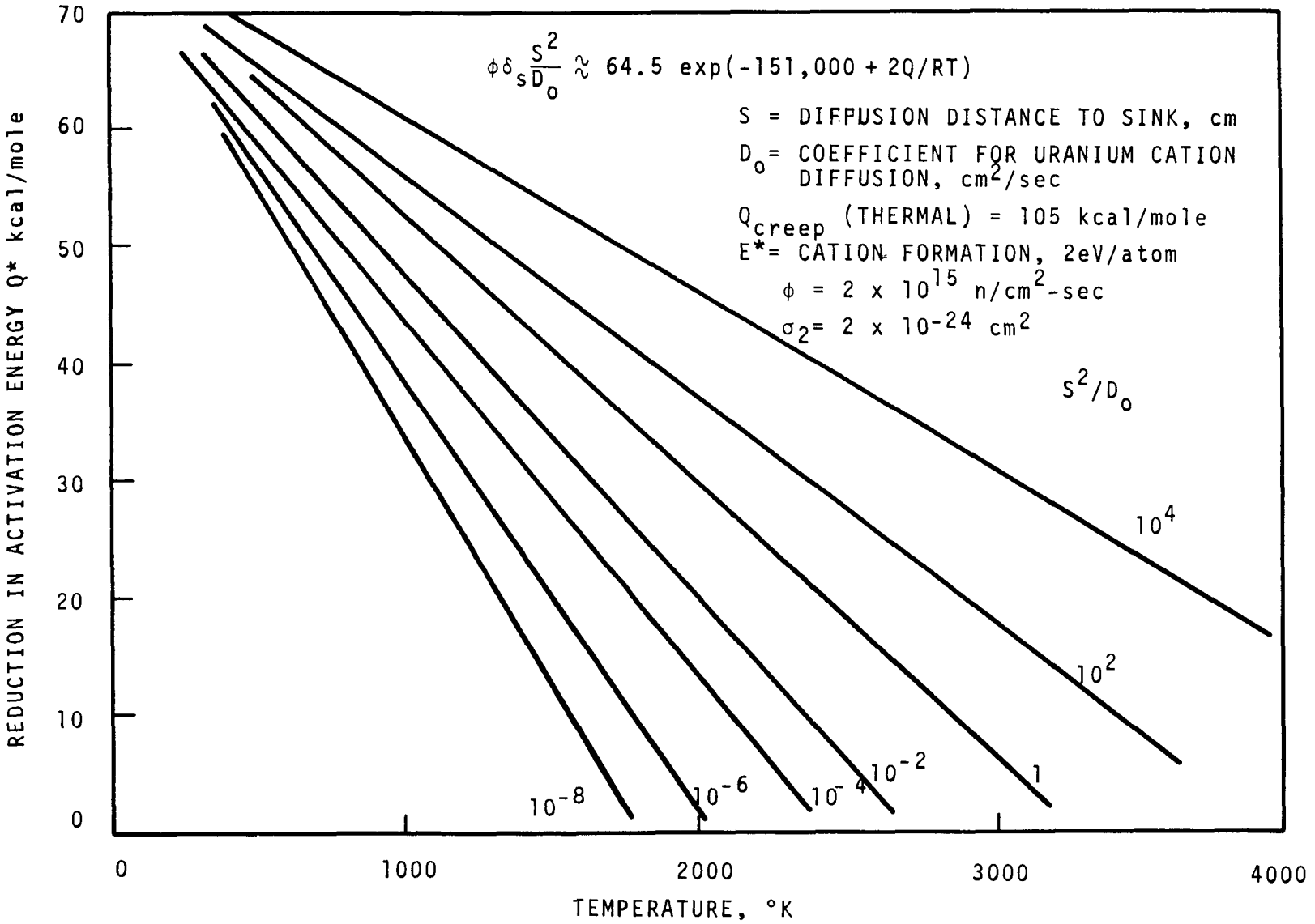

FIGURE VII-39 *Reduction in Activation Energy for Creep of Mixed Oxide for Various S^2D_O.*

over 100 hours without failure. This sample was then assumed to be structurally sound and was placed in the capsule under no load to determine whether the stresses developed from thermal gradients were sufficient to cause sample failure. The other mixed-oxide sample and the UO_2 were loaded in a position for application of loads of 1250 psi and 1835 psi, respectively, during testing.

The capsule was inserted into the reactor and the temperature maintained at 900°C. After 44 hours, erratic behavior was noted on the monitoring thermocouple and two hours later the control thermocouple opened. Consequently, the test was discontinued and the capsule was removed from the reactor.

Subsequent examination of the capsule revealed that all the samples had failed (fractured) during testing. Each sample, including the unloaded mixed-oxide specimen, had broken into two pieces. Metallography is presently being conducted to determine the extent of grain growth and noncatastrophic crack development.

The failure of all three specimens was sufficient evidence to conclude that successful creep measurements by the present method are virtually impossible. On the basis of this test, and in light of previous difficulty in obtaining mixed-oxide samples suitable for bend testing, a decision was made to discontinue the creep studies.

7. Mixed Oxide Swelling

a. Evaluation of Spatial Distribution of Pore Morphology in Irradiated Mixed Oxide Fuel

D. C. Bullington, B. Mastel, H. A. Treibs and L. A. Hartcorn

The radial and axial distributions of pores in irradiated mixed oxide fuel are being determined (12163 FP-E) to better understand the swelling of mixed oxide due to the accumulation of gaseous and solid fission products. Comparison of the size distribution of pores with that of the fuel before irradiation makes possible a better understanding of both swelling and sintering of the oxide fuel during irradiation.

1) Pore Distribution in PNL X-7 Pin

An evaluation of the void area fraction and its distribution in a transverse fuel section of PNL X-7D was performed using a 50X enlarged photomosaic of the fuel cross section. The Quantimet was used to evaluate the area fraction of cracks, porosity, and central void in area of columnar grains, as well as the area of equiaxed grains and unrestructured area. The results are shown in Table VII-12. The section of PNL X-7 examined reached a measured burnup of 8500 MWd/MTM at a linear power of 10.4 kW/ft. The analysis was performed to show a comparison of the void volume in the three regions of the pellet. The absolute magnitude of the void area is not reliable, because the analysis was performed on a photomosaic of an etched structure at low magnification (50X). A large uncertainty exists in the intergranular pore area. The procedure is, however, useful for estimating the area of large features such as cracks and central voids. Work is now underway to obtain composite photomosaics of fuel at higher magnification before etching.

2) Pore Distribution in PNL 2-3 Pin

Two unetched transverse sections of the fuel from PNL 2-3 were examined with the Quantimet to determine the radial distribution of intergranular pellet porosity. The first section was two inches from the bottom of the fuel and was calculated to have reached 4.1 atom% burnup of heavy metal at a local power of 8.2 kW/ft. The fuel at the section operated at a calculated peak fuel temperature of 3200 °F and a surface temperature of 1140 °F. Figure VII-40 shows the measured void volume as a function of $(r/R)^2$ where r is the local radius and R is the total pellet radius. The absicissa is a useful parameter for estimating total area fraction.

TABLE VII-12
AREA FRACTION* OF VOIDS IN PNL X-7D

	Unrestructured Area (outer 63.8%)	Area of Equiaxed Grain Growth (intermediate 26.7%)	Area of Columnar Grains (inner 9.5%)	Total Area Fraction of Feature
Central Void	----	----	0.23%	0.23%
Cracks	4.67	1.79	0.41	6.87
Porosity	2.12**	5.21	2.30	9.63
Fuel-Cladding Gap	2.31	----	----	2.31
Total Void (%)				19.04

* Area Fractions represent fraction of total Fuel Pellet Area

** 0.6% of the 2.12% thought to be residual fabricated porosity

Initial Smear Density of PNL-X7 87.17% (128% void) = 4.8×10^{-3} in.^{2}

ΔA of cladding ID change $\pi[(0.111)^2 - (0.109)^2]$ = $\underline{0.4 \times 10^{-3}}$ in.^{2}

Total Void Area Expected = 5.2×10^{-3} in.^{2}

Total Void Area Measured by Quantimet $(0.19)\pi(0.111)^2$ 7.37×10^{-3} in.^{2}

Unaccountable Void Area 2.17×10^{-3} in.^{2} or 5.7%

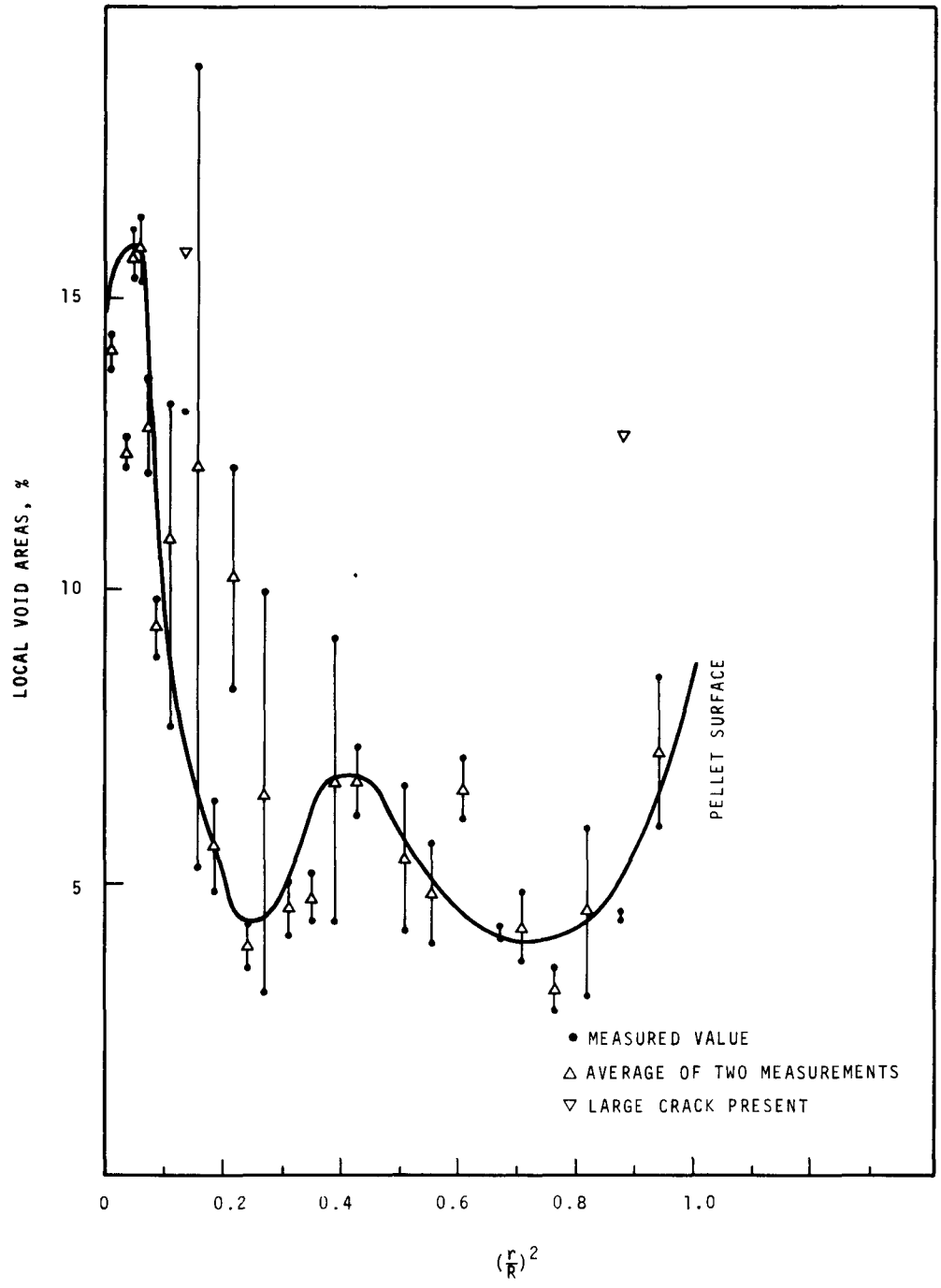

FIGURE VII-40 *Local Pore Area vs $(r/R)^2$ for PNL 2-3B. Calculated Burnup 4.1%. Calculated Power 8.2 kW/ft. Average Fuel Density in Pin, 10.45 gm/cm^3.*

Figure VII-41 is similar plot showing the pore distribution near the center of the fuel pin that achieved a calculated burn-up of 5.2 atom% heavy metal at a local calculated linear power of 10.3 kW/ft. This section had a calculated center temperature of 3640 °F and a fuel surface temperature of 1320 °F. Both figures are the result of two measurements with the Quantimet across 300X enlargements of the unetched pellet radii. Neither section had a region of columnar grains or central void. Although considerable scatter exists in the data, three regions of increased pore density are apparent in both sections. The void density reaches approximately 15% of the area at the fuel center and 8% at the surface of both sections. A third region near a (r/R^2) of 0.5 showed an increase in void volume of about 1% for the low power section and 3% for the higher power section above that of the 5.5% average void volume of the pin. (Volume percentage and area percent pore volume of a section should be identical). The two higher density annuli on either side of this central portion are quite apparent in 75X photomosaics of the total fuel cross sections. The outer portions of the pellets still contain pores as large as 8 mils in diameter which are thought to be the remains of fabricated porosity. Integration of a visual best-fit of the data in each graph indicated a volume increase of 0.9 volume % for the low power section and 2.9 volume % for the higher power section, based upon a fabricated theoretical pellet density of 94.5%.

The data are being compared with the change in fuel-cladding gap size to identify what portion of fuel swelling is manifested in gap closure.

b. Experimental Fuel Swelling Program

F. E. Panisko, E. T. Weber and J. A. Christensen

This program is to determine the effects of fuel density, temperature, temperature gradient, fission rate, burnup and fuel restraint on the fission

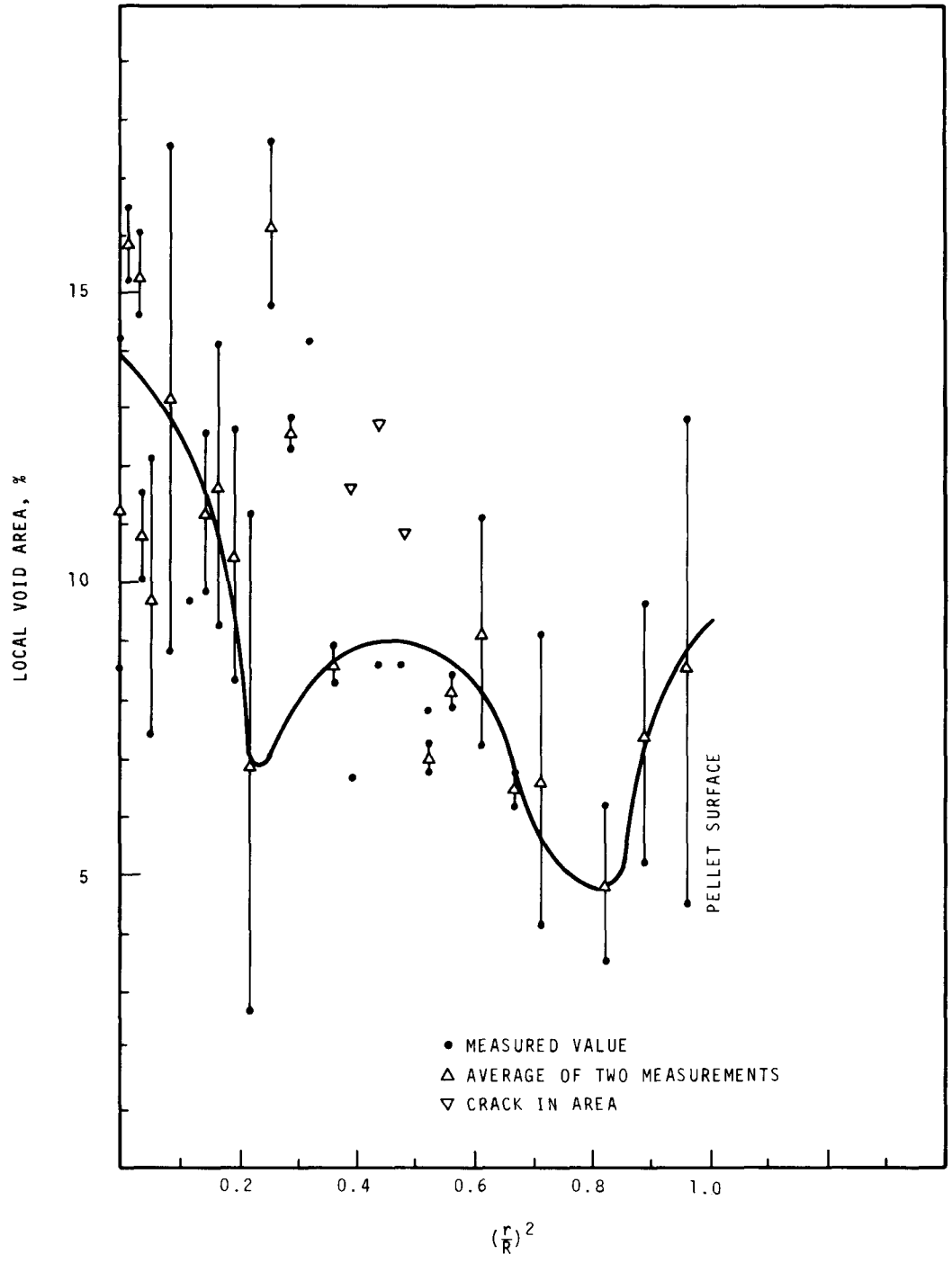

FIGURE VII-41 *Local Pore Area vs $(r/R)^2$ for PNL 2-3G. Calculated Burnup 5.2%, Calculated Power 10.3 kW/ft.*

gas swelling of UO_2 - 25 wt% PuO_2. (12213)

The first capsule was irradiated last quarter. The specimens were recovered intact. Figure VII-42 is a photograph of a 75X mosaic of an isothermal cross-section of one of the irradiated specimens. A statistical determination of the void size distribtuion is in progress using data from both light photomicrographs and from photographs of replicas from the scanning electron microscope. Photographs of replicated, as-polished fuel surface taken at 1500 and 3000X indicate an absence of <1μ diameter pores. Postirradiation examination of the microstructure of this specimen showed neither melting nor significant grain growth. Therefore, the maximum fuel temperature was probably between 1000° and 1600°C. Additional tests are planned.

Figure VII-43 is a photograph of a model of the fuel swelling capsule. The fuel wafers are held in position by molybdenum spacers; stainless steel tubing, 0.005-in. wall, clads the molybdenum rod. This assembly is positioned in a NaK annulus inside the heater. The NaK is pressurized by He gas that compresses a NaK-filled metal bellows. Heat is transferred from the heater and fuel, mainly by conduction through metal fins, to the pressure shell, which conducts heat to the coolant. Figure VII-44 is a photograph of the molybdenum rod and 0.005-in. wall stainless steel clad that was used in the first capsule. Thermocouples are located in grooves in the molybdenum. The fuel compartments have threaded walls to reduce heat transfer.

8. Theoretical Density

D. C. Bullington and D. S. Dutt

An empirical expression was developed and programmed (12163 FA-E) for use on the WANG calculator for caluclating the theoretical density of mixed oxide fuel as a function of stoichiometry, weight percent uranium and plutonium and isotopic content of heavy metal. The density (δ) in grams/cm^3 is

$$\delta = K[5.8755 + 0.497Q + 2.54\$]$$

FIGURE VII-42 *Mosiac of an Isothermal Cross Section of an Irradiated Specimen.*

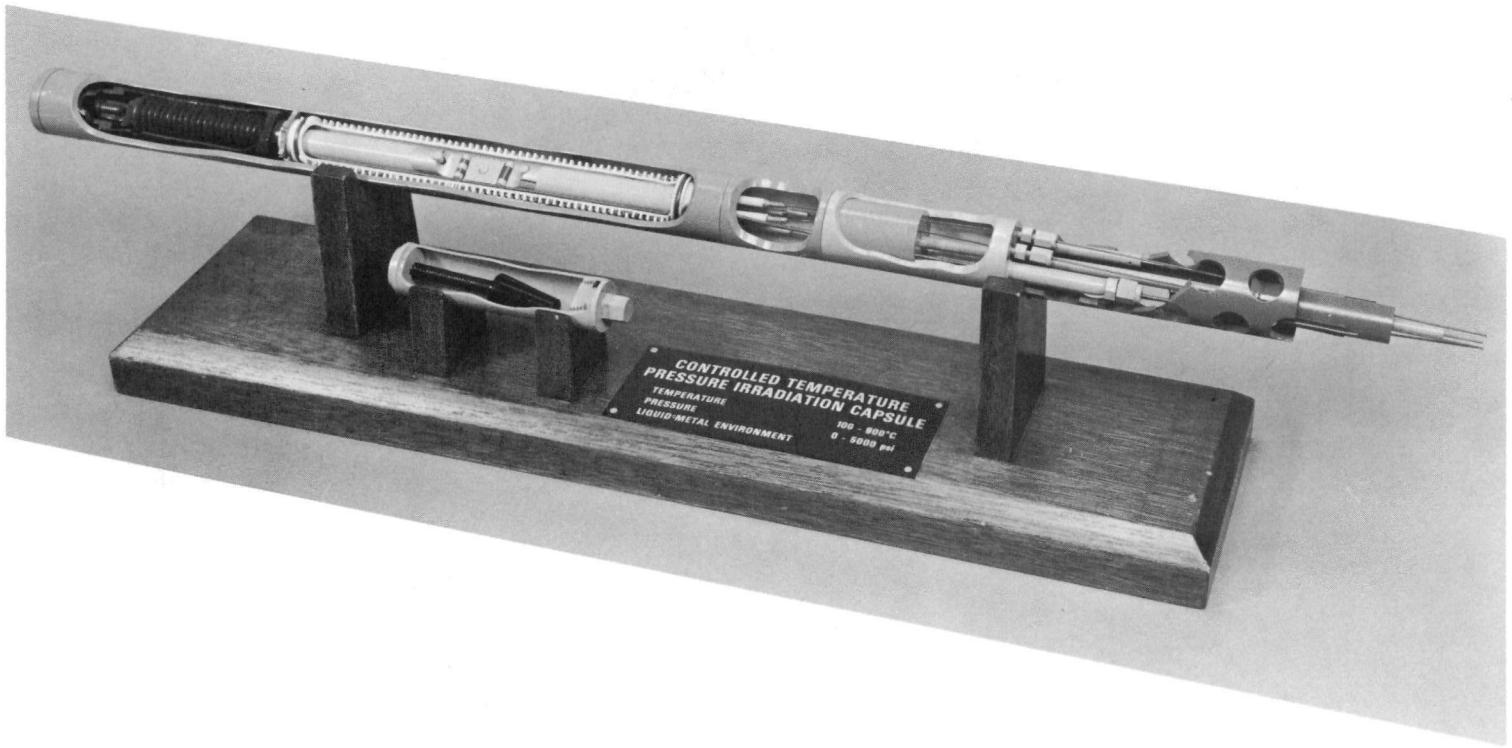

FIGURE VII-43 *Model of the Fuel Swelling Capsule.*

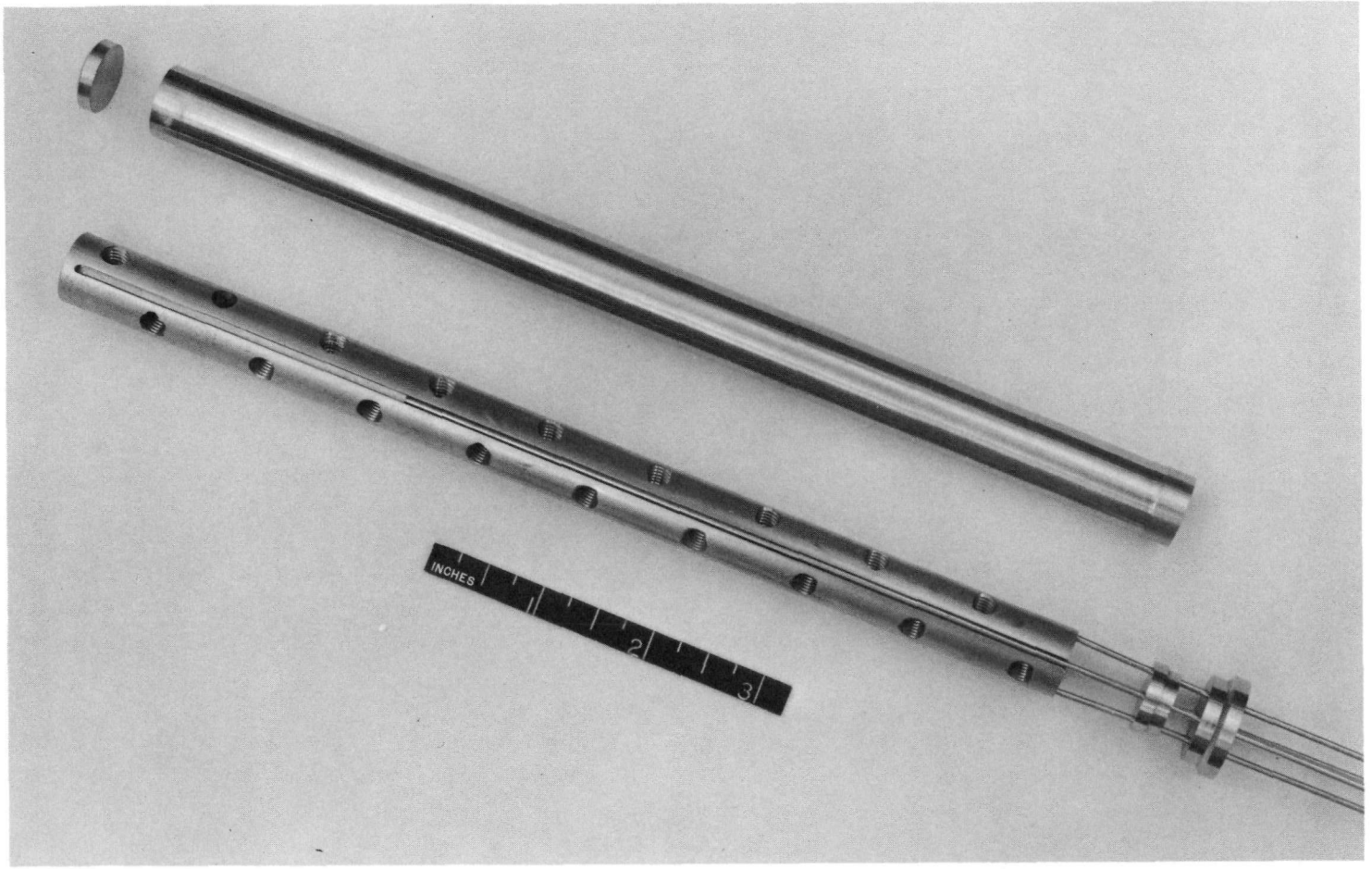

FIGURE VII-44 *Molybdenum Rod and 0.005-in. Wall Stainless Steel Clad.*

where

Q = w% plutonia (15-30)

Q = A/(A+B)

where

A = w% plutonium

B = w% uranium

K = isotopic ratio

K = (M+N) 237.98

$ = stoichiometry (1.95 to 2.00)

where

$$M = \frac{(1-Q)}{100} [234W + 235X + 236Y + 238Z]$$

$$N = \frac{Q}{100} [238E + 239F + 240G + 241H + 242J]$$

where W,X,Y,Z = uranium isotopic weight percent 234, 235, 236 and 238 and E,F,G,H,J = plutonium isotopic weight percent 238, 239, 240, 241 and 242

This computer code has been used to calculate the theoretical density of the fuel used in the 37 pin assemblies PNL 3, 4, and 5 for inclusion in the data storage and retrieval center.

C. IRRADIATION EFFECTS IN STAINLESS STEEL

1. Tensile Studies

A. L. Ward and J. J. Holmes (12215, 12186)

This program will provide mechanical property and metallurgical stability data for candidate LMFBR vessel and structural materials, particularly those selected for the FFTF. The data provide assurance of adequate lifetime performance under anticipated FTR service conditions.

A system for predicting tensile properties using fast reactor-induced swelling data is being developed for annealed 304 and 316 stainless steels. Dislocation theory predicts that the change in yield strength caused by voids in a metal should follow the relationship,

$$\Delta\sigma = \frac{2Gb}{\ell}$$

where $\Delta\sigma$ is the change in yield strength, G is the shear modulus, b is the Burgers vector and ℓ is the planar spacing between voids. If ℓ is taken as $(ND)^{-1/2}$, where N is the volumetric void number density and D the average void diameter, the change in stress becomes,

$$\Delta\sigma = \frac{K(\Delta V/V)^{1/2}}{D}$$

where K is a constant and $(\Delta V/V)$ is the volume change. The terms $\Delta V/V$ and D have been described in terms of fluence and irradiation temperature using empirical models at HEDL. Since changes in strength are related to $\Delta V/V$ and D, the swelling and void diameter equations can be used to calculate changes in strength due to irradiation.

Tensile flow stresses for annealed AISI Types 304 and 316 SS, representing irradiation and test temperatures ranging from 371 to 482°C (700 to 900°F) and fluences from 0.4 to 3.7 x 10^{22} n/cm^2 (E> 0.1 MeV), were plotted as a function of the parameter, $P = (\Delta V/V)^{1/2} D^{-1}$. The results of these correlations, obtained from a computerized least-squares curve fitting technique, are summarized in Figure VII-45. Consistent with the theory, the data were fitted to linear expressions with the results shown

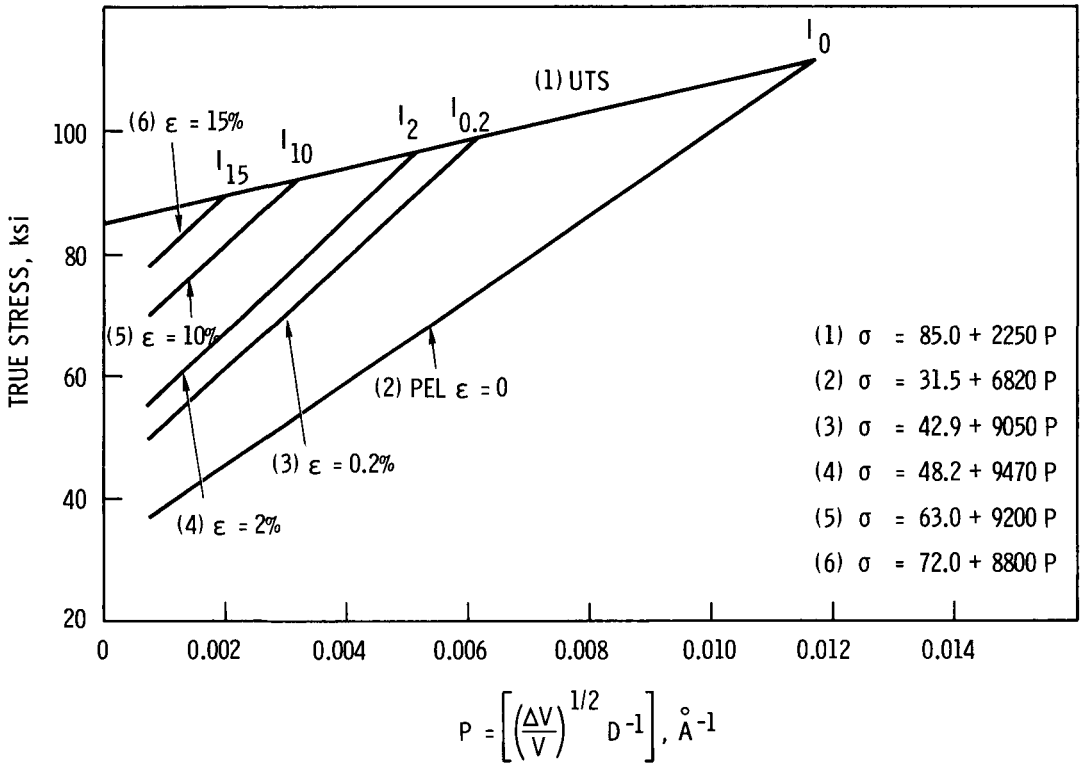

FIGURE VII-45 *Correlation of Tensile Stresses with a Structural Parameter for Various Plastic Strain Increments.*

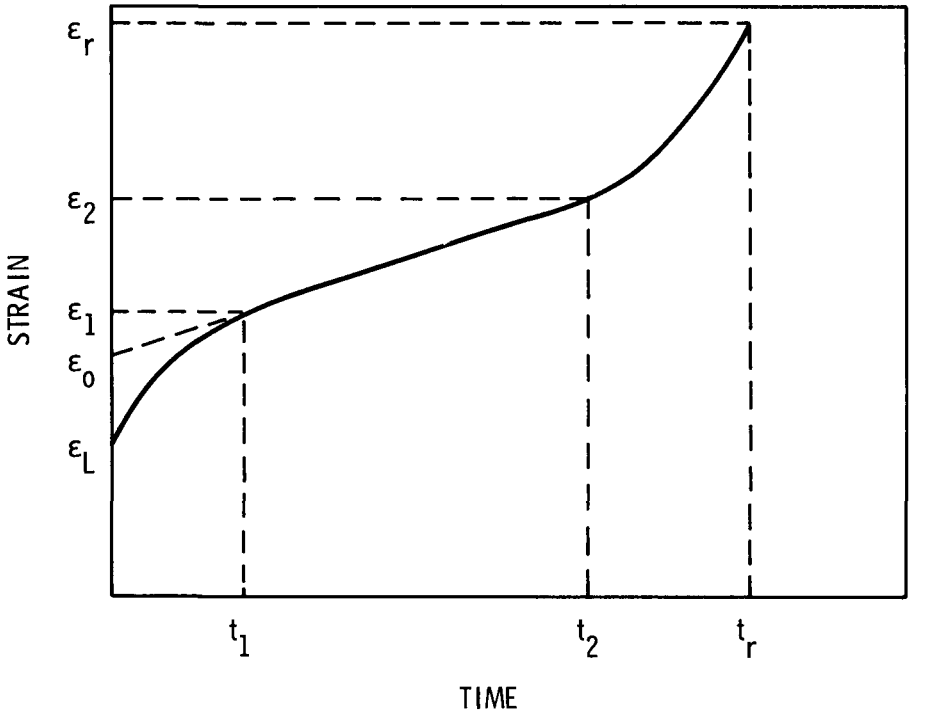

FIGURE VII-46 · *Schematic Diagram of Creep Curve.*

by equations (1) through (6) (Figure VII-45). These equations give the flow stress as a function of P for a variety of strain values. Intersections of the lines represented by equations (2) through (6) with that of equation (1) identify values of strain and P associated with the onset of plastic instability. For example, simultaneous solution of equations (1) and (2) yields a value of $P = I_{\varepsilon=0}$ [$I_{\varepsilon=0}$ = value of P corresponding to the intersection of (1) and (2)] such that when $P \geq I_{\varepsilon=0}$ no uniform plastic flow can occur; that is, the proportional elastic limit and the UTS coincide.

The primary significance of these results lies in the ability to use previously developed empirical equations for volume change and void diameter to map these parameters (I_ε) into a fluence-temperature plane. The result of such a mapping can be expressed as:

$$(\phi t) = \exp\left[\frac{\ell n\, I\varepsilon - \ell n\, [(T-40)^{1/2} \times 10^{-5}] - 8.81 + 0.0075T + 850/T}{0.875 - 13.5/\Theta + 63/\Theta^2}\right]$$

where t = neutron fluence, 10^{22} n/cm^2 (E > 0.1 MeV)

T = temperature, °K

$\Theta = T-623$

The above equation may be used to estimate the fluence beyond which uniform plastic flow greater than ε cannot occur in annealed Types 304 and 316 SS in the range from 700 to 900°F. Further, once the correlations are established for a series of strain increments, it is a simple exercise to construct a stress-strain diagram based upon any selected fluence and temperature utilizing a P value calculated from empirical or theoretical swelling equations.

This analysis is as yet not fully refined, and is limited by material scatter and uncertainty in fluence and irradiation temperature. However, the technique appears capable of predicting the shape of the stress-strain curve up to the point of plastic instability at any fluence in the 700 to 900°F range where swelling data exist, and may be capable of utilizing

extrapolated swelling data to calculate tensile data where actual tensile data do not exist. Further development of this method of data analysis is in progress.

2. Creep Studies

a. Effect of Prior Creep Deformation on the Residual Tensile Properties of Unirradiated Austenitic Stainless Steels

A. J. Lovell, L. D. Blackburn and J. J. Holmes (12215, 12186)

A current FFTF design criterion requires that heavy section SS components, such as the vessel, core barrel, and core support structure, retain a residual tensile elongation of at least 10% at end of life. With an FTR bulk sodium outlet temperature of 1100°F, heavy section components may operate in the 1000 to 1050°F range. At these temperatures, creep deformation of stressed components can occur. It is, therefore, necessary to assure that creep deformation does not produce some form of damage which results in low residual tensile elongation that could limit design or operation of FTR components. To study this problem, a number of creep tests on unirradiated, annealed Type 304 and Type 316 SS were interrupted prior to rupture, and the specimens were then tensile tested at elevated temperatures to determine the residual tensile properties.

Experimental Results.- A schematic creep curve is shown in Figure VII-46. The total deformation in a creep test is composed of the time-independent elastic plus plastic loading strain, ε_L, and the time-dependent creep strain obtained in primary, secondary, and tertiary creep stages. Results from creep-rupture tests on both the Type 304 and Type 316 SS show that the creep strain at rupture, $\varepsilon_r - \varepsilon_L$, is essentially independent of stress and rupture life in the temperature range of 1000 to 1200°F. Values of creep strain at rupture are presented in Table VII-13.

For both materials, rupture strains are low at 1000°F, but increase significantly at higher temperatures.

The tensile properties of annealed and of aged SS determined at a crosshead speed of 0.002 in./min (specimen gage length 1.125 in.) are

TABLE VII-13
CREEP STRAIN AT RUPTURE FOR AUSTENITIC SS

Material	Test Temperature (°F)	Creep Strain at Rupture ($\varepsilon_r - \varepsilon_L$, %)
304	1000	5 ± 2
	1100	13 ± 3
	1200	33 ± 5
316	1000	5 ± 1
	1100	13 ± 3
	1200	44 ± 5

presented in Table VII-14. Thermal aging in the absence of an applied stress does not reduce the total elongation; in fact, aging at 1200°F significantly increases tensile elongation.

Tensile properties of specimens subjected to prior creep deformation are presented in Table VII-15. Stresses and elongations were calculated using the original specimen dimensions prior to any creep deformation. A set of stress-strain curves for annealed, aged, and creep tested Type 316 SS at 1100°F are shown in Figure VII-47. Curves for creep-tested specimens are offset on the strain axis by the total elongation, ε, accumulated in the creep test. In this figure, then, the elongation at fracture represents the total deformation of the specimen, i.e., the creep test loading strain, ε_L, the time-dependent creep strain, $\varepsilon-\varepsilon_L$, and the residual tensile strain, ε_R. These curves show quite graphically that the sum of the creep elongation and the residual tensile elongation is significantly less than the original tensile elongation. The reduction in elongation becomes larger the greater the creep strain. Comparisons of stress-strain curves for other test temperatures and for Type 304 SS were

TABLE VII-14
TENSILE PROPERTIES OF SS AFTER CREEP DEFORMATION

Creep Test Conditions						Tensile Properties					
Temp (°F)	Stress (1000 psi)	Duration (hr)	Creep Stage	Creep Strain (%)	Total Strain (%)	Temp (°F)	PEL (1000 psi)	0.2% Yield Strength (1000 psi)	Ultimate Strength (1000 psi)	Uniform Elongation (%)	Total Elongation (%)
304 SS											
1100	20	1180	2nd	3.2	3.6	1100	19.8	25.7	43.9	18.7	26.2
1100	22	1300	3rd	5.3	6.0	1100		~28.6	~43.0	~16.1	~23.0
1200	14	1000	2nd	7.2	7.2	1200	19.4	24.4	31.5	8.1	37.2
1000	30	286	2nd	2.3	4.4	1000	30.9	33.3	53.5	20.3	24.6
316 SS											
1000	36	9500	2nd	2.9	7.2	1000	39.6	40.7	55.8	11.6	12.6
1000	32	2200	1st or 2nd	~0.6	6.1	1000	28.9	34.7	61.2	30.8	35.4
1100	30	3900	3rd	6.8	10.9	1100	39.1	39.5	51.3	8.4	12.3
1100	26	5000	2nd	2.6	6.7	1100	32.2	37.6	53.3	12.4	27.2
1100	26	1500	2nd	2.6	5.4	1100	29.4	36.1	53.4	14.7	32.0

TABLE VII-15
TENSILE PROPERTIES OF ANNEALED AND AGED SS

Material	Condition	Test Temp (°F)	PEL (1000 psi)	0.2% Yield Strength (1000 psi)	Ultimate Strength (1000 psi)	Uniform Elongation (%)	Total Elongation (%)	Site Sequence Number
304 SS	Annealed	1000	10.7	14.8	54.0	32.0	35.3	H07598
	Annealed	"	7.3	17.1	54.2	32.6	37.1	H06223
	Annealed	"	8.1	17.9	56.9	31.4	38.7	H06224
	Aged 800°F*	"	13.5	17.7	53.3	29.1	34.4	H07417
	Aged 900°F	"	11.1	16.9	52.4	34.7	39.6	H06721
	Aged 1000°F	"	15.5	19.4	59.5	27.6	34.5	H07405
	Annealed	1100	7.3	15.0	45.7	27.7	33.3	H06225
	Aged 800°F	"	13.0	18.4	45.5	22.7	29.5	H07418
	Aged 900°F	"	14.9	18.4	43.6	25.7	36.0	H06719
	Aged 1100°F	"	10.8	19.4	43.5	22.8	37.6	H07455
	Annealed	1200	9.8	13.7	32.9	18.9	34.5	H07599
	Annealed	"	8.5	16.8	35.4	18.0	24.4	H06226
	Aged 800°F	"	10.7	14.4	32.8	18.6	35.2	H07419
	Aged 900°F	"	10.2	17.0	33.6	20.9	35.7	H06720
	Aged 1200°F	"	11.4	18.0	33.6	15.9	50.0	H07466
316 SS	Annealed	1000	14.3	18.8	67.2	39.8	44.3	H07135
	Annealed	"	13.4	18.8	67.7	36.3	43.7	H07136
	Annealed	"	11.8	15.5	66.0	40.1	45.9	H07146
	Annealed	"	11.5	16.2	66.3	41.3	49.7	H07147
	Annealed	"	11.8	18.3	63.7	43.7	47.2	H06880
	Aged 800°F*	"	13.5	17.1	65.6	38.8	45.3	H07047
	Aged 1000°F	"	12.8	17.6	68.4	40.0	48.7	H07059
	Annealed	1100	9.2	16.2	54.6	30.4	42.3	H07186
	Annealed	"	12.2	17.1	51.7	27.3	36.8	H06881
	Aged 800°F	"	13.0	16.8	57.0	29.4	37.5	H07048
	Aged 1100°F	"	12.7	19.0	54.9	29.6	48.4	H07103
	Annealed	1200	13.5	17.2	43.5	21.3	39.4	H07148
	Annealed	"	12.3	15.7	43.7	22.2	41.2	H07149
	Annealed	"	13.3	17.2	43.7	20.9	34.0	H06882
	Annealed	"	17.5	20.7	45.2	22.6	41.1	H07137
	Annealed	"	12.6	18.7	45.0	20.0	37.8	H07138
	Annealed	"	13.3	19.5	46.3	23.1	49.3	H07139
	Aged 800°F	"	12.1	18.4	41.9	22.2	56.4	H07049
	Aged 1200°F	"	11.2	17.6	41.3	19.6	62.9	H07116

*All aging for 3050 hr

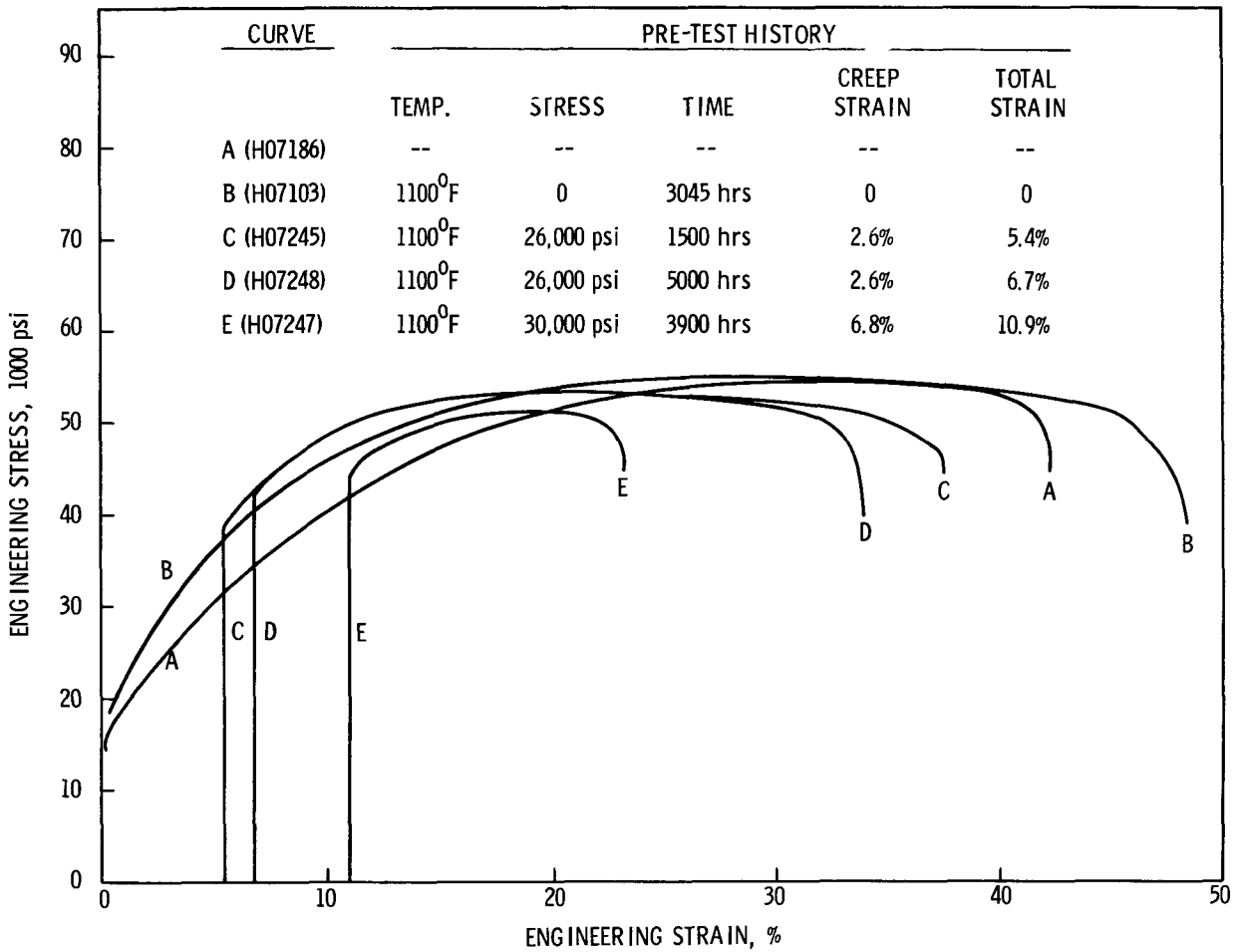

FIGURE VII-47 *Stress-Strain Curves For 316 Stainless Steel at 1100°F After Prior Creep Deformation.*

quite similar to that shown in Figure VII-47.

A correlation between creep strain and residual tensile elongation is shown in Figures VII-48 and VII-49 for Type 304 and Type 316 SS, respectively. In these figures, the point plotted at zero creep strain is the average tensile elongation in the absence of any creep deformation obtained from Table VII-14. The point plotted at zero residual tensile elongation is the creep strain at fracture obtained from Table VII-13. When the data from creep tested specimens are then included in the figures, it appears that there is a linear relationship of residual tensile elongation to creep strain between the two end points.

It is interesting to note that the data at 1200°F for Type 304 SS appears to reflect the increased tensile elongation resulting from thermal aging at this temperature. Although the data for Type 316 SS in Figure VII-49 are near the lower side of the band, note that these specimens were subjected to somewhat larger creep loading strains than were the Type 304 SS specimens. If creep deformation were introduced at lower stresses, where loading strains are smaller, slightly higher residual tensile elongation values might be obtained.

Discussion.- The present data show clearly that prior creep deformation can significantly reduce the residual tensile elongation of Type 304 and Type 316 SS. This effect must now be considered in terms of the 10% residual elongation limit for FTR components to see whether it has any impact on FTR design or operation. Since heavy section stainless steel components will be made of Type 304 SS, the following discussion will focus on this alloy.

The amount of creep strain required to reduce the residual tensile elongation to the 10% level was determined from the linear relationships in Figures VII-48 and VII-49, and this value is plotted against temperature in Figure VII-50. This limiting creep strain value increases from about 4% at 1000°F to about 9% at 1100°F and then to values above 20% at 1200°F. It is unlikely that heavy section FTR components will be designed to allow as much as 9% creep strain during operation. Therefore, the creep

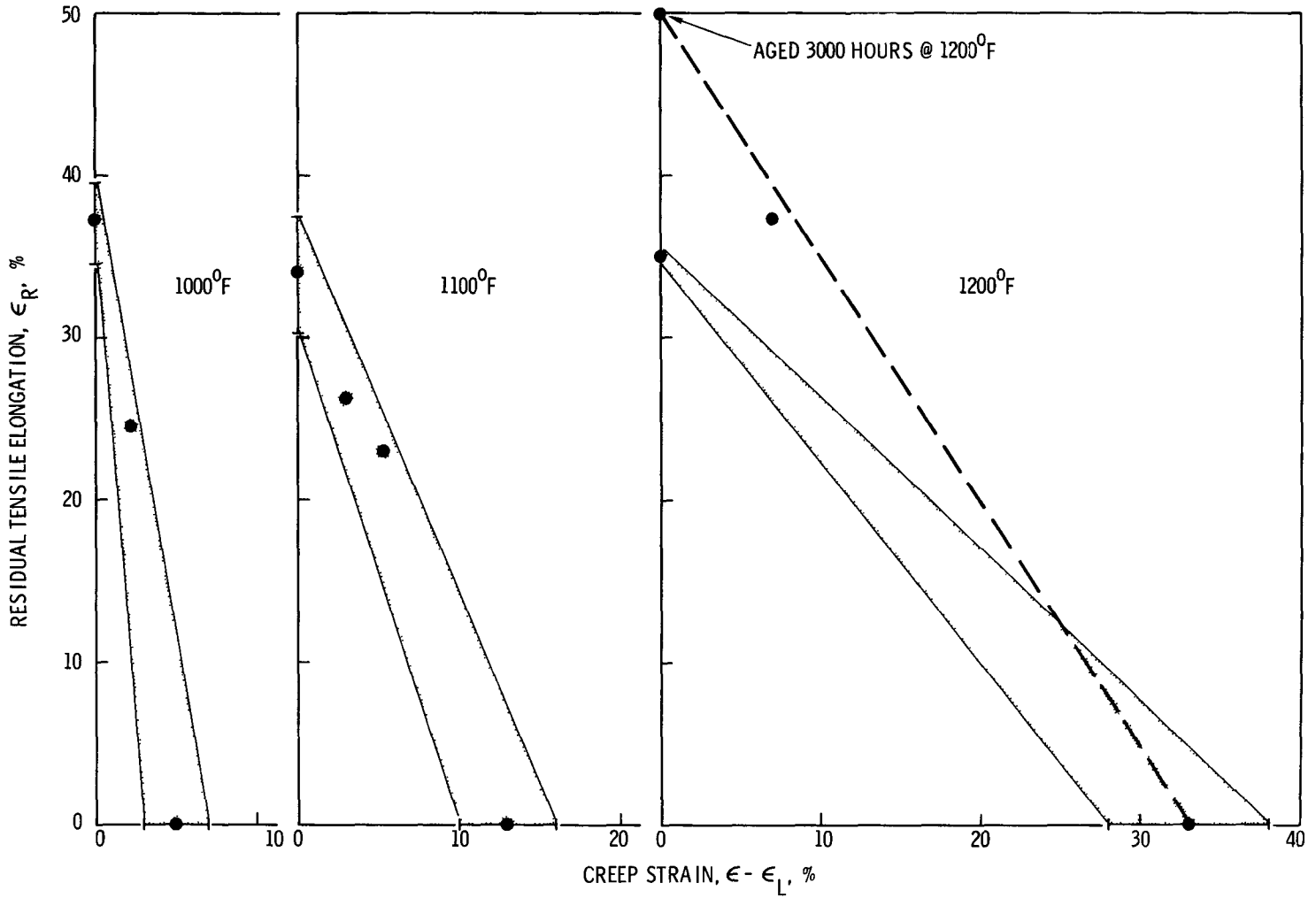

FIGURE VII-48 *Effect of Prior Creep Deformation on The Residual Tensile Elongation Of Type 304 Stainless Steel.*

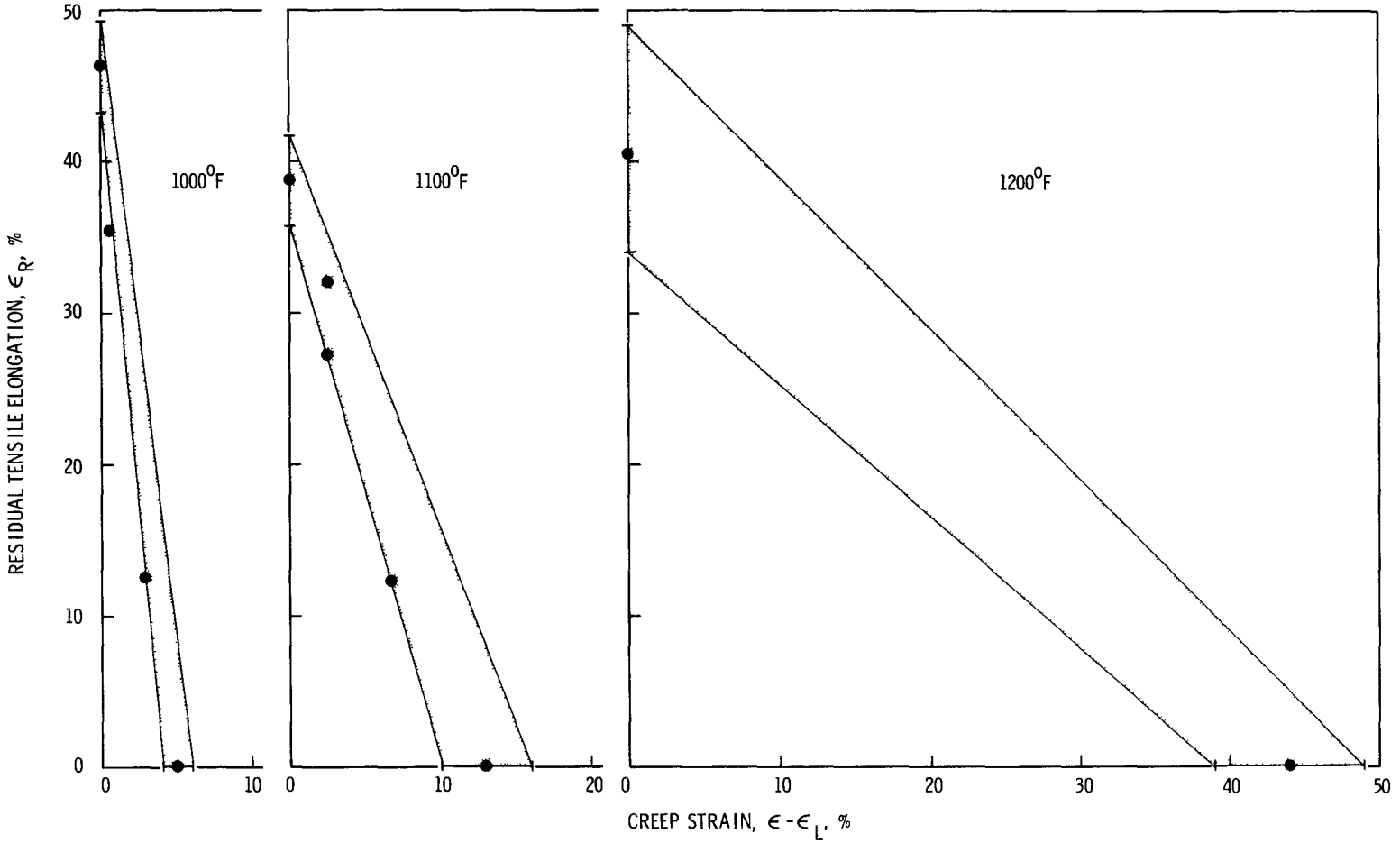

FIGURE VII-49 *Effect of Prior Creep Deformation on the Residual Tensile Elongation Of Type 316 Stainless Steel.*

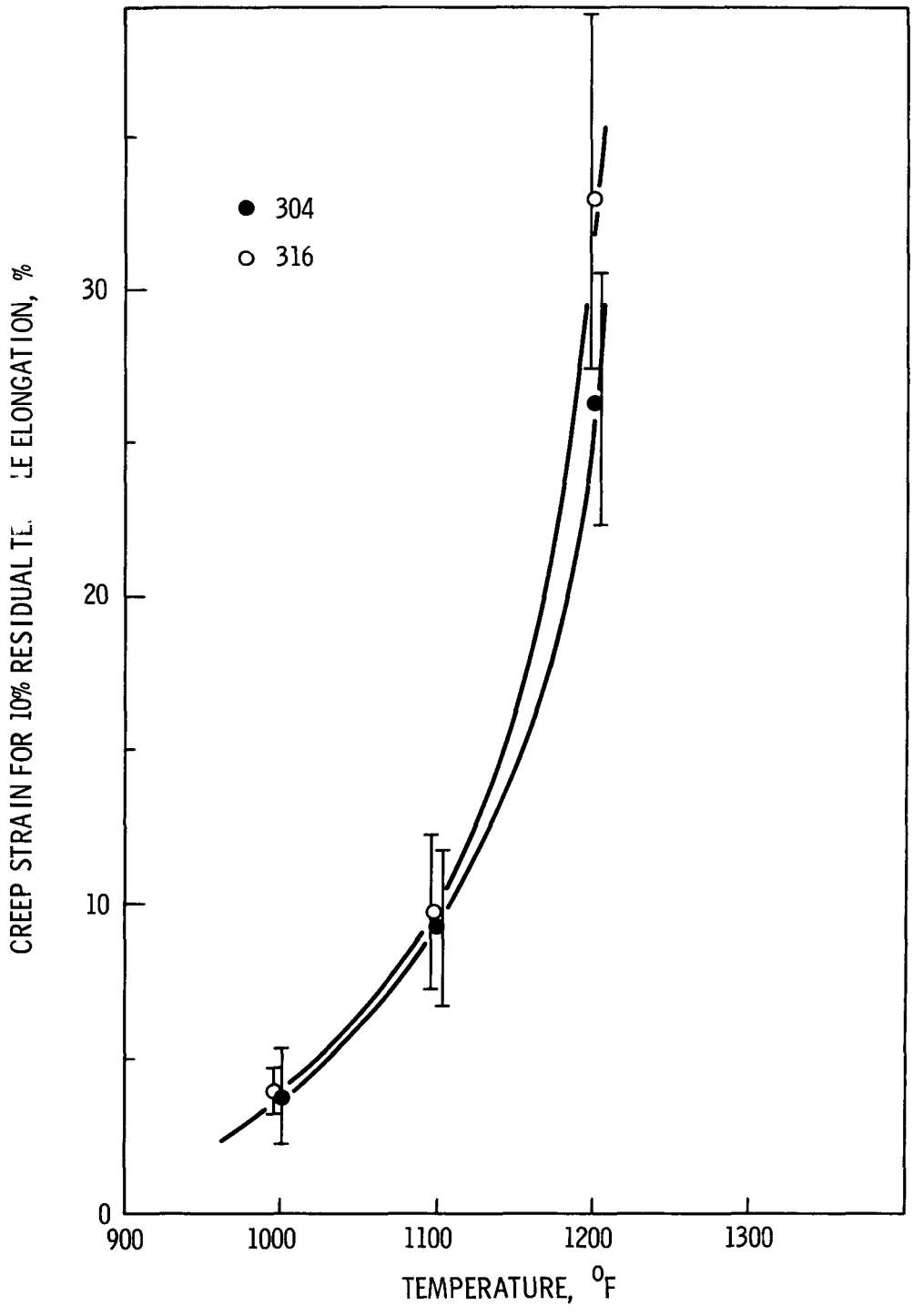

FIGURE VII-50 *Temperature Dependence of Creep Strain Required to Reduce Residual Tensile Elongation to 10% level.*

damage effect does not appear to be a significant factor at temperatures of 1100°F and higher. However, it is necessary to consider creep behavior at 1000°F in more detail, since only 4% creep strain will reduce residual tensile elongation to the 10% level.

Results determined from creep-rupture tests of the Type 304 SS show that the creep strain at the end of second-stage creep, $\varepsilon_2 - \varepsilon_L$, is about 4%, and is essentially independent of stress. The time to the end of second-stage creep was then plotted against stress and extrapolated to 150,000 hr, (20 years of FTR operation at 75% plant factor) yielding a stress value of 22,000 psi to produce 4% creep strain in 150,000 hr. The design stress intensity for Type 304 SS at 1000°F (from Section VIII of the ASME Boiler and Pressure Vessel Code) is 12,500 psi. Therefore, times far in excess of the projected FTR lifetime would be required to reach 4% creep strain, and thus 10% residual tensile elongation, in Type 304 SS using current allowable stress values.

It must be emphasized that this analysis applies to unirradiated material. Both the original tensile elongation and the creep strain at rupture can be reduced after irradiation; therefore, the creep strain limits may be much smaller if irradiated steels are found to be susceptible to creep damage.

The basic causes leading to the creep damage effect have not yet been investigated. However, since the tensile flow stress curves for creep-tested specimens closely approximate those for aged, undeformed specimens, it is unlikely that the loss in ductility can be attributed to a strengthening effect resulting from a strain aging process. It is possible that creep damage is related to the wedge-type intergranular cracks which form during creep at low test temperatures (i.e., 1000 and 1100°F), and then act to reduce the residual tensile elongation.

Although creep damage can occur in austenitic stainless steels at operating temperatures of FTR components, the use of current design allowable stresses appears to be acceptable for maintaining at least 10% residual tensile elongation in unirradiated material at end of life. Further

study of irradiated materials is required to fully define the importance of creep damage effects in FTR components.

b. Unirradiated 20% Cold-Worked 316 SS

M. M. Paxton and J. J. Holmes

The pre-irradiation characterization of creep-rupture properties of 20% cold-worked 316 SS from Heat No. 87210 is continuing. The fabrication schedule and chemical analysis, for the portion of the heat used to obtain 0.270-in. diameter rod with nominally 20% cold work, are shown in Table VII-16. The microstructures before and after the final pass are shown in Figure VII-51. The updated tabulation of the data is shown in Table VII-17. The effect of stress and temperature on the rupture life is shown in igure VII-52. The lines through the data at a given temperature are tending to curve on the log-log plot. It is apparent that some recovery is taking place in the material at longer test times. The same tendency is apparent in Figure VII-53, which shows the effect of stress and temperature on the minimum creep rate.

Creep tests on this material depart significantly in form from normal creep curves. Very short primary and secondary stages are observed, with the majority of the creep strain being accumulated in third stage. An example of the creep curve from the FFTF heat of Type 316 SS is compared to a creep curve from Progrow heat Type 316 SS in Figure VII-54. Usually third stage creep is associated with the onset of failure either by plastic instability or by grain boundary cracking. The very long third stage in this material suggests that failure processes are not occurring; rather, the material is becoming less resistant to creep with increasing test time. This effect could arise from recovery of the 20% cold work during testing.

The nature of the extended third-stage creep is being clarified. Post-test metallographic examination of failed specimens from each test temperature and varying stresses are in progress. Preliminary examination

TABLE VII-16
FABRICATION SCHEDULE AND CHEMICAL ANALYSIS OF BAR 53, HEAT NO. 87210

Fabrication Schedule		
1.187 → 1.050 → 0.950 22% 18%	36% Cold-Work Anneal	1925°F/15 min
0.950 → 0.850 → 0.800 → 0.750 19.8% 11.5% 12.2%	37.7 Cold-Work Anneal	1925°F/15 min
0.750 → 0.680 → 0.634 → 0.600 17.8% 13.2% 11.25%	36% Cold-Work Anneal	1925°F/15 min
0.600 → 0.540 → 0.500 → 0.470 18.8% 14.4% 11.6%	38.6% Cold-Work Anneal	1925°F/15 min
0.470 → 0.420 → 0.390 → 0.370 20.4% 13.6% 9.9%	38% Cold-Work Anneal	1925°F/15 min
0.370 → 0.340 → 0.320 → 0.300 16% 11.3% 11.8%	34.4% Cold-Work Anneal	1925°F/15 min
0.300 → 0.270 = 18.9% Reduction in Area		

Chemical Analysis Report*

Element	wt(%)	Element	wt(%)
C	0.055	Ni	13.50
Mn	1.49	Cr	16.57
P	0.013	Mo	2.45
S	0.007	Ni	0.011
Si	0.51	B	0.0005
Cu	0.009	Co	0.07

*Lukens Steel Company

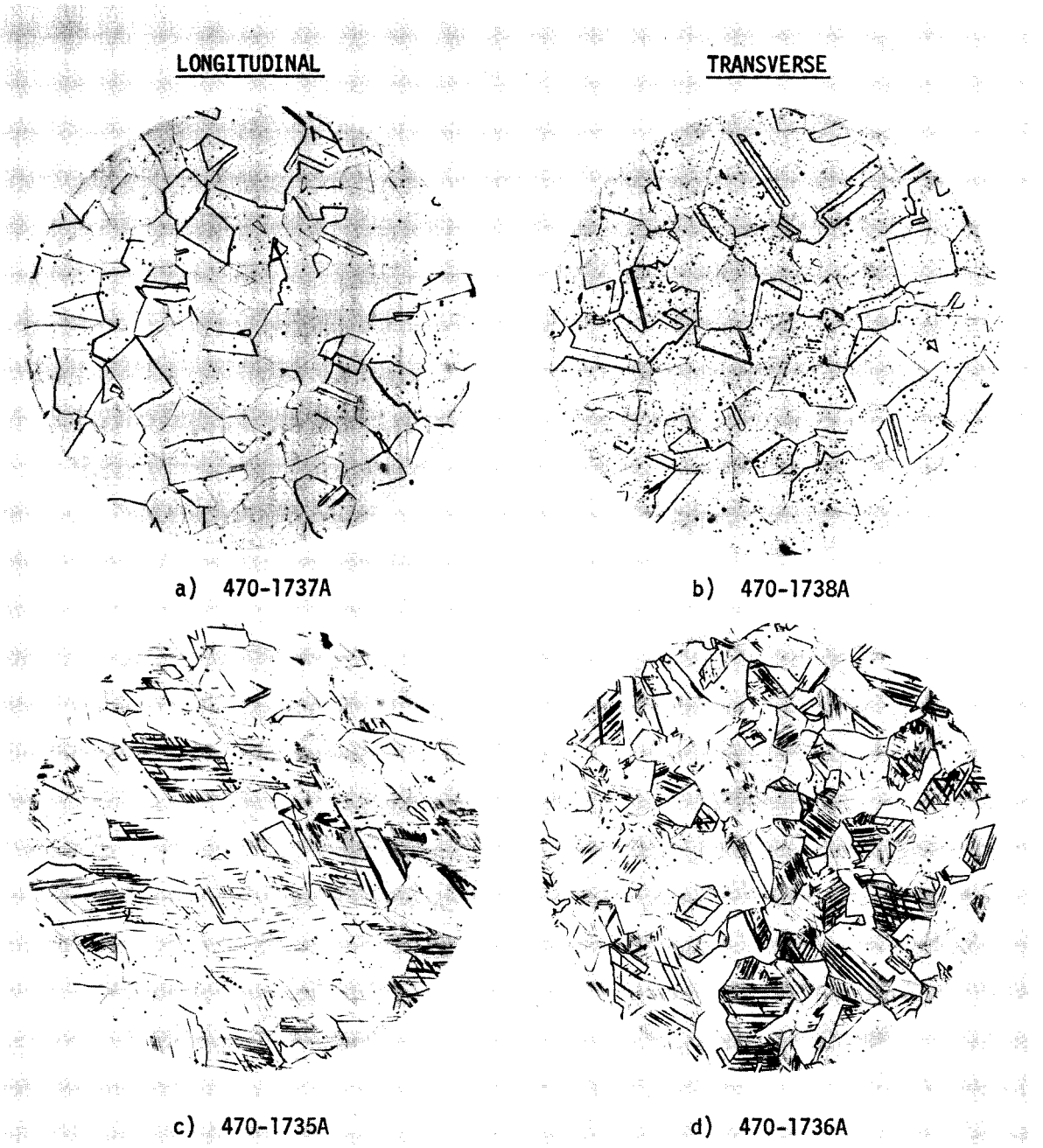

FIGURE VII-51 *Microstructure of 316 Stainless Steel, Heat No. 87210. 250X*

a) Longitudinal section before final draw.
b) Transverse section before final draw.
c) Longitudinal section after final draw, ∿20% cold-worked.
d) Transverse section after final draw, ∿20% cold-worked.

TABLE VII-17
CREEP AND CREEP-RUPTURE RESULTS FOR 20% COLD-WORKED 316 SS

Temperature (°F)	Stress (psi)	Minimum Creep Rate (10^{-7}% hr)	Rupture Time (hr)	Total Elongation (%)
1000	70,000	20.8	353.0	10
	65,000	2.36	630.5	11
	60,000	0.96	1316.5	8
	50,000	0.38	Stopped at 985 hrs	--
1100	63,000	4620	4.5	21
	60,000	566	11.1	21
	57,000	198	26.5	19
	55,000	100	46.4	16
	50,000	45	96.6	26
	45,000	21.4	196.4	25
	40,000	5.37	939.4	18
	36,000	6.14	950.3	21
1200	45,000	1960	4.45	30
	40,000	170	26.8	29
	35,000	106	79.8	31
	30,000	21.5	364.6	30
	25,000	3.8	On Test	--
1400	30,000	12600	0.8	37
	25,000	2520	4.0	36
	20,000	539	15.8	40
	17,000	44.5	92.0	17
	15,000	18.8	188.5	11
	11,000	7.6	549.9	15

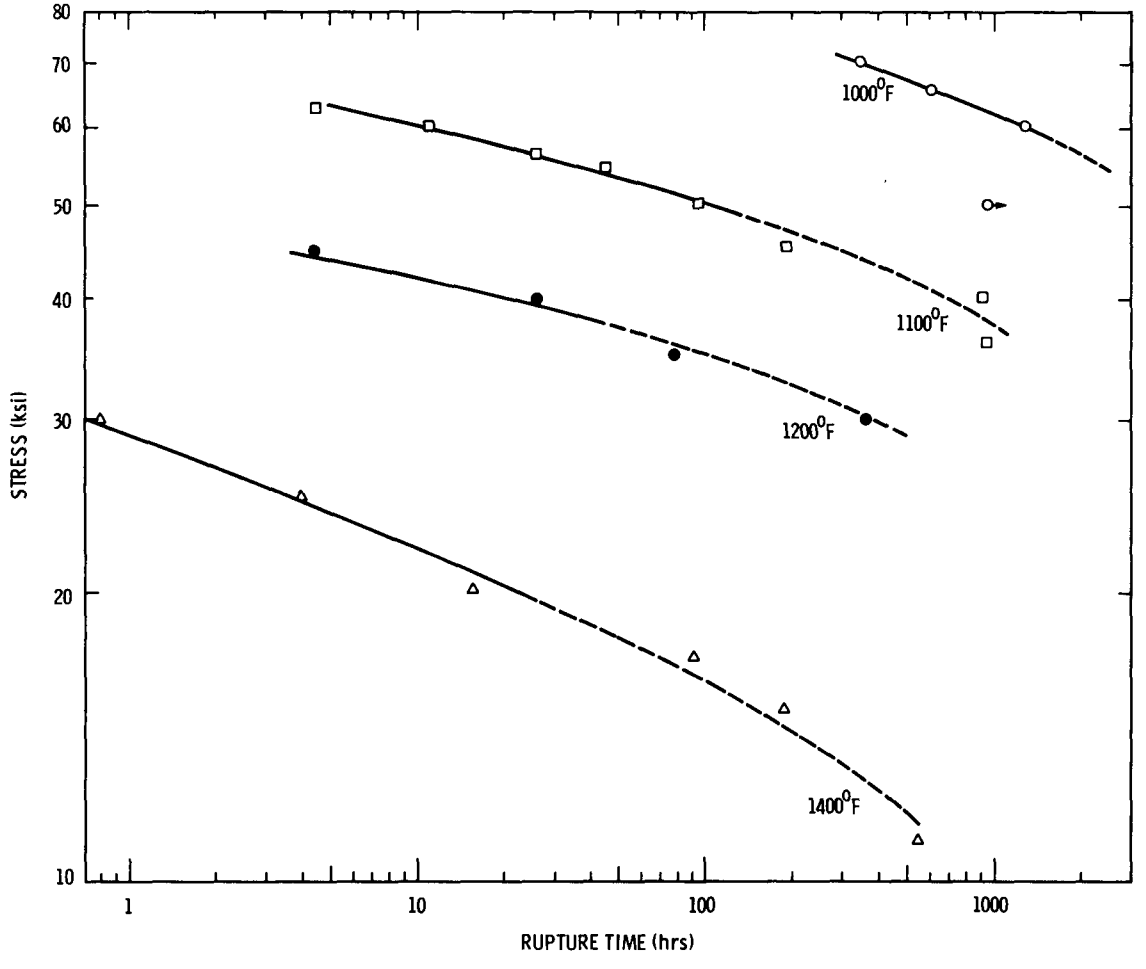

FIGURE VII-52 *Effect of Stress and Temperature on the Rupture Life of 20% Cold Worked 316 Stainless Steel (FFTF Heat 87210 Rod 53)*

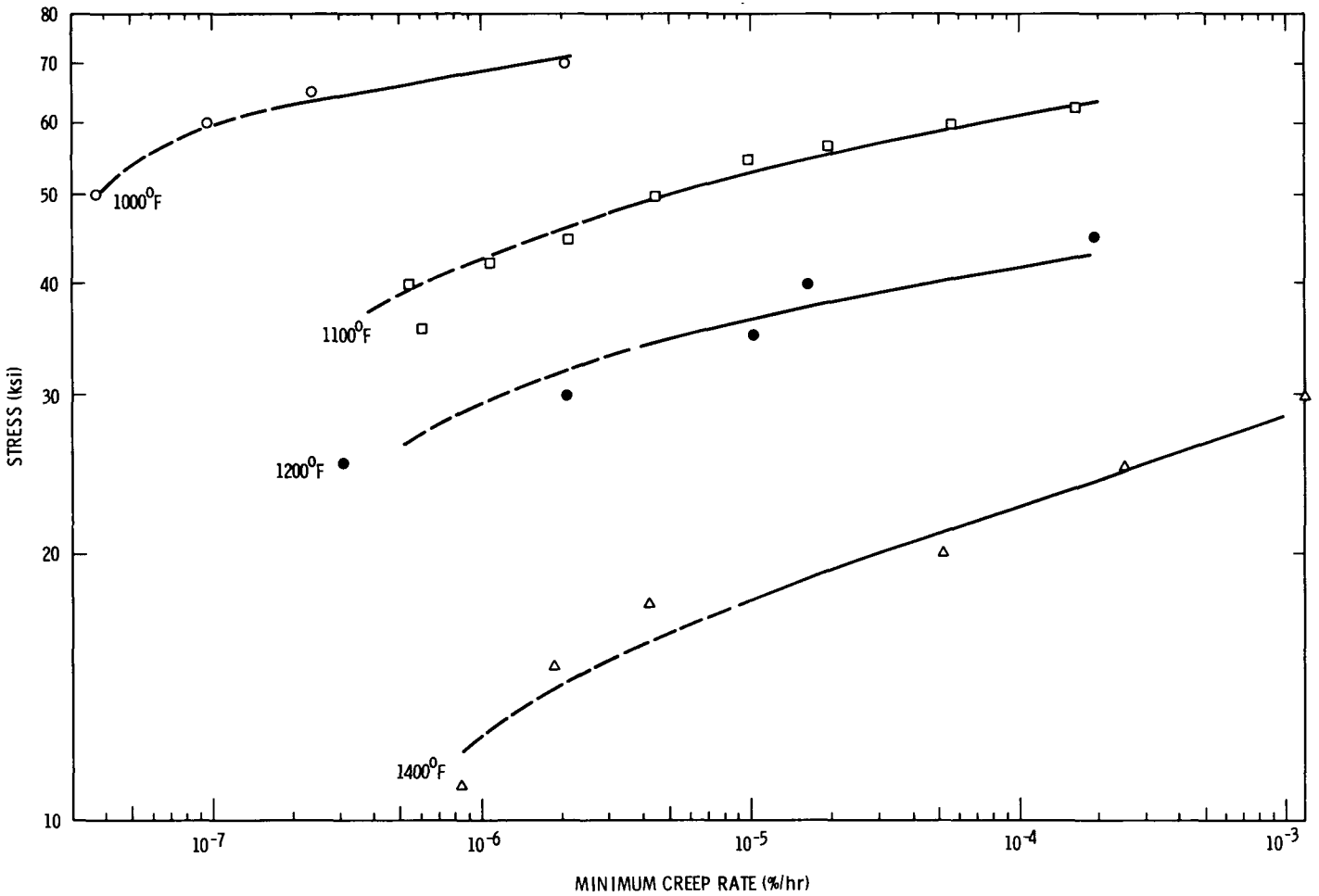

FIGURE VII-53 *Effect of Stress and Temperature on the Minimum Creep Rate of 20% Cold Worked 316 Stainless Steel (FFTF Heat 87210 Rod 53).*

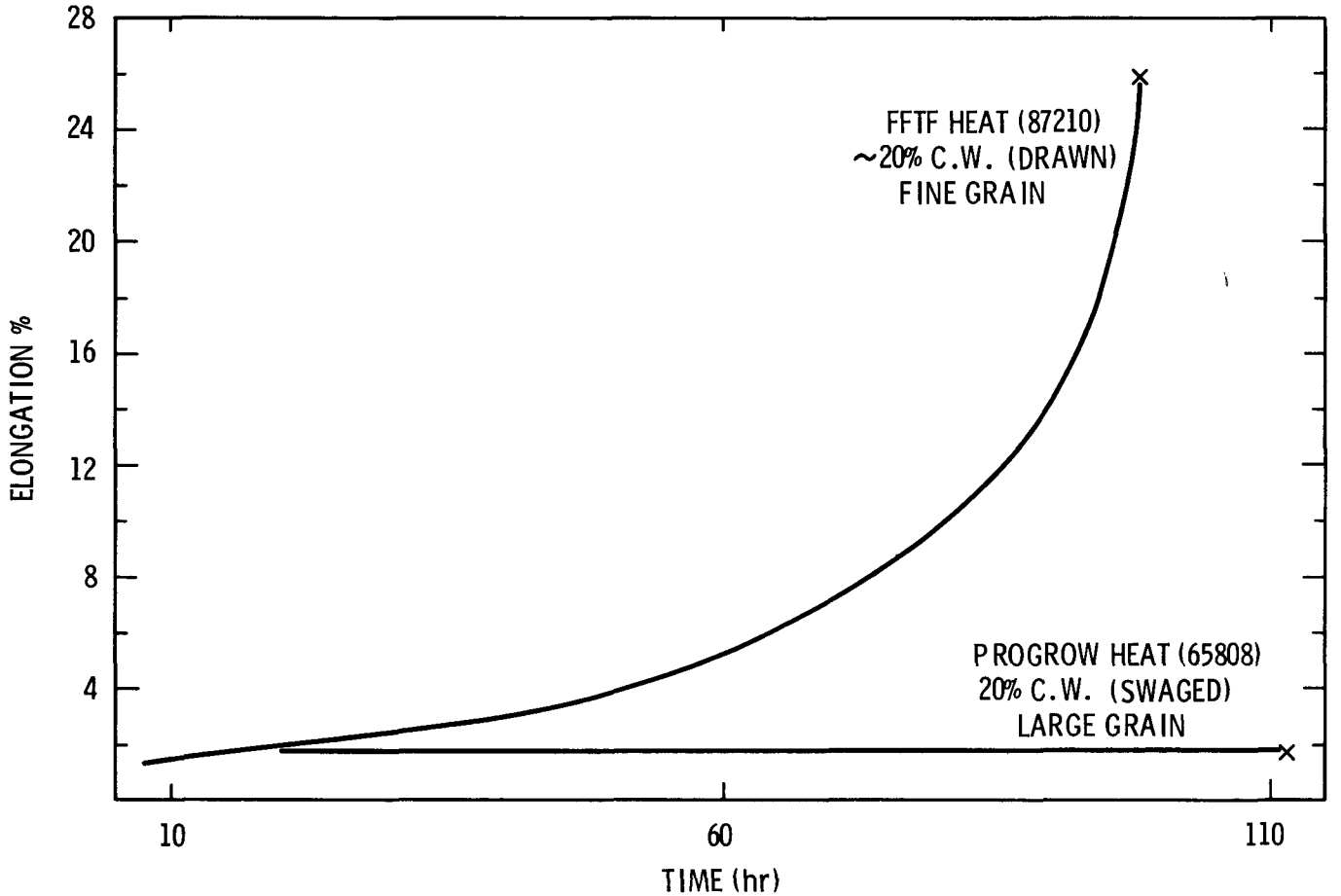

FIGURE VII-54 *Effect of Heat and Fabrication Variation On The Creep Curves of 20% Cold Worked 316 Stainless Steel (Tests at 1100°F, 50,000 psi)*

indicates that the amount of microcracking and voiding in the tested specimens depend on test temperature and stress (test duration). See Figure VII-55. The lower temperatures (1000°F and 1100°F) tend to form many microcracks, with little tendency for the microcracks to open up in the longitudinal direction. There also appears to be very little tendency for the grain to elongate. The higher temperature tests tend to have the microcracks opened up to form voids at triple points. The grains near the fracture have generally elongated substantially at the higher temperatures (1200 and 1400°F). The number and size of voids are strongly dependent on both temperature and test duration or stress. However, the relationship between cracking and the shape of the creep curve is not yet clear. Additional work will be conducted to clarify this point.

c. Irradiated 304 SS

M. M. Paxton and J. J. Holmes

New results from post-irradiation creep-rupture tests on 304 SS at 900°F and 1200°F are presented in Table VII-18. A specimen irradiated to a total fluence of $1.4 \times 10^{22} n/cm^2$ at 845°F shows approximately a four-fold loss in rupture life, which is attributed to a reduction in ductility. Previous results from specimens irradiated to a total fluence of $1.6 \times 10^{22} n/cm^2$ at 900°F showed about a 30-fold reduction in rupture life at a test temperature of 1000°F.

Previous work on irradiated 304 SS has centered on the test temperature range of 1000 to 1100°F. The results in Table VII-18 give preliminary information on irradiation effects at a test temperature of 1200°F. For a total fluence of about $3 \times 10^{22} n/cm^2$, the ductility is decreased markedly, but this is offset by reduced creep rates, so that rupture life is virtually unaffected. The results for the two specimens are very similar, even though there was a large difference in irradiation temperature (1130°F versus 860°F). These tests at 1200°F represent one of the few instances where substantial third-stage creep has been observed in irradiated 304 or 316 SS.

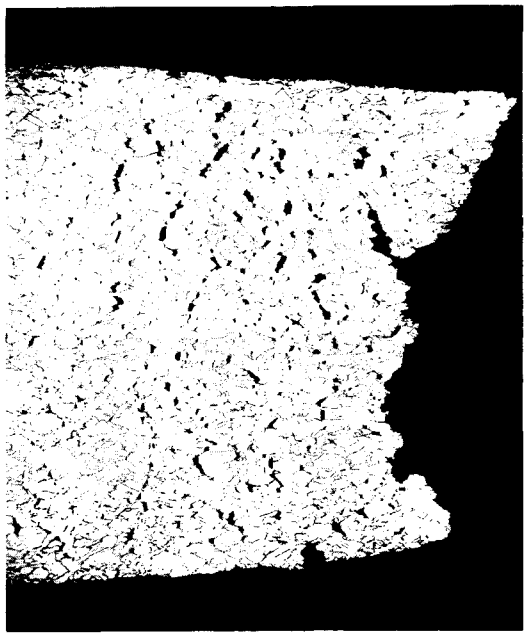

5702673 (a) 50X

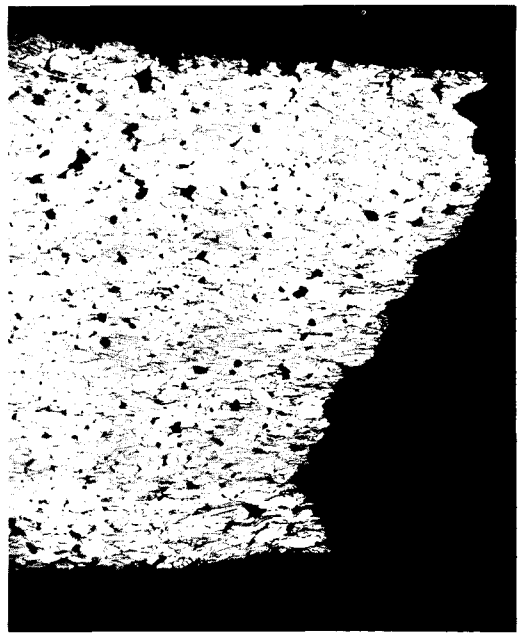

5702676 (b) 50X

5702679 (c) 50X

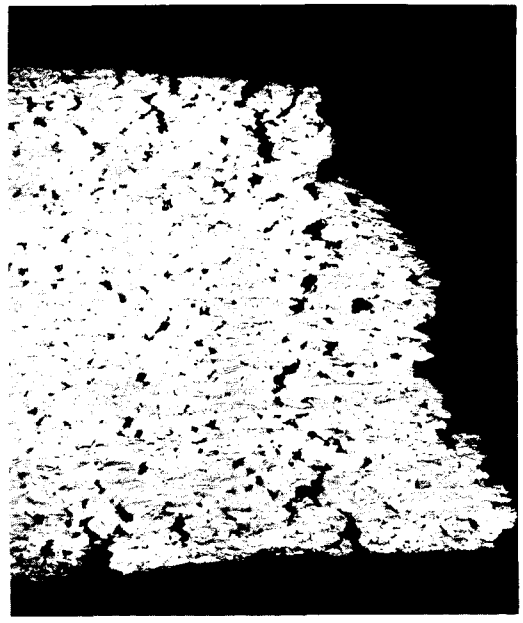

5702682 (d) 50X

FIGURE VII-55 *Post test Longitudinal Sections of Failed 20% Cold Worked Creep-Rupture Specimens a) 1000°F, 60,000 psi, 1300 hours, b) 1100°F, 40,000 psi, 930 hours, c) 1200°F, 30,000 psi, 365 hours, d) 1400°F, 1500 psi, 185 hours.*

TABLE VII-18
UNIAXIAL CREEP-RUPTURE PROPERTIES OF IRRADIATED 304 SS

Site Sequence Number	Fluence (10^{22} n/cm^2)		Irrad. Temp (°F)	Test Temp (°F)	Test Stress (psi x 10^3)	Minimum Creep Rate (10^{-5} in/in/hr)		Rupture Life (hr)		Total Elongation (%)	
	Total	E > 0.1 MeV				Irrad.	Control	Irrad.	Control	Irrad.	Control
B02151/B02045*	1.4	0.9	845	900	50	~0.18	~0.3	482.6	1800	1.5 (a)	24.8
B02150/B02125*	2.7	2.0	860	1200	20	7.6	76.6	137.5	257.7	3.1 (a)	32.2
B02152/B02125*	3.5	3.0	1130	1200	20	6.65	76.6	204.7	257.7	4.1 (a)	32.2

(a) Values from creep curve.

* Control

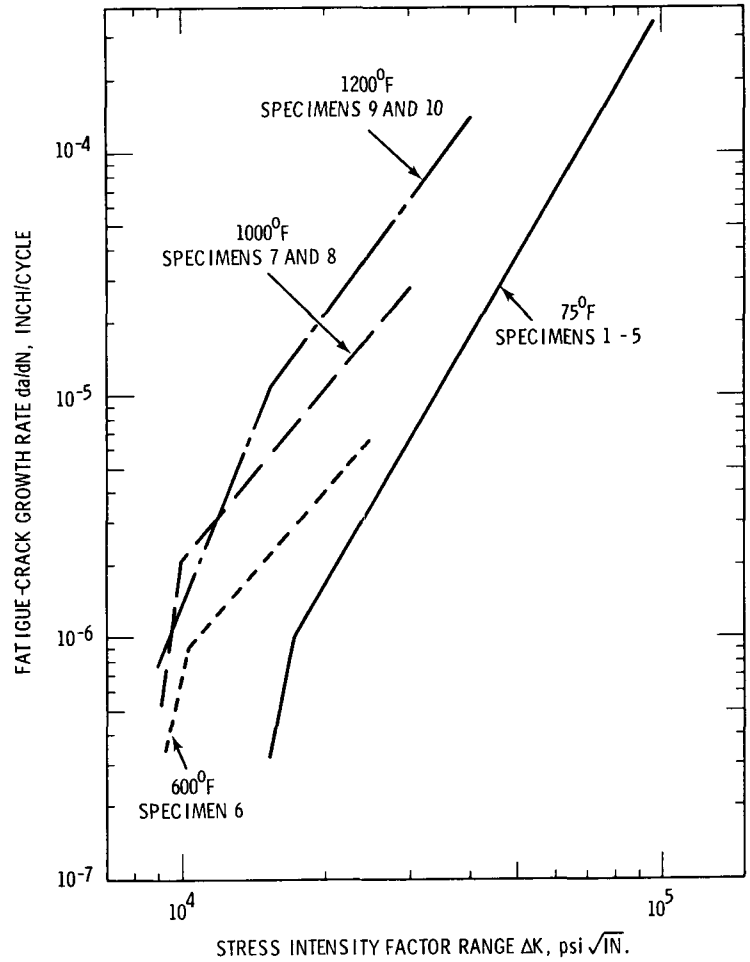

FIGURE VII-56 *Summary of Fatigue-Crack Propagation Behavior of Type 304 SS.*

3. Materials Cracking Properties

L. A. James and R. L. Knecht (12184)

Knowledge of the anticipated cracking properties of principal FFTF structural materials (Types 304 and 316 SS) under simulated FFTF service conditions is necessary for estimating the service life of structural components. In practical terms, this means the number of load cycles required for a crack in a component to grow from a finite size (associated with NDT detection capabilities) to a size that can be detected through leakage monitoring. This type of analysis has been recently completed for FFTF components (Ref 32).

Six structural locations in the reactor vessel and primary piping system were analyzed. These locations were:

- Reactor vessel upper shell course
- Reactor vessel lower shell course
- Primary piping outlet
- Primary piping inlet
- Pump housing
- Intermediate heat exchanger shell

The method of analysis may be summarized as follows:

- An initial crack size was assumed.
- Through the power law of fatigue crack propagation the number of load cycles necessary for the crack to grow to a designated size was estimated.

References

32 James, L. A., "FFTF Vessel and Piping Crack Growth Behavior," Unpublished Data, August 1970.

- By knowing the crack length and crack boundary displacements, the sodium flow rate through the crack was estimated by means of fluid mechanics.
- Designated crack lengths were based on assumed values of the flow stress.
- The fatigue behavior was based on assumed crack growth rates in sodium in the presence of neutron irradiation.

In view of the significant number of assumptions involved, it was recommended that these factors be better characterized experimentally.

Work is continuing on characterizing the fatigue-crack propagation under simulated FFTF operating conditions. The effect of elevated temperature on the fatigue-crack growth rate of Type 304 SS has been determined. As may be seen in Figure VII-56 (taken from Ref 33), increasing the temperature has a profound effect on increasing the fatigue-crack growth rate. The crack growth rate at 1200°F is 10 or 12 times that at 75°F for the same stress intensity factors. Other important parameters such as cyclic frequency, stress ratio, cyclic waveform, and effects of weldments are presently being investigated for Type 304 SS. A less comprehensive study is being made on Type 316 SS; preliminary results indicate that at room temperature, the fatigue-crack propagation rate is slightly higher than for Type 304 SS. Plans are being finalized to irradiate a limited number of fatigue specimens (Types 304 and 316 SS) in EBR-II in order to evaluate the effect of irradiation upon the fatigue-crack growth rate.

References

33 James, L. A. and Schwenk, E. B., "Fatigue-Crack Propagation Behavior of Type 304 Stainless Steel at Elevated Temperatures", presented at the Fourth National Symposium on Fracture Mechanics, August 24-26, 1970, Pittsburgh, Pennsylvania, (Report WHAN-SA-17)

4. Notch Effects on FFTF Materials

J. M. Steichen and R.L. Knecht (12186)

The degradation of stress-rupture properties of certain materials due to the presence of stress concentrations can cause components to fail in service. This notch sensitivity, as it is normally identified, is usually expressed as a ratio of notch strength to unnotched strength, e.g., stress rupture strength (psi) of the net cross section at the notch of a notched specimen to the stress rupture strength of an unnotched bar. Notch sensitivity problems have been identified for certain austenitic stainless steels used in turbine components and pressure piping in the power generating industry and for some superalloys used for turbine rotor components in jet engines.

A literature survey on this subject and a study of the applicability of existing data were required.

The literature survey has been completed and general summary information on the austenitic stainless steels follows:

1) Specimen size and notch geometry can significantly affect notched stress rupture results.
2) Notch sensitivity of the austenitic stainless steels is temperature- and time-dependent.
3) Type 304 SS appears to be slightly notch weakened at 1100°F after rupture lives of about 100 hr.
4) Type 304 SS is notch strengthened at 1500°F for rupture lives up to ∿10,000 hr.
5) Type 316 SS (solution annealed) base metal or weld metal does not appear to be notch weakened at 1100 or 1500°F for rupture times to ∿10,000 hr.

6) Type 321 SS is slightly notch weakened in stress rupture tests at 1100°F for times of about 70 to 200 hr but not at 1500°F.

7) Type 347 SS base metal is not notch weakened at 1100°F, but Type 347 heat-affected zone weld metal is very notch weakened at the same temperature.

It appears that only limited information is available under high temperature conditions, and the application of such information can be only from the standpoint of identifying possible materials and material conditions that might be susceptible to premature service failures due to stress concentrations. Type 304 SS is notch-weakened to an unknown extent under some conditions. No known data are available on cold worked 316 SS and no known data are available on the effect of irradiation for any austenitic stainless steel.

The review further indicates that, for most materials, notch stress rupture properties can be correlated between various specimen sizes and notch geometries. These correlations are obtained through the use of major specimen and test parameters; these include notch strength ratio, notch radius, notch depth and specimen diameter.

5. High Stain Rate Effects

J. M. Steichen and R. L. Knecht (12184)

The results of this program will provide information on the behavior of the vessel and core components during conditions of rapid loading by evaluating the effects of high strain rates on the mechanical properties of materials expected to be used in the FTR vessel and core components.

High strain rate testing has been completed on unirradiated 304 SS at strain rates from 0.01 to 100.0 in/in/sec and test temperatures from 600 to 1400°F. A summary of the mechanical properties obtained is presented in Table VII-19 and illustrated in Figures VII-57 through VII-60.

TABLE VII-19
THE EFFECT OF STRAIN RATE AND TEST TEMPERATURE ON THE MECHANICAL PROPERTIES OF 304 SS

Strain Rate (Sec)	Test Temp(°F)	Stress (psi x 10^3)		Elongation % (1.125 in.Gauge)		Reduction of Area (%)
		Ultimate	Yield*	Total	Uniform	
0.01	R.T.	85.10	42.56	55.0	49.9	73.5
	600	62.20	30.09	31.0	25.3	70.4
	800	60.60	27.96	33.7	27.7	71.5
	1000	56.33	26.65	29.7	24.1	70.5
	1200	47.65	21.86	28.4	23.0	70.5
	1400	33.41	18.89	37.7	20.2	65.0
0.1	R.T.	83.58	48.78	50.1	43.7	74.3
	600	63.19	31.11	33.1	27.9	69.7
	800	63.88	30.10	31.4	25.8	57.7
	1000	59.24	28.43	32.2	27.8	69.0
	1200	51.52	23.90	30.9	25.1	71.2
	1400	39.14	18.91	33.9	23.5	72.0
1.0	R.T.	86.70	48.81	46.1	40.1	68.5
	600	58.59	30.22	33.5	27.4	70.3
	800	59.78	28.16	30.6	25.8	72.7
	1000	55.93	25.02	30.6	25.6	67.4
	1200	47.94	20.50	30.2	25.2	75.3
	1400	34.39	16.74	31.3	24.1	77.5
10.0	R.T.	88.43	53.56	48.0	43.2	65.6
	600	61.36	34.12	35.7	27.9	69.9
	800	55.08	31.62	32.0	24.2	71.0
	1000	45.51	24.70	30.5	25.7	66.5
	1200	42.41	19.80	31.7	23.1	70.6
	1400	39.69	19.03	30.9	23.8	73.4
100.0	R.T.	91.52	58.00	47.5	41.7	62.1
	600	62.26	34.61	35.4	28.3	69.8
	800	57.03	34.46	33.7	26.9	73.5
	1000	53.25	28.46	32.2	26.3	73.7
	1200	48.36	26.56	33.3	23.0	77.9
	1400	41.23	21.02	32.0	25.0	78.4

*The yield strength values are slightly high due to prestraining of the tensile specimens during machining.

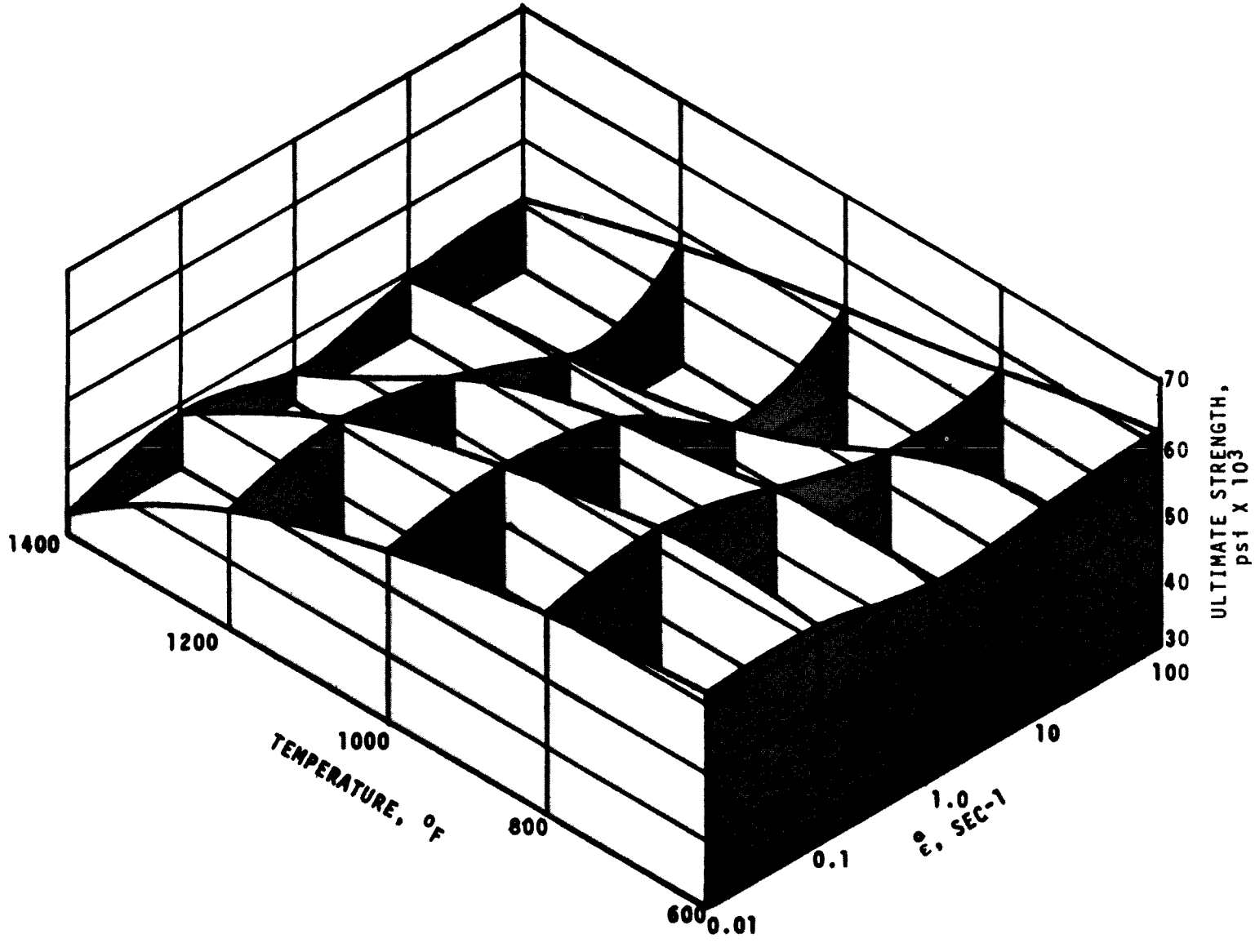

FIGURE VII-57 *The Effect of Strain Rate and Test Temperature on the Ultimate Strength of 304 Stainless Steel.*

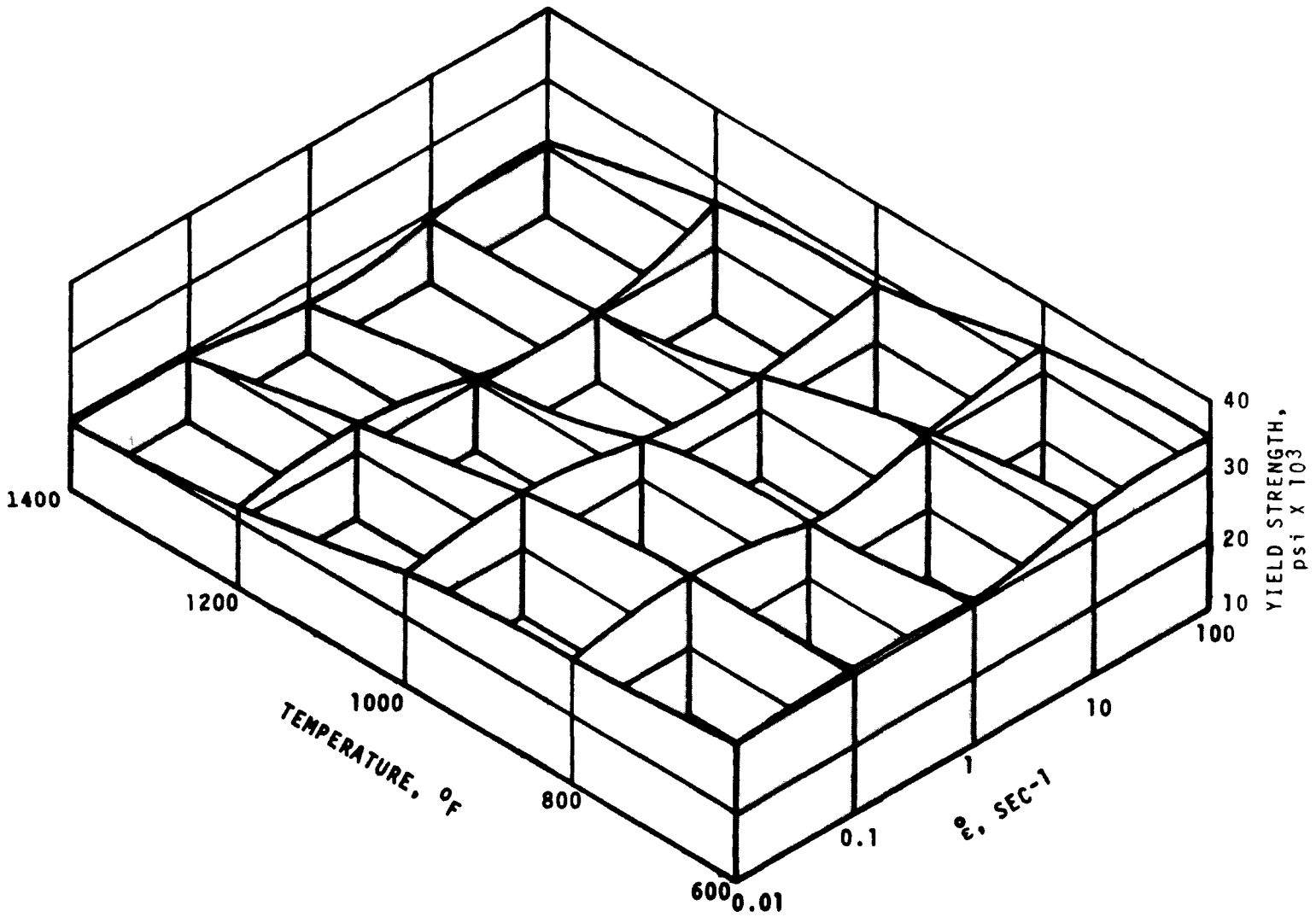

FIGURE VII-58 *The Effect of Strain Rate and Test Temperature on the Yield Strength of 304 Stainless Steel.*

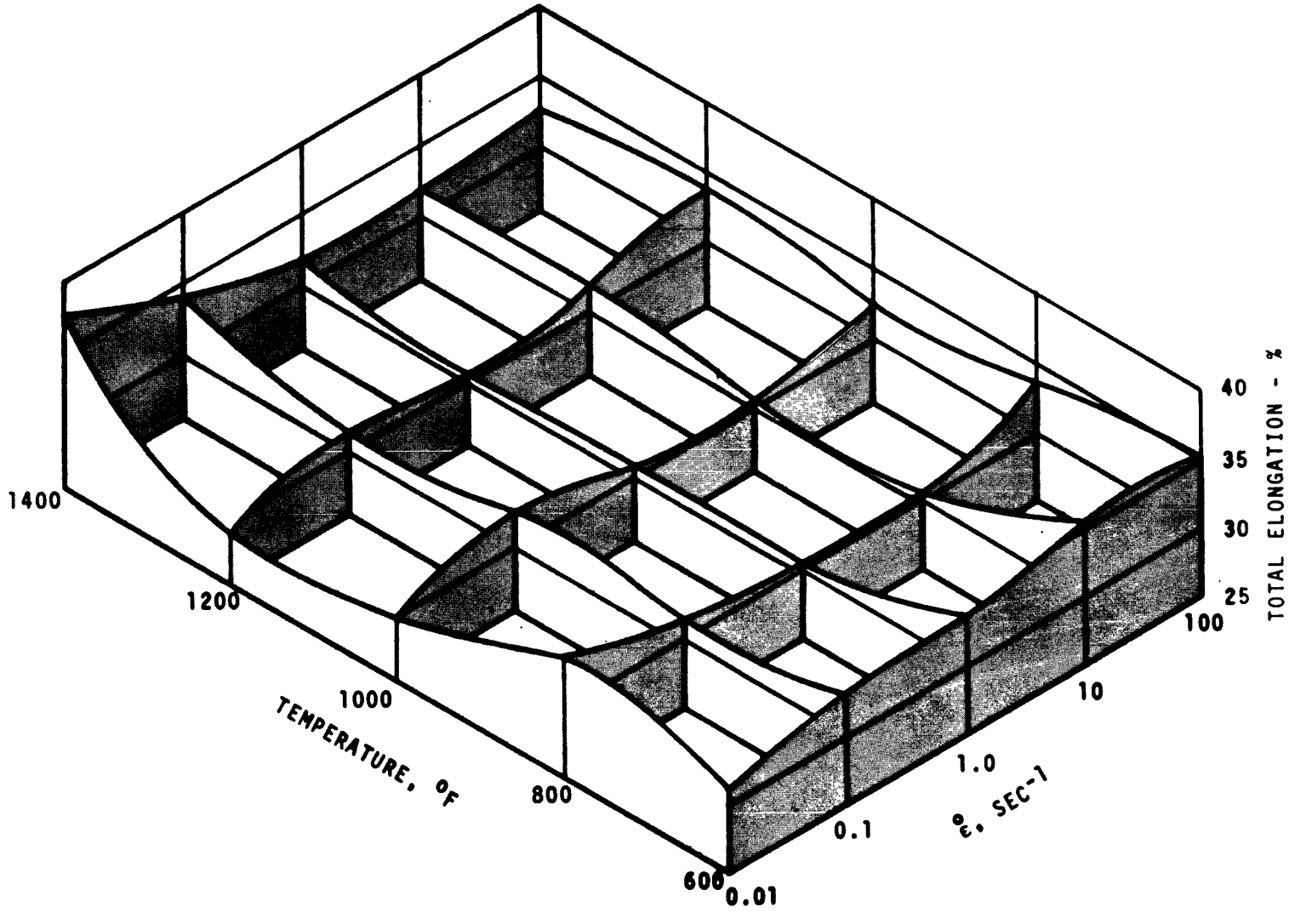

FIGURE VII-59 *The Effect of Strain Rate and Test Temperature on the Total Elongation of 304 Stainless Steel.*

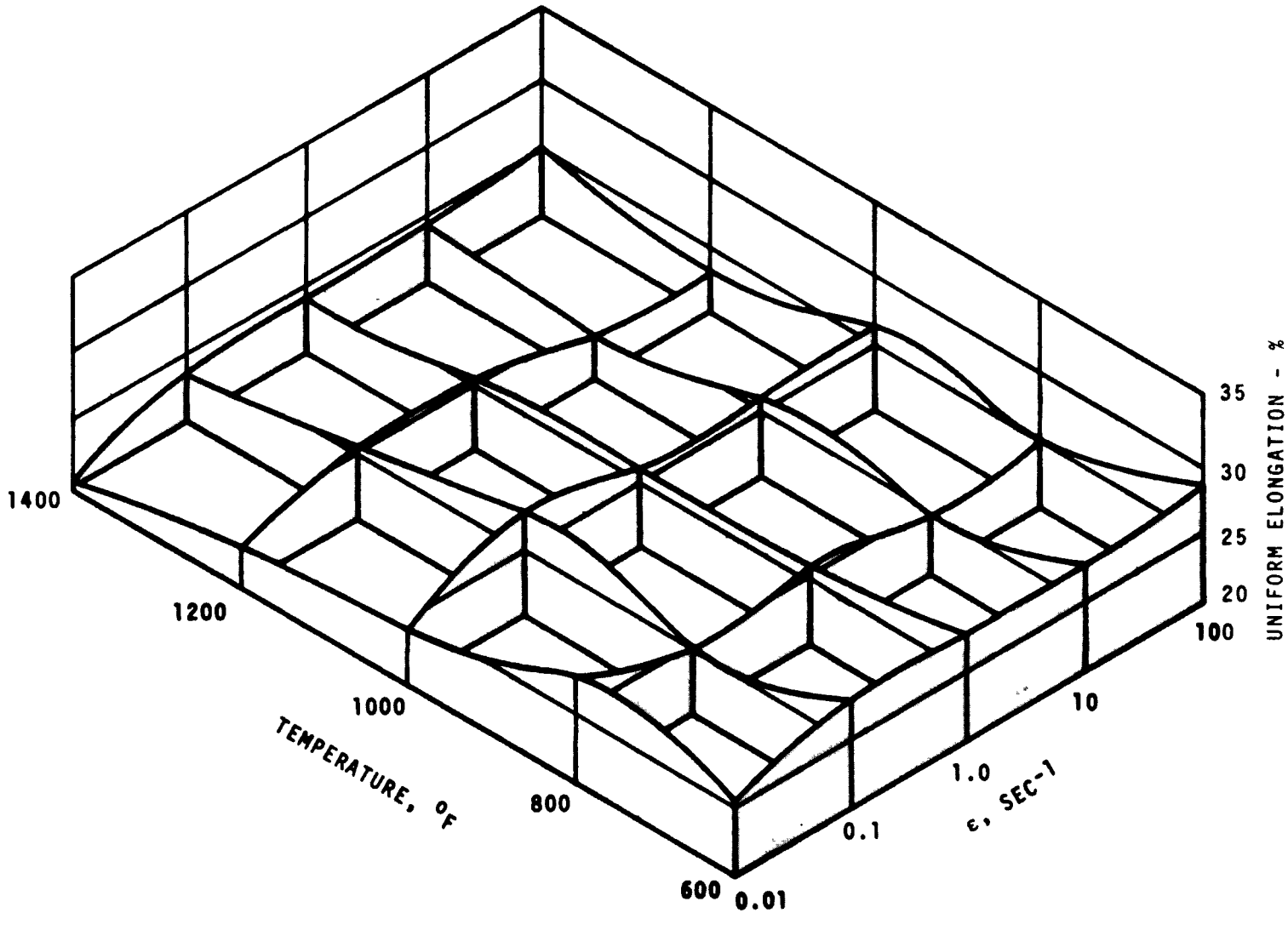

FIGURE VII-60 *The Effect of Strain Rate and Test Temperature on the Uniform Elongation of 304 Stainless Steel.*

General trends observed of the effect of strain rate on the mechanical properties of 304 SS are:

1) The ultimate strength decreases with increasing temperature at all strain rates. It is nearly constant at 600°F, but at 800, 1000, 1200, and 1400°F, minimums in strength are observed (Figure VII-57). These minimums in ultimate strength form a trough at 1400°F and 1 in/in/sec and extend to 800°F and 10 in/in/sec.

2) Yield strength slightly increases or remains constant with strain rate at all test temperatures (Figure VII-58). Minor variations at certain strain rates are observed.

3) Total elongation is not greatly affected by strain rate, but the general trend (although minor variations are observed) is that total elongation slightly increases with increasing strain rate at test temperatures to 1200°F (Figure VII-59). At 1400°F, total elongation decreases with increasing strain rate.

4) Uniform elongation appears to remain constant or to slightly increase with strain rate at all test temperatures (Figure VII-60). At 1400°F, significant increases in uniform elongation are observed.

High strain rate testing has been initiated on 20% cold worked 316 SS. Test parameters to be evaluated include test temperature to 1600°F and strain rates to 100 in/in/sec. Several irradiated 304 SS specimens will be tested this fiscal year.

6. Biaxial Stress-Rupture Studies on Alloy 12R72HV - 12215

R. W. Barker and J. J. Holmes

This program is for evaluating materials potentially useful for cladding in advanced cores of the FFTF or in later demonstration reactors. The Swedish alloy 12R72 HV appears to have attractive stress-rupture properties that would make it a candidate for such reactor systems. This alloy is basically a 316 type austenitic stainless steel containing high carbon, a titanium stabilizer, and higher nickel content to stabilize the alloy against sigma phase formation. The material is being tested in the cold worked condition. The grain size (shown in Figure VII-61) is duplex, having a band of very fine grains (ASTM 10) at both the inner and outer tube surfaces, with a coarse central zone of grains whose size is about ASTM 7.

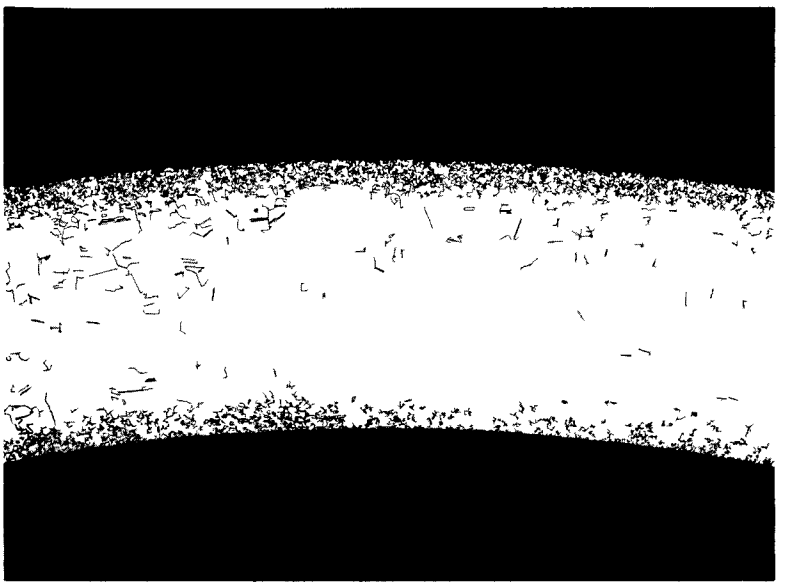

100X

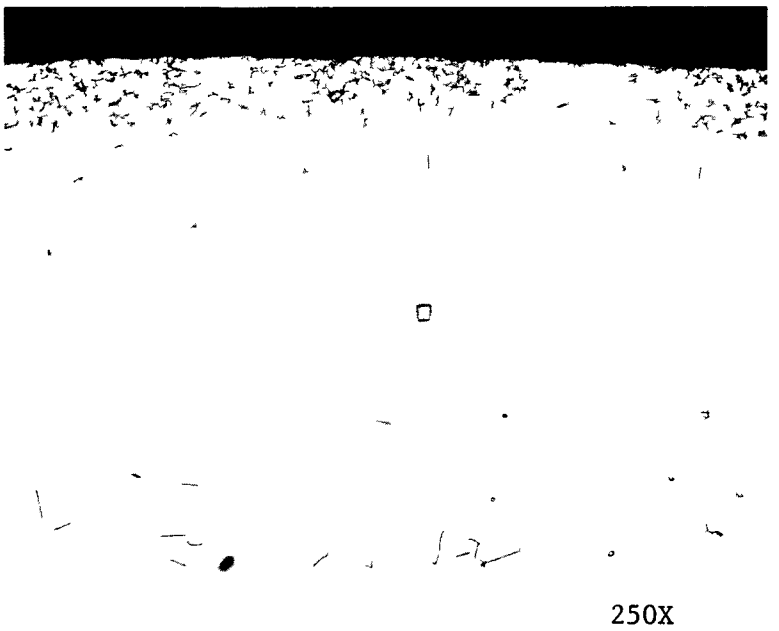

250X

FIGURE VII-61 *Grain Size and Microstructure of Cold Drawn 12R72 HV SS Tubing.*

Biaxial stress-rupture tests have been conducted on 12R72 to rupture times up to ∿5000 hours at test temperatures of 1000, 1200, and 1400°F. The results are shown in Figure VII-62 plotted as log hoop stress versus log rupture time. The rupture stress ranges from well over 80,000 psi at 1000°F for short rupture times to 10,000 psi at 1400°F at ∿5000 hours. A sharp break occurs in the curve formed by the 1400°F data at about 1200 hours, apparently the result of recovery processes. Data scatter at all test temperatures appears to be minimal.

The rupture stress of this material is, as might be expected, superior to that of mill-annealed Type 316 SS currently being evaluated. It is also superior, in terms of rupture stress, to the 20% cold-worked Type 316 SS (0.230-in. dia. x 0.015-in. wall) reported by Paxton. Comparisons of these data indicate 12R72 possess a rupture stress advantage of about 15% at 1000°F at comparable rupture times. At 1200°F and 1400°F, the rupture stress advantage is about 50%.

Strain at rupture for 12R72, which is shown in Figure VII-63, plotted as log strain versus log rupture time, appears low in comparison with the 20% cold-worked 316 SS. The 12R72 suffers a slight ductility disadvantage at 1000°F which becomes substantial at 1200°F. Relative values at 1200°F are about 6% for the Type 316 and about 3% for the 12R72. Further, the ductility values published for the Type 316 are more conservative, being established well away from the ruptured area, while the strain at rupture for the 12R72 is measured at the point of failure for those specimens which are not fragmented. At 1400°F, 12R72 appears to pass through a ductility minimum at 300 to 400 hours rupture time.

At all temperatures, failure is generally typified by the formation of grain boundary cracks in the zone of coarse grains immediately adjacent to the zone of fine grains at the outer tube surface. At 1000 and 1200°F (and to some extent at 1400°F), these cracks elongate with time. This results in a significant decrease in the tube wall thickness until a critical stress is reached and the tube fails by plastic instability.

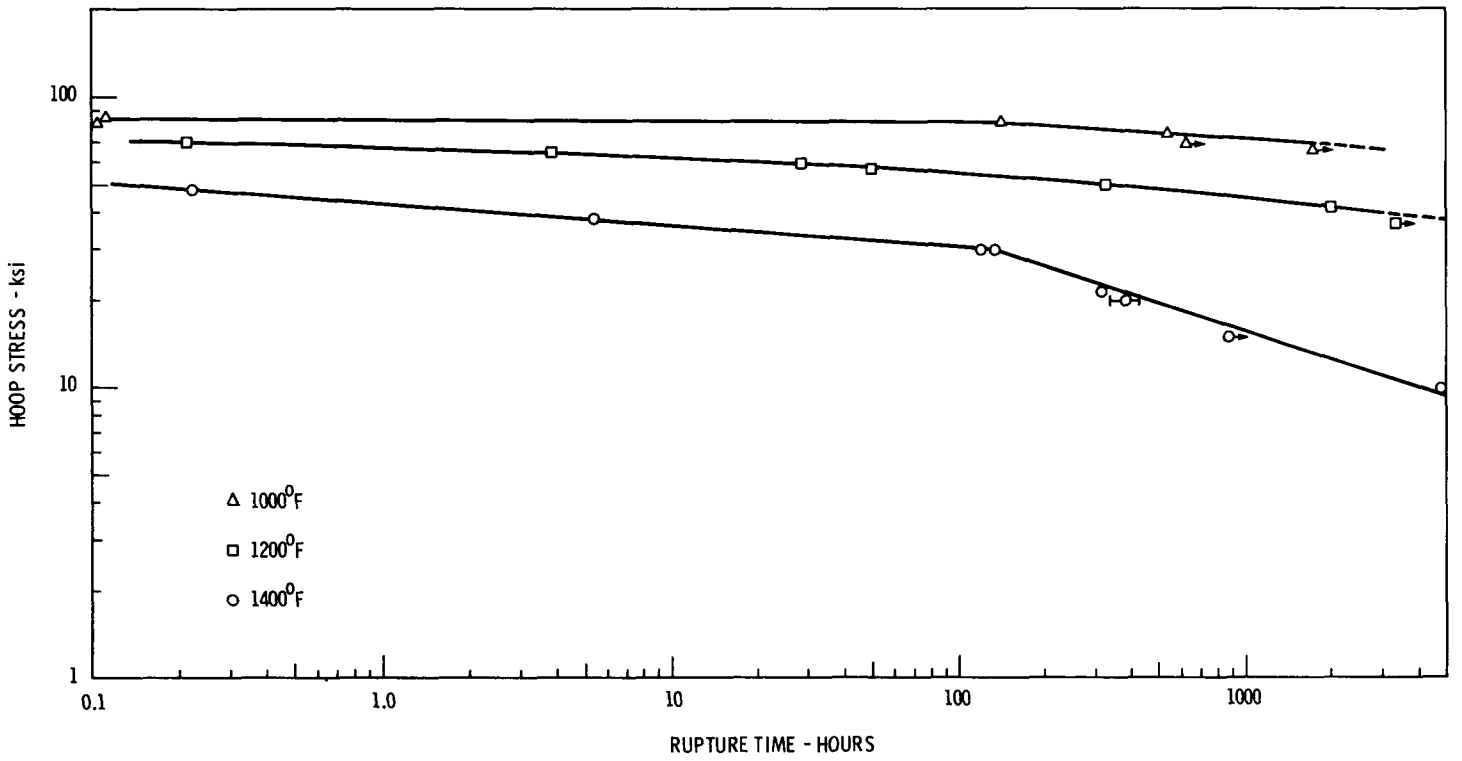

FIGURE VII-62 *Effect of Stress and Temperature on the Rupture Life of 12R72 HV SS Tested Under Biaxial Stress.*

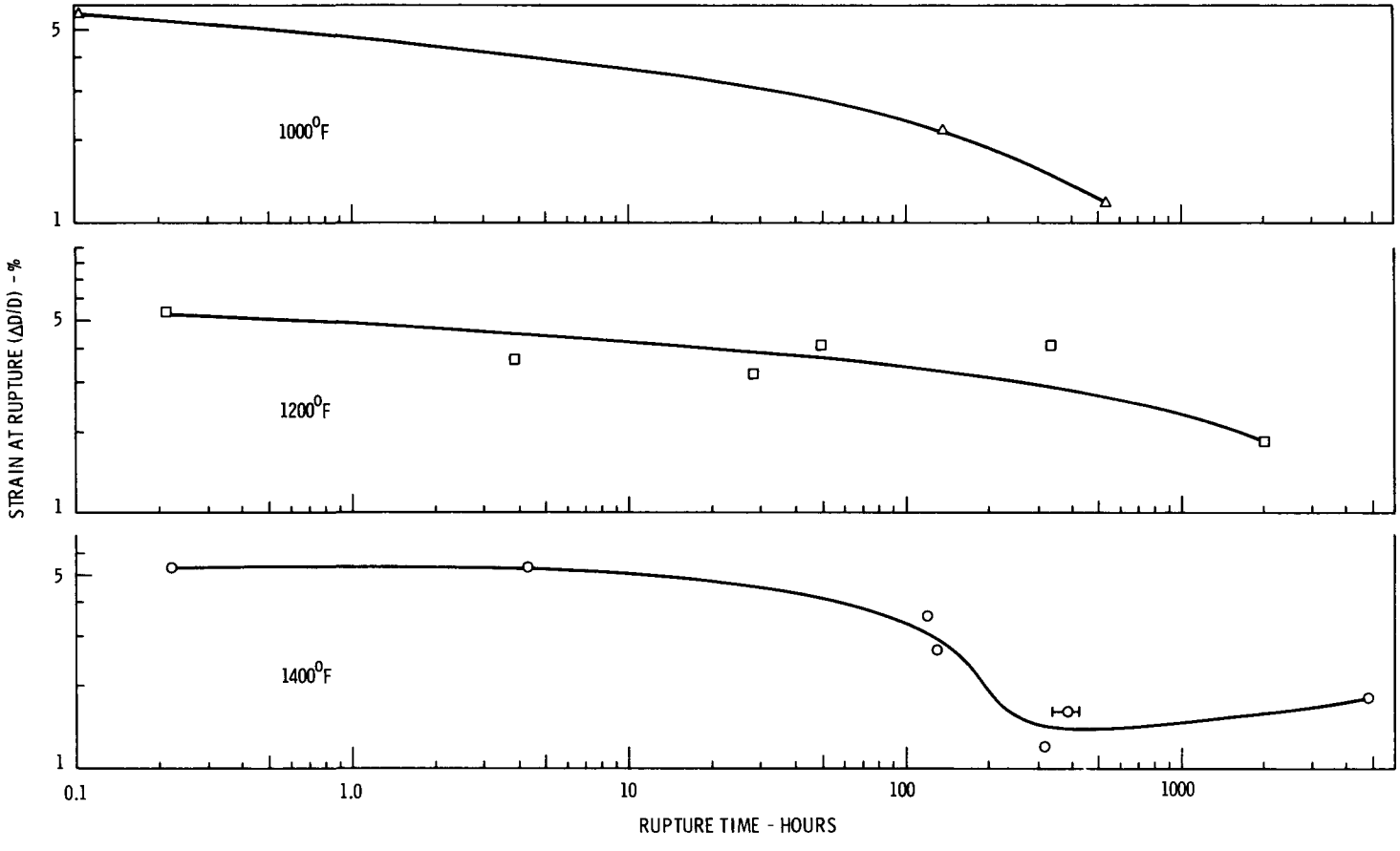

FIGURE VII-63 *Effect of Rupture Time on the Ductility (ΔD/D) of 12R72 HV SS Tested Under Biaxial Stress.*

Examples of these failures are given in Figures VII-64, VII-65 and VII-66. The fine grained area at the inner and outer tube surfaces appears more resistant to grain boundary cracking than the coarse grained material. At 1400°F, the formation of grain boundary cracks appears to be the result of a different mechanism than at lower temperatures. At 1400°F, cracks are formed by the linking up of numerous round type cracks which expand into the large cracks observed in Figure VII-66. At lower temperatures, the round type cracks are not as prevalent. Instead, a combination of round type cracks and wedge type cracks at triple points appears to cause crack growth.

The recovery processes, which are undoubtedly the cause of the sharp break in the 1400°F stress-rupture curve in Figure VII-62, are evidenced by the presence of recrystallization and grain growth observed in Figure VII-66. The recovery processes probably play a role in producing the ductility minimum at 1400°F (Figure VII-63). In addition, the unusual granular structure seems to be a factor in the initial formation of cracks leading to failure. It is not understood whether the ductility of 12R72 is low (in comparison with other cold-worked materials) because of the amount of cold work, per se, or because of the unusual structure.

7. Mechanical Testing of Fuel Pin Cladding (12138)

R. L. Fish and J. J. Holmes

This program is to provide a basis for evaluating the combined effects of fuel cladding interaction, fluence and operating temperature on the post-irradiation burst and stress-rupture properties of fuel pin cladding.

Previously reported burst test results on fueled specimens from the PNL-1 series fuel pins (clad with Type 304 SS, E-lot) revealed that specimens from above the fuel midplane exhibited a drastic reduction in burst strength and ductility after long periods of internal air exposure (> 8 months). Every specimen tested from above the midplane that had been exposed long enough experienced a low strength, intergranular failure.

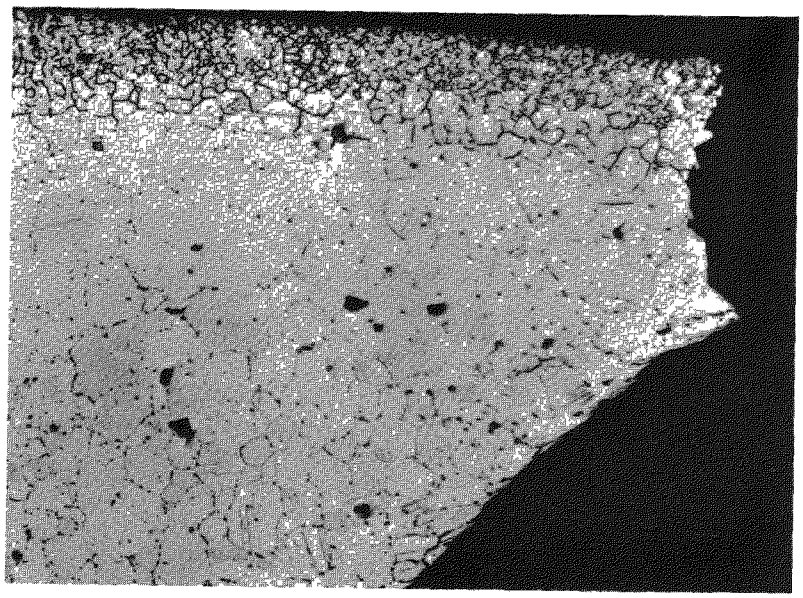

250X

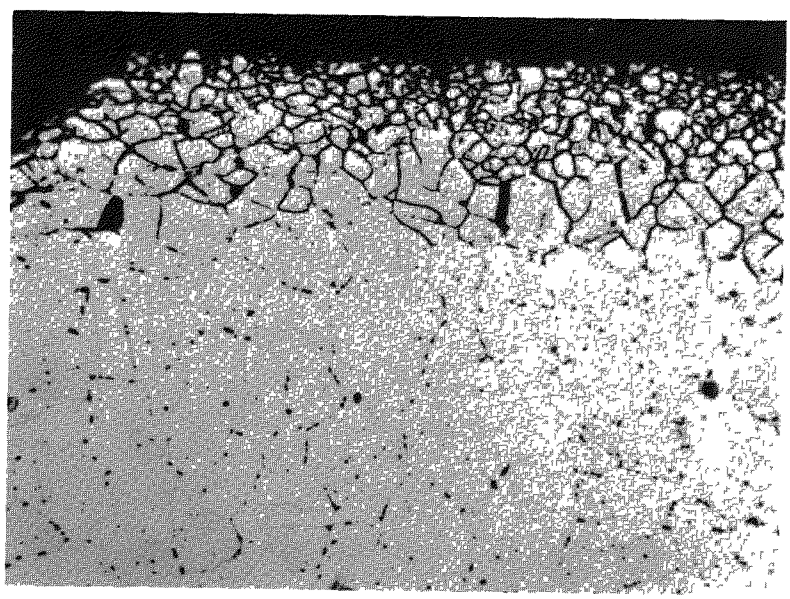

500X

FIGURE VII-64 *Transverse Section of 12R72 SS Tubing Tested at 75,000 psi Hoop Stress and 1000°F showing Rupture Mode and Microstructure. Rupture occurred in 536 hours.*

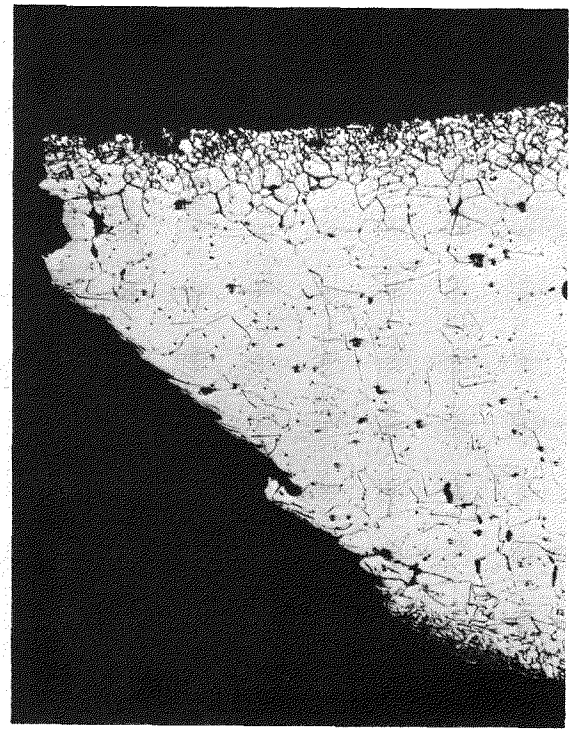

250X

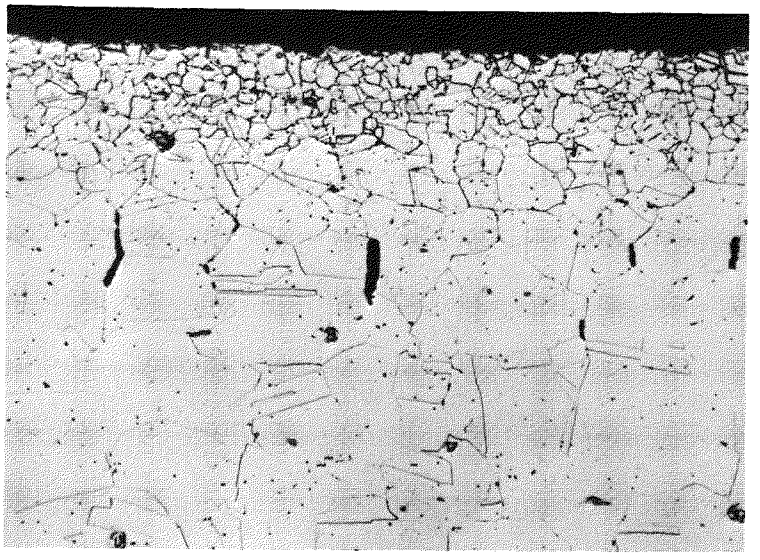

500X

FIGURE VII-65 *Transverse Section of 12R72 SS Tubing Tested at 60,000 psi Hoop Stress and 1200°F showing Failure Mode and Microstructure. Rupture occurred in 28 hours.*

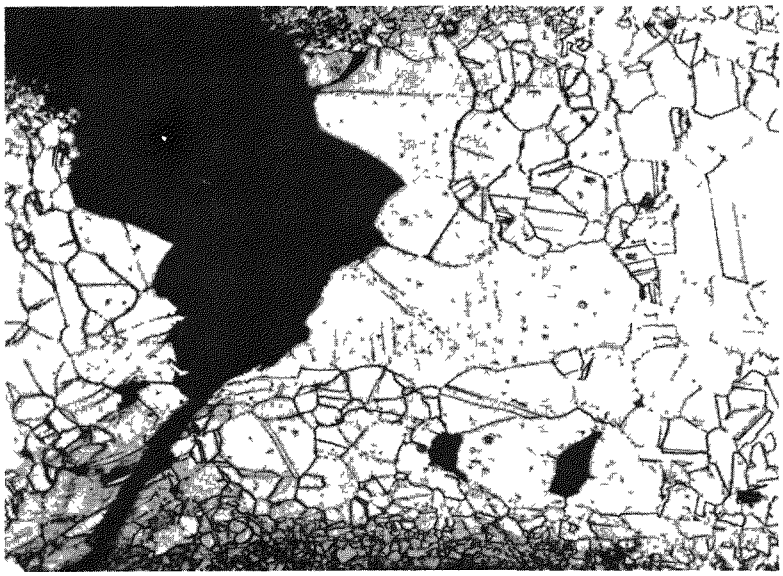

250X

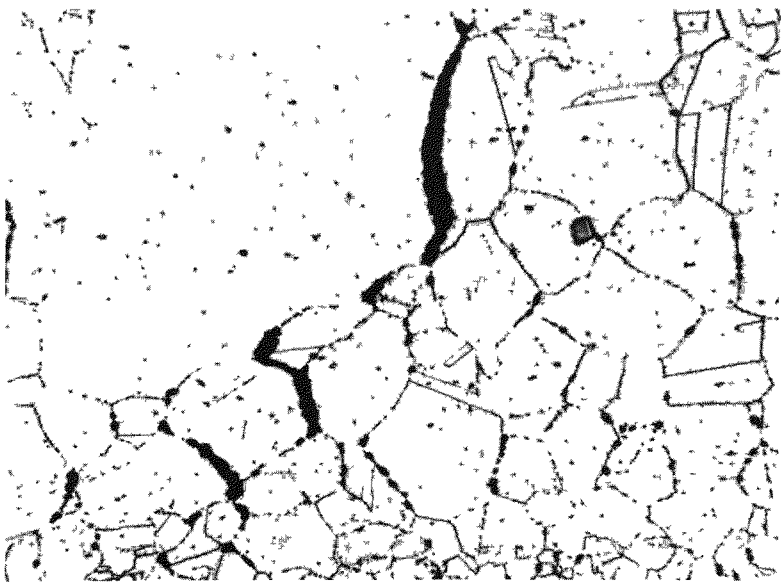

500X

FIGURE VII-66 *Transverse Section of 12R72 SS Tubing Tested at 30,000 psi Hoop Stress and 1400°F showing Failure Mode and Microstructure. Rupture occurred in 119 hours.*

Subsequent burst tests performed on specimens from above the midplane in fuel pins PNL 1-17 and 1-19 have revealed a variation from this established pattern. These two burst specimens had been internally exposed to hot cell air for 10 to 12 months, but failed with good rupture strength (65,150 and 57, 120 psi, respectively) and relatively high strain values.

Table VII-20 compares the biaxial properties of these specimens with the PNL-1 pin specimens tested earlier from above the fuel column midplane. The table illustrates the inconsistency of the data when comparing PNL 1-17 and 1-19 specimen behavior with the previously obtained results.

Postirradiation examination of the PNL 1-17 fuel and cladding microstructure indicates that this pin operated at a lower temperature than the heat transfer calculations had postulated. The PNL 1-19 fuel pin operated with a larger fuel-cladding gap than the other pins. Although the PNL 1-17 cladding irradiation temperature may explain the strength of that specimen, the PNL 1-19 results can only be attributed to the larger fuel-cladding gap.

TABLE VII-20
COMPARISON OF PNL-1 BURST TESTS
(TEST TEMP 900 °F)

Specimen	Avg Clad ID Temp(°F)	Fluence (E> 0.1 MeV)	Internal Air Exposure(Mo.)	Max. Rupture Hoop Stress(psi)	Strain (ΔD/D %)
PNL 1-3:G4	970	3.7×10^{21}	10	38,940	0.2
1-6:G1	940	4.2×10^{21}	8	22,040	0.6
1-6:G2	940	3.0×10^{21}	10	27,180	0.4
1-16:H	935	4.3×10^{21}	10	<740*	Negl.
1-18:H	965	5.0×10^{21}	10	<740*	Negl.
1-18:J	970	3.3×10^{21}	10	<740*	Negl.
1-15:G2	960	4.0×10^{21}	11	31,190	0.2
PNL 1-17:G2	965	4.5×10^{21}	12	65,150	3.6
1-19:G3	980	3.8×10^{21}	10	57,120	5.2

* Specimens revealed fissures during leak test.

Burst and stress-rupture testing of PNL-2 series fuel pins has been initiated. These mixed-oxide fuel pins were clad with Type 304 SS (E lot) and irradiated in the EBR-II to a peak fuel burnup of about 47,000 MWd/MTM (peaking cladding fluence $\sim 2.5 \times 10^{22}$ n/cm^2, E > 0.1 MeV).

Two fueled specimens sectioned from pins PNL 2-3 and 2-6 were burst tested at 1000 and 1200°F. The results are summarized in Table VII-21. These burst strengths reflect the irradiation-hardening behavior expected of this material.

TABLE VII-21
PNL-2 BIAXIAL TEST RESULTS

Specimen	Average Cladding I.D. Temp(°F)	Fluence (E> 0.1 MeV)	Test Temp(°F)	Maximum Rupture Hoop Stress(psi)	Strain (ΔD/D%)
Control (Unirrad)	--	--	1000	54,000	∿ 15-20
PNL 2-3:K	935	2.2×10^{22} n/cm^2	1000	70,600	5.0
Control (Unirrad)	--	--	1200	45,000	∿ 15-20
PNL 2-6:J	930	2.3×10^{22} n/cm^2	1200	57,100	6.4
PNL 2-6:K (Stress-Rupture Specimen)	930	1.9×10^{22} n/cm^2	1200	25,760 (Rupture Life = 108 hr.)	3.0

A stress-rupture test performed on a PNL 2-6 specimen at 1200°F and a maximum hoop stress level of 25,760 psi, failed with a rupture life of 108 hr. The target rupture life for this stress level and material was calculated to be 100 hr. Thus, no evidence of property degradation by fission product-fuel cladding interaction was found.

Based on these results, we conclude that, for these irradiation and test conditions, there is no effect of fuel-cladding interaction on the

biaxial properties. Therefore, a general biaxial property surveillance program is planned for this and subsequent fueled cladding subassemblies using only selected specimens, temperature, and stress levels to obtain an overview of the interaction effects. If the change in properties becomes significant, detailed stress-rupture testing will be used to fully characterize the interaction and its effect on the biaxial properties.

8. Prediction of Low Cycle Fatigue

D. C. Bullington and D. S. Dutt (12163)

For many metals which undergo repetitive strain cycling at elevated temperature, the cycles before failure (N_f) can be predicted by the relationship:

$$\Delta E_t = \frac{3.5\sigma u}{E} (N_f)^{-0.12} + D^{0.6}(N_f)^{-0.6}$$

where:

ΔE_t = total elastic and plastic strain/cycle

E = Modulus of elasticity (psi)

σu = ultimate tensile strength (psi)

$D = \ln \left(\frac{100}{100-R}\right)$

R = percent reduction in area during tensile test

The above expression was programmed into a FORTRAN V computer program called CYCLE, which is capable of predicting the cycles to failure iteratively once the strain/cycle and the material properties are determined. Material properties are computed as a function of temperature in external subroutines.

9. Fuel Pin Clad Swelling (12163)

R. J. Jackson, R. D. Leggett, E. O. Ballard, J. W. Weber, R. B. Baker, E. A. Schnaible and J. E. Hanson

Fuel pins PNL 2-3 and 2-6 have been examined after irradiation to a fluence of about 2.5×10^{22} (E > 0.1 MeV) at a calculated peak cladding temperature of approximately 980°F. The actual diameter increases along

the pins agree quite well (Figures VII-67 and VII-68) with those predicted. The cladding swelling was calculated using the equation:

$$\Delta V/V = (\phi t)\left\{2.05 - (27/T - 623) + [78/(T - 623)^2]\right\}[(T-40)\times 10^{10}]$$
$$\times \exp[-0.015T - (5100/T) + 32.6].$$

where:

$\Delta V/V$ = increase in cladding volume, %
T = cladding mid wall temperature, °K
ϕt = cladding fluence ($E > 0.1$ MeV), 10^{22} n/cm^2.

This indicates that the diameter increase from fission gas pressure was not significant. Check analyses are being conducted to predict the contribution of irradiation creep to diameter increase to assist in confirming the irradiation creep model.

10. In-Reactor Creep Experiments (12215)

D. C. Kaulitz, E. R. Gilbert, J. J. Holmes

a. EBR-II Creep Capsule (B-51)

A fully instrumented creep capsule is being constructed for use in the EBR-II. This capsule contains a bellows loading system, electrical heating and thermocouples for temperature control and an externally driven micrometer screw for strain measurement. The capsule is designed to meet ASTM recommendations for creep testing with respect to bending moment, load stability, and temperature control.

A "Data Package and Hazards Analysis," for this capsule has been prepared and approved by Argonne National Laboratory. This analysis describes in detail the relationships between capsule functions and the safety of EBR-II. In order to minimize possibility of failure of the tube pressurizing the loading bellows, the tube is surrounded by a secondary pressure containment

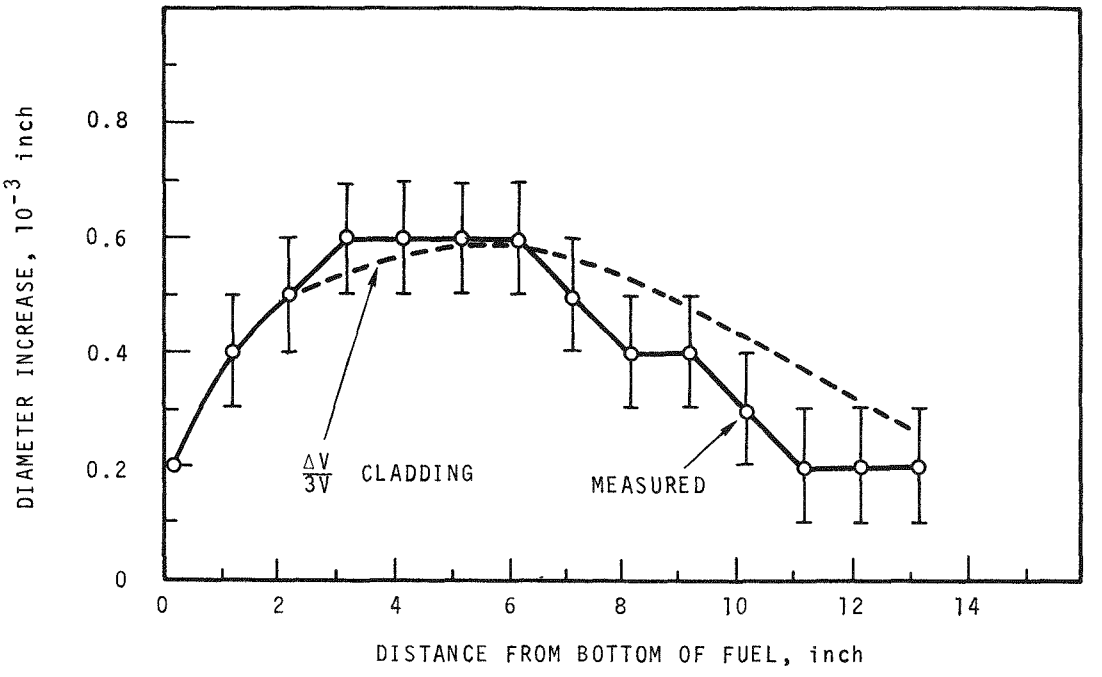

FIGURE VII-67 *Fuel Pin PNL 2-3--Comparison Between Measured Diameter Increase and Calculated Cladding Swelling.*

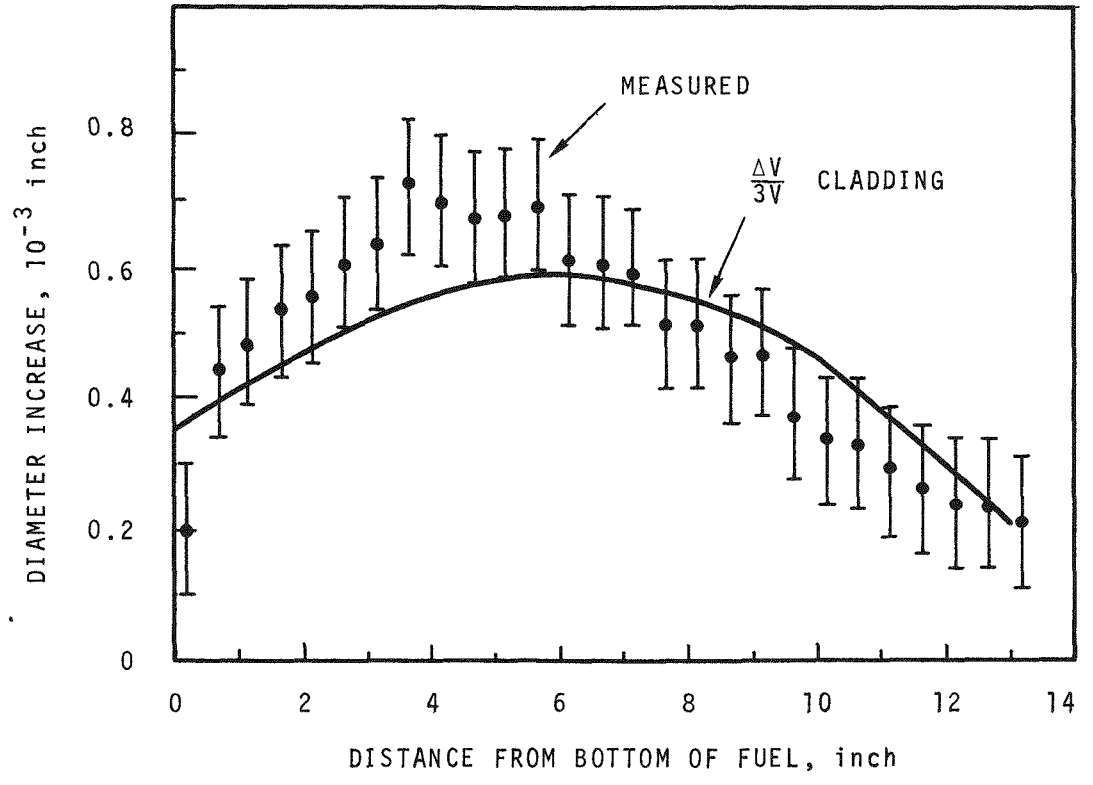

FIGURE VII-68 *Fuel Pin PNL 2-6--Comparison Between Measured Diameter Increase and Calculated Cladding Swelling.*

tube and is protected with a rupture disk that limits operating pressures to a small fraction (0.02) of the rated tube pressure.

In order to investigate the possibility of gas release directly from the bellows to the reactor coolant a plexiglass mock-up of a flow channel was constructed and a bellows failure performed under simulated reactor operating conditions. The results of this test demonstrated that the gas bubble created by bellows failure travels less than six in. against the sodium flow, and is quickly dissipated by the fluid flow.

Acceptance of the "Data Package and Hazards Analysis," marks a new phase in this effort. The capsule can now be completed and made ready for EBR-II irradiation. It is anticipated that the capsule will be operational in . nuary 1971.

An unirradiated control creep test on 20% cold-worked 316 SS was conducted at 20,000 psi and 1000°F, (the initial set of conditions proposed for the EBR-II Creep Capsule). Extrapolated data and a creep test performed on 20% cold-worked 316 SS characterized by a 130 micron grain intercept showed negligible thermal creep at these conditions. The control test performed on the EBR-II creep capsule specimen material, however, showed creep comparable to that expected from irradiation enhancement. These data are shown in Figure VII-69. A test conducted on a solution-treated specimen of the large 130 micron grained material is also shown in Figure VII-69. The creep of the solution-treated 316 and the 20% cold-worked EBR-II creep capsule material is not greatly different. Hardness measurements have verified the cold-work in the EBR-II creep capsule material.

As a consequence of the large thermal creep component in the EBR-II creep capsule material at 1000°F and 20,000 psi, the decision was made to lower the test temperature to approximately 900°F. The appreciable

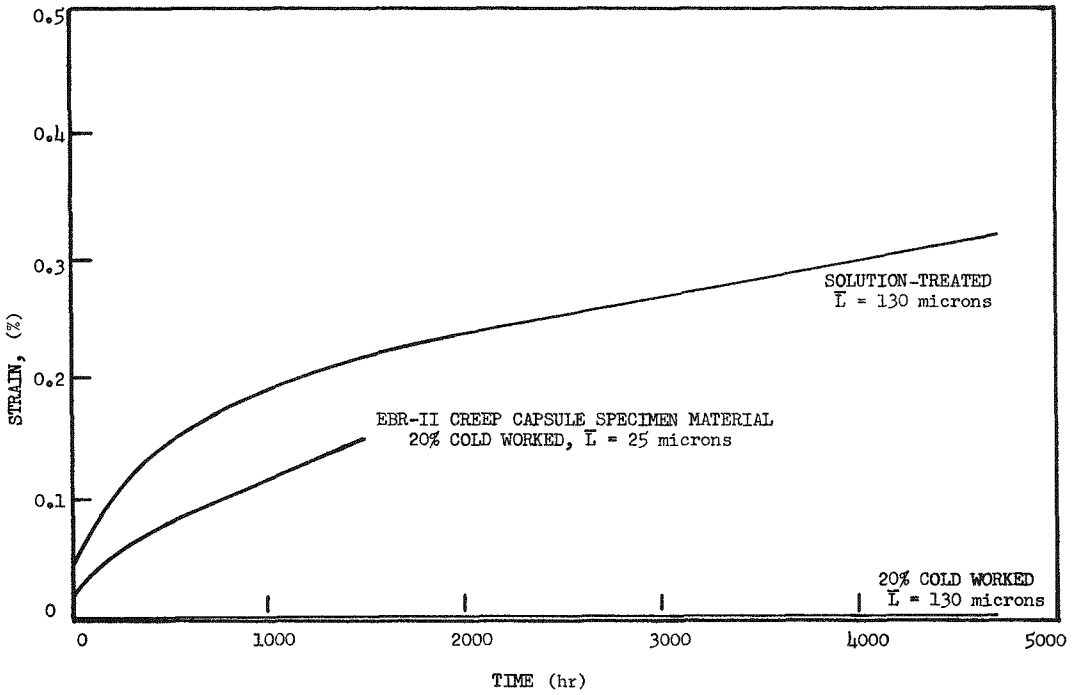

FIGURE VII-69 *Creep Curves for 316 SS at 1000°F and 20,000 psi.*

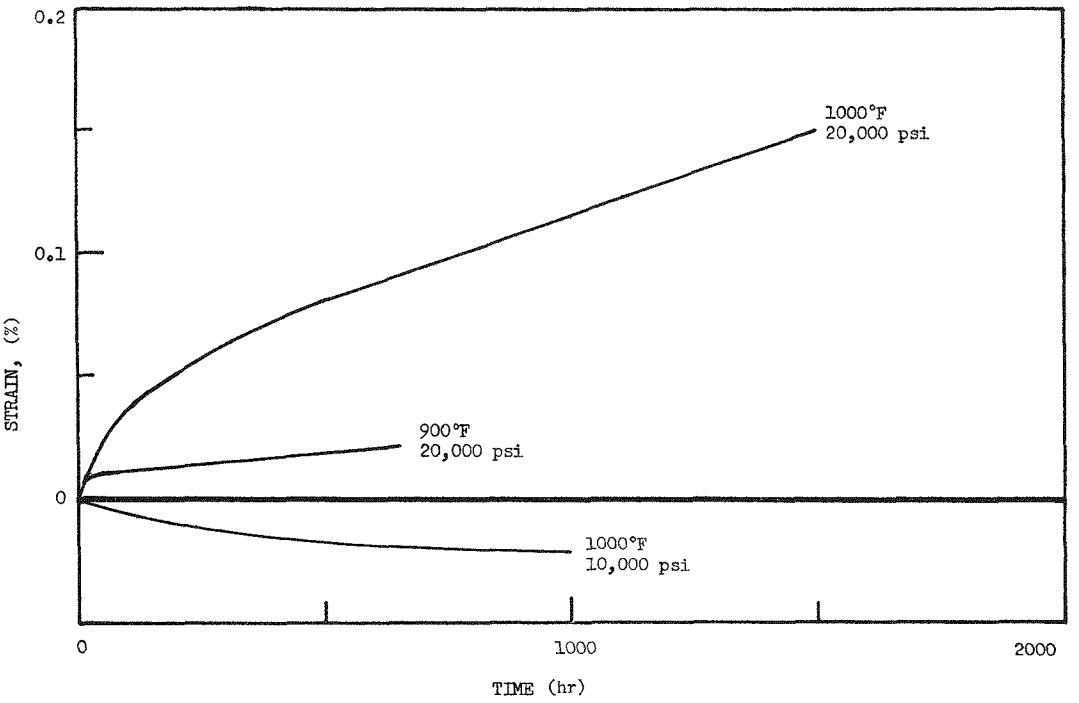

FIGURE VII-70 *Creep Curves for EBR-II Instrumented Creep Capsule Specimen Material with Data on 20% Cold-Worked 316 SS at 1000°F.*

reduction in thermal creep thus attained is shown in Figure VII-70. Also shown in Figure VII-70 is a test conducted at 1000°F and 10,000 psi. This specimen was observed to shorten slightly. This shortening effect is expected to make the evaluation of irradiation-induced creep more difficult. It has been observed in both 304 and 316 SS at low stresses, where the shortening effect was larger than the creep strain. In certain instances, it has obscured the measurement of irradiation-induced creep. It is anticipated that, at 900°F and 20,000 psi, the irradiation-induced creep rate will be large enough in the EBR-II to offset the shortening phenomenon.

The strain rate of the EBR-II creep capsule specimen material is compared with other materials in Figure VII-71. At low stresses, a divergence is observed, with the EBR-II creep capsule specimen material becoming relatively weaker. Other HEDL data on 20% cold-worked 316 stainless steel at 1000°F show a trend similar to that predicted. (Ref 33a)

b. 100 K E Capsule

A creep capsule capable of being operated in a fuel channel in the K East reactor is being designed. This capsule will operate in a flux tailored and enhanced region of the reactor. This capsule, designated K-II, is nearly identical to the previous model (KI) used in Hanford reactors for over two years. The objective of the new capsule development is to provide facilities for conducting in-reactor creep tests at a somewhat higher fast flux than was possible in the KI model.

The initial test planned for the K-II capsule is on 20% cold-worked AISI type 316 stainless steel. This test will be operated at conditions identical to the EBR-II test, namely, 20,000 psi stress and 900°F. Should the initial creep rate under these conditions be very low, the stress level will be increased.

The K-II test is scheduled for completion in February 1971. A three month test duration is planned.

References

33a Biancheria, A., Bishop, A. A., Boltax, A., Ray, W. E., and Riley, B., Oxide Fuel Element Development Quarterly Progress Report for the Period Ending December 31, 1968, WARD-3791-32 (1969) 16.

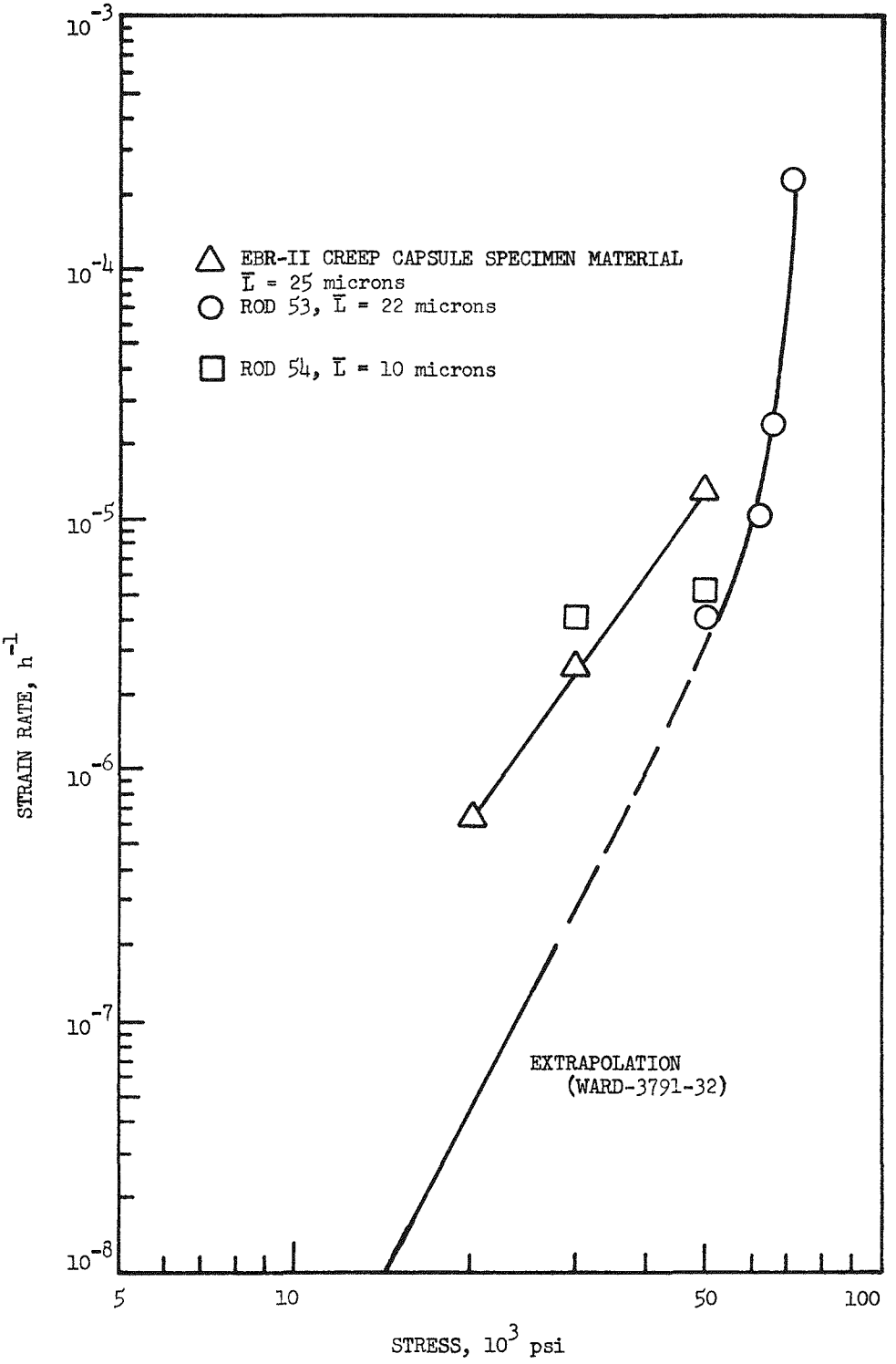

FIGURE VII-71 *Comparison of Creep Rates for EBR-II Instrumented Creep Capsule Specimen Material with Data on 20% Cold-Worked 316 SS at 1000°F.*

11. Analysis of Irradiation-Induced Creep (12215)

E. R. Gilbert and J. J. Holmes

An attempt to provide correlation of irradiation-induced creep data on annealed austenitic stainless steels was made using the creep equation form proposed by McVetty (Ref 34).

$$\varepsilon = A\sigma \quad (1 - e^{-\phi t/B}) + C\sigma\phi t \qquad (1)$$

which was used by Hesketh (Ref 35) to describe the creep of annealed EN58B springs in the Herald Reactor. In this equation, ε is the irradiation-induced strain; σ is applied stress; ϕ is neutron flux; t is time; and A, B, and C are constants for a given temperature, material and reactor position. Data were used from tests conducted in tension on Type 304 SS in a Hanford thermal reactor KI test facility (Ref 36), in torsion on EN58B in the Herald reactor (Ref 35), pressurized tube experiments on Type 304 SS in the EBR-II (Ref 37), and torsion on Type 316 SS in the DFR (Ref 38).

The creep rates determined in these tests are plotted in Figure VII-72 vs neutron flux. Broken points represent predicted creep rates for the Hanford thermal reactor K-II test facility, the EBR-II instrumented creep test, and the FTR Driver I. (Ref 39). The creep rate is normalized for stress in accordance with equation (1). It is also normalized for state of stress by using effective strain and effective stress for non-conservative-volume irradiation-induced creep (Ref 40) as follows:

$$\bar{\varepsilon}/\bar{\sigma} = \gamma/3\tau = \varepsilon/6\sigma = 4\varepsilon_h/33\sigma_h \qquad (2)$$

where $\bar{\varepsilon}/\bar{\sigma}$ is the effective strain per unit effective stress, γ/τ is the shear strain per unit shear stress in a torsion test, ε/σ is the tensile strain per unit tensile stress in a uniaxial tensile test, and ε_h/σ_h is the hoop strain per unit hoop stress for the tangential direction in a pressurized tube. The strain rate is also compensated for temperature by α, defined as (Ref 39):

$$\alpha = \exp\ (1.41 - 0.0027T) \qquad (3)$$

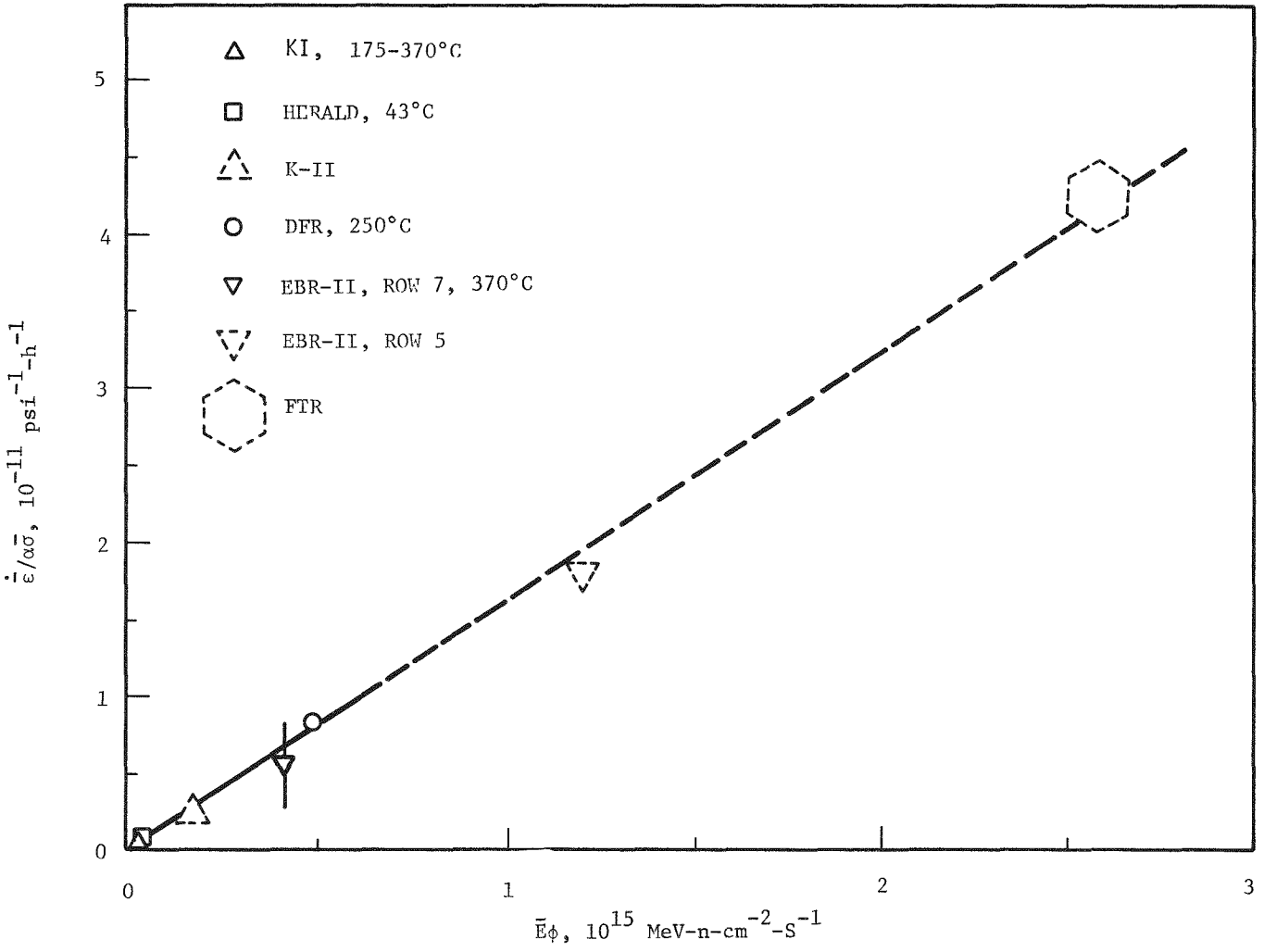

FIGURE VII-72 *Effect of Neutron Flux on Creep Rate for Annealed Austenitic Stainless Steels. Creep rate is normalized for stress, state of stress, and temperature. Flux is normalized for spectral differences with the average neutron energy.*

where T is temperature, °K. The relationship in equation (3) normalized the temperature to 250°C, the temperature of the DFR creep experiments. The neutron flux is normalized for differences in spectra by using the average neutron energy $\bar{E}$. It was found in a damage function analysis (7) that the effectiveness of a reactor test facility in producing creep was proportional to $\bar{E}$. Figure VII-72 shows that the irradiation-induced creep rate is proportional to the product of the neutron flux and the average neutron energy.

Creep Mechanisms.-The formation (Ref 35) of small Frank dislocation loops on preferred planes in an applied stress field, as well as their subsequent growth by point defect absorption (Ref 41), have been considered as mechanisms for irradiation-induced creep at low temperatures in nonfissile metals and alloys. These loops are generated by the coalescence of irradiation-generated point defects and subsequent collapse into loops. During neutron irradiation at high temperatures, the extrinsic loops in austenitic stainless steel grow until they reach a critical size, then become unfaulted. The unfaulting process is described in terms of the nucleation of a Schockely partial dislocation which sweeps across the Frank partial to form a unit dislocation according to a reaction of the type

$$a/6\ [11\bar{2}] + a/3\ [111] \rightarrow a/2\ [110]. \qquad (4)$$

Consideration of the difference in energy between the faulted loop and the unfaulted loop shows that the reaction is energetically favorable (Ref 42) when

$$\gamma > \frac{Ga^2}{24\ \pi R} \frac{(2 - \nu)}{(1 - \nu)} \ln\left(\frac{R}{r_o}\right) \qquad (5)$$

where γ is the stacking fault energy, G is the shear modulus, a is the lattice parameter, R is the loop radius, ν is Poisson's ratio, and r_o is the radius of the dislocation core. The details of the nucleation of the Schockely partial have not been described in detail, but the change in loop energy with faulted loop radius is very large (about 2 eV per Angstrom

change in radius) so that thermal energy fluctuations probably do not significantly assist the nucleation of the Schockely partial. The unfaulting shows a strong temperature dependence (Ref 43), however, which is probably due to the temperature-dependence of diffusion through which loops grow to a critical radius and become unfaulted. The critical radius for unfaulting of a Frank partial loop in an austenitic stainless steel with a stacking fault energy of 17 ergs/cm^2 at a temperature of 500°C is 650 Å.

The creep rate due to unfaulting of Frank partials can be developed from the Orowan equation, which expresses strain as the product of mobile dislocation density, Burger's vector and dislocation displacement. Differentiation with respect to time yields:

$$\frac{d\gamma}{dt} = bx\frac{d\rho}{dt} + b\rho\frac{dx}{dt} \qquad (6)$$

where γ is strain, t is time, b is the Burger's vector, ρ is dislocation density, and x is dislocation displacement. The first term arises from the nucleation rate of dislocations or the rate at which irradiation-induced Frank partial loops become unfaulted, and their subsequent glide until they are held up at obstacles. Stress and temperature will assist in the bowing of loop segments from which a stress and temperature dependence will arise; however, due to the large activation area, stress will have the dominant influence. The second term arises from the rate of motion of unfaulted loop segments beyond the glide radius where dislocations become pinned. The stress and temperature dependence is similar to that for thermal creep. The combined expression for the creep rate by this mechanism is:

$$\frac{d\gamma}{dt} = b\pi\left(r_p^2 - r_c^2\right)\frac{d(N)}{d(\phi t)}\,\phi f(\sigma,T) + \left(\frac{N\pi r_p^2}{\rho}\,\frac{d\gamma}{dt}\right)_{\text{Thermal}} \qquad (7)$$

where N is the number of loops per unit volume, r_p is the radius at which unfaulted loops are pinned, r_c is the critical radius for unfaulting, ϕ is

neutron flux, t is time, σ is stress, T is temperature, and ρ is dislocation density. The second term is expected to have only a small effect on creep in most cases. An estimate of the influence of the first term based on $r_p = 10^3$ Å, $r_c = 650$ Å, and $d(N)/d(\phi t) = 10^{-6}$ loops-cm^{-3}-n^{-1}-cm^2 for EBR-II is a creep rate on the order of 10^{-6} to 10^{-5} h^{-1} at stresses from 10,000 to 20,000 psi. The expected rate is sensitive to microstructure, stress, and temperature.

References

34. McVetty, P. G., Trans. ASME, 55 (1933) 99.

35. Hesketh, R. V., "Collapse of Vacancy Cascades to Dislocation Loops," Proc. Intern. Conf. Solid State Physics Research with Accelerators, BNL-50083 (C-52) (1967) 389.

36. Gilbert, E. R., Work in progress, WADCO Corporation, Richland, Washington (1970).

37. Walters, L. D., Walter, C. M., Pugacz, M. A., Tesk, J. A., Carlander, R. and Li, Che-Yu, "EBR-II In-Pile Creep Experiments on Stainless-Steel Tubing," Trans. Am. Nucl. Soc., 13 (1970) 145.

38. Mosedale, D., Lewthwaite, G. W., Leet, G.O., and Sloss, W., "Irradiation Creep in the Dounreay Fast Reactor," Nature, 224 (1969) 1301.

39. McElroy, W. N., Dahl, R. E., Jr., and Gilbert, E. R., "Neutron-Energy-Dependent Damage Function for Analysis of Austenitic Steel Creep Data," to be published in Nucl. Eng. Design.

40. Gilbert, E. R., and Straalsund, J. L., "A Relationship for Non-Conservative-Volume Creep under Different States of Stress," Nucl. Eng. Design, 12 (1970) 421.

41. Kosevich, A. M., Saralidze, Z. K., and Slezov, V. V., "Effect of Irradiation on the Diffusional-Dislocational Flow of Crystals," Soviet Physics-Solid State, 9 (1967) 697.

42. Hull, D., "Dislocations in Face-Centered Cubic Crystals," Introduction to Dislocations, Pergamon Press (1968) 100.

43. Brager, H. R. and Bates, J. F., "Microstructural Analysis of Swelling in EBR-II Irradiated Stainless Steels," Trans. ANS, 13 (1970) 146.

12. Irradiation Effects on the Fracture of Heavy Section Pressure Vessel Steels (12242)

C. W. Hunter, J. A. Williams, J. A. Ulseth, R. L. Knecht and H. H. Yoshikawa

a. Specimen Irradiations

Specimen irradiations were resumed in the M-3 hot water loop of the ETR at the beginning of reactor cycle 108, after the addition of loop heaters to allow temperature control of the M-3 specimen assembly over a temperature range from 125°F to 600°F.

Two specimen tubes of the M-3 irradiation capsule were modified for the irradiation of Charpy specimens. The capsule, as charged during cycle 108 contained 12 one-in. CT specimens, 24 Charpy-V specimens and 21 tensile specimens. Of the CT specimens, 8 were WR orientation A533 B HSST plate 02, with goal exposures being 2×10^{19} and 8×10^{19} n/cm^2(E>1 Mev) for two groups of four, respectively. The balance of 4 CT specimens are weld center material of A533 B (submerged arc) with a goal exposure of 8×10^{19} n/cm^2 (E>1 Mev). The Charpy-V specimens include five each WR and RW A533 B, with a goal exposure of 2×10^{19} n/cm^2(E>1 Mev), and 7 each WR and RW, with goal exposure of 8×10^{19}n/cm^2 (E>1 Mev). Nine and eight A533 B transverse tensile specimens are to be irradiated to 2 and 8×10^{19}n/cm^2(E>1 Mev), respectively. Four weld center tensile specimens were inserted for a goal fluence of 2×10^{19}n/cm^2(E>1 Mev).

A dosimeter pin with monitor sets selected to provide the energy-dependent absolute integral flux (10^{-10} to 18 Mev) at three axial positions in the M-3 capsule was included for irradiation during cycle 108. Previous flux determinations have been made using Fe and Al-0.1% Co wire dosimeters and a calculated spectrum. Determination of the actual spectrum will increase the degree of confidence placed on previous flux determinations, or will provide the necessary correction factors.

b. Base Material Studies of ASTM A533 B

Irradiated 1T CT specimens from 12-in. ASTM A533 Grade B Class 1-HSST

plate 02 were tested at temperatures as high as 175°F and as low as -125°F. Specimens were of RW orientation, irradiated to approximately 2 x 10^{19} n/cm^2 (E>1 Mev) at 540°F. The results of completed irradiated fracture toughness studies are given in Table VII-22. The fracture toughness for irradiated A533 B (Figure VII-73) exhibits a considerable sensitivity to irradiation embrittlement. In terms of arbitrary toughness levels of 40 and 60 ksi, the shift in properties is approximately 240°F and 210°F, respectively. The start of transitional behavior is indicated only through the use of invalid fracture toughness, K_Q, data. The unirradiated K_Q data shown closely represents the fracture behavior of A533 B compared to the data of Shabbits, Pryle and Wessel (Ref 44) for the same material; it is surmised that the irradiated K_Q values represent, at least, a temperature range in which an increase in toughness would actually be observed. Eventual verification of transitional behavior will depend on the results of valid fracture toughness measurement.

TABLE VII-22
FRACTURE TOUGHNESS OF IRRADIATED ASTM A 533, GRADE B,
HSST PLATE 02 HEAVY SECTION STEEL, RW ORIENTATION

Specimen	Test Temp (°F)	Crack Length, a (in.)	Yield Strength (psi x 10^3)	Irradiation Exposure 10^{19} n/cm^2(E>1 MeV)	K_Q Ksi$\sqrt{in}$	$2.5(\frac{K_Q}{\sigma_{ys}})^2$	K_{Ic} Ksi$\sqrt{in}$
02GA10	-120	1.026	115	1.85	27.6	.145	27.6
02GA24	-100	1.119	107	2.28	40.5	.358	40.5
02GA23	- 25	1.063	101	2.10	32.8	.264	32.8
02GA22	26	.971	97	1.82	41.8	.458	41.8
02GA 1	85	.973	94	1.85	43.1	.525	43.1
02GA 4	120	.924	92	1.83	47.0	.654	47.0
02GA 9	125	.994	92	1.7	82.3	1.98	
02GA 3	145	.991	91	1.85	69.7	1.47	
02GA 2	175	1.014	89	1.92	79.6	2.0	

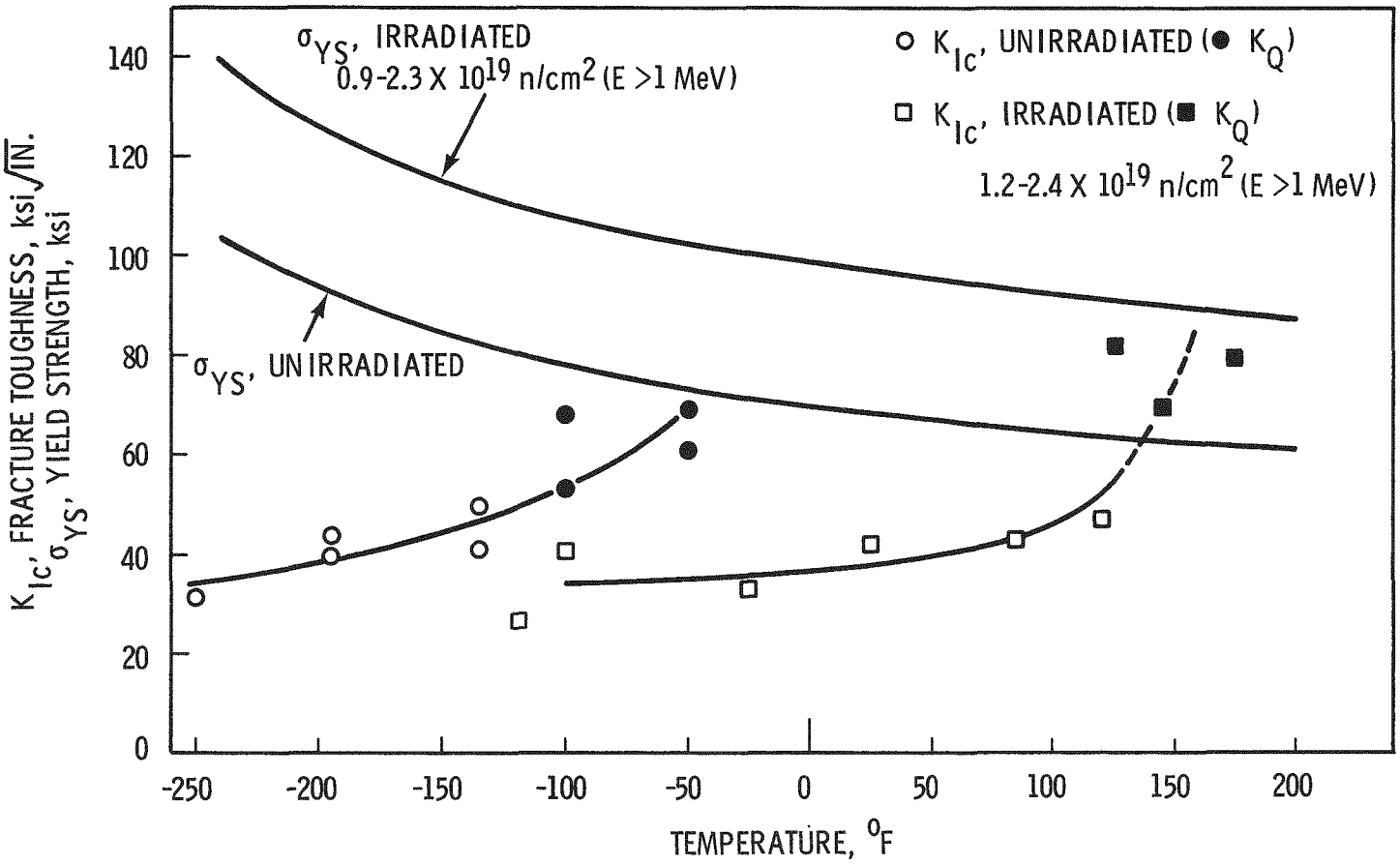

FIGURE VII-73 *Fracture toughness and yield strength of irradiated and unirradiated A533 Grade B, Class 1 Steel as a Function of Temperature. The properties are for the RW orientation of HSST plate 02.*

An analysis incorporating the combined effects of irradiation, stress and temperature on a simple structure of A533 B, a plate six inches thick with a crack of depth "a" and of unit plane strain length (Ref 45), is shown in Figure VII-74. The critical flaw depth under conditions of yield loading has been calculated from fracture toughness data. Temperatures above which significant flaw sizes can be tolerated can readily be seen. The temperature shift in this type of analysis is of significance, because the effect of irradiation on both the yield strength and decrease in the fracture toughness have been accounted for.

The fracture appearances of irradiated A533 B specimens over the temperature range investigated are shown in relation to the fracture toughness curve in Figure VII-75. An increasingly tougher appearance is observed with increasing test temperature. The most pronounced shear lips and fracture toughness is observed between 145 and 175°F.

Tensile specimens and CT specimens irradiated to $8 \times 10^{19} n/cm^2$ (E>1 Mev) are presently in various stages of testing and preparation for testing. Tensile specimens will be tested between -100°F and 500°F prior to testing the fracture toughness specimens.

c. Fatigue Crack Preparation in CT Specimens

In linear elastic fracture toughness determination, the critical stress intensity (K_{Ic}) is that for fracture initiation from a sharp fatigue crack. Hence, the preparation of a fatigue crack in the fracture specimens is a necessary preliminary to actual toughness determinations. Consideration of the loading conditions during such fatigue crack preparation provides an opportunity to extract some information on fatigue crack behavior. To be sure, these loading conditions were not intended to provide pure propagation data, such as the crack growth rate per cycle (da/dn) versus cyclic stress intensity (ΔK) relationship developed by Paris (Ref 46). Nevertheless, this information does offer some examples of and insight into the practical situation of crack initiation, stalling, and re-initiation, (incubation) as well as propagation.

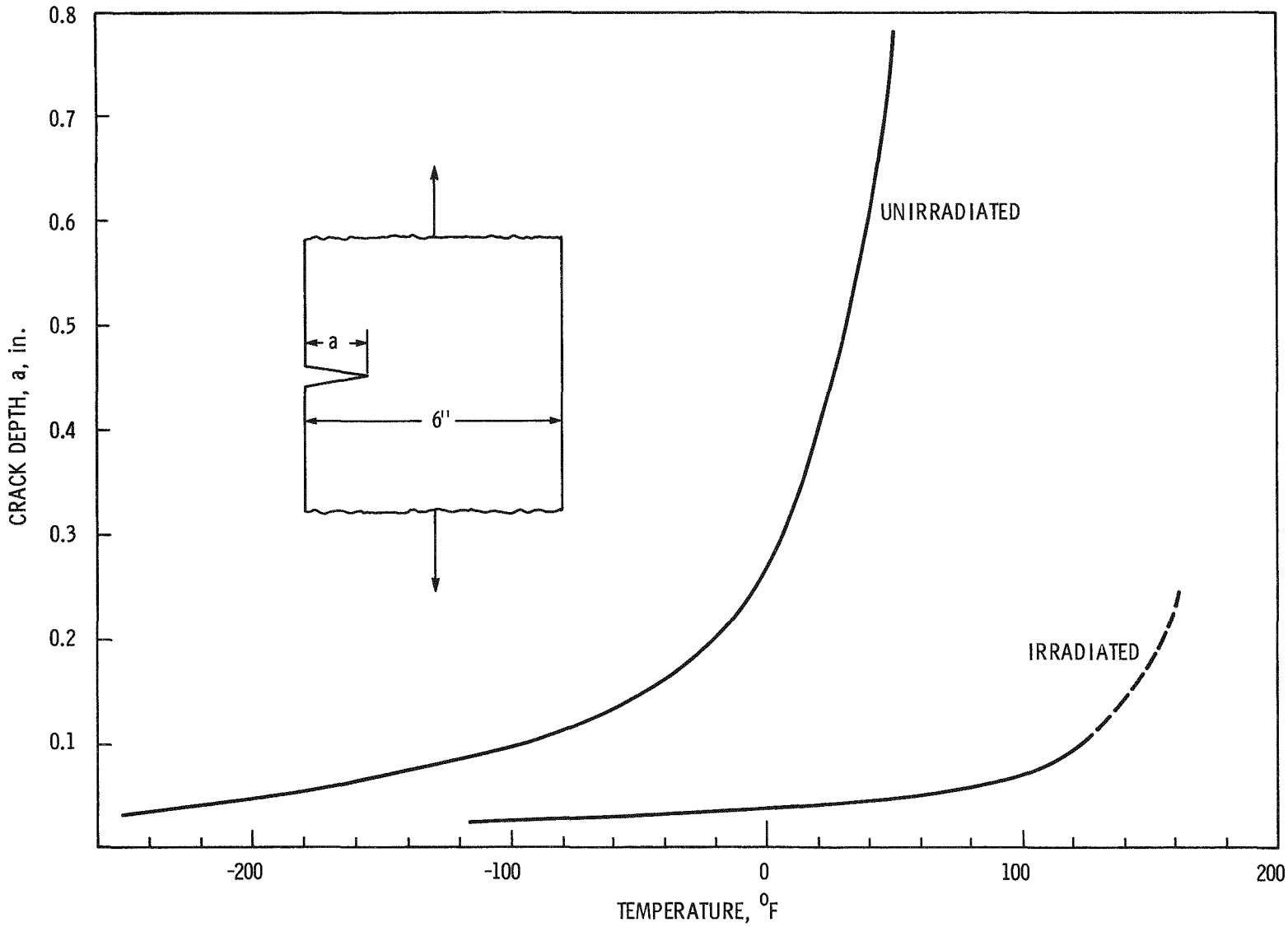

FIGURE VII-74 *Critical Flaw Size as a Function of Temperature in a Simple Structure of Irradiated and Unirradiated A533 B. The observed shift is of significant importance because the effect of irradiation on both the yield strength and the fracture toughness has been considered in the analysis.*

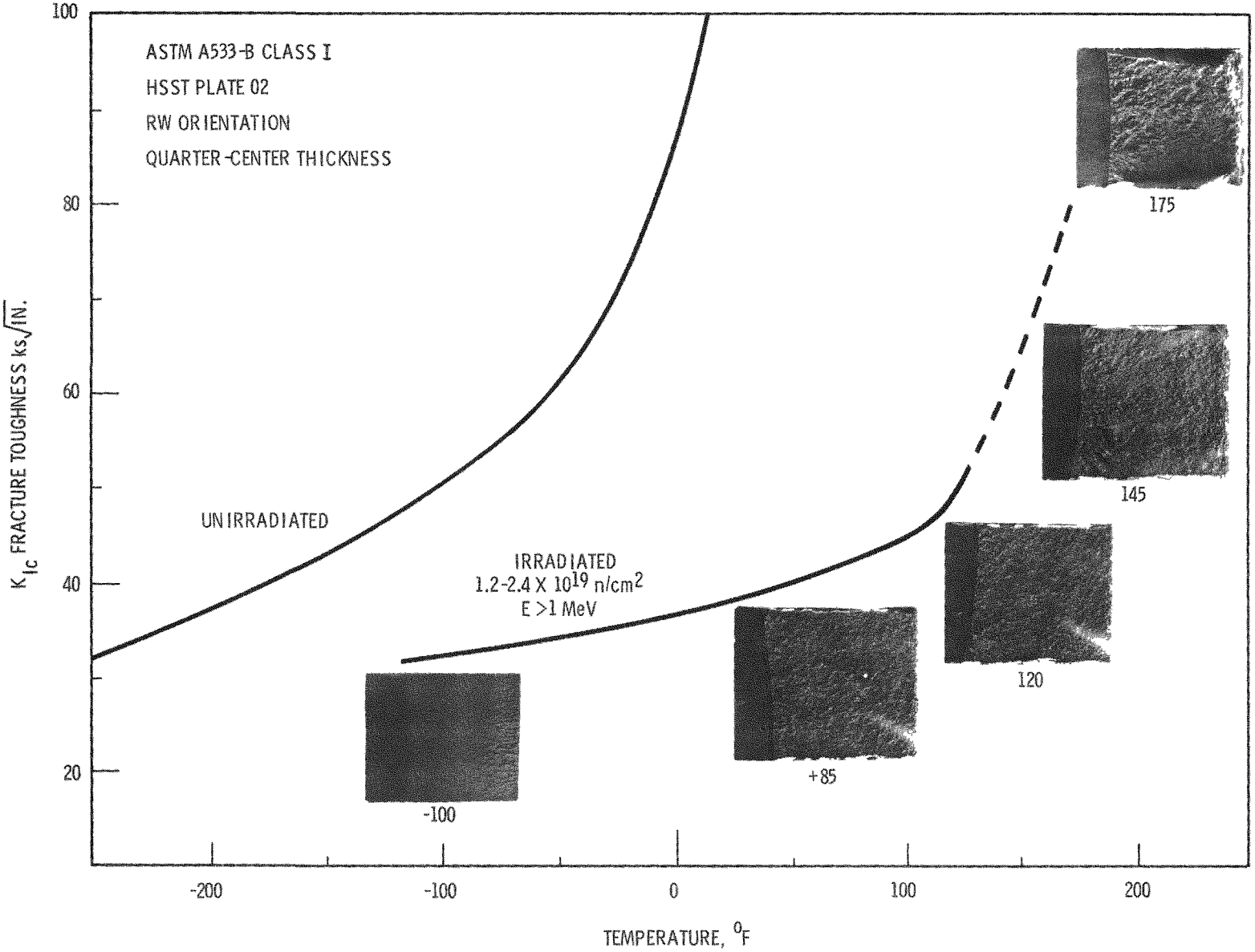

FIGURE VII-75 *Fracture Surfaces from one-in. Thick Specimens of Irradiated ASTM A533 B Pressure Vessel Steel in Relation to Toughness Characteristics. The Test Temperature of Each Specimen is Noted.*

The details of the fatigue cracking have been previously described. The effective crack growth for initiation and propagation in the base material and weldment approached pure crack propagation rates, with a distinct propensity for hindrance. The fatigue crack propagation in irradiated base material specimens has provided an opportunity for a cursory assessment of the irradiation effect on fatigue. The comparison in Table VII-23 suggests a doubling of the effective propagation rate due to irradiation. However, this observation must be considered preliminary, because a different crack monitoring system was used in the hot cell on the irradiated specimens than on the unirradiated ones.

TABLE VII-23
IRRADIATION INFLUENCE ON THE EFFECTIVE FATIGUE CRACK EXTENSION BEHAVIOR IN IT CT SPECIMENS OF ASTM A533 B FROM HSST PLATE 02

Fatigue Step	Unirradiated		Irradiated ($1.5\text{-}2.5 \times 10^{19}$ n/cm^2)	
	ΔK (psi $\sqrt{\text{in}}$)	Crack Rate (in/cycle)	ΔK (psi $\sqrt{\text{in}}$)	Crack Rate (in/cycle)
1 (from machined notch)	26,100	1.22×10^{-6}	26,060	2.44×10^{-6}
2	22,200	1.73×10^{-6}	21,700	2.71×10^{-6}
3	18,000	1.07×10^{-6}	17,200	1.06×10^{-6}
4	13,300	0.31×10^{-6}	12,700	0.62×10^{-6}

References

44. Shabbits, W. O., Pryle, W. H., and Wessel, E. T., "Heavy Section Steel Technology Program Technical Report No. 6-Heavy Section Fracture Toughness Properties of A533 Grade B, Class I, Steel Plate and Submerged Arc Weldment", Westinghouse Atomic Power Division, WCAP-7414, December 1969.

45. Paris, P. C. and Sih, G. C.,"Stress Analysis of Cracks", ASTM STP 381-Fracture Toughness Testing and Its Applications, American Society for Testing and Materials, PP. 44, 1964.

46. Johnson, H. H. and Paris, P. C., "Subcritical Flaw Growth", Engineering Fracture Mechanics, Vol. 1, pp. 3-45, 1968.

13. Physical and Microstructural Changes in Irradiated FTR Candidate Materials - 12215

J. L. Straalsund, H. R. Brager, J. F. Bates, J. J. Laidler, G. L. Guthrie and T. K. Bierlein

The dimensional and microstructural changes produced by neutron irradiation of austenitic stainless steels are being characterized to provide information needed to interpret fast reactor irradiation effects, to assist in formulating material irradiation behavior models, and to establish bases for improving the performance of austenitic stainless steel in reactor environments.

Changes in density and microstructure of a series of irradiated AISI 316 and 304 SS and some nickel alloys with varying degrees of cold work are being evaluated. The results show that, for irradiation temperatures between 700°F and 1400°F and fluences between 2 and 3 x 10^{22} n/cm^2 (E>0.1 MeV), cold work reduces swelling in 316 SS to negligible amounts.

a. Density Measurements

Tentative results for the density measurements are listed in Table VII-24. The irradiation temperatures were estimated by assuming radial heat flow only; these will be revised when more detailed heat transfer calculations are done. The fluence values were calculated on the basis of the irradiation history given in Table VII-25 and will be updated when dosimetry results are available.

The following trends are evident for 316 SS:

1) The data in Table VII-24 was normalized to a fluence of 3 x 10^{22} n/cm^2 by assuming a fluence dependency of the form $\Delta V/V \sim (\phi t)^{1.7}$ and was plotted as a function of temperature in Figure VII-76. The figure shows that both 25 and 75% cold work essentially eliminate swelling in the AISI 316 stainless steel. Only one cold-worked specimen (25% cold work irradiated at 900°F) was found to exhibit swelling (0.08%).

TABLE VII-24
DENSITY MEASUREMENTS OF SPECIMENS IRRADIATED IN PIN NO. BNWL-24 IN EBR-II

Specimen	Identity	Fluence, 10^{22} n/cm^2 (E > 0.1 MeV)	Calculated Temp (°f)	Density (g/cm^3)	Spread (%)	Δv/v (%)	Calculated Δv/v(%)*
7D-1	316-Ann.	1.83	700	7.9442	0.15	0.27	0.23
7D-2	316-25% CW			7.9718	0.14	-.07	
7D-3	304-50% CW			7.9017	0.12	-.02	
7D-4	316-75% CW			7.9717	0.10	-.07	
5D-1	316-Ann.	2.35	800	7.9359	0.14	.38	0.7
5D-2	316-25% CW			7.9730	0.05	-.09	
5D-3	304-50% CW			7.8882	0.07	0.15	
5D-4	316-75% CW			7.9737	0.06	-.10	
3D-1	316-Ann.	2.90	1100	7.9768	0.13	-.14	1
3D-2	316-25% CW			7.9769	0.14	-.14	
3D-3	304-50% CW			7.8914	0.09	0.11	
3D-4	316-75% CW			7.9737	0.11	-.10	
1D-1	316-Ann.	3.05	1300	7.9767	0.11	-.14	0.52
1D-2	316-25% CW			7.9801	0.11	-.18	
1D-3	304-50% CW			7.9072	0.12	-.09	
1D-4	316-75% CW			7.9747	0.08	-.11	
1V-1	316 Ann.	3.05	1400	7.9740	0.13	-.10	0.33
1V-2	316-25% CW			7.9726	0.10	-.08	
1V-3	304-50% CW			7.9162	0.11	-.20	
1V-4	316-75% CW			7.9771	0.07	-.14	
2V-1	316-Ann.	2.99	1200	7.9623	0.07	0.04	0.76
2V-2	316-25% CW			7.9758	0.06	-.13	
2V-3	304-50% CW			7.8590	0.06	0.523	
2U-4	316-75% CW			7.9718	0.07	-.08	
4U-1	316-Ann.	2.63	1000	7.9546	0.10	0.14	1.05
4U-2	316-25% CW			7.9680	0.11	-.03	
4U-3	304-50% CW			7.9068	0.06	-.08	
4U-4	316-75% CW			7.9699	0.10	-.05	
5U-1	316-Ann.	2.07	900	7.9454	0.06	0.26	0.73
5U-2	316-25% CW			7.9591	0.06	0.08	
5U-3	304-50% CW			7.8845	0.09	0.20	
5U-4	316-75% CW			7.9689	0.07	-.04	
7U-5	Ni-200 Ann.	1.83	900	8.7255	0.14	1.81	
7U-6	Ni-200-50% CW			8.8166	0.12	0.79	
7U-7	Inconel 600 Ann.			8.4466	0.05	0.05	
7U-8	Inconel 600-50% CW			8.4481	0.06	0.03	
5U-5	Ni-200-Ann.	2.35	1000	8.7356	0.11	1.70	
5U-6	Ni-200-50% CW			8.7828	0.09	1.17	
5U-7	Inconel 600 Ann.			8.4467	0.06	0.06	
5U-8	Inconel 600-50% CW			8.4458	0.03	0.06	
3U-5	Ni-200-Ann.	2.90	1100	8.8320	0.11	0.61	
3U-6	Ni-200-50% CW			8.7821	0.03	1.17	
3U-7	Inconel 600-Ann.			8.4435	0.10	0.09	
3U-8	Inconel 600-50% CW			8.4372	0.01	0.16	
2D-5	Ni-200 Ann.	2.99	1200	8.8449	0.07	0.47	
2D-6	Ni-200-50% CW			8.8315	0.20	0.62	
2D-7	Inconel 600-Ann.			8.4416	0.10	0.11	
2D-8	Inconel 600-50% CW			8.4434	0.13	0.09	
4D-5	Ni-200 Ann.	2.63	800	8.6496	0.09	2.66	
4D-6	Ni-200-50% CW			8.7316	0.15	1.74	
4D-7	Inconel 600-Ann.			8.4313	0.06	0.23	
4D-8	Inconel 600-50%			8.4337	0.05	0.20	

TABLE VII-25
IRRADIATION DATA ON PIN NO. 24

Irradiation History	Specific Value
EBR-II Runs	30 through 40, inc.
Position	2D-1 except for run 38B (62MW) in which the pin occupied position 5D-2 (exposure in this position was 770 MW days)
Total Exposure	10,014 MWd
Calculated Peak Fluence	$3.05 \times 10^{22} n/cm^2 (E > 0.1 MeV)$

2) Almost all of the cold-worked 316 specimens and some of the solution-treated specimens, irradiated at high temperatures, increased in density. Because this may be due to a thermally induced solid-state phase transformation (producing $M_{23}C_6$ σ) the densities of a specimen of 25% cold worked 316 SS obtained from the same stock used in preparing the irradiated specimens, were measured before and after thermal aging for 260/700 hr at 1200°F. The results are summarized in Table VII-26.

TABLE VII-26
DENSITY CHANGES IN 25% COLD-WORKED TYPE 316 SS DURING AGING

	Density (g/cm^3) Avg of 4 measurements	Range(%)
Before Aging	7.9623	± .03
After Aging	7.9741	± .01
Change in density	.15%	

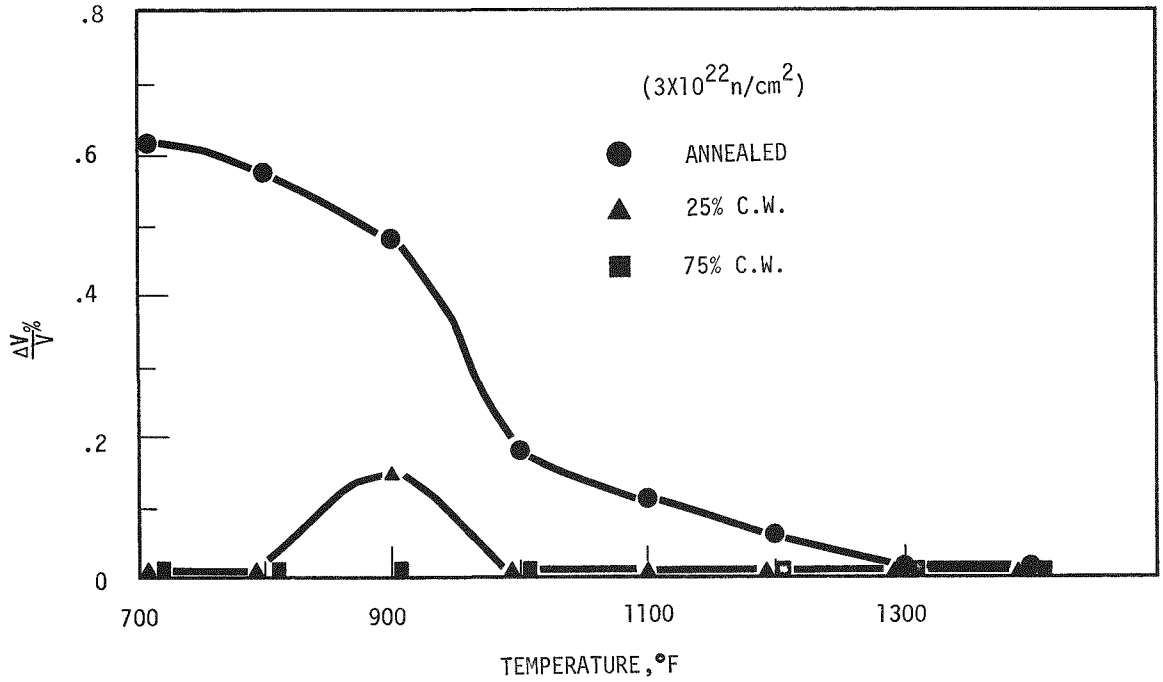

FIGURE VII-76 *Temperature-Dependence of Swelling in Annealed and Cold-Worked 316 SS.*

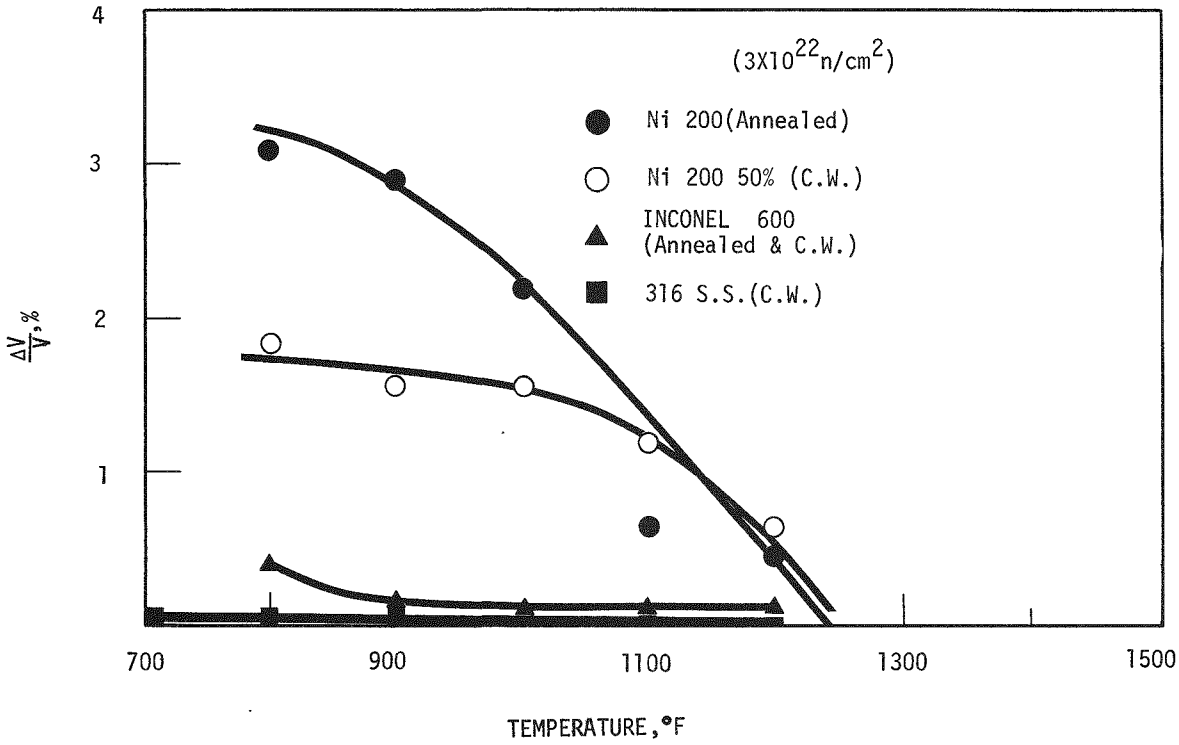

FIGURE VII-77 *Swelling In Candidate Reflector Alloys.*

A similar increase in density (0.17%) was found for a 50% cold-worked sample from the same heat of material. This increase in density is of the same magnitude as that observed for the irradiated specimens. Therefore, the density decreases observed in the irradiated specimens are probably due to this effect. The primary significance of this result is that it confuses the interpretation of small density changes measured in irradiated cold-worked samples by immersion techniques. Specimen 7D-1, for example, may have a void volume fraction as high as 0.37%, even though the density change measured was only 0.27%.

3) The results for the 50% cold-worked 304 indicate that, at 700°F, the cold work suppresses swelling, similar to the results for AISI 316. For the intermediate temperature range of 800°F to 1100°F, the swelling appears to be suppressed by cold work, but not nearly to the extent as that for 316. Finally, at 1200°F, the density change is essentially that expected for annealed material. These results suggest that the swelling resist cold work structure is more thermally stable in 316 than in 304 SS.

The density changes measured for the nickel alloys were normalized to a common fluence of $3 \times 10^{22} n/cm^2$ by assuming a linear fluence dependency. These normalized results are plotted as a function of temperature in Figure VII-77, which shows that the results for Nickel 200 confirm the high degree of swelling expected for relatively pure nickel alloys. For irradiation temperatures up to 1000°F, cold work reduces the swelling found in the nickel; however, more swelling was found for the cold-worked material at 1100°F and 1200°F. It appears likely that the recrystallization temperature for the Nickel 200 with 50% cold work lies between 1000°F and 1100°F. The reason for the cold-worked material offering less swelling resistance than the annealed material for the high temperatures is not apparent.

The maximum amount of change in density found in Inconel-600 was 0.23%. The low amount of swelling and the relatively high nickel content suggests that Inconel-600 may be a useful reflector alloy. In contrast to the results observed for the other alloys, no effect of cold work on swelling in Inconel-600 was found.

b. Transmission Microscopy

Both the annealed and cold-worked 316 specimens are being examined with transmission electron microscopy. The results, summarized in Table VII-27, are consistant with the density measurements. While considerable void formation was found in the solution-treated material, few, if any, voids were found in the cold-worked steels.

The microstructures of the 25% cold worked steels irradiated at calculated temperatures of 800 and 900°F (samples 5D-2 and 6U-2) are shown in Figures VII-78 and VII-79. Stereo examination showed that the light objects shown on the micrographs are near the surface of the foil and are probably surface pits. Essentially no voids were found in these samples. Faulted loops, however, are clearly visible in the diffraction contract micrographs. Figure VII-80 shows a twinned region in sample 6U-2.

The structure of the solution-treated steels irradiated at a calculated temperature of 800°F is shown in Figure VII-81. The sample contains voids, loops and a low dislocation density network. Faulted loops and dislocations in the sample are shown in Figure VII-82.

The microstructure of this particular sample appears to be inconsistant with the results of previous studies and in fact, from the other results from this study. Relative to other studies, the microstructure of this specimen appears more representative of an irradiation temperature of 1000°F than 800°F. One possible explanation for the discrepancy with previous studies is differences in alloy chemistry and process variables. This possibility was suggested earlier, when it was noted that the bulk density results for this material deviated

TABLE VII-27
SUMMARY OF FAST REACTOR IRRADIATED 316 SS DATA

Calculated Irradiation Temp (°F)	Fast Neutron Fluence (E> 0.1 MeV)	Cold-Worked Steel			Solution-Treated Steel				
		Specimen No.	Voids	Interstitial Cluster Morphology	Specimen No.	Average Cavity Size (Å)	Cavity Number Density (cc^{-1})	Void Volume (%)	Interstitial Cluster Morphology
800	2.4×10^{22}	5D-2	(b)	Complex High Density Dislocation Network and Faulted Loops	5D-1	280	1.5×10^{14}	0.2	Faulted Loops & Dislocation Network
900	2.1×10^{22}	6U-2	(b)		6U-1	238	5×10^{14}	0.5	"
1100	2.9×10^{22}	3D-2	(b)	Moderate Dislocation Density	3D-1	296	3×10^{13}	0.06	Low Number Density Dislocation Network
1300	3.0×10^{22}	1D-2	(b)	"	1D-1	108(a)	3×10^{13}	-	"

(a) Probably helium bubbles

(b) Few or no voids visible

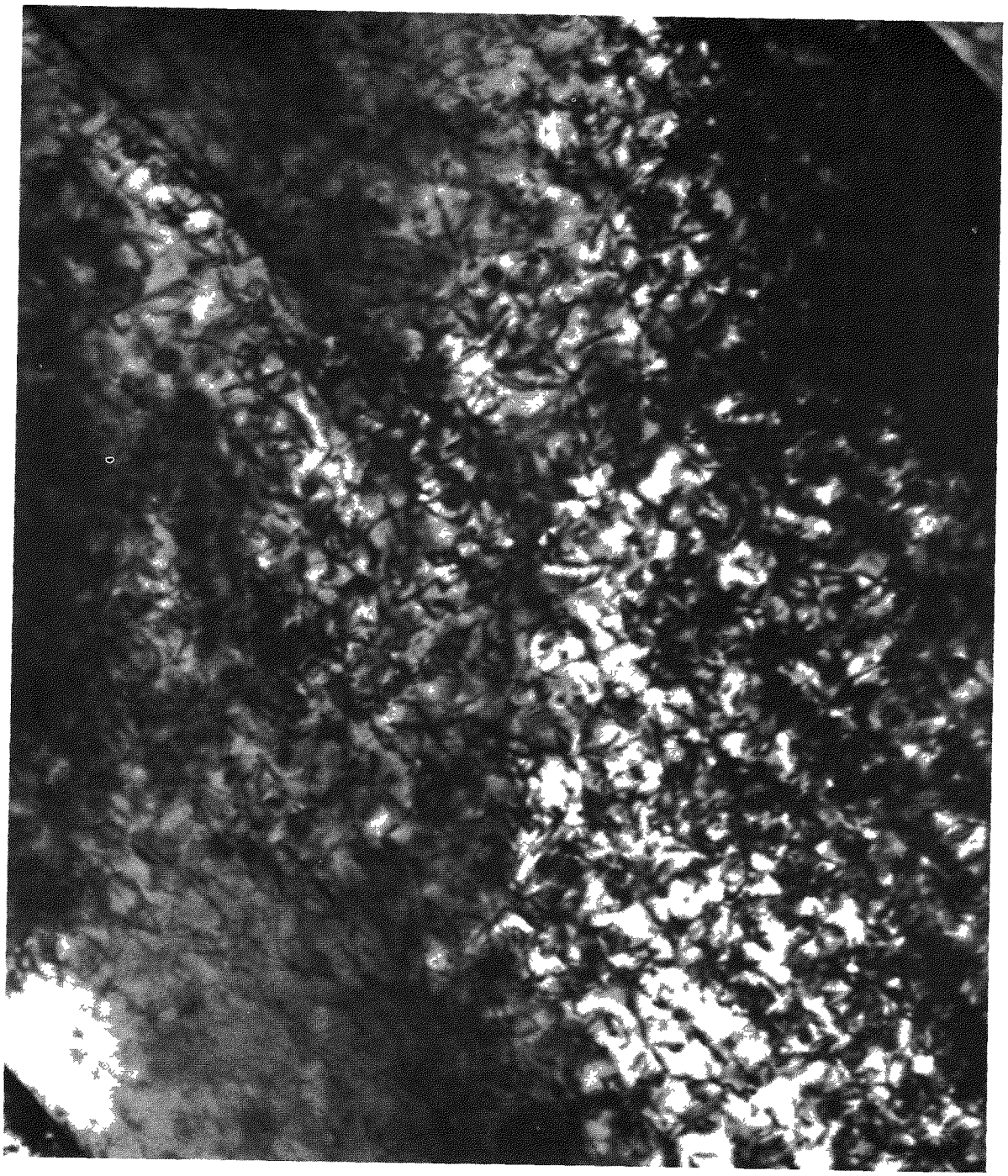

98,000X

FIGURE VII-78 *25% C.W. 316 SS Irradiated at 800°F to 2.4 x 10^{22} n/cm^2 (E > 0.1 MeV). The Bright Field Micrograph Shows a Complex Dislocation Network and Faulted Loops in the Matrix Oriented to a 110 zone axis.*

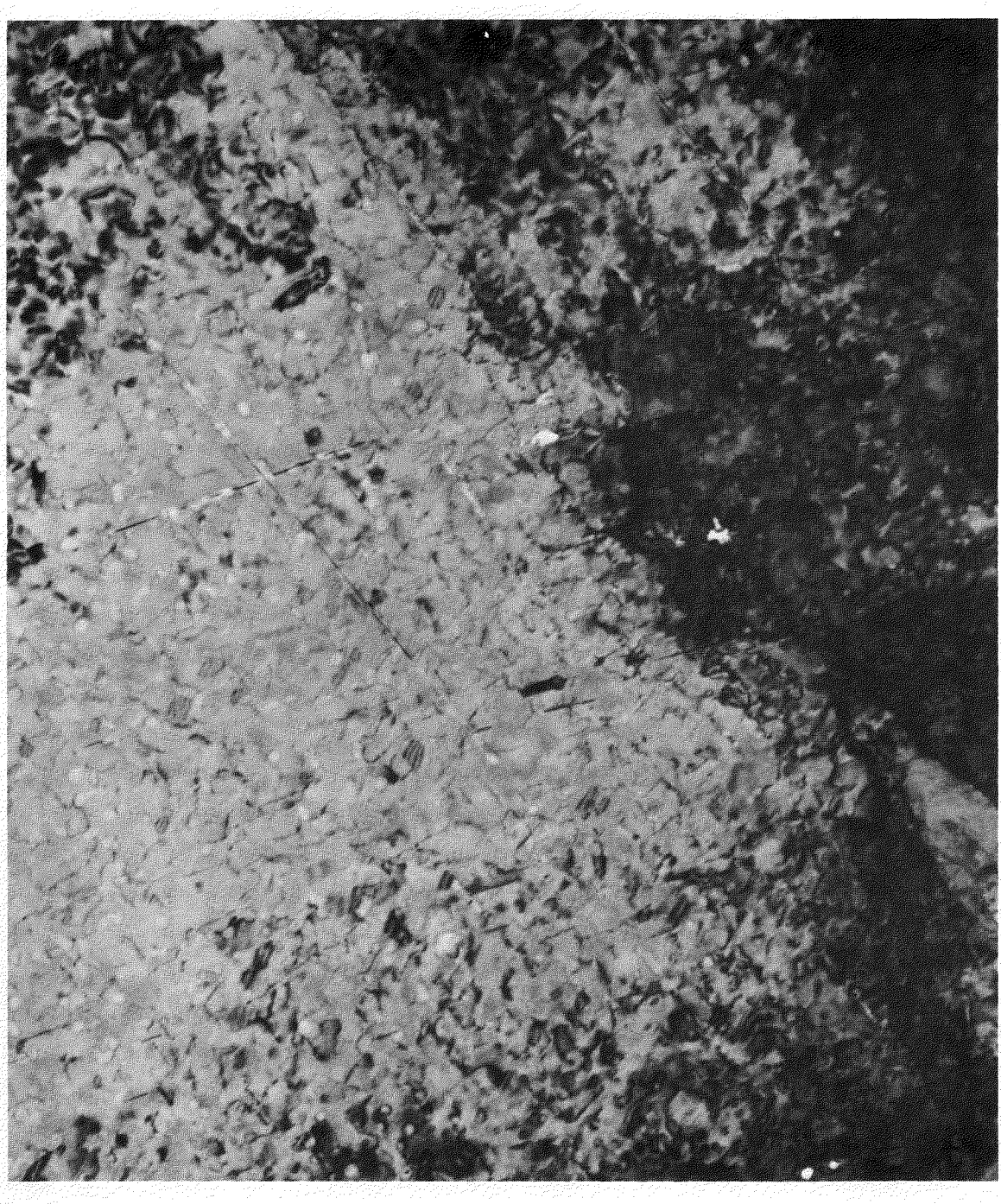

90,000X

FIGURE VII-79 *Same Material and Crystal Orientation as in Figure VII-78 Irradiated at 900°F to 2.1 x 10^{22}n/cm^2(E > 0.1 MeV).*

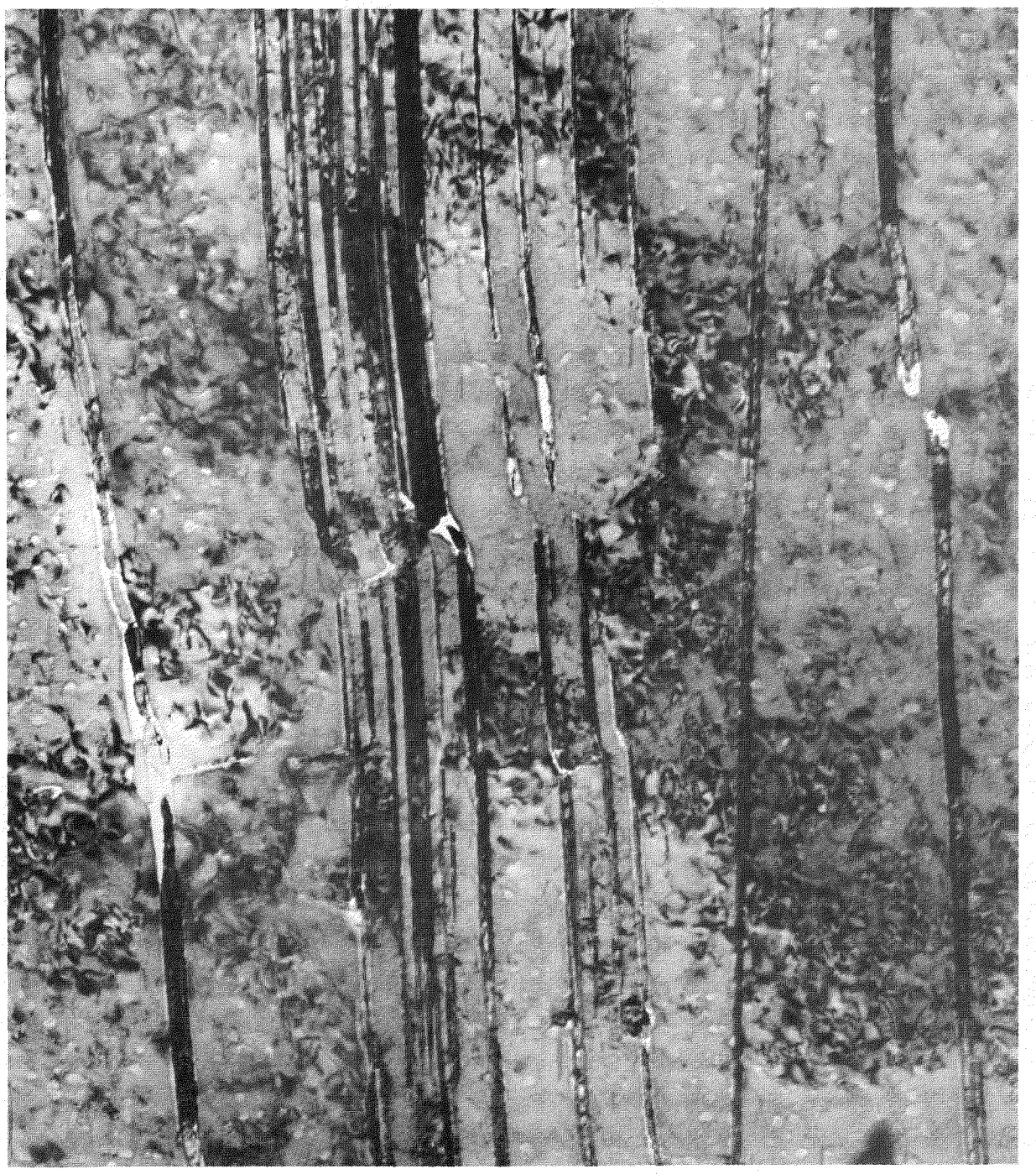

90,000X

FIGURE VII-80 *Distorted Twinned Regions in the 25% C.W. 316 SS Irradiated at 900°F.*

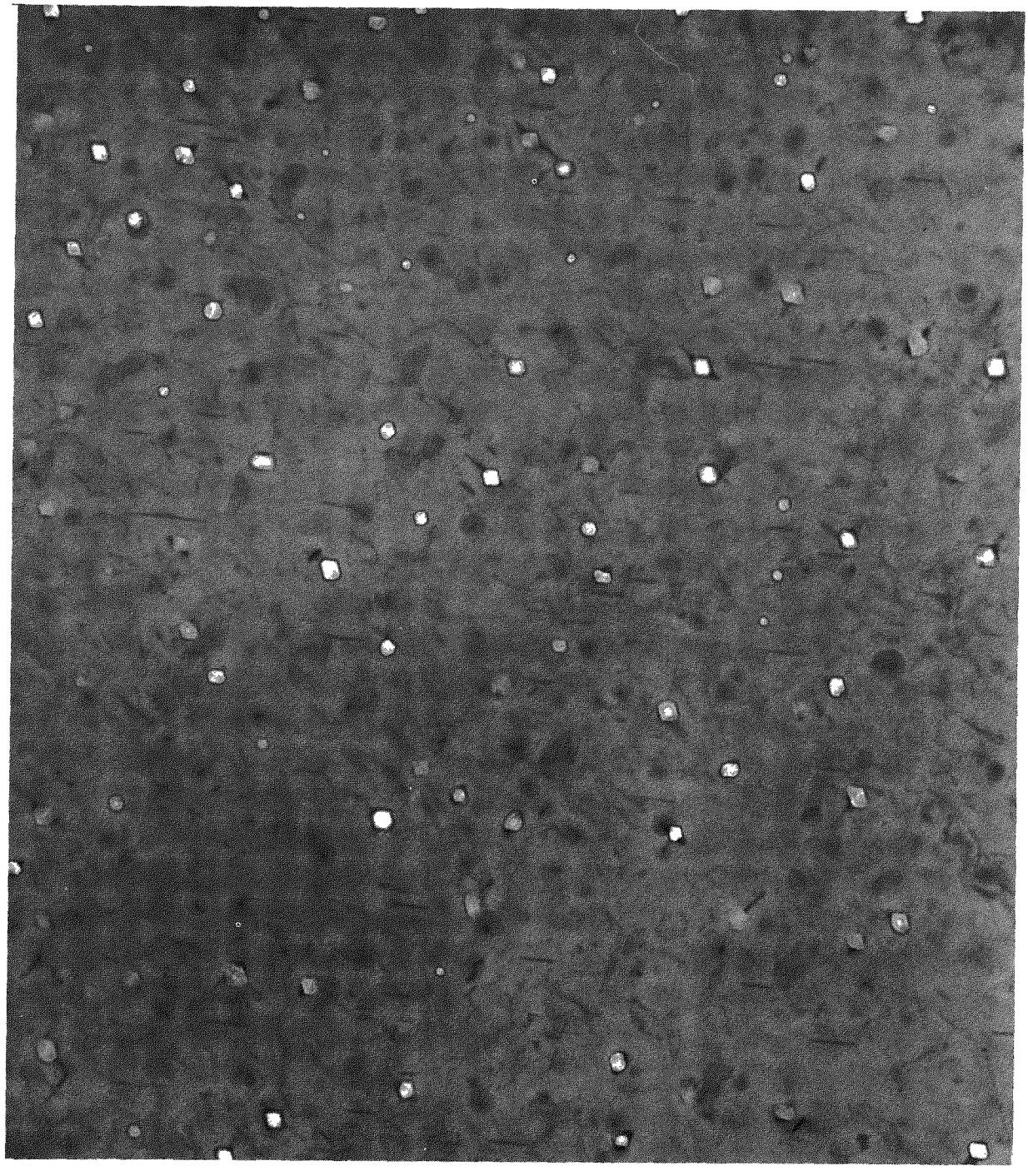

90,000X

FIGURE VII-81 *Solution-treated 316 SS Irradiated at 800°F to 2.4 x 10^{22} n/cm^2 (E > 0.1 MeV). This sample is the Companion Specimen of the Material Shown in Figure VII-78. The Void Number Density of 1.5 x 10^{14}/cc and Average Diameter of 280 Å Produce a Void Volume of 0.2%.*

90,000 X

FIGURE VII-82 *Faulted Loops and a Dislocation Network in the Same Sample as Figure VII-79 but viewed under Diffraction Contrast (110 zone axis.)*

so much from previously established trends. Moreover, the microstructure of the "800°F" specimen appears inconsistent with the microstructural trends of the present study, which relates entirely to the same heat of material. Figure VII-83 shows the microstructure obtained for the annealed 316 specimen irradiated at a calculated temperature of 900°F. A comparision shows that the microstructures in Figures VII-81 and VII-82 appear to be representative of an irradiation temperature as high or higher than for Figure VII-83. The temperature of the "800°F" specimens was maintanined by γ heating and a gas gap between the sodium-filled capsule containing the specimens and the reactor coolant sodium. For the particular location of the 800°F capsule, the reactor coolant temperature was 700°F, so that the capsule and gap were designed to operate at a 100°F temperature differential. Considering uncertainties in γ heating, emissivities, etc., the calculated temperature differential may easily have been in error by as much as 100°F.

Precipitates are not discernable in the cold-worked 800°F and 900°F temperature sample. The 800°F solution-treated sample had small ($\sim$500 Å long) rod-shaped precipitates (usually associated with voids) and are probably (Fe-Cr)σ. Also some small (50 to 200 Å) precipitates are shown which are probably $M_{23}C_6$. The 900°F sample appears to contain only the small carbide precipitates.

As at the lower irradiation temperatures, no significant number of voids were discernible in stereographs of the cold-worked steel irradiated at 1100°F and 1300°F, as may be seen in Figures VII-84 and VII-85 respectively. The samples did contain significant amounts of precipitates, which may account for the increased bulk density of the heat-treated irradiated and unirradiated samples.

Figure VII-86 shows the analysis of an area of the 25% cold-worked sample irradiated at 1300°F. Selected area electron diffraction patterns of the region shown in Figure VII-86 conclusively proved that the smaller size (200 to 1000 Å) particles are $M_{23}C_6$. The upper right

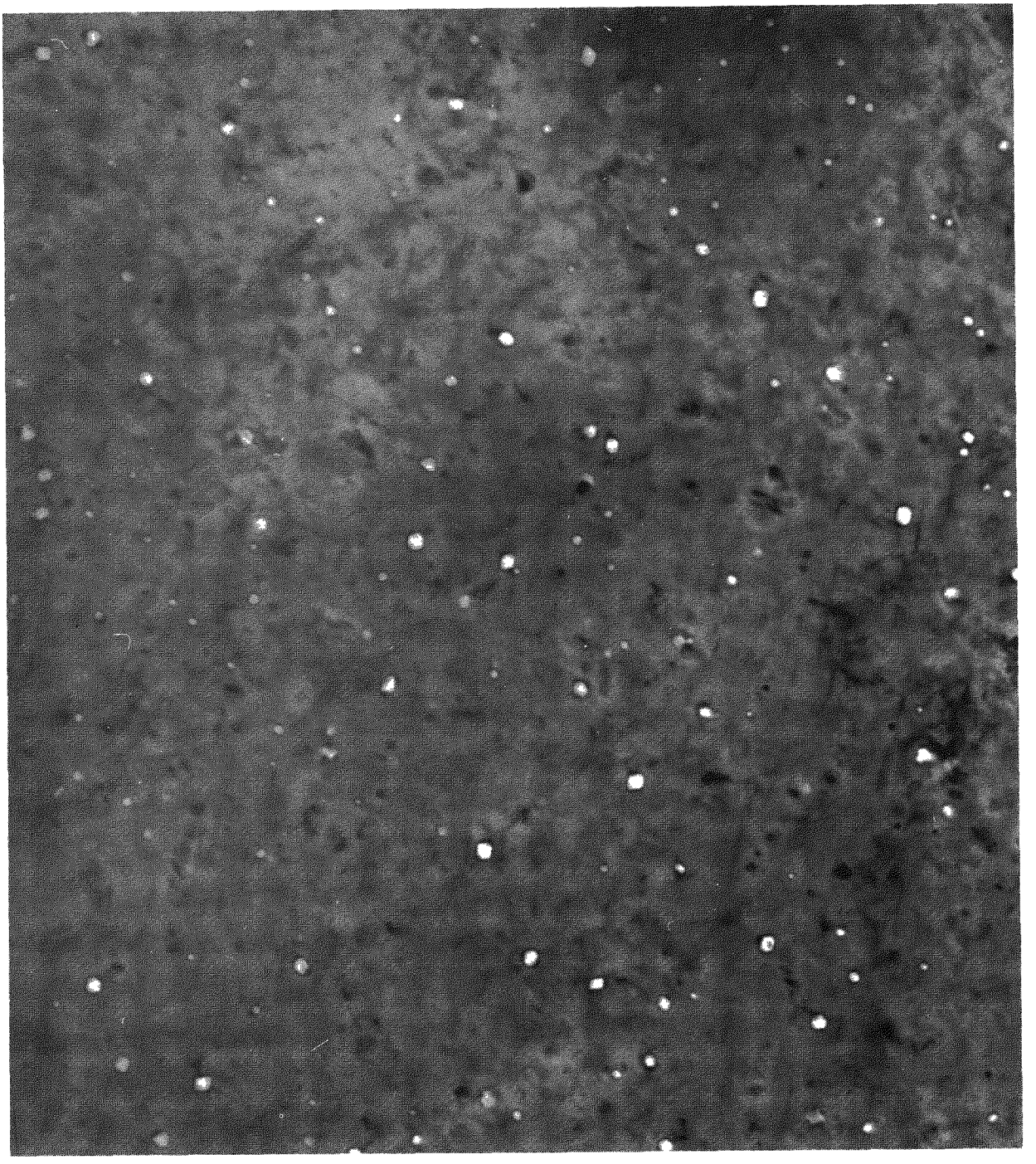

90,000X

FIGURE VII-83 *Solution-treated 316 SS Irradiated at 900°F in Conjunction With Sample Shown in Figure VII-79. Absorption Contrast Shows Voids Occupying 0.5% Void Volume.*

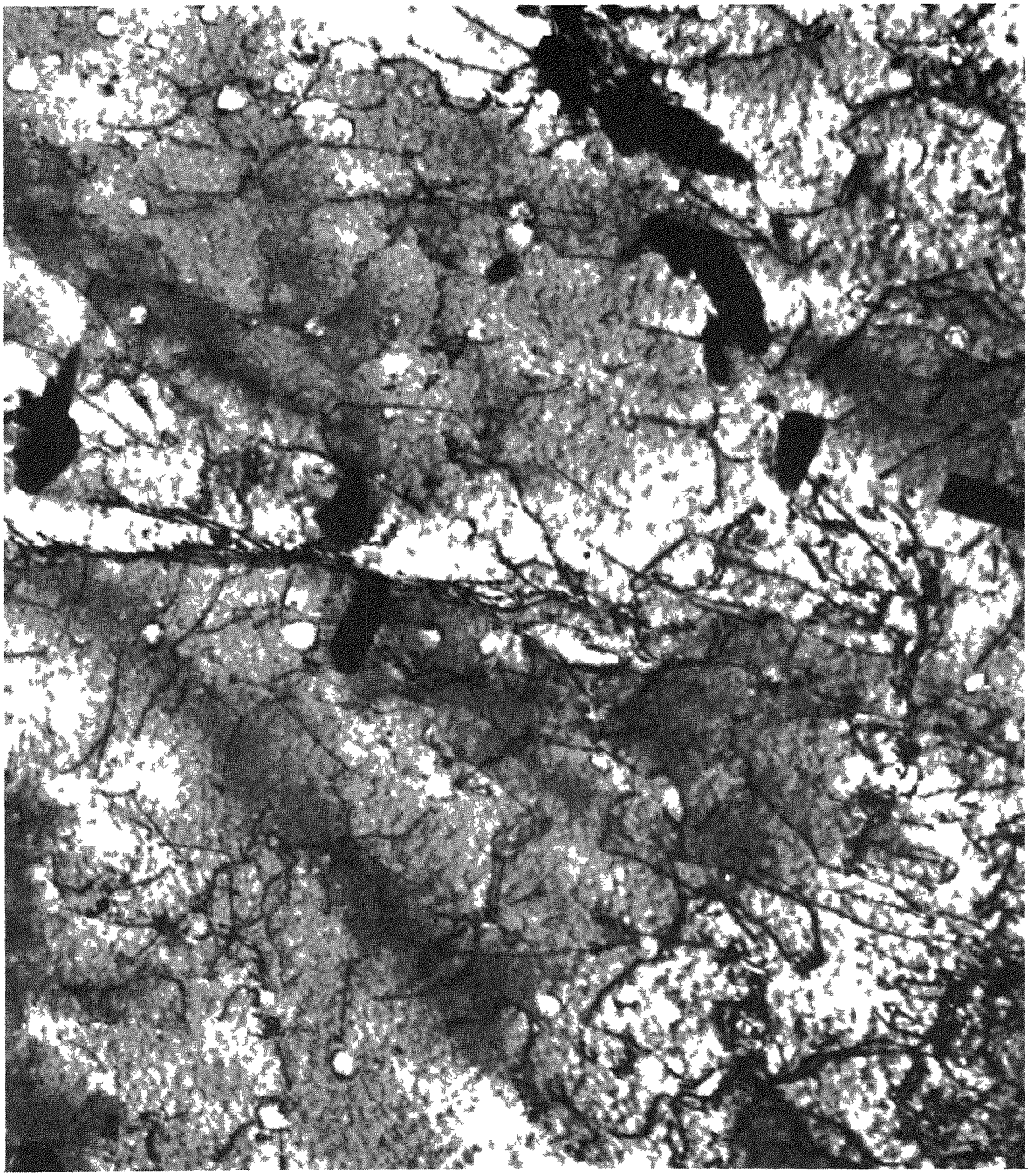

90,000X

FIGURE VII-84 *Diffraction Contrast Showing Dislocations and Large Precipitates in 25% CW 316 SS Irradiated at 1100°F to 2.9 x 10^{22} n/cm^2 (E > 0.1 MeV).*

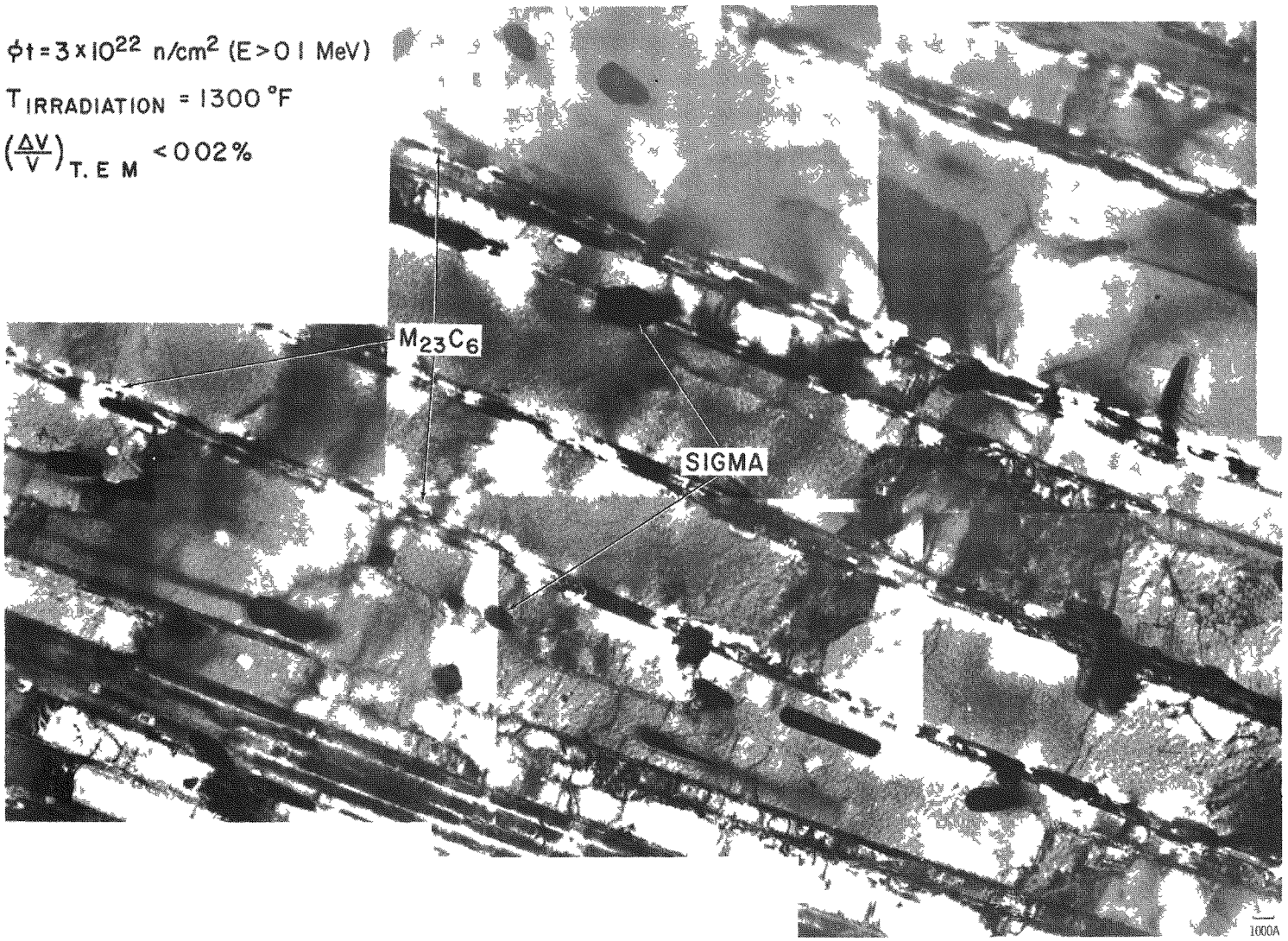

FIGURE VII-85 *Large (Fe-Cr) σ and $M_{23}C_6$ Precipitates in 25% CW 316 SS Irradiated at 1300°F to 3.0 x 10^{22} n/cm^2 (E > 0.1 MeV).*

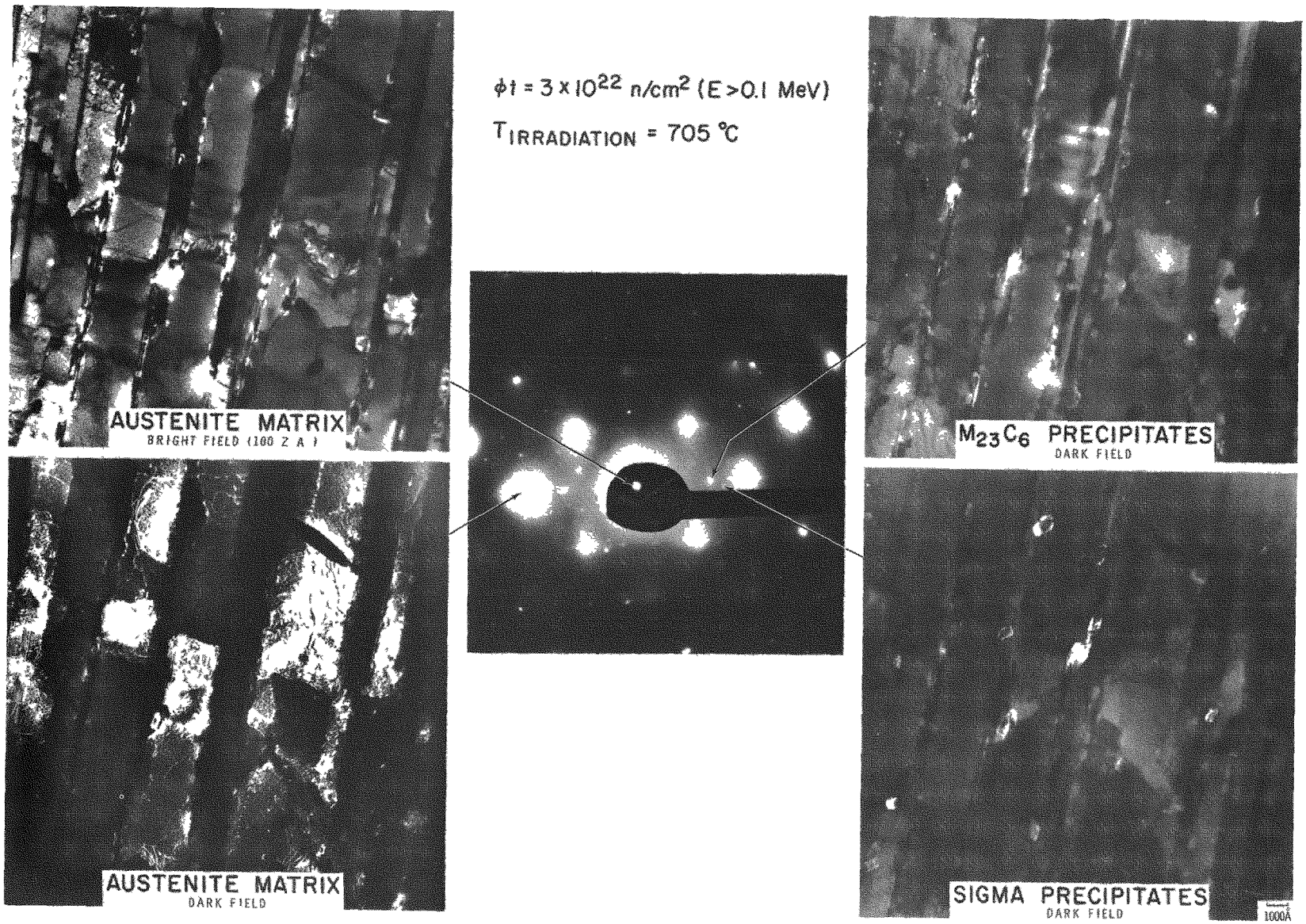

FIGURE VII-86 *Identification of $M_{23}C_6$ and σ Phases in Same Material Shown in Figure VII-85.*

hand dark-field micrograph shows that the $M_{23}C_6$ particles are preferentially located next to the dislocation slip lines. In the bright-field micrograph, the $M_{23}C_6$ carbides are related to regions that also show up as lighter areas. Stereoscopic analysis of the foil showed that the lighter regions are not uniformly located throughout the foil, but are near the surfaces, indicating that the electropolishing has preferentially attacked the "sensitized" regions adjacent to the $M_{23}C_6$ particles. In addition to the $M_{23}C_6$ carbides, the irradiated matrix also contained larger (1000 to 5000 Å) precipitates. The lower right hand dark field micrograph of Figure VII-84 shows that the large particles are also preferentially precipitated on or near dislocation slip lines. Analyses of the diffraction spots produced by the larger precipitates are consistent with both (Fe-Cr) σ phase or with M_6C particles. The "d" spacing of these large precipitates are not consistent with γ, α, χ, $M_{23}C_6$ or ε phases. It appears that the precipitates are Fe-Cr σ, since M_6C carbides are normally not the stable carbide formed in 18-8 SS; recent analysis of thermally aged 25% cold-worked type 316 SS has determined the presence of the (Fe-Cr) σ phase.

The higher irradiation temperature caused significant dislocation recovery in the cold-worked steel, but no appreciable recrystallization. These high irradiation temperatures and the "enhanced" diffusion due to displacement damage should promote recovery. Recrystallization was probably hindered by both the matrix hardening produced by displaced atoms and by the precipitates which formed.

The microstructure of the cold worked irradiated or control steel varies considerably throughout each sample, Figure VII-87. Cold working the matrix produced regions deformed by either mechanical twinning, multiple slip-dislocation interaction forming crystal subgrains, or dislocation channeling. This variation in microstructure of the cold worked 316 SS does not appear to significantly influence void formation in the fast neutron irradiation of steel.

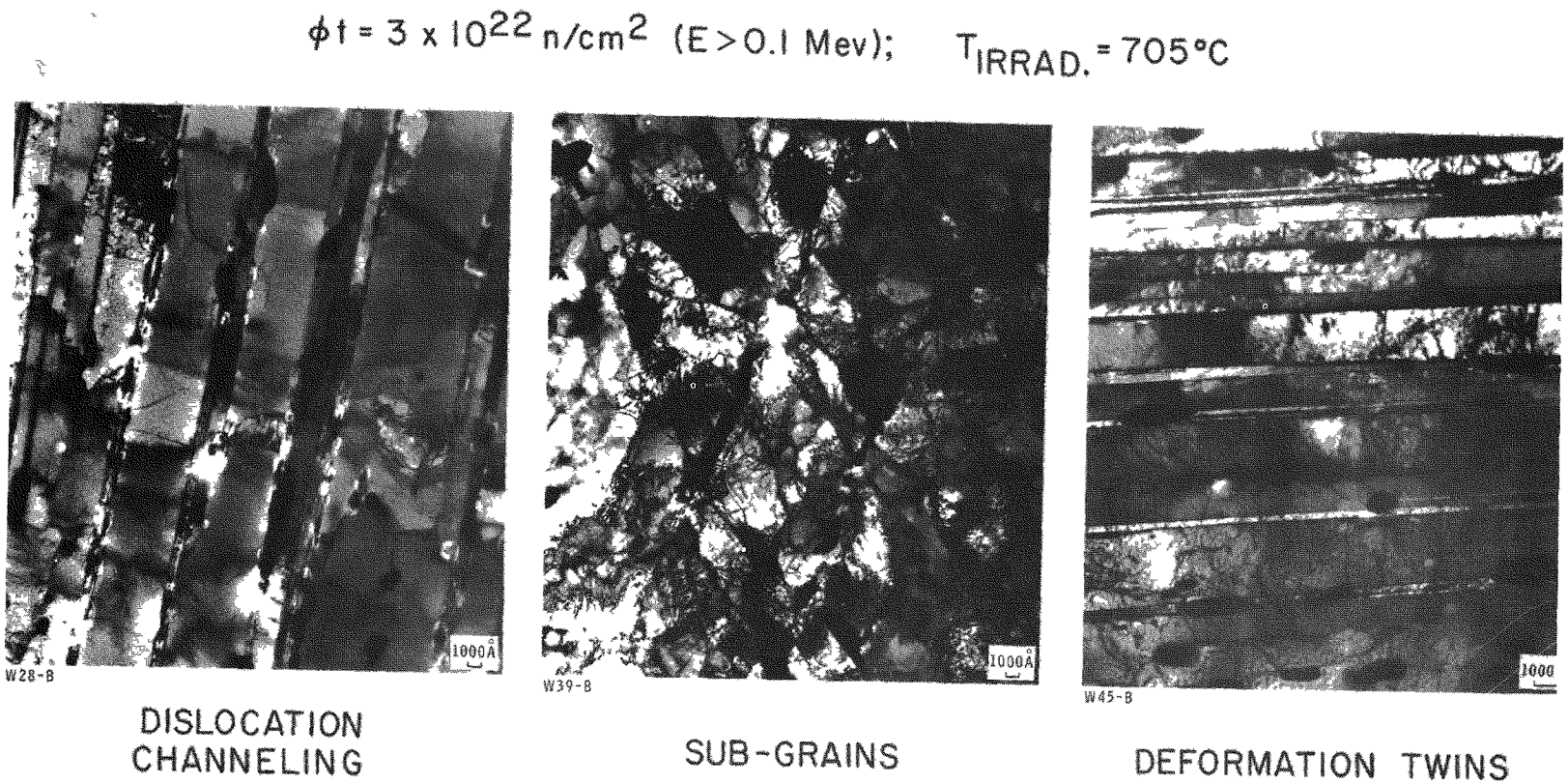

FIGURE VII-87 *Three Modes of Deformation in CW 316 SS Irradiated at 1300°F to 3.0 x 10^{22} n/cm^2 (E > 0.1 MeV)- Dislocation Channeling, Sub-grains and Deformation Twinning.*

Micrographs of the solution-treated steels irradiated at 1100°F and 1300°F are shown in Figures VII-88 and VII-89. The 1100°F steel contains a low number density ($\sim 3 \times 10^{13}$/cc) of large ($\bar{d}$ = 296 Å) voids. Nearly all the voids are associated with rod-shaped precipitates which are probably (Fe-Cr)σ phase. In addition, polyhedral $M_{23}C_6$ precipitates are formed.

At the 1300°F irradiation temperature, a low number density ($\sim 3 \times 10^{13}$/cc) of small cavities ($\bar{d} \sim 108$ Å) is present both at grain boundaries and in the matrix. These cavities are probably helium-filled bubbles, since voids are normally not found at grain boundaries and the expected void size should be over 300 Å.

Only large (0.1 to 0.5 μ) polyhedral shaped $M_{23}C_6$ precipitates were formed in the solution-treated steel and mostly at grain boundaries. In addition to an absence of large voids, the rod-shaped precipitates (Fe-Cr) σ, which are normally attached to voids, were not present.

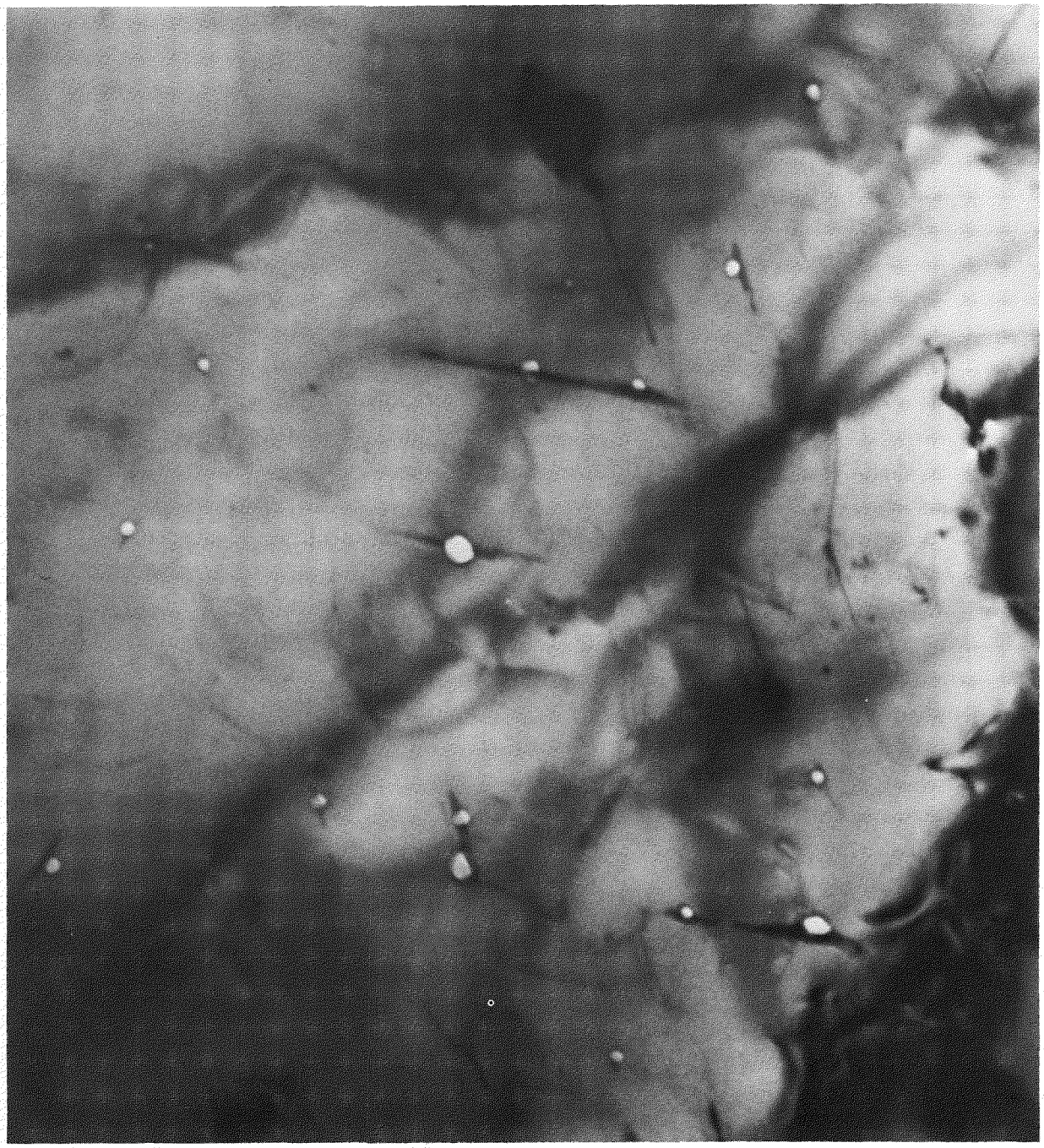

90,000X

FIGURE VII-88 *Large Voids Predominately formed on Rod-Shaped Precipitates, Probably (Fe-Cr) σ Phase in Solution-Treated 316 SS Irradiated @ 1100°F to 2.9 x 10^{22} n/cm^2 (E > 0.1 MeV). The Material was Irradiated Adjacent to the Cold Worked Sample Shown in Figure VII-84 . Polyhedral Precipitates are $M_{23}C_6$ Carbides.*

90,000X

FIGURE VII-89 *Polyhedral $M_{23}C_6$ Precipitates in Solution-Treated 316 SS Irradiated at 1300°F to 3 x 10^{22} n/cm^2 (E > 0.1 MeV). The Low Number Density (3 x 10^{13} /cc) Small Cavities (d = 100 A) Located on the Grain Boundary and in the Matrix are Probably Helium Filled Bubbles.*

D. FAST REACTOR CONTROL MATERIALS

1. B_4C Characterization (12435)

W. A. Ross and D. E. Mahagin

Commercially produced B_4C pellets with the boron enriched to 92% B^{10} will be irradiated in a control materials test. To evaluate irradiation effects related to material characteristics, the pellets will be characterized both before and after irradiation.

The vendor has fabricated and supplied pellets upon which structural and chemical composition characterization has begun. The characterization data on pre-irradiated material reported here will pertain primarily to microstructure and crystallography.

Pellets from the material have been examined, and four characteristics noted:

1) The pellets contain numerous small metallic inclusions. Figure VII-90 shows an area containing more than the average number of such inclusions. An impurity analysis of a similar pellet shows the presence of 0.2% Fe, which is probably the major component of the metallic phase. A microprobe analysis will be used to confirm the composition of the inclusions.

2) The pellets contain a graphite phase (Figure VII-91). The B/C ratio of the pellets has not been accurately determined because of analytical limitations, but the graphite phase indicates a B/C ratio of less than 4.

3) Porosity varies in size and amount between the ends of the pellet and its center (Figure VII-92 and VII-93). This can be expected from hot-pressed pellets due to the stress distribution throughout the pellet during forming. The large variation in porosity size and shape can also be observed in Figure VII-90.

4) The etched microstructure shows that a high degree of twinning occurs in B_4C grains. In these ~90% T.D. pellets, the grain structure is not highly developed. Figure VII-94 shows the etched microstructure and indicates a large variation in grain size. Grain size was determined by random line intercept method for the 87.4 and 91.7% T.D. pellets. The values, which are not corrected for porosity, were 8.0 and 10.1 microns, respectively.

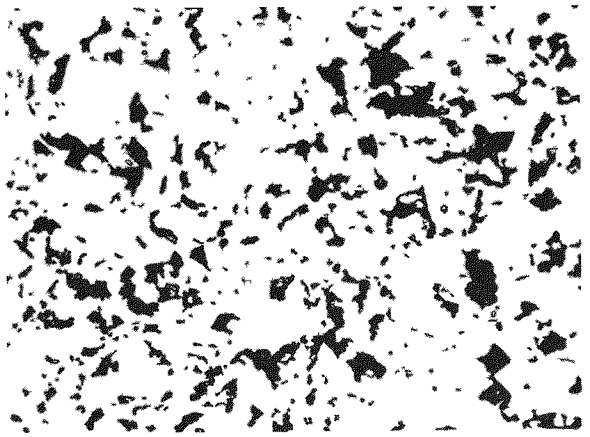

500X

FIGURE VII-90 *Enriched 87.4% T.D. B_4C Pellet. The very light spots are apparently metallic inclusions.*

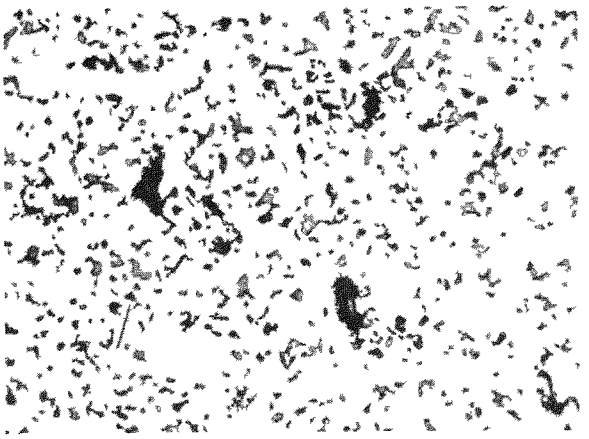

200X

FIGURE VII-91 *Enriched 86.6% T.D. B_4C Pellet under Polarized Light. The darkest regions are graphite.*

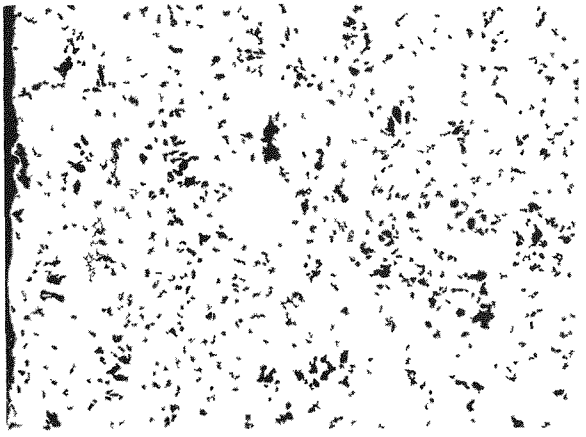

100X

FIGURE VII-92 *Enriched 91.7% T.D. B_4C Pellet Showing Porosity Distribution near Surface.*

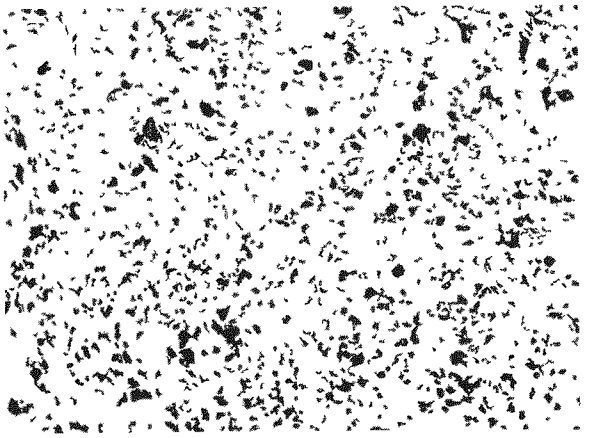

100X

FICURE VII-93 *Enriched 91.7% T.D. B_4C Pellet Showing Porosity Distribution near Pellet Center.*

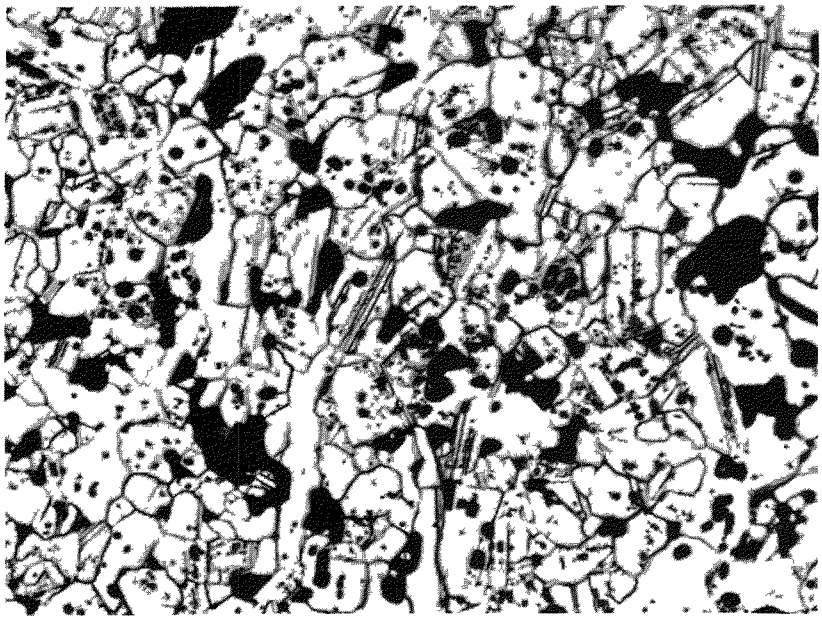

400X

FIGURE VII-94 *Etched 91.4% T.D. Enriched B_4C Pellet.*

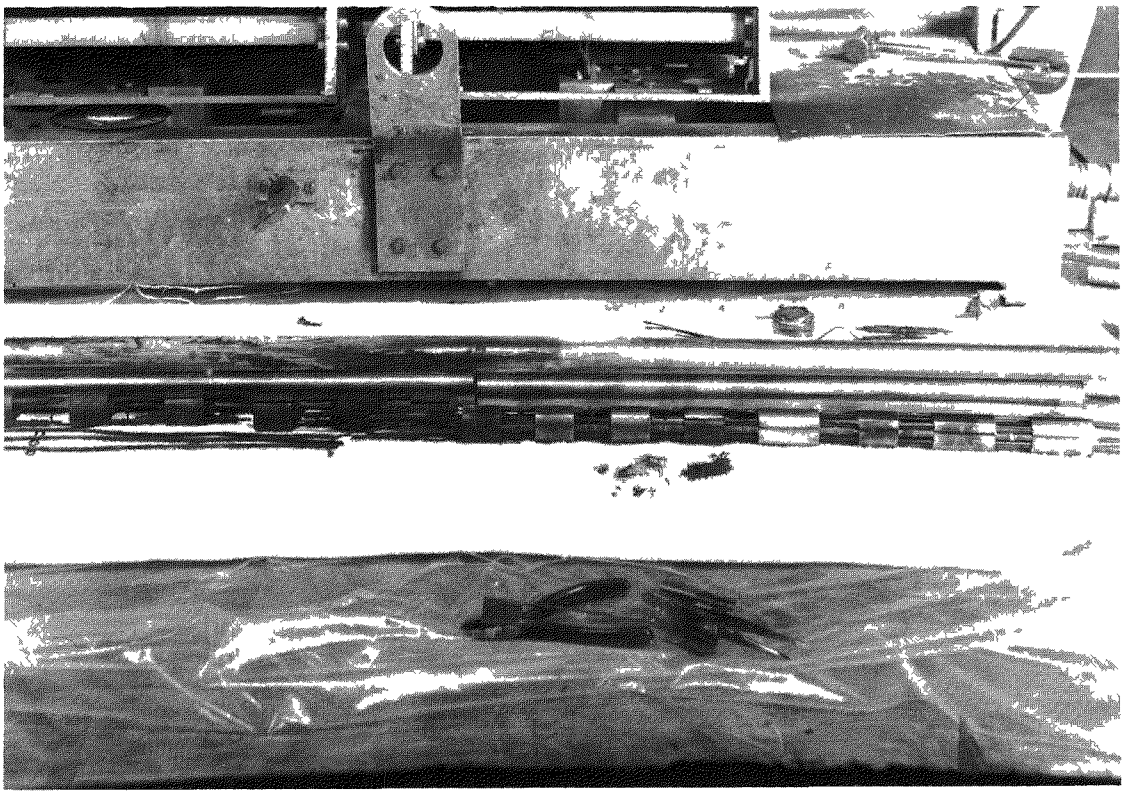

FIGURE VII-95 *Partially Disassembled BNW-7-1 Sample Holder Showing Burned-off Leads at Hottest Section of Capsule.*

2. Radiation Effects on Boron Carbide and Tantalum (12226)

A. L. Pitner and D. E. Mahagin

The BNW-7-1 capsule containing enriched (92% B^{10}) and depleted (98.5% B^{11}) (as well as tantalum specimens) completed a one-cycle irradiation in an ETR flux hardened by cadmium and boral filters and has been disassembled. Reactor heating in the test position was greater than expected, which resulted in capsule temperatures higher than desired. The specimen temperatures and estimated exposures are summarized in Table VII-28. The temperature of each specimen was monitored by a chromel-alumel thermocouple and in-reactor gas release in the enriched B_4C pellets was measured by gas tubes leading to external pressure gauges. The high temperatures caused some instrumentation failure in the capsule, but two gas-pressure monitoring systems operated reliably throughout the irradiation. These indicated that Sample No. 3 (99% T.D. B_4C irradiated at $\sim$ 1300°F to $\sim$ 5 x 10^{20} captures/cc) released 25% of the helium generated; Sample No. 7 (70% T.D. B_4C irradiated at $\sim$ 1700°F to $\sim$ 8 x 10^{20} captures/cc) released 45% of the helium generated during the irradiation. The capture density values are based on estimated burnups and are subject to revision after final burnup analysis.

Following discharge of the capsule, disassembly was performed at an NRTS hot cell. Figure VII-95 shows the appearance of the sample-holder train after its removal from the capsule. It is apparent that there has been considerable interaction between the B_4C pellets and their 304 SS holders in the hotter section of the capsule. Most of the instrumentation leads and the tubes containing flux monitors have parted at this location. Maximum capsule temperatures in this region probably exceeded 2200°F some time during the irradiation. In spite of this interaction, most of the B_4C pellets (33 out of 39) and all three tantalum samples were recovered in good condition. Figure VII-96 shows a typical appearance of the samples after removal from their holder. These particular samples are from Cell No. 7, which operated at $\sim$ 1700°F. Although the 316 SS wafer (included for compatibility studies) has reacted with the B_4C, the pellets appear to have retained good integrity.

TABLE VII-28
BNW-7-1 IRRADIATION CONDITIONS

Sample Number	Material	Average Temperature (°F)	Estimated Exposure
1	Tantalum	950	1.3×10^{20} n/cm^2 (E > 1 MeV)
2	Tantalum	1270	2.1×10^{20} n/cm^2 (E > 1 MeV)
3	99% TD Enriched B_4C	1290	4.7×10^{20} captures/cc
4	Tantalum	1480	3.4×10^{20} n/cm^2 (E > 1 MeV)
5	90% TD Enriched B_4C	1500	6.9×10^{20} captures/cc
6	70% TD Enriched B_4C	1590	7.5×10^{20} captures/cc
7	70% TD Enriched B_4C	1680	8.4×10^{20} captures/cc
8	90% TD Enriched B_4C	1760	9.3×10^{20} captures/cc
9	90% TD Depleted B_4C	1840	5.9×10^{20} n/cm^2 (E > 1 MeV)
10	70% TD Enriched B_4C	1900	10.0×10^{20} captures/cc
11	99% TD Enriched B_4C	1940	10.9×10^{20} captures/cc
12	90% TD Enriched B_4C	1920	10.9×10^{20} captures/cc
13	99% TD Enriched B_4C	1830	9.5×10^{20} captures/cc
14	90% TD Depleted B_4C	1700	5.6×10^{20} n/cm^2 (E > 1 Mev)

TABLE VII-29
TANTALUM DENSITY DECREASE

Sample ID	Temperature (°F)	Est. Exposure (E > 1 MeV)	$\Delta\rho$	$\Delta\rho/10^{20}$nvt
1	950	1.3×10^{20} nvt	-0.08%	-0.06%
2	1270	2.1×10^{20} nvt	-0.18%	-0.08%
3	1490	3.4×10^{20} nvt	-0.23%	-0.07%

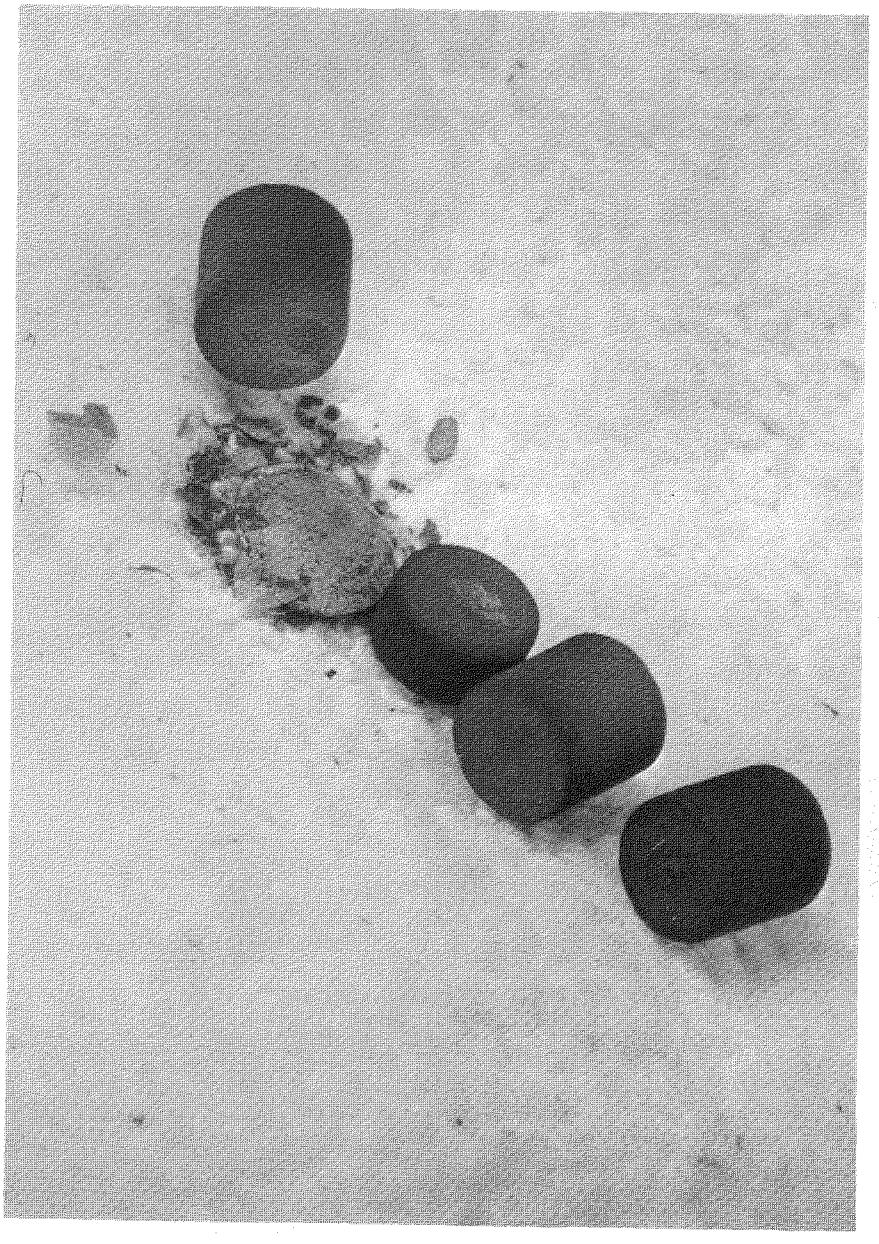

FIGURE VII-96 *B_4C Pellets Irradiated at 1700°F to ~ 8 x 10^{20} Captures/cc. Thin wafer is 316 SS included for compatibility studies.*

The samples have been returned to HEDL and post-irradiation analysis is presently underway. Dimensional, density, and thermal conductivity measurements have been completed. Preliminary results indicate that the thermal conductivity of the B_4C pellets decreased approximately 25%, as measured by the pulse diffusivity technique. The results of the density measurements on the tantalum samples are given in Table VII-29. It is interesting to note that the ratio of density change to neutron exposure is nearly constant in spite of the 540°F span of temperature. However, these data points are too few for firm conclusions to be drawn from these observations. Also, these results are different from earlier data (Ref 47) obtained from EBR-II irradiations of tantalum, where density decrease was seen to be quite dependent on temperature in the 1300 to 2100°F range.

Dimensional measurements made on the B_4C pellets were quite scattered, and no significant trends were detectable in the length changes of the 75 and 90% T.D. pellets. The 99% T.D.-enriched B_4C and the 90% T.D.-depleted B_4C pellets showed apparent growths of 0.3 to 0.5%. Densities were measured on the pellets by immersion weighing the samples after coating them with a water-impermeable substance. The results are given in Table VII-30. Weight losses as a result of the irradiation are also shown. At irradiation temperatures below 1600°F, weight losses were negligible, but at higher temperatures, some significant weight changes did occur. Although some of the weight changes can be attributed to breaking off of small particles, it is suspected that significant weight loss occurred as a result of interaction with the stainless steel holders at the higher temperatures. Within each pellet type, swelling increases with exposure and temperature. Sufficient data are not yet available to separate the variables of exposure and temperature. A surprising observation, however, is that, for roughly similar burnup and temperature conditions, swelling appears to decrease with increasing density in the enriched B_4C. Previous thermal reactor tests (Ref 48) have shown that helium gas release decreases with increasing pellet density, so it might be expected that swelling would increase with increasing density. These data, however, indicate the opposite to be true. The data pertaining to the depleted B_4C pellets do

TABLE VII-30
B_4C PELLET SWELLING AND WEIGHT CHANGE

Sample	% TD (Nominal)	Irrd Temp (°F)	Est Exposure	ΔW	ρo (/cc)	ρ Irrd (/cc)	ΔV	Avg ΔV
6-1	75	1590	7.5 x 10^{20}C/cc	-0.4%	1.774	1.692	+4.8%	+5.8%
6-2	"	"	"	-0.6%	1.764	1.669	+5.7%	
6-3	"	"	"	-0.5%	1.840	1.723	+6.8%	
7-1	75	1680	8.4 x 10^{20}C/cc	-3.7%	1.814	1.682	+7.8%	+6.5%
7-2	"	"	"	-3.0%	1.786	1.669	+7.0%	
7-3	"	"	"	-3.7%	1.774	1.693	+4.8%	
5-1	90	1500	6.9 x 10^{20}C/cc	-0.0%	2.097	2.030	+3.3%	+3.9%
5-2	"	"	"	-0.7%	2.158	2.064	+4.6%	
5-3	"	"	"	-0.0%	2.199	2.117	+3.9%	
8-1	90	1760	9.3 x 10^{20}C/cc	-9.4%	2.145	2.080	+3.1%	+5.0%
8-2	"	"	"	-5.6%	2.156	2.054	+5.0%	
8-3	"	"	"	-5.1%	2.190	2.050	+6.8%	
12-1	90	1920	10.9 x 10^{20}C/cc	-6.1%	2.180	2.010	+8.5%	+8.5%
12-2	"	"	"	-6.2%	2.133	1.961	+8.8%	
12-3	"	"	"	-12.1%	2.161	1.996	+8.3%	
3-1	98	1290	4.7 x 10^{20}C/cc	-0.0%	2.354	2.285	+3.0%	+2.9%
3-2	"	"	"	-0.0%	2.321	2.258	+2.8%	
13-1	98	1830	9.5 x 10^{20}C/cc	-0.3%	2.336	2.267	+3.0%	+3.2%
13-2	"	"	"	+0.5%	2.305	2.226	+3.5%	
14-1(Depleted)	90	1700	5.6 x 10^{20}n/cm^2 (E>1 Mev)	+1.5%	2.354	2.304	+2.2%	+2.2%
14-3 "	"	"	"	-18.4%	2.354	2.312	+1.8%	
9-1(Depleted)	90	1840	5.9 x 10^{20}n/cm^2 (E>1 Mev)	-5.9%	2.347	2.162	+8.6%	+6.9%
9-2 "	"	"	"	-3.6%	2.330	2.210	+5.4%	
9-3 "	"	"	"	-6.9%	2.307	2.162	+6.7%	

not appear to be in good agreement. Although irradiation conditions were not very different between the two groups of samples, swelling rate varies by over a factor of three.

Post-irradiation analysis is continuing on the test samples. Efforts are presently underway to determine burnup by B^{10}/B^{11} isotopic analysis. The 316 SS wafers included in the irradiation test and the B_4C microscopy samples are being prepared for metallographic examination. The enriched B_4C pellets will also be annealed and the helium gas given off will be measured to determine the fraction of gas released during the irradiation.

A second filtered-irradiation of enriched boron carbide is being planned. This experiment will investigate the effect of density in the 90 to 99% T.D. range and also the effect of a heavy-metal impurity (1% ir( ) on the irradiation behavior of B_4C. Temperatures will range from 1000 to 1600°F, and in-reactor gas release will again be monitored. The capsule will be identified as WDC-1-1. Maximum exposures in the test are aimed at 30 x 10^{20} captures/cc, probably requiring about five reactor cycles of irradiation.

3. Swelling in Tantalum and Tantalum-Based Alloys (12226)

J. F. Bates, J. L. Straalsund and T. K. Bierlein

The magnitude and nature of swelling in irradiated tantalum and tantalum-based alloys and the effect of cold work on swelling are being studied.

Work has been initiated on an irradiation experiment which will allow study of the compatibility of commercially pure Ta, Ta-10W, T-111 and T-222 with 316 SS cladding in the 20% cold worked condition. Typical compatibility specimens to be used in this experiment are shown in Figure VII-97.

A thermal test pin has been fabricated for irradiation in the EBR-II during Run 46. This pin is identical in design to the four pins of the swelling study to be conducted in support of the FFTF Control Rod Development Program. This pin is designed to provide a comparison of calculated and measured irradiation temperatures for 62.5MW operation of the EBR-II.

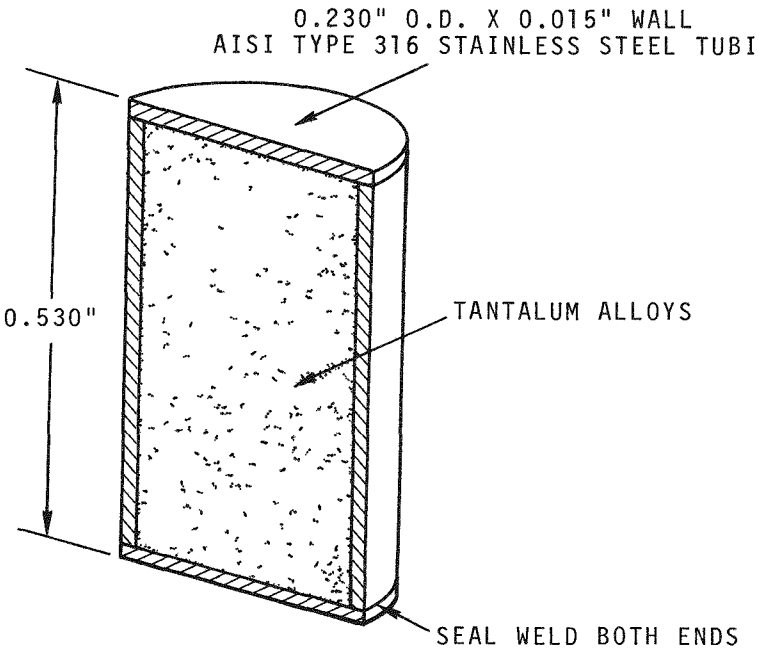

FIGURE VII-97 *Typical Compatibility Specimen.*

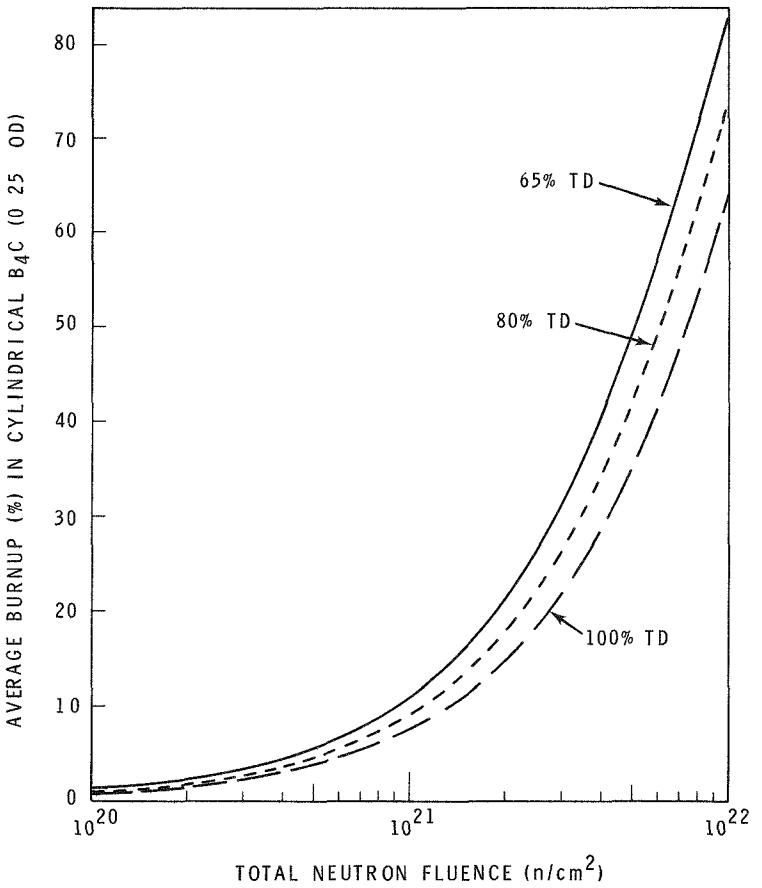

FIGURE VII-98 *Average Burnup in B4C Cylinders.*

Silicon carbide monitors will be used to determine the temperature of each axial specimen position in the pin.

The temperatures in the different levels of all of the pins are calculated and controlled by means of a gas gap between the inner pin wall and the outer subcapsule wall. With tantalum, where gamma heating is extremely severe, small variations in this gap can cause variations in temperature of several hundred degrees. Thus, it is important to know with accuracy the inner diameter of the pin wall. A 30-in. extension for the Diatest equipment has been purchased which will allow measurement of the inner diameter of the tubes to $\pm$ 0.0001 in.

4. EBR-II Subassembly BCM-1 (12163)

H. C. F. Ripfel and J. E. Hanson

A request for Approval-In-Principle for irradiation testing of control material in EBR-II, subassembly BCM-1, was submitted to AEC-DRDT. It contains technical data such as given in Table VII-31. Design of B_4C test capsules is 90% complete. The design will be finished and fabrication of the capsules will begin upon receipt of the AIP. An engineering test plan has been drafted.

5. Damage Analysis Control Materials

G. E. Russcher and H. H. Yoshikawa

Thermal reactor irradiations of the fast reactor control materials are a necessary part of the LMFBR development program. As a first step in the use of such data for estimating performance in LMFBR conditions, an irradiation analysis of such tests is necessary. An analysis has been completed of Hanford K reactor irradiations of boron carbide.

In order to determine burnup levels and reaction profiles in experimental specimens, the B^{10} atom density distributions were calculated for three different boron carbide densities as a function of neutron fluence. Burnup calculations were made for boron carbide of theoretical density, 2.52 g/cm^3, 80% TD and 65% TD for fluences ranging from 5×10^{19} to 1×10^{22} n/cm^2. These represent the nominal densities of the specimens

TABLE VII-31
CONTROL MATERIAL EBR-II SUBASSEMBLY BCM-1
(POISON PIN PARAMETERS)

Poison Composition	B_4C
Poison Type	pellet
Poison Dimensions (in.)	0.344 OD x 13.5 long L/D ratio ∿ 1
Average Poison Smeared Density	90 ± 2% TD
Poison B^{10} Enrichment (%)	92
Poison Volume (cm^3)	20.6
Poison Weight (g)	46.4
Reflector Material	Inconel
Reflector Dimensions (in.)	0.344 OD x 5 long (at each end of poison)
Reflector Volume (cm^3)	7.6
Reflector Density (g/cm^3)	8.9
Reflector Weight (g)	67.6
Cladding Material	316 SS
Cladding Dimensions (in.)	0.435 OD x 0.043 thick
Poison-to-cladding Gap (in.)	0.005 Cold as fab. ±0.0005
Gas for Poison Pin	He
Gas Volume (cm^3)	10.3
Gas Pressure at Room Temp	1 atm.

and include the exposure range of these experiments.

Self-shielding in these cylinders was calculated by an extension of the methods described by Rockwell (Ref 49). The approximation used was intermediate between maximum and minimum self-shielding models.

The burnup of the B^{10} is calculated from the B^{10} atom density distribution. An average burnup for the entire specimen is determined with the following relationship:

$$\overline{BU} = \sum_{i=1}^{500} BU_i \, V_{fi} / V_{total}$$

Where V_{total} is the volume of the specimen and BU_i and V_{fi} are the burnup and volume fractions for the i^{th} spatial zone respectively. In these calculations, the zones were cylindrical shells of input length. These computer calculations thus give an almost continuous B^{10} atom distribution and a reasonable description of the neutron fluence attenuation in the absorber.

In Figure VII-98, summarized results show average B^{10} burnup ($\overline{BU}$) in cylindrical specimens as a function of the total neutron fluence for typical B_4C specimen densities. The relationship between the localized burnup (BU) profile and the specimen averaged burnup ($\overline{BU}$) is shown in Figure VII-99 and Table VII-32.

Helium production as a function of fluence was also calculated for the specimens. The results are shown in Figure VII-100. The gas volume produced is determined by the number of B^{10} atoms transmuted. For example, at a fluence of 10^{21} n/cm^2, average burnup is 7.6% in 100% TD material, but 10.9% in 65% TD material. However, Figure VII-100 shows approximately equal helium production for these specimens. At higher fluences, the theoretical helium production is higher for the fully dense material than for the 65% TD material.

The large thermal-neutron absorption cross section of B^{10} is known to cause considerable self-shielding within B_4C specimens in a thermal neutron irradiation. Consequently, sample geometry could influence the irradiation behavior of boron carbide. Moreover, in thermal reactor

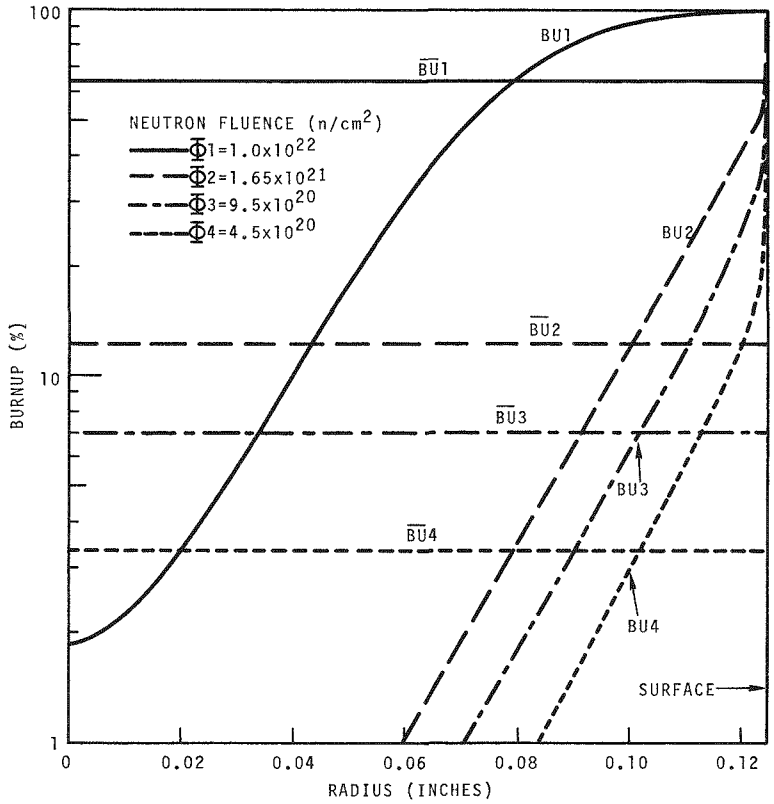

FIGURE VII-99 *Local (Bu) and Average ($\overline{BU}$) B^{10} Burnup in 0.250 in. O.D. Cylinders of 100% T.D. B_4C.*

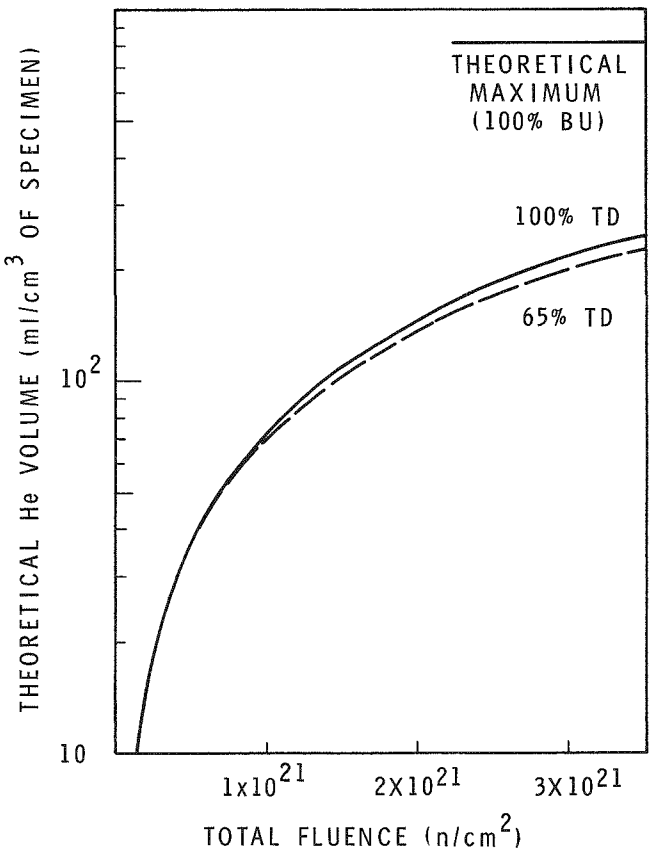

FIGURE VII-100 *Theoretical He Production.*

TABLE VII-32
AVERAGE B^{10} BURNUP FOR
REPRESENTATIVE FLUENCES AND B_4C DENSITIES

Total Neutron Fluence	Average Burnup	Density
Φ (n/cm^2)	$\overline{BU}$ (%)	ρ (%TD)
$\Phi 1 = 1.0 \times 10^{22}$	$\overline{BU1} = 64$	100
	$= 74$	80
	$= 83$	65
$\Phi 2 = 1.65 \times 10^{21}$	$\overline{BU2} = 12$	100
	$= 15$	80
	$= 18$	65
$\Phi 3 = 9.5 \times 10^{20}$	$\overline{BU3} = 7.0$	100
	$= 8.6$	80
	$= 10.3$	65
$\Phi 4 = 4.5 \times 10^{20}$	$\overline{BU4} = 3.3$	100
	$= 4.1$	80
	$= 4.9$	65

testing of B_4C, while the thermal portions of the spectra are basically similar for the various reactors, epithermal and high-energy portions of the spectra can vary significantly. Therefore, damage in B_4C resulting from interactions with higher-energy neutrons could conceivable result in different overall performance of B_4C in various reactors under similar temperature and burnup conditions.

References:

47. Fast Flux Test Facility Quarterly Technical Progress Report - March, April, May, June, 1970, BNWL-1394.

48. Pitner, A. L., Irradiation of Boron Carbide Pellets and Powders in Hanford Thermal Reactors, WHAN-IR-24, October 1970.

49. Rockwell, T., III, ed., Reactor Shielding Design Manual, U. S. Atomic Energy Commission (1956).

E. SIMULATIONS OF IRRADIATION DAMAGE

1. Heavy Ion Bombardment of Stainless Steel (12215)

J. J. Laidler, J. L. Straalsund, H. R. Brager, G. L. Guthrie and T. K. Bierlein

A paucity of information about the nature of defects produced in austenitic stainless steel by high-temperature, high-fluence fast reactor irradiation provides strong incentive for development of means to simulate these conditions in short times. A method which has been selected is bombardment with heavy ions, in this case 5 MeV Ni^{++}. Heavy ion bombardment by nickel ions offers some pronounced advantages over other simulation techniques:

1) Accurate temperature measurement and control.
2) A displacement rate nearly 10^6 times as great as with EBR-II neutrons (Ref 50).
3) No significant change in the chemical composition of the target material, since the bombarding species is one of the major alloy elements in the steel.

Disadvantages of the method as presently employed are the limited range of the ions in the target material ($\sim 10^{-3}$ mm) the lack of the helium build-up characteristic of neutron irradiations and the higher supersaturation of defects relative to those induced by reactor neutron fluxes. The degree of simulation or neutron equivalence is uncertain as yet, but means of establishing equivalence is now under study.

The first series of specimens to be bombarded included both solution-annealed and 20% cold-worked AISI Type 316 SS; neither material was doped with helium prior to irradiation. The ion bombardment experiments were carried out over a range of irradiation temperatures from 280°C to 585°C. Fluences ranged from 0.3×10^{15} to 1.2×10^{7} ions/cm^2, which, basing equivalence on the total number of atom displacements, correspond to "equivalent" EBR-II fluences of 6×10^{20} n/cm^2 to 2×10^{23} n/cm^2. Significant void concentrations were found only in specimens bombarded at 565 to 585°C with ion fluences in excess of 1×10^{16} ions/cm^2. The results of this first series of ion bombardment experiments and near-term

plans for further experimentation are presented and discussed in the following sections.

a. Solution-Annealed 316 SS

High-fluence Ni^{++} bombardment of 316 SS at 585°C produces voids at fluences in excess of 1 x 10^{16} Ni^{++} /cm^2. An example of the microstructure after 3 x 10^{16} Ni^{++}/cm^2 at 585°C is shown in Figure VII-101. The average void diameter, 300 Å, is somewhat smaller than is observed after a fast neutron fluence of 3 to 5 x 10^{22} n/cm^2 at a similar temperature, while the void density, 3.3 x 10^{13} cm^{-3}, is significantly lower than in the case of neutron irradiation. This is based on a comparison with work on neutron-irradiated specimens done in this laboratory; in comparison with work performed elsewhere, the distinction is somewhat different, Using HEDL results, the void size and density are similar to those after neutron irradiation to about 7 x 10^{21} n/cm^2 (E > 0.1 MeV) at ∿ 565°C. Figure VII-102 is histogram giving the void size distribution for the ion-bombarded specimen. Lower heavy ion fluences at the same temperature (585°C) primarily result in the formation of faulted dislocation loops; the void density at a fluence of 1 x 10^{16} Ni^{++}/cm^2 is less than 10^{11} cm^{-3}, and no voids at all were observed after a fluence of 3 x 10^{15} Ni^{++}/cm^2. The distribution of faulted loops is initially nonuniform, (Figure VII-103); the loops lie in strings aligned along <011> directions on {111} planes. There appears to be a fine precipitate associated with these strings, but its identity has not been established. At a higher fluence (Figure VII-104), loop nucleation has occurred at sites between the strings. The size of the faulted loops varies in a peculiar manner, first increasing and then decreasing with increasing fluence. Formulation of a model to explain this behavior is considered premature, since the observations involve single specimens and the post-irradiation history of the specimens is poorly documented.

Bombardment of 316 SS with 5 MeV Ni^{++} ions at 475°C produces a very high density of small dislocation loops, but no voids even at the highest fluence used (1.2 x 10^{17} Ni^{++}/cm^2). The defect structure after bombardment at 475°C to a fluence of 1.2 x 10^{17} Ni^{++}/cm^2 is typified by Figure

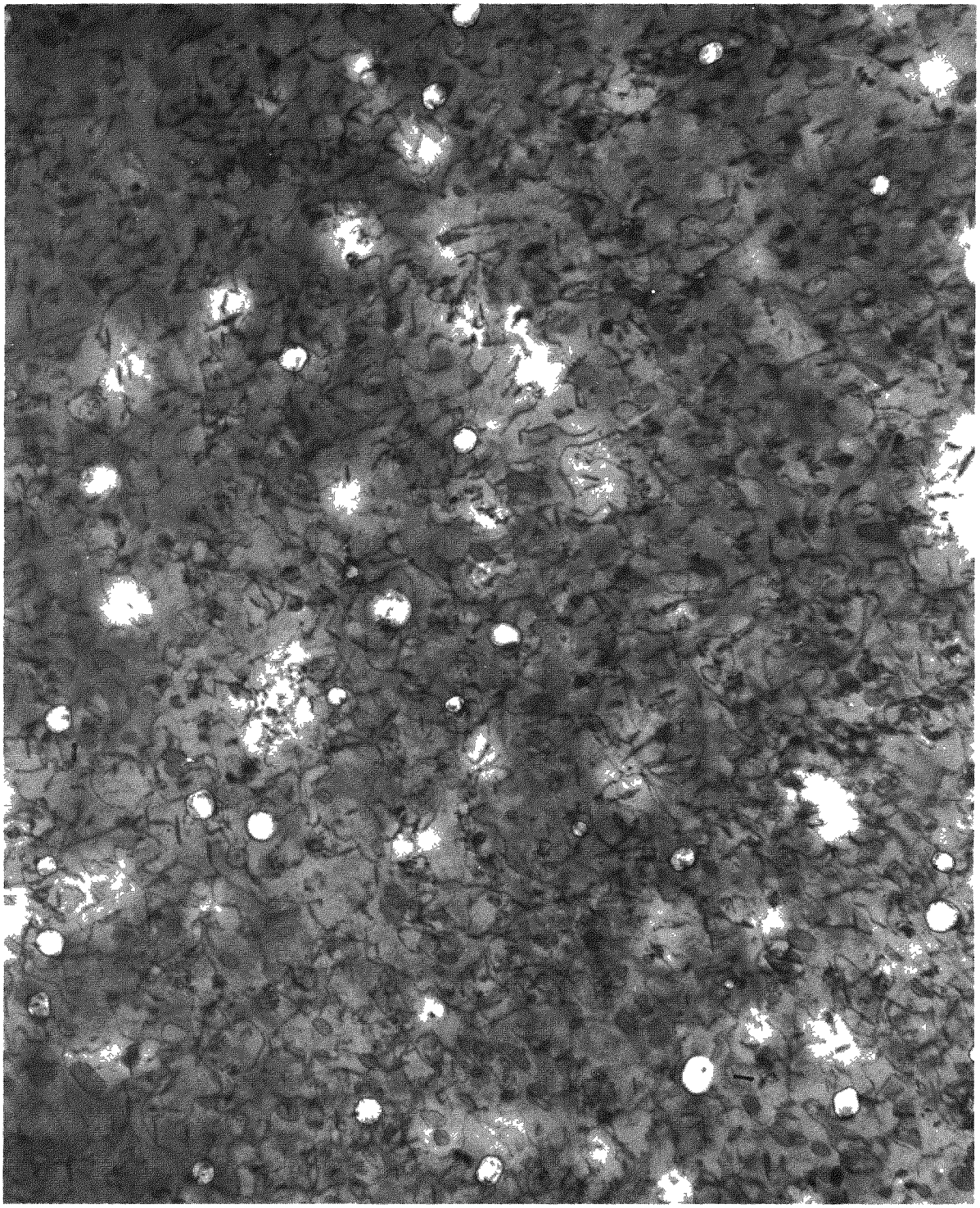

94,200X

FIGURE VII-101 *Solution-annealed 316 SS Bombarded With 5 MeV Ni^{++} at 585°C to 3 x 10^{16} Ni^{++}/cm^2.*

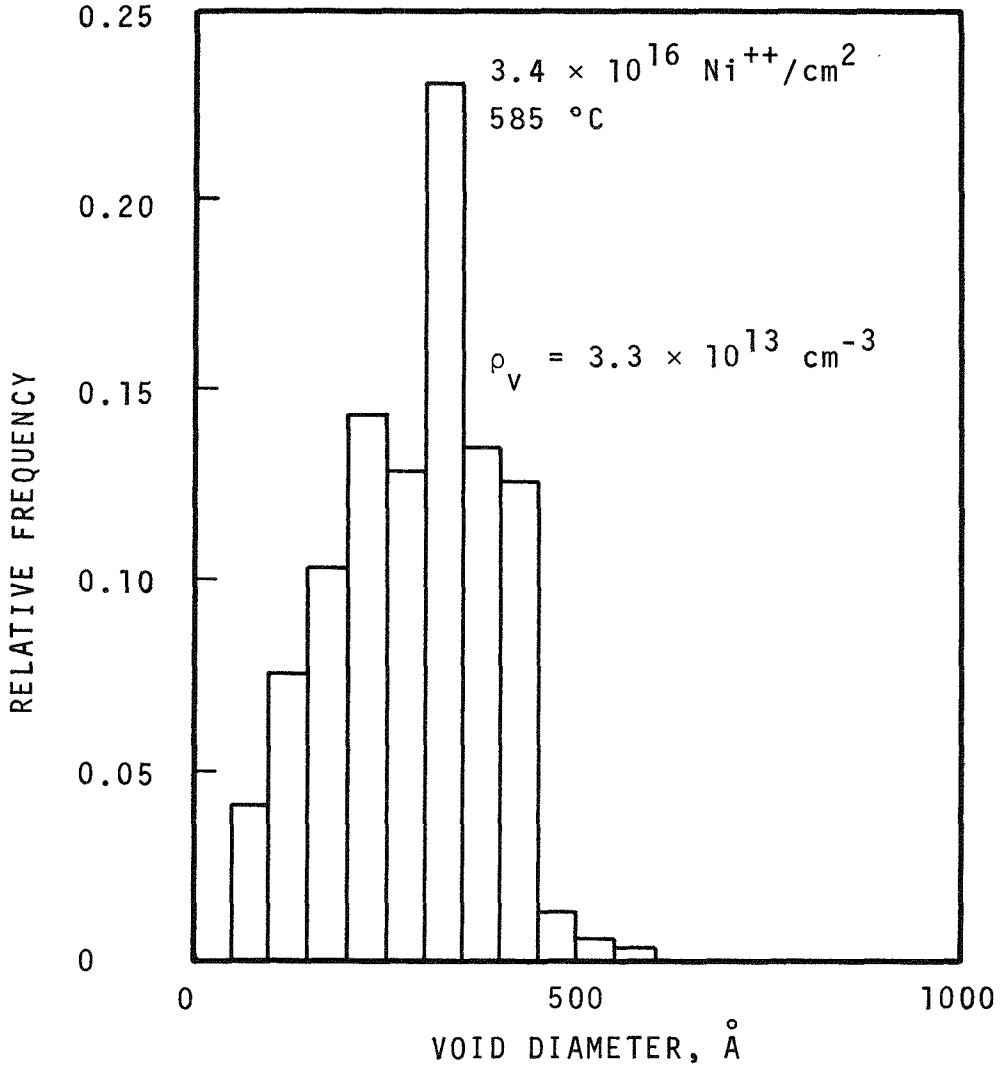

FIGURE VII-102 *Histogram of Void Size Distribution in Solution-annealed 316 SS, 3 x $10^{16}Ni^{++}/cm^2$ at 585°C.*

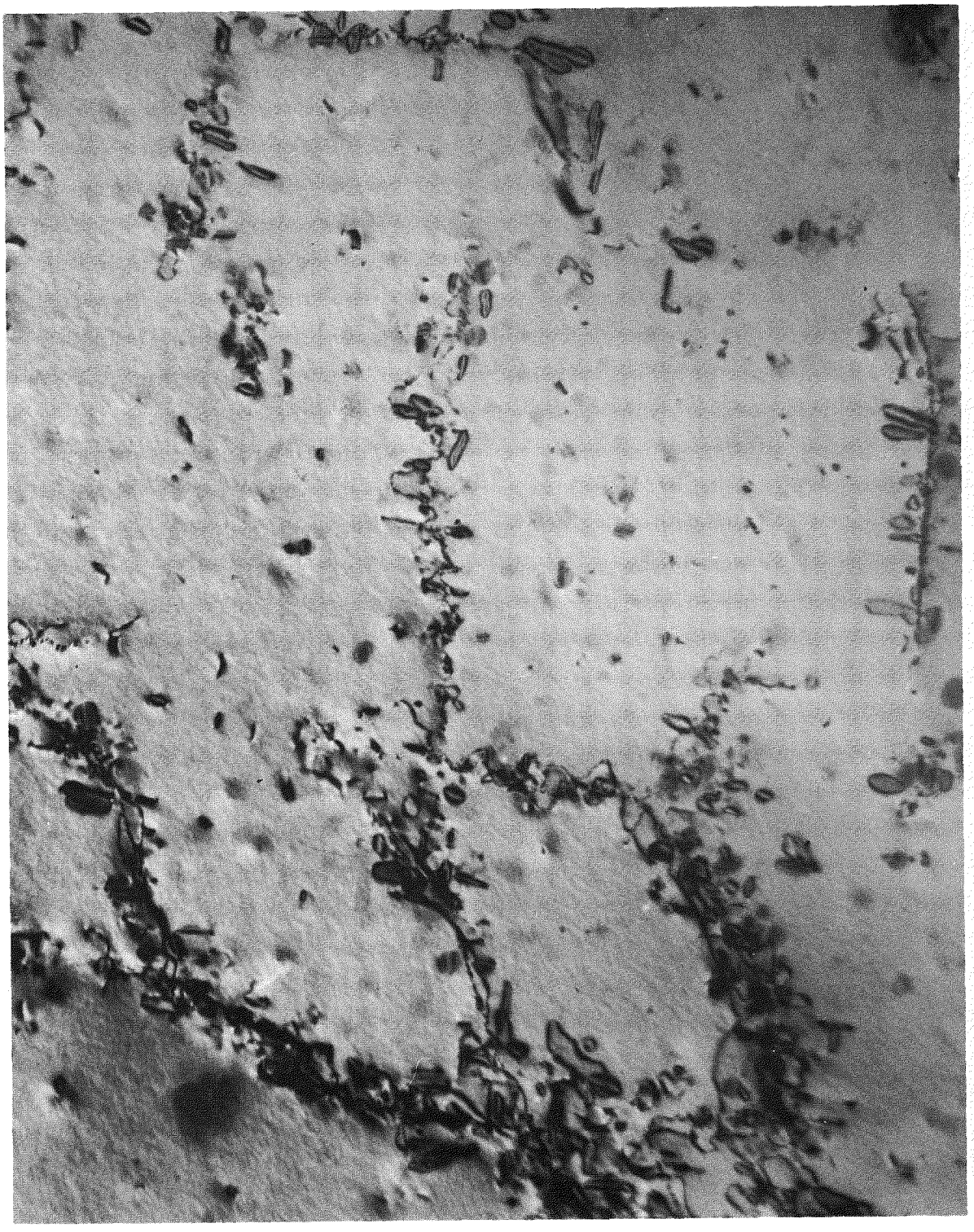

94,200X

FIGURE VII-103 *Solution-annealed 316 SS, Bombarded with 5 MeV Ni^{++} at 585°C to 3 x $10^{15} Ni^{++}/cm^2$.*

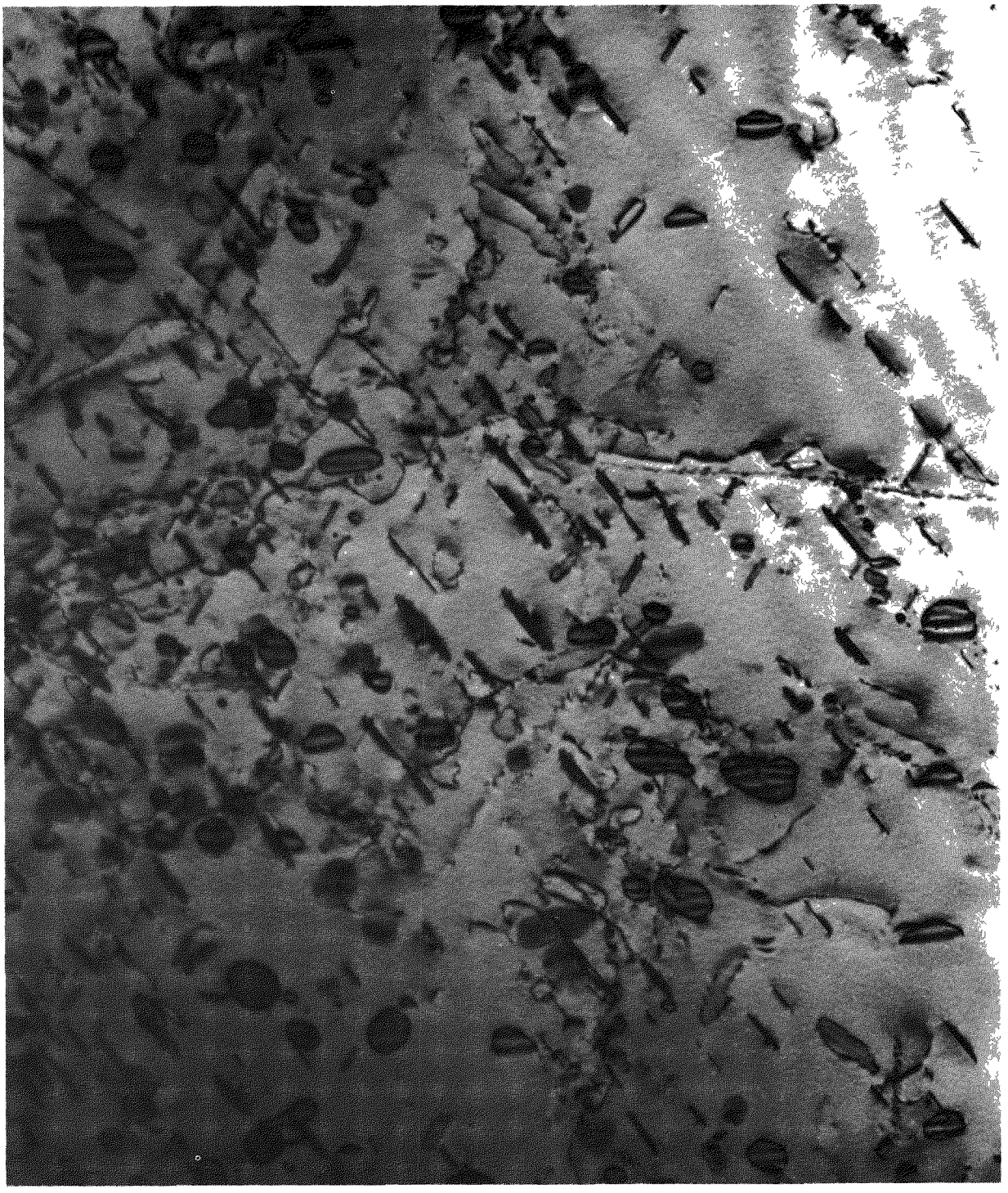

94,200X

FIGURE VII-104 *Solution-annealed 316 SS Bombarded with 5 MeV Ni^{++} at 585°C to 1 x $10^{16} Ni^{++}/cm^2$.*

VII-105; the structure is similar to that of a lower-fluence, higher-temperature specimen (Figure VII-104). The loops appear to have nucleated at small precipitates lying in strings on 111 planes. The loops are faulted, (Figure VII-106), a dark-field electron micrograph of the same region. The same structure prevails at a lower fluence of 3×10^{16} Ni^{++}/cm^2 (T_{irr} = 475°C), (Figure VII-107) with the exception that the nonuniform loop distribution was not observed under these conditions.

The structure after bombardment to a fluence of $3 \times 10^{16} Ni^{++}/cm$ at 370°C is similar to the 475°C structure, except that the loop size is smaller and the loop density is greater in Figure VII-108. The dark-field image of this area, Figure VII-109, reveals the loops to be faulted.

b. 20% Cold-Worked 316 SS

Type 316 SS foil specimens, previously reduced 20% in thickness by rolling at room temperature, have been bombarded with 5 MeV Ni^{++} ions over temperature and fluence ranges comparable to those reported above for solution-annealed material. Voids have been observed in only one case, a specimen bombarded at 585°C to a fluence of 3×10^{16} Ni^{++}/cm^2; the microstructure under these conditions is as shown in Figures VII-110a and VII-110b The average void diameter is 250 Å and the void density is 3×10^{13} cm^{-3}, very nearly the same values as determined for a solution-annealed specimen at the same temperature and fluence. Lower-fluence bombardment at the same temperature did not result in the production of either voids or faulted loops; Figures VII-111a and V11-111b are illustrative examples of the microstructure of 20% cold-worked material after 1×10^{16} Ni^{++}/cm^2 and $3 \times 10^{14} Ni^{++}/cm^2$ at 585°C. Specimens bombarded at 425°C (797°F) and 500°C (932°F) to a fluence of 3×10^{16} Ni^{++}/cm^2 contained faulted loops but not voids, as shown in Figures VII-112 and VII-113, respectively.

At the present time, there is insufficient information for quantitative comparison of heavy ion bombardment and neutron irradiation effects in cold-worked 316 SS. There appears to be a serious discrepancy between the two irradiation processes, in that 25% cold-work suppresses void

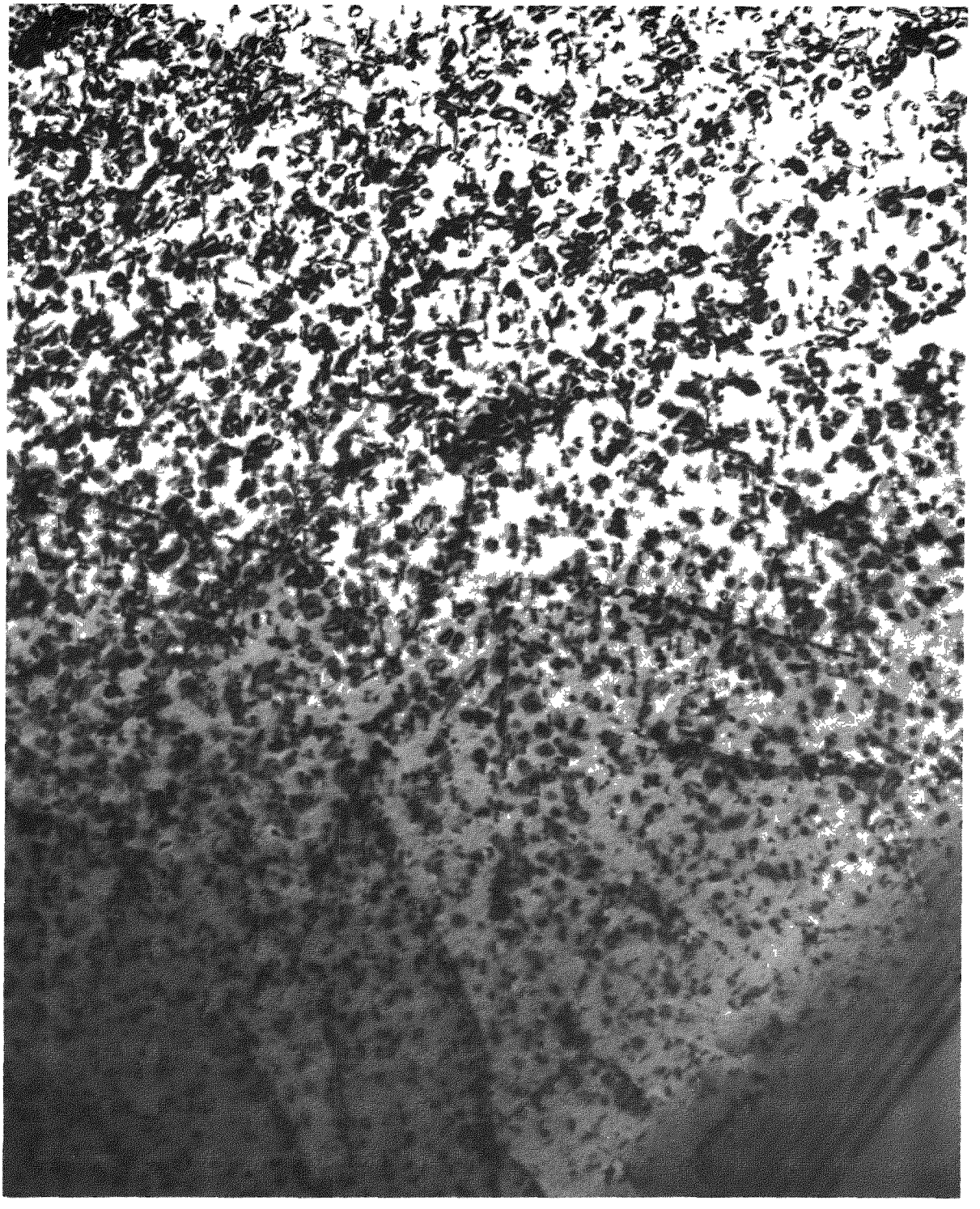

94,200X

FIGURE VII-105 *Solution-Annealed 316 SS, Bombarded with 5 MeV Ni^{++} at 475°C to 1.2 x 10^{17} Ni^{++}/cm^2.*

188,400X

FIGURE VII-106 *Solution-Annealed 316 SS, Bombarded with 5 MeV Ni^{++} at 475°C to 1.2 x 10^{17} Ni^{++}/cm^2. Dark Field.*

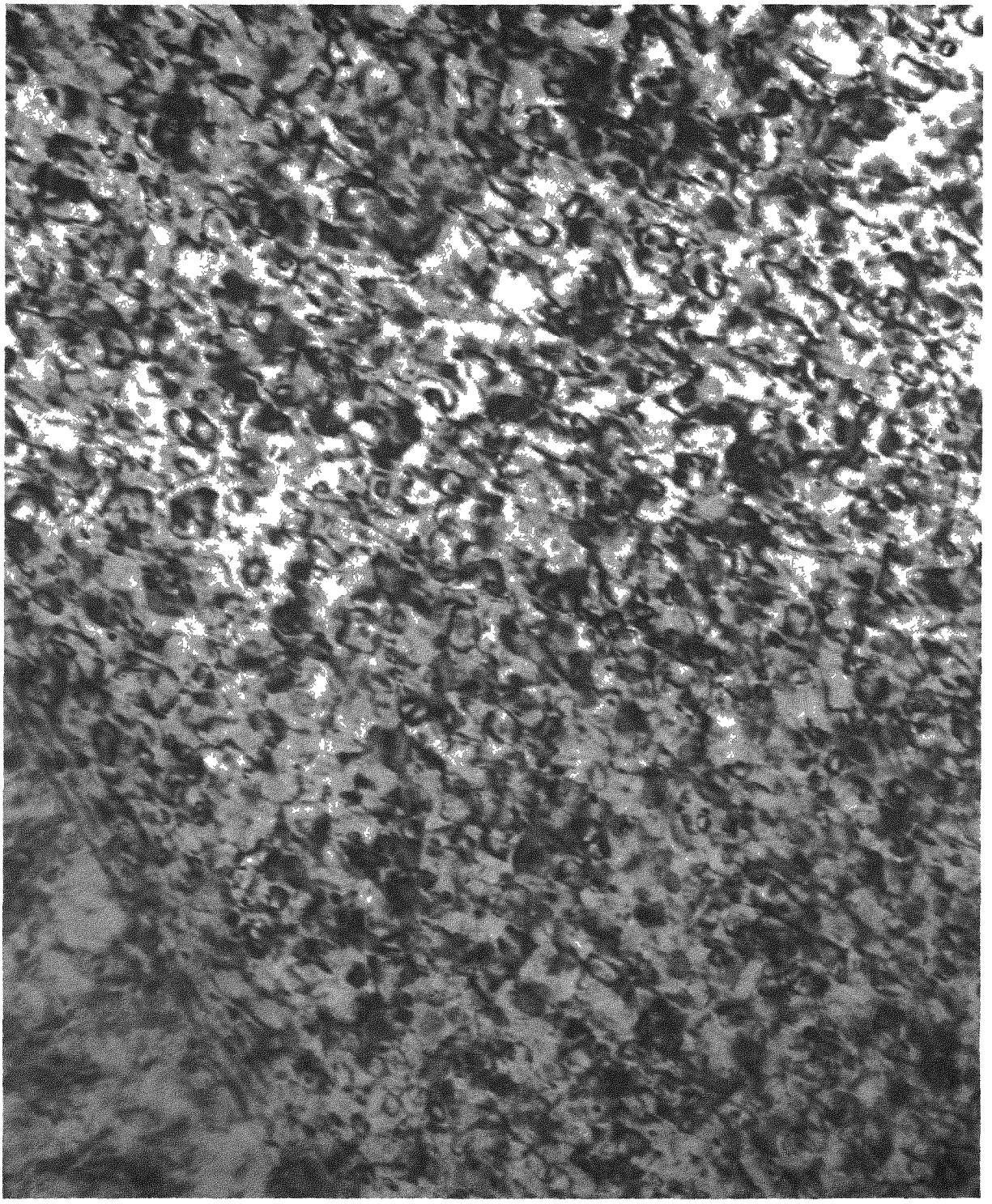

188,400X

FIGURE VII-107 *Solution-Annealed 316 SS, Bombarded with 5 MeV* Ni^{++} *at 475°C to 3 x* 10^{16} Ni^{++}/cm^2.

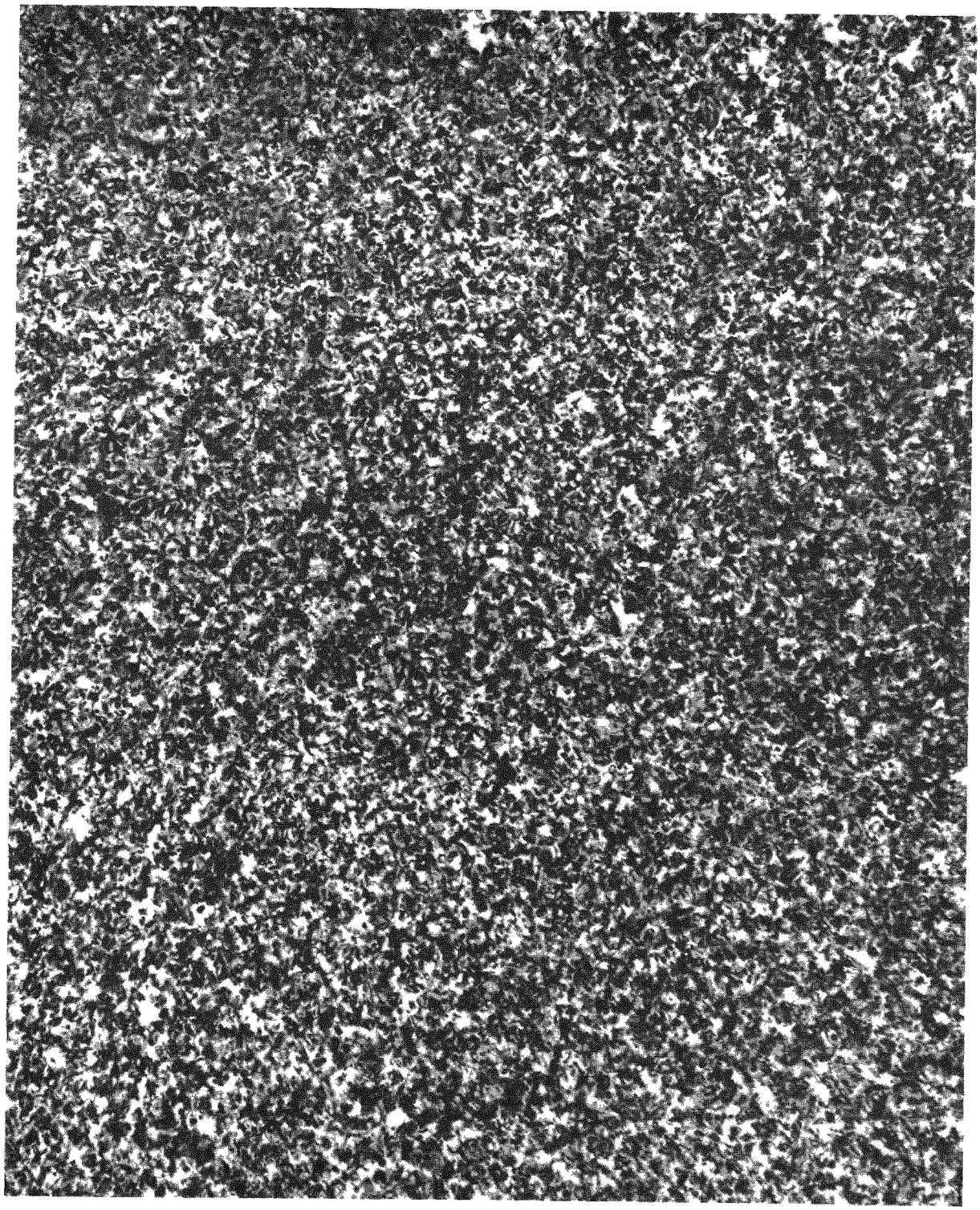

94,200X

FIGURE VII-108 *Solution-Annealed 316 SS, Bombarded with 5 MeV Ni^{++} at 370°C to 3 x 10^{16} Ni^{++}/cm^2.*

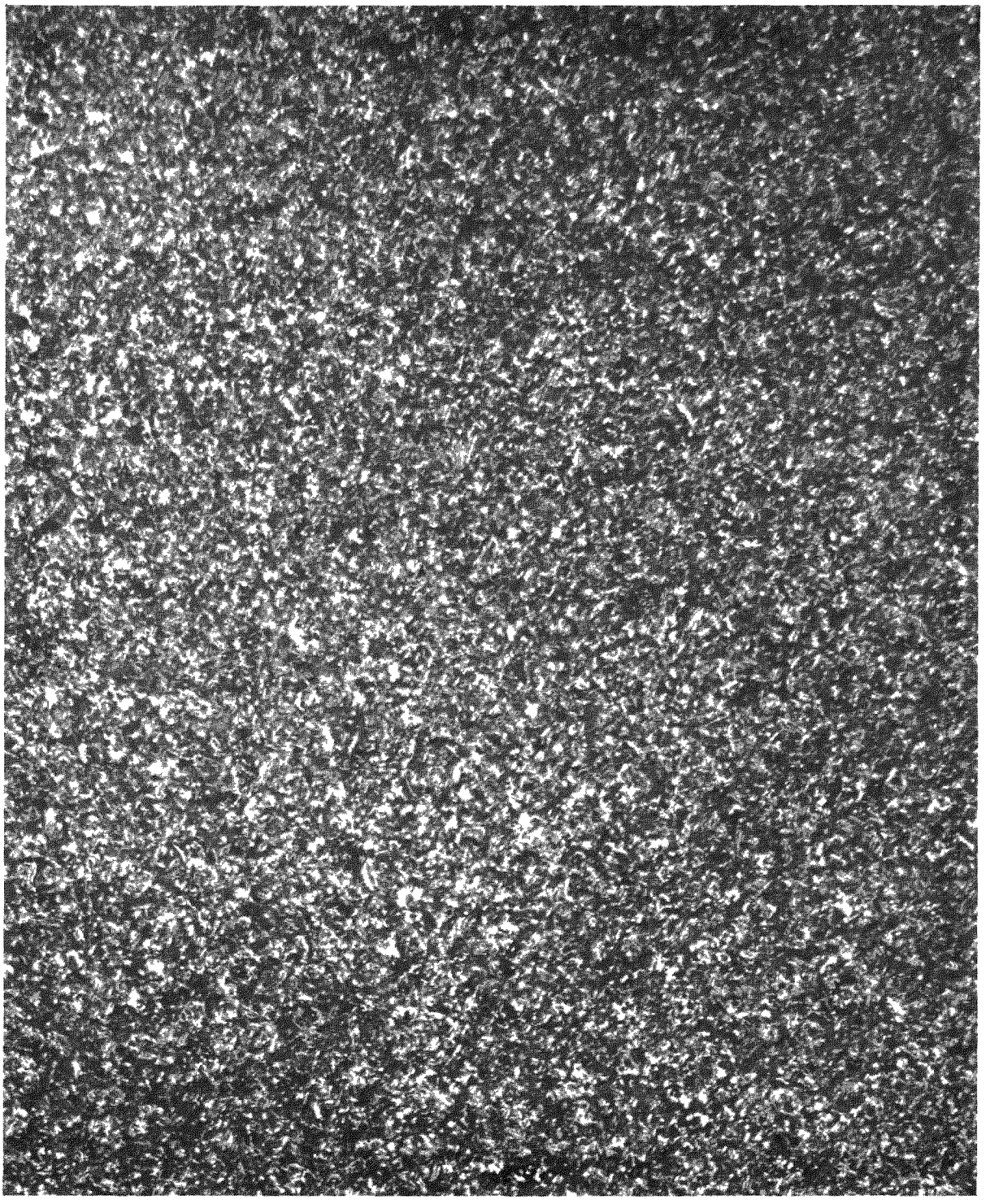

94,200X

FIGURE VII-109 *Solution-Annealed 316 SS, Bombarded with 5 MeV Ni^{++} at 370°C to 3 x 10^{16} Ni^{++}/cm^2 - Dark Field.*

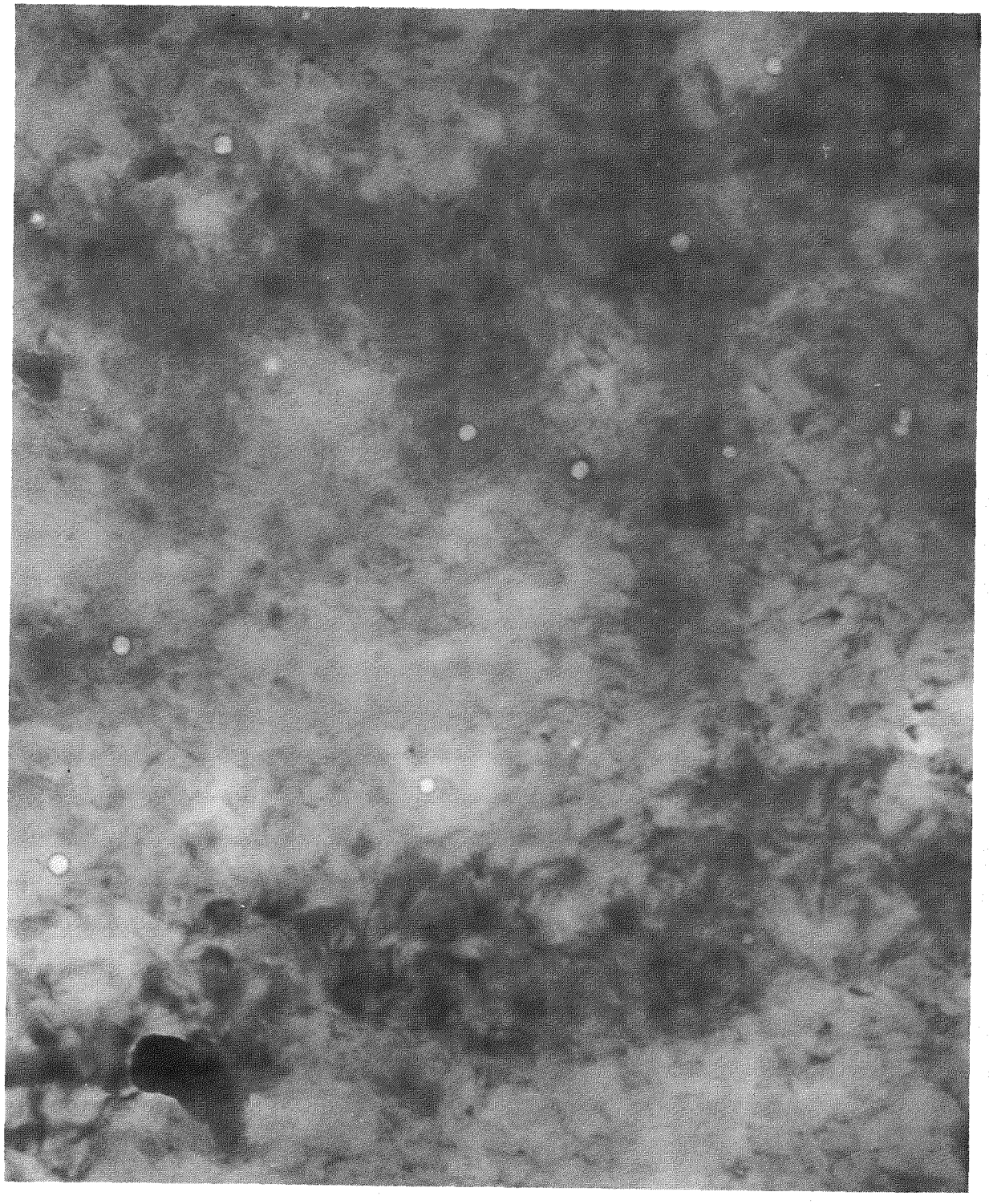

150,000X

FIGURE VII-110a *20% CW 316 SS Bombarded with 3 x $10^{16}Ni^{++}$ Ions/cm^2 (E = 5 MeV) at 585°C.*

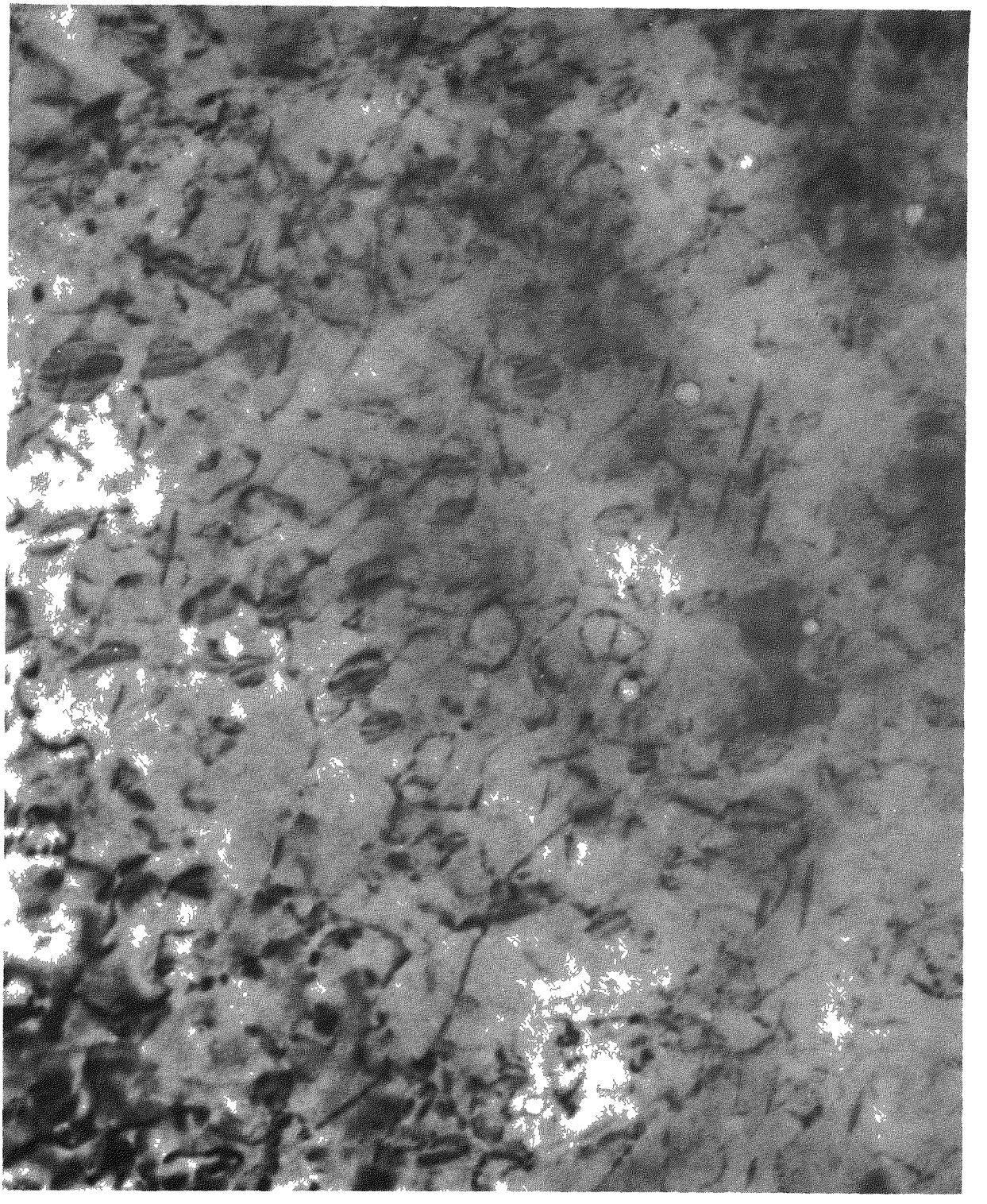

190,000X

FIGURE VII-110b *Same Sample Oriented to Show Faulted Loops and Dislocations.*

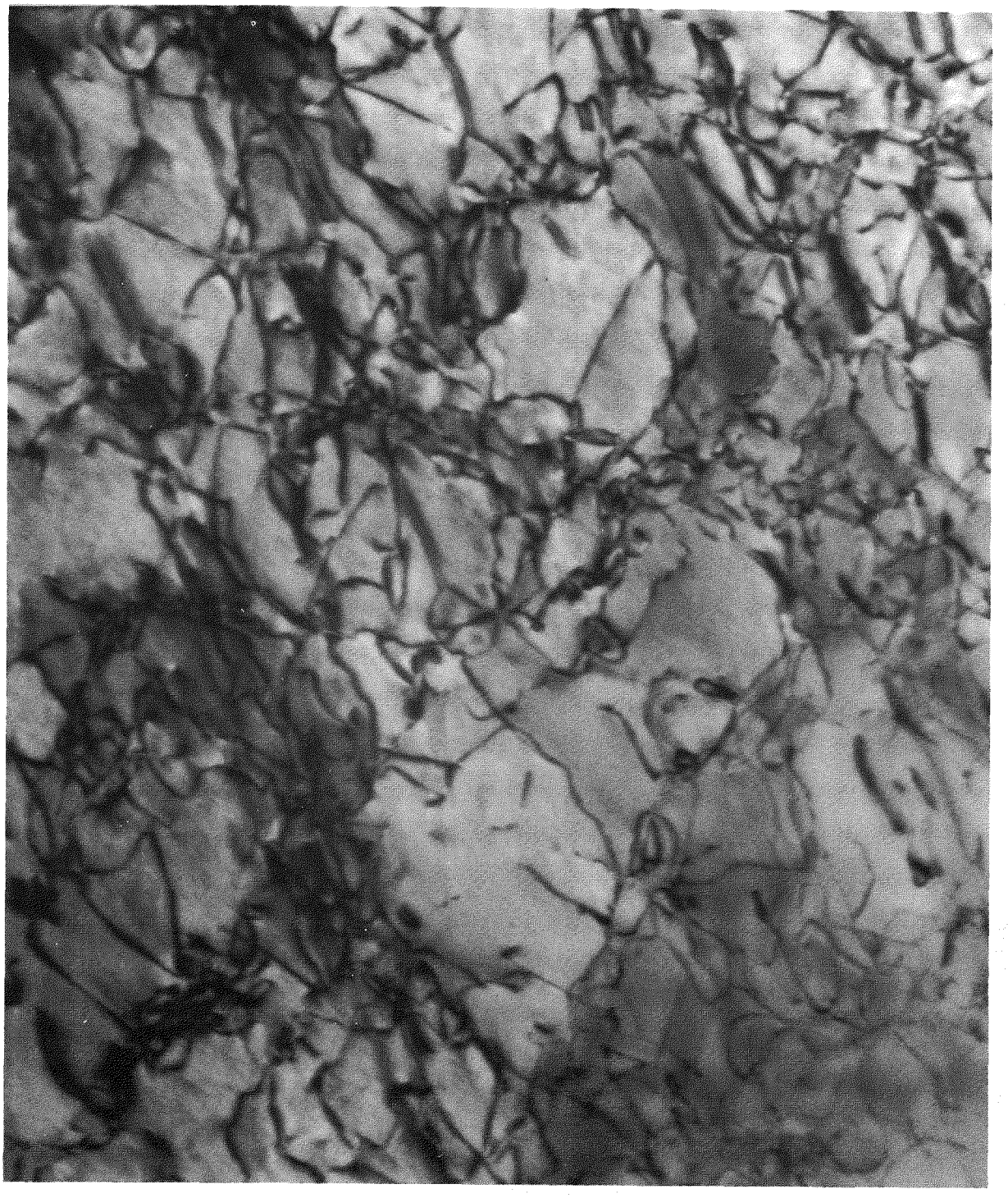

150,000X

FIGURE VII-111a *20% CW 316 Bombarded to 10^{16} Ni^{++} Ions/cm^2 (E = 5 MeV) at 585°C.*

190,000X

FIGURE VII-111b *20% CW 316 SS Bombarded to 3 x 10^{14} Ni^{++} Ions/cm^2 (E = 5 MeV) at 585°C.*

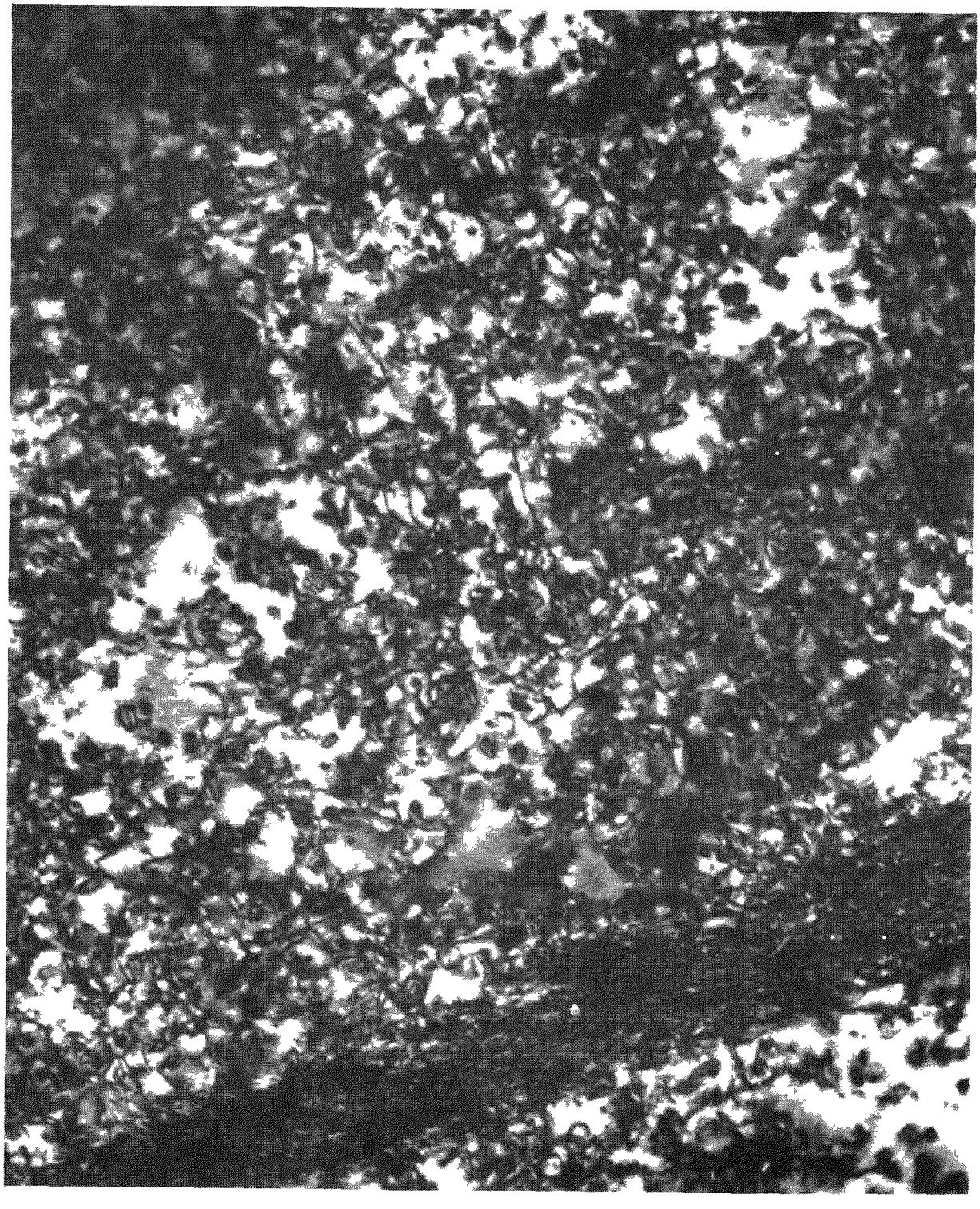

150,000X

FIGURE VII-112 *Presence of Faulted Loops, a Complex Dislocation Network, and Absence of Voids in 20% CW 316 SS Bombarded at 425°C to 3 x 10^{16} Ni^{++} ions/cm^2 (E = 5 MeV).*

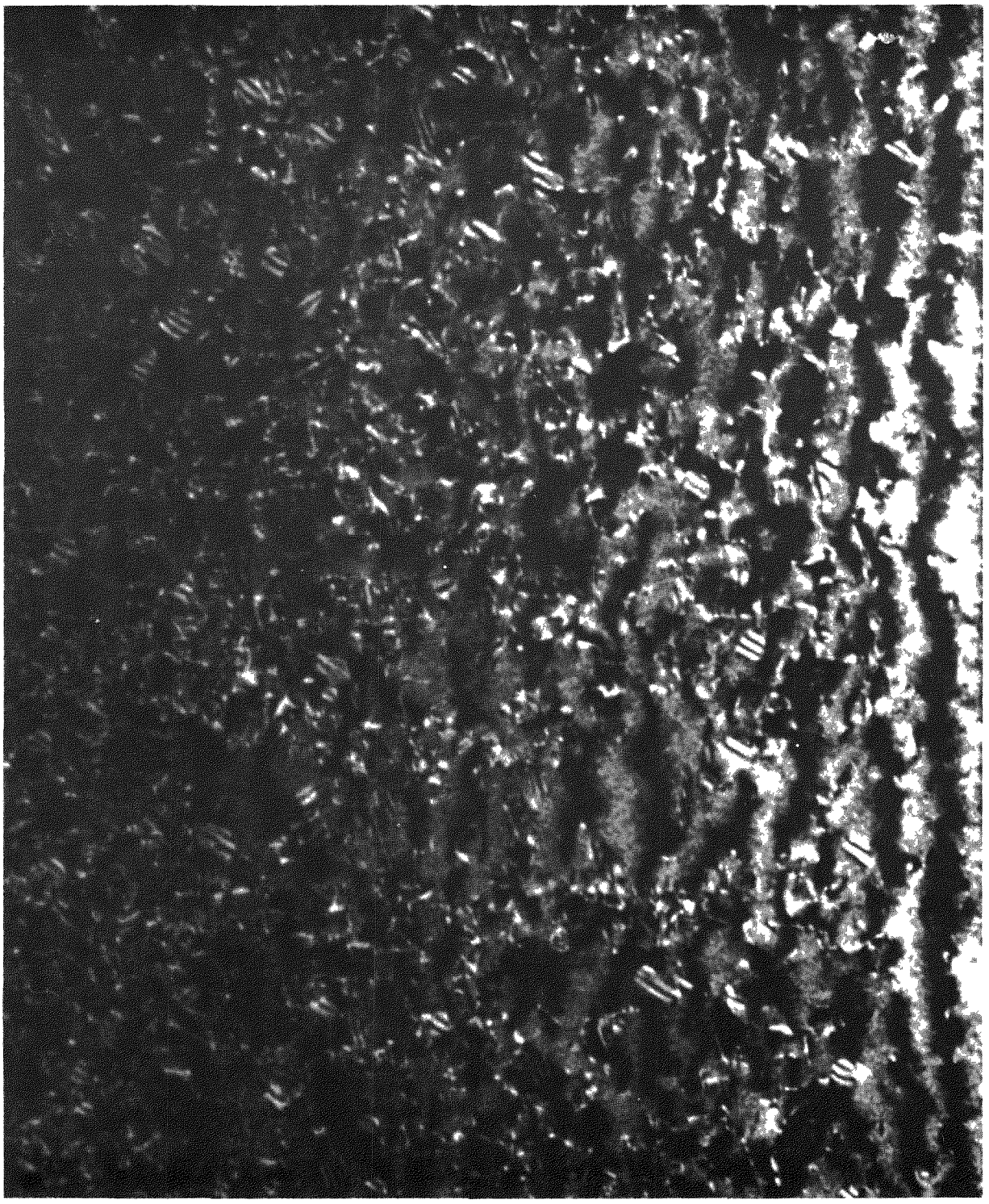

190,000X

FIGURE VII-113 *Dark-Field Micrograph Showing Faulted Loops in 20% CW 316 SS Bombarded at 500°C to 3 x 10^{16} Ni^{++} Ions/cm^2 (E = 5 MeV).*

formation in 316 SS neutron-irradiated to 3 x 10^{22} n/cm^2 (E > 0.1 MeV) over the temperature range 427°C to 705°C. An upper limit to the void concentration in the cold-worked, neutron-irradiated steel is about 3 x 10^{12} cm^{-3}, an order of magnitude less than observed in the ion-bombarded specimen. At a neutron fluence of 3 x 10^{22} n/cm^2, faulted loops are present in cold-worked 316 irradiated at 427°C and 482°C, but irradiation at 593°C and above results in the formation of a dislocation network with no loops.

c. Flux Effects

From the preliminary results reported above, it is increasingly evident that the temperature threshold for void formation is higher for ion-bombarded specimens. That is, while voids are observed in stainless steels which have been neutron-irradiated at 370°C, voids are not observed in heavy ion bombarded stainless steel for irradiation temperatures less than about 450°C. Some understanding of phenomena such as this is necessary in order to place a correct interpretation of ion-bombardment results as they apply to the prediction of results expected from high fluence neutron irradiations. A rationale, or model, is being developed to correlate the damage states of neutron-irradiated and ion-bombarded specimens.

The effect of dose rate on the defect state development may be expected to depend on both the nucleation and growth mechanisms for voids. Unfortunately, no satisfactory nucleation mechanisms are yet available. It appears, however, that the essential features of the temperature shift may be partially understood on the basis of growth theory. It can be shown that, for the high super-saturations of vacancies and interstitials to be expected during neutron irradiation and ion bombardment, classical diffusion theory predicts the following growth rate for a spherical pore:

$$\frac{d(r^2)}{dt} = 2\Omega(D_v C_v - D_i C_i) \qquad (1)$$

where r is the pore radius, D_v and D_i are the diffusivities for vacancies and interstitials, respectively, Ω is the atomic volume, and C_v and C_i are the concentrations of free vacancies and interstitials, respectively,

produced by the irradiation. To a first approximation, these concentrations may be calculated by assuming that they are steady-state concentrations, such that the rate of production is balanced by the rate of recombination and diffusion to sinks:

$$\frac{dn_v}{dt} = G\phi - \frac{30D_i\Omega^2 C_i C_v}{a^2} - SD_v C_v = 0 \qquad (2)$$

$$\frac{dn_i}{dt} = G\phi - \frac{30D_i\Omega^2 C_i C_v}{a^2} - S'D_i C_i = 0 \qquad (3)$$

where $G\phi$ is the defect production rate, a is the recombination distance, and S is a geometrical term describing the efficiency of the various sinks for vacancies. For example, if the sinks are "ideal", the major components of S would be:

$$S = 4\pi N_v r_v + 4\pi N_p r_p + \rho_D$$

where: N_v = number of voids/unit volume

r_v = average void radius

N_p, r_p pertain to incoherent precipitates

ρ_D = dislocation density, and

S' is the sink term for interstitials. Because of the larger strain field associated with an interstitial and the accompanying stress-assisted diffusion effects, S' is generally expected to be slightly larger than S. It should be pointed out that, in the development of the equation for void growth, it was assumed that the strain field around voids was negligible. This assumption appears reasonable for large voids, in the absence of externally applied stresses. One may introduce equations (2) and (3) into equation (1) to obtain the following growth equation:

$$\frac{d(r^2)}{d\phi t} = 2\Omega G\left(\frac{S' - S}{S'S}\right)\left\{\frac{D_v C_v}{G\phi} - \frac{S}{}\right\} \qquad (4)$$

From inspection of equation (4) it is seen that the growth rate may be considered in two parts, the first part being independent of dose rate

and dependent only on the relative distribution of sinks. The second part of the growth rate, in curly brackets, may be recognized merely as the fraction of defects which diffuse to sinks or, in other words, are not annihilated through recombination. Simultaneous solution of equations (2) and (3) yields:

$$\frac{D_v C_v S}{G\phi} = \frac{-1 + (1 + 4\xi)^{1/2}}{2\xi} \qquad (5)$$

$$\xi = \frac{30 G\phi}{SS' a^2 D_v}$$

so when ξ becomes very small (corresponding to low damage rates, high sink densities or high temperatures) the ratio becomes unity and the growth equation is rate insensitive. This situation corresponds to negligible amounts of recombination. As ξ is increased, however, the fraction of defects diffusing to sinks is decreased (due to increased recombination) and according to equation (4), for the same sink densities, the void size is reduced. The following "reasonable" values were chosen to calculate the variation in the ratio $D_v C_v S/G\phi$ with temperature.

$$S \sim 10^{10}/cm^2$$

$$D_v \sim e^{-30,000/RT}$$

$$G \sim 10/n\text{-}cm$$

The results for these assumptions are shown in Figure VII-114. The results for two flux levels are shown: 10^{15} n/cm^2-sec, which is equivalent to the neutron flux levels obtained in EBR-II; and 10^{18} n/cm^2-sec, which is roughly equivalent to the simulated neutron flux attained in the ion bombardment experiments. By comparing these two curves, one may readily see a plausible reason for the absence of voids in material bombarded at 400°C compared to their presence in neutron-irradiated material. In the neutron-irradiated case, approximately 90% of the defects survive recombination and diffuse to sinks, whereas for the higher dose rate,

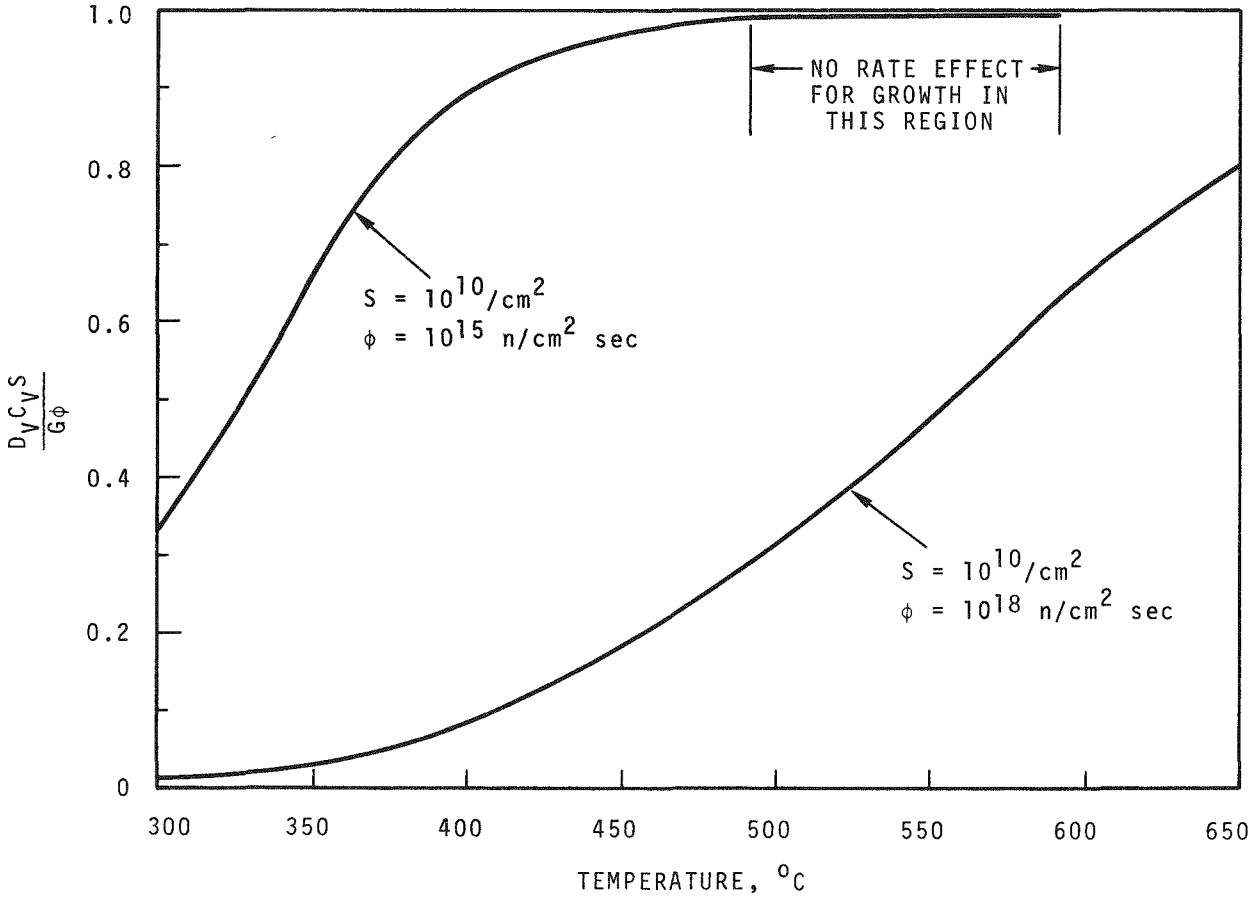

FIGURE VII-114 *Fraction of Defects Diffusing to Sinks as Calculated from Simple Defect Theory.*

only about 8% of the defects arrive at sinks. Assuming the same constant sink densities and noting that, at 400°C, voids in neutron-irradiated metals are about 100 Å in diameter, the use of equation (4) suggests that voids in the ion bombarded material would be expected to be about 30 Å in diameter or essentially below the resolution limit. Of course, the exact numbers and results of this analysis must be taken in a qualitative sense. The nature of defect production and migration is very poorly known and the effects of flux on nucleation have not been taken into account. However, the essential nature of the analysis is probably correct: as the dose rate is increased radically (as in bombardment experiments), the relative percentage of recombination increases, leaving for a given fluence fewer point defects available, particularly at low temperatures, for the formation of secondary defects such as large clusters, loops and voids.

The hypothesis that a flux effect should exist is verified not only by the observation of the higher temperature threshold for void formation in ion-bombarded stainless steel, but also by the presence of voids in ion-bombarded cold-worked stainless steel when there are none in specimens of the same material after neutron irradiation. Furthermore, direct evidence for a flux effect has been found upon examination of solution-annealed Type 316 stainless steel specimens bombarded with 5 MeV Ni^{++} at 425°C (798°F) at fluxes of 5×10^{11}, 5×10^{12}, and 5×10^{13} Ni^{++}/cm^2-sec. Representative microstructures of these specimens are shown in Figures VII-115, VII-116 and VII-117, respectively. The ion fluence in these three specimens is the same, 1×10^{15} Ni^{++}/cm^2, which is too low for the formation of resolvable dislocation loops. However, it can be seen that the concentration of defect clusters decreases with increasing ion flux. Preliminary determinations of defect concentrations are (in order of increasing flux) 6×10^{16}, 3×10^{16}, and 1×10^{16} clusters/cm^3. It therefore appears that not only the growth rate, but also the nucleation rate, of secondary defects are flux-dependent. These calculations and results will be analyzed in further detail during the next quarter.

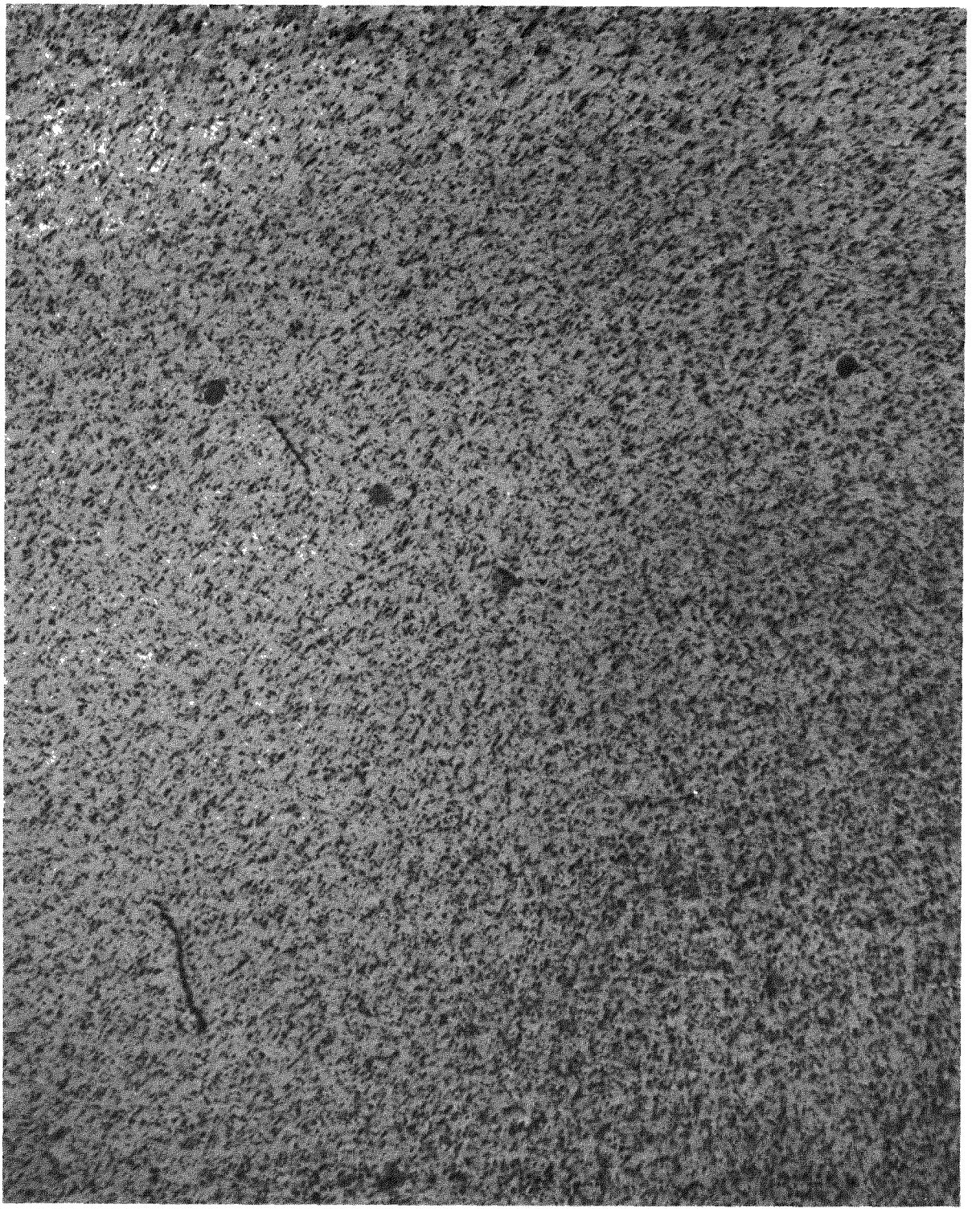

94,200X

FIGURE VII-115 *Solution Annealed 316 SS, Bombarded With 5 MeV Ni^{++} at 425°C to 1 x 10^{15} Ni^{++}/cm^2; Flux 5 x 10^{11} Ni^{++}/cm^2-sec.*

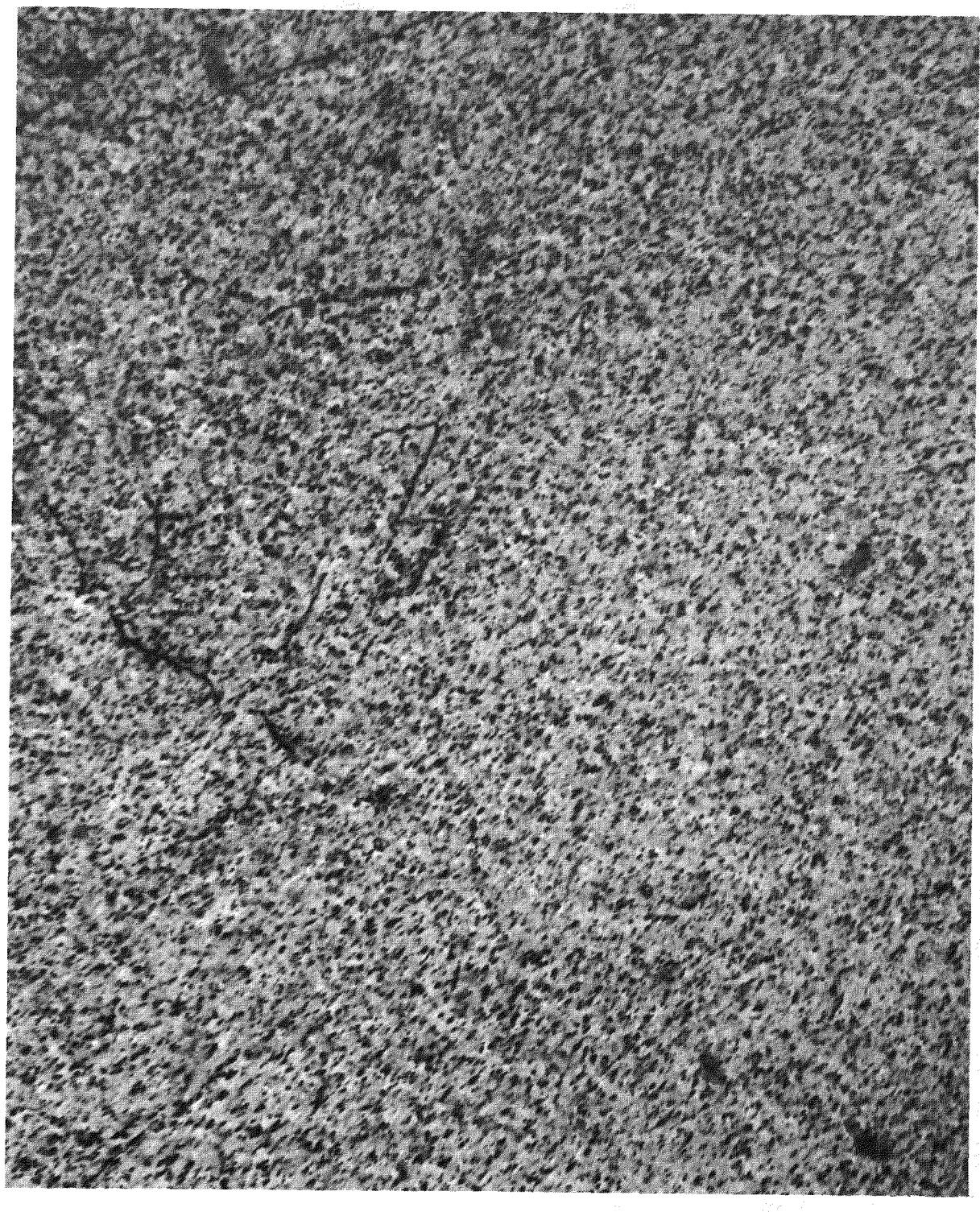

94,200X

FIGURE VII-116 *Solution-Annealed 316 SS, Bombarded With 5 MeV Ni^{++} at 425°C to 1 x 10^{15} Ni^{++}/cm^2; Flux 5 x 10^{12} Ni^{++}/cm^2-sec.*

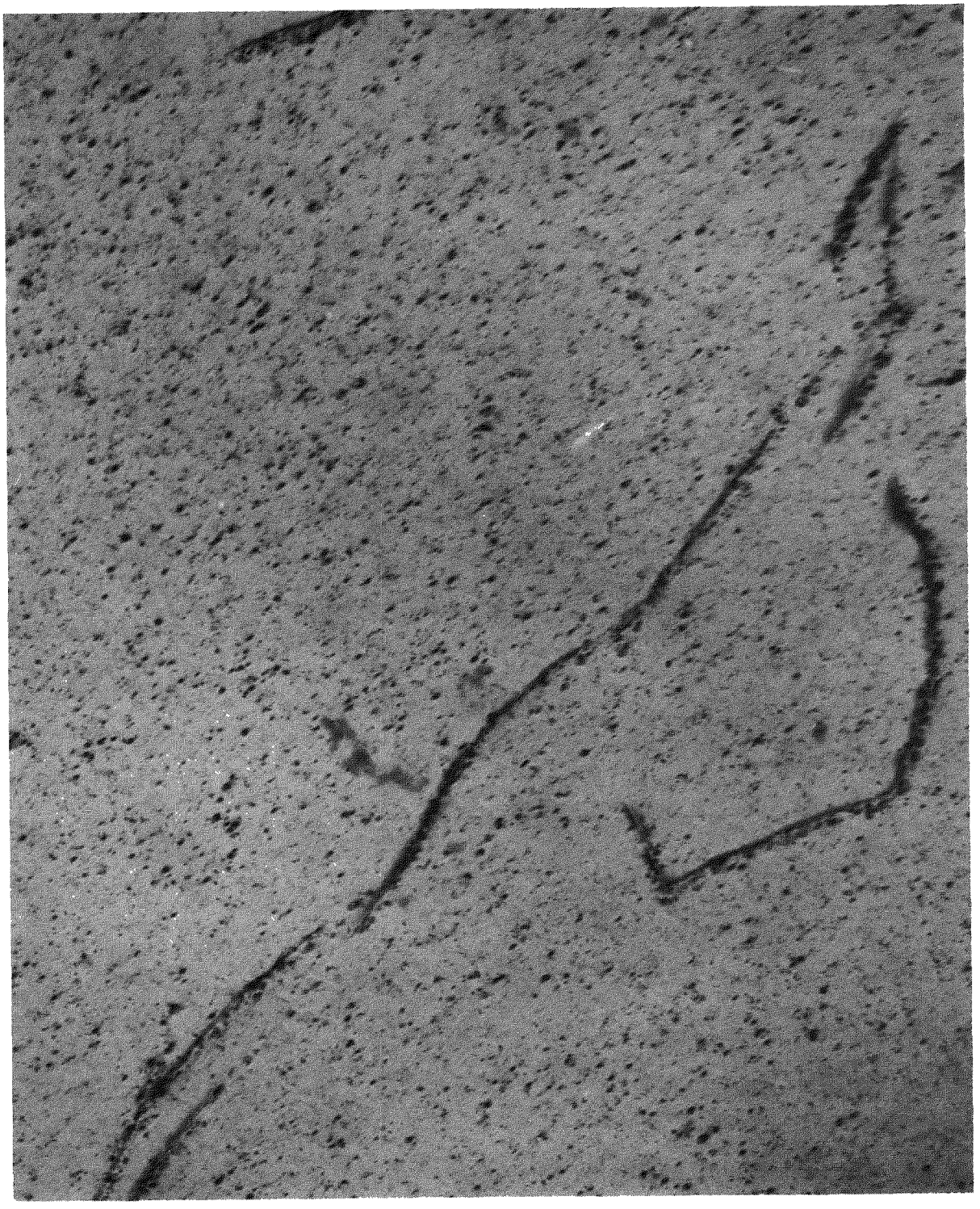

94,200X

FIGURE VII-117 *Solution-Annealed 316 SS, Bombarded With 5 MeV Ni^{++} at 425°C to 1 x 10^{15} Ni^{++}/cm^2; Flux 5 x 10^{13} Ni^{++}/cm^2-sec.*

d. Screening Experiments

Ion bombardment experiments, because of their accelerated damage rates and consequent short turnaround time, may be of considerable use in screening material variables for further study in fast reactor irradiation experiments. As an example, thermomechanical treatment is being explored as a means of improving the swelling resistance of stainless steel. The resistance to swelling is expected to be derived from the presence of a high density of NbC-decorated extrinsic stacking faults, which are efficient sinks for vacancies and, further, are thermally stable. A thermomechanically-treated (TMT) 348 SS specimen was bombarded at 375°C to a fluence of 1×10^{16} Ni^{++}/cm^2. The effectiveness of the thermomechanical treatment in producing a material that resists swelling in a fast reactor neutron flux has not yet been fully evaluated, since the first EBR-II irradiated TMT 348 specimens will not be discharged until later this year. Figure VII-118 shows the microstructure of a TMT 348 specimen after ion bombardment under the conditions given above. The results confirm that the stacking faults act as vacancy sinks, and, in so doing, have altered the nature of secondary defect formation. The faulted regions have disappeared, indicating vacancy absorption, and the characteristic bands of NbC precipitates remain. The remaining irradiation-produced defects have agglomerated into small clusters, as opposed to the faulted loops produced in Type 316 stainless steel at the same temperatures (Figures VII-108 and VII-109). These results are quite encouraging as they suggest that it may indeed be possible to produce a swelling-resistant microstructure. Since, as discussed in the preceding section, recombination should predominate over diffusion to sinks, the material should function even more effectively in a fast reactor environment. Additional specimens have been bombarded at 625°C and are awaiting examination.

e. Helium Injection Studies

The problem of gradually depositing a uniform distribution of helium nuclei throughout the region of the sample foils undergoing defect production during ion bombardment studies has been considered. The ion

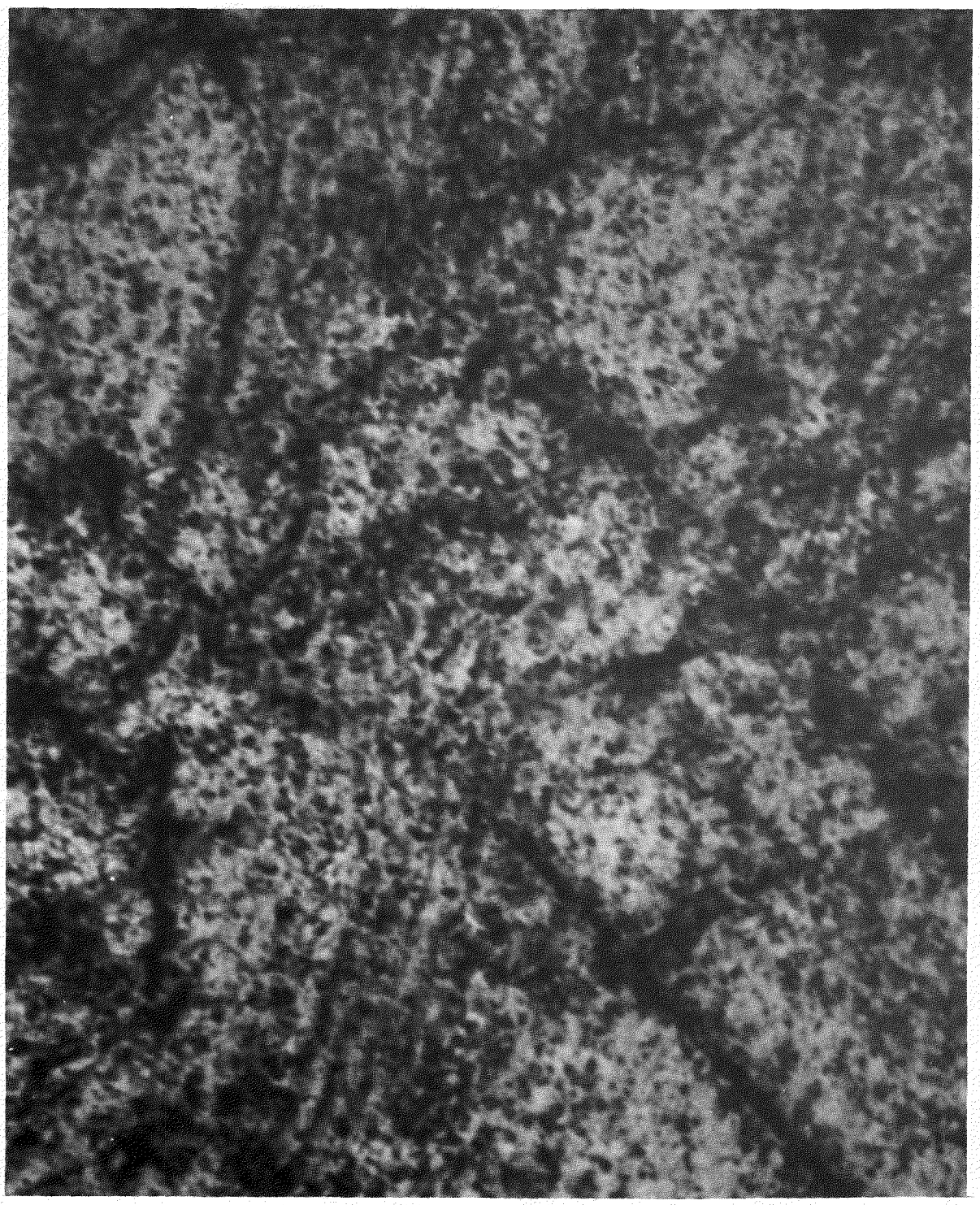

136,500X

FIGURE VII-118 *Thermomechanically treated 348 SS, Bombarded with 5 MeV* Ni^{++} *at 375°C to 1 x* 10^{16} Ni^{++}/cm^2.

bombardment is intended to simulate the radiation damage which occurs in nuclear reactor irradiations. The reactor exposure takes place under conditions where alpha particles are steadily introduced into the solid. These alpha particles or helium atoms are believed to serve as nucleation points for void formation and to also affect void growth kinetics. If the ion bombardment is to simulate the corresponding reactor experiment accurately, or if it is to be of maximum possible use in developing theoretical understanding of the reactor experiment kinetics, we must be able to simulate the gradual introduction of helium atoms into the region undergoing damage.

In the ion bombardment experiments, it is extremely difficult to operate a helium source and a pseudo primary knock-on source simultaneously, so it is necessary from a practical and economic standpoint to bombard alternately the stainless steel foil samples with Ni and He ions. This is not necessarily a disadvantage, as the continuous helium introduction of the reactor experiments can be approximated to any degree desired. For reasons of advancing theoretical understanding, it is actually desirable to be able to control the point in time when the helium is introduced so as to be able to observe the effect of its presence or absence at various stages of the damage experiment.

Recent studies by J. Weitman, N. Daverhog, and S. Farvoldan have shown that the helium production in a reactor does not occur at a steady rate and may in some cases actually be more rapid near the end of a particular constant flux reactor experiment.

Calculations have shown (Ref 50) that, when stainless steel is bombarded with 5 MeV Cu^{++} ions, the damaged region is distributed so that the maximum equivalent neutron fluence occurs at a depth of 0.95 microns below the incident surface. It was found that the equivalent fluence fell off only about 15 or 20% over a region 0.3 μ wide centered about the region of maximum equivalent fluence.

Experimentally then, the problem with helium is to inject it over a broad enough region to cover the damaged region at the location given by Kulcinski, Laidler and Doran (Ref 50), and to inject at times which either aid theoretical understanding or simulate reactor injections as currently understood.

The methods of obtaining the time distribtuion are obvious, although it now appears that the time distribtuion for reactor simulation depends upon the impurities in the steel and the degree of hardness of the spectrum.

As an aid to planning space distribtuions of helium, calculations have been made of the depth of penetration, R, and straggling, ΔR, of He ions of various energies injected into Ni, Fe, and Cu. The calculations were made following the method of Schiott, (Ref 51) who used Lindhard's (Ref 52) approach. The results are tabulated below in Table VII-33.

TABLE VII-33
RANGE OF HE IONS INTO FE, NI, AND CU

	Fe		Ni		Cu	
E (KeV)	R (μ)	ΔR (RMS)	R (μ)	ΔR (RMS)	R (μ)	ΔR (RMS)
100	0.3	0.09	0.28	0.11	0.30	0.10
200	0.52	0.12	0.48	0.12	0.52	0.12
300	0.72	0.13	0.66	0.12	0.72	0.14
400	0.92	0.15	0.83	0.13	0.90	0.15
500	1.05	0.15	0.97	0.14	1.10	0.16
600	1.24	0.16	1.11	0.15	1.27	0.17

It appears that the width of the region containing helium from a single energy of incident ion is uncomfortably narrow from an experimental point of view. The thinning procedure in the electron microscopy will be much less critical if bombardments of He are carried out at two or three different energies. An alternate experimental approach would be to gradually insert a wedge-shaped shield in front of the target during the helium bombardment. The relative merits of these two approaches are presently being considered, and the most practical one will be employed in proposed ion bombardment experiments.

f. Further Studies

A second series of ion bombardment experiments is now beginning. Bombardment temperatures and fluences will be extended to higher levels, and flux effects will be studied at temperatures above the void formation threshold. A number of specimens of 316 SS have been uniformly injected with 3 atom ppm He and will be bombarded in an experiment which serves as a precursor to irradiations in which He is gradually introduced. An irradiation has been completed in which the effects of holding the bombarded specimen at the irradiation temperature for various times will be determined. If a difference is noted, redesign of the specimen heater in the ion bombardment facility will be necessary.

References

50. Kulcinski, G. L., Laidler, J. J., and Doran, D., "Simulation of High Fluence Fast Neutron Damage with Heavy Ion Bombardment." To be published in Radiation Effects.

51. Schiott, H. E., Mat. Fys. Med 35 No. 9 (1966).

52. Lindhard, J., Scharff, M., and Schiott, H. E., - Mat. Fys. Med 33 No. 14. 1963.

2. Computer-Based Modeling of Irradiation Damage

D. G. Doran and H. H. Yoshikawa

The purpose of formulating damage models is to provide a basic scientific frame of reference within which experimental data on radiation-induced changes in material properties can be evaluated and correlated.

The objective of the present effort is to model correctly the production of displacement damage and the subsequent nucleation of extended defects, as functions of fluence and temperature. Computer experiments with single displacement cascades have led to the development of a new computer code to study the consequences of a high degree of cascade overlap, and to the development of an FCC version of the HAPBCC code that simulates short-term annealing in a BCC lattice; these codes provide temperature corrections to displacement cascades simulated by computer at an effective irradiation temperature of 0°K.

Displacement Cascade Overlap.-In the previous quarterly, some results were presented of computer experiments in which displacement cascades were produced in damaged lattices. Also reported was an attempt to approximate these results by simply superposing the cluster distributions appropriate to the pre-cascade damage state and the cluster distributions appropriate to cascades produced in perfect lattices. The results were rather poor approximations to the actual computer experiments.

A spatial superposition has now been performed. Two cases were studied using eight 20 keV cascades simulated in α-iron. The primary knock-on atoms producing these cascades had a common take-off point, but had different directions selected randomly within one-half of an octant ($0 \leq \theta \leq \pi/2$, $0 \leq \phi \leq \pi/4$). In the first case, annealed PASS 1 cascades were spatially superposed on the input damage state for PASS 3 runs (reported in the last quarterly). It should be noted that the "PASS" terminology has the following significance. The term PASS 1 refers to the simulation of several cascades in a perfect lattice using the CASCADE-CLUSTER computer codes. These cascades were subjected to a simulated short term anneal using the HAPBCC (Hybrid Anneal Program-BCC) code to account for nonzero irradiation temperatures. The resulting damage configuration for

a typical cascade, modified for long term effects by eliminating mobile defects and rearranging clusters in more stable configurations, was used as the input damage state for PASS 2 (same take-off points and directions as in PASS 1); an annealed PASS 2 cascade served as input for PASS 3, etc. Results through PASS 4 were reported last quarter.

The second case was a similar treatment of PASS 4. The superposition results are considered to be good approximations to the PASS 3 and PASS 4 runs.

Averaged results for both cases are shown in Figures VII-119 through VII-122. Each plot suggests that superposition produced larger clusters than the original runs. However, the peak in each plot corresponding to the largest clusters is due to the particular cascade from which the initial damage distribution was derived. Thus it represents a cascade superposed on itself and can be ignored as a highly unlikely event. Superposition did produce a small excess of mobile defects and total defects. The similarity of the superposition results to the runs obtained by simulating cascades in damage lattices does not imply that lattice damage does not significantly influence cascade formation. Such information simply cannot be extracted from the CASCADE-CLUSTER codes, because realistic lattice damage cannot be simulated with them; specifically, the damage description is limited to specifying the occupancy of a lattice or interstitial site.

These results have led in part to the development of a computer code, called HIFLUF (High Fluence FCC), which is now being written to describe the superposition of a large number of cascades in a finite volume. The goal is a temperature-sensitive model that spans the gap in scale from atomic simulation to transmission electron microscopy, while retaining at least approximately the spatial and temporal variations of defect densities inherent in the production of defects by the cascade process.

This code should be completed and tested in its initial form during the next quarter.

FCC Annealing Code.-The programming of the code HAPFCC, which will handle short term anealing in an FCC lattice (γ-iron), is estimated to be 70% complete.

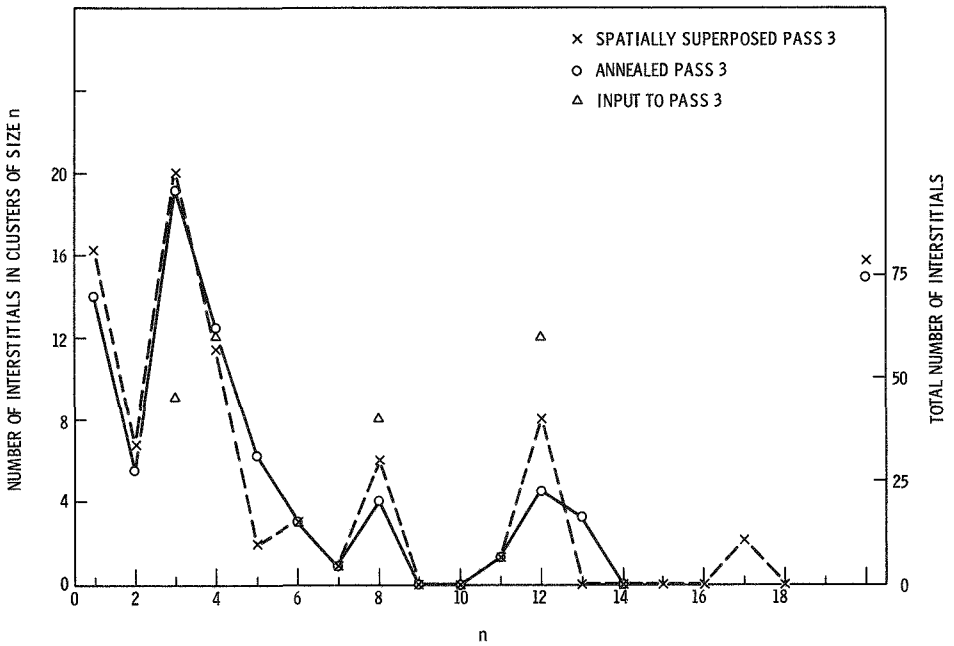

FIGURE VII-119 *Comparison of the Interstitial Cluster Size Distribution, Obtained by Spatially Superposing Annealed PASS 1 Cascades on the Indicated Input Distriubtion (obtained from PASS 2), with the Cluster Size Distribtuion Obtained from Annealed PASS 3 Cascades.*

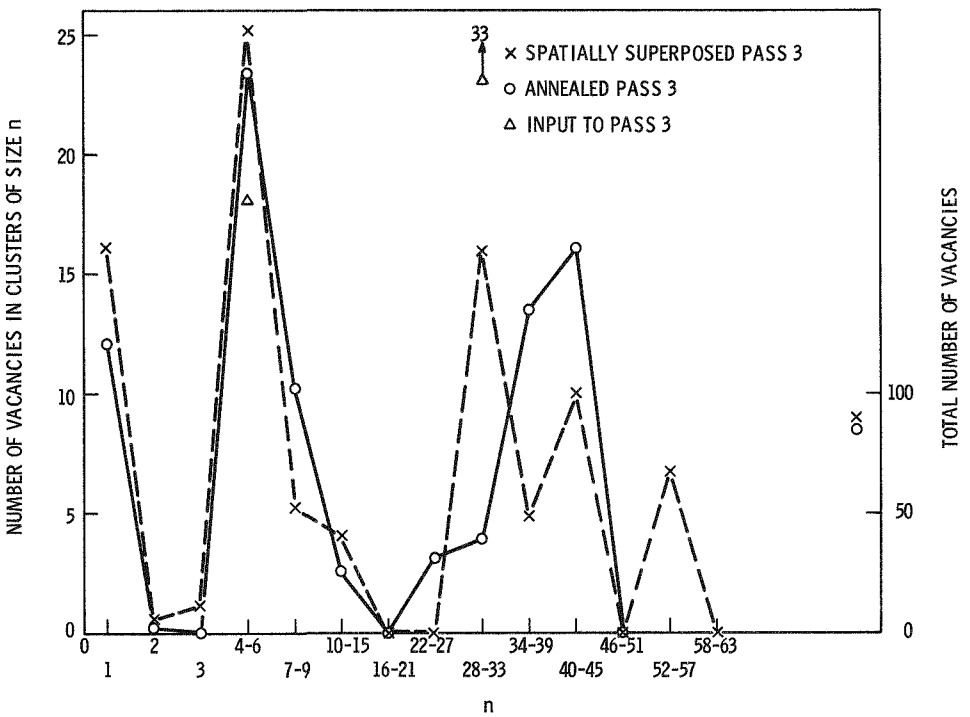

FIGURE VII-120 *Same Comparison as in Figure VII-119 but for Vacancies.*

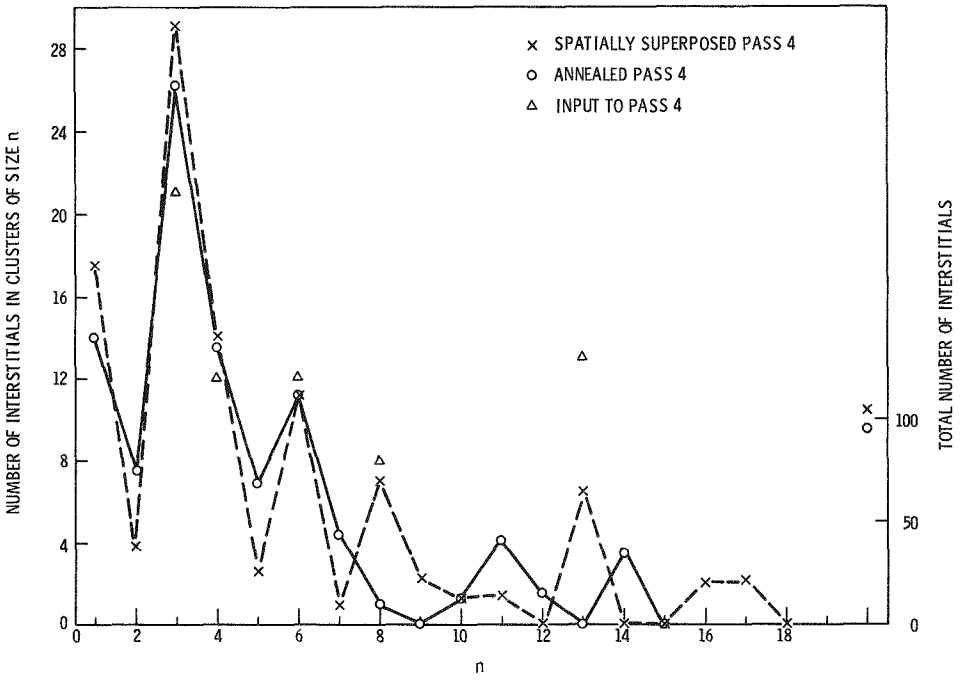

FIGURE VII-121 *Comparison of the Interstitial Cluster Size Distribution, Obtained by Spatially Superposing Annealed PASS 1 Cascades on the Indicated Input Distribution (obtained from PASS 3), with the Cluster Size Distribution Obtained from Annealed PASS 4 Cascades.*

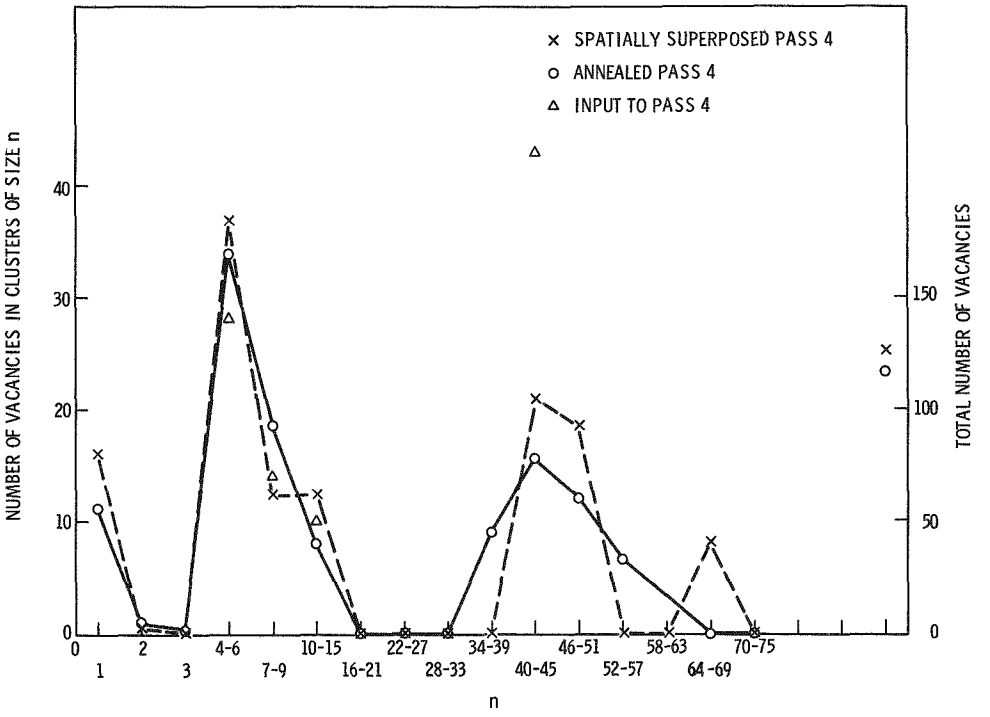

FIGURE VII-122 *Same Comparison as in Figure VII-121 but for Vacancies.*

F. MICROSTRUCTURAL MODIFICATIONS TO STAINLESS STEELS

J. J. Laidler, J. F. Bates, J. L. Straalsund, G. L. Guthrie and T. K. Bierlein

The purpose of this work is to seek means for improving the stability of austenitic stainless steels in fast reactor environments through microstructural modifications. Such modifications may be produced by selected variations in chemical composition and/or by use of thermomechanical treatments.

Discussion of the concept of a damage-resistant microstructure in thermomechanically-treated (TMT) AISI Type 348 SS, and the effects of variations in composition and TMT processing parameters on mechanical properties have been included in previous quarterly reports. This report will survey microstructures produced under various processing treatments being considered.

The expected resistance to fast reactor radiation damage of TMT 348 SS has its origin in the manner in which NbC precipitates from supersaturated solution upon aging in the narrow temperature range of 650 to 750°C. As the NbC precipitates, extrinisic stacking faults are generated by a mechanism originally identified by Silcock (Ref 53). Further precipitation occurs on the leading (Frank) partial of the growing stacking fault, resulting in a faulted structure copiously decorated with NbC. Additional precipitation may occur at unextended dislocations and at isolated sites in the matrix. This extensive precipitation not only enhances the elevated temperature tensile strength and creep resistance, but additionally provides a very high concentration of sinks and traps for point defects. The extrinsic stacking faults appear to be very effective sinks for vacancies, as disclosed in the ion bombardment section of this report. The existence of a highly specific sink for vacancies also appears to upset the normal defect nucleation scheme, so that void nucleation may be completely suppressed. Final proof of this concept must await examination of specimens ion-bombarded at higher temperatures and neutron-irradiated to high fast fluences. The precipitates at isolated sites in the matrix are also expected to play an important role. It has been

reported (Ref 54) that helium bubbles form on matrix NbC precipitates during 600°C neutron irradiation; a high density of such precipitates should serve to trap a significant portion of the helium generated by (n, α) reactions and reduce the extent of grain boundary helium agglomeration and consequent embrittlement.

The method for production of the faulted structure in 348 SS is rather uncomplicated; essential to the process is a very high solution-annealing temperature to maximize the amount of niobium and carbon in solution. A solution treatment of one hour at 1300°C has been used throughout these experiments, followed by either water quenching or an interrupted quench involving a hold for one hour at 700°C. The latter method will be referred to as a "direct aging" treatment. Following the solution treatment, the alloy may be plastically deformed and then aged or simply aged without deformation. An aging treatment of 100 hours at 700°C has been adopted as a basic reference treatment in this study.

Although the research effort is continuing and the state of understanding of the active precipitation processes is evolving, an "optimum" thermomechanical treatment of 348 SS has not been achieved. At present, the particular type of TMT must be chosen to fit the intended function of the alloy. There are four basic functionally-directed types of thermomechanical treatments. For simplicity of notation, these will be referred to as TMT-A, -B, -C, and -D. The first, TMT-A, has as its function the production of a high density of stacking faults which will serve as vacancy sinks. A typical example of the microstructure produced by TMT-A is shown in Figure VII-123a. This TMT involves a direct aging treatment followed by stress-aging (at about 1-2% strain) at 700°C and a final treatment of 100 hours at 700°C. With this method, it has been possible to achieve areal stacking fault densities as high as 5×10^5 cm^2/cm^3, which represents absorption capacity for $\sim 2 \times 10^{20}$ vacancies per cm^3. Figure VII 123b is a dark-field micrograph of the same structure, made with the NbC (002) reflection, to demonstrate that the precipitates seen are NbC. The large particle in the center of the field is undissolved $M_{23}C_6$. The maximum density of gas atom traps is produced by TMT-B, which

35,000X

FIGURE VII-123a *348 SS, Solution-Treated 1 hr at 1300°C, Direct Aged 1 hr at 700°C, Cooled to RT, Stress-Aged 1/2 hr at 700°C at 1% Strain, Unloaded, and Aged 100 hr at 700°C.*

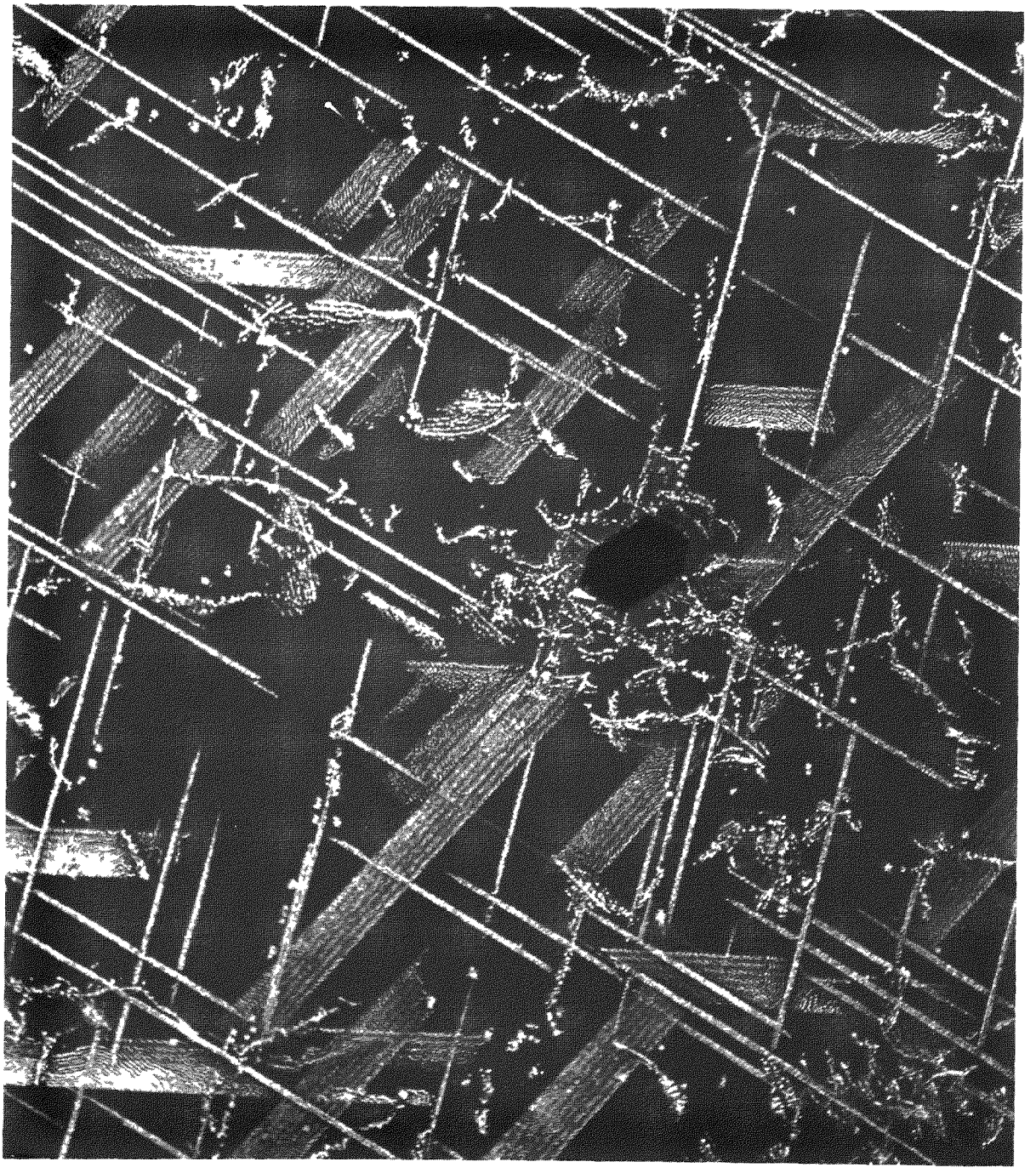

35,000X

FIGURE VII-123b *Same Treatment as in 123a; Dark-Field Image with NbC (002) Reflection.*

involves water quenching, room temperature prestraining to 1 to 3% strain, and the standard aging treatment. This microstructure is shown in Figure VII-124. The highest concentration of isolated matrix precipitates yet achieved is 3×10^{13} cm^{-3}. Higher plastic strains are required for maximum mechanical strengthening. Maximum 650°C creep strength is produced by TMT-C, which is identical to TMT-A with the exception that stress-aging is carried out at 3-5% strain. Figure VII-125 illustrates the microstructure produced by TMT-C. The elevated temperature creep resistance of TMT 348 SS has been shown to arise from the presence of the NbC-precipitated stacking faults (Ref 55); short-time elevated temperature tensile strength, on the other hand, is provided by a high density of NbC-decorated dislocations, as produced by TMT-D. This TMT is similar to TMT-B, with the exception that prestrains of 10-20% are required. The resultant microstructure is illustrated in Figure VII-126. This structure is not thermally stable and over-ages rapidly.

A fifth treatment, TMT-E, which involves aging without plastic deformation, produces a microstructure such as shown in Figure VII-127. This "TMT" included a direct aging treatment followed by aging for 1000 hours at 700°C. It is typical of the direct aging process in that precipitation at isolated sites in the matrix is suppressed.

Thermomechanically-treated Type 348 SS swelling specimens irradiated in EBR-II to 3×10^{22} n/cm^2 ($E > 0.1$ MeV) in the X-018A subassembly will become available during the next quarter. A large number of foil specimens, representing 18 different thermomechanical treatments, were loaded in the Metallurgical Variables assembly, and will be available in about two years. In the meantime, limited screening tests employing heavy ion bombardment will be conducted.

35,000X

FIGURE VII-124 *348 SS, Solution-Treated 1 hr at 1300°C, Water-Quenched, Strained 3% at RT, and Aged 100 hr at 700°C.*

21,000X

FIGURE VII-125 *348 SS, Solution-Treated 1 hr at 1300°C, Direct Aged 1 hr at 700°C, Cooled to RT, Stress-Aged 1/2 hr at 700°C at 3% Strain, Unloaded, and Aged 100 hr at 700°C.*

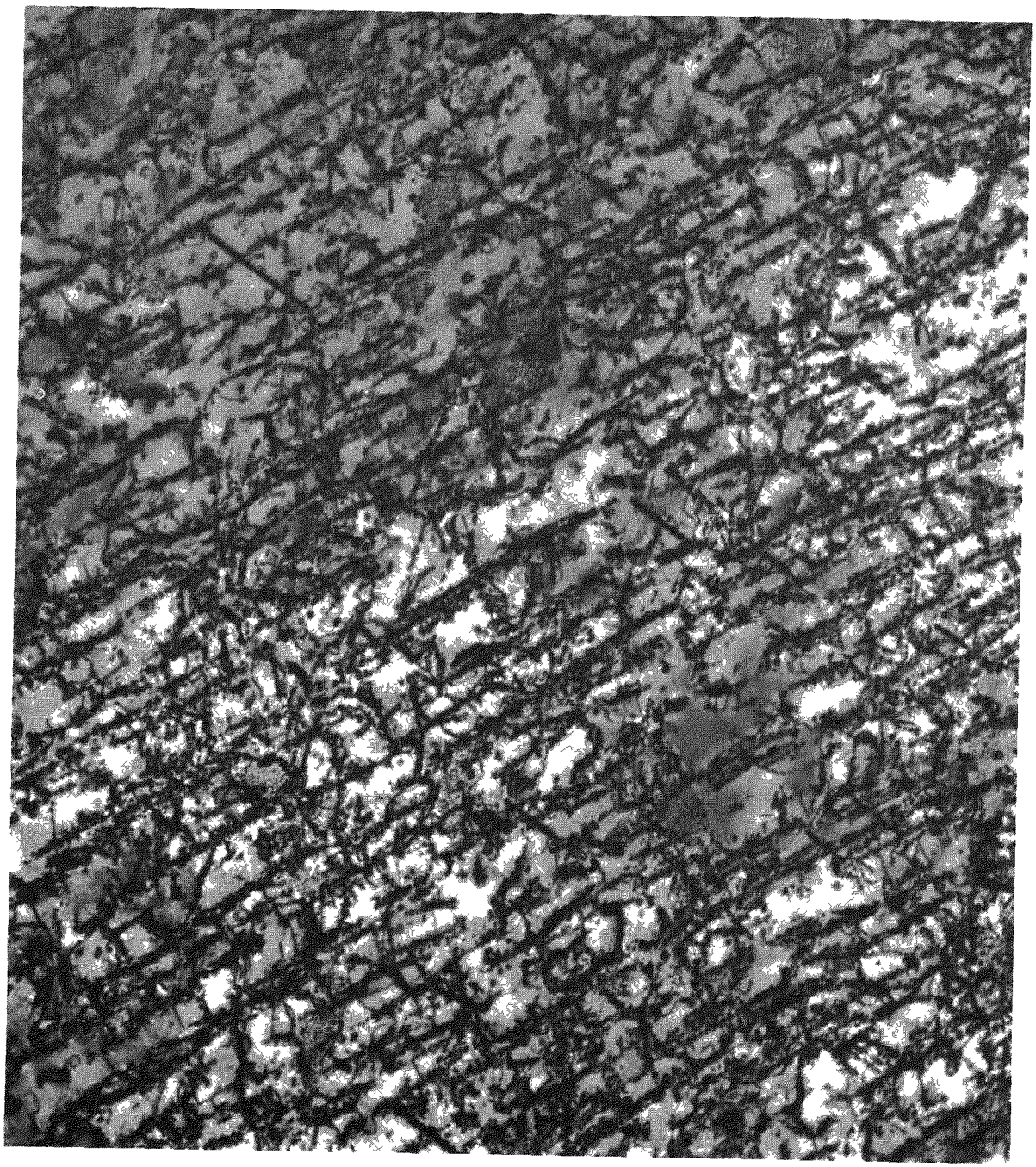

35,000X

FIGURE VII-126 *348 SS, Solution-Treated 1 hr. at 1300°C, Water-Quenched, Strained 10% at RT, and Aged 100 hr at 700°C.*

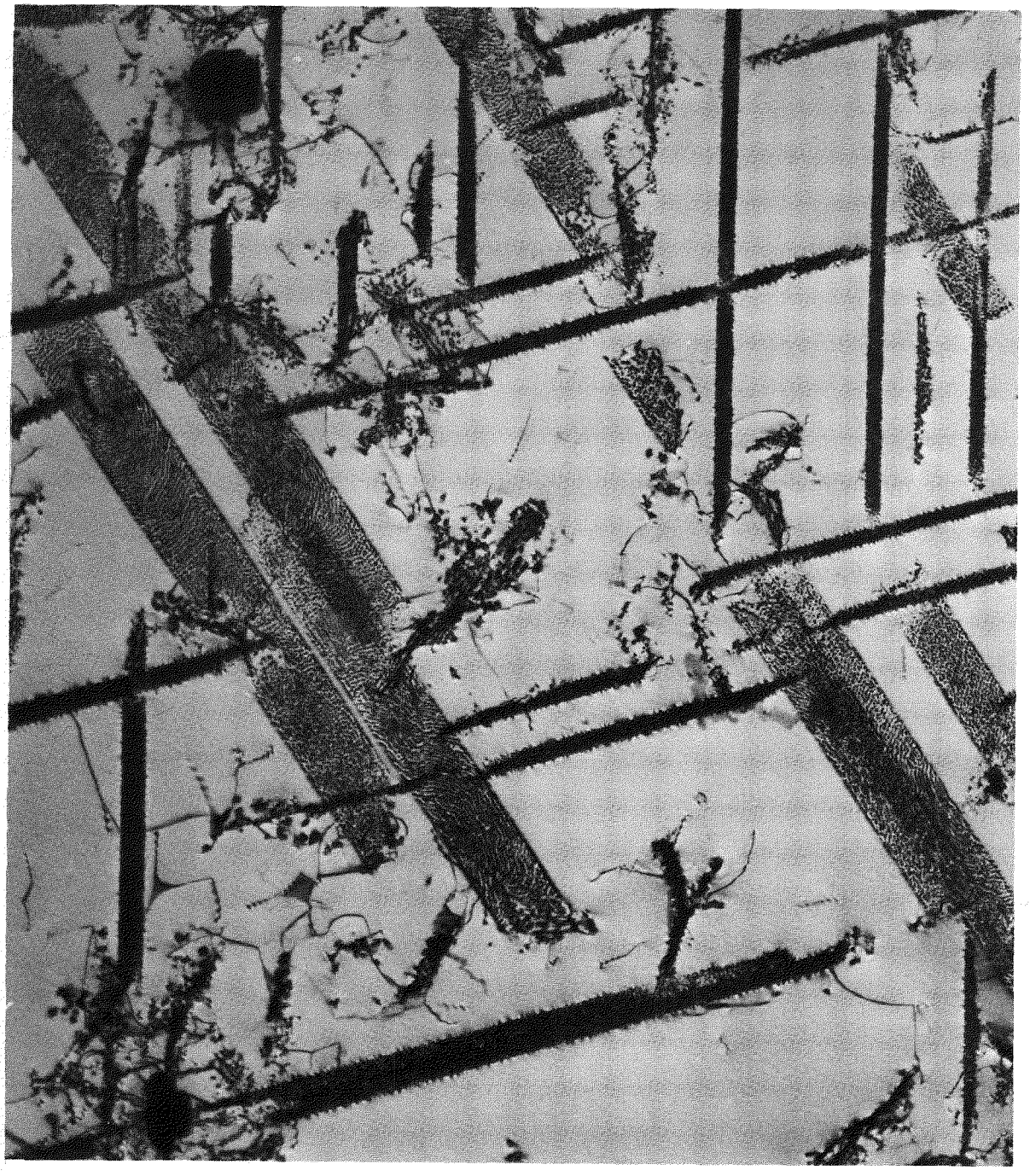

35,000X

FIGURE VII-127 *348 SS, Solution-Treated 1 hr at 1300°C, Direct Aged at 700°C, Cooled to RT, Then Aged 1000 hr at 700°C.*

References:

53. Silcock, J. M. and Tunstall, W. J., "Partial Dislocations Associated with NbC Precipitation in Austenitic Stainless Steels, Phil. Mag., 10 (1964) 361.

54. Shepherd, J. P., "Irradiation-Induced Precipitation in a Niobium-Stabilized Stainless Steel," Metal Sci. J., 3 (1969) 229.

55. Naybour, R. D., "Hardening by Stacking Fault Precipitation in an 18 Cr-12 Ni-Nb Austenitic Steel," J. Iron and Steel Inst., 204 (1966) 1200.

VIII. FUELS PROCESSING AND FABRICATION

A. FUELS TECHNOLOGY

1. Sintering Behavior of Mixed Oxide Pellets

R. L. Gibby, E. T. Weber and W. A. Ross

This program identifies the basic parameters controlling the sintering behavior of physically mixed UO_2 - 25 wt% PuO_2 powder compacts to establish optimum conditions for production sintering of mixed-oxide fuel pellets.

The sintering rates of mixed-oxide pressed pellets will be determined by following their shrinkage as a function of time and temperature using a recording dilatometer.

At present, a high-temperature dilatometer has been constructed and installed in a plutonium glove box. The technical specifications of this system are shown in Table VIII-1.

TABLE VIII-1
SPECIFICATIONS OF HIGH TEMPERATURE DILATOMETER

Furnace	Tungsten elements; molybdenum heat shields; water-cooled cold wall type; Max Temp 2500°C @ 7 kW; programmable heating cycle.
Thermocouple	Tungsten 5% vs W 26% Re
Vacuum	Oil diffusion pump high vacuum system (5×10^{-6} torr)
Atmosphere	N_2, He, Ar, Ar 8% H_2
Transducer	LVDT 3 kHz input signal (sensitivity >limits of calibration)
Push Rod	High purity tungsten
Calibration Standards	Low temperature - fuzed silica High temperature - high purity tungsten

A schematic of the apparatus is shown in Figure VIII-1. The dilatometer itself consists of a linear variable differential transformer (LVDT) to measure the changes in pellet length during sintering. The sample holder and push rod are constructed of tungsten. The furnace consists of a tungsten mesh heater surrounded by molybdenum heat shield and a water cooled copper jacket. The entire system is enclosed in a stainless steel vacuum chamber that can be pumped down to approximately 5×10^{-6} torr, or can be filled to atmospheric pressure with inert or reducing gases.

The system is presently being checked for leaks; after this is complete, the tungsten furnace will be tested under vacuum to determine the maximum temperature attainable with the available power supply. Measurements of shrinkage rates for mixed-oxide powder compacts will be initiated during the next quarter.

2. Fabrication of Mixed Oxide for EBR-II Subassemblies

W. E. Warden and J. P. Keenan

Fabrication and characterization of fuel for PNL-10 and PNL-11 pins was completed. The fuel consists of 65% enriched U^{235} mixed-oxide in the EBR-II test composition of 75% UO_2-25% PuO_2. Sixteen kilograms of fuel were sintered in four lots (FE-79, FE-92, FE-93, and FE-94) for the 156 required pins. The final fuel pellet data for PNL-10 and PNL-11 are shown in Table VIII-2 and VIII-3, respectively.

3. FTR Fuel Specifications

C. A. Strand and R. E. Bardsley

Fuel pin specifications and material specifications, written as RDT Standards for use in the RFP package for the Fuel Vendor Qualification program, were prepared. These drafts and associated drawings, prepared by WADCO and ARD, reflect agreements on use of the 0.0075-in. maximum, cold pellet to clad diametral gap and a pellet tolerance of ± 0.0015 in. The RDT Standards for the fuel pin, components, and materials are listed in Table VIII-4.

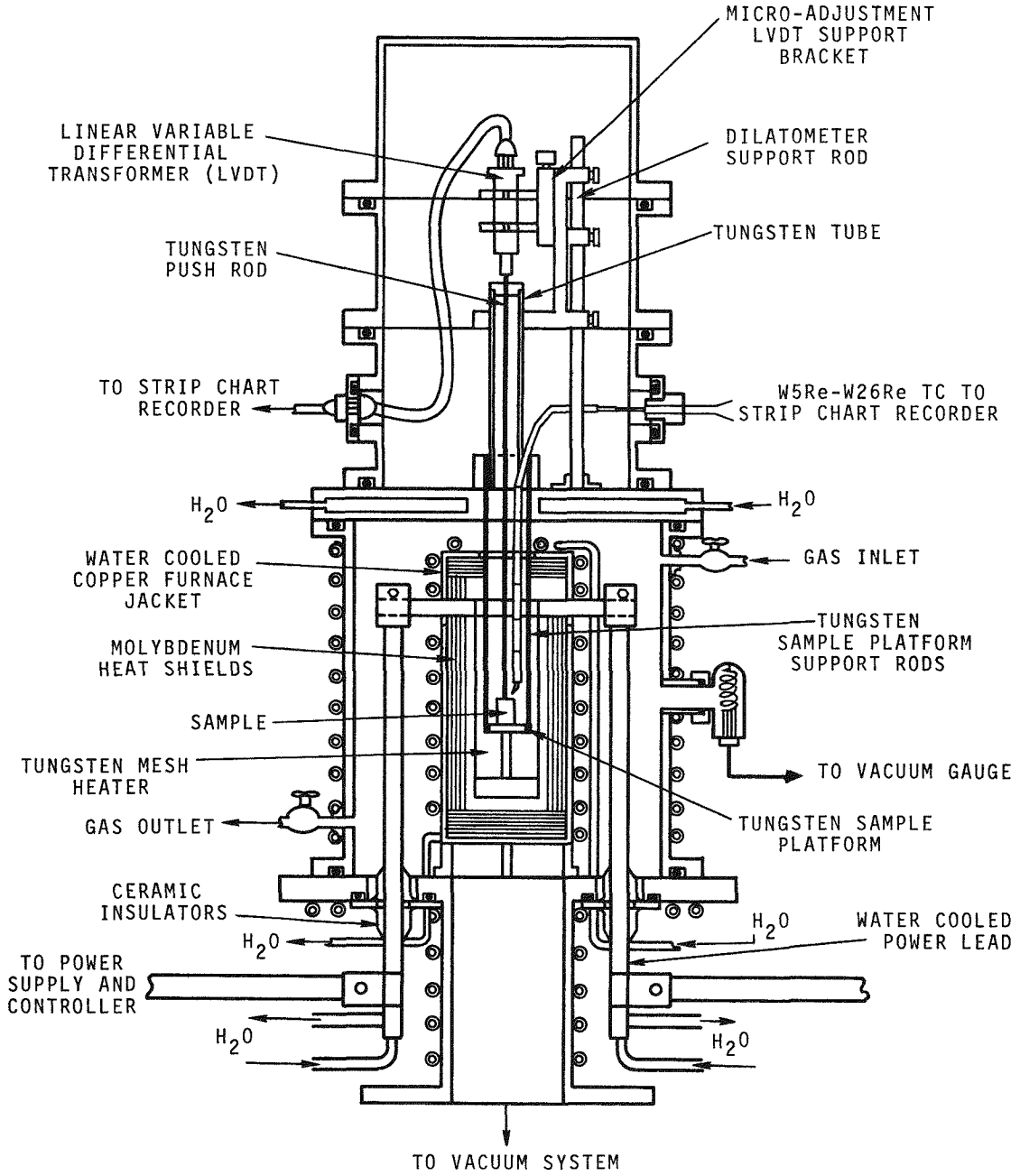

FIGURE VIII-1 *High Temperature Dilatometer.*

TABLE VIII-2

SINTERED PELLET DATA - SUBASSEMBLY PNL 10

Batch No.	Average Sintered Density (e)	Standard Deviation Sintered Pellets (f)	wt% Pu (a)	wt% Pu (b)	wt% U (c)	Off-gas (d) (cc/g)	H_2O (ppm) @200	H_2O (ppm) @800	Cl (ppm)	F (ppm)	C (ppm)	O/M	U^{235} (wt%)
FE-79.0	10.06 g/cc	0.06 g/cc	22.2	25.1	65.8	0.03	18	20	<10	<5	185	1.975	65.0
	91.79% TD	0.55% TD	22.2	25.1	66.2	0.03	10	15	<10	<5	140	1.978	65.0
			22.2	25.1	----	----	13	13	<10	5	130	1.974	65.0
			22.3	25.2	66.1	0.03	16	18	<10		100	1.979	
			22.1	25.0		0.02	16	17	<10			1.975	
						0.01						1.973	
												1.977	
												1.980	
												1.978	
			22.2	25.1	66.0	0.024	14.6	16.6	<10	<5	139	1.9765	65.0
FE-92.0	9.81 g/cc	0.05 g/cc	22.2	25.1	66.1	0.02	23	26	<10	<5	130	1.969	65.1
	89.67% TD	0.46% TD	22.1	25.0	66.1	0.02	25	25	<10	<5	100	1.967	65.0
			22.0	24.9	66.0	0.02	24	26	<10	<5	120	1.965	65.0
			22.0	24.9		0.01	22	31	<10		90	1.963	
			22.1	25.0		0.02	30	34	<10		100	1.967	
									<10			1.963	
												1.963	
												1.970	
												1.964	
			22.1	25.0	66.1	0.018	24.8	28.4	<10	<5	108	1.9654	65.0

(a)Basis of wt% Pu is $Pu/(U, Pu)O_{2-x}$
(b)Basis of wt% Pu is Pu/(Pu+U)
(c)Basis of wt% U is $U/(U, Pu)O_{2-x}$

(d)Total off-gas released to maximum of 1600°C
(e)Theoretical density is based on actual O/M and isotopic content.
(f)The standard deviation was calculated using data from 60 pellets for lot FE-79.0 and 80 pellets for lot FE-92.0.

TABLE VIII-3

SINTERED PELLET DATA SUBASSEMBLY HEDL-P-11

Batch No.	Average Sintered Density (e)	Standard Deviation Sintered Pellets (f)	wt% Pu (a)	wt% Pu (b)	wt% U (c)	Off-gas (d) (cc/g)	H_2O (ppm) @200	H_2O (ppm) @800	Cl (ppm)	F (ppm)	O/M	U^{235} (wt%)
FE-93	9.96 g/cc	0.03 g/cc	22.0	25.0	66.0	0.02	8	15	<10	8	1.968	65.0
	90.87% TD	0.27% TD	22.2	25.2	65.9	0.02	7	13	<10	7	1.979	65.1
			22.0	25.0	66.1	0.02	9	15	<10	7	1.980	65.0
			22.2	25.2		0.03	9	14			1.983	
			22.2	25.2		0.02	7	18			1.981	
											1.979	
											1.973	
											1.965	
											1.975	
			22.1	25.1	66.0	0.02	8	15	<10	7.3	1.976	65.03
FE-94	10.01	0.05 g/cc	22.2	25.1	66.4	0.02	<5	<5	<10	17	1.973	64.7
	91.67% TD	0.46% TD	22.2	25.1	66.3	0.02	10	18	<10	15	1.967	64.6
			22.2	25.1	66.2	0.02	<5	8	<10	12	1.980	64.3
			22.2	25.1		0.02	<5	6			1.981	
			22.1	25.0		0.02	<5	8			1.965	
											1.977	
											1.973	
											1.970	
											1.971	
			22.2	25.1	66.3	0.02	<5	10	<10	14.6	1.973	64.5

(a) Basis of wt% Pu is $Pu/(U,Pu)O_{2-x}$
(b) Basis of wt% Pu is Pu/(Pu+U)
(c) Basis of wt% U is $U/(U,Pu)O_{2-x}$

(d) Total off-gas released to maximum of 1600°C
(e) Theoretical density is based on actual O/M and isotopic content.
(f) The standard deviation was calculated using data from 30 pellets for each batch.

TABLE VIII-4
RDT STANDARDS FOR FFTF DRIVER FUEL

RDT Std No.	Title
E 13-1	FFTF Ceramic Grade Plutonium Dioxide
E 13-2	FFTF Ceramic Grade Uranium Dioxide
E 13-3	FFTF Uranyl Nitrate Solution
E 13-4	FFTF Plutonium Nitrate Solution
E 13-5	FFTF Driver Fuel Pin
E 13-6	FFTF Driver Fuel Pin Mixed Oxide Fuel Pellet
E 13-7	FFTF Driver Fuel Pin Insulator Pellet
E 13-8	FFTF Driver Fuel Pin Seamless Cladding Tube
E 13-9	FFTF Driver Fuel Pin End Caps
E 13-10	FFTF Driver Fuel Pin Reflector
E 13-11	FFTF Driver Fuel Pin Plenum Spacer
E 13-12	FFTF Driver Fuel Pin Plenum Spring
E 13-13	FFTF Driver Fuel Pin Wire Wrap

4. Analytical Methods for Fuels

C. A. Strand and R. E. Bardsley

Drafts of the following analytical methods were prepared for incorporation into FFTF Analytical Chemistry Methods in Support of Driver Fuel Fabrication, WHAN-IR-5.

1) Americium 241 by Anion Exchange and Alpha Analysis
2) Oxygen-to-Metal Ratio by Thermogravimetry (Revision)
3) Determination of Residual Chloride on Fuel Pins and Components.

5. Prequalification of LMFBR Fuel Suppliers

J. F. Williams and D. A. Stranik

During the previous quarter, the three fuel suppliers participating in this program completed delivery of a small quantity (65 to 125) of FFTF driver fuel pins and additional pellets fabricated to a specification approximating the final RDT Standard. Evaluation of these products is complete and all three contractors were briefed on the results.

All three contractors demonstrated the ability to produce PuO_2-UO_2 fuel pins and improved their quality assurance capabilities in the process.

The planning, documentation, and use of procedures, methods and techniques accomplished as part of the Prequalification Program is a major step toward achieving an overall capability for manufacturing Fast Flux Test Facility (FFTF) LMFBR fuel pins.

6. Material Control and Data Acquisition System

J. C. Watkins, A. W. DeMerschman and R. A. Harvey

The previously installed Systems Engineering Laboratory (SEL) 810-B digital computer was operated successfully for real-time data acquisition and concurrent batch processing using the Foreground-Background Operating System.

A criticality inventory system has been implemented on the computer. The system operates in real time, with five remote terminals located in the fabrication area. Hard copy reports of the results of the operation of the system are available in the computer room.

A fuel fabrication process data system is presently being implemented on the computer. The system is to provide storage and retrieval of fuel fabrication process data in direct support of the fabrication operation.

Four programs have been developed and are currently running on the SEL 810-B. Two additional programs are in development.

The Ground and Sintered Pellet Density Analysis Program, code name "PELLET", will perform the following function. Given two fuel pellet end diameters, middle diameter, land width, length and weight, the program will

calculate and translate average diameter, length between dishes, average dish depth, taper, hour glassing and density. For each column of measurements, the program provides standard deviation, mean, maximum and minimum upper and lower confidence bounds, and upper and lower tolerance limits.

The Green Pellet Density Analysis Program, code "GRENP 2", is basically the same as the "PELLET" program. Given one end diameter, middle diameter, land width, length and weight, the program will give average dish depth, length between dishes and density with related statistics for each column.

The Green Pellet Single Diameter Analysis Program, code name "GRENP 1", has the same input as "GRENP 2", except only the middle diameter is used. The same output is generated.

The fourth program on file is a demonstration program code name "WOW 38-D".

In final stages of development is the Spectrometer Probe Program, code name "SPECTRO". The conversion code software for "SPECTRO" is currently being tested.

A Generalized Regression Program will begin this quarter.

7. WADCO Model 60 Shipping Container

F. M. Smith and A. W. DeMerschman

There are, at present, no approved shipping containers available for shipment of unirradiated FFTF driver fuel pins. A container will be needed for the fuel vendor qualification program in the last quarter of FY '71. The WADCO Model 60 shipping container, capable of transporting 120 fuel pins, has been designed to meet this requirement. A prototype has been built and a report describing the container and the criticality safety analysis has been issued (WHAN-IR-34)(Ref 1) to serve as application for a DOT Special Permit. This report shows that the Model 60 will have a Transport Index of 4.2 units. Twelve containers may be shipped at any one time in the same vehicle.

8. Pellet Fabrication for Prototype Fuel Pins

H. T. Blair, J. E. Sammis, and R. E. Bardsley

In pellet fabrication for prototype fuel pins, control of sintered fuel pellet oxygen-to-metal ratios was a problem. A major contributor to the problem was the polyvinyl alcohol (PVA) used as a pore former and binder to obtain the 91% TD fuel pellets. After the use of PVA was discontinued, oxygen-to-metal ratio control improved, and sintered pellet carbon content has decreased, as shown in Table VIII-5.

TABLE VIII-5
EFFECT OF PVA BINDER ON SINTERED PELLET O/M AND CARBON CONTENT

Batch No.	Carbowax (20m)	PVA (%)	O/M	Carbon Content (ppm)
03A10	2.5	0.75	1.953	75
03A11	2.5	0.75	1.950	70
03A13	2.5	0.75	1.960	100
03A14	2.5	0.75	1.938	77
05A5	2.5	2.50	1.897	100
05A6	2.0	2.50	1.877	85
05A7	2.5	3.00	1.855	180
05A8	2.0	3.00	1.860	125
07A1A2	3	0	1.975	<50
07A3	3	0	1.964	<50
08A1C1	3	0	1.968	<55
08A1C2	3	0	1.963	<50
09C1	3	0	1.968	--

The oxygen-to-metal ratio of sintered fuel pellets is directly related to the furnace load mass and inversely related to the sintering soak temperature and gas flow rate. It is expected that enough data will be obtained during the prototypic fuel pin fabrication to make a regression analysis and develop a formula for these relationships.

9. Production of Dished-End Pellets

J. E. Sammis and R. E. Bardsley

The last Quarterly Progress Report described the development effort to fabricate dished-end fuel pellets of 91% TD on a "once through" basis involving reduced milling efficiency and the addition of PVA (poly-vinyl alcohol) as a "pore-forming" binder. Although initial results were successful, reproducibility of the sintered density from lot to lot was lacking. After this approach to achieving low densities was exhausted, it was decided to explore the double pressing approach, wherein the powder is preslugged to form hard granules which resist compaction during the final pressing operation. An experiment was run to determine the main effects and interactions of preslugging and forming pressure upon green density, and firing shrinkage. A 2 x 2 factorial design was employed, with preslug pressures at 25k and 50k psi and forming pressures at 20k and 30k psi. Experimental results are summarized in Figures VIII-2 and VIII-3. Note that there are only four actual data points, and that additional element lines were interpolated. Because of lot-to-lot differences, these graphs are not intended to be used for predicting sintered density. Rather, they aid in correcting sintered density by indicating how much of a change in preslug pressure or forming pressure is required to achieve the specified density.

References:

1. WADCO Model 60 Fissile Material Shipping Container - Basis for DOT Special Permit. F. M. Smith, WHAN-IR-34 September 1970.

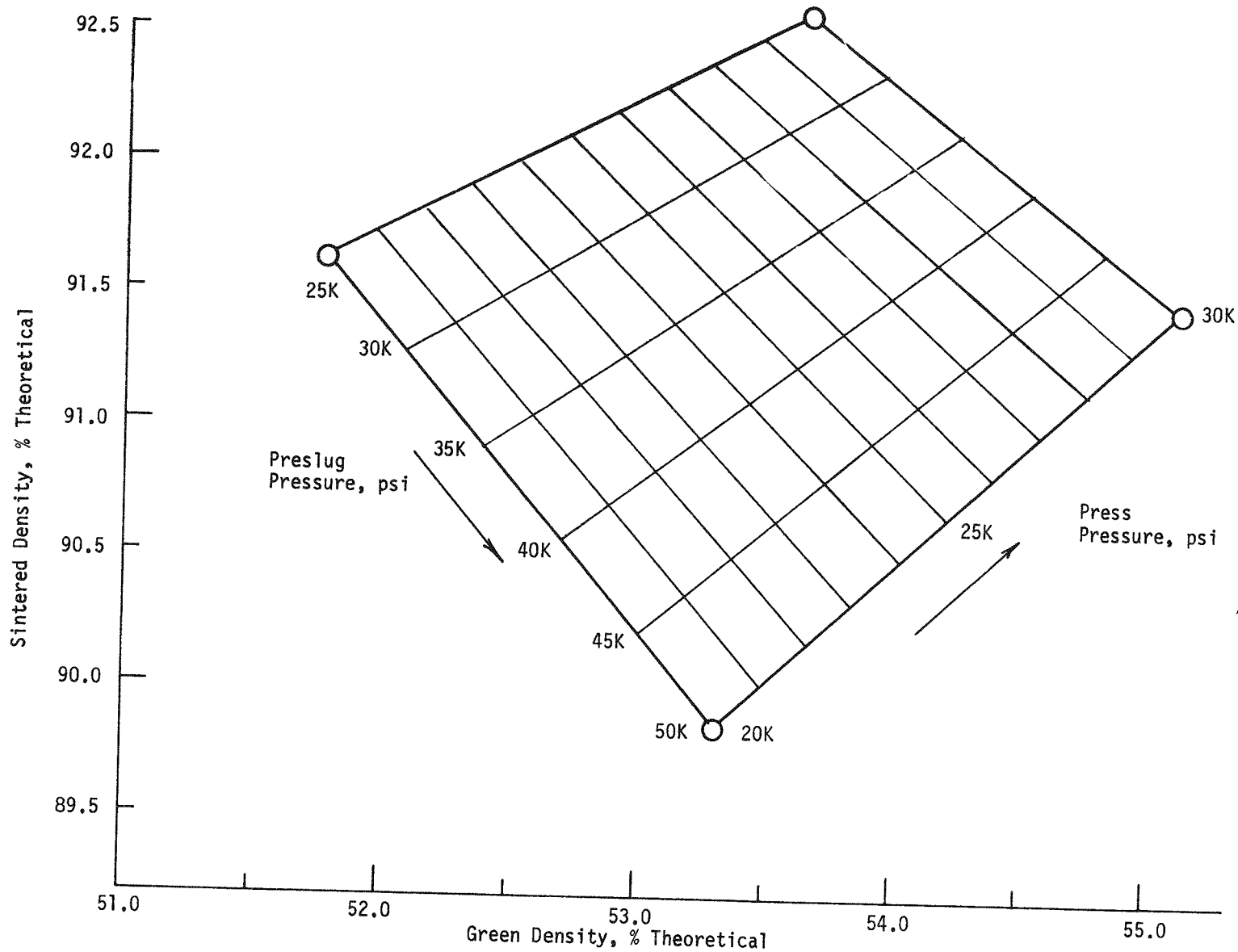

FIGURE VIII-2 *Sintered and Green Density vs Preslug and Press Pressure.*

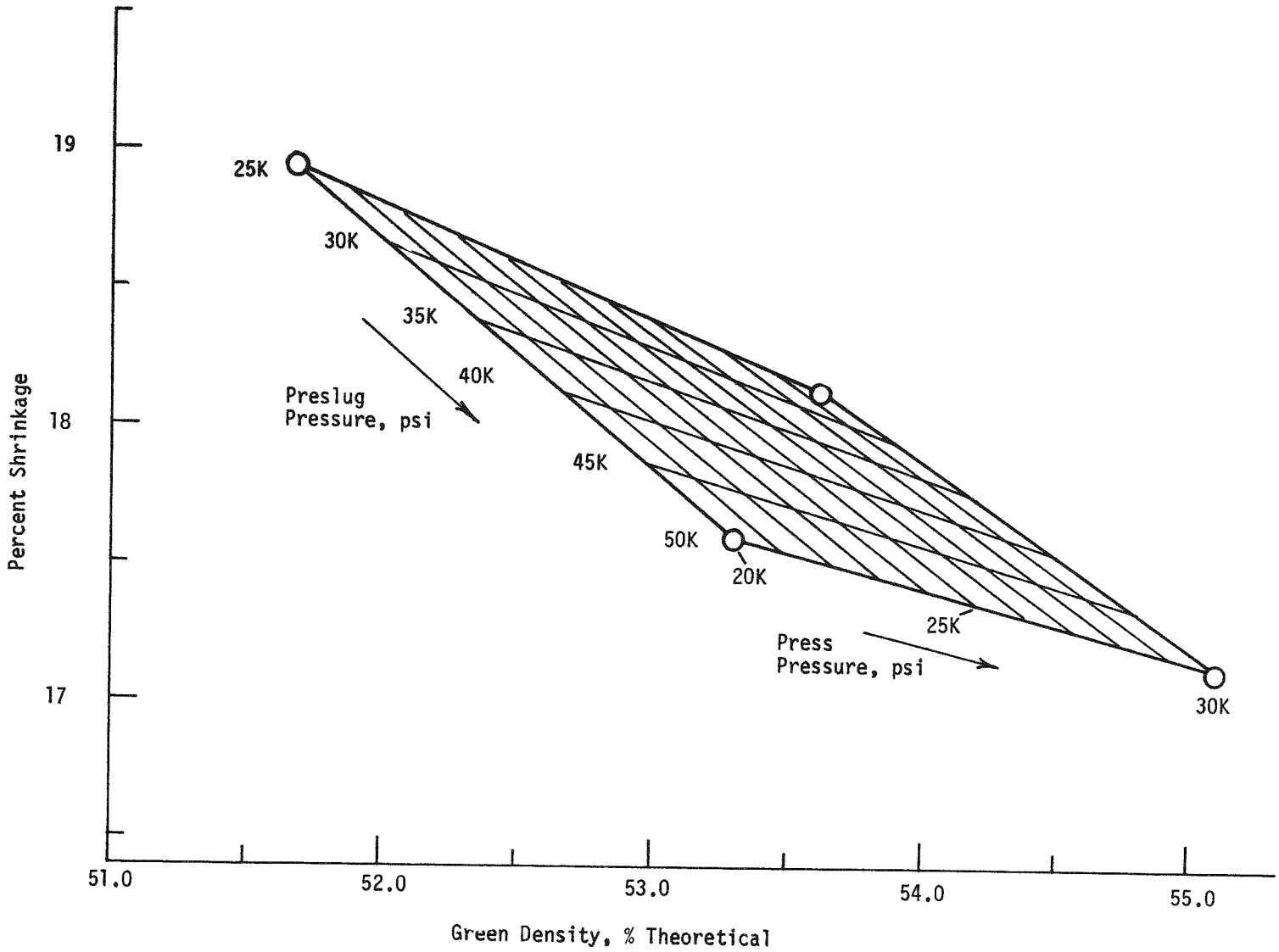

FIGURE VIII-3 *Percent Shrinkage and Green Density vs Preslug and Press Pressure.*

B. CLADDING TECHNOLOGY

1. Non-Destructive Testing

R. R. Studer, D. W. Dragnich, R. J. Lobsinger and J. V. Tverberg

a. Standards

Vidigage standards to establish statistical control of the ultrasonic wall thickness testers have been completed. Figure VIII-4, a reproduction of drawing H-3-32036, shows the as-built standard used for the finished cladding tube. The standard has three different wall thicknesses, which cover the manufacturing specifications, and an eccentricity equal to the maximum allowable. Assemblies 1 and 2 of this standard were cemented into the ends of ultrasonic notch standard illustrated in Figure VIII-5, a reproduction of drawing SK-3-15593. This makes up a complete standard now known as "NDT STANDARD No. 1". A second standard is being fabricated as backup.

The Vidigage sections of the standard were certified in the WADCO Standards lab. A Vidigage standard for CarTech's tube hollows was also built. This standard also contained three different wall thicknesses as well as three degrees of eccentricity. This allows statistical calibration of both wall thickness and eccentricity. The as-built standard is illustrated in Figure VIII-6, a reproduction of drawing SK-3-15602.

b. Ultrasonic Testing of Wall Thickness

The type of uniformity of test results obtainable by ultrasonic testing of wall thickness is illustrated in Figure VIII-7. These results are for CarTech's ultrasonic wall thickness tester using a standard produced by Los Angeles Gage Company. The sample trace shown in Figure VIII-7 represents consecutive runs on that part of the standard with 5%, 10%, and 20% wall eccentricity. Uniformity of response is excellent and the plot of these values is nearly a straight line.

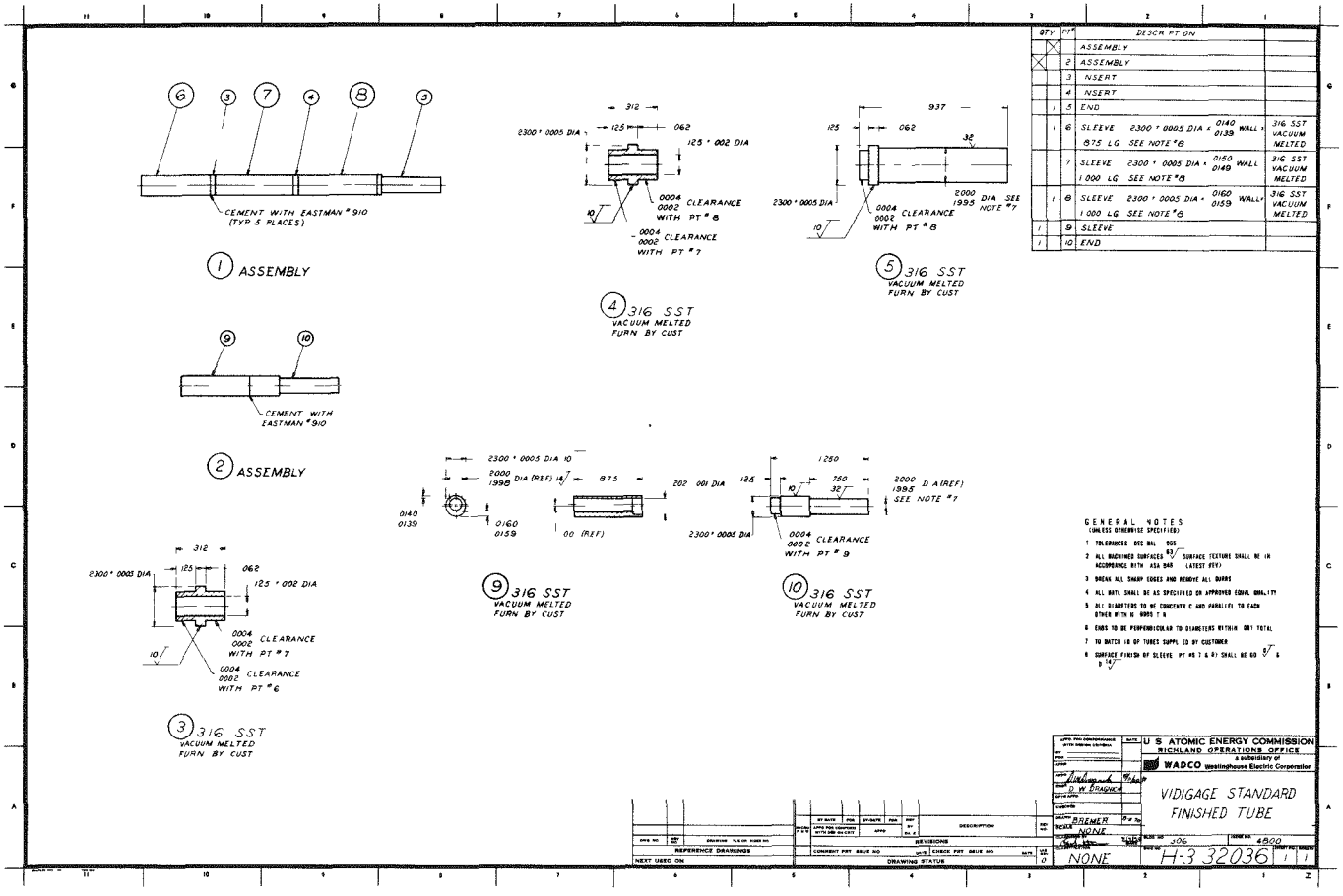

FIGURE VIII-4 *Finished Tube Eccentricity and Wall Thickness Standard for Calibration of the Ultrasonic Wall Thickness Tester.*

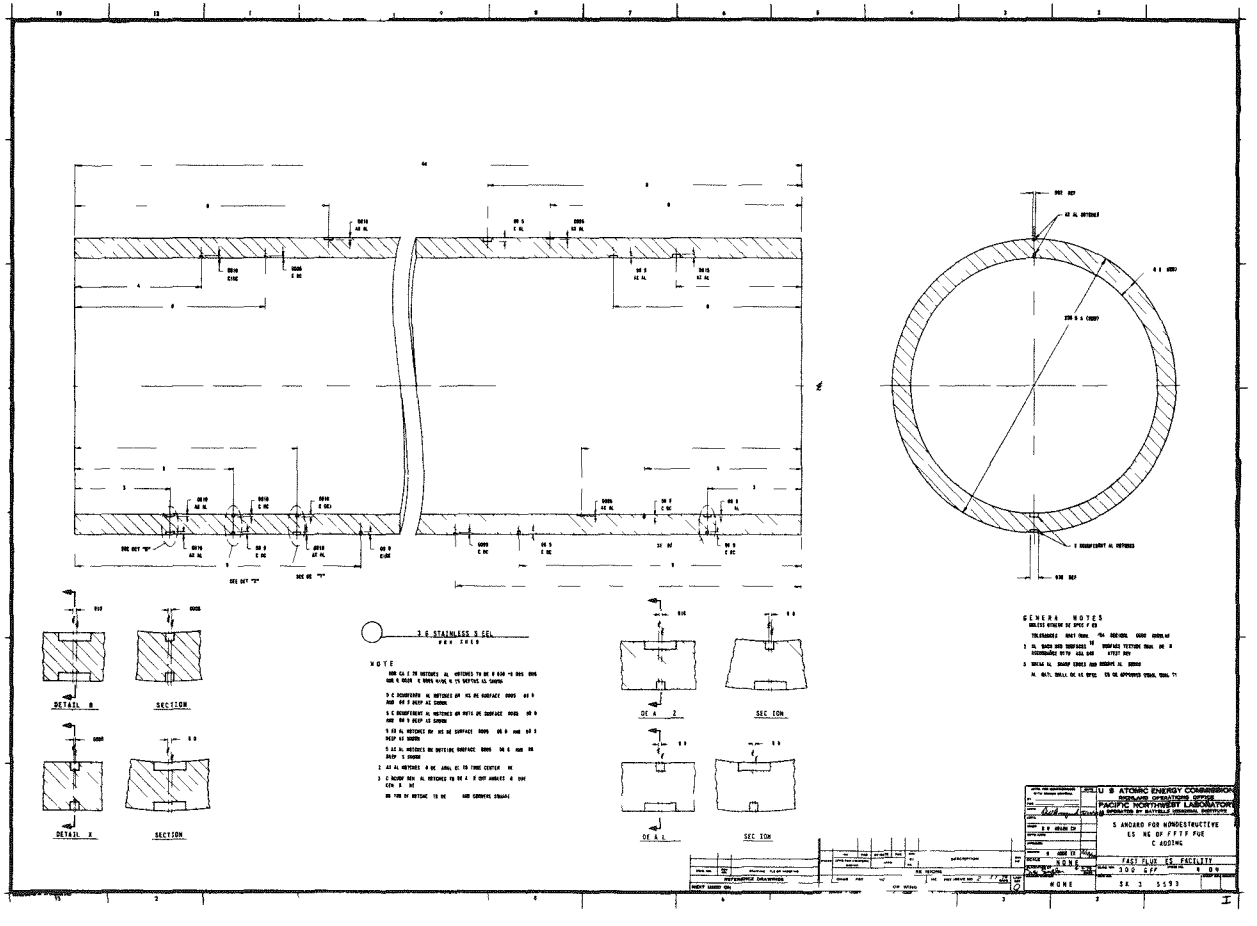

FIGURE VIII-5 *Multinotch Ultrasonic Defect Standard. This standard allows statistical calibration of the tester and shows the effect of overlapping notches.*

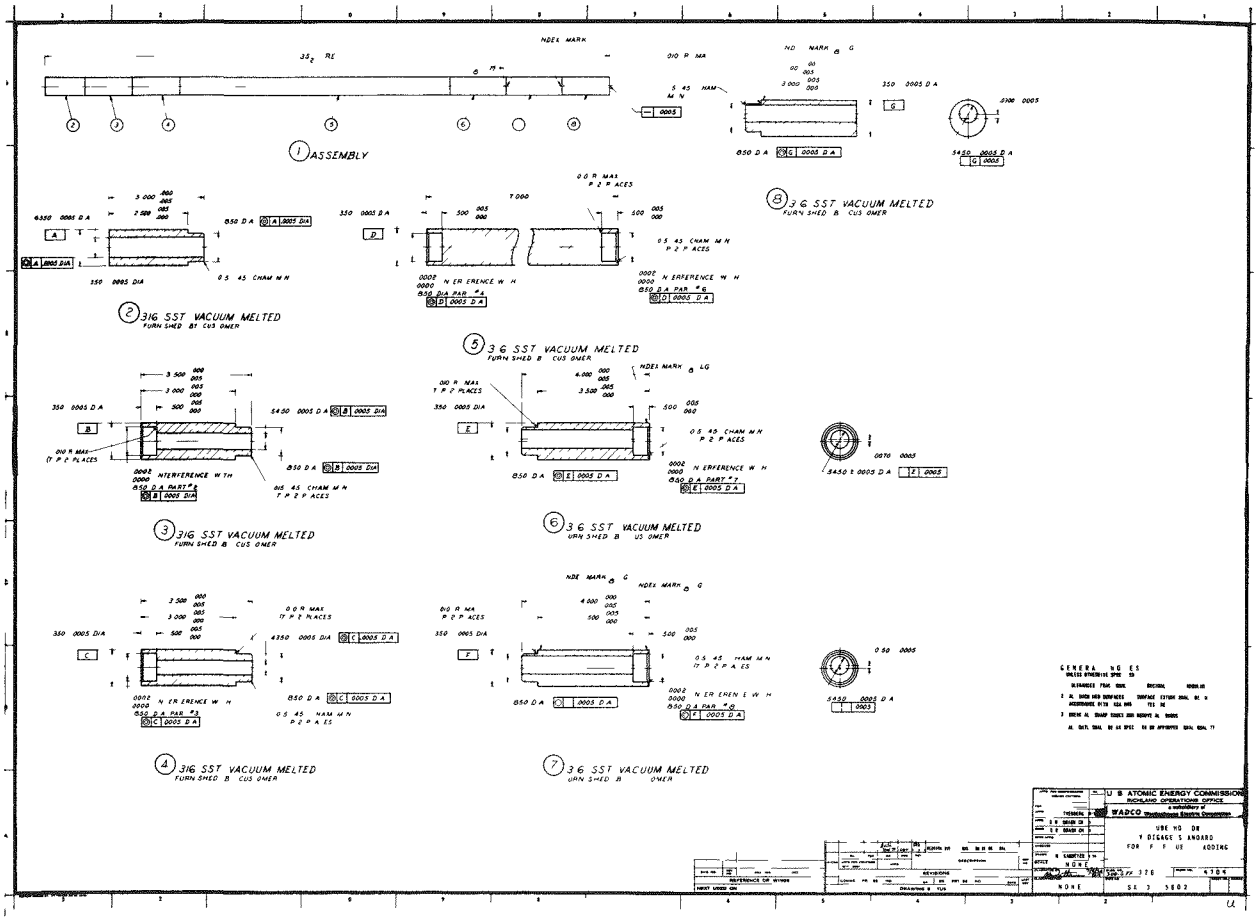

FIGURE VIII-6 *Specific Design for a Tube Hollow Wall Thickness and Eccentricity Standard to Allow Calibration of the Carpenter Technology Corporation Testers. This calibration allows compliance with the product specification for FFTF fuel cladding.*

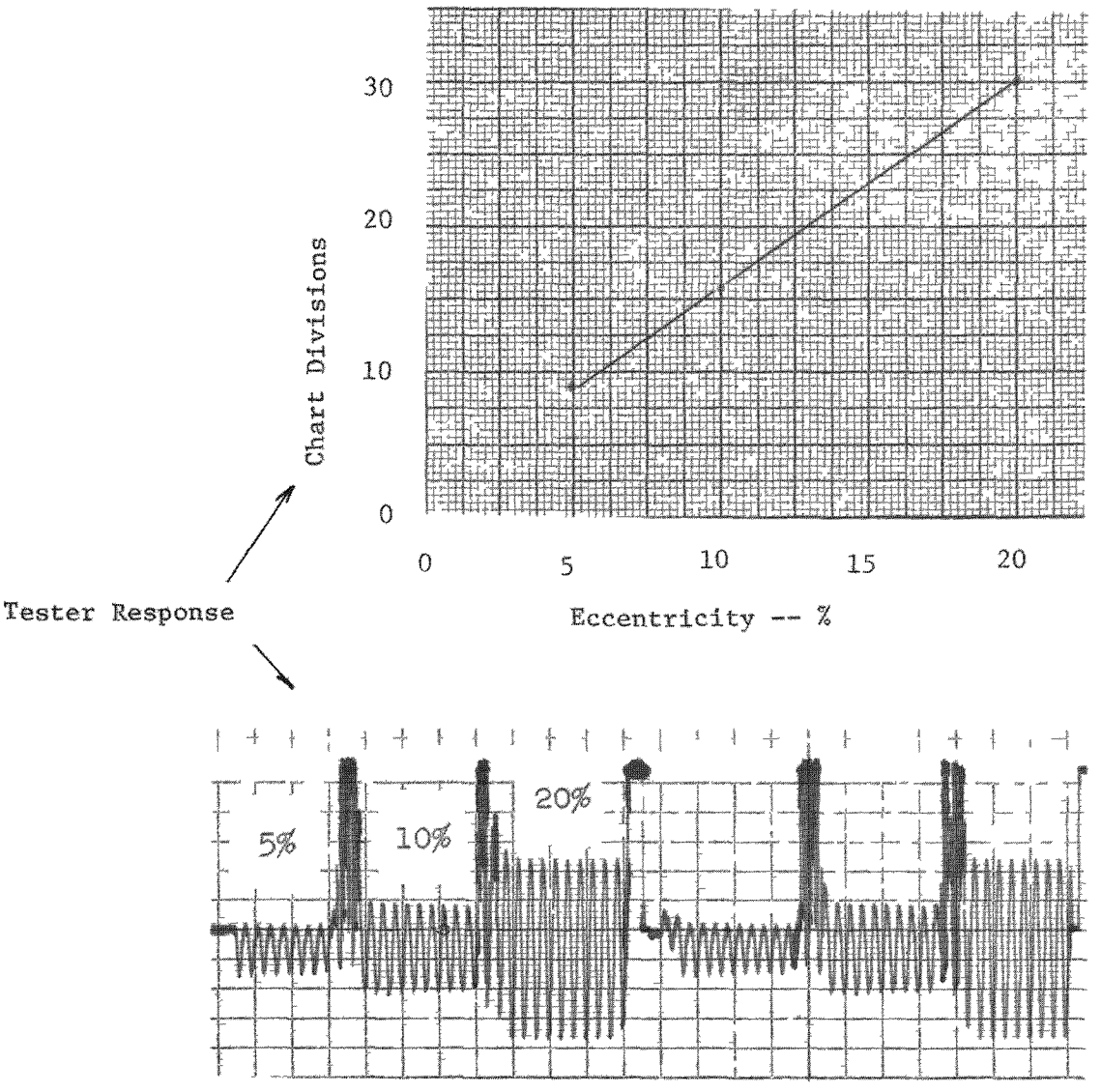

FIGURE VIII-7 *Calibration of Ultrasonic Wall Thickness Tester.*

2. Cladding Vendor Qualification

J. C. Tverberg, R. C. Aungst

A detailed program for qualification of the Fuel Cladding Vendors was established. This is being published as WHAN-IR-40 "Criteria for Qualification of FFTF Fuel Cladding Vendors". Basically, this document allows for a four-step qualification procedure: a pre-judging stage; a process evaluation stage; a plant audit; and evaluation of typical FFTF tubing. A similar procedure was established for the steel producers.

Each of the vendors participating in the Vendor Development Program will be evaluated according to this procedure.

3. Cladding Procurement

J. C. Tverberg, R. J. Lobsinger, and R. C. Aungst

FFTF Control Rod Cladding.-Two different sizes of control rod cladding were ordered and received: 0.435 in. x 0.043 wall, and 0.230 in. x 0.023 wall. On-site receiving inspection is being performed on the tubing prior to fabrication into irradiation test assemblies.

30% Cold-Worked Cladding.-Procurement was initiated for 1000 feet of 316 SS cladding 0.230 in. OD by 0.200 in. ID with 30% cold work.

Electroslag Melting of Stainless Steel.-Vacuum-arc melted bar furnished the Bureau of Mines Station at Albany, Oregon, was electroslag remelted. Examination for nonmetallic inclusion content and distribution is under way at the USBM, but detailed results are not yet available.

FFTF Fuel Cladding - 30,000 ft. Order.-Two hundred ultrasonic reject tubes were purchased from the vendor for use in establishing natural defects for nondestructive testing, the effect of natural defects on mechanical property testing and for determining effects of natural defects on irradiation testing. All material has been received on this order.

4. Measuring Halogen Contamination

W. T. Wood and J. P. Keenan

A method was developed to measure surface chlorides on cladding and completed fuel pins. Random measurements were obtained on 14 cladding and 14 fuel pin samples. The results are:

	Surface Chlorides (a) (mg/in^2)	
	Max Value	Avg Value
Cladding(b)	0.00018	0.00008
Completed Fuel Pins(c)	0.00021	0.00010

(a) Acceptable limit is 0.0005 mg/in^2

(b) Cladding from PNL-10 had been stored approximately three weeks.

(c) The fuel pins (all from PNL-10) were ready for shipment when unpacked and tested.

The method for measuring surface chlorides involves washing the cladding or the fuel pin with a hot detergent solution and then evaporating the solution to a 10-ml volume. The chloride concentration is measured with a chloride ion electrode and a high input impedance millivolt meter. The value measured from the concentrated solution is then compared to a calibration curve obtained from solutions with known chloride concentrations. Before each test a calibration curve is made.

The procedure is too time-consuming to test all the cladding and fuel pins which make up a subassembly. Therefore, the test will be used on a statistical basis. The data obtained from PNL-10, ANL-14, and PNL-11 should be adequate to develop a reasonable sampling plan for future fabrication control.

A similar method will be developed to measure surface fluorides once the chloride procedure has been finalized.

5. Acceptance Testing and Clad Characterization (12164)

M. M. Paxton and J. J. Holmes

The clad characterization program is being conducted to insure that high quality stainless steel cladding is obtained and utilized throughout

the FFTF fuels development and associated irradiation testing programs. Under this program, selected mechanical properties are determined and analyzed to evaluate fabrication variables and assist in vendor qualifications.

The current status of characterization for tubing Lots E, F, G, H, N-1, N-2, N-3, K, L and M is given in Tables VIII-6 through VIII-15. Tensile tests at a strain rate of 0.01 min^{-1} have been completed on Lots N-3, K, L and M. In the mill annealed condition, K lot tubing is weaker than Lots G and H. The relative weakness of K lot can be attributed to lower nitrogen, vacuum melting and grain size effects.

Biaxial stress rupture tests are being conducted on artifically defected 20% cold worked Lot N tubing. All artifical defects were made by EDM machining. A limited number of defected specimens are now being irradiated in EBR-II to a target fluence of $3 \times 10^{22} n/cm^2$ (E >0.1 MeV).

Initial results at 1200 and 1400°F indicate that,when a defect 3.3% of wall thickness causes premature failure, this reduction can be predicted from the geometry of the defect. If stress calculations (Ref 2) are made based on the tube dimensions at the base of the defect:

$$\sigma = \frac{P\,(a^2+b^2)}{(a^2-b^2)} \qquad (1)$$

where P = Internal gas pressure
a = Inside radius
b = Outside radius

and this value of stress is used to calculate the reduction in rupture life in accordance with (Ref 3);

$$t_r = A \exp \frac{Q_{creep}}{RT}\, \sigma^{-n} \qquad (2)$$

where t_r = time to rupture
Q_c = Activation energy for creep
σ = stress
A and n = empirical constants

TABLE VIII-6
MECHANICAL PROPERTIES--PNL TUBE LOT E, MILL ANNEALED 304 SS
0.250-in. OD X 0.218-in. ID

	Burst Test			Tensile Test					Stress Rupture			
Test Temp(°F)	Press. (psi)	Max Hoop Stress (psi)	ΔD/D	ε min^{-1}	0.2% YS	UTS	U.E.(%)	T.E.(%)	Max Hoop Stress (psi)	Rupture Time(hr)	ΔD/D%	$\Delta D/D^{\varepsilon}\%$ hr^{-1}
RT	10,700	78,540	-	0.01	42,090	97,940	73.9	86.3				
RT	10,700	78,540	-	1.0	46,550	93,110	53.6	63.9				
RT	10,800	79,270	-	10.0	51,300	93,110	40.6	61.7				
800				0.01	21,580	74,120	40.5	43.7				
800				1.0	23,840	68,360	36.7	42.1				
800				10.0	24,180	66,670	36.3	40.7				
1000	7,390	52,240	-	0.01	18,950	68,220	40.1	43.9	50,000	38.0	12.6	0.3315
1000									49,000	40.8	10.8	0.2647
1000	7,430	54,540	-	1.0	20,900	62,710	34.5	40.0	47,000	74.9	10.1	0.1348
1000	7,410	54,390	-	10.0	22,370	62,260	35.2	41.1	46,000	177.3	7.8	0.0439
1000									42,000	409.0	7.2	0.0176
1000									38,200	1720.1	6.3	0.0037
1200	6,260	45,950	-	0.01	16,780	48,550	26.7	33.9	35,300	9.8	9.3	0.9489
1200	6,230	45,730	-	1.0	20,190	54,350	30.1	35.3	29,000	44.5	10.9	0.2449
1200	6,280	46,095	-	10.0	21,530	54,750	31.6	36.8	28,050	80.0	----	------
1200									27,150	125.0	5.7	0.0456
1200									24,300	268.2	4.1	0.0152
1200									22,100	821.0	----	------
1200									22,100	853.0	----	------
1200									19,150	4173.0	7.5	0.0017
1400	5,000	36,700	-	0.01	15,710	28,980	15.6	40.1				
1400	5,020	36,850	-	1.0	17,740	39,660	26.3	45.9				
1400	5,060	37,140	-	10.0	16,950	43,670	28.2	38.9				
1600	3,510	25,760	-	0.01	10,310	12,970	7.5	36.6				
1600	3,530	25,910	-	1.0	15,820	26,660	19.8	59.0				
1600	3,550	26,060	-	10.0	14,750	31,470	22.2	60.7				
1800	2,340	17,175	-									
1800	2,460	18,060	-									
1800	2,600	19,080	-									

TABLE VIII-7
MECHANICAL PROPERTIES--PNL TUBE LOT F, MILL-ANNEALED 304 SS
0.250-in. OD X 0.218-in. ID

	Burst Test			Tensile Test					Stress Rupture			
Test Temp(°F)	Press (psi)	Max Hoop Stress (psi)	ΔD/D	ε min^{-1}	0.2% YS	UTS	U.E.(%)	T.E.(%)	Max Hoop Stress (psi)	Rupture Time(hr)	ΔD/D%	ε ΔD/D % hr^{-1}
RT	9,950	73,030	-	0.01	46,810	101,440	68.6	83.6				
RT	9,950	73,030	-	1.0	50,510	93,820	50.6	62.4				
RT	9,900	72,670	-	10.0	54,010	94,800	43.5	52.4				
800				0.01	23,480	67,600	33.8	38.0				
800				1.0	30,760	66,070	32.0	36.3				
800				10.0	25,420	64,740	34.2	39.0				
1000									49,000	16.8	17.5	1.0416
1000	7,020	51,530	-	0.01	23,700	64,310	34.3	40.8	48,000	26.4	15.5	0.5871
1000	7,070	51,890	-	1.0	21,020	57,910	30.0	35.2	47,000	31.0	14.7	0.4741
1000	7,075	51,930	-	10.0	24,580	58,650	32.3	38.7	46,000	50.3	12.8	0.2544
1000									44,000	119.3	10.6	0.0888
1000									42,000	231.3	9.	0.0389
1000									39,000	1105.1	7.1	0.0069
1000									37,500	1683.5	6.2	0.0037
1000									36,200	2526.5	7.4	0.0029
1200	5,790	42,500	-	0.01	20,110	44,210	24.5	47.5	27,800	17.8	11.3	0.6348
1200	5,820	42,720	-	1.0	19,960	51,190	26.9	31.4	26,900	41.8	----	------
1200	5,830	42,790	-	10.0	20,450	50,396	28.9	34.6	24,300	112.5	----	------
1200									21,650	281.9	7.7	0.0273
1200									18,950	1388.6	6.1	0.0043
1200									16,800	4729.0	9.2	0.0019
1200									15,250	6690.7	7.3	0.0010
1400	4,460	32,740	-	0.01	13,930	22,970	16.5	59.6				
1400	4,450	32,660	-	1.0	17,290	36,190	23.4	51.2				
1400	4,400	32,300	-	0.0	19,710	42,200	26.4	39.8				
1600	3,170	23,270	-	0.01	8,420	10,540	14.8	43.3				
1600	3,200	23,490	-	1.0	14,960	22,090	18.8	65.8				
1600	3,090	22,680	-	0.0	14,520	29,040	22.2	66.3				
1800	2,040	14,970	-									
1800	2,000	14,680	-									
1800	2,100	15,410	-									

TABLE VIII-8
MECHANICAL PROPERTIES--PNL LOT G, MILL-ANNEALED 316 SS
0.250-in. OD X 0.218-in. ID

	Burst Test			Tensile Test					Stress Rupture			
Test Temp(°F)	Press (psi)	Max Hoop Stress (psi)	ΔD/D	ε min^{-1}	0.2% YS	UTS	U.E.(%)	T.E.(%)	Max Hoop Stress (psi)	Rupture Time(hr)	ΔD/D%	ε ΔD/D % hr^{-1}
RT	10,950	80,370	-	0.01	42,230	92,740	65.7	79.8				
RT	11,100	81,470	-	1.0	46,470	93,110	42.4	59.6				
RT	10,700	78,540	-	10.0	51,530	96,000	38.6	56.9				
800				0.01	27,350	80,280	65.7	79.8				
800				1.0	27,460	71,130	33.6	37.1				
800				10.0	27,230	70,740	34.2	37.4				
1000	8,110	59,530	-	0.01	24,040	75,200	34.0	38.3	58,000	217.4	16.0	0.0735
1000	8,300	60,920	-	1.0	25,310	66,890	30.6	33.3	56,000	504.0	11.9	0.0236
1000	8,150	59,820	-	10.0	24,750	66,670	32.6	36.8	55,000	712.5	10.6	0.0148
1000									53,500	626.1	10.2	0.0163
1000									52,000	901.9	9.6	0.0106
1200	6,960	51,090	-	0.01	21,100	53,470	19.5	44.4	37,800	8.3	15.7	1.8915
1200	7,220	52,990	-	1.0	21,240	59,100	27.6	33.0	34,700	20.9	16.1	0.7703
1200	7,210	52,920	-	10.0	22,150	60,680	28.3	32.9	32,300	42.4	13.7	0.3231
1200									30,170	84.2	17.7	0.2102
1200									30,310	94.9	14.1	0.1485
1200									28,190	172.1	11.7	0.0679
1200									26,940	327.8	11.7	0.0356
1200									23,860	818.4	9.7	0.0118
1200									21,360	1926.1	14.0	0.0072
1200									20,000	2606.9	18.8	0.0034
1200									19,890	2913.0	10.3	0.0035
1200									19,000	4256.6	8.8	0.0021
1400	5,610	41,180	-	0.01	16,980	28,670	12.0	59.0				
1400	5,620	41,250	-	1.0	20,230	43,110	22.9	48.0				
1400	5,640	41,400	-	10.0	19,660	49,490	26.6	39.3				
1600	4,050	29,730	-	0.01	11,440	14,040	9.2	46.7				
1600	4,160	30,530	-	1.0	15,650	27,520	17.8	65.8				
1600	4,060	29,800	-	10.0	18,250	35,530	19.6	60.7				
1800	2,780	20,405	-									
1800	2,740	20,110	-									
1800	2,980	21,870	-									

TABLE VIII-9
SELECTED MECHANICAL PROPERTIES--PNL TUBE LOT H, MILL-ANNEALED 316 SS
0.250-in. OD X 0.218-in. ID

Test Temp(°F)	Burst Test Press.	Burst Test Max Hoop Stress	Burst Test ΔD/D	Tensile Test ε min^{-1}	Tensile Test .2% YS	Tensile Test UTS	Tensile Test U.E.%	Tensile Test T.E.%	Stress Rupture Max Hoop Stress	Stress Rupture Rupture Time (hr)	Stress Rupture ΔD/D%	Stress Rupture $\Delta D/D^{\varepsilon}$% hr^{-1}
R T	18,560	134,200	1.3	0.01	91,800	117,110	15.5	24.5				
R T	18,200	131,950	1.0									
R T	19,080	138,330	1.3									
800	14,610	105,920	1.6	0.01	72,100	96,600	7.4	9.7				
800	14,600	106,290	.9									
800	15,080	109,330	1.3									
1000	13,120	95,120	.9	0.01	70,800	91,200	8.5	10.6				
1000	13,720	99,720	1.1						65,200	785.6	1.04	0.0013
1000	13,660	99,040	1.0						63,800	816.6	0.86	0.0011
1000									62,000	1107.0	1.26	0.0011
1000									60,000	1570.0	1.00	0.0006
1000									56,000	2101.3	0.97	0.0005
1000									52,000	3355.8		
1200	10,950	79,390	1.7	0.01	55,600	64,100	3.6	22.3	56,000	2.7	5.2	1.9259
1200	11,260	81,640	1.3						49,000	10.6	5.1	0.5809
1200	10,720	77,720	2.3						44,000	28.1	6.5	0.2313
1200									35,000	270.1	6.3	0.0233
1200									30,000	739.6	2.4	0.0032
1200									39,000	114.9	6.4	0.0557
1200									28,000	1543.0	4.3	0.0028
1200									27,000	1010.0	5.7	0.0030
1200									25,000	3393.0		
1400	8,150	59,090	4.1	0.01	34,600	39,000	1.6	38.8	32,000	2.1	14.1	6.714
1400	8,230	59,670	2.4						28,000	6.0	7.2	1.200
1400	8,050	58,360	3.9						24,000	17.4	8.5	0.4885
1400									20,000	23.0	12.9	0.5609
1400									21,000	37.3	5.0	0.1340
1400									19,500	62.2		
1400									18,000	70.0	4.6	0.0657
1400									15,000	169.0	9.6	0.0568
1400									14,600	286.1		
1400									12,000	473.6	8.7	0.0184
1600	6,100	44,230	5.7	0.01	18,800	21,100	1.4	41.5				
1600	5,750	41,690	7.0									
1600	5,660	41,040	5.5									

TABLE VIII-10
SELECTED MECHANICAL PROPERTIES PNL TUBE LOT N-1 MFG'S LOT 83628
AND 83629, 20% CW 316 SS
0.230 in. OD X 0.200 in. ID

	Burst Test			Tensile Test					Stress Rupture			
Test Temp(°F)	Press (psi)	Max Hoop Stress (psi)	ΔD/D	ε min^{-1}	0.2% YS	UTS	U.E.(%)	T.E.(%)	Max Hoop Stress (psi)	Rupture Time(hr)	ΔD/D%	ε ΔD/D % hr^{-1}
RT	18,560	134,560	.8	0.01	90,990	119,210	14.2	21.1				
RT	18.220	132,090	.7									
RT	18,640	135,140	.9									
800	14,980	108,600	.8	0.01	75,540	98,850	7.5	9.1				
800	14,460	104,840	.7									
800	15,230	110,780	1.1									
1000	13,770	99,830	.6	0.01	70,860	91,810	9.5	11.9	65,200	744.3	1.34	0.0018
1000	13,580	98,460	1.0						63,800	904.5	1.26	0.0014
1000	13,850	100,410	1.2						63,000	1107.0	1.21	0.0010
1000									60,000	1458.8	1.50	0.0010
1000									56,000	2051.1	1.10	0.0005
1000									52,000	4017.1		
1200	11,400	82,650	1.6	0.01	54,060	64,090	3.2	19.7	61,630	1.2	1.8	0.6667
1200	10,700	77,580	1.1						49,000	9.5	6.3	0.6631
1200	10,920	79,170	1.6						43,500	32.8	5.7	0.1737
1200									36,250	193.6	6.6	0.0340
1200									33,000	404.3	3.5	0.0087
1200									29,000	1042.3	5.4	0.0051
1200									28,000	1697.0	5.6	0.0033
1200									27,000	2503.0	3.5	0.0014
1200									23,000	3975.1		
1400	8,460	61,340	2.5	0.01	83,170	37,460	1.5	29.0	36,000	0.7	8.9	12.71
1400	8,420	61,050	3.6						32,000	1.9	9.5	5.00
1400	8,260	59,890	2.7						28,000	5.1	10.0	1.961
1400									24,000	14.0	10.6	0.7571
1400									21,000	37.3	9.8	0.2627
1400									20,500	54.6		
1400									19,000	62.2		
1400									18,000	70.0	7.2	0.1029
1400									15,000	142.0	9.1	0.0641
1400									12,000	357.6	9.6	0.0268
1600	5,560	40,310	8.1	0.01	6,370	19,440	2.0	39.7				
1600	5,760	41,760	6.6									
1600	6,000	43,500	4.2									

TABLE VIII-11
SELECTED MECHANICAL PROPERTIES PNL TUBE LOT N-2, MFG's LOT 83626, 83627 and 83531 20% CW 316 SS
0.230-in. OD X 0.200-in. ID

	Burst Test			Tensile Test					Stress Rupture			
Test Temp(°F)	Press (psi)	Max Hoop Stress (psi)	ΔD/D	ϵ min^{-1}	0.2% YS	UTS	U.E.(%)	T.E.(%)	Max Hoop Stress (psi)	Rupture Time(hr)	ΔD/D%	ϵ ΔD/D % hr^{-1}
RT	11,000	80,740	-	0.01	44,400	94,780	57.2	73.0				
RT	10,650	78,170	-	1.0	48,360	89,830	45.2	57.2				
RT	10,900	80,010	-	10.0	51,300	94,010	40.6	55.8				
800				0.01	26,130	78,450	38.1	41.4				
800				1.0	29,490	72,160	33.1	36.7				
800				10.0	27,120	69,036	31.8	39.7				
1000	7,770	57,030	-	0.01	23,870	75,370	35.9	39.6	56,000	272.1	11.2	0.0411
1000	8,260	60,630	-	1.0	23,160	66,440	30.0	32.9	57,000	358.8	14.0	0.0390
1000	8,280	61,510	-	10.0	24,740	65,650	32.0	36.5	55,000	444.7	41.9	0.0267
1000									52,500	670.0	9.8	0.0146
1000									51,000	1018.8	9.4	0.0092
1200	7,120	52,260	-	0.01	21,270	51,550	22.7	39.4	34,720	10.5	10.8	1.0285
1200	6,940	50,940	-	1.0	23,280	59,320	29.3	35.3	31,430	33.5	13.6	0.4059
1200	7,140	52,410	-	10.0	21,020	59,890	24.0	33.4	30,170	60.5	13.7	0.2264
1200									20,440	222.9	12.8	0.0574
1200									23,860	665.1	9.3	0.0139
1200									21,730	1581.9	13.6	0.0085
1200									20,410	1762.0	11.3	0.0064
1200									19,000	5016.0	17.1	0.0014
1200									17,000	8206.0	6.8	0.0008
1400	5,440	39,030	-	0.01	17,630	28,870	12.9	58.2				
1400	5,340	39,200	-	1.0	20,110	41,240	21.2	47.0				
1400	5,450	40,000	-	10.0	18,870	48,530	26.0	39.1				
1600	3,880	28,480	-	0.01	10,310	14,430	7.7	46.5				
1600	3,820	28,040	-	1.0	19,600	28,580	15.8	64.2				
1600	3,950	28,990	-	10.0	16,380	34,070	19.5	61.1				
1800	2,680	18,940	-									
1800	2,630	19,300	-									
1800	2,640	19,380	-									

TABLE VIII-12
SELECTED MECHANICAL PROPERTIES 83638, 83639, 83640, 8077201, and 8077206 20% CW 316 SS
0.230-in. OD X 0.200-in. ID

	Burst Test			Tensile Test					Stress Rupture			
Test Temp (°F)	Press. (psi)	Max Hoop Stress (psi)	ΔD/D	ε min^{-1}	.2% YS	UTS	U.E.(%)	T.E.(%)	Max Hoop Stress (psi)	Rupture Time (hr)	ΔD/D%	$\Delta D/D^{e}\%\ hr^{-1}$
R T	19,830	143,800	1.3	0.01	95,100	118,100	18.1	23.0				
R T	19,000	137,800	0.9									
R T	19,380	140,500	1.3									
800	15,100	109,500	0.9	0.01	74,900	96,500	11.5	13.3				
800	14,280	103,500	0.4									
800	14,940	108,300	0.9									
1000	13,440	97,400	0.9	0.01	70,900	91,600	8.5	11.2	65,250	821.0	1.3	0.0016
1000	13,840	100,300	0.9						63,000	1091.0	1.2	0.0011
1000	13,290	96,400	0.9						62,000	1013.6	1.1	0.0011
1000									56,000	2296.5		
1200				0.01	55,600	69,100	3.8	22.7	50,000	5.4	2.5	0.4630
1200	10,980	79,600	0.9						43,500	37.9	6.5	0.1715
1200	11,340	82,200	1.3						36,500	141.4	4.7	0.0332
1200	10,960	79,500	1.3						33,000	358.1	2.8	0.0078
1200									29,000	989.3	3.1	0.0031
1200									28,000	1668.3		
1200									27,000	2729.0		
1200									25,000	4096.8		
1400	8,600	62,400	1.7	0.01	28,600	34,800	2.2	44.9	32,000	1.8	8.9	5.444
1400	8,660	62,800	2.2						28,000	6.1	7.1	1.164
1400	8,670	62,900	1.7						24,000	17.2	11.5	0.6686
1400									21,000	33.3	7.9	0.2372
1400									18,000	111.3	11.9	0.1069
1400									15,000	156.2	12.1	0.0775
1400									12,000	331.7	6.8	0.0205
1400									7,000	1121.3		
1600	5,780	41,900	6.1	0.01	16,400	19,600	2.0	41.5				
1600	6,060	43,900	3.9									
1600	5,720	41,500	3.9									

TABLE VIII-13
SELECTED MECHANICAL PROPERTIES PNL TUBE LOT K, MFG's LOT 83632 and 83633 MILL-ANNEALED 316 SS
0.230-in. OD X 0.200-in. ID

Test Temp(°F)	Burst Test			Tensile Test					Stress Rupture			
	Press.	Max Hoop Stress	ΔD/D	min^{-1}	.2% YS	UTS	U.E.%	T.E.%	Max Hoop Stress	Rupture Time (hr)	ΔD/D	ΔD/D $\%hr^{-1}$
R T	9,860	71,500	16.0	0.01	37,500	87,100	62.2	81.2				
R T	9,660	70,000	16.0									
R T	10,440	75,700	17.0									
800	7,700	55,800	13.0	0.01	23,400	72,700	40.6	43.7				
800	7,780	56,400	15.0									
800	7,620	55,200	13.0									
1000	7,210	52,300	12.0	0.01	20,400	68,600	40.1	42.8	52,000	373.0	15.8	0.0424
1000	7,300	52,900	13.0						51,000	350.5	13.4	0.0382
1000	7,400	53,700	12.0						48,000	552.0	10.4	0.0188
1000									46,000	1381.0	13.0	0.0094
1200	6,540	47,400	13.0	0.01	19,000	47,000	26.4	56.4	35,000	5.5	21.3	3.8727
1200	6,560	47,600	11.0						32,000	12.0	19.3	1.6083
1200	6,600	47,900	13.0						32,000	15.8	19.1	1.2089
1200									29,000	33.5	16.3	0.4866
1200									29,000	36.0	13.0	0.3611
1200									26,000	82.7	17.6	0.2128
1200									25,000	169.7	20.1	0.1184
1200									21,000	555.4	15.8	0.0284
1200									20,000	947.2		
1200									19,000	1184.7		
1400	5,260	38,100	17.0	0.01	16,600	25,900	14.5	86.3	23,000	1.1	24.9	22.63
1400	5,200	37,700	13.0						20,000	3.6	19.1	5.306
1400	5,320	38,600	17.0						17,000	17.6	16.9	0.9441
1400									14,000	34.0	18.6	0.5471
1400									13,000	142.6		
1400									10,000	628.3		
1600	4,160	30,200	11.0	0.01	11,100	14,200	10.5	83.1				
1600	4,140	30,000	21.0									
1600	4,100	29,700	21.0									

TABLE VIII-14
SELECTED MECHANICAL PROPERTIES PNL TUBE LOT L, MFG'S LOT 83694
5% CW 316 SS 0.230-in. OD X -.200-in. ID

	Burst Test			Tensile Test					Stress Rupture			
Test Temp(°F)	Press. (psi)	Max Hoop Stress (psi)	ΔD/D	ε min^{-1}	0.2% YS	UTS	U.E.(%)	T.E.(%)	Max Hoop Stress (psi)	Rupture Time (hr)	ΔD/D%	$\Delta D/D^{\varepsilon}\%\ hr^{-1}$
RT	10,680	77,430	9.1	0.01	55,900	89,800	62.8	70.3				
RT	10,760	78,010	10.0									
RT	10,800	78,300	10.9									
800	8,400	60,900	9.1	0.01	43,000	74,600	33.7	37.7				
800	8,340	60,470	8.7									
800	8,240	59,740	8.7									
1000	7,840	56,840	7.8	0.01	38,600	70,600	33.0	38.1	57,000	25.6		
1000	7,700	55,830	7.0						56,000	274.8	13.5	0.0491
1000	7,700	55,830	7.8						54,000	363.9	7.2	0.0198
1000									50,000	551.5		
1000									49,000	582.0	13.5	0.0232
1200				0.01	32,800	48,900	20.5	53.7	43,000	0.7		
1200	6,980	50,600	7.0						39,500	2.0	26.1	10.04
1200	6,990	50,680	8.7						35,500	10.0	20.2	2.020
1200	7,050	51,110	8.3						34,000	16.8	20.8	1.238
1200									30,000	70.1	19.2	0.2739
1200									28,000	142.6	21.8	0.1535
1200									26,500	193.0	22.9	0.1187
1200									24,000	384.8	20.0	0.0520
1200									22,000	1158.1	22.6	0.0195
1200									20,000	1818.6		
1400	5,420	39,300	14.3	0.01	24,000	27,300	9.2	82.5	25,000	1.1	19.3	17.55
1400	5,420	39,300	13.0						22,000	2.6	10.4	4.000
1400	5,440	39,440	14.3						19,000	8.9	27.5	3.090
1400									16,000	31.1	20.0	0.6431
1400									13,500	139.9	13.0	0.0929
1400									10,000	1402.3	6.2	0.0044
1600	4,360	31,610	16.1	0.01	14,800	16,200	2.1	78.8				
1600	4,180	30,310	18.3									
1600	4,180	30,310	6.5									

TABLE VIII-15
SELECTED MECHANICAL PROPERTIES PNL TUBE LOT M, MFG'S LOT 83695
10% CW 316 SS 0.230-in. OD X 0.200-in. ID

	Burst Test			Tensile Test					Stress Rupture			
Test Temp(°F)	Press (psi)	Max Hoop Stress (psi)	ΔD/D	ε min^{-1}	0.2% YS	UTS	U.E.(%)	T.E.(%)	Max Hoop Stress (psi)	Rupture Time (hr)	ΔD/D%	$\Delta D/D^{\varepsilon}\%$ hr^{-1}
RT	13,900	100,770	1.7	0.01	74,000	96,000	41.7	51.5				
RT	13,050	94,610	2.2									
RT	13,290	96,350	1.7									
800	10,400	75,400	2.2	0.01	58,700	79,700	2.3	2.6				
800	10,320	74,820	1.3									
800	10,300	74,680	1.7									
1000	9,720	70,470	1.7	0.01	58,400	75,900	2.1	2.6	65,250	354.5	2.6	0.0073
1000	9,740	70,620	1.3						63,000	420.3	2.7	0.0064
1000	9,880	71,630	2.6						61,000	521.7	1.1	0.0021
1000									59,000	746.3	1.1	0.0015
1000									55,000	1874.1	1.5	0.0008
1000									52.500	2563.2	1.7	0.0007
1200	8,000	58,000	3.0	0.01	46,200	53,800	0.7	4.0	39,000	10.0	5.2	0.5200
1200	8,060	58,440	2.6						34,000	59.2	9.0	0.1520
1200	8,060	58,440	2.2						30,000	207.4	9.2	0.0444
1200									26,000	744.3	6.3	0.0085
1200									24,000	1673.0		
1400	6,220	45,100	5.2	0.01	29,800	31,900	1.5	68.0	29,000	1.0	16.5	16.50
1400	6,320	45,820	7.4						26,000	3.2	9.0	2.813
1400	6,200	44,950	6.1						23,000	6.2	16.9	2.729
1400									20,000	40.6	9.3	0.2291
1400									17,000	155.3	9.1	0.0586
1400									14,000	415.5	6.8	0.0164
1400									10,000	1755.0		
1600	4,720	34,220	4.3	0.01	16,600	18,800	1.3	59.3				
1600	4,680	33,930	8.7									
1600	4,780	34,660	7.8									

Then a predicted reduction in rupture life for each defect size can be made. However, all tests with a rupture time less than 400 hours have failed away from the defect. These initial results would indicate that 20% cold-worked 316 SS tubing is not notch sensitive.

J. H. Shively recently reported (Ref 4) tube shortening on wire-wrapped biaxial stress-rupture specimens. The results of measurements on two K Lot specimens show tube shortening of approximately the same proportion, 0.1%. Additional tests are planned on K Lot and N Lot specimens.

6. LMFBR Fuel And Cladding Information Center

F. R. Shober and B. R. Hayward

The LMFBR Fuel and Cladding Information Center, a computerized data storage, retrieval, and analysis system, is operated by WADCO for the USAEC. The system contains data and information on LMFBR fuel pins, their materials, fabrication, irradiation, and postirradiation examination pertinent to the evaluation of their irradiation performance. The system has seven discrete sections; cladding fabrication, fuel fabrication, fuel pin fabrication, fuel subassembly fabrication, irradiation history, post-irradiation examination, and irradiation-induced property changes in nonfissile materials. The computer programs for data storage and retrieval are of fixed format type written in Fortran IV.

a. Cladding Fabrication

The cladding fabrication file is designed to list all data pertaining to the manufacture and characterization of thin-wall seamless tubing. The data for cladding used in the fabrication of experimental fuel pins and from the cladding development programs are placed on file. The files contain data for 22 lots of Types 304 and 316 SS cladding.

The files are being constantly updated with data additions and revisions. Latest additions include inventory and tensile data for PNL lots N-1, N-2, N-3, M, and L of 316 SS. Tensile data from 327 tests made over the 800 to 1600°F temperature range are now on file.

b. Fuel Fabrication

The fuel fabrication file provides for detailed data storage of LMFBR/FFTF fuels fabrication data. The data fields for this file have been listed, programming is complete for data storage, and the file is ready to receive data. A draft version of the data input forms has been sent to industry for comments. Comments have been received suggesting some minor revisions in data fields and format. Data for storage from several sources can be expected during the next quarter.

c. Fuel Pin Fabrication

Data on fuel pin fabrication, preirradiation measurements, and cross-indexing of materials fabrication are included in this file. Major revisions were made in the file. These revisions included reorganization of data fields in areas of pre-irradiation, irradiation testing, and post-irradiation examination to represent sequentially the process and test operations, analyses, and detailed characterization descriptions.

Three data systems, EBR-II, GE (PA-10 program), and the WADCO Data Acquisition System for FFTF fuel fabrication, are major sources of data for the Fuel and Cladding Information Center. Contacts have been made with each of the three organizations to discuss the Center's capabilities and needs and how to develop interfaces between the center and the three systems. The EBR-II presently produces a timely run report that gives the major EBR-II operating characteristics, subassembly identities, and core locations. Some software problems are anticipated in interfacing with the EBR-II system: e.g., program languages, magnetic tape densities, and data blocking.

An exchange with GE of data forms, program formats, and test examples is in progress. GE has three main areas of data collection; pre-irradiation, reactor environment, and post-irradiation results.

The WADCO Data Acquisition System (DAS) has produced a set of data input forms for fuel and fuel pin fabrication data that has been reviewed by laboratory and data center personnel. This DAS will be the collection point for the FFTF vendor fabrication data, as well as the fuel development program data.

Fuel pin component data will be stored in the fuel pin fabrication section. Computer Sciences Corporation has made important improvements in the fuel pin component data collection forms. Many of these components (clad, end caps, plenum tube, etc.) may originate from the same heat of material and have many identical fabrication operations. Instead of having individual files for each component, the file structure was reorganized to eliminate these duplications.

A total of 920 fuel pins, either irradiated or being irradiated in the EBR-II, have been listed, and data related to their positions in the reactor, subassembly numbers, the fabricators, and irradiation history stored. Fabrication and pre-irradiation data for about 200 of these pins have also been stored. A complete set of data for fuel pins in subassemblies PNL-3, 4, and 5 was retrieved to check for completeness and accuracy of data on file. A copy of the set for PNL-5 was sent to ANL in support of their EXPO-I program.

d. Fuel Subassembly Fabrication

Collection of process data from experienced vendors has started for the preparation of the subassembly fabrication file.

e. Irradiation History

Reports have been requested from EBR-II Project, ANL, to supplement the operating history data of the EBR-II currently on file at HEDL.

f. Post-irradiation Examination

This post-irradiation examination file is ready to receive data. Data collection and storage will be initiated in about six weeks.

g. Radiation-Induced Property Changes

The mechanical properties file on austenitic stainless steel was updated, bringing the total of tensile tests on file to 2703.

References:

2. Roark, R. S., Formulas For Stress and Strain, McGraw-Hill Book Co., Inc. 1943, pg. 264.

3. Garofolo, F., Fundamentals of Creep and Creep-Rupture in Metals, The Macmillan Co. 1965, pg. 210.

4. Shively, J. H., "Biaxial Creep and Stress Rupture of Wire Wrapped Cladding in 1200°F Sodium Under ΔT Conditions. Interim Report." AI-AEC-12944 April 1970.

C. CORE COMPONENT FABRICATION AND ASSEMBLY TECHNOLOGY

1. Prototypic FTR Fuel Pin Fabrication

H. T. Blair, J. E. Sammis and R. E. Bardsley

During this reporting period, 100 prototypic FTR fuel pins were fabricated. Several innovations in fuel pin fabrication were evaluated during pin assembly. The first is a reverse loading procedure, in which the top end cap is welded into the cladding tube. The plenum spacer, plenum spring, and top reflector are then loaded into the cladding prior to attaching the tubes to a glovebox for loading the insulator pellet and fuel pellet column. The tubes are protected along their exterior length by a thick-walled nylon sleeve during all the remaining process steps up to nondestructive testing. The insulator pellets and fuel columns are loaded into the cladding tubes through a thick stainless steel sleeve which extends 1/4 in. into the cladding tubes. After loading, a five-in. section of the bottom reflector is placed in the cladding tube while it is still attached to the loading glovebox to provide a barrier between the fuel column and the decontamination process. Using a second innovation, decontamination time was reduced by using a modified power tool. The final closure weld is then made using a modified bottom end cap, which has a one-in. internal plug portion that comprises the remainder of the bottom reflector. (See Figure VIII-8)

Seventy-six of the completed fuel pins were nondestructively tested.

During fabrication of the top and bottom end caps for this demonstration, it was found that the concentricity requirements specified in Drawings H-3-29515, Revision 3, Part No. 4; H-3-29870; and H-3-29678, Revision 1, could not be met. The concentricity tolerances which had been specified relative to the upper end of the end caps, were changed - first, to relate to the plug end of the end cap, and second, to specify a tolerance that would make routine fabrication feasible without compromising fuel pin assembly. These end cap design changes were noted in Drawings H-3-32414; H-3-29870, Revision 2; and H-3-29678, Revision 3. A second change

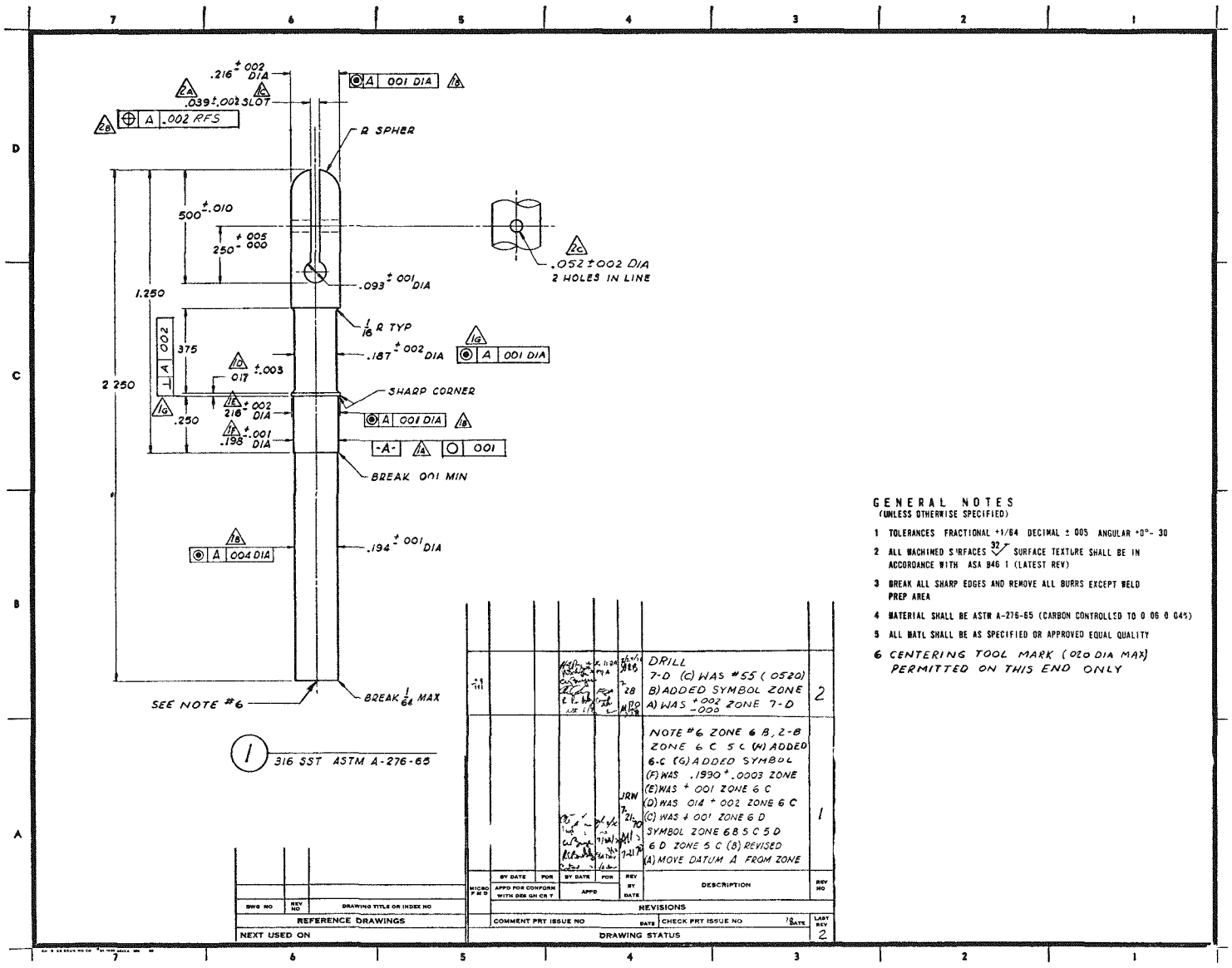

FIGURE VIII-8 *Prototypic FTR Fuel Pin Bottom End Cap Detail for Reverse Loading Demonstration.*

sheet to the FFTF Engineering Test Plan for Fabrication of FTR Prototypic Fuel Pins, A-0166, was written to include these new end cap drawings.

The second change sheet also included a change in the requirements for the welds attaching the plenum plug to the plenum spacer tube. The original design called for two tack welds 180 deg. apart on the joint between the plenum plug and plenum tube. The change requires the welds to be located 0.05 ± 0.07 in. from the end of the tube where it butts to the plenum plug.

The requirement for analyses for samarium, europium, gadolinium, dysprosium, sulfur, and tungsten on the source oxides and finished fuel and insulator pellets was removed from the ETP because the capability to perform such analyses had not been developed at the start of fabrication. Requirements for weld fusion zone intergranular attack and for intergranular corrosion and corrosion rate were also removed from the ETP for the same reason.

2. Assembly of Test Pins for Irradiation in EBR-II

S. W. Binegar and J. W. Thornton

Eighty-two fuel pins for PNL-10 were completed. Sixty-one of these pins were shipped to EBR-II on July 7. Of the remaining 21 pins, 17 are spares and the other 5 are archive specimens. A total of 90 pins was originally fabricated to yield the 77 test and spare pins and 5 archive samples (defective pins). Of the 90 fuel pins fabricated, seven were rejected due to weld concavity and porosity (4% of 180 welds), four for pits in the cladding, and two for damage during handling.

3. Non-Uniform Behavior of Fuel Pin End Cap Stock

R. R. Studer, D. W. Dragnich, R. J. Lobsinger and J. C. Tverberg

Investigation was continued to determine the reasons for the non-uniform welding behavior of one lot of vacuum-melted 316 SS procured for use as fuel pin end cap stock. The only data obtained to date showing differences in this lot as compared to a normal lot is in grain size and distribution (Figure VIII-9a and b). Material showing low weld penetration

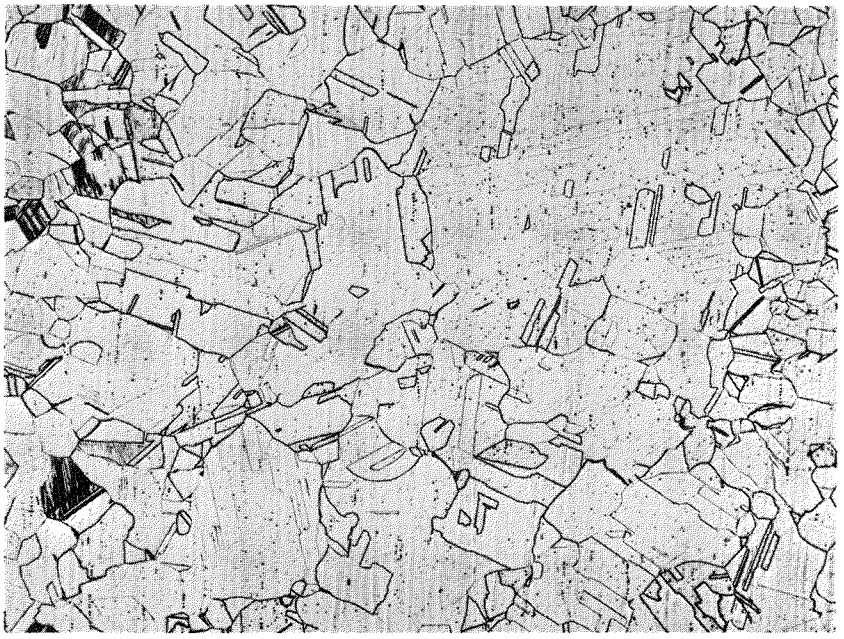

470-1605A 100X
Grain Structure in Center of Low Weld-Penetration Material

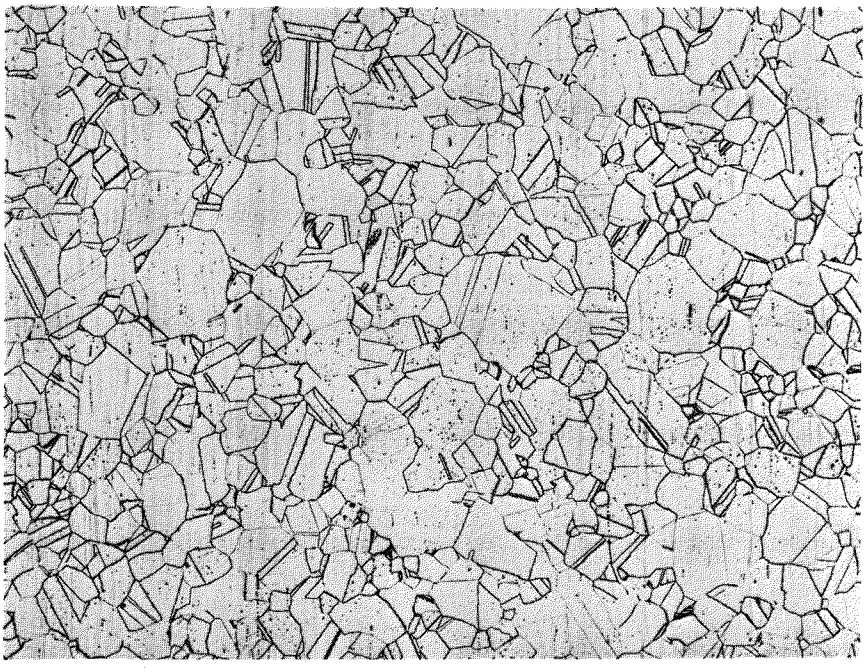

470-1605C 100X
Grain Structure Near Surface of Low Weld-Penetration Material

FIGURE VIII- 9a *Grain Size Variations in 316 SS Bar.*

contained a duplex grain structure with an ASTM size of 4 to 5 in the and 1 to 2 near the surface. Material showing high weld penetration contained a relatively uniform grain structure of ASTM size 6-7. No satisfactory reason has been found to explain how these grain size differences would affect welding behavior.

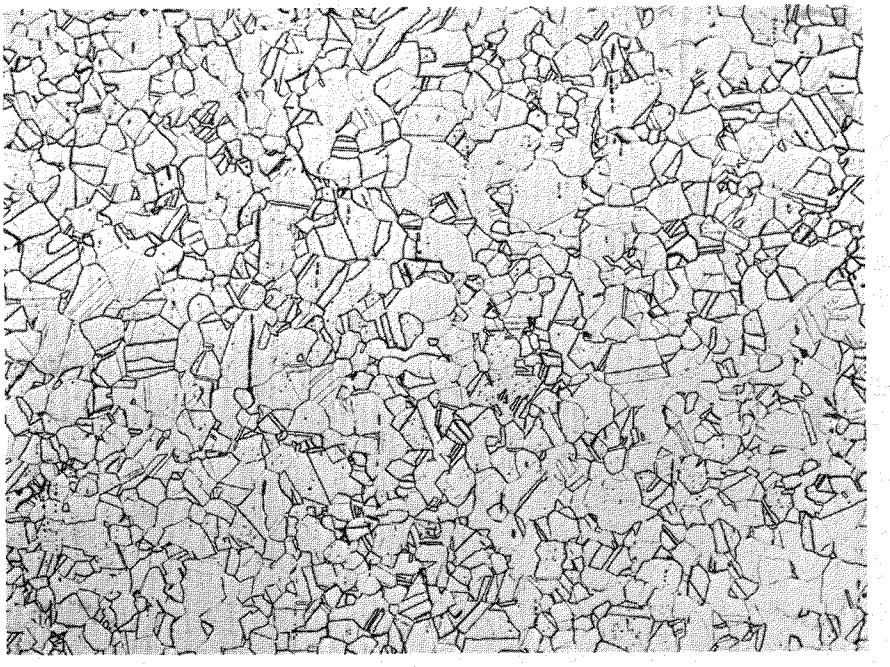

470-1610C 100X

FIGURE VIII-9b *Grain Size Variations in 316 SS Bar Showing Grain Structure Typical of High Weld-Penetration Material.*

4. End Closure Weld Parameter and Tolerance Study

J. P. Keenan and R. M. Crawford

A factorial experiment for fuel pin end closure welding, designed to determine the effect of end cap machining tolerances, welding parameter variations, and their interactions on the closure weld, was completed. Two replications of each combination of levels resulted in 64 welds. These welds were visually and dimensionally inspected, radiographed, and metal-

lographically examined for weld penetration, throat thickness, and cracking. The following is a summary of the data evaluated to date from this study.

1) Results to date indicate the present welding system is not oversensitive to weld parameter variations or machining tolerances.

2) As-welded maximum diameter was 0.2302 in. - 0.2317 in.

3) Radiography: Three of the 64 weld samples were rejected by radiography for weld concavity or insufficient throat thickness. These welds were all made at the conditions that provide the minimum filler material and the maximum heat input. These three welds represent 38% of the welds made under these conditions.

4) Metallographic Examination: The 64 sample welds were examined metallographically in two positions. The minimum weld throat thickness measurements on the 128 sections examined ranged from 0.01366 in. to 0.01733 in. Two of the sections were rejects, and were 0.0034-in. below the minimum acceptable throat thickness.

5. Biaxial Stress-Rupture of Closure Welds

R. W. Crawford and J. P. Keenan

Biaxial stress rupture testing of the bottom end closure weld in conjunction with the cladding characterization program is continuing. To date, results have been received on 52 samples. Of the samples reported, two failed in the weld. The weld failures in both cases occurred very close to the time predicted for cladding failure at that temperature and stress level.

6. Ferrite Weld Studies

R. R. Studer, D. W. Dragnich, R. J. Lobsinger and J. V. Tverberg

Metallographic examination was completed on six of 45 different alloy variations of type 316 SS, produced by Carpenter Technology Corporation for the Metallurgical Variables Capsule Program. The composition of each of these alloys is given in Table VIII-16. The amount of ferrite in each weld is determined by a) metallographic examination, b) Severn ferrite indicator and c) calculations from the Schaeffler diagram. First results from the Severn ferrite indicator are presented in Table VIII-17.

TABLE VIII-16

FERRITE WELD STUDY SAMPLES

Alloy Number	Heat Number	C	Mn	Si	P	S	CR	Ni	Mo	Cu	Co	B	N
1	V00470	0.003	0.92	0.40	0.009	0.008	16.95	12.01	2.35	0.10	0.11	0.0011	0.007
2	V00471	0.046	0.96	0.37	0.010	0.007	16.91	12.15	2.35	0.10	0.12	0.0011	0.119
3	V00472	0.047	0.94	0.39	0.010	0.007	16.99	12.05	2.33	0.10	0.12	0.0008	0.050
4	V00473	0.127	0.96	0.38	0.012	0.008	17.06	12.08	2.32	0.10	0.11	0.0010	0.006
5	V00474	0.128	0.97	0.43	0.011	0.008	17.00	12.10	2.34	0.10	0.11	0.0008	0.111
6	V00460	0.048	0.92	0.35	0.001	0.004	16.89	11.99	2.36	0.12	0.12	0.0005	0.054
7	V00461	0.046	0.96	0.37	0.003	0.007	17.06	12.13	2.35	0.10	0.11	0.0005	0.052
8	V00462	0.046	0.97	0.38	0.003	0.018	17.14	12.14	2.32	0.11	0.11	<0.0005	0.054
9	V00463	0.045	0.96	0.37	0.004	0.036	17.09	12.17	2.32	0.11	0.11	<0.0005	0.055
10	V00464	0.047	0.93	0.37	0.011	0.004	17.09	12.04	2.35	0.11	0.11	0.0005	0.052
11	V00465	0.045	0.95	0.39	0.021	0.005	16.95	12.03	2.31	0.11	0.12	<0.0005	0.054
12	V00466	0.046	0.93	0.36	0.039	0.004	17.01	12.12	2.33	0.11	0.11	<0.0005	0.057
13	V00467	0.051	0.98	0.40	0.003	0.004	16.95	12.09	2.34	0.11	0.11	0.0012	0.057
14	V00468	0.046	0.98	0.39	0.003	0.004	17.09	12.10	2.31	0.11	0.11	0.0030	0.054
15	V00469	0.047	0.96	0.39	0.004	0.004	17.05	12.14	2.32	0.10	0.11	0.0057	0.052
16	V00475	0.045	<0.01	0.43	0.011	0.008	16.92	12.15	2.45	0.10	0.11	0.0011	0.047
17	V00476	0.046	0.92	0.38	0.009	0.007	17.00	12.07	2.33	0.10	0.11	0.0012	0.052
18	V00477	0.047	2.04	0.38	0.010	0.008	17.17	11.91	2.21	0.10	0.11	0.0016	0.054
19	V00478	0.044	3.89	0.37	0.009	0.007	17.03	11.98	2.30	0.10	0.11	0.0012	0.056
20	V00479	0.048	0.96	0.40	0.010	0.008	16.92	12.07	2.32	<0.01	0.11	0.0010	0.049
21	V00480	0.045	0.96	0.38	0.010	0.008	16.99	12.05	2.34	0.10	0.11	0.0012	0.048
22	V00481	0.044	0.94	0.38	0.009	0.007	16.96	12.04	2.35	0.99	0.11	0.0012	0.052
23	V00482	0.044	0.95	0.39	0.010	0.008	16.96	12.27	2.35	2.94	0.11	0.0012	0.052
24	V00483	0.044	0.95	0.39	0.011	0.008	17.00	11.91	2.35	4.47	0.11	0.0013	0.055
25	V00484	0.046	0.95	<0.01	0.010	0.008	16.88	11.98	2.31	0.10	0.11	0.0011	0.052
26	V00485	0.045	0.94	0.48	0.009	0.008	17.00	12.12	2.34	0.11	0.11	0.0010	0.054
27	V00486	0.045	0.94	0.95	0.011	0.007	17.06	12.19	2.35	0.10	0.11	0.0007	0.049
28	V00487	0.044	0.93	1.47	0.010	0.008	17.07	12.30	2.38	0.10	0.11	0.0007	0.054
29	V00488	0.045	0.94	1.96	0.010	0.007	17.13	12.39	2.41	0.11	0.11	0.0010	0.050
30	V00489	0.044	0.99	0.40	0.010	0.007	16.89	12.31	<0.01	0.10	0.11	0.0011	0.049
31	V00490	0.041	0.98	0.38	0.010	0.007	16.86	12.04	0.11	0.10	0.11	0.0011	0.048
32	V00491	0.045	0.99	0.40	0.010	0.008	16.90	11.99	1.00	0.10	0.11	0.0012	0.049
33	V00492	0.047	0.92	0.38	0.011	0.008	16.96	12.09	3.03	0.10	0.11	0.0012	0.049
34	V00493	0.045	0.87	0.40	0.011	0.008	17.09	12.24	4.93	0.10	0.11	0.0010	0.051
35	V00494	0.044	0.96	0.41	0.010	0.007	16.89	12.03	2.31	0.10	0.02	0.0010	0.049
36	V00495	0.045	0.93	0.40	0.009	0.006	17.12	12.03	2.32	0.10	0.20	0.0010	0.049
37	V00496	0.046	0.91	0.41	0.009	0.009	16.97	11.89	2.29	0.10	0.50	0.0010	0.051
38	V00497	0.043	0.85	0.38	0.010	0.008	17.03	11.99	2.26	0.11	0.98	0.0010	0.050
39	V00498	0.042	0.90	0.38	0.011	0.008	17.00	12.04	2.30	0.10	4.45	0.0013	0.049
40	V00499	0.045	0.95	0.40	0.010	0.007	14.86	9.96	2.29	0.10	0.12	0.0013	0.050
41	V00500	0.046	0.96	0.38	0.009	0.007	14.89	12.01	2.35	0.10	0.11	0.0013	0.052
42	V00501	0.046	1.00	0.39	0.009	0.008	15.13	14.04	2.32	0.10	0.11	0.0008	0.048
43	V00502	0.047	0.93	0.40	0.009	0.007	16.85	12.12	2.35	0.10	0.11	0.0005	0.052
44	V00503	0.041	0.90	0.41	0.011	0.007	18.97	12.11	2.35	0.10	0.11	0.0010	0.049
45	V00515	0.012	1.12	0.41	0.010	0.007	16.98	12.12	2.31	0.10	0.11	0.0012	0.13

TABLE VIII-17
VARIATIONS IN WELD FERRITE CONTENT
AS DETERMINED BY SEVERN FERRITE INDICATOR

Alloy Number	Ferrite in Weld (%)
1	1.5 to 2.5
5	0.5
28	0.5 to 1
29	1.5 to 2.5
34	1.5 to 2.5
44	1.5 to 2.5 at edge of weld; 1.0 to 1.5 for rest of weld

D. REPROCESSING TECHNOLOGY

1. Application of Aqueous Technology to LMFBR Separations Processes (12543)

a. Solvent Performance

G. L. Richardson and J. M. Atwood

The Purex process, or a modification thereof, is currently favored for reprocessing LMFBR fuels. Because of the expected high burnups and high specific powers, solvent radiation exposures will be much higher than in present plants. The resulting degradation of the TBP extractant may impose a limitation on the separations performance of the solvent extraction system. An experimental study, using multistage miniature contactors, has been undertaken to obtain quantitative information on solvent performance in a dynamic, countercurrent system under high levels of radiation.

The test stand for this study is shown in Figure VIII-10. It will use the flow diagram shown schematically in Figure VIII-11. The desired radiation level (up to 10 watts/liter in the feed) will be supplied by a mixture of $Ce^{144}Pr^{144}$ and concentrated Purex Plant high level waste. The blended feed will be pumped continuously, together with the TBP solvent, to a single-stage extraction contactor. The holdup time of the solvent in this contactor will be adjusted to provide the desired absorbed radiation dose to the solvent(up to 2W-hr/liter). The solvent will then be separated from the high level feed via a miniature centrifuge. The solvent extract, having a composition comparable to the solvent product from a Purex (or LMFBR) 1A column, will then pass through a succession of multistage, miniature centrifugal contactors which provide the functions of 1A column scrub section for fission product removal, a 1B extraction column for plutonium removal, and a 1C column for uranium removal. The solvent finally passes through a single stage contactor, where it is treated with dilute Na_2CO_2 to remove most of the degradation products and residual solutes. If desired, the washed solvent can be recycled immediately to the irradiation contactor to determine the effect of continued

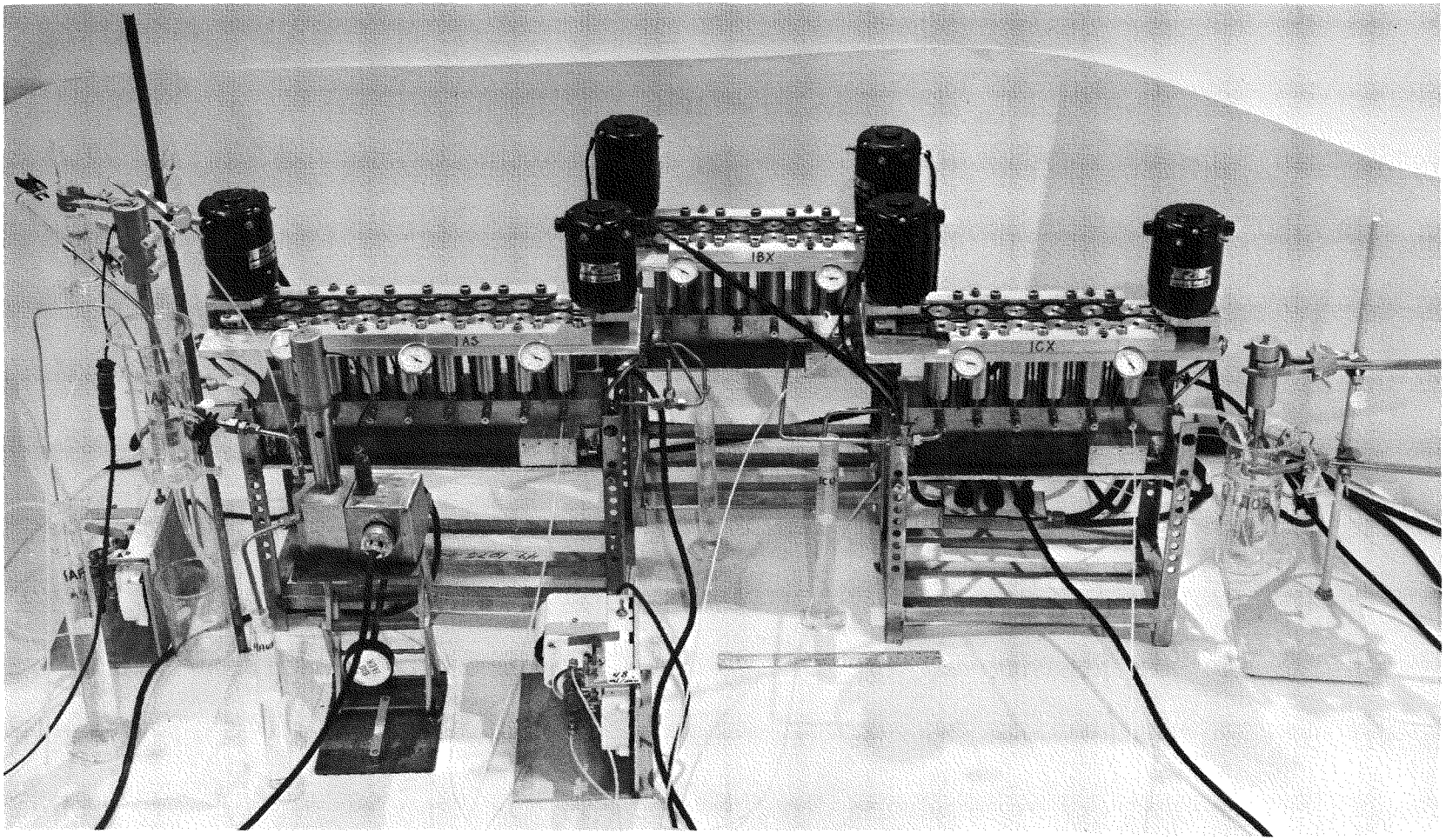

FIGURE VIII-10 *LMFBR Solvent Extraction Test Stand.*

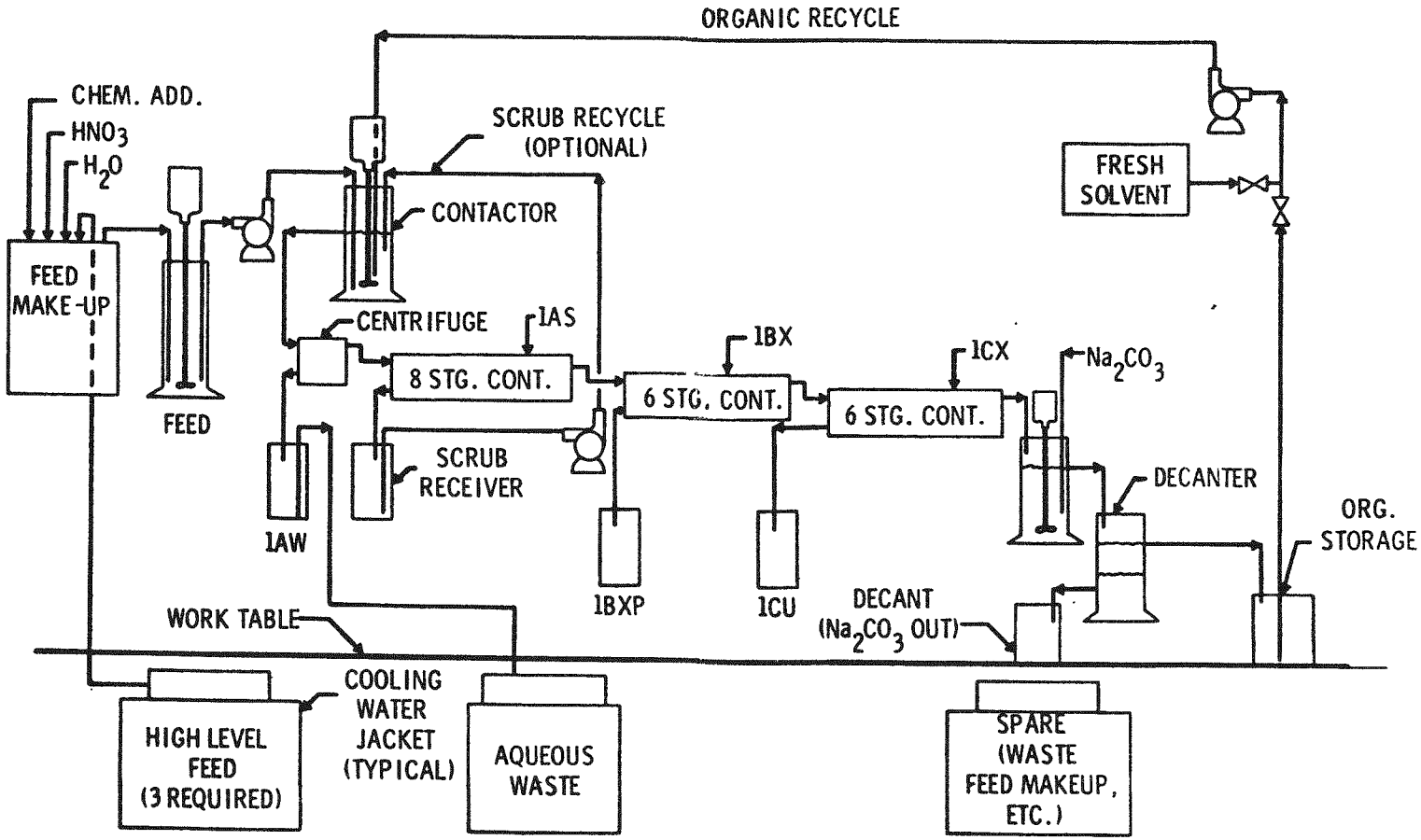

FIGURE VIII-11 *Schematic LMFBR Solvent Extraction Test Stand.*

recycle on the buildup of deleterious degradation products.

The performance will be compared with that obtained in current Purex plants processing LWR and production reactor fuels. Several test runs will be made under current Purex process flowsheet conditions to confirm the validity of this approach.

Progress to date includes completion of the experimental design, (Ref 5) hot cell modifications, and experimental equipment design and fabrication. Cold testing is essentially complete; hot cell installation and hot operation are planned early next quarter.

To assist in flowsheet calculations, the SEPHIS computer program developed at ORNL (Ref 6) for predicting transient and steady-state concentration profiles in stage-wise solvent extraction equipment has been modified to cover a wider range of TBP and solute concentrations, to correct for volume changes caused by mass transfer of macro components. The new program hasn't been fully tested, but should be applicable for developing LWR and LMFBR flowsheets for TBP concentrations from 10 to 40%, aqueous HNO_3 concentrations from 0 to 5M, and temperatures from 20 to 60°C.

b. Fuel Dissolution Characteristics

R. E. Lerch and J. M. Atwood

Nitric acid dissolution of fuel is an essential head-end step for the Purex solvent extraction process. Successful application of the Purex process to processing of LMFBR oxide fuels demands a detailed knowledge of the dissolubility and dissolution properties of such fuels in nitric acid. This information is vital to determine if simple chop-leach head-end technology will apply generally and uniformly to LMFBR oxide fuels and, if not, to provide a basis for establishing alternative head-end dissolution procedures.

To obtain quantitative information on the effect of fabrication variables on the dissolution properties of mixed oxide fuels, an experimental study has been initiated which first looks at unirradiated fuels made by the three candidate oxide fuel fabrication processes (mechanically

blending, Sol Gel, and coprecipitation). Progress to date includes completion of an experimental design (Ref 7) and completion of initial dissolubility studies using mechanically blended mixed oxide fuel.

Following preliminary laboratory investigations, a statistical, fractional factorial experiment was performed (Ref 8) to determine the effect of six fuel fabrication variables on the dissolubility of unirradiated, mechanically blended PuO_2-UO_2 fuels. In this experiment, dissolubility refers to the fraction of plutonium and uranium which dissolves when the oxide fuel is exposed to boiling 12M nitric acid for two 6-hour treatments. Of the six fabrication variables investigated, sintering temperature, source of PuO_2 and weight percent PuO_2 had major effects on dissolubility; rate of temperature rise during sintering, sintering time, and press pressure had minor effects on dissolubility.

Typical major effects:

1) As the sintering temperature was increased from 1400°C to 1700°C, the dissolubility of the fuel increased; the largest increase with temperature was noted for UO_2-25 wt% PuO_2 fuel pellets.
2) As the source of PuO_2 was changed, dissolubility increased in the order: calcined nitrate < calcined oxalate < burned metal.
3) As the weight percent PuO_2 was increased from 15 to 25 wt% PuO_2, the dissolubility decreased.

The statistical design of the experiment was a 1/3 replica of a full factorial experiment for three variables at three levels, and three variables at two levels. Such a design results in 72 treatment conditions or "cells". Two or three pellets were dissolved for each cell and the mean of the weight dependent variable in the experiment was the weight percent of the pellet variables shown in Table VIII-18. The amount of undissolved residue ranged from 0.0 to 9.1 % of the original weight.

The statistical model that was employed in the first attempt at estimating the effect of each independent variable was a full quadratic model, that is, a model that considered all possible two-factor interactions (e.g., X_1^2, X_1X_2, X_1X_3, etc.) of all six variables. After deleting the terms from the full quadratic model which were not significant, the

TABLE VIII-18
VARIABLES FOR STATISTICAL, FRACTIONAL FACTORIAL EXPERIMENT ON DISSOLUTION OF MECHANICALLY BLENDED PuO_2-UO_2 FUEL

Variable		Statistical Designation	Levels
X_1	Source of PuO_2	-1 0 1	burned metal calcined nitrate calcined oxalate
X_2	Weight Percent of PuO_2	-1 0 1	15 20 25
X_3	Sintering Temp (°C)	-1 0 1	1,400 1,550 1,700
X_4	Sintering Time (hr)	-1 1	1 6
X_5	Rate of Temperature Rise During Sintering (°C/hr)	-1 1	100 250
X_6	Press Pressure (psi)	-1 1	25,000 50,000

following equation resulted:

$$Y = 4.862 + 0.532\,X_1 + 0.940\,X_2 - 2.244\,X_3 - 0.243\,X_4 + 0.753\,X_5 - 0.136\,X_6 - 1.873\,X_1^2 - 0.355\,X_3^2 - 0.369\,X_1X_2 + 0.147\,X_1X_5 - 0.514\,X_2X_3 - 0.354\,X_2X_4 \quad (1)$$

In equation 1, Y is the weight percent undissolved and the X's are the statistical designations of the particular variable and are defined to run from -1 to +1. By inserting the appropriate values for the various X's, this equation can be used to give the predicted or expected weight percent undissolved. A negative percent undissolved would indicate that the pellet is completely soluble. The equation can also be used to calculate response curves which show the effect of going from one level

to another within a given variable.

To measure the accuracy of the model, a "goodness of fit" was prepared to compare the observed weight percent undissolved for the 72 observations as a function of the weight percent undissolved predicted by the model. Figure VIII-12 shows the observed weight percent undissolved to be very close to that predicted. The standard deviation that expresses the scatter of these points about the line is ± 0.53. Another way to express the adequacy of the model is in terms of the amount of the total variation of weight percent undissolved explained by the model. In this experiment, the multiple correlation coefficient was 0.976. This means that the model used explained approximately 95% of the total variation (calculated by multiplying 100 times the square of the multiple correlation coefficient) which indicates that the model was very effective in accounting for the overall variation.

The residue samples remaining after dissolution were dissolved in 12M HNO_3-0.05M HF and the resulting solutions were analyzed for uranium and plutonium. Preferential dissolution of uranium was found to occur in every sample. The plutonium oxide/uranium oxide ratio in the residues ranged from 3.9 to 16.0 as compared to starting ratios of 0.18, 0.25, and 0.33 for 15, 20, and 25 weight percent PuO_2 pellets, respectively.

2. Fast Fuels Radiation Exposure and Refabrication (12529)

R. C. Smith and J. M. Atwood

The scope of the Fast Fuels Radiation Exposure and Refabrication program encompases three general tasks. The program's major emphasis is on measuring the radiation characteristics of high exposure plutonium, developing calculational techniques for predicting the dose rates expected during the manufacture of LMFBR plutonium enriched fuels, measuring the shielding attenuation of high efficiency neutron shielding materials and developing shielding codes. The second task consists of a study of the actual radiation exposures encountered on the FFTF demonstration fuel fabrication line and correlation of the personnel exposure measurements with process conditions, fuel inventory and throughput. The third task

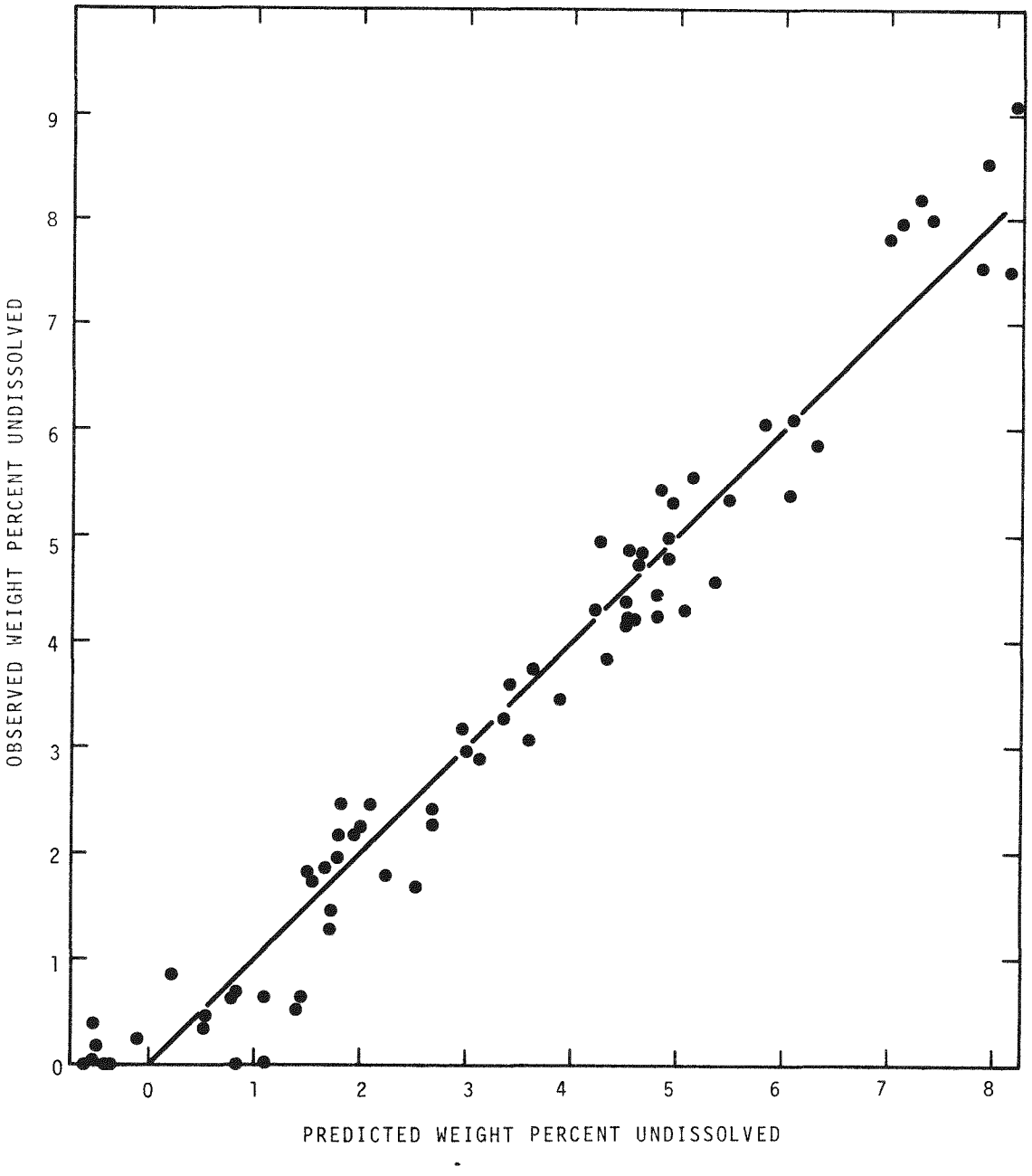

FIGURE VIII-12 *Predicted Weight Percent Undissolved vs Observed Weight Percent Undissolved.*

is to evaluate the overall fast reactor fuel fabrication process with respect to the increased radiation exposure, criticality and other special handling problems resulting from the use of high plutonium content fuels and with respect to the large fuel throughput necessary for economical fast reactor fuel manufacture.

Measurements of the gamma radiations from plutonium, plutonium dioxide and plutonium fluoride, the gamma energy spectra and the buildup of gamma radiation from the daughter products of plutonium are nearly complete. A computer code (PUSHLD) was developed and has been verified by actual measurement to accurately predict the surface dose rate, through a variety of shielding materials, as a function of plutonium isotopic composition. The effect of radiation buildup from decay isotopes is also accurately evaluated in the latest version of the PUSHLD code. A final modification of the code is currently underway; this modification will incorporate source geometry factors and will predict the dose rate, through shielding, at distances up to one meter from the source.

The neutron dose measurements and calculational techniques are more difficult to accomplish and evaluate. Acceptable accuracies are achieved in the measurement of neutron yields from plutonium dioxide. But minor amounts of impurities in metal samples are frequently found to cause variations in the neutron yields of up to 40 percent, due to (α, n) reactions with light element impurities. The accuracy of the (α, n) yield for several light elements commonly found in ceramic reactor fuels has not been verified and is currently under study. A theoretical evaluation of the (α, n) yield from O^{17} and O^{18} was recently completed and is in reasonably good correlation with measured data.

An important factor in evaluating neutron dose rate is the application of a quality factor relating the measured "rad" dose reading to the biological equivalent "rem" dose. Knowledge of the neutron energy spectra is absolutely necessary for accurate applications of such a quality factor but to date the low energy portion of the PuO_2 neutron spectra, below approximately one MeV, has not been satisfactorily resolved. A reasonably accurate definition of the plutonium spontaneous fission

energy spectra above about 0.8 MeV and the high energy portion of the PuO_2 spectra have been resolved.

Shielding attenuation measurements have shown most of the gamma radiation from plutonium to be relatively low in energy and a reduction of 10^3 in the gamma radiations can be accomplished by relatively minor shielding (e.g., 1/2 in. of lead or less). Preliminary neutron attenuation measurements indicate four or five in. of polyethylene may be required to reduce the neutron dose by a factor of 10. Further measurements are necessary to confirm what actual attenuation might be achieved on the neutron dose rate from various high exposure plutonium compounds. Most of the spontaneous fission neutrons from a plutonium metal sample are generated by the even-numbered plutonium isotopes (Pu^{238}, Pu^{240} and Pu^{242}) so the neutron yield can vary widely with isotopic composition according to the amounts of plutonium isotopes other than Pu^{238} contained in the sample. Furthermore, the (α, n) reaction-generated neutrons can essentially double the total neutron yield for a PuO_2 compound and can increase the neutron yield by a factor of 35 to 50 for a PuF_4 compound. For example, the spontaneous fission neutron yield for a plutonium metal sample, containing about 22 wt% Pu^{240} was measured to be about 249 n/g-sec. A PuO_2 sample of approximately the same Pu^{240} content measured $\sim$450 n/g-sec., and a PuF_4 sample measured 11,800 n/g-sec. Neutron yields, spectra, (α, n) evaluations and attenuation measurements are being continued.

References:

5. Richardson, G. L., "Application of Aqueous Technology to LMFBR Separations Processes. Program Plan for Task T-1: Solvent Performance," WHAN-FR-32, in publication.

6. LMFBR Fuel Cycle Studies Progress Report for Dec. 1969, No. 10, ORNL-TM-2819, January 1970.

7. Lerch, R. E., Application of Aqueous Technology to LMFBR Separations Processes. Program Plan for Task T-2: Fuel Dissolution Characteristics, WHAN-FR-33, in publication.

8. Lerch, R. E., The Effect of Fabrication Properties on the Dissolubility of Unirradiated Mechanically Blended Mixed Oxide Fast Reactor Fuel, WHAN-FR-34, in publication.

E. OTHER CORE COMPONENTS

1. B_4C Pellet Fabrication

W. A. Ross and E. T. Weber

We are presently defining the fabrication conditions for specific material characteristics needed for materials irradiation studies in EBR-II; pellets with selected properties are being provided for irradiation tests. The first tests will require approximately 400 pellets in four groups with combinations of two variables: grain size and stoichiometry.

The major efforts to date have been to develop capabilities for hot pressing pellets. Control systems are being incorporated into the hot press temperature control system and hydraulic load system to increase the reproducibility from run-to-run during production of the large number of pellets. To increase the number of pellets, the load train has been modified to provide multiple pellet pressing with a single die assembly.

Trial runs have been made with a natural B_4C powder (Norbide 325F). In the first trial, a 7-pellet die of ATJ graphite, SBGF spacers between punch and pellet, and POCO punches was used. Temperatures of about 2150°C and pressures of 4000 psi yielded pellets which ranged from 90.13 to 91.98% T.D. This was within the goal of 90 ± 2% T.D. A second die, with capacity for 20 pellets, was fabricated. The same type of graphite was used for components. This run, with the same conditions as above, resulted in 95% yield with densities from 90.28% to 91.98% T.D. The die and punch is designed to remove the load from the pellet when the desired pellet density is reached. The previously designed dies with this feature had only a single acting punch; this resulted in rather large density variations within a pellet. The present design has a double acting punch to reduce the density variation. The variation in diameter of the pellets fabricated to date has been within a range of 0.003 in., but will require centerless grinding to meet specifications.

No. of Copies	AEC Div. of Reactor Dev. and Tech.
28	Director, RDT Asst. Director for Nuclear Safety Analysis & Evaluation Br, RDT:NS Asst. Dir for Plant Engr., RDT Facilities Br, RDT:PE Components Br, RDT:PE Instrument & Control Br, RDT:PE Liquid Metal Systems Br, RDT:PE Asst. Dir for Program Anal, RDT Asst. Dir for Project Mgmt, RDT Liquid Metals Projects Br, RDT:PM FFTF Project Manager, RDT:PM (3) Asst. Dir for Reactor Engrg, RDT Control Mechanisms Br, RDT:RE Core Design Br, RDT:RE (2) Fuel Engineering Br, RDT:RE Fuel Handling Br, RDT:RE Reactor Vessels Br, RDT:RE Coolant Chemistry Br, RDT:RT Fuel Recycle Br, RDT:RT Fuels & Materials Br. RDT:RT Reactor Physics Br, RDT:RT Special Technology Br, RDT:RT Asst. Dir for Engrg. Standards: RDT LMFBR Project Manager, RDT:PM
1	AEC Div. of Reactor Licensing Director, DRL
1	AEC San Francisco Operations Office Director, Reactor Division
5	AEC Site Representatives Argonne National Laboratory - ID Argonne National Laboratory - AR Atomics International General Electric Company Westinghouse Electric Corporation
1	Atomics International Westinghouse Field Manager J. S. Theilacker
10	Bechtel Corporation Project Admin., FFTF J. J. Teachnor
2	SEFOR Facility Breeder Reactor Division P. O. Box 847 Fayetteville, Arkansas 72701 Q. L. Baird - WADCO Corp. K. L. Berrett - WADCO Corp.
16	Westinghouse Electric Corporation Advanced Reactor Division D. C. Spencer, Mgr, FFTF R. J. Cregan, Mgr, LMFBR
1	AEC Chicago Patent Group G. H. Lee

OFFSITE

No. of Copies	
271	AEC Div. of Tech. Info. Ext.
1	AEC Idaho Operations Office Nuclear Technology Division C. W. Bills, Director
1	Aerojet General Corporation S. G. Harbison
5	Argonne National Laboratory R. A. Jaross LMFBR Program Office (3) A. Travelli
1	Atomic Power Development Assoc. Document Librarian
6	Atomics International FFTF Program Office (5) FBR Project Definition Phase W. T. Morgan
2	Babcock & Wilcox Co. Atomic Energy Division S. H. Esleeck G. B. Garton
1	Combustion Engineering 1000 MWe Follow-on Study W. P. Staker, Project Manager
1	Combustion Engineering Mrs. Nell Holder, Librarian
4	General Electric Co. Advanced Products Operation Karl Cohen (3) Breeder Reactor Dev. Operation L. F. Fidrych
1	General Electric Co. Nucleonics Laboratory P. O. Box 836 Pleasanton, Calif. 94566 Dr. H. W. Alter, Mgr.
2	Gulf General Atomic Inc. General Atomic Division D. Coburn
1	Idaho Nuclear Corporation J. A. Buckham
1	Liquid Metal Engineering Center R. W. Dickinson
2	Liquid Metal Information Center A. E. Miller
2	Oak Ridge National Laboratory W. O. Harms P. Partiarca
1	United Nuclear Corporation Research and Engrg. Center Library R. F. DeAngelis

ONSITE-HANFORD

No. of Copies

1 AEC Chicago Patent Group

R. K. Sharp (Richland)

1 AEC Richland Operations Office

J. M. Shivley

3 Battelle-Northwest

Technical Library

1 Bechtel Corporation

W. A. Smith (Richland)

2 RDT Asst Dir for Pacific Northwest Programs

2 Vitro-Hanford Engineering Services

J. M. Frame

86 WADCO Corporation Staff

G. J. Alkire
H. J. Anderson
J. M. Atwood
D. L. Ballard
R. E. Bardsley
R. A. Bennett
T. K. Bierlein
C. L. Boyd
R. D. Brown
W. L. Bunch
C. A. Burgess
C. P. Cabell (2)
T. T. Claudson
L. J. Defferding
W. H. Esselman
E. A. Evans
V. F. Fitzpatrick
W. M. Gajewski
J. W. Hagan
J. P. Hale
J. E. Hanson
K. M. Harmon
L. A. Hartcorn
T. O. Harves
R. A. Harvey
E. N. Heck
R. E. Heineman
C. W. Higby
P. L. Hofmann
J. J. Holmes
K. M. Horst
D. I. Hulbert
J. N. Judy
D. C. Kaulitz
J. P. Keenan
W. C. Kinsel
R. L. Knecht
H. T. Knight
G. A. Last
F. J. Leitz
C. E. Linderoth
W. W. Little
D. E. Mahagin
W. B. McDonald
J. S. McMahon
J. W. Mitchell
R. L. Moore
C. A. Munro
J. M. Norris
D. G. Ott
H. N. Pedersen
R. E. Peterson
H. G. Powers
W. E. Roake
G. J. Rogers
V. K. Rutkauskas
F. A. Scott
D. W. Shannon
C. B. Shaw
P. F. Shaw
W. F. Sheely
F. R. Shober
A. A. Simmons
D. E. Simpson
W. G. Spear
D. D. Stepnewski
C. D. Swanson
J. W. Thornton
J. C. Tobin
K. G. Toyoda
J. C. Tverberg
R. C. Walker
E. T. Weber
J. E. Werle
J. H. Westsik
J. F. Wett
L. A. Whinery
J. B. Williams
J. F. Williams
T. W. Withers
B. Wolfe
W. R. Wykoff
J. M. Yatabe
H. H. Yoshikawa

23 WADCO Corporation Files

Document Control-3201 (15)
FFTF File (5)
Technical Publications (3)